

Geology, geochemistry and petrology of the Foss stratiform  
barite - base metal deposit and adjacent Dalradian metasediments,  
near Aberfeldy, Scotland.

Norman R. Moles

(B.Sc. Aberdeen)

Doctor of Philosophy  
University of Edinburgh

May 1985



## ABSTRACT

The Foss deposit is located ~7km NW of Aberfeldy in the central Scottish Highlands, within steeply inclined metasediments of the Easdale Subgroup (ca. 620My). The syngenetic mineralization, which occurs in a zone of 2.2km strike-length explored in detail to depths of ~300m by Dresser Minerals International Inc., consists of granoblastic barite rock ( $\geq 2$ M tonnes), Ba-feldspar-rich cherts and schists ( $> 10$ Mt) and carbonate rocks with disseminated to massive pyrite, sphalerite and galena ( $< 0.5$ Mt). These lithologies occur in seven horizons, of which two are laterally extensive ( $> 1$ km) and up to 12m thick. They are part of a 10m - 200m thick, upper division of the Ben Eagach Schist, which largely comprises Ba-, Zn- and Pb-enriched, graphitic quartz muscovite schists. This mineralized zone also contains subordinate quartzitic and dolomitic turbidites, calcareous mica schists, and volumetrically minor ( $< 5\%$ ) metabasite layers of pyroclastic and intrusive origin. Despite diagenetic and metamorphic alteration, the metabasites retain an immobile-element tholeiitic petrochemistry indicative of a subcontinental source region, although subsequent more voluminous basaltic magmatism with an 'oceanic' petrochemistry suggests incipient continental rifting.

Major, E-W isoclinal folds repeat the mineralized zone three times in the 3km<sup>2</sup> study area, and complex fold structures of 10-60m amplitude overturn and locally attenuate the strata. Continuity of the zone is also interrupted by subsequent block faulting. However, a three-dimensional reconstruction of the original form of the deposit has been achieved from a detailed evaluation of the distribution, thickness and lateral facies variations of both the stratiform mineralized lenses and the enclosing metasediments intersected in over sixty drillholes. Primary features of the mineralization are related to syndepositional faulting which controlled the locus of hydrothermal vents, the pulsatory exhalative activity, and the palaeotopography of the marine basin. Sulphide-dominated mineralization (up to 12% Zn+Pb) enclosed by thick meta-sediments indicate locally anoxic, basinal environments. Elsewhere, shallower water environments are suggested by thick (up to 20m) composite barite units, with little detrital input but evidence of sedimentary reworking between and during successive hydrothermal emanations.

Primary variations in sphalerite iron-content (range, 0-17 mol% FeS) and in <sup>32</sup>S:<sup>34</sup>S ratios ( $\delta^{34}\text{S}_{\text{Sulphides}} = +15$  to  $+28\%$ ) support



these environmental interpretations, and indicate the derivation of reduced sulphur from both seawater sulphate ( $\delta^{34}\text{S} = +35\%$ ) and hydrothermal sources.  $\delta^{34}\text{S}_{\text{barite}}$  values (+28 to +42‰) increase with bed thickness, also suggesting a mixed source. Hyalophane pseudomorphs of diagenetic sulphate (?gypsum) occur rarely in cherty mineralized sediments, and traces of ?diagenetic witherite, baryto-calcite and norsethite ( $\text{BaMg}(\text{CO}_3)_2$ ) have survived metamorphism. Newly described from the deposit are rare baoite ( $\text{Ba}(\text{Ti},\text{Fe})_2\text{SiO}_7(\text{Cl},\text{F})$ ) and crichtonite-group minerals (e.g.  $(\text{Ti},\text{V},\text{Cr},\text{Ba},\text{Fe})_{22}\text{O}_{38}$ ). More widespread are minor cymrite ( $\text{BaAl}_2\text{Si}_2\text{O}_8 \cdot \text{H}_2\text{O}$ ), Ba- and Ba-Cr-muscovites (up to 16% BaO, 9%  $\text{Cr}_2\text{O}_3$ ), Ba-biotites, talc and Cr-rutile.

Amphibolite facies metamorphism which accompanied deformation during the Grampian Orogeny (530-500My) induced localized K-Na metasomatism, recrystallization and mineralogical/isotopic equilibration on various scales ( $\mu\text{m}$  to m). Calcite-dolomite, garnet-hornblende and garnet-biotite geothermometry, plus sphalerite-pyrite-pyrrhotite and two silicate geobarometers, indicate peak T-P conditions of  $530 \pm 30^\circ\text{C}$ ,  $9 \pm 1$  kbar. Textural features and the experimental T-P location of the  $\text{cymrite}_{\text{ss}} = \text{celsian}_{\text{ss}} + \text{H}_2\text{O}$  reaction, place constraints on the uplift history which was initially near-isothermal and accompanied by partial re-equilibration. Erosion has since removed much of the deposit, but three areas with further exploration potential are identified.

## DECLARATION

The work presented in this thesis is my own except where acknowledged as otherwise. It has not been submitted for a degree at any other university, but material in chapter 8 and part of chapter 7 has been published by the author prior to submission of the thesis.

-----  
Norman R. Moles.

## Acknowledgements.

I am grateful to Drs. Steve Laux, Colin Graham and Roy Gill for initiating and supervising the project, and to the Department of Education, Northern Ireland, for a three year grant and other financial assistance. The project would not have been possible without the support of Dresser Minerals International Inc., who provided access to the deposit and gave permission to examine and sample drillcore. This phase of my work benefitted from the guidance of company staff, in particular Mark Boast, Alan Burns, Steve Laux and Alan Matthews. I appreciated the assistance of Dr. Bob Cheeney and Robin Thomson in transporting samples and equipment.

I express my thanks to the technical staff of the Grant Institute for assistance throughout my research work, especially in preparing a large number of thin sections, photographing samples and printing the B&W plates (for which I particularly thank Diana Baty). Mike Saunders planned and assisted with the wet chemical analytical work, and Dr. Pete Hill provided guidance in the operation of the electron microprobe particularly to obtain good analyses of my problematic barium-rich minerals. Dodie James helped with modifying the XRF data-reduction program, and most of the tables and figures of analytical data in chapters 3-7 could not have been prepared without Andy Walker's excellent computer programs. My thanks are also due to Drs. Max Coleman and John Rouse (formerly of B.G.S., London) who provided advice on sulphur isotope work, and I am grateful to Richard Benmore (University College, London) and Ken Greig (Edinburgh University) for analysing additional samples. I acknowledge the Natural Environment Research Council for supporting the microprobe and experimental petrology facilities at Edinburgh and the stable isotope laboratory of the British Geological Survey in London.

I wish to thank Dr. Neil Fortey (B.G.S., London) and Drs. Mike Gallagher and Graham Smith (B.G.S., Edinburgh) for their interest in my research and for assisting me to attend several conferences and field excursions. For discussions and constructive criticism of manuscripts submitted for publication, I am indebted to my supervisors and to Tim Dempster and Dave Pattison of Edinburgh University, Dr. Allan Hall, Professor Mike Russell and Robert Willan

of Strathclyde University, and Dr. David Vaughan (Aston), Dr. Giles Droop (Oxford) and Dr. Roger Powell (Leeds).

For assistance with typing, I gratefully thank the secretarial staff of the Grant Institute and especially Mrs. Marcia Wright, who efficiently word processed the bulk of the thesis (including many horrendous tables). I dedicate this tome to my fiancée, Fiona Taylor: words cannot adequately thank her for constant moral support throughout my time at Edinburgh, for patiently converting my illegible first drafts into typescript, and for her persistence in setting deadlines for me to complete the thesis. I could not have succeeded in this without John Craven, whom I thank for his light-hearted critique, advice on graphic presentation, and efforts to maintain room temperatures conducive to efficient work output. Also special thanks to Steve Laux for agreeing to read it through a second time, and to Jean for the regular supply of hot chocolate. Last, but certainly not least, I thank my parents for their encouragement and support throughout my educational career, and Richard for stimulating his younger brother's interest in rocks and minerals.

**Frontispiece:** The view east from Craig an Chanaich, with Farragon Hill (780m O.D.) on the skyline to the right, and to the left at a greater distance, Ben Eagach (689m O.D.). Just visible at upper left, beyond Ben Eagach, is Ben Vrackie (841m O.D., 15km). The ridge in the middle distance is that of Creagan Loch: I.G.S. borehole 3 intersected >6m of barite rock near the farthest visible point on the track, which runs approximately along the strike of the poorly exposed mineralized zone in Foss East. Borehole 1 intersected >15m thickness of barite rock where the track deflects sharply to the south (left centre), close to the northward-flowing Frenich Burn. This occupies a valley along the Frenich Burn Fault, which produces a sinistral displacement of ~250m in the mineralized zone between Foss East and Foss West.

On the near side of the stream amidst heather-covered peat, light-coloured outcrops of barite form a knoll (lower centre) which is the site of borehole 2. The building just visible at the base of the view is near the entrance to the adit driven by Dresser Minerals beneath Creag an Chanaich. Outcrops in the foreground are of quartzite and graphitic schist which lie stratigraphically below (to the north side of) the steeply inclined mineralized zone. Note the more abundant outcrop and grassy vegetation associated with the calcareous Ben Lawers Schist, which lies stratigraphically above the mineralized zone (upper right) and also forms the summit of Farragon Hill.



## CONTENTS

### VOLUME I:

page

#### CHAPTER 1: Introduction, regional geology, previous work and objectives of this study.

1.1	Location and exploration of the Aberfeldy deposits.	1
1.2	Regional geology and structural-stratigraphic setting.	
1.2.1	Deposition and tectonic environment	3
1.2.2	Deformation	5
1.2.3	Metamorphism	6
1.3	Summary of previous work on the mineralization.	8
1.3.1	Components of the mineralized zone	9
1.3.2	Distribution of the mineralization	10
1.3.3	Previous genetic models	11
1.3.4	Results of investigations of the Foss deposit by Dresser Minerals	12
1.4	Objectives and methods of the present study.	
1.4.1	Mineralization and basinal development	14
1.4.2	Lithogeochemistry	14
1.4.3	Mineralogy	15
1.4.4	Stable isotopes	16
1.4.5	Analytical methods	17
1.5	Thesis layout.	18

#### CHAPTER 2: Geological structure and lithostratigraphy of the Foss deposit.

2.1	Introduction.	27
2.2	Surface geology of the Foss area.	
2.2.1	Cryptic barium enrichment and subdivision of the Ben Eagach Schist	27
2.2.2	The northern limb of the Creag na h-Iolaire Anticline	30
2.2.3	The mineralized zone between Meall Tairneachan and Creagan Loch	32
2.3	Sub-surface geology of the mineralized zone: Foss West.	
2.3.1	General introduction	37
2.3.2	Foss West drillhole intersections	38
2.3.3	The Foss adit	44
2.3.4	Foss West: a lithostratigraphical synthesis	45
2.4	Sub-surface geology of the mineralized zone: Foss East.	
2.4.1	The Frenich Burn area: shallow intersections	48
2.4.2	The Frenich Burn area: deep intersections and the upper mineralized zone	50
2.4.3	Central Foss East	54

2.4.4	The Creagan Loch area	58
2.4.5	Deep intersections in central Foss East	63
2.4.6	Foss East: a lithostratigraphical synthesis	64
2.5	The depositional and structural history of the Foss deposit: a summary.	
2.5.1	Deposition of the mineralized zone	68
2.5.2	Deformational history	71

### CHAPTER 3: Petrography and geochemistry of the mineralized strata.

3.1	Introduction.	106
3.2	Petrography.	
3.2.1	Barite rock	107
3.2.2	Sulphide rocks	108
3.2.3	Mineralized carbonate rocks	110
3.2.4	Quartz celsian and cymrite rocks	112
3.2.5	Hyalophane rocks	115
3.3	Post-depositional changes in mineralogy and texture.	
3.3.1	Hyalophane pseudomorphs of probable diagenetic sulphate crystals	116
3.3.2	Formation and decomposition of barium carbonates	119
3.3.3	Post-depositional mobility of sulphur and metals	121
3.4	Geochemistry and rock type classification.	
3.4.1	Previous work: I.G.S. drillcore analyses	122
3.4.2	Rock type classification and selection of material for analysis	124
3.4.3	Mineralized basic igneous and sedimentary material	126
3.5	Proximity to exhalative centres and metal zonation.	
3.5.1	Distribution of mineralized metabasite and sulphidic carbonate rocks	129
3.5.2	Pb/Zn and Ag/Pb ratios	130
3.6	Summary.	132

### CHAPTER 4: Petrography and geochemistry of the metasediments.

4.1	Introduction.	143
4.2	Petrography.	143
4.2.1	Carn Mairg Quartzite and similar quartzites in the Ben Eagach Schist	144
4.2.2	Unit A lithologies	145
4.2.3	Unit B lithologies	147
4.2.4	Unit C lithologies	149
4.2.5	Unit D lithologies	150
4.3	Geochemistry: previous studies and sampling rationale.	
4.3.1	Previous work	151
4.3.2	This study: objectives and sample selection	152
4.4	Element associations and mineralogical components.	
4.4.1	Multivariate analysis	153
4.4.2	Alkali element associations	156



	page
4.5 Comparative lithogeochemistry.	
4.5.1 Bulk compositional characteristics of the litho-stratigraphical units.	158
4.5.2 Comparison of the Ben Eagach Schist with other Dalradian metasediments and average shales.	160
4.6 Nature of the sedimentary environment and post-depositional changes.	
4.6.1 Composition of the sedimentary material	161
4.6.2 Diagenetic and epigenetic changes in the meta-sediments	163
4.6.3 Alkaline element mobility during metamorphism	164
4.7 Metasediment geochemistry: a summary.	166
 CHAPTER 5: <u>Petrography and geochemistry of the metabasites.</u>	
5.1 Introduction.	181
5.2 Petrography.	
5.2.1 Amphibolites (type B1)	182
5.2.2 Chloritic metabasites (type B2)	182
5.2.3 Calcite biotite schists (type B3)	184
5.2.4 Dolomite muscovite schists (type B4)	184
5.3 Element mobility and the diagenetic/metamorphic alteration of metabasite compositions.	
5.3.1 Previous studies	185
5.3.2 Alkaline element enrichment in the Foss metabasites	187
5.3.3 Sodium depletion and enrichment	188
5.3.4 Silica depletion	189
5.4 Immobile element chemistry of Foss and other Middle Dalradian metabasites.	
5.4.1 The Ben Vrackie and Farragon Beds suite	190
5.4.2 Metabasites at Foss and Ben Eagach	191
5.4.3 Stratigraphical and geochemical constraints on the time and mode of magma emplacement	193
5.5 Petrogenetic affiliations and their tectonic significance.	
5.5.1 Trace element discrimination diagrams	195
5.5.2 The tectonic significance of metabasites at Foss and Ben Vrackie	197
5.6 Metabasite geochemistry: a summary.	199
 CHAPTER 6: <u>Silicate mineral chemistry.</u>	
6.1 Introduction.	220
6.2 Plagioclase, barium-potassium feldspars and cymrite.	221
6.2.1 Plagioclase	221
6.2.2 Celsian, hyalophane and orthoclase	223
6.2.3 Cymrite	225
6.3 Micas.	227
6.3.1 Muscovite and barian muscovite	227

	page
6.3.2 Chromium and vanadium muscovites	230
6.3.3 Biotite, phlogopite and barium biotite	232
6.3.4 Compositional variations in coexisting micas	236
6.4 Other ferromagnesian silicates and minor phases.	
6.4.1 Chlorite	237
6.4.2 Talc	237
6.4.3 Garnet	238
6.4.4 Hornblende	241
6.4.5 Epidote group minerals	242
6.4.6 Tourmaline and sphene	242
6.4.7 Baoite	243
6.5 Summary.	244
 CHAPTER 7: <u>Non-silicate mineral chemistry.</u>	
7.1 Introduction.	277
7.2 Oxides.	277
7.2.1 Magnetite	278
7.2.2 Rutile and ilmenite	278
7.2.3 Cassiterite and crichtonite group minerals	279
7.3 Sulphides.	280
7.3.1 Iron and copper sulphides	281
7.3.2 Sphalerite	283
7.3.3 Galena, tennantite and arsenopyrite	290
7.4 Sulphate (barite).	292
7.5 Carbonates.	
7.5.1 Introduction	293
7.5.2 Calcite and dolomite	293
7.5.3 Barytocalcite, norsethite and witherite	295
7.5.4 Siderite and siderite-smithsonite solid solutions	296
7.6 Phosphates.	297
7.7 Primary mineralogy, element partitioning and metamorphic equilibration.	299
 CHAPTER 8: <u>Geothermometry, geobarometry and metamorphic evolution.</u>	
8.1 Introduction.	319
8.2 Geothermometry.	
8.2.1 Garnet-hornblende	320
8.2.2 Garnet-biotite	321
8.2.3 Calcite-dolomite	322
8.3 Geobarometry.	
8.3.1 Plagioclase-biotite-garnet-muscovite	323
8.3.2 Biotite-muscovite-chlorite-quartz	324
8.3.3 Sphalerite-pyrite-pyrrhotite	325
8.3.4 Cymrite-celsian	326
8.3.5 Discussion of peak metamorphic pressure estimates	328

8.4	Metamorphic evolution in central Perthshire.	329
8.5	Conclusions.	331

## CHAPTER 9: Sulphur isotope studies.

9.1	Introduction.	339
9.2	Sulphur isotope systematics.	339
9.2.1	Sources of sulphur	340
9.2.2	Fractionation	341
9.2.3	Open and closed systems	342
9.2.4	Isotopic equilibration during metamorphism	342
9.3	Previous sulphur isotope investigations of the Aberfeldy deposits.	343
9.4	Objectives and methods of the present study.	345
9.5	Isotopic equilibration and sulphur mobility during metamorphism.	
9.5.1	Evidence for and against small-scale isotopic equilibration	348
9.5.2	Sulphur mobility during diagenetic and metamorphic reactions	355
9.6	Stratigraphical and lateral variations in $\delta^{34}\text{S}$ ratios.	
9.6.1	The Creagan Loch area	357
9.6.2	The Frenich Burn area and central Foss East	359
9.6.3	Foss West	361
9.6.4	Summary of new results from the Foss deposit	363
9.7	Sources of sulphur and the depositional environment.	
9.7.1	Barite	364
9.7.2	Sulphides	367
9.8	Summary and conclusions.	370

## CHAPTER 10: Petrogenesis of the Foss deposit and its host rocks.

10.1	Introduction.	393
10.2	The conditions and effects of metamorphism.	
10.2.1	Depositional and metamorphic history	393
10.2.2	Primary and metamorphic mineralogy	395
10.2.3	The effects of metamorphism on isotope ratios	396
10.2.4	Changes in bulk composition	397
10.3	Tectonic setting and depositional environment of the Foss deposit.	
10.3.1	Sedimentation and magmatic activity	399
10.3.2	Interaction of the hydrothermal fluids with the marine environment	402
10.3.3	Diagenetic changes in the mineralized strata	405
10.4	Comparisons with other sedimentary-exhalative deposits and models of ore genesis.	
10.4.1	Classification and characteristics	406
10.4.2	Comparative mineralogy	408

10.4.3	Composition, temperature and origin of the hydrothermal fluids	410
10.5	Other deposits in the Easdale Subgroup and potential for further exploration.	
10.5.1	Historical review	416
10.5.2	Exploration methods and targets	417
10.5.3	Suggested further sub-surface exploration at Foss	418
10.6	Summary and suggestions for further research.	418
	References.	430
	Published paper: Sphalerite composition in relation to deposition and metamorphism of the Foss stratiform Ba-Zn-Pb deposit, Aberfeldy, Scotland (Moles, 1983).	453

## VOLUME II:

### Appendices:

A	<u>Drillcore logs.</u>	460
B	<u>Location, description and summary of petrographical data for samples referred to in the text.</u>	500
C	<u>Portable XRF operation and calibration.</u>	
	C.1 Technique	513
	C.2 Precision, accuracy and calibration	513
	C.3 Data presentation	514
D	<u>X-ray fluorescence analysis of rock samples.</u>	
	D.1 Introduction and summary	517
	D.2 Sample preparation	517
	D.3 Standards	518
	D.4 Correction procedures for mass adsorption and interference effects	520
	D.5 Precision and accuracy of the XRF analyses	522
E	<u>Electron microprobe operating conditions and analytical techniques.</u>	
	E.1 General method and precision of W.D.S. analyses	530
	E.2 Analysis of barium feldspars and cymrite	531
	E.3 Interference between Ti, V, Cr and Ba	532
	E.4 Sulphur peak shift in barite	533
F	<u>Preliminary data on carbon and oxygen isotopic composition of carbonates from the Aberfeldy deposits.</u>	
	F.1 Introduction	537
	F.2 Stable isotope abundances, reservoirs and fractionation mechanisms	537
	F.3 Previous studies of the isotopic composition of carbonates in metamorphic rocks	540
	F.4 Analytical methods	542

	page
F.5 Sample description and results	543
F.6 Discussion and conclusions	545
G <u>Experimental study of cymrite<sub>ss</sub>-celsian<sub>ss</sub> equilibria at 8 kbar.</u>	
G.1 Preparation of gels for celsian and cymrite synthesis	549
G.2 Synthesis of cymrite and celsian for use in reversal runs	550
G.3 Cymrite-celsian reversal runs and assessment of the results	551
H <u>Sulphur isotope analysis: sample preparation and method.</u>	
H.1 Separation of pure sulphides and barite from polymineralic samples	555
H.2 Procedure for isotopic analysis	556

## Plates.

list in back pocket

## Tables

2.1 Class interval frequencies of barium content in relation to occurrence of garnet and sulphides in 'G-series' outcrop samples	74
2.2 Deformational history and macroscopic/microscopic characteristics.	74
3.1 Average composition of major components of the mineralized zone, from Coats et al. (1981).	134
3.2 XRF analyses of mineralized rocks.	135
4.1 Metasediment samples: mineral assemblages.	168
4.2 XRF analyses of metasedimentary rocks.	169
4.3 Partial analyses of metasediments intersected in I.G.S. boreholes, averaged by unit.	172
4.4 Average compositions of unit B samples from outcrop and from drillcore.	173
4.5 Comparative compositions of Dalradian and world average pelites.	174
4.6 Reduced carbon and volatile contents of Ben Eagach Schist samples.	175
4.7 Major element composition of clay minerals expressed on a volatile-free basis.	175
5.1 Metabasite samples: mineral assemblages and modal percentages.	201
5.2 XRF analyses of metabasite samples.	202
5.3 Analyses of metabasites intersected in I.G.S. boreholes (data from Coats et al., 1981).	204
5.4 Average compositions of Dalradian metabasites and of MORB.	205
5.5 XRF analyses of metabasites from the Ben Vrackie complex and Farragon Beds.	206

	page
6.1 Plagioclase analyses.	248
6.2 Barium-potassium feldspar analyses.	249
6.3 Cymrite analyses.	252
6.4 Muscovite analyses.	253
6.5 Ba-Cr and Ba-V-Cr muscovites.	256
6.6 Biotite, phlogopite and barian biotite analyses.	257
6.7 Altered biotites.	259
6.8 Chlorite analyses.	260
6.9 Talc analyses.	260
6.10 Garnet analyses.	261
6.11 Hornblende analyses.	262
6.12 Epidote group minerals.	262
6.13 Tourmaline and sphene analyses.	263
6.14 Baoite analyses.	263
7.1 Rutile and ilmenite analyses.	303
7.2 ?Crichtonite-group minerals.	303
7.3 Pyrite, pyrrhotite and chalcopyrite analyses.	304
7.4 Sphalerite analyses.	304
7.5 Galena, tennantite and arsenopyrite.	305
7.6 Barite analyses.	305
7.7 Calcite and dolomite analyses.	306
7.8 Barium carbonate analyses.	307
7.9 Siderite (smithsonite) analyses.	307
7.10 Mineral species identified in the Foss deposit and host rocks.	308
8.1 Previously published, peak metamorphic P-T estimates for the Aberfeldy area.	332
8.2 Formulations of geothermometers and geobarometers used.	333
8.3 Garnet, hornblende, biotite, plagioclase and muscovite compos- itions and derived P-T estimates.	334
8.4 Activity data and pressure estimates from biotite-muscovite- chlorite-quartz geobarometry.	335
9.1 Sulphur isotope data, sample locations and descriptions.	373
9.2 Sulphur isotope fractionations and derived temperatures.	376
9.3 Mass balance calculations.	377
9.4 Summary of $\delta^{34}\text{S}$ features in Foss and in other sedimentary exhalative sulphide/barite deposits.	378
10.1 Stratigraphical features and metal contents of selected sedi- mentary exhalative deposits.	422
10.2 Characteristic features of sedimentary exhalative, stratiform Pb-Zn-Ba deposits (Large, 1981) and corresponding features observed at Foss.	423

	page
D.1 Major element compositional ranges of standards and samples analysed by XRF.	524
D.2 Gravimetric and uncorrected XRF determinations of Ba contents	524
D.3 Absorption-corrected major element analyses of dilution series and synthetic Ba-Al-Si oxide gels.	525
D.4 Major element and trace element analyses of Ba-spiked metabasite sample.	525
D.5 Comparison of XRF analyses of duplicate, untreated and ignited rock samples.	526
D.6 XRF calibration data.	527
E.1 Electron microprobe standards and elements routinely determined in common phases.	534
E.2 Detection limit and precision of representative W.D.S. analyses.	535
F.1 $\delta^{13}\text{C}$ and $\delta^{18}\text{O}$ determinations in carbonates.	547
G.1 Solution batch preparation for celsian synthesis.	552
G.2 Theoretical composition of starting materials and XRF analyses of gels.	552
G.3 Microprobe analyses of synthetic celsian.	553
G.4 Cymrite-celsian hydrothermal reversal experiments.	553
H.1 Separation methods used in sample preparation for sulphur isotope analysis.	557

## Figures

1.1 Outline geology of Scotland with location of stratabound mineralization in the Middle Dalradian.	20
1.2 Topographic and drainage map of the Aberfeldy area with distribution of zinc in stream sediments.	21
1.3 General solid geology of the area south of Loch Tummel with location of the area mapped.	21
1.4 Schematic stratigraphical column of the Dalradian Supergroup, with main formations in SW and central Highlands, and tectono-sedimentary summary.	22
1.5 Block diagram of major structures in the SW and central Highlands.	23
1.6 NW-SE cross-section of the central Highlands through the Foss area.	24
1.7 Geological map of the Creag an Chanaich area, Foss West, from Coats et al. (1980).	24
1.8 Vertical sections showing lithologies intersected and Ba content, BHs 1, 2 and 11, from Coats et al. (1981).	25
1.9 Sketch of the Foss deposit area looking west from Farragon Hill.	26
2.1 Topographic map of the Foss deposit area with location of areas covered by figs. 2.2-2.4.	75

2.2	1:5000 topographic map of the Foss area with location of G-series samples.	*
2.3	VLF-EM map of same area showing areas of high and low resistivity.	*
2.4	Geological map of the same area.	*
2.5	Lithostratigraphic column of formations, units and marker horizons at Foss.	76
2.6	Barium distribution in deep overburden and geology of Foss East; Coats et al. (1981).	77
2.7	Geological map with horizontal projection of drillholes, Foss East.	78
2.8	Geological map with horizontal projection of drillholes, Foss West.	79
2.9	BHs 10, 9 and 2: T.V.D. profiles with barium content of analysed intervals.	80
2.10	Foss West: vertical projection of drillholes.	81
2.11	Geological cross-section, DHs 406 and 407, Meall Tairneachan.	82
2.12	Geological cross-section, DHs 404, 405, 417 and 429, east of Meall Tairneachan.	83
2.13	Geological cross-section, BH9 and DHs 401/2/3 and 427, Creag an Chanaich; (a) previously published, (b) alternative interpretation.	84
2.14	Geological cross-section, BH2 and DHs 415, 416, 507 and 508, east of Creag an Chanaich.	86
2.15	T.V.D. profiles of deeper intersections of the mineralized zone in Foss West.	87
2.16	Vertical projection of Foss West drillholes with thickness isopachs of (a) unit B sediments, (b) metabasites.	88
2.17	Sketches of structural features in the Foss adit and DH 102.	89
2.18	Foss East: vertical projection of drillholes with sectors described.	90
2.19	Foss East: vertical projection of drillholes with mineralized intersections.	*
2.20	Geological cross-section, DHs 101/2/5, Frenich Burn.	91
2.21	Geological cross-section, DHs 712 and 714, Frenich Burn.	91
2.22	Annotated T.V.D. profiles of mineralized intersections in DHs 104 and 105.	92
2.23	T.V.D. profiles of upper and lower mineralized zone intersections in DHs 207, 203 and 408 and BH11, Frenich Burn area.	93
2.24	Geological cross-section, BHs 1 and 11, DHs 408 and 409.	94
2.25	Geological cross-section, DHs 106, 715, 701 and 601, east of Frenich Burn.	95
2.26	Geological cross-section showing faulted isoclinal fold, DH 702.	96
2.27	Geological cross-section, DHs 703, 704 and 201, central Foss East.	97
2.28	T.V.D. profiles of mineralized zone intersections in central Foss East.	98
2.29	T.V.D. profiles of the M3 horizon intersected in Foss East drillholes.	99
2.30	T.V.D. profiles of mineralized zone intersections in the Creagan Loch area.	101
2.31	Geological cross-section, DHs 705 and 202, Creagan Loch.	102
2.32	Geological cross-section, DHs 706/7/8, 204 and 602, east of Creagan Loch.	103



	page
2.33 T.V.D. profiles of the mineralized zone in deep intersections in Foss East.	104
2.34 Simplified profiles of the mineralized zone in Foss East sectors.	105
3.1 Sketches from thin sections of tabular hyalophane structures in N81-80 and CYR 6.	136
3.2 Log $\Sigma S$ against (a) T, (b) log $fO_2$ to illustrate location of pyrite-pyrrhotite-magnetite equilibrium.	137
3.3 Activity diagram to illustrate relationships between witherite, calcite, barite, gypsum and normal seawater composition.	137
3.4 $Al_2O_3$ -BaO-SiO <sub>2</sub> diagram of I.G.S. drillcore analyses and of samples analysed in this study.	138
3.5 Frequency distribution of Ti contents in I.G.S. drillcore analyses and in samples analysed in this study.	139
3.6 Classification scheme for rock types at Foss with areas proportional to volumetric abundance in drillcore examined.	140
3.7 Graphic estimation of 'mineralized component' in a sample of mineralized basic rock, based on TiO <sub>2</sub> as a fixed component.	141
3.8 Pb/Pb+Zn ratios in drillhole intersections of M3, Foss East.	142
4.1 Pie diagrams to show proportions of samples analysed from each lithostratigraphic unit in (a) this study, (b) I.G.S. drillcore.	176
4.2 Factor analysis element groupings for metasediments and mineralized sediments analysed in this study.	177
4.3 Na <sub>2</sub> O vs. BaO in metasediment samples, subdivided by units.	178
4.4 Na <sub>2</sub> O-BaO-K <sub>2</sub> O diagram of metasediment samples, subdivided by units.	178
4.5 K <sub>2</sub> O/Al <sub>2</sub> O <sub>3</sub> vs. Na <sub>2</sub> O/Al <sub>2</sub> O <sub>3</sub> diagram of metasediment samples.	
4.6 Modified A'KF diagram of metasediments and typical muscovite, biotite and chlorite compositions.	179
4.7 Comparative major & selected trace element distributions of metasediment groups.	180
5.1 T-X <sub>CO<sub>2</sub></sub> section at P(total) = 8 kbar to illustrate relationship between metabasite mineral assemblages and key fluid-buffering reactions.	210
5.2 Histograms of major and selected trace element distributions in metabasite samples.	211
5.3 Rb vs. K <sub>2</sub> O showing correlation in metasediments and metabasites from Foss.	212
5.4 Sr vs. CaO in metasediments and metabasites from Foss	212
5.5 Metabasite bed thickness vs. K <sub>2</sub> O content of samples analysed.	213
5.6 Na <sub>2</sub> O-BaO-K <sub>2</sub> O diagram of Foss metabasites.	213
5.7 Na <sub>2</sub> O vs. CaO in metabasites from Foss, Ben Vrackie and Farragon Beds.	214

5.8	Compositional ranges (mean $\pm$ std. dev.) of Foss and Ben Vrackie metabasite suites.	215
5.9	Variation diagrams of $TiO_2$ , $P_2O_5$ , Y, V, Cr and Ni vs. differentiation index, for metabasites from Foss, Ben Vrackie and the Farragon Beds.	216
5.10	V vs. Ti in metabasites from Foss, Ben Vrackie and Farragon Beds.	217
5.11	'Spidergram' of chondrite-normalized, immobile trace and minor element distributions.	218
5.12	Zr-Ti-Y diagram of Foss and Ben Vrackie metabasite suites.	219
6.1	Histogram of An content in plagioclase, analysed in various rock types from Foss.	264
6.2	T- $X_{An}$ diagram of peristerite solvi at different pressures.	264
6.3	Na-Ba-K diagram of barium feldspars and cymrite analysed.	265
6.4	Na vs. K in barium feldspars to illustrate ranges in K/Na ratios.	265
6.5	Histograms of mol% K+Na feldspar solid solution in analysed celsian and cymrite.	266
6.6	Histogram of Ba cations in analysed di-octrahedral micas.	266
6.7	Na-Ba-K diagram of all micas analysed in samples from Foss.	267
6.8	Na+K vs. Ba cations in all mica analyses	268
6.9	K+Si vs. Ba+Al <sup>iv</sup> cations in di-octrahedral micas, showing coupled substitution.	268
6.10	Al <sup>iv</sup> vs. Ba cations in di-octrhedral micas.	268
6.11	Fe+Mg vs. Si cations illustrating phenitic substitution in di-octahedral micas.	268
6.12	Total Y-site cations excluding Al, vs. total Al cations in all micas.	269
6.13	Wt% $Cr_2O_3$ vs. BaO to show correlation in Ba-Cr muscovites.	269
6.14	Fe/Fe+Mg vs. total Al cations in all mica analyses showing similar Fe:Mg ratios in coexisting biotite and muscovite.	270
6.15	Fe/(Fe+Mg) vs. Ti cations in all micas.	271
6.16	Fe/(Fe+Mg) vs. wt% F in all micas.	271
6.17	Octahedral site cation deficiency vs. Ti cations in tri-octahedral micas.	271
6.18	Al <sup>iv</sup> vs. Ti cations showing loose correlation in tri-octahedral micas.	271
6.19	Fe/(Fe+Mg) ratios of muscovite vs. coexisting biotite in samples with both micas.	272
6.20	Al <sup>vi</sup> cations in muscovite vs. Al <sup>vi</sup> cations in biotite in samples with both micas.	272
6.21	Fe/(Fe+Mg) vs. Si cations in chlorites and altered biotites.	273
6.22	Garnet compositions in samples from Foss and Grantully area on triangular diagram of (Mn+Ca)-Mg-Fe.	274
6.23	Compositional profiles of zoned garnets in five samples from Foss.	275
6.24	Compositional maps of zoned, spiral-shaped garnet in sample N81-88.	276

7.1	Histogram of mol% FeS contents of sphalerite grains analysed in 705-20.	309
7.2	Mol% MnS vs. FeS in all sphalerite analyses.	309
7.3	Summary of textural/compositional relationships in sphalerite observed in samples from Foss.	310
7.4	T.V.D. profiles of M3 horizon in 9 Foss East drillholes showing mol% FeS contents of sphalerites analyses.	311
7.5	Silver vs. lead content of drillcore intervals and Ag contents of galena analyses.	314
7.6	Histogram of mol% SrSO <sub>4</sub> contents of barite analysed in various rock types from Foss.	315
7.7	Triangular diagrams to show compositional ranges of all Ca-Mg-Fe-Mn carbonates analysed.	316
7.8	Mol% FeCO <sub>3</sub> vs. MgCO <sub>3</sub> contents of analysed calcites from mineralized and other lithologies.	315
7.9	Triangular diagram of Ca-(Fe+Mg+Mn)-(Ba+Sr) analysed carbonates to show barium carbonate compositions.	317
7.10	MnCO <sub>3</sub> -FeCO <sub>3</sub> -ZnCO <sub>3</sub> diagram of siderite-smithsonite <sub>ss</sub> in samples from BH4.	318
7.11	Equilibration times for various sulphides involved in solid-state reactions as a function of temperature.	318
8.1	Mol% FeCO <sub>3</sub> vs. MgCO <sub>3</sub> contents of calcite coexisting with dolomite in six samples from Foss, contoured for T at P=7 and 9 kbar.	336
8.2	P-T diagram showing results from several geothermometers and barometers.	337
8.3	Histogram of mol% FeS in sphalerite equilibrated with pyrite + pyrrhotite, with pressure calibration.	338
8.4	P-T diagram with possible uplift paths for the Aberfeldy and Foss areas and location of the cymrite = celsian + H <sub>2</sub> O equilibrium.	338
9.1	Variation in sulphur isotope composition of marine sulphate with geological time.	379
9.2	Sulphur isotope equilibrium fractionations between pyrite, barite, sphalerite and galena, plotted against 1/T <sup>2</sup> ; the trisulphide geothermometer.	380
9.3	Geological map of Foss deposit with locations of samples analysed.	381
9.4	Frequency distribution of $\delta^{34}\text{S}$ ratios obtained from the Foss and Ben Eagach deposits.	383
9.5	Frequency of $\delta^{34}\text{S}$ ratios in sulphides from different lithologies at Foss.	383
9.6	Frequency distribution of temperatures indicated by sulphur isotope fractionation in samples from Foss and Ben Eagach, compared with temperatures of modern and ancient hydrothermal fluids and of metamorphism.	384
9.7	Grain size data for selected samples analysed.	384
9.8	Location of sampled material and isotopic results, sample 705-30B.	385
9.9	Location of sampled material and isotopic results, 708-6.	385

	page
9.10 Diagram to compare $\delta^{34}\text{S}$ ratios obtained from sulphide rocks, barite rocks, and sulphidic barite rocks.	386
9.11 Stratigraphic (TVD) profiles of M3 intersections with $\delta^{34}\text{S}$ ratios and Zn+Pb contents, BH3 and DHs 705, 708, Creagan Loch area.	387
9.12 Stratigraphic profile and $\delta^{34}\text{S}$ data, DH 104, Frenich Burn area.	389
9.13 Barite bed thickness vs. $\delta^{34}\text{S}$ ratios in barite samples from Foss and BH4.	390
9.14 Postulated $\delta^{34}\text{S}$ distributions of aqueous sulphate and sulphide reservoirs at Foss.	390
9.15 Stratigraphic variation in $\delta^{34}\text{S}$ ratios in (a) McArthur (Australia) and (b) Rammelsberg (W. Germany).	391
9.16 Schematic block diagram of Foss East during deposition of M3 to illustrate relationships between depositional environment and isotopic compositions.	392
10.1 Location of syndepositional faults, and geological map and stratigraphical section of the Middle Dalradian succession in western Argyll, from Anderton (1979).	424
10.2 Schematic longitudinal section of the Middle Dalradian between Jura and Glenshee during Ben Eagach Schist times, from Coats et al. (1984b).	424
10.3 Seawater convection model for the genesis of the Aberfeldy deposits with particular reference to formation of cymrite precursor, from Russell et al. (1984).	425
10.4 NW-SE sections showing inferred structural settings of the Dalradian during Easdale Subgroup and Southern Highland Group times, from Plant et al. (1984).	426
10.5 Simplified, schematic cross-section of the Foss deposit showing distribution of stratiform mineralization and postulated growth faults.	427
10.6 Cross-sections of the McArthur, Hilton, Mt. Isa and Broken Hill ore deposits, Australia, from Hutchison (1983).	428
10.7 Schematic cross-section of the Tom stratiform Pb-Zn-barite deposit, Yukon; modified from Carne (1979).	429
10.8 Distribution of mineralization in the Dalradian of the Grampian Highlands and Shetland, from Smith et al. (1984).	429
C.1 Calibration curves for portable XRF determinations of barium content in drillcore and outcrop samples.	515
C.2 Cumulative frequency diagram of portable XRF measurements for barium in G-series samples.	516
D.1 Log-log diagram of wt% BaO values obtained by XRF and gravimetric analyses.	528
D.2 Correction factors for major element XRF analyses of Ba-rich samples.	528
D.3 Empirical corrections for trace element XRF analyses of Ba-rich samples.	529

	page
D.4 Log-log diagram of Zn values obtained by XRF and AAS analyses.	529
E.1 Diagram of Ba vs. Al cations in Ba-K feldspar analyses processed using different mass absorption coefficients.	536
E.2 Diagram of Na vs. K cations in Ba-K feldspar analyses, as above.	536
F.1 Carbon and oxygen isotope data from Foss and other areas.	548
G.1 Summary P-T diagrams showing results of cymrite-celsian reversal experiments of Nitsch (1980) and of this study.	554

\* Figure located in back pocket.

## CHAPTER 1: Introduction, regional geology, previous work and objectives of this study.

### 1.1 Location and exploration of the Aberfeldy deposits.

Stratabound barium-zinc mineralization occurring in late Precambrian - early Cambrian metasediments of the Dalradian Supergroup (Argyll Group), was discovered in 1975 near Aberfeldy in the central Scottish Highlands (fig. 1.1) by the Institute of Geological Sciences (IGS; now the British Geological Survey). The Aberfeldy deposits, which "represent almost certainly the major non-energy mineral discovery in Scotland in the present century" (Coats et al., 1981) were found in a follow-up stream sediment survey and geological reconnaissance after the identification of anomalously high Ba, Zn and Pb concentrations during part of a regional drainage geochemistry survey (Coats et al., 1978, 1980). Subsequent exploration, and mineralogical and chemical studies, revealed the presence of major amounts of unusual barium minerals, principally celsian and barian muscovite, in addition to potentially economic quantities of barite and sulphides of zinc, lead and silver.

The Aberfeldy deposits occupy a zone typically 100m in thickness, developed over a combined strike-length of 5km in steeply inclined, amphibolite facies metasediments of the Ben Eagach Schist formation. This formation consists largely of graphitic muscovite schists and quartzites, and crops out along the axis of an ENE-trending hill range which forms the watershed between the glaciated valleys of Straths Tay and Tummel (60-150m above O.D.). The ridge has a broadly convex profile but rises to a number of distinct peaks including Meall Tairneachan, Farragon Hill (both 780m above O.D.) and Ben Eagach (689m) (fig. 1.2). Areas of good or sporadic exposure are separated by large tracts of peat-covered glacial overburden (frontispiece). Geophysical surveys, in particular Very Low Frequency Electromagnetic (VLF-EM) mapping, were successfully applied by the IGS to delineate the lateral extent of mineralized beds in areas of poor exposure (Coats et al., 1980 and 1981; Parker,

1980). Integrated geological, geochemical and geophysical surveys were supplemented by shallow boreholes, of which eleven were completed by the IGS in 1977-78.

West of Ben Eagach (fig. 1.2), the outcrop pattern of the Ben Eagach Schist and adjacent formations is complicated due to the effects of two major folds, the axial traces of which are sub-parallel to the strike. By virtue of these major structural features, which Sturt (1961) named the Creag na h-Iolaire Anticline and the Sron Mhor Syncline, the Ben Eagach Schist outcrop has a strike-length of 10km within an east-west distance of 3km. Most of the mineralization in this area is located on the southern, overturned limb of the Creag na h-Iolaire Anticline, between its westerly-plunging closure near Meall Tairneachan and the steep eastern flank of Creagan Loch, a distance of just over 2km (figs. 1.2, 2.2). This portion of the mineralized zone, which was referred to as the Western Sector in previous publications, lies within the Foss Estate and is the subject of the present study. Apart from two areas of low-grade mineralization on Farragon Hill, the 2.5km strike-length of the Ben Eagach Schist east of Creagan Loch appears to be barren (Coats et al., 1981). Potentially economic mineralization occurring in the Ben Eagach - Creag an Fhithich area is referred to here as the Ben Eagach deposit (the Central and Eastern Sectors of previous authors; Gallagher, 1983).

Dresser Minerals International Inc. obtained exploration and mining rights on the Foss Estate in 1979, and undertook a major programme of diamond core-drilling to evaluate the commercial potential of the area. Drillcore from over forty closely-spaced (<100m) intersections of the mineralized zone at shallow, mid-depth and deep levels (to about 350m below land surface), have been examined and sampled in this study. Field mapping was supplemented with information on temporary exposures obtained in overburden trenching by the company. Underground exploration by Dresser Minerals, initially involving 100m of drift mining beneath Creag an Chanaich (fig. 2.2), was subsequently extended for ~400m by Aberdeen Barytes Company. This was also made available for inspection and sampling.

## 1.2 Regional geology and structural-stratigraphic setting.

### 1.2.1 Deposition and tectonic environment.

The Ben Eagach Schist formation which hosts the stratabound mineralization, together with the stratigraphically underlying Carn Mairg Quartzite and the overlying Ben Lawers Schist and Farragon Beds formations (fig. 1.4), comprise the Easdale Subgroup of the Middle Dalradian Argyll Group (Harris and Pitcher, 1975). The Dalradian Supergroup consists of a 20-25km thick sequence of marine and deltaic detrital sediments, limestones, tillite, and eruptive and intrusive basaltic rocks, which accumulated in the late Proterozoic (Riphean and Vendian) and Cambrian (approximate age span, 720-530 M.y.: see Harris et al., 1978 and compilation by Willan and Coleman, 1983, fig. 2). The base of the Argyll Group is taken as the base of the Port Askaig Tillite, which is correlated with the Varangian glaciation of Scandinavia (revised Rb-Sr age determined by Pringle, 1972: 688  $\pm$  7 M.y.). The older Grampian and Appin Groups consist of relatively thin (<1km) and laterally extensive formations of micaceous sands, carbonaceous muds, and shallow-water carbonates deposited on a stable, slowly subsiding marine shelf. The diversity of sediment types and marked lateral thickness and facies changes in the Argyll Group, which are particularly evident in the SW Highlands (Anderton, 1979 and 1982; Litherland, 1980), are evidence for increasing crustal instability and basin formation in the Vendian.

The complex structure and metamorphic deformation in the central Grampian Highlands hinders the recognition of synsedimentary basins such as those identified in the SW Highlands (Anderton, op. cit.). However, the fault-controlled development of steep slopes and basins in this area may be indicated by complimentary variations in the thickness of the pebbly quartzites and carbonaceous pelites of the Carn Mairg Quartzite and Ben Eagach Schist respectively. The latter formation, which is considered to represent a deeper water facies (Harris et al., 1978), is locally absent in the Ben Vrackie area 10km NE of the Aberfeldy deposits (fig. 1.2). It is also absent immediately NE of recently discovered barium mineralization in the uppermost Ben Eagach Schist at Loch Lyon, 45km WSW of the Aberfeldy deposits (fig. 1.1) (Coats et al., 1984b). Coats et al. (op. cit.) envisage a number of 'second-order' basins



(the Easdale, Aberfeldy and Glen Shee Basins) of 20-100km strike-length, which are separated by 'palaeo-highs' of attenuated, predominantly clastic sedimentation, within the epicratonic Dalradian basin in mid-Argyll Group times. A major change in the tectono-sedimentary environment is indicated by the subsequent, widespread deposition of calcareous pelites of the Ben Lawers Schist formation (the Craignish Phyllites of the SW Highlands).

This period of crustal instability culminated in the SW Highlands with a period of voluminous basaltic volcanism (Graham, 1976a) represented by the Tayvallich Volcanics. These metabasites, and the less abundant metabasites of similar and older ages in Perthshire, have a tholeiitic chemistry characterized by strong differentiation trends resembling those of modern ocean ridge basalts, but with incompatible-element patterns which are transitional between oceanic and continental basalts (Graham, *op. cit.*, Graham and Bradbury, 1981). The petrochemistry, the style of magma emplacement (largely as sills), and the nature and extent of rock-alteration processes (spilitization) in the Middle Dalradian metabasite suite, suggest the development of 'quasi-oceanic crust' in the SW Highland area (Soper and Anderton, 1984; Graham and Borradaile, 1984), which may have been analogous to that now forming at the head of the Gulf of California (*cf.* Einsele *et al.*, 1980).

The current consensus (Phillips *et al.*, 1976; Anderton, 1982, Soper and Anderton, 1984) is that the Argyll Group and overlying Southern Highland Group sediments and volcanics were deposited in an abortive continental rift, which was peripheral to the site of contemporaneous rupturing and opening of the Iapetus Ocean to the SE. The Southern Highland Group (fig. 1.4) consists of about 2km of coarse, immature, quartzo-feldspathic sediments which were deposited as turbidite fans prograding out from a continental area to the SE, or from raised areas within the Dalradian basin (Harris *et al.*, 1978). Subsequently, in late Cambrian - early Ordovician times, a marine transgression spread over the present NW Highlands foreland to deposit orthoquartzites, carbonates and evaporitic sediments (Russell *et al.*, 1984). This transgression may have been a consequence of regional subsidence on a continent marginal to the spreading ocean, together with the increasing volume of mid-ocean ridges. Broadly similar depositional histories in the Caledonides

of NW Newfoundland, Greenland and Scandinavia are noted by Kennedy (1979), Higgins and Phillips (1979), Nicholson (1979) and Anderton (1982).

### 1.2.2 Deformation.

Following the deposition of The Southern Highland Group, the Dalradian sedimentary pile underwent complex, polyphase deformation and metamorphism in the Lower Ordovician Grampian Orogeny (ca. 520-460 M.y.), which Lambert and McKerrow (1976) attribute to northwesterly subduction of the Iapetus Ocean. Grampian structure is characterized by large, often recumbent, primary folds which diverge southeast and northwest away from a central 'root zone', giving rise to an "involute mushroom structure" in the SW and possibly central Highlands (e.g. Roberts, 1974; Roberts and Treagus, 1979; Thomas, 1979) (fig. 1.5). Although the structural pattern is still controversial in detail, it is generally agreed that recumbent folds such as the Tay Nappe and the Ardrishaig - Aberfoyle Anticline (which is equated with the Creag na h-Iolaire Anticline by Roberts and Treagus, op. cit.) are early D<sub>1</sub> structures which are refolded by upright D<sub>2</sub>-D<sub>3</sub> folds such as the Boyndie Syncline, the Cowal Antiform, and the Sron Mhor Syncline (which was formerly regarded as a primary structure: Sturt, 1961) (figs. 1.5 and 1.6).

The early movements were accompanied by the development, in pelitic rocks, of a penetrative schistosity which is generally parallel to the sedimentary bedding. In the area of the Aberfeldy deposits, the second major phase of deformation (D<sub>3</sub> in the scheme of Roberts and Treagus, op. cit.) produced a strong crenulation cleavage at a high angle to the bedding in pelitic rocks, and a westward-plunging rodding lineation in granoblastic lithologies (such as the barite rock). Subsequent deformation was of low intensity except in the vicinity of NW-trending folds (D<sub>4</sub> in local terminology) on Ben Eagach and Ben Vrackie (fig. 1.2).

A consequence of the early formation of nappe structures is that much of the currently exposed Dalradian succession is inverted, particularly in the southern part of the Grampian Highlands (the Loch Tay flat belt). Tracts of flat, domed or gently dipping strata are separated by steeply dipping zones (fig. 1.5), which are variously interpreted as roots to the nappe structures (e.g. the Loch Awe syncline and the structurally deeper Ossian steep belt:

Thomas, 1979), as deep-seated rotation zones associated with gravitational over-turning (such as the Tummel steep belt: Bradbury et al., 1979), or as loci of secondary, upright folding (e.g. the Highland Border downbend/Aberfoyle Anticline: Harris et al., 1976). Zones of thinning or complete excision of parts of the stratigraphic succession, for which Bailey (1910) introduced the term 'slides', have been widely mapped within the Dalradian terrain. However, there is considerable disagreement over the location, extent, and significance of these slides (e.g. Johnson et al., 1979), many of which emplace younger rocks over older and thus have the geometry of 'lags' rather than thrusts. Soper and Anderton (1984) have shown that the Dalradian slides may have been initiated as syn-depositional extensional faults which were only modified, and not formed, during the Grampian Orogeny.

### 1.2.3 Metamorphism.

Early studies of Dalradian metamorphism established the presence of regional variations in both metamorphic grade and facies series across the Grampian Highlands. 'Barrovian' metamorphism is characterized by an extensive chlorite zone at low grades in the south and SW, and by the occurrence of biotite, almandine, kyanite and sillimanite at successively higher grades which are encountered in the central Highlands (e.g. Atherton, 1977). 'Buchan' metamorphism in the eastern Scottish Dalradian also ranges from greenschist to upper amphibolite facies but is characterized by the occurrence of andalusite and cordierite at higher grades, and was considered to represent a lower pressure, intermediate facies series (Miyashiro, 1961; Chinner, 1973). Fettes et al. (1976) have demonstrated a gradual transition between the two facies series which they relate to variations in regional geothermal gradients rather than to the exposure of differing structural levels in the SW and NE (cf. Chinner, 1966).

Several recent studies have striven to quantify the spatial variations in climactic pressure-temperature conditions by constructing petrogenetic grids and applying experimentally calibrated geothermometers and barometers (e.g. Harte and Hudson, 1979; Wells and Richardson, 1979; Dempster, 1983; Baker, 1985; Watkins, 1985). The consensus from several authors is that in the central Highlands, temperatures of 550-600°C were reached at pressures of 8-10 kbar

(corresponding to depths of burial of ~30-35km), but there is considerable areal variation with lower pressures (6-7 kbar) south of the Tummel Steep Belt and higher temperatures further NE (up to about 800°C in the Glen Muick area: Baker, 1985). The attainment of maximum temperatures probably post-dated the D<sub>3</sub> fold phase in the Aberfeldy area as suggested by the growth of cross-cutting hornblende 'garbenschiefer' in calcareous pelites of the Ben Lawers Schist. An early high P, low T phase accompanying the major regional deformation is indicated by relict blueschist facies assemblages in the Irish Dalradian (Gray and Yardley, 1979) and possibly in the SW Highlands (Graham and Harte, 1985). These authors consider that the high pressure phase occurred in a setting of reduced heat flow, probably associated with overthrusting or above a subduction zone, whereas Richardson and Powell (1976) show that the subsequent Barrovian metamorphism can be accounted for by a normal geothermal gradient and heat flux from the underlying crust.

Syn-orogenic intrusions, notably the 'Older Granites' of NE Scotland and the gabbros, quartz diorites and granites of Connemara, are spatially associated with areas of steeper geothermal gradients and it is likely that these intrusions were an additional, local heat source (Fettes, 1979; Harte and Hudson, 1979). These intrusions, and smaller, foliated granites in central Perthshire such as Ben Vuirich and Dunfallandy Hill (fig. 1.2), carry the imprint of the later phase of ductile deformation, and their radiometric ages of 510-490 M.y. (Pankhurst and Pidgeon, 1976) therefore approximate to the age of the metamorphic climax (Bradbury et al., 1976). However, Dempster (1985) presents isotopic evidence which shows that the climax of metamorphism was diachronous across the SE and central Grampian Highlands.

The presence of a northerly-directed subduction zone beneath the Dalradian (as suggested by Phillips et al., 1976) is supported by the chemistry of the Connemara syn-orogenic basic intrusions, which are clearly affiliated with modern volcanic arcs (Yardley and Senior, 1982; Yardley et al., 1982). In the late Silurian - Lower Devonian Caledonian Orogeny (415-400 M.y. ago), which was associated with the closure of Iapetus, the cooling and uplifted Dalradian metasedimentary pile and the non-metamorphic accretionary wedge of the Southern Uplands were intruded by large, forceful and permissive

granite plutons (the 'Newer Granites'). During the same period, oblique continental collision (Phillips et al., op. cit.) may have been responsible for generating the system of sinistral strike-slip faults with downthrown SE sides, which includes the Loch Tay Fault (lateral displacement about 6km) and the Great Glen Fault (total displacement about 65km, but partly due to post-Devonian movements).

### 1.3 Summary of previous work on the mineralization.

Although shallow excavations and a small trial adit were made by early prospectors, Sturt (1961) was the first to mention mineralization in the area south of Loch Tummel. Sturt mapped an "intensely brecciated tectonic inclusion of quartzite" within the Ben Eagach Schist SW of the summit of Ben Eagach. The quartzite is described as extensively mineralized with quartz, barite, galena, pyrolusite, pyrite and chalcopryrite, and similar mineralization is noted at Craig an Chanaich and at other localities at the junction of the Ben Eagach Schist and the Ben Lawers Schist. However, Sturt considered the mineralization to be "later than the F3 movements" (i.e. D<sub>4</sub>, which formed the Ben Eagach Antiform: fig. 1.3), and apparently did not recognise the unusual mineralogy of the 'quartzites' (quartz celsian rocks) or the stratiform nature of the source to the mineralized veins.

The initial discovery and investigation of the Aberfeldy deposits by the IGS has been described above. The presence of cryptic barium enrichment in the muscovitic metasediments adjacent to the stratabound mineralization was initially recognised with a portable X-ray fluorescence analyser (Grout and Gallagher, 1980). Willan (1981a) subsequently used both portable and laboratory-based XRF methods to determine the lateral and across-strike dispersion of Ba, Zn and Pb enrichment in the Ben Eagach Schist surrounding the deposits (up to 1.3km and 250m respectively). Previous studies of sulphide mineral chemistry (Willan, 1981b and 1983), sulphur isotopes (Willan and Coleman, 1983) and lead isotopes (Swainbank et al., 1981) in the Aberfeldy deposits, are summarized following a general description of the deposits based on the work of Coats et al. (1980 and 1981), and Fortey and Beddoe-Stephens (1982).

### 1.3.1 Components of the mineralized zone.

The zone delineated by Coats et al. (1980, 1981), which includes both the stratabound mineralization and the associated, barium-enriched metasediments, is 60-110m thick and extends through a vertical distance of at least 370m within the combined strike-length of about 5km. This mineralized zone contains a variety of interbedded lithologies which form layers or impersistent lenses ranging in thickness from a few centimetres to tens of metres. On the basis of dominant mineralogy and bulk geochemistry, six principal rock types are distinguished. In order of generally decreasing volumetric abundance, these are:

(1) Graphitic quartz muscovite schists, containing varying amounts of carbonate, chlorite and sulphides, and variably enriched in Ba (up to 4 wt%), which is usually contained in barian muscovite.

(2) Quartz barian-muscovite schists which are similar to the above, but are free of graphite and consequently are pale-coloured.

(3) Quartz celsian rocks with 5-25 wt% Ba and varying in appearance from cherty and occasionally breccia-textured, to coarsely crystalline or schistose, and often containing sulphide bands.

(4) Massive, white or grey, granoblastic barite rock, which is typically fairly pure but often contains minor or trace quartz, carbonates, sulphides and magnetite.

(5) Sulphide-rich carbonate rocks; a heterogeneous group which includes rocks consisting largely of calcite or of dolomite, some with a fragmental texture, and often enriched in manganese.

(6) A small group of calcareous chlorite- and biotite-rich schists which are geochemically distinctive, and in particular have high Ti contents ( $>0.7$  wt%), which are identified as metabasites. These were found to be common only in the Creag an Chanaich area (fig. 1.7).

Other minor components of the mineralized zone, which are more abundant outwith this zone, include calcareous mica or chlorite schists, and quartzites. The former are petrographically similar to rocks in the Ben Lawers Schist formation but are enriched in barium, whereas some of the quartzites are coarse-grained and resemble those in the Carn Mairg Quartzite formation. Thin beds of 'dark

limestone' (carbonaceous, fine-grained dolomite rock) occur occasionally in the graphitic schist and may be preferentially enriched in sulphides.

### 1.3.2 Distribution of the mineralization.

From the available evidence, Coats et al. (1981) considered the westernmost part of the mineralized zone to be of most economic significance (from Meall Tairneachan to the Frenich Burn: fig. 1.3). On Creag an Chanaich they demonstrated that a 3.6m band of barite rock sandwiched by quartz celsian rocks exposed at the surface, is the same thickness at a depth of 30m in IGS borehole (BH) 9. This bed was mapped along strike for about 400m, despite the effects of open F3 folds (sensu Roberts and Treagus, 1979) which are some 30m in amplitude and are a prominent feature of this part of the deposit (fig. 1.7). A thick intersection (nearly 10m) of the barite bed in BH2 is explained by repetition due to a horizontal fold closure (fig. 1.8). However, it is not clear whether the sharp reduction with depth in the 'true' thickness of the barite bed in the Frenich Burn area (from 15.5m in BH1, close to the surface, to 2.3m at a depth of 90m in BH11: fig. 1.8), is due to folding, faulting, or pronounced lenticularity. Immediately west of this area, a new NNE-SSW trending fault zone was recognised (fig. 1.3), which has about 250m of sinistral strike-slip displacement and is probably a member of the Loch Tay Fault system. This 'Frenich Burn Fault' is used by Willan and Coleman (1983) and in this study to divide the 'eastern sector' into Foss East and Foss West areas (fig. 1.3).

Coats et al. (1981) found evidence throughout the Aberfeldy deposits for two distinct stratigraphic horizons of barium enrichment within the mineralized zone, of which only the upper horizon was found to contain barite in Foss West and in the Creag an Fhithich district (fig. 1.3). However, near Creagan Loch (in Foss East) a 6.4m barite bed was intersected in a shallow borehole (BH3) through the lower horizon, and the upper horizon contains only quartz celsian cherts. Both here and near the summit of Ben Eagach, base metal-rich carbonate rocks accompany barite rock, and in BH 4 (fig. 1.3) the zinc and lead contents reach levels comparable with those of economic deposits (8.5% Zn and 3.6% Pb over a true thickness of 4.3m). However, the Ben Eagach area is structurally complex due to folding and tectonic disruption associated with the post-F3

Ben Eagach Antiform, and Coats et al. (op. cit.) considered this mineralization to have a limited along-strike extension.

In the Creag an Fhithich district (fig. 1.3), three lenses or fault-disrupted bands of barite (enclosed by quartz celsian rocks) have a lateral extent of 350m, but the barite decreases in total thickness from 11.3m at surface to 6.0m at a depth of 14m (BH5), and to 1.4m at about 28m below surface (BH7). In this area, 40-100m of barium-enriched, calcareous mica schist underlies the mineralization, which in turn is separated from the Ben Lawers hornblende calc-mica schist by a similar thickness of graphitic schist, which wedges out to the west (BH6: fig. 1.3). Only weak mineralization is present at this stratigraphic level to the east of Creag an Fhithich (BH8), but a thick unit of quartz celsian rock is exposed further north in the Allt Coirein a' Chinn. This represents a stratigraphically lower horizon which Dresser Minerals have since shown to extend west along strike to the outcrops of mineralization on Ben Eagach, and to contain a major portion of the barite and base-metal reserves in the Aberfeldy deposits (barite thickness up to 28m; Gallagher, 1983).

### 1.3.3 Previous genetic models.

Coats et al. (1980, 1981) concluded that a pre-metamorphic and synsedimentary origin for the deposits is supported by the strati-form nature of the mineralization, the abrupt contacts between chemically distinct lithologies and the interbanding of sedimentary and mineralized components, and the textural and structural evidence of similar metamorphic and deformational histories in these lithologies. The barite and manganoan carbonate rocks are considered by Coats et al. to be products of rapid chemical precipitation from an exhalative, hydrothermal brine which contained significant amounts of Ba, Fe, Zn, Pb, Mn, Si and perhaps Ca, Mg, Al and minor amounts of Ti and Cr. These elements were leached from the underlying sedimentary pile by meteoric, connate or possibly juvenile waters, and carried into a euxinic basin accumulating carbonaceous sulphidic muds.

The alternation of barite, celsian and sulphidic carbonate rocks is attributed to the varying rate of input and mixing of the dense brine with oxidizing seawater, with vigorous mixing resulting in sufficiently high oxidation potentials to precipitate the



barite-magnetite assemblage. Coats et al. (op. cit.) found little petrographical evidence for reaction between barite and barium feldspar, and proposed three alternative precursors for the celsian: a Ba-Al-Si gel; a mixture of silica and barium zeolite; or the hydrous barium aluminosilicate, cymrite (Fortey and Beddoe-Stephens, 1982). The 'cryptic' barium enrichment in muscovitic and graphitic schists peripheral to, and of greater lateral extent than the mineralized horizons, is ascribed to the sedimentary or diagenetic adsorption of barium onto clay minerals from pore waters enriched by hydrothermal fluids.

This model of formation is supported by other studies of the mineralization. Willan (1980) derived metamorphic equilibration pressures of 6-7 kbar from sphalerite geobarometry, and concluded that the low nickel and cobalt contents of the iron sulphides indicates deposition in a "hydrothermally-influenced sedimentary environment". Sulphur isotope results obtained by Willan and Coleman (1983) are considered to indicate unequilibrated pre-metamorphic compositions which are interpreted in terms of a dual supply of sulphur from the hydrothermal brines (which precipitated much of the sulphide) and from the contemporaneous, basinal seawater sulphate (which precipitated most of the barite). Lead isotope ratios in Aberfeldy galena examined by Swainbank et al. (1981) give model ages of roughly 600 M.y. and record an older, possibly Lewisian age (ca. 2500 M.y.), which suggests the derivation of base metals from craton-derived Dalradian sediments mixed with lead from a basic igneous (mantle) source. Recently, Russell et al. (1984) have discussed the palaeogeographic environment of the Dalradian basin and adjoining shelf areas, and have developed a model to explain the source of the huge tonnage of chemically-precipitated aluminium (now in the form of barium feldspars), which appears to be a unique feature of the Aberfeldy deposits. These authors postulate that the alumina was carried in solution in alkaline basinal brines which drained from the adjacent evaporitic shelf-seas, rather than in the hydrothermal fluids.

#### 1.3.4 Results of investigations of the Foss deposit by Dresser Minerals.

Previously published results from Dresser Minerals' investigations are limited to an abstract (Swenson et al., 1981) and one

geological cross-section incorporating information from deep drilling in the Creag an Chanaich area (reproduced by Smith, 1981, Willan and Coleman, 1983, and in fig. 2.13a). This drilling programme, in addition to extending the barite and base-metal reserves of the Foss deposit, considerably increased geological knowledge of the Foss deposit. Notable results reported by the company geologists are summarised below.

(1) Correlation of five laterally impersistent mineralized horizons in the Foss East area, of which the basal contains the most barite rock. Up to three horizons are present in parts of Foss West, but the bulk of the barite is contained within the upper, most extensive horizon.

(2) Subdivision of the Ben Eagach and Ben Lawers Schists into five distinct lithostratigraphic units (of which four are retained in this study: sections 2.2 and 2.5). The lowest division, which generally underlies the mineralized zone, is characterised by the presence of garnet and the absence of barium enrichment.

(3) Recognition of pronounced lateral and down-dip variations in facies and thickness of both the mineralized beds and the host metasediments, particularly in Foss East where deeper drillholes established the absence of barite rock >150m below the surface.

(4) Location of N-S fault zones east of Creagan Loch, which define the eastern limit of the Foss deposit, and in the Frenich Burn area.

(5) Illustration of the contrasting structural styles in each part of the deposit, with generally near-vertical dips in Foss East but complex folding throughout Foss West due to the imposition of F3 fold axes sub-parallel to the major E-W early fold axis.

From an analysis of the distribution of the mineralization and host metasediments, company geologists proposed a model of basinal development during the period of hydrothermal activity. An important outcome of this approach was the correlation of high-grade barite or significant base-metal mineralization, with thin or thick developments respectively of the lithostratigraphical unit containing the mineralized horizons.

## 1.4 Objectives and methods of the present study.

### 1.4.1 Mineralization and basinal development.

The initial definition of the project was broad in scope and involved a detailed study of the geology, petrochemistry and genesis of the mineralization and surrounding rocks in the Foss Estate area, using (together with surface exposures) the extensive new drillcore obtained by Dresser Minerals. In the light of the new information from this drilling programme, a major objective of the study is to refine the model of basinal development and ore formation through detailed logging of drillcore material and field mapping, combined with the use of the portable XRF analyser to detect 'cryptic' barium enrichment. Field studies are supplemented with petrographical examination and laboratory-based analyses of whole-rock, mineral and isotopic compositions. Of particular interest is the correlation of the several mineralized horizons and their lateral facies equivalents, and the identification of features associated with proximity to exhalative vents, of which no direct evidence (such as feeder pipes) are observed. Because of the complex tectonic history, a careful evaluation of the effects of penetrative deformation, folding and faulting is a prerequisite to the three-dimensional reconstruction of the original form of the deposit.

### 1.4.2 Lithogeochemistry.

Lithogeochemical studies by Coats et al. (1981) and Willan (1981) show the usefulness of this approach in elucidating the original nature of the rock types associated with the deposit (especially the metabasites), and also compositional changes associated with hydrothermal activity, diagenesis and metamorphism. Rather than undertaking a systematic programme of outcrop or sequential drillcore analyses, which would largely duplicate the published work summarised above, a more selective approach was adopted to address several specific objectives. These are:

(1) To clarify the original nature and composition of a selection of mineralized lithologies including several of unusual mineralogy which were not previously encountered.

(2) To further characterise the metasediments constituting the several lithostratigraphic subdivisions of the Ben Eagach and Ben Lawers Schists, and to deduce the geochemistry of the sedimentary

environment and the contribution from hydrothermal, authigenic and allochthonous sources.

(3) To compare the metabasic rocks of the Foss area with those elsewhere in the Dalradian (in particular in the Ben Vrackie metabasite complex and in the Farragon Beds: fig. 1.4), and if possible, ascertain both the tectonic setting and intrusive or extrusive origin of the metabasic lenses and sheets occurring at Foss. An integral part of this study is to investigate the nature of diagenetic/metamorphic alteration of the original igneous chemistry.

#### 1.4.3 Mineralogy and experimental petrology.

The objectives of mineralogical investigations are threefold:

(1) To characterise the mineral phases present and to establish their compositional ranges within individual samples and in the spectrum of rock types associated with the deposit.

(2) To identify compositional features related to the conditions of metamorphism and to the mode of formation of the various minerals, and to assess mutual variations in the composition of coexisting mineral phases may reflect the influence of either bulk rock composition or metamorphic element partitioning. Compositional zoning is of particular interest in relation to the prograde growth and/or retrograde alteration of the more refractory minerals (e.g. feldspars, garnet, sphalerite).

(3) To derive estimates of the intensive parameters of metamorphism using experimental and empirical calibrations of various mineral equilibria, including the garnet-biotite, garnet-hornblende and calcite-dolomite geothermometers and the sphalerite-pyrite-pyrrhotite geobarometer. Textural features relating mineral growth to the deformational history are examined in order to properly interpret the estimates of metamorphic conditions derived using these mineral equilibria.

The presence of the platy mineral, cymrite ( $\text{BaAl}_2\text{Si}_2\text{O}_8 \cdot \text{H}_2\text{O}$ ), and textural evidence in the Aberfeldy mineralization for the replacement of cymrite by celsian ( $\text{BaAl}_2\text{Si}_2\text{O}_8$ ) after fabric development (Fortey and Beddoe-Stephens, 1982), is of particular significance since the reaction  $\text{cymrite} = \text{celsian} + \text{H}_2\text{O}$  (Essene, 1967) has been located in P,T space in hydrothermal experiments by Nitsch (1980). Nitsch confirmed that cymrite is the stable phase under

higher pressure - lower temperature conditions. Further experiments have been performed to bracket this equilibrium using compositions and P-T conditions appropriate to the natural occurrences in the Foss deposit, for application in metamorphic thermobarometry.

#### 1.4.4 Stable isotopes.

Stable isotope studies of ore deposits, and of metamorphic rocks and minerals, usually provide information on several or all of the following: (1) the nature and origin of the source materials, e.g. their derivation from hydrothermal solutions or from organic activity; (2) changes in the depositional system indicated by spatial or temporal variations in primary compositions; (3) the mechanisms of diagenetic or metamorphic mineral reactions and extent of fluid infiltration or devolatilization; (4) the extent to which inter-phase equilibrium was attained (if at all) during deposition and/or subsequent metamorphism; and (5) if equilibration can be demonstrated, the temperature at the time this occurred. An extensive literature on the oxygen isotope ratios of silicates, and on the carbon and oxygen isotope ratios of carbonates (reviewed by Hoefs, 1980; O'Neil, 1979), illustrates the wide range in the effects of metamorphism on primary hydrothermal or sedimentary isotopic distributions. Whereas pervasive alteration and/or homogenization of carbon and oxygen isotope ratios in carbonates may accompany even low-grade metamorphism, broad variations in sulphur isotope composition often appear to survive high-grade metamorphism (Rye and Ohmoto, 1974).

This contrasting influence of metamorphism on carbon-oxygen isotope ratios and sulphur isotope compositions is demonstrated by studies of minerals from the Aberfeldy deposits. A preliminary study of the isotopic composition of carbonates in nine samples of mineralized and host rock lithologies (with carbonates of sedimentary, hydrothermal and probable metamorphic origin), described in Appendix F, confirmed that presumably diverse primary compositions have been overprinted by extensive metamorphic alteration. In a previous sulphur isotope investigation of barite and sulphides from the deposits, Willan and Coleman (1981, 1983) established the presence of considerable large- and small-scale isotopic variation which they concluded was unaffected by the metamorphism. However, their data for most coexisting barite-sulphide pairs yield equil-

ibrium fractionation temperatures in the range appropriate to amphibolite facies metamorphism (450–600°C), which suggests that isotopic exchange may have affected original compositions in samples with more than one sulphur-bearing phase. Furthermore, their interpretation of large-scale isotopic variations may not be valid since barite is now known to have been sampled from more than one horizon in the Foss deposit.

A more detailed study of sulphur isotopes using material from the Foss area examined in the present study, has the following aims:

(1) To specifically assess the scale and extent of metamorphic equilibration, particularly in rocks with textural and chemical evidence of pre-metamorphic sulphide compositional variations (notably in sphalerite), and of sulphur mobility during diagenesis and/or metamorphism.

(2) To determine temporal and spatial variations in the isotopic composition of both barite and sulphides in the several mineralized horizons, and to establish the relationship between these variations and changes in the sulphur source and/or the nature of the depositional environment as established from stratigraphical, geochemical and mineralogical studies.

(3) To further investigate the isotopic compositions of sulphides of probable non-exhalative origin in metasedimentary and metabasic rocks surrounding the deposit, and of sulphides in distal stratigraphic equivalents of the mineralized horizons.

#### 1.4.5 Analytical methods.

Samples were collected in the course of detailed field mapping of about 3km<sup>2</sup> of the Foss Estate (figs. 1.3 and 2.2) and from parts of some 3km of drillcore which was re-logged in this study (Appendix A). Semi-quantitative determinations of barium content in over two hundred outcrop samples and in drillcore was performed at the field base using a portable XRF analyser (which was kindly loaned by the IGS). Subsequently about two dozen of these outcrop samples, together with a set of three core sections used in routine calibration of the portable XRF (Appendix B) were analysed using laboratory procedures.

Laboratory-based work utilised a Philips PW1450 automated XRF spectrometer with measurement and data correction procedures

modified to incorporate barium as a major element (Appendix D). Major element data was obtained for one hundred and six rock samples plus sixteen spiked and synthetic materials used in BaO calibration. Trace element data were also obtained by XRF in all but eight of these samples, for the elements Sc, V, Cr, Ni, Cu, Zn, Rb, Sr, Y, Zr, Nb, La, Ce, Nd, Ba, Pb and Th. XRF calibration of barium as a major element (ie. >1wt% BaO) was based on gravimetric determinations of Ba content in seven samples.

Polished thin sections were prepared by technical staff from a large number of samples, and these have been examined in transmitted and reflected light and with a cold-source cathodoluminoscope (plate 45). Over two thousand mineral analyses were obtained with a Cambridge Instruments Microscan Mark 5 electron microprobe (Appendix E). Hydrothermal cymrite-celsian experiments (Appendix G) utilised facilities in the Experimental Petrology Unit, also at Edinburgh University. Carbon and oxygen isotope ratios were determined at the Scottish Universities Research and Reactor Centre at East Kilbride, on a triple-collecting Philips 903 mass spectrometer using standard preparation methods (Appendix F). Following the purification of mineral separates using conventional magnetic, heavy liquid, and hand-picking techniques, sulphur isotope ratios were determined in the Isotope Geology Unit at the British Geological Survey in London (Appendix H), using a VG Micromass 602C double-collecting spectrometer.

### 1.5 Thesis layout.

The following eight chapters need not necessarily be read sequentially since each covers a clearly defined aspect of the study. Chapter 2 presents the results of mapping and core logging, and endeavours to unravel the depositional and structural history to reconstruct the original form and development of the Foss deposit and its host rocks. Structural and stratigraphical nomenclature, used in all subsequent chapters, is summarized in section 2.5. Chapters 3 to 5 cover petrographical and geochemical studies of the mineralization, the metasediments, and the metabasites in that order. Chapters 6 and 7 are concerned with investigations of the mineralogy and mineral chemistry of silicates and non-silicates, respectively. Chapter 8 is a summary of the approach to, and

interpretation of, thermobarometric studies and the metamorphic history of the study area, which are described in greater detail in two published papers incorporated in this volume (from page 453 ~~and in back pocket~~). Chapter 9 introduces sulphur isotope systematics and reviews the previous results from the deposit, before examining the evidence for a metamorphic overprint and the primary controls on isotopic variation. Finally, chapter 10 integrates the diverse information pertaining to both metamorphic and depositional processes which is presented in the previous chapters, to construct a unified model for the petrogenesis of the deposit. Comparisons are made with other sedimentary exhalative and metamorphosed stratiform deposits, and implications for further exploration of the Aberfeldy deposits and of mineralization elsewhere in the Dalradian are briefly discussed.

Tables and figures follow the text of each chapter, whereas photographic plates 1 - 116 and Appendices A - H are incorporated in Volume II. Representative rock samples, rock powders, mineral separates and thin sections (with photographs showing microprobe sites) are lodged with the Grant Institute of Geology at Edinburgh University. The complete set of microprobe analyses is held on computer files in the Edinburgh Multi-Access System (see Appendix E).



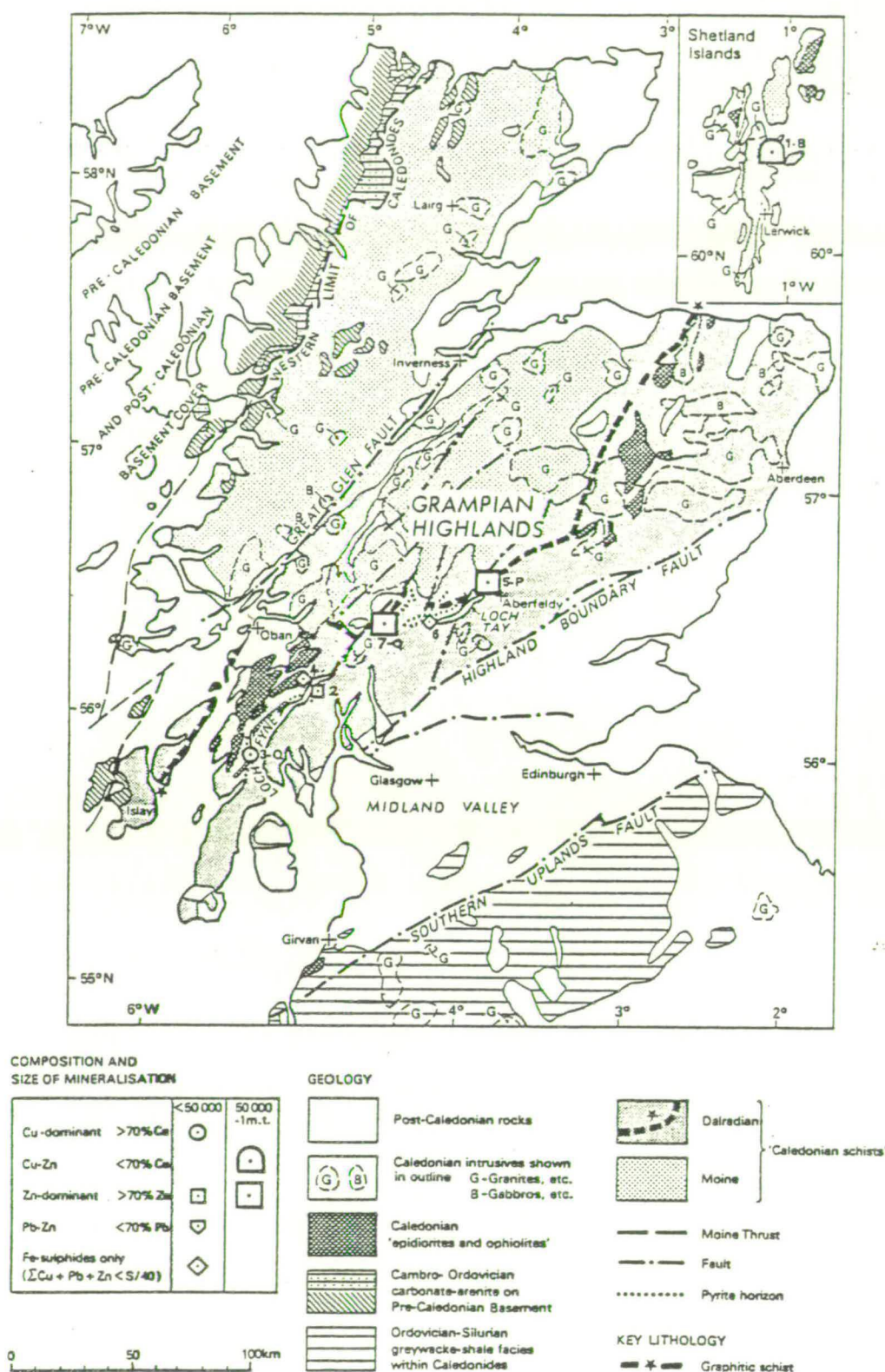


Fig. 1.1: Outline geology of the Scottish Highlands, slightly modified from Coats et al. (1981), showing location of mineralization in the Middle Dalradian: 1 Vidlin, 2 McPhun's Cairn, 3 Meall Mor, 4 Coille Braghaid, 5 Aberfeldy, 6 Loch Tay, 7 Auchtertyre and Ben Challum. Host rocks: B basic volcanics, P graphitic schist, Q quartzite.



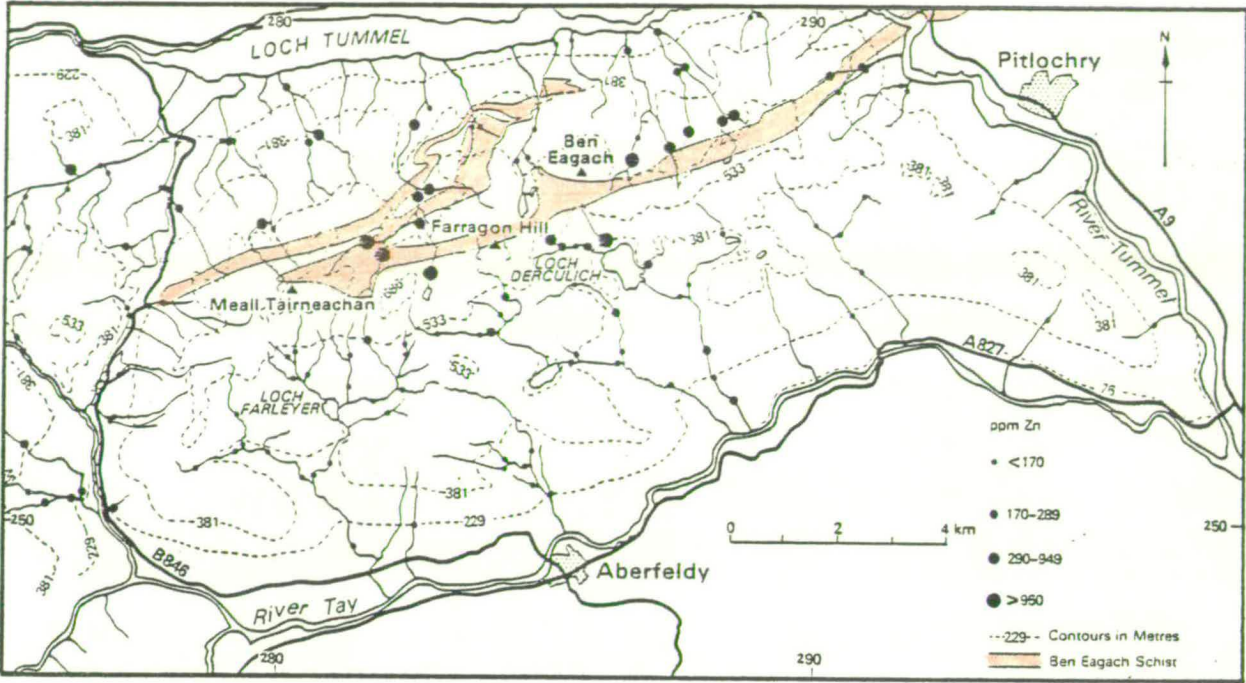


Fig. 1.2: Map of the Aberfeldy area, from Coats et al. (1980), showing topography, drainage, outcrop of the Ben Eagach Schist formation, and distribution of zinc in stream sediment samples.

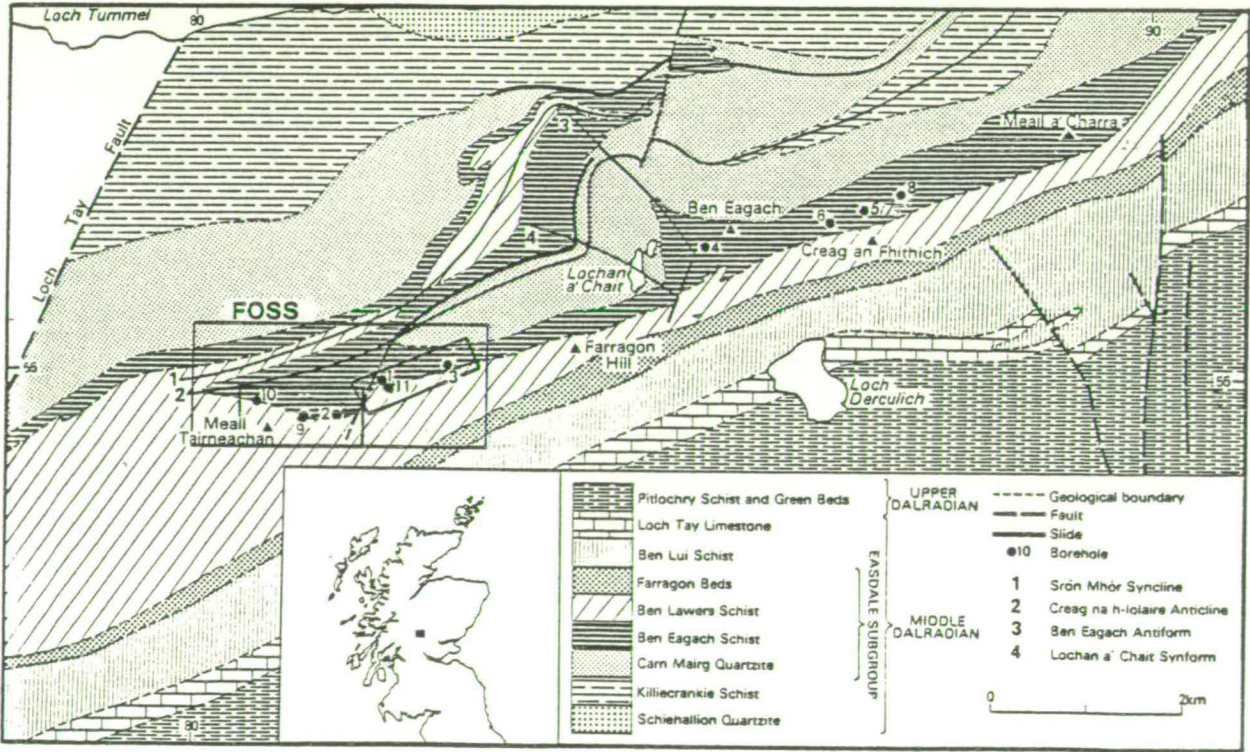


Fig. 1.3: General geology of the area south of Loch Tummel, from Coats et al. (1980), modified to show locations of the Ben Eagach and Foss deposits and the area examined in this study.



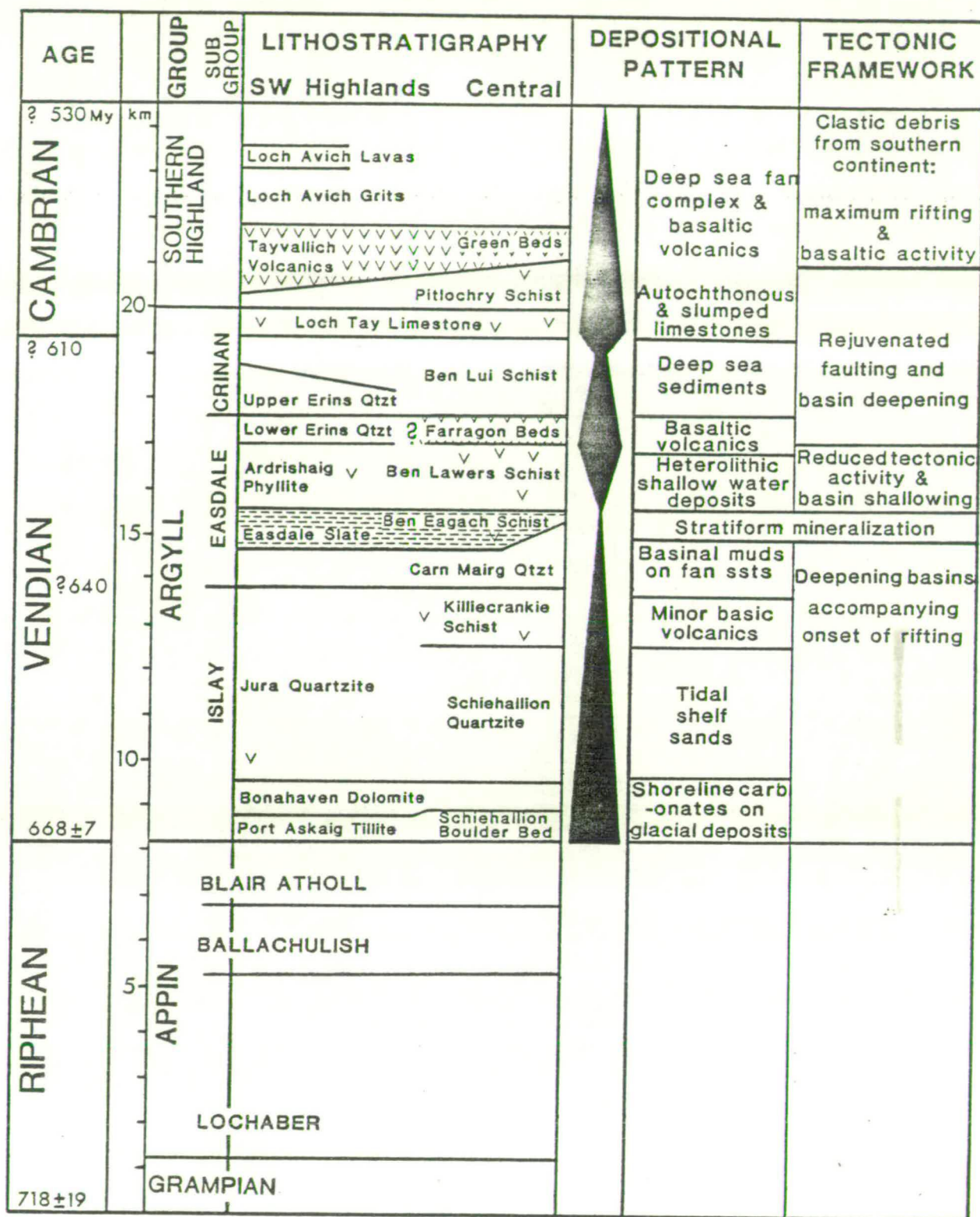


Fig. 1.4: Schematic stratigraphical column (approximately to scale) of the Dalradian Supergroup showing subdivisions, the main formations in the SW and central Scottish Highlands, and an interpretation of the depositional pattern and tectonic framework (from Graham & Bradbury, 1981). Column adapted from Willan & Coleman (1983) using diagrams of Harris & Pitcher (1975) and Harris et al. (1978); age dates from Willan & Coleman (1983). vv = metabasites interpreted as extrusive in origin. Dashed ornament indicates the formation which hosts the Aberfeldy deposits. ▲ = basin deepening; ▼ = basin shallowing (Graham & Bradbury, 1981).

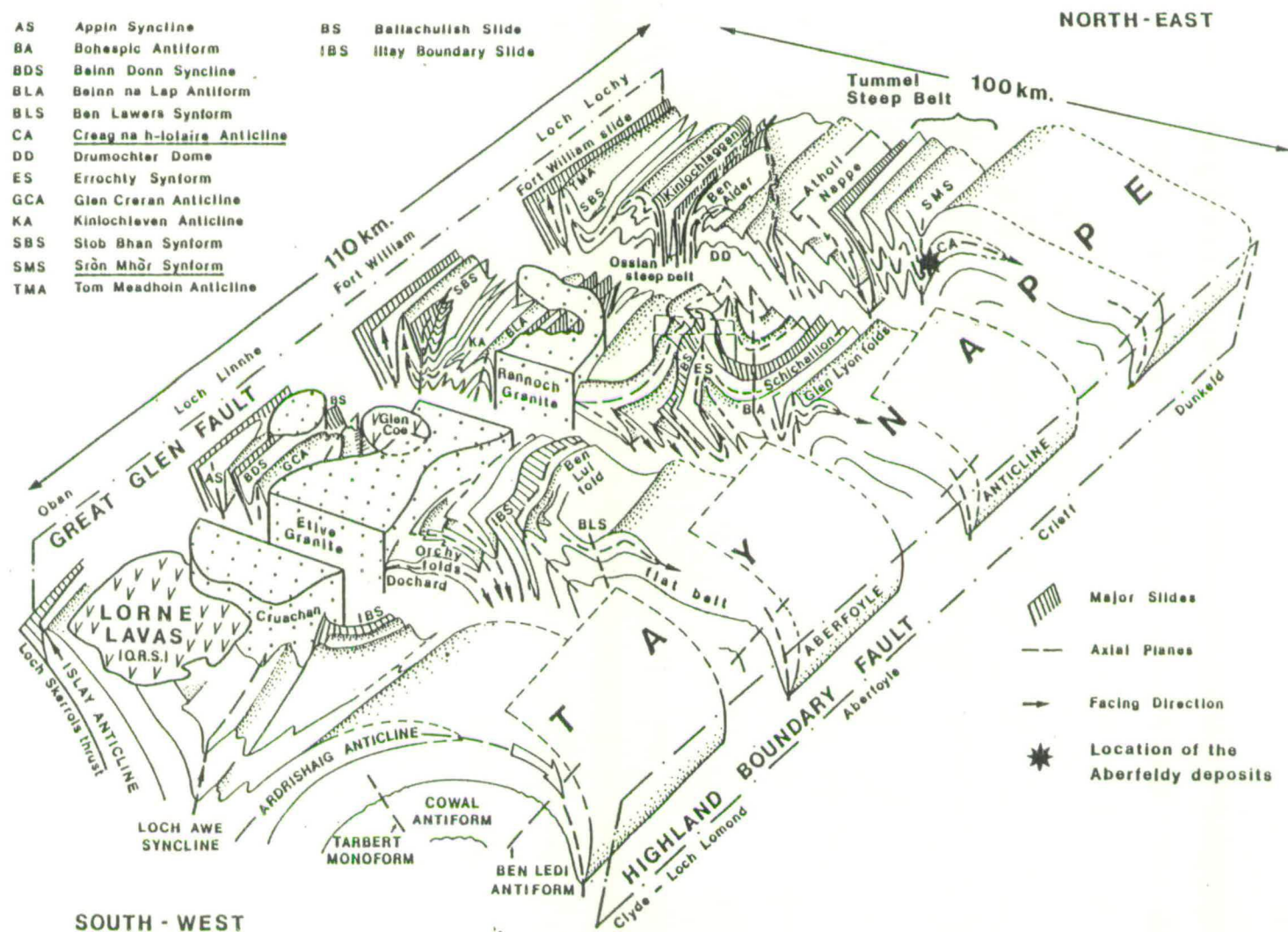


Fig. 1.5: Block diagram of major structures in the SW and central Highlands, omitting faults and minor intrusions, from Thomas (1979). The locations of the Tummel Steep Belt and the Aberfeldy deposits have been added.



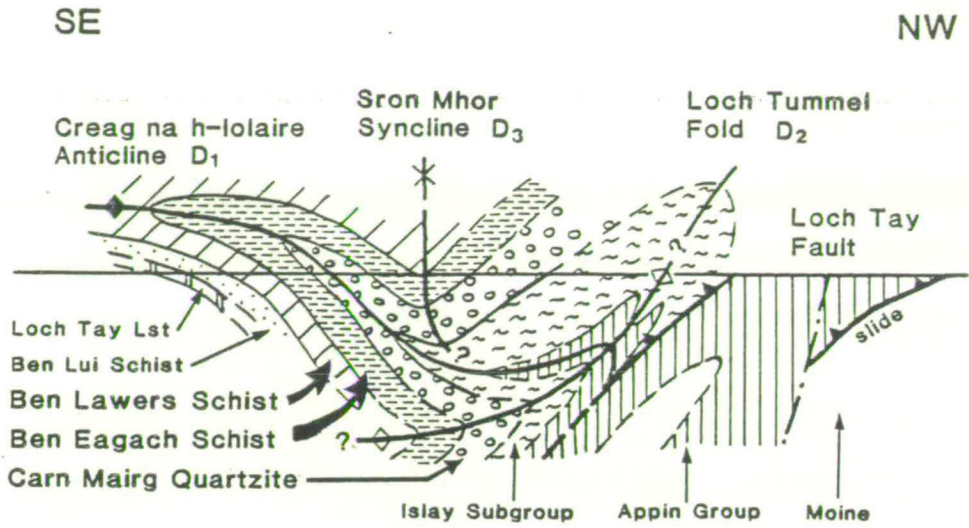


Fig. 1.6: NW-SE cross-section of the central Highlands through the Foss area showing the major structures and formations, adapted from Roberts & Treagus (1979). The horizontal line represents the present erosion level; the section is about 8km in length.

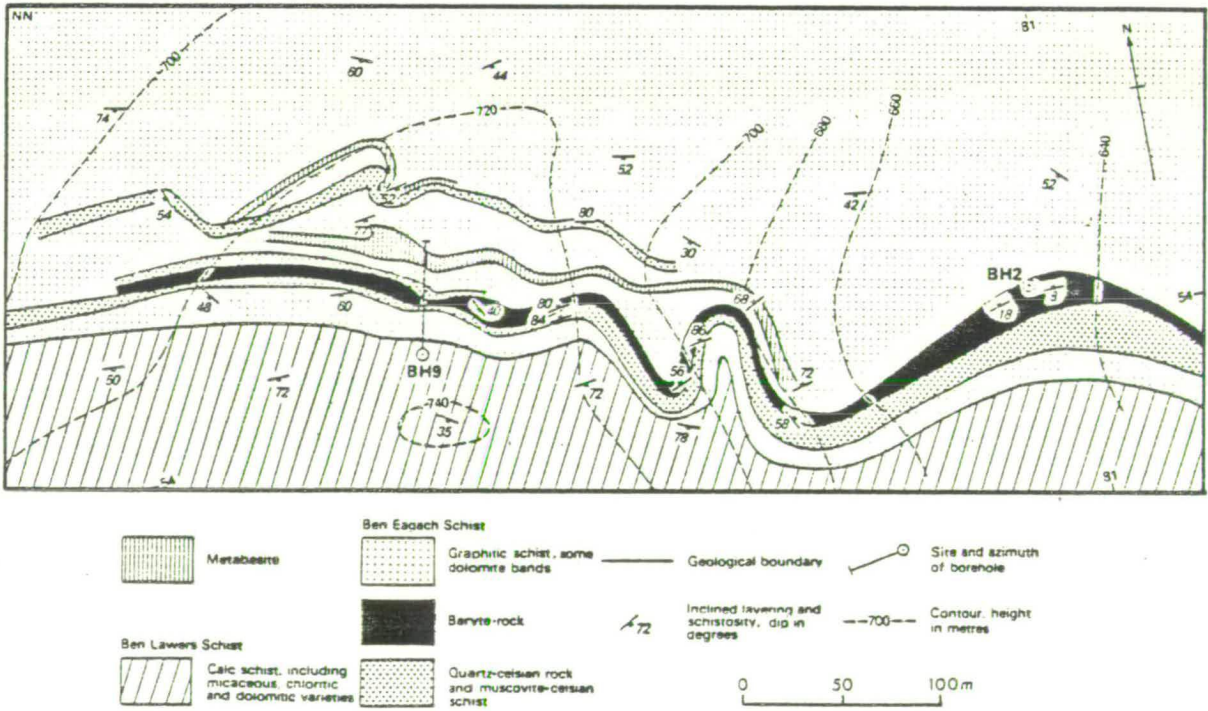
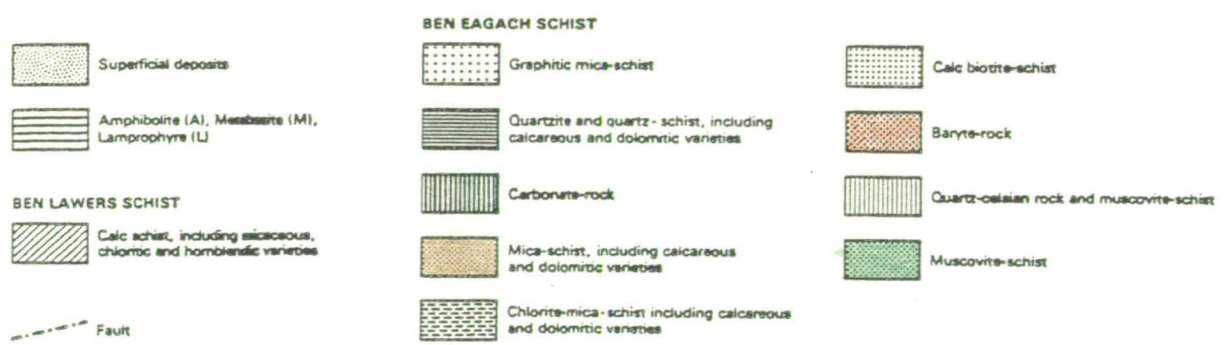
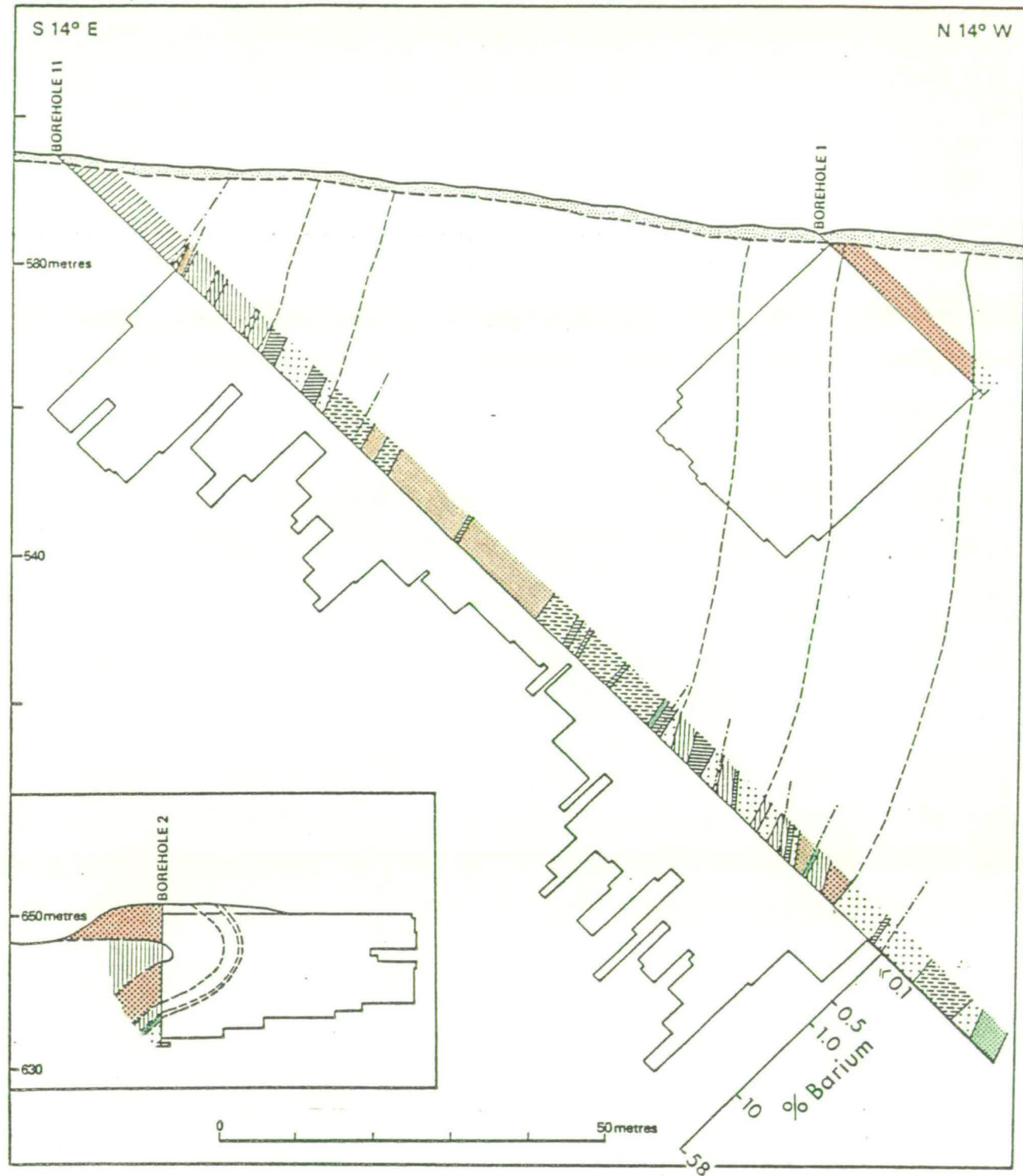
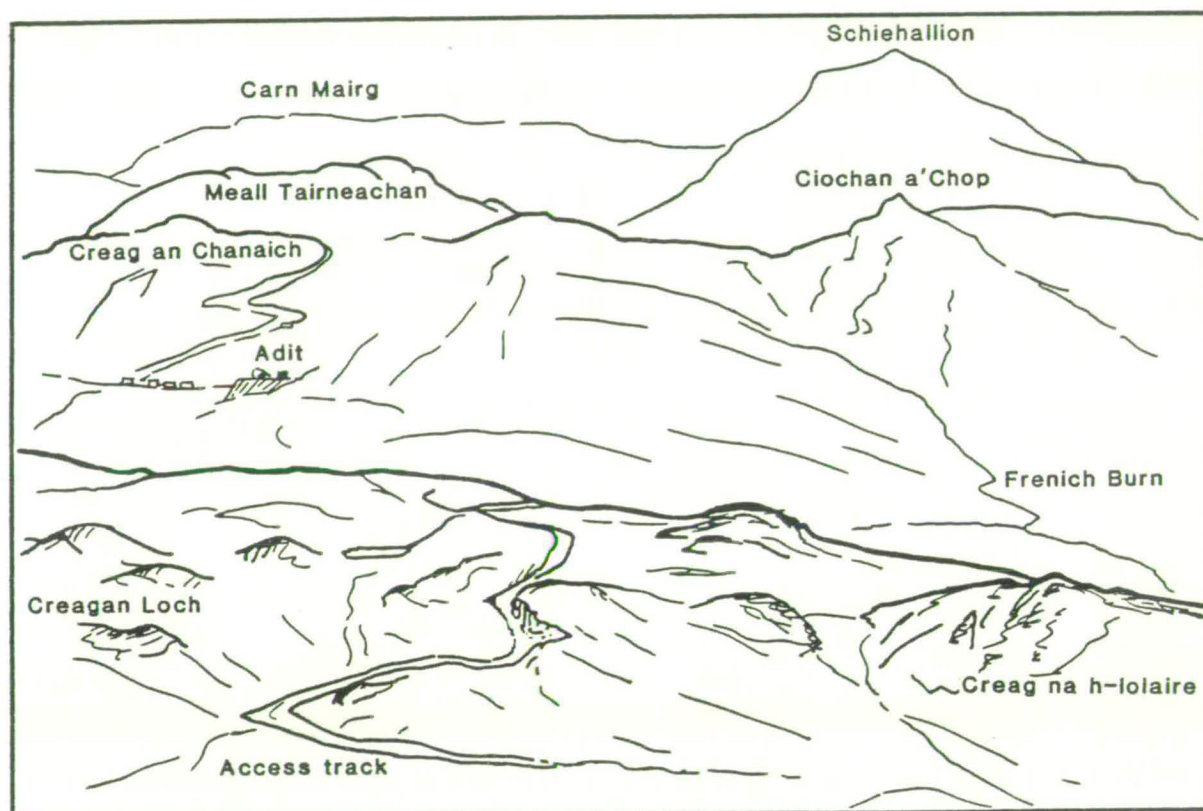


Fig. 1.7: Geological map of the Creag an Chanaich area, Foss West, from Coats et al. (1980). (Fig. 2.8 shows the same area mapped in this study).



**Fig. 1.8:** Vertical sections showing lithologies intersected in BHs 1 and 11 (Frenich Burn) and BH2 (eastern Foss West: inset), with plots of Ba content (on a logarithmic scale), from Coats et al. (1981). Note the two zones of mineralization intersected in BH11, each containing several discrete beds of barium-enriched strata. (Fig. 2.24 shows revised lithostratigraphic correlations).



**Fig. 1.9:** View of the Foss deposit area looking west from Farragon Hill (see frontispiece), showing the steep, eastward-facing slopes of Creagan Loch, Creag na h-Iolaire and Creag an Chanaich. In the distance are the quartzite mountains of Carn Mairg and Schiehallion (see tailpiece).

## CHAPTER 2: Geological structure and lithostratigraphy of the Foss deposit.

### 2.1 Introduction.

Much of the material presented in this chapter is necessarily graphic and descriptive: 34 figures accompany the text (including four located in the back pocket), and logs of >2.5km of drillcore are provided in Appendix A. Since structural and stratigraphical aspects are inseparable in an analysis of the geological setting of the deposit, a geographical approach is adopted in which structural features are described and stratigraphical nomenclature is introduced in the appropriate areas.

The first section (2.2) describes the results of surface mapping, and integrates spatial information from geophysical and geochemical surveys (including a lithogeochemical sampling programme) to define the distribution and components of the mineralized zone and surrounding rocks in the Foss area. The following two sections describe and interpret the sub-surface geology of the mineralized zone on the southern limb of the Creag na h-Iolaire Anticline, in a west-to-east progression across Foss West (section 2.3) and Foss East (section 2.4). This account is based on the examination of core from over forty drillhole intersections, supplemented by underground exposures afforded by mine development in Foss West. Structural and stratigraphical syntheses are presented in each section, and are integrated in the final section (2.5), which summarizes the lithostratigraphy and development of the deposit and its structural history.

Note that unless specified otherwise, the terms 'upper', 'lower', 'above', 'below', 'overlying' and 'underlying' refer to the stratigraphical way-up rather than to the present orientation of the strata described.

### 2.2 Surface geology of the Foss area.

#### 2.2.1 Cryptic barium enrichment and subdivision of the Ben Eagach Schist.

Outcrops of the various lithologies constituting the Ben Eagach Schist formation, and its boundaries with the Carn Mairg Quartzite



and the Ben Lawers Schist, were mapped in the area between Meall Tairneachan, Doire Leathan and Creagan Loch (figs. 2.1, 2.2). Rock exposure varies from nearly complete on the craggy, east-facing slopes of Creag an Chanaich and Creagan Loch, to minimal in the broad valley occupied by the eastern headwater tributary of the Frenich Burn, where there are extensive tracts of peat-covered glacial overburden.

During the 1981 field season, over two hundred samples of graphitic schist were collected from outcrop in the Foss area, and following preparation of cut faces perpendicular to the dominant schistosity, were analysed for barium content using a portable XRF spectrometer at the field base (Appendix C). Sample collection utilised the 60m exploration grid established by the I.G.S. in the area north of Creag an Chanaich (fig. 2.2), but elsewhere sample distribution is determined by the limited outcrop available. Detailed sampling transects follow the courses of the Frenich Burn tributaries. Of the total sample collection, about 20% are from Foss East, and another 5% are from outcrops on the N limb of the Sron Mhor Syncline between Ciochan a'Chop and Doire Leathan (fig. 2.2). Where several samples of different lithologies were collected at outcrop, the distribution of barium enrichment shown in fig. 2.2 refers to that of the most pelitic component. A cumulative frequency plot of barium contents (Appendix C, fig. C.2) shows two inflexion points at concentrations corresponding to 0.4 and 1.1 wt% Ba. The lower value equals that taken by Willan (1982) as the threshold between background and anomalous populations, and is also adopted here for this purpose. On this basis, about 20% of the samples measured are anomalously enriched in barium.

Table 2.1 illustrates the antipathetic relationship between barium enrichment (expressed as sample frequency in class intervals of estimated barium content) and the presence of garnet in samples of the Ben Eagach Schist. The relative proportion of samples containing disseminated pyrite (visible in hand specimen) also greatly increases with increasing barium enrichment. These features are the principal criteria used in defining the two lithostratigraphic subdivisions of the Ben Eagach Schist, which were first introduced by Dresser Minerals' geologists working on drillcore from Foss East (A. M. Boast, pers. comm. 1981) (fig. 2.5). The strati-

graphically lower division, termed 'unit A', consists largely of garnet mica quartzites with wispy intercalations of graphitic schist, and of leaden-grey coloured (weakly graphitic), garnetiferous and chloritic quartz muscovite schists which lack barium enrichment. 'Unit B', which hosts much of the mineralization, is characterized by mid-grey to black, well-foliated and crenulated, graphitic quartz muscovite schists, which are often enriched in barium ( $>0.4\%$ ). However, it should be noted that in over one third of the outcrop samples collected, neither garnets nor sulphides were discernible in hand specimen, and no barium enrichment was detected with the portable XRF (table 2.1). Further petrographical and geochemical features which characterise unit A and unit B metasediments are described in chapter 4. It is noteworthy that Bailey (1925) also recognized differences between the upper and lower parts of the Ben Eagach Schist, the lower part containing much intercalated quartzite.

In the Creag an Chanaich area (fig. 2.2), outcrops are sufficiently frequent to allow mapping of the boundary between units A and B. Additional constraints on the location of this boundary, which allows extrapolation from the limited exposures on the northern limb of the Creag na h-Iolaire Anticline in Foss West (fig. 2.4), are provided by (i) the distribution of electrically neutral or resistant bedrock (unit A?) and conductive bedrock (unit B) indicated by the VLF-EM survey (fig. 2.3), and (ii) the distribution of anomalous Ba and Zn in deep overburden samples (data obtained by Coats et al., 1981, and by Dresser Minerals). Between the sites of BH2 (east of Creag an Chanaich) and BH3 (Creagan Loch), the location of the unit A/unit B boundary is projected from drillcore intersections (fig. 2.7).

Graphitic schists with anomalous contents of barium also outcrop on the N limb of the Sron Mhor Syncline (fig. 2.2), where anomalous barium concentrations are also indicated by deep overburden sampling. Anomalous levels of Ba in the Ben Eagach Schist may extend as far west as the Loch Tay Fault (fig. 1.3) (Willan, 1981a), although no mineralization has been observed despite several well-exposed transects (e.g. in the bed of Allt Tarruinchon: fig. 2.2). To the northeast of Ciochan a'Chop, barium enrichment in the Ben Eagach Schist appears to die out and garnetiferous schists

similar to those of unit A were found. Outcrop is sparse in this area (south of Doire Leathan), which was not covered by the VLF-EM survey, so it is not possible to ascertain whether this transition is fault-related or due to lateral facies variation.

The outcrop width of unit B metasediments (i.e. the across-strike thickness of the mineralized zone, minus the mineralization itself) is narrowest in the vicinity of the Frenich Burn West, where only a few metres of graphitic schist separate barite rock from garnetiferous schists lying to the north. East of Creag an Chanaich, the thickness is about 20m and appears to rapidly increase to 50-60m in central Foss West. On the northern limb of the Creag na h-Iolaire Anticline, unit B metasediments (incorporating at least 50m of quartzite) average 200m in thickness. North of Ciochan a'Chop, barium-enriched graphitic schists interbedded with quartzites, constitute a large part or possibly the entire thickness (about 180m) of the Ben Eagach Schist on the northern limb of the Sron Mhor Syncline. Although shallow angles of dip locally give the impression of a wider mineralized zone (such as to the east of Creag an Chanaich), no structural explanation plausibly accounts for the enormous variation in unit B thickness in the Foss area, which is interpreted as an original depositional feature associated with lateral facies variation in the Ben Eagach Schist. These facies and thickness changes in the metasediments of the mineralized zone, and their relationship to variations in nature and distribution of the stratiform mineralization, are examined after a more detailed description of the mineralization from surface and drillcore observations (parts 2.3.4, 2.4.6 and 2.5.1).

### 2.2.2 The northern limb of the Creag na h-Iolaire Anticline.

During field mapping and lithogeochemical sampling, particular attention was given to the areas of sparse outcrops north of Creag an Chanaich and southeast of Ciochan a'Chop, where the Ben Eagach Schist lies on the northern limb of the Creag na h-Iolaire Anticline. Here, outcrops of minor celsian mineralization in the bed of the western Frenich Burn tributary were reported by Coats et al. (1981), in an area where the VLF-EM survey showed clearly-defined, ENE-trending bands of alternating electrically resistive and conductive units (fig. 2.3).

Several more outcrops of mineralized lithologies were traced intermittently along a north-facing topographic bluff for about 350m ENE from the southernmost of the two previously recorded outcrops in Frenich Burn West. The mineralization consists of pyritic quartz celsian and hyalophane cherts, some containing a bright green mica (subsequently identified as Cr-Ba-muscovite), and is associated with strongly crenulated pyritic graphitic schists which are also enriched in barium (see following section and fig. 2.2). Scattered outcrops of massive, calcareous and chloritic rocks identical in appearance to the metabasites mapped by Coats et al. (1981) in the vicinity of Creag an Chanaich, also occur in this area. A quartzite bed at least two metres in thickness, and containing both folded lamellae and disseminations of sphalerite and galena, is marked by a small waterfall at 8122 5506, and can be traced for about 200m to the ENE where anomalous concentrations of Pb and Zn were discovered in both the IGS follow-up drainage survey and in deep overburden sampling by Dresser Minerals in 1979. This quartzite bed coincides with an electrically resistive band in the Ben Eagach Schist (fig. 2.3) which is, however, greater in lateral extent (over 2km) and thickness (30-50m) and probably reflects a composite unit of graphite- and sulphide-poor, garnetiferous quartzitic schists which are enclosed by pelitic schists with higher graphitic contents.

A tentative interpretation of the geology of the area around Frenich Burn West has been made by extrapolating the limited outcrop information using the VLF-EM map (figs. 2.3, 2.4). Evidence for certainly two and possibly four NNE-trending faults, each with 20-60m of sinistral strike-slip displacement, is provided by matched offsets of zones of high resistivity and conductivity, and of correlated quartzitic, metabasic and mineralized horizons in this area. Reductions in the intensity of the electromagnetic response associated with these offsets, and the generally constant strike directions measured in outcrops ( $080^{\circ} \pm 10^{\circ}$ ), further suggest that the offsets are related to faulting subparallel to the more major Frenich Burn Fault, rather than to asymmetrical folding such as that seen in the Creag an Chanaich area (figs. 2.4, 2.8).

Both geophysical and geological evidence suggests that a major change in the lithostratigraphy of the Ben Eagach Schist occurs directly west of Frenich Burn West, where the band of relatively

high conductivity associated with the celsian mineralization described above, is replaced by a wide zone of relatively low conductivity which extends west towards the nose of the Ben Eagach Schist in the Creag na h-Iolaire Anticline (fig. 2.3). Despite the moderately good exposure on the col between Ciochan a'Chop and Meall Tairneachan, no mineralization or metabasites were observed in outcrop or float material, and quartzitic, calcareous and graphitic schists from this area are neither garnetiferous nor barium-enriched (see below and fig. 2.2). As noted above, similar lithologies occur in outcrops of the Ben Eagach Schist which lie on the northern, steeply inclined limb of the Sron Mhor syncline north of Ciochan a'Chop.

### 2.2.3 The mineralized zone between Meall Tairneachan and Creagan Loch.

The distribution and thickness of barite rock, and the presence of two horizons of barium enrichment in this area, were initially determined by IGS investigations (Coats et al., 1981) which have been described in section 1.3. Overburden sampling and the VLF-EM survey (figs. 2.6 and 2.3) both provide evidence for the continuity of the mineralized zone across areas of poor exposure, i.e. between BHs 9 and 10, NE of Meall Tairneachan; in the broad valley of the Frenich Burn East between BHs 1 and 2; and east of BH1 towards Creagan Loch (frontispiece). However, the resolution of the geophysical survey is insufficient to distinguish individual horizons within the mineralized zone, which is defined by an elongate band of relatively high conductivity corresponding to the outcrop of sulphidic, graphitic schists of unit B (figs. 2.3, 2.4). The zone is clearly offset by about 250m of sinistral, strike-slip displacement along the Frenich Burn Fault, and possible fault drag associated with this displacement is suggested by the curvature of both the resistive zone and the overburden anomalies immediately west of the barite bed exposed in the stream section.

#### 2.2.3.1 Frenich Burn East, and the definition of unit C.

Further exploration in Foss East has confirmed that the distribution of barium enrichment in overburden samples faithfully defines the suboutcrop of mineralization. The zone of Ba and Zn enrichment in overburden (fig. 2.6) broadens from 30m to ~100m east

from the Frenich Burn and separates into two parallel bands in the area of no exposure. These bands coalesce and narrow again to the NW of Creagan Loch. New outcrop information from track and trench exposures, extrapolated using information from over twenty shallow to mid-depth drillholes (described in section 2.4), has enabled a more detailed geological map of the Foss East area to be compiled (fig. 2.7). These drillholes have confirmed that the thick barite bed near the surface at Frenich Burn (BH1) splits into four or five separate mineralized horizons, both along-strike to the east, and with increasing depth (e.g. in BH11).

Track exposures about 250m E of the BH1 site in central Foss East clearly demonstrate the presence of three chert and barite horizons, separated by over 10m of rapidly-weathering, calcareous quartz mica schists, which lie above the graphitic schists enclosing the lowermost barite-chert bed. The calcareous mica schists resemble those observed in outcrops upstream of the Frenich Burn barite bed and intersected in BH11, and are also similar to metasediments occurring stratigraphically beneath the mineralization on Creagan Fhithich (see section 1.3). These calcareous mica schists are variably enriched in barium (0.2-1.2% in BH11 core intervals) and for this reason were considered by Coats et al. (1981) to be part of the Ben Eagach Schist formation. However, lithologies of similar appearance also occur within the Ben Lawers Schist, although hornblende and garnetiferous calc mica schists are more characteristic of this formation. To avoid confusion arising from the use of different formation names for the same rock type, all calcareous quartz mica schists are referred to here as 'unit C', whereas the garnet- and hornblende-bearing varieties are designated as 'unit D' (fig. 2.5). In a later section (2.4) it is demonstrated that unit C lithologies occur within both formations in the Foss East area, and that this rock type represents a geochemically distinct lithofacies possibly associated with oxidizing conditions during sedimentation (sections 4.5, 4.6).

A fifth lithostratigraphical division was distinguished by company geologists from deeper drillhole intersections in the Frenich Burn area of Foss East. This unit comprises interbedded graphitic schists, muscovite schist and quartz celtsian cherts, and reaches a maximum thickness of 30m in BH11 (figs. 2.23, 2.24). These

lithologies are also found in sparse outcrops parallel to the course of the Frenich Burn and along the track west of the collar to BH11 (figs. 2.2 and 2.7). However, detailed examination described below (part 2.4.2) suggests that this unit represents a fault repetition of the mineralized zone. This is at variance with previous interpretations which correlated the upper unit with the upper mineralized horizon at Creagan Loch (Coats et al., 1981), or invoked a localized reversion to Ben Eagach Schist-type sedimentation associated with a second phase of mineralization during Ben Lawers Schist times (A.M. Boast, pers. comm. 1981).

#### 2.2.3.2 Creagan Loch.

The construction of an access track past the BH3 site north of Creagan Loch has increased the available outcrop information from the area (fig. 2.7). Banded barite rock up to 5.2m thick occurs in steep, east-facing crags (at 8270 5503) which represent the easternmost exposure of this lithology at Foss. The barite progressively decreases in thickness west of this point, and is absent about 100m to the west where ~4.5m of massive, sulphide-banded quartz celsian rocks represent the same mineralized horizon. No further exposures of this horizon are seen further west, where overburden sampling by IGS (fig. 2.6), a lithogeochemical sampling transect (fig. 2.2) and a Dresser Minerals drillhole (DH 503) all suggest the absence of mineralization within the Ben Eagach Schist in this 100-150m of strike-length. (However, the drillhole data is amenable to an alternative explanation, discussed in part 2.4.3).

Quartzites are a major component of the Ben Eagach Schist north of Creagan Loch, and occur both within the 150m thickness of unit A south of the boundary with the Carn Mairg Quartzite, and within the mineralized zone which is between 60 and 100m thick in this area. Coats et al. (1981) observed graded bedding in a coarse quartzite bed south of the track, and in this study, samples of both garnetiferous and sphalerite-bearing quartzite (e.g. N80-29: fig. 2.7) were collected during field mapping. Several small outcrops of massive, chloritic metabasite rock were also recorded in this area, and another exposure of calcite-biotite metabasite similar to that on the hilltop near BH3, was discovered at the north side of the quartz celsian rock exposed in the road section. The occurrence of significant amounts of quartzite within the mineralized zone at

Creagan Loch suggests that the lithostratigraphy in this area could be comparable to that on the northern limb of the Creag na h-Iolaire Anticline in Foss West (see part 2.2.2 and fig. 2.4).

Lateral offsets in exposures of quartz celsian rocks marking the upper mineralized horizon about 75m SE of BH3, were mapped by Coats et al. (1981) as an open, monoclinic fold (fig. 2.6). However, detailed examination reveals no structural evidence for this deflection in strike (fig. 2.7), but suggests that the mineralized horizon is offset by a fault. Another horizon of celsian-bearing quartz schists (earlier mapped as quartzite) cropping out about 80m ESE of the BH3 collar, cannot be traced further west. The hypothesis that a N-S fault parallels the base of the steep eastern face of Creagan Loch and Creag na h-Iolaire (figs. 2.2 and 2.7), is supported by evidence of fault displacements in one drillhole (DH 706) and of an abrupt facies change in this and in other intersections of the mineralized zone east of BH3 (part 2.4.4). Further drilling by Dresser Minerals has established the presence of at least two other major fault planes in the topographic depression east of Creagan Loch. However, the broad continuity of the Ben Eagach Schist suboutcrop across this valley suggests that displacements were largely in a vertical sense.

#### 2.2.3.3 Foss West.

A similar offset in the strike of the upper mineralized horizon in Foss West occurs between the base of the steep slope of Creag an Chanaich and the small hillock of barite rock which is the site of BH2 (fig. 2.8 and frontispiece). This suggests the presence of another N- to NNE-trending fault, and several shear zones have been noted in drillcore from this area. Other NNE-trending shear zones with displacements of up to 10m have been observed in underground development beneath the western slopes of Creag an Chanaich ('Bimbo's Fault'), and may account for the topographic low between this hill and Meall Tairneachan (fig. 2.2).

Information from temporary trench exposures in the ground NE of Meall Tairneachan, where the westernmost headwater tributary of the Frenich Burn rises in a deep, peat-filled depression (plate 2), has extended the previously known lateral continuity of both upper and lower mineralized horizons. About 300m WNW of the adit entrance, barite in the upper horizon wedges out, and its place is taken by



sulphidic quartz celsian rock which is notably rich in remobilized galena. In this same area, barite appears in the lower horizon and increases in thickness to over 2m (fig. 2.8). A reversion to the situation on Creag an Chanaich, namely with cherts in the lower horizon and barite rock in the upper, occurs a further 120m to the west on the northern flank of Meall Tairneachan. However, this bed is of limited lateral (and down-dip) extent, and barite is absent in the vicinity of BH10 (about 700m WNW of the adit). Here, quartz celsian rock is abundant in surface float, and forms four bands totalling about 2.5m in thickness (fig. 2.9), intersected at depths of 8-20m below the surface. The celsian rock is interbanded with muscovite schists and 7.5m of metabasic rock (barium-enriched, calcareous quartz biotite schists). Coats et al. (1981) correlated this zone with the lower mineralized horizon and attributed the absence of the upper band to faulting at the junction of the Ben Lawers and Ben Eagach Schists, observed in BH10A. A pyrite-banded, cherty 'quartzite' (sample G191: fig. 2.2) occurring at this junction in track exposures about 70m NW of the BH10 collar, could be the lateral equivalent of the upper horizon. No mineralization has been observed either in outcrop or in percussion drillholes to the west of this point.

Only one mineralized band (corresponding to the upper horizon) was previously observed on the eastern slopes of Creag an Chanaich. Here, exposure is sufficiently complete to trace this barite bed with its mantle of quartz celsian rock through three large, near-horizontal folds (plate 3), whose median limbs are up to 60m long (fig. 2.8). In 1982, an exposure of the lower mineralized horizon was found near the first (uphill) bend in the mine access track, which represents the easternmost outcrop of this band in Foss West. In the track section, a 30cm bed of cherty quartz celsian rock, with lenticular pyrrhotite and pyrite bands, is enclosed by graphitic schists with a 50cm bed of metabasite in direct contact with the chert on the north (stratigraphically lower) side. This sequence is similar to the intersection of the same horizon in BH9, some 120m further west, where, however, the chert bed is 6m thick (fig. 2.9). At the surface directly above the BH9 intersection, 60cm of barite rock occurs near to the stratigraphic base of the lower mineralized horizon, which is also underlain by barium-enriched metabasic rock

(~1% Ba: sample N81-81). Metabasite at the same stratigraphic horizon can be traced further west (fig. 2.8) and may be equivalent to that encountered in BH10, where three metabasite bands are interdigitated with the mineralization (fig. 2.9). The significance of this metabasite as a marker bed for the lower mineralized horizon is demonstrated in subsequent sections.

Two other, lenticular metabasite units occur within graphitic schists between the upper and lower mineralized horizons in the Creag an Chanaich area, and total at least 12m in thickness in the BH9 intersection (figs. 2.8, 2.9). These metabasite bodies diminish in thickness both laterally and down-dip, as illustrated by the previously published geological section (fig. 2.13a). A thin metabasite bed (apparently not recognized as such by Coats et al., 1981) was also intersected within graphitic schists near the base of BH2 (fig. 2.9) and in drillholes by Dresser Minerals in this area (fig. 2.14). This could be the lateral equivalent of the metabasite which underlies the lower mineralized horizon on Creag an Chanaich, but only a single mineralized band is present in the BH2 area (this is discussed further in part 2.3.4).

## 2.3 Sub-surface geology of the mineralized zone: Foss West.

### 2.3.1 General introduction.

Much of this account is based on over sixty drillhole (DH) intersections obtained by Dresser Minerals, which are equally divided between Foss East and Foss West. These are given three-digit numbers: the first digit identifies the series (of which there are six) and the next digits are chronologically consecutive drillhole numbers in each series (prefixes indicating year and drill type have been omitted). Drillhole locations are shown on horizontal and vertical projections (figs. 2.7, 2.8, 2.10 and 2.18).

Most intersections of the mineralized zone in Foss East have been relogged, using the portable XRF to identify cryptic barium enrichment and mineralization not recognised in the initial logging (data presented in figs. 2.23, 2.28, 2.30 and 2.33). Structural and lithological information obtained in this work, together with the locations of sampled intervals, are presented in Appendix A. Only a few drillholes from Foss West were relogged in detail, and much of

the information from this area is the unpublished work of company geologists (A R Burns, S J Laux and A M Boast). Drillhole information is presented in two forms: (i) as geological cross-sections for a selection of complete intersections (figs. 2.11-2.14, 2.20, 2.21, 2.24-2.27, 2.31 and 2.32); and (ii) as true vertical distance (TVD) profiles of the mineralized zone, in which the thickness of each lithological unit has been calculated directly from structural measurements, or derived from the geological cross-sections after removing the effects of fold repetition (figs. 2.15, 2.22, 2.23, 2.28, 2.30 and 2.33). Structural features observed in the mine adit are important to the interpretation of drillhole intersections, and are described in part 2.3.3. Structural-stratigraphical syntheses conclude each section, and section 2.5 presents an overview of the depositional and structural history.

### 2.3.2 Foss West drillhole intersections.

Figures 2.8 and 2.10 show that most drillhole trajectories in Foss West are arranged to form a series of coplanar cross-sections of the mineralized zone to depths of ~300m below the surface. All of the drillholes were collared to the south of the mineralized zone in the Ben Lawers Schist. Intersections of interest are described from east to west.

#### 2.3.2.1 DHs 406 and 407.

These were collared about 190m SSE of BH10 and intersect mineralization at elevations of 550-650m in the Meall Tairneachan area. DH 406 intersected an amphibolite bed about 20m above the unit C/unit B boundary, in a corresponding position to an amphibolite mapped at the surface (fig. 2.8). Beneath this boundary are three cherty quartz felsic bands 1-5m in thickness, enclosed by about 35m of graphitic schist which does not contain any metabasites (fig. 2.11). The lowest and thickest chert band is underlain by about 2m of barite rock, but the base of this bed (and the underlying metabasite?) is displaced out of the section by a low-angle fault. A similar stratigraphic sequence is seen in DH 419 (figs. 2.8, 2.10) in which three chert horizons were also intersected: the uppermost is close to the unit C/unit B boundary and the lowermost contains a central band of subgrade barite.

The upper two chert bands are absent from DH 407, due to down-dip non-continuity or to faulting near the unit C/unit B boundary (as in BH10A). The lower mineralized horizon is intersected twice due to folding (fig. 2.11). A fold nose in the lower intersection is indicated by structural features and the symmetrical repetition of lithologies (graphitic schist, a 20-40cm metabasite bed, quartz celtsian rock and a core of subgrade barite rock at least 50cm thick). However, the upper intersection is significantly different from the lower, in that neither barite nor metabasite are present and the cherts have a different appearance.

#### 2.3.2.2 DHs 404, 405, 417 and 429.

These intersections, together with surface information from trenching, span a 350m-length cross-section of the southerly-dipping mineralized zone (fig. 2.12). However, the drillholes are not sufficiently close-spaced to accurately locate the decimetric fold structures which are inferred from intersections further east (e.g. fig. 2.13). A further problem is that the first two drillholes were terminated within unit B schists and failed to intersect the lower mineralized horizon, which from surface information would be expected to occur 25-30m below the upper horizon. However, there is little evidence for this lower horizon in the two deeper intersections which penetrated unit A lithologies (fig. 2.12).

Barite rock is absent from the upper horizon at the surface in this section, but is present in significant amounts in all four drillhole intersections (thicknesses range from 2.3m in DH 405, to 7.5m in DH 429). In the upper two intersections, the mineralized horizon is separated from the unit C/unit B boundary by some 10m of graphitic and muscovitic schists, whereas this metasediment interval decreases abruptly in thickness to <1m in DH 417 and is absent in DH 429. Near the surface, unit B graphitic schists underlying the mineralized horizon are approximately 50m thick, but this interval decreases to about 25m in DH 417 and ~10m in DH 429, where a 10m thick metabasite bed (not present in DH 417) also occupies this zone (fig. 2.12). A 30cm bed of metabasite also occurs directly beneath the mineralized strata in DH 429. Sulphide, quartz and carbonate impurities are relatively more abundant in the barite intersection in DH 429, which is overlain by a 1.3m bed of calcareous, sulphidic cherts.

A very similar picture of down-dip variation is provided by the DH 418-423-428 coplanar section (located on figs. 2.8 & 2.10), except that here only 2.6m of barite was intersected at a similar elevation to DH 429, and the underlying metabasite is also thinner (1.3m rather than 10m).

### 2.3.2.3 BH9 and DHs 401, 402, 403 and 427.

The cross-section constructed with information from these drillholes has been published previously (fig. 2.13a). The flat-lying folds depicted between the BH9 and DH 401 intersections are projected from surface exposures on the steep eastern slopes of Creag an Chanaich, and DHs 401-403 constrain four box-shaped folds which throw the mineralized zone into tight corrugations lying within a fold envelope which dips south at  $55^\circ$  in this plane. Multiple intersections of the mineralization in DHs 401, 402 and 427 suggest that a second phase of folding about horizontal axes (such as seen on the eastern slopes of Creag an Chanaich and at BH2), is superimposed on earlier folds which have axial planes dipping steeply to the north. The deepest drillhole is particularly interesting because, as originally depicted (fig. 2.13a), the single barite horizon lies subparallel to the core and is intersected five times over a lateral distance of 45m, due to open folds with southerly-dipping axial planes. Over this interval, the barite progressively decreases in thickness from about 5m to 5cm. Since the barite grade remains unchanged through these repeated intersections (unpublished assay data), this pronounced decrease in thickness was attributed to structural attenuation rather than to a primary wedging-out of the barite layer (A.R. Burns, pers. comm. 1981). However, detailed logging of this interval (Appendix A) shows several significant differences between these mineralized intersections, notably the presence of a metabasite bed stratigraphically beneath quartz celsian cherts in only the two lowest intersections. An alternative structural-stratigraphical interpretation which invokes two separate horizons containing barite rock (the upper, 1.3-5m in thickness, the lower 5-10cm), is shown in figs. 2.13b and 2.15.

Apart from the likely presence of two mineralized horizons in DH 427, this profile is similar to the DH 429 profile (figs. 2.12, 2.15) in containing a thick metabasite bed (>4m) within a relatively

thin graphitic schist unit (<12m) between the mineralization and the unit B/unit A boundary. The thin, lower barite bed intersected in DH 427 is tentatively correlated with a 17cm barite band within quartz celsian cherts beneath the main barite bed in DH 429. Implicit in this correlation is the assumption that the intervening metasediments "wedge-out" between these intersections (this is discussed further in subsequent sections). The appearance of graphitic schists between the upper mineralized horizon and unit C, and an increase in unit B metasediment thickness with increasing elevation, are features seen in both cross-sections (figs. 2.12, 2.13). Although the lower mineralized horizon appears to be absent in DH 403 (as in DH 417), this chert horizon with its basal metabasite bed can be traced from the surface through BH9, DH 401 and DH 402. Both of the two thick metabasite lenses between the mineralized horizons become thinner with depth, and the lower unit appears to transgress to a position just above the lower chert horizon in DH 401 (Appendix A), below which it cannot be traced. This evidence supports the previous interpretation (Coats et al., 1981) that these metabasites were intrusive sills.

A fine-grained quartzite bed within unit C, which was intersected in DHs 403 and 427 (and also DHs 404, 429; fig. 2.13a), has been erroneously described by Willan and Coleman (1984) as quartz celsian chert. Since the rock in question does not contain any visible sulphide, and its barium content is below the detection limit of the portable XRF (probably <0.2%), the extension of the mineralized zone a further 100m into the Ben Lawers Schist, as proposed by these authors, is not justified. However, weak barium enrichment (~0.5%) was detected with the portable XRF in muscovitic quartzite containing galena and iron sulphides, at an inclined depth of 294m in DH 401 (Appendix A). This was previously considered to be the Ben Eagach Schist/Carn Mairg Quartzite boundary, but although quartzite is abundant in the intersection, it is fine-grained, frequently chloritic and garnetiferous, and does not resemble the pebbly orthoquartzites seen in surface exposures of the Carn Mairg Quartzite formation. Therefore, unit A metasediments are at least 120m thick in this part of Foss West, a thickness comparable to that in the Creagan Loch area (fig. 2.4).

#### 2.3.2.4 DHs 420, 421, 422 and 424.

This coplanar section (not illustrated) lies 100m to the east of the BH9 - DH 427 section, with which it is similar both in structure and stratigraphical variation. A 1m-thick bed of granular pyrite rock (containing minor sphalerite but no galena) directly underlies 3.8m of barite rock in the upper horizon intersected in DH 420. This pyrite bed can be correlated with exposures in the track section on Creag an Chanaich and in the adit (where it was sampled for an isotopic study by Willan and Coleman, 1983, fig. 13). Sulphidic cherts also occur beneath the barite bed in DHs 421 and 422. A 20cm interval of chert directly above the lower of the two metabasites intersected in DH 420 may represent the lower mineralized horizon, but this horizon was not encountered at greater depths. The mineralized zone in the deepest intersection, DH 424 (Appendix A and fig. 2.15), closely resembles that in DH 429, with only 80cm of metabasite and chert between unit C and the thick (5.8m) barite bed. The barite bed consists of alternating magnetite- and sulphide-bearing barite units and is underlain by 1.6m of sulphidic quartz celsian rocks with a basal, 15cm thick, metabasite bed. Another thin (55cm) metabasite occurs within the unit B metasediments, which total 11m in thickness.

#### 2.3.2.5 DHs 501, 502 and 425.

This cross-section is located immediately east of the Creag an Chanaich escarpment on a N-S line which passes the adit entrance (figs. 2.8 & 2.10 and plate 1). In DH 501, two dextral faults with displacements of about 10m result in repeated intersections of the barite bed which lies on a N-dipping fold limb some 35m in length. A thin metabasite bed underlies this mineralized horizon in DHs 501 and 502, but faulting has displaced the upper and lower boundaries of the barite bed intersected at depth in DH 425. Unit B metasediments beneath the mineralization are about 7-10m thick in the upper two intersections and 12-14m thick in DH 425, and there is no evidence for a discrete lower mineralized horizon (fig. 2.15). Amphibolite bands occur near to the top of unit C in all three intersections, and a thin, post-metamorphic basic dyke cuts the barite in DH 501.

#### 2.3.2.6 BH2 and DHs 415, 416, 507 and 508.

These intersections provide a relatively complete cross-section

of the mineralized zone (fig. 2.14). Again, multiple intersections of the barite bed in the shallowest drillhole (DH 415) constrain a N-dipping fold limb which lies below an extensive zone of flat-lying barite rock (140m across in this plane of section), the northern closure of which was pierced by BH2. A return to southerly dips is recorded by deeper intersections in DHs 416, 507 and 508, in which barite thicknesses are estimated at ~5m, ~8m and 1.6m respectively. An 8cm-thick metabasite layer was positively identified directly beneath the mineralized horizon in DH 507, but is not recorded in the other intersections (including BH2). However, a thin metabasite bed occurs within unit B sediments, 2-3m below the mineralization in BH2 and DHs 415 and 416, which could perhaps correlate with that in DH 507. Graphitic and muscovitic schists and an upper 'cherty' horizon (not assayed by Dresser Minerals) are recorded near the surface in DH 415, but graphitic schist above the barite does not persist to depths greater than 30m in this area. The DH 508 intersection is unusual for the paucity of chert (<30cm) mantling the barite, and the relatively greater thickness of the underlying unit B graphitic schists (~27m) compared with the other intersections (13m in DH 507, ~20m in DHs 415 and 416: figs. 2.15 and 2.16a).

Drillholes 507 and 508 also intersected a major shear zone dipping steeply to the south, probably at a low angle to the plane of section. These may represent the faults trending 010° which are indicated by the topographic linear at the base of the Creag an Chanaich escarpment. Extensive shearing is also seen in two mid-depth drillholes (412 and 413), 80m further to the east (figs. 2.8 & 2.10). The easternmost intersection of the mineralized zone west of the Frenich Burn Fault is provided by DH 414, where the upper horizon is represented by only 17cm of barite and a similar thickness of quartz felsian rock (Appendix A). Unit B metasediments in this intersection are 10.5m thick (fig. 2.15), and metabasite is absent. A deeper drillhole in this area (DH 426) intersected 15m of unit B lithologies with no mineralization, and no evidence of fault disruption at this level.



### 2.3.3 The Foss adit.

The adit entrance is at an elevation of 665m on the eastern flank of Creag an Chanaich (frontispiece), and when examined in May 1982, drift mining at this elevation had extended over 400m to the west. This exploration confirms the underground continuity of the upper barite horizon and the presence of westward-plunging fold pairs of the type interpreted from surface exposures and drillhole intersections, although the first such structure encountered (50-60m from the entrance) is smaller in amplitude than seen elsewhere. Minor (parasitic) F3 folds with near-vertical axial planes also plunge at 20-25° to the west (plate 32), together with bedding surface lineations and a rodding fabric seen in coarse barite rock (cf. plate 45). Gentle undulations about subhorizontal axial planes are attributed to the later phase of folding (?F4), and the barite is strongly jointed parallel to this plane.

Variation in the barite thickness (on average about 3.5m) may be largely attributed to attenuation associated with the F3 fold structures, in the vicinity of which thicknesses fluctuate between 2m and 5m over ten metre intervals. Pronounced thinning of the barite is observed in the structural equivalent to the upper, flat-lying fold limb exposed in the track section on Creag an Chanaich (fig. 2.8), where the barite thickness is reduced to 5cm at one point. At another location in the adit, the footwall pyrite horizon (now gossan) is extremely attenuated in the core of an inverted, isoclinal anticline of barite rock, which is itself attenuated in the associated synclinal structure (fig. 2.17). Near the western limit of the mine when examined, fold noses of siliceous chert are seen 'intruding' an attenuated barite bed, at which point banding in the barite is discordant to the chert/barite boundary (fig. 2.17).

The adit intersects many minor faults and three major shear zones, which displace the barite bed by between a few centimetres (plate 5) to at least ten metres. Most faults trend N-S to NE-SW, and sinistral displacements with downthrown eastern sides appear to be the most frequent. A major NE-trending fault zone some 330m from the adit entrance (north of the DH 418 collar: fig. 2.8) contains large (>3cm) euhedral barite crystals infilling cavities in a chert breccia, and prominent slickensides are seen in the adjacent barite

rock. The continuation of this fault in the footwall graphitic schists is marked by a thick, irregular quartz vein. A short southerly offshoot of the main adit midway between this point and the entrance, reveals a metre-thick zone of fault gouge along the Ben Eagach Schist - Ben Lawers Schist boundary, comparable to that seen in BH10A.

Stratigraphical orientation of the folded and faulted barite bed is facilitated by the presence of distinctive footwall and hanging wall lithologies. As previously noted, a pyrite horizon is characteristic of the stratigraphical base to the barite bed and attains a thickness of over 1m near the adit entrance. This is underlain by dark-coloured pyritic cherts and siliceous graphitic schists (plate 19) which are typically 1-2m thick. Overlying the barite bed are a similar thickness of cherty rocks, initially banded with barite lamellae and subsequently containing disseminated or laminated sulphides (plate 20). Two samples from this horizon (collected from locations >100m apart) have a breccia texture in which irregular rod- or plate-like fragments (1-20cm across) of a mid-grey coloured, siliceous chert are set in a matrix of lighter grey, cherty quartz-celsian rock which contains about 8% pyrite, minor carbonate and rutile (plates 17 & 18). This breccia-textured rock forms a discontinuous layer about 20cm thick, enclosed within undisturbed layers of similar rocks, and could either be of synsedimentary or tectonic origin (see part 3.2.4). The hanging wall cherts are overlain by graphitic schists or pyritic and siliceous graphitic rocks generally about 2m thick, followed by a variable thickness of pale green-coloured muscovite schists beneath the unit B/unit C boundary.

#### 2.3.4 Foss West: a lithostratigraphical synthesis.

The continuous exposure afforded by underground mining of the barite rock confirms the interpretation of sub-surface structures deduced from drillhole intersections, but also demonstrates that variations in lithological thickness between these intersections could reflect tectonic thickening and thinning in addition to primary (depositional) variations. In general, deformational attenuation is likely to account for thickness variations in closely-spaced, fold-repeated intersections of barite beds in

several drillholes such as 427 (fig. 2.13b) and 415 (fig. 2.14). However, the previous interpretation of extreme attenuation in the former (fig. 2.13a) may be incorrect if, as detailed logging suggests (Appendix A.13), there are two discrete mineralized horizons containing barite. It seems reasonable to expect that the fissile, graphitic schist host rocks have also suffered localized tectonic attenuation and thickening, particularly in the Creag an Chanaich area where the F3-F4 folding appears to have been more intensive than elsewhere.

Despite this structural overprint, stratigraphical thicknesses estimated from drillhole intersections in Foss West show consistent patterns of large-scale variations which are considered to be depositional in origin. An 'unfolded' isopach map of unit B graphitic and muscovite schist thickness (fig. 2.16a), which also shows the boundary between regions containing one or two mineralized horizons, suggests that the mineralized zone can be divided into two sectors. An eastern area near the surface, which extends laterally with depth (sector I), is characterized by relatively thin unit B metasediments (10-20m) with a single mineralized bed at the top (except in DH 427). This sector contains the thickest barite (up to 8m), but thicknesses are variable and decrease towards the eastern margin (DHs 412, 413, 414). The central, near-surface zone (sector II) is characterized by greater unit B thicknesses, reaching about 50m at the surface NE of Meall Tairneachan (fig. 2.8), and by the presence of two mineralized horizons, the upper of which contains barite with a fairly uniform thickness of 2-4m. Graphitic and muscovite schists, typically 2-5m thick, occur above the upper mineralized bed in this sector, and in adjacent areas beneath Creag an Chanaich (fig. 2.16a). The dividing line between the two sectors plunges to the west at 20°-30°, an angle which is similar to the regional structural plunge defined by both minor and major structural features (rodding lineations, F3 fold axes and the Creag na h-Iolaire Anticline). In both shallow and mid-depth intersections beneath Meall Tairneachan (BH10, DHs 406, 407 and 419), barite dies out and a third quartz celsian chert horizon appears between the upper and lower horizons (figs. 2.9 and 2.11).

Fig. 2.16b shows that total metabasite thickness within the mineralized zone is not related to the thickness of the unit B

metasediments, nor to the distribution of barite. Metabasites exceeding 1m in thickness are confined to the central part of Foss West, and only BHs 9 & 10 and DHs 427 & 429 intersected over 4m of metabasite. However, a thin (0.1-0.5m) metabasite layer is present directly beneath the lower mineralized horizon, or the single mineralized bed in sector I, in at least ten of the thirty-one intersections (and may have been mistaken for muscovite schist of pelitic origin in a similar number: fig. 2.16b). The equivalent metabasite bed was mapped at surface for a strike-length of about 500m (fig. 2.8). It is invariably enriched in potassium and barium (see chapter 5) and is considered to be eruptive (pyroclastic) rather than intrusive in origin because of its limited thickness but lateral extent at one particular time-horizon. Its significance as a marker bed for stratigraphic correlations in Foss East is discussed in the following section.

The correlation suggested in fig. 2.15 between the thin, lower mineralized horizon in DH 427 and the basal part of the single mineralized bed in DH 429, may be extended throughout the Foss West area on the basis of the underlying metabasite 'marker horizon'. It is suggested that the single mineralized horizon in sector I generally represents a composite bed formed from two discrete events of hydrothermal-exhalative activity (of unequal magnitude), which only formed two horizons in sector II where unit B sediments (now up to 30m thick) continued to accumulate in the intervening period. In this sector, the deposition of sediments now represented by graphitic and muscovite schists, also continued for some time after the upper mineralized horizon was formed. The absence of these overlying unit B lithologies in sector I could be due to (a) non-deposition until the start of Ben Lawers Schist (unit C) sedimentation, or (b) contemporaneous deposition of unit C lithologies here, implying that the unit B/unit C boundary is diachronous across the area.

The absence (where genuine) of the basal, eruptive metabasite layer may be attributed to sedimentary reworking, particularly in areas of slow deposition. This hypothesis may also account for the absence of the lower mineralized horizon in such areas, although exposures on Craig an Chanaich suggest that mineralization at this horizon diminishes eastwards and may therefore not have been

deposited to the east of this area. The westward-plunging boundary between sectors I and II could represent a former 'hinge zone' between relatively uplifted and down-sagging parts of the upper Ben Eagach Schist seafloor (fig. 2.35), and the particularly abrupt changes in unit B sediment and barite thicknesses in the vicinity of DHs 429 and 507 (fig. 2.16a) may indicate the former presence of growth faults. This palaeogeographic-stratigraphic reconstruction is discussed further in section 2.5 in the context of the entire Foss deposit area.

## 2.4 Sub-surface geology of the mineralized zone: Foss East.

Most drillhole intersections of the mineralized zone in Foss East (figs. 2.18, 2.19) are within 100m of the surface, with only seven intersections beneath 150m sub-surface. The intersections are divided into six groups on the basis of similar stratigraphical characteristics, and these are described in a general west to east order except for sector F, which comprises four of the deeper intersections (fig. 2.18).

### 2.4.1 The Frenich Burn area: shallow intersections.

This relatively small area, extending for about 80m to either side of the Frenich Burn East and to 50-100m below the surface, is of interest because of the exceptional thickness of barite rock. Barite about 16m in thickness outcrops in the stream bed and a similar thickness was proven in a shallow borehole drilled by IGS (BH1: Coats et al., 1981). Subsequently, Dresser Minerals completed two drillholes 70-85m in length (DHs 712 and 714), and an intensive shallow (~ 50m) drilling programme was undertaken by Aberdeen Barytes Company in 1982. Six of these intersections (DHs 101-106) were examined and sampled in this study.

The most significant features shown by these intersections (figs. 2.20 - 2.22) are evidence for syn-sedimentary reworking, and an eastwards and down-dip splitting of the single barite bed, initially into two bands, the lower of which then divides into three with increasing distance from the BH1 intersection. The three lower barite units can be distinguished in DHs 102, 104, 105, 712 and 714 (fig. 2.22), where they are separated by thin bands (2-90cm) of

finely foliated, quartz dolomite biotite schists which are geochemically comparable to unit C lithologies (chapter 4). In several places, these have a conglomeratic texture with folded, lenticular fragments of granoblastic dolomite rock and occasionally barite, set in a dark matrix subsequently shown to contain biotite, albite and hyalophane (plate 13). A 15cm band of this conglomeratic lithology also occurs within the BH1 barite intersection (plate 14) and was referred to by Coats et al. (1981) as a quartz-biotite schist with "laminations thrown into tight ptygmatic folds" (subsequent examination shows that it is rich in dolomite and celsian).

Conglomeratic and breccia textures of probable pre-metamorphic origin were also observed in the lower part of the composite barite unit and in basal 'cherts' intersected in DHs 105 and 106, and in barite rock near the top of the unit in DH 102. In these rocks, a matrix of darker coloured, sulphidic barite rock (with ~5% pyrite, 1% sphalerite) contain white, sulphide-poor 'clasts' of barite rock which have diffuse, annealed outlines (plates 11 & 12), and quartz chert fragments occur within calcareous or sulphidic quartz celsian rocks similar to those observed in the adit (plates 16-18). A small, constricted isoclinal fold nose of barite rock at the basal chert/barite rock boundary in DH 106 (plate 11), which contrasts with the parallel lithological banding elsewhere in this intersection, could be interpreted as a sedimentary load structure associated with the rapid deposition of barite precipitates and the overlying intraformational barite breccia. Highly complex and irregular folding (with opposite facing fold noses) of the basal chert/metabasite boundary in DH 102 (fig. 2.17) is also possibly of synsedimentary origin. Cross-cutting internal boundaries in banded barite rocks, and a few examples of unconformable contacts between coarsely conglomeratic metasediment and the overlying barite rock (plate 15), suggest that periods of erosion and sedimentary reworking occurred during the deposition of the composite barite bed.

The uppermost barite unit is separated from the lower group by an interval of unit C schists in DHs 102, 104 and 105, which rapidly increases in thickness from 0.8m to over 4m with decreasing elevation (fig. 2.20). At greater depths (fig. 2.24) and further to the east (fig. 2.21), graphitic and muscovite schists appear between the upper barite bed and the lower composite barite unit, and reach

a thickness of ~12m in DH 714 (Appendix A). Here, however, the upper barite bed is displaced out of the intersection by a steeply inclined fault (not recognized in previous logging). Two other drillholes in this area (DHs 103 and 106) were probably not extended sufficiently far to intersect this stratigraphically upper horizon.

Shearing and fracturing are particularly common in the vicinity of the Frenich Burn, and faulting subparallel to the core in DH 101 makes this intersection difficult to interpret. Both in surface exposures and in BH1, faulting has displaced the footwall cherts stratigraphically beneath the composite barite unit. In non-disrupted intersections (other than DH 104), these quartz celsian cherts are 0.7-1.4m thick and are separated from the underlying graphitic schists by a 10-50cm thick metabasite bed (plate 28). In DH 104 (fig. 2.22), a basal barite band is directly underlain by a 20cm bed of quartz-hyalophane rock containing evenly distributed carbonate spots (~25%) and pyrrhotite (~10%) (sample 104-45A; Appendix B). Chemical analyses (part 3.4.2) confirm that this represents metabasic material which has been impregnated with barium, which supports the contention that this thin and laterally extensive metabasite layer was formed as a pyroclastic deposit immediately preceding the emanation of hydrothermal fluids (part 5.4.3). Metabasite is not present at any other stratigraphic horizon in this area.

#### 2.4.2 The Frenich Burn area: deep intersections and the upper mineralized zone.

In part 2.2.3, the occurrence was noted of calcareous graphitic schists and interbanded quartz celsian cherts to the south of the barite bed at BH1, and separated from it by about 70m of unit C schists (fig. 2.7). Despite contrary evidence from the pattern of barium enrichment in deep overburden samples from Foss East (fig. 2.6), Coats et al. (1981) correlated this upper mineralized band with the upper quartz celsian chert bed seen at Creagan Loch. Subsequent exploration by Dresser Minerals has shown this correlation to be incorrect, as the composite barite bed at BH1 splits into four horizons each of which can be traced eastwards across central Foss East (in drillhole intersections described in the following section, and in track exposures mentioned in part 2.2.3),

to the Creagan Loch area. Detailed relogging of the BH11 core and of three other deep drillhole intersections in the Frenich Burn area (DHs 408, 203 and 207: fig. 2.23 and Appendix A), revealed features which suggest that the upper band of graphitic schist with cherts actually represents a fault-repetition of the same mineralized zone which is intersected again at depth.

#### 2.4.2.1 BH11 and DH 408.

The lower mineralized zone in BH11, intersected at depths of 70-90m below the surface exposures in Frenich Burn West, consists of five bands of quartz celsian rock totalling 12m in thickness, plus 2m of barite rock which is mostly contained in the basal horizon (figs. 2.23, 2.24). These bands are separated by a similar thickness of graphitic schists, muscovite schist, quartzite and calcareous mica schist. Garnetiferous lithologies characteristic of unit A occur from about 8.5m beneath the basal horizon, which directly overlies a very thin layer (2cm) of quartz dolomite muscovite schist containing pyrrhotite and rutile. Compositional and textural features noted in microscopic examination of this lithology, indicate that it is probably metabasic in origin (see part 5.2.4), allowing correlation with the footwall metabasite noted in near-surface intersections. The same thin metabasite layer is present in a second drillhole (DH 408) which intersects the lower mineralized zone 12-15m beneath BH11 (fig. 2.24). Here, however, the top of the basal barite bed is truncated by faults, and the metasedimentary lithologies between the succeeding chert bands are different from those in BH11 (fig. 2.23).

Several shears were also recorded by Coats et al. (1981) in the BH11 intersection, within both the lower and the upper mineralized zones. The most prominent shear plane (at 21.85m inclined depth) places unit D schists against the top of the upper mineralized zone. This zone comprises two quartz celsian chert bands (again totalling 12m) underlain by ~28m of graphitic schists, quartzite and calcareous mica schist, with two intervals of barium-enriched (<4%) muscovite schist (fig. 2.23). Barium contents decrease abruptly in sheared unit C schists beneath the lower muscovite schist band, which has a 50cm basal layer described in IGS logs as 'calcareous biotite-quartz schist' (Coats et al., 1981). A partial analysis





shows high contents of  $\text{TiO}_2$  (1.4%) and  $\text{Fe}_2\text{O}_3$  (10.2%) (CYD 766: table 5.3), and on the basis of petrographical and chemical criteria discussed in section 3.4, this rock is considered to be metabasic in origin. A similar lithology, ranging in thickness from 5–10cm, was logged at the base of the upper mineralized zone intersected in DHs 408, 203 and 207 (fig. 2.23 and Appendix A), and a full XRF analysis confirms its metabasaltic affinities (sample 207-5; tables 5.1 and 5.2).

#### 2.4.2.2 Other intersections of the upper zone.

In the two western intersections of the upper mineralized zone (DHs 203 and 207: figs. 2.19, 2.23), this also consists of four bands of quartz celsian rock or barium-enriched muscovite schist, interbedded with unit B and unit C metasediments including quartzites and graphitic dolomite rocks. This assemblage is over 40m thick in BH11, but reduces to about 18m in DH 203 and 14m in DH 207 as both the mineralized and metasedimentary units become thinner. In all intersections, the zone is bounded by shear planes which are interpreted as major, subvertical, ENE-trending faults which parallel the steeply inclined strata (fig. 2.24). Subsidiary faults result in omissions and duplications of the sequence, for instance in DH 207 where the basal chert horizon is intersected twice (fig. 2.19). A deep drillhole (DH 409) from the same collar as DH 408, intersected a narrow, fault-bounded mineralized zone containing only two chert horizons, which suggests that the major faults transgress the stratigraphical sequence and converge with depth.

Nearly 200m east of BH11, the upper mineralized zone is again intersected in DH 410 (figs. 2.19, 2.28 and Appendix A). Here, at 30–40m below the surface, the 5m thick zone consists of two bands of quartz celsian chert and barium muscovite schist, which are underlain by barium-enriched unit C schists enclosing a 12cm layer of biotitic metabasite rock (sample 410-4B: tables 5.1 and 5.2). This horizon conformably overlies about 20m of unit C schists, which are separated from the lower mineralized zone by a gossanous shear zone. Mid-way between this intersection and BH11, an upper mineralized zone was not intersected in DH 701, but there is evidence for two major faults, one of which is again directly above the lower mineralized zone. Here, a calcite-cemented fault breccia contains fragments of graphitic schist, which suggests a large displacement

since no comparable lithology occurs in the adjoining lithological succession (Appendix A).

The conclusion that the upper mineralized zone in western Foss East represents a fault repetition of the main (lower) zone, is based on (i) correlation of the metabasite marker bed beneath the lowest mineralized horizon in each zone, (ii) the general similarity between the upper and lower zones in their lithological components and thicknesses (although in detail, lateral variations are rapid as illustrated by BH11 and DH 408), and (iii) the presence of shear zones marking major ENE-trending faults which bound the upper zone.

Of equal interest are the differences between the two zones. In the upper zone, barite is absent and the lowest horizon is represented only by barium-enriched muscovite schists, which are enclosed within unit C calcareous mica schists. No graphitic schist occurs between the metabasite marker and the faults which separate the upper and lower zones. This occurrence of unit C lithologies beneath the lower mineralized horizon appears to be unique in the Aberfeldy deposits. Another significant difference is the markedly lower base metal content of the upper zone mineralization and enclosing metasediments (Coats et al., 1981, Appendix II, Table XI). These features suggest that the upper zone represents a part of the deposit which was more distal from the exhalative centres, and perhaps formed in a more oxidizing environment (indicated by the high carbonate content and low reduced carbon and sulphide contents). Considering the increase in barite thickness and coalescence of the mineralized horizons with increasing elevation in the French Burn area, it is postulated that the upper zone was upfaulted to its present position by near-vertical faults with displacements of at least 90m (the depth of the BH11 lower zone intersection).

#### 2.4.2.3 DHs 203 and 207.

The previous discussion omitted reference to lower mineralized zone intersections in DHs 203 and 207 (figs. 2.19, 2.23). The absence of the metabasite marker bed in both intersections reduces the confidence attached to stratigraphic correlations, particularly as only three mineralized horizons occur in this zone in DH 203. Here, over 9m of barite rock occurs in the lowest horizon at an elevation of approximately 500m, similar to that of the BH11 intersection 120m to the east. This suggests that the thick barite

present near the surface at Frenich Burn and further east, forms a wedge-shaped volume deepening to the west in the direction of the structural plunge. The base of this bed is 13m above the unit B/unit A boundary, and the presence of a thin barite band in the third horizon (labelled M5 for reasons explained in the following section), supports the correlation with the BH11 profile shown in fig. 2.23. In a much deeper intersection, unit B lithologies at least 24m thick were not bottomed at an elevation of 300m in DH 207, where the lowest horizon consists of a thin (15-85cm) quartz celsian chert band intersected twice due to folding (fig. 2.19 and Appendix A). The down-dip transition in the lower mineralized horizon from thick to thin barite rock, then to quartz celsian cherts and finally to barian muscovite schists, is a consistent feature seen throughout Foss East, and is illustrated further in the following sections.

#### 2.4.3 Central Foss East.

This section is concerned with 450m of strike-length in which the mineralized zone was intersected within 100m of the surface by eight drillholes: 715, 701, 410, 702, 504, 704, 703 and 503 (figs. 2.18, 2.19). Two of the three geological cross-sections provided (figs. 2.25-2.27) incorporate information from deeper intersections (DHs 601 and 201), which are considered in more detail in part 2.4.5. Fig. 2.28 shows TVD sections of the mineralized zone in five of the drillholes. These were constructed from detailed structural, lithological and portable XRF logs of the core preserved for examination (Appendix A).

The cross-sections and TVD profiles show that the mineralized zone in this area is about 50m thick and contains four distinct mineralized horizons, of which three are laterally persistent, as previously noted from surface exposures (part 2.2.3). The lower horizon contains 0.2-3.5m of barite rock sandwiched by quartz celsian and carbonate rocks (detailed TVD sections are shown in fig. 2.29). This horizon is again characterized by a 8-50cm thick, basal metabasite bed (absent in DH 410 due to faulting), and is situated 5-12m above the unit A/unit B boundary. The upper three horizons, or two horizons in the east of the area, are usually separated by 1-7m of unit C schists which also extend above the mineralized zone. The interval of unit B lithologies between the lower horizon and the

upper group appears to show large differences in thickness between closely-spaced intersections (e.g. 17m in DH 715, 6m in DH 701: fig. 2.28).

#### 2.4.3.1 Folding.

As far as possible, the effects of repetitions of the stratigraphic succession due to small-scale, tight or isoclinal folding have been removed in constructing the TVD profiles in figures 2.28 and 2.29. This fold repetition is readily discerned in the distinctive, heterogeneous mineralized lithologies of the third mineralized horizon in DH 701 (labelled M6, as explained below), and in all four horizons in DH 702 (figs. 2.26, 2.28 and Appendix A). However, much of the intervening metasediment consists of monotonous fissile graphitic schists (unit B) and calcareous mica schists (unit C) in which evidence of bedding is sparse and isoclinal folds may not have been recognized. Such folding, and attenuation through strain-slip movements, could account for some of the large differences in metasediment thickness between the mineralized horizons noted above.

Attenuation associated with the relatively large isoclinal fold pair which accounts for a treble intersection of the basal cherts of the lower horizon cherts in DH 702 (fig. 2.26), is manifested by thickness changes between each intersection (110cm in the top intersection, 70-80cm in the lower pair), and by boudinage in a 2cm-thick dolomite band within the barite rock (plate 9). Banding in the barite rock also shows curvature for 3-8cm on either side of a high-angle fault, which appears to have been annealed and therefore may pre-date the thermal maximum (plate 10). This fault results in about 1m of stratigraphical displacement and is interpreted as a coeval structure which accommodated the contrasting competencies between barite rock, cherts and enclosing pelitic schists during deformation. Isoclinal folding and faulting also disrupt the lower horizon in DH 504, 110m to the east. The absence of distinctive lithologies and poor core condition (possibly transposed during assay sampling), preclude a confident interpretation of this intersection (fig. 2.29). Note that faulting may have substantially reduced the thickness of both the lower and uppermost mineralized horizons intersected in DH 701 (figs. 2.28, 2.29).

#### 2.4.3.2 Continuity of the upper horizons.

Dresser Minerals' geologists were not able to follow the upper set of mineralized horizons between DH 702 and the Creagan Loch area, and did not recognise any mineralization in DH 503 (fig. 2.18). Regrettably, core from the relevant part of the DH 504 intersection was discarded, but nearby surface exposures (fig. 2.7) indicate continuity of the two horizons of barium enrichment, which were also located during relogging of DHs 703, 704 and 503 using the portable XRF analyser (figs. 2.28 and 2.30). DH 703 was collared directly above the lower of these two horizons, which consist of quartzitic rocks with a schistose fabric, containing barian muscovite, biotite and/or carbonates in addition to celsian, cymrite and pyrrhotite, but only traces of base metal sulphides. Subsequent analytical work confirms that these lithologies are of mixed hydrothermal-sedimentary origin and contain 2-10% BaO (part 3.4.2).

#### 2.4.3.3 DH 503.

With the aid of the portable XRF, two lower horizons of barium enrichment were located in the lower third of the unusually thin (~30m) mineralized zone in DH 503. Both bands consist mostly of muscovite schist and quartz dolomite muscovite schist, but a 90cm interval of calcareous celsian rock (green in colour due to chloritic alteration) occurs at the top of the upper band. This is terminated abruptly by a 90cm interval of fault breccia which is overlain by graphitic schists lacking any discernable barium enrichment (fig. 2.30). Between the fault zone and the upper barium-enriched horizons are a variety of interlayered lithologies including garnetiferous and chloritic graphitic schists and quartzites, and several thin metabasite bands. These lithologies are absent from the mineralized zone further west, but are developed extensively east of DH 503 (fig. 2.30) where the total thickness of the zone is much greater (>60m: see following section). It is therefore suggested that a significant change in the sedimentary succession occurs in the vicinity of DH 503, and that post-metamorphic fault displacements have removed part of the succession from this intersection. This contention is supported by evidence that the celsian band beneath the fault breccia in DH 503 does not correlate with the 'lower mineralized horizon' described previously from Foss East, but represents one of two stratigraphically earlier

horizons of limited lateral extent. A NNW-trending fault with a dextral displacement and/or a downthrow to the NE (of the order of 20m) can account for the absence of the 'lower mineralized horizon' in DH 503 and in the surface exposures nearby (figs. 2.3, 2.7).

#### 2.4.3.4 Correlation of M1-M7.

Portable XRF logging located one or two thin (<1m) bands of quartz celsian rock and barian muscovite schist lying stratigraphically below the main 'lower' horizon (with its metabasite marker bed) in five other drillholes in central Foss East. The lowermost mineralized horizon, designated 'M1', is represented by 60-70cm of celsian rock in DHs 703 and 704 and 10cm of celsian-bearing rock in DH 504, but by only barian muscovite schist about 100m further east and west of these intersections (fig. 2.28). The second horizon of celsian rock ('M2') does not exceed 30cm in thickness, which is developed towards the east in DHs 503 and 505 (fig. 2.30). Both horizons appear to be absent from DH 705, which did not penetrate the unit B/unit A boundary beneath the main lower horizon (fig. 2.31), and in DH 505 a much greater interval of graphitic schist (15-20m) separates the two horizons of barium enrichment than in the other drillholes (generally <3m). The significance of these features is discussed in part 2.4.6.

The distinctive metabasite marker bed beneath the main 'lower' mineralized horizon (henceforth designated 'M3') allows correlation with the succession in the Frenich Burn area, where in deeper intersections, four subsequent mineralized horizons ('M4'-'M7') were identified (fig. 2.23). However, both in shallow intersections in the Frenich Burn area, and in central Foss East, only three (or locally two) horizons occur above M3. These horizons cannot be confidently correlated with those in the Frenich Burn deep intersections because of the absence of other marker beds. In the scheme adopted (figs. 2.19, 2.28, 2.30), mineralization corresponding to the M4 horizon is regarded as absent in central Foss East, but its position may be marked by a band of weak barium enrichment in metasediments beneath the upper horizons (M5-M7), detected in deeper intersections (DHs 201, 601: fig. 2.33) and in the Creagan Loch area (DHs 505, 506 and 705). However, considering the limited extent of M1 and M2, more than one horizon of laterally impersistent barium enrichment is likely to be present between 'M3' and 'M5'. Therefore,

seven is regarded as the minimum number of such horizons in Foss East. The wider correlation of these horizons and the significance of major stratigraphical differences between western and central Foss East, are discussed in sections 2.4.6 and 10.3.

#### 2.4.4 The Creagan Loch area.

Surface exposures of the mineralized zone in this area, which extends for about 300m east of DH 503, were described in part 2.2.3. In that section, the diversity of both metasedimentary and mineralized rock types and the presence of more than one metabasite band was noted, and evidence for several major N-S faults was discussed. These faults divide the area into two blocks of unequal strike-length. The western block was penetrated by BH3, DH 503 (described above) and DHs 505, 705, 506 and 202, of which the last two are relatively deep intersections (fig. 2.19). DH 706 penetrates the upper part of the mineralized zone in the eastern block, but several shear zones were encountered at greater depths and the lower mineralized horizon (M3) is either displaced out of the section by faulting (fig. 2.32), or drilling was terminated before this bed was reached. The M3 horizon is intersected by DH 707 at a higher elevation and a short distance east from its anticipated position in DH 706, but in DH 707 the characteristics of both the mineralization and the metasedimentary succession differ from those of the western block, as described below. Another partial intersection of the mineralized zone in this block is provided by DH 708, which unlike most other drillholes in the area, was collared north of the zone in unit A lithologies (figs. 2.7, 2.32). A deep intersection (DH 204) shows the presence of only one horizon (at the unit C/unit B boundary), and other deep drillholes which penetrated the Creagan Loch Faults (DHs 602 and 205: fig. 2.7 and 2.18) failed to locate any mineralization.

##### 2.4.4.1 Metasedimentary succession in the western block.

The upper parts of the mineralized zone intersected 100m apart in DHs 503 and 705 are very similar (fig. 2.30). In both intersections, an unusually thick bed (3-4m) of dark grey, graphitic dolomite rock containing 5% pyrrhotite and minor sphalerite in thin, folded lamellae, occurs directly beneath a similar thickness of beige and pale green coloured, celsian-bearing quartz mica schists

(Appendix A). In DH 705, a stratigraphically higher band of similar barium-enriched schists is interbedded with unit C calcareous mica schists, and the graphitic dolomite rock is repeatedly intersected due to small folds with S-dipping axial planes (fig. 2.31). Beneath this carbonate bed, weak barium enrichment also occurs in quartz muscovite schists enclosing another thin celsian-bearing band (equated with M4; fig. 2.30). This is underlain by alternating thin beds of chloritic metabasite, graphitic schist, quartzitic graphitic schists with chlorite (identical to unit A lithologies), graphitic dolomite rock and either calcareous or sulphide-banded quartzites. Two 10-50cm thick beds of coarse-grained, feldspathic quartzites, similar to those of the Carn Mairg Quartzite formation except for the enrichment in Zn and Pb, are repeatedly intersected in DHs 705 and 202 due to folding (fig. 2.31). A similar sequence is seen in DHs 505 and 506, although the upper mineralization is extremely thin in the former and unusually thick in the latter (fig. 2.30 and Appendix A). Unfortunately DH 506 terminated prematurely before reaching the M3 horizon.

A striking difference between DH 705 and DH 505 (which intersects the mineralized zone about further 50m east and a similar distance down-dip), is the considerable increase in thickness of the metasediments between M3 and M5, which are estimated at 44m and 84m respectively (fig. 2.30). This eastward-thickening trend appears to be supported by the thin intersection in DH 503, but as previously noted, an unknown interval including the M3 horizon is absent from DH 503 due to a fault displacement. The thickness of the unit B graphitic schist interval beneath the M3 horizon is also greatly increased in DH 705 (>25m: unit A lithologies were not reached) and DH 505 (estimated at 27m), in comparison with central and western parts of Foss East (range, 5-13m). Sufficient information on bedding orientations is present to argue against extensive fold-thickening in both intersections (fig. 2.31 and Appendix A), particularly as no repeat intersections of the M1 and M2 horizons occur in DH 505 (note the absence of these bands of barium enrichment in DH 705). A genuine increase in stratigraphic thickness is also supported by information from BH3 and nearby surface exposures, about 100m east of DH 705. BH3 intersected unit B graphitic schists at least 14m thick stratigraphically below the M3 horizon, and the



across-strike distance to the unit B/unit A boundary in surface outcrop is about 23m (fig. 2.7). However, the interval of unit B schists beneath the distal equivalent to the M3 horizon in DH 202, about 200m below the surface, is reduced to <5m (figs. 2.31, 2.33).

#### 2.4.4.2 Components of the M3 horizon and lateral variations.

The progressive westward decrease in thickness and disappearance of barite rock in the lower (M3) horizon in surface exposures at Creagan Loch was described in part 2.2.3. However, 50m below the surface near track exposures where barite is absent, DH 705 intersected two bands of barite rock totalling 1.8m, enclosing a 1.2m-thick bed of massive, coarsely crystalline pyrite rock. The barite is sandwiched by 2m of quartz celsian cherts (figs. 2.29 and 2.31). A 3.0m bed of barite rock, partly sulphidic and sub-grade, was also intersected by DH 505 nearly 100m below the surface further to the east (fig. 2.19). Although thin beds of mineralized carbonate rock occur in both intersections, the extensive development (>4m) of this lithology below the barite rock seen in surface exposures and BH3 (fig. 2.29), is absent at depth. Clearly, pronounced lateral changes occur in the nature and thickness of both the mineralization and the metasediments in this area.

An unusual, banded quartz sulphide manganoan-calcite rock, containing about 10% pyrite and 5% each of sphalerite and galena, forms 10-14cm layers which occur both above and below the massive pyrite bed in DH 705 (Appendix A). This repetition of similar lithologies cannot be explained by folding despite the low core-to-bedding angles observed in this intersection. The low-angle intersection reveals at least two discordant lithological boundaries which are oblique to the bedding (plates 24 and 25), although the drillcore is continuous with no evidence of post-metamorphic fracturing. Thin section examination of the lower discordant junction between sulphidic carbonate rock and the underlying, magnetite-bearing barite rock, shows the boundary to be slightly diffuse (over 1-2mm) with small barite inclusions in 1-2mm pyrite metablasts near the contact. This is interpreted as an annealed fault, and it is speculated that these discordant junctions could represent syn-depositional displacements associated with formation of the massive pyrite rock.

This pyrite bed occupies an unusual stratigraphical position

compared with other massive sulphide beds at Foss, which are normally located at or near the base of mineralized horizons such as in the adit and DH 701 (fig. 2.29). The sulphide bed in DH 705 is also compositionally unusual in that sphalerite is subordinate to galena, which occurs as coarsely crystalline patches averaging about 2% over the interval. This is reflected in exceptionally high Pb/Zn ratios, which are also high ( $>1$ ) in the mantling sulphidic carbonate rock, and in impure barite rock in the upper part of the DH 505 intersection (assay data of Dresser Minerals: see fig. 3.8). Possible evidence for syn-depositional disruption, in the form of fragmental textures, is also noted at this stratigraphic horizon in DH 505 (Appendix A) and in the basal carbonate rock in BH3 (Coats et al., 1981) (fig. 2.29). Attention is also drawn to the position of the thin footwall metabasite marker bed, which is within rather than beneath the basal part of the mineralization in these intersections (fig. 2.29). Taken together, these stratigraphical, textural and chemical features are considered to indicate a proximal setting with respect to the sites of hydrothermal exhalation, and it is suggested that the massive pyrite rock in DH 705 could have been a sulphide "chimney" from which some of the hydrothermal fluids debouched.

#### 2.4.4.3 The eastern block.

Bands of massive sulphide rock, typically consisting of similar amounts of sphalerite and pyrite with minor galena, are a common constituent of the 7-9m thick M3 horizon intersected in DHs 707 and 708 (fig. 2.29). A very thin ( $<10\text{cm}$ ) layer of barite rock occurs together with sulphidic carbonate rock near the top of the horizon in both intersections, in which sulphidic and cherty quartz celsian rocks predominate. Quartz dolomite barian-muscovite schists, about 2m thick, separate the base of these cherts from the thin (4cm) metabasite marker bed in DH 707. Hyalophane (K-Ba-feldspar)-bearing quartz muscovite schists, 0.7m thick, occupy a similar position in DH 708 where the basal metabasite is over 20cm thick (Appendix A). The components of the M3 horizon are therefore similar in these intersections, but the paucity of barite and carbonate rocks and the abundance of incorporated sedimentary material and of base metal sulphides (up to 12% Zn+Pb in DH 708), contrasts with the western block described above. Other geochemical and isotopic evidence for major differences in the mineralization between these blocks is

discussed in chapters 3 and 9.

Further indications that the mineralized zone in the eastern block was not originally contiguous with that further west, are derived from differences in the metasedimentary successions. The most notable differences are the reversion to 'normal' thicknesses (4-8m) of unit B graphitic schists beneath the M3 horizon in the eastern block, and the abundance of quartzites (both garnetiferous and sulphide-banded varieties) interbanded with graphitic schists stratigraphically above this horizon (figs. 2.32, 2.34). A thick (3.3m) chloritic metabasite bed with overlying garnetiferous quartzites was intersected a short distance stratigraphically above the M3 horizon in DH 708, and may correlated with a similar unit (4.7m thick) in DH 706 (fig. 2.32), but this metabasite is absent from the DH 707 intersection, possibly due to fault displacement. Two distinct bands of barium enrichment occur in the upper part of the mineralized zone intersected by DH 706 and mapped in surface exposures (figs. 2.34, 2.7). Combining the incomplete information from outcrop and drillhole intersections in this block (figs. 2.18, 2.32) allows the thickness of the mineralized zone to be estimated at 80-85m (cf. 110m in DH 505).

Drillhole 204 intersected a single horizon of quartz muscovite celsian schists on the unit C/unit B boundary approximately 160m below the surface in this area (figs. 2.19, 2.32). No other barium enrichment was detected with the portable XRF in the underlying succession of alternating unit B graphitic schists and unit A quartzitic graphitic schists and garnet dolomite mica quartzites, which total at least 100m (Appendix A). The drillhole terminated in a major shear zone, which if correlated with shear zones at a lower elevation in DH 602 and near the surface in DH 710 (fig. 2.18), would indicate a N-S fault plane dipping at 79°W (A.M. Boast, pers. comm. 1981). Both DH 602 and DH 205 (another deep drillhole 110m further east) failed to intersect mineralization in the Ben Eagach Schist east of the aforementioned fault, and demonstrate that a ~50m sinistral displacement is accompanied by lithostratigraphic changes suggesting a significant vertical component. These results are consistent with the absence of mineralization and unit B-type graphitic schists in the moderately well-exposed ground between the

valley of Lochan Lairig Laoigh and Farragon Hill, which was briefly examined during field mapping (see also Willan, 1981).

#### 2.4.5 Deep intersections in central Foss East.

Drillholes 202, 201, 411 and 601 intersect the mineralized zone (incompletely in DH 411) over a 600m strike-length at progressively lower elevations to the west (fig. 2.19). Despite the large separation between these intersections, they present similar lithostratigraphic profiles (fig. 2.33) with thick intervals of chloritic and garnetiferous graphitic schists and quartzites occurring between the upper group of carbonate- and sulphide-rich mineralized horizons, and the lower (M3) horizon, which is thin and weakly developed. The deepest intersection of M3 in Foss East, at an elevation of 280m in DH 601 (fig. 2.19), comprises 50cm of quartz dolomite barian-muscovite schist with 20cm of quartz celsian rock and banded quartz pyrrhotite dolomite rock. This overlies 8cm of muscovitic metabasite and at least 1m of siliceous graphitic schist (Appendix A). Portable XRF logging of the core from DHs 201 and 202 located zones of weak barium enrichment (up to 1.2% in sample 202-R: tables 4.1, 4.2) in pelitic metasediments directly above a thin metabasite layer (4cm and 12cm respectively) at a stratigraphic position corresponding to the M3 horizon (fig. 2.33).

Three discrete 'upper' horizons were intersected in DHs 411 and 601 (M5-M7: fig. 2.33), of which the uppermost quartz celsian chert bed is the least thick (10-20cm). The 5.4->6m thick M6 horizon consists of calcareous and sulphidic quartz cherts and massive dolomite rocks, both of which contain minor celsian (<10%). These lithologies often exhibit breccia textures (cf. plates 22, 31) attributed to tectonic disruption of alternating quartz and dolomite layers, and to the remobilization of sulphides (average about 5% sphalerite + galena, 2-10% pyrrhotite with subordinate pyrite). The M5 horizon is similar in thickness but is of contrasting appearance and composition, with a higher celsian content, much less sphalerite and galena, and pyrite as the dominant iron sulphide (~5%). Talc was identified in this horizon in DHs 411, 601 and 201 and is occasionally a major constituent of breccia-textured rocks in which talc and celsian form a schistose matrix to 1-5cm diameter fragments

of granular dolomite rock and quartzose chert (plate 23). In DH 201, lithologies characteristic of the M6 horizon are stacked directly above those of the M5 horizon, whereas in DHs 601 and 411, 3m and 8m of intervening graphitic muscovite and dolomite schists are present (fig. 2.33). The distribution of celsian and sulphides in the single mineralized bed in DHs 202 and 506 also suggests that this is a composite horizon (Appendix A).

Above the M6 horizon in DHs 201, 202 and 506, several thin (5-20cm) bands of dark brown coloured, quartz biotite cymrite schists occur within barium-enriched calcareous quartz mica schists. Similar biotite cymrite schists are also found at this stratigraphical position in DHs 410, 706 and 204 (Appendix A), and geochemical analyses demonstrate that this lithology is of mixed hydrothermal-sedimentary origin (part 3.4.2).

A diffuse interval of barium enrichment associated with muscovite schists was also detected some distance below the M5 horizon in DHs 601, 201 and 202 (fig. 2.33). In DH 601, this interval overlies barium-poor garnetiferous quartzites and chloritic graphitic schists which extend to 6.5m beneath the M5 horizon, whereas the possible equivalent in DH 202 underlies similar lithologies. If this 'M4' correlation is correct, this indicates that the thicker sequence of garnetiferous quartzite and graphitic schist in the DH 202 intersection was largely deposited between the M4 and M5 time-horizons (see fig. 2.31). Between this area and DH 601, a garnet- and chlorite-bearing quartz mica schist located about 10m below M5 in DH 201, was found to be barium-enriched (2.1% BaO in sample 201-K: Appendix B and table 4.2). Together with one sample of garnetiferous graphitic schist collected from outcrop in Foss West (G13: fig. 2.2) which contains 0.5% BaO, these are the only recorded occurrences of barium-enrichment in garnetiferous lithologies at Foss (cf. part 2.2.1 and table 2.1).

#### 2.4.6 Foss East: a lithostratigraphical synthesis.

The more expansive description of Foss East than of Foss West partly reflects a more detailed examination of this area, but is also necessitated by the diversity of lithostratigraphical features exhibited by this part of the deposit. Although the effects of folding are more localized and generally on a smaller scale than in

Foss West, several major faults are shown to have juxtaposed blocks of the mineralized zone which are unlikely to have been contiguous during deposition. Since the foregoing account has been subdivided partly on the basis of these natural discontinuities, it is pertinent to emphasize here both the similarities and the major differences between these structural blocks.

#### 2.4.6.1 Thickness of metasediments between mineralized horizons.

At least three discrete horizons of barium enrichment are seen throughout Foss East (except in DH 204), and seven such horizons can be correlated although not more than five occur in any one intersection (fig. 2.19). At the surface and in shallow intersections in the Frenich Burn area, the thick barite bed splits laterally into four discrete bands. However, the lower three remain closely associated and are separated only by thin layers (<1m) of metasediment, whereas the interval of metasediment between this group and the upper horizon increases rapidly in thickness to over 20m (fig. 2.21). A radical change must occur in the 30m strike-length between DHs 103-104 and DHs 106-715-701 (figs. 2.19, 2.24 and 2.25), east of which the pattern characteristic of much of Foss East is established, namely with an upper group of horizons isolated from the lower horizon by a relatively large interval of metasediments (fig. 2.34).

The thickness of this interval of unit B metasediments above M3 is, however, highly variable in closely-spaced drillholes in this part of central Foss East (6-40m: fig. 2.28). Unusually, unit B lithologies also occur above M5 in this area (DHs 702, 411 and 601: figs. 2.28 and 2.33), in place of the unit C calcareous mica schists which more frequently overlie this horizon. Therefore, rapid lateral facies and thickness changes perhaps associated with syndepositional faulting could account for the radical change in lithostratigraphy noted above. However, evidence for the presence of post-metamorphic faults which may provide a more plausible explanation, is seen in the vicinity of DH 106 where a deflection in the strike of the barite rock was observed in trench exposures adjoining an area of very deep overburden (>7m). Several faults with unknown displacements were intersected in DHs 715, 701 and 601 (fig. 2.25).

The lithostratigraphic sequence near the surface in the Frenich Burn area is also different to that intersected at depth in BH11 and DH 408, where five equally-spaced mineralized horizons (M3-M7) are

interlayered with a similar volume of metasediment (figs. 2.23 and 2.24). As described in part 2.4.2, the 'upper mineralized zone' intersected by these and other drillholes in this area, probably represents an upfaulted block containing a more distal equivalent of the same ('lower') mineralized zone present to the north and intersected at depth. Considering the close spacing of drillholes it is difficult to envisage another major shear zone separating the 'lower' zone intersections in BH11 - DH 408 from those in BH1 - DHs 712, 714 (fig. 2.24), unless perhaps the displacement of the M7 barite bed in DH 714 is much larger than shown.

#### 2.4.6.2 Lithostratigraphical variation in eastern Foss East.

Two lithostratigraphical discontinuities in eastern Foss East appear to coincide with evidence for faulting observed in DHs 503 and 706, both of which failed to intersect the M3 horizon because of post-metamorphic displacements. However, since the part of the mineralized zone above and west of the fault in DH 503 has close affinities in lithostratigraphy with the block further east, this fault alone cannot account for the lithostratigraphical change east of DHs 703-704 (figs. 2.18, 2.28 and 2.30). Significant differences were also noted between deeper intersections in DHs 201 and 202 (part 2.4.5) which straddle this area. Poor surface exposure precludes direct examination of the intervening ground, and the present evidence for the syn-depositional or post-metamorphic nature of this discontinuity is inconclusive.

Convincing evidence is present for major syn-depositional facies and thickness changes east of DH 503 in the Creagan Loch area. Here, barite rock reappears in the M3 horizon as a westward-plunging lense up to 6.4m thick in BH3, and the thickness of unit B metasediment increases both below and above this horizon (to 27m and 75m respectively in DH 505: fig. 2.30). M3 rapidly diminishes to merely a thin band of barium-enriched metasediment above the metabasite marker bed in DH 202, about 130m down-dip of the DH 705 intersection (fig. 2.31), where an unusual massive pyrite + galena bed enclosed within sulphidic carbonate and barite rocks is considered to represent a hydrothermal vent deposit. A proximal setting with respect to an exhalative centre in this area is also suggested by (i) high Pb/Zn ratios associated with this sulphide bed, and at the same stratigraphic level in the DH 505 barite bed, (ii) the

development of thick sulphidic carbonate rocks beneath the barite in the vicinity of BH3, and (iii) incorporation of the metabasite marker bed into the basal part of the mineralized bed intersected in BH3 (fig. 2.29), suggesting an earlier start to the deposition of hydrothermal precipitates than elsewhere.

Barite is only present as a thin (<10cm) band near the top of the M3 horizon intersected further east in DHs 707 and 708. Here, the mineralized bed largely consists of sulphidic and cherty quartz celsian rocks (averaging 33m% Zn+Pb in DH 708), with a large (~2m thick) admixture of sedimentary material towards the base of the horizon (fig. 2.29). Two possible explanations for this are: (a) an influx of sediment accompanied the hydrothermal fluids, perhaps due to contemporaneous slumping; (b) a much longer than usual period of time elapsed between the initial exhalation of mineralizing fluids and ore deposition, during which normal sedimentation continued beneath a brine pool. This abrupt change in mineralized facies supports the interpretation of strike offsets which suggest a sinistral fault parallel to the Creagan Loch escarpment (part 2.2.3). The 'normal' unit B thickness (4-8m) beneath the M3 horizon in this area (fig. 2.32), together with the presence of thick quartzite and metabasite units and two discrete upper mineralized horizons, is further evidence for a major vertical displacement relative to the western block at Creagan Loch.

#### 2.6.4.3 Deeper intersections.

Evidence for a down-dip decrease in grade and disappearance of mineralization at the M3 horizon in central Foss East (figs. 2.25, 2.27 and 2.31), is consistent with the interpretation of the 'upper mineralized zone' in the Frenich Burn area (fig. 2.23) as an upfaulted and relatively distal part of the deposit (part 2.4.2). The similar metasedimentary successions in deep intersections across central Foss East, and the occurrence in DH 601 of quartz celsian rock at a lower elevation than weak barium-enrichment at this horizon in DHs 201 and 202, suggest a west-plunging boundary between the 'shallow' and 'deep' sectors in this area. A similar orientation was noted for the wedge of thick barite extending from east of the Frenich Burn to DH 203, and the boundary between sectors I and II in Foss West (fig. 2.16). The sector represented by deeper intersections in central and eastern Foss East was distal from the



exhalative centres during formation of the M3 horizon, and received a greater influx of clastic sediments, represented by the garnet-iferous quartzites within the mineralized zone.

## 2.5 The depositional and structural history of the Foss deposit: a summary.

### 2.5.1 Deposition of the mineralized zone.

#### 2.5.1.1 Lithostratigraphical units.

The base to the mineralized zone is usually defined by an abrupt transition between two petrographically (and geochemically) distinct lithostratigraphical subdivisions of the Ben Eagach Schist (fig. 2.5). The lower division is comprised of interbedded mica quartzites and weakly-graphitic quartz muscovite schists, both of which commonly contain garnet and chlorite, and lack barium enrichment ('unit A'). The upper division is largely comprised of well-foliated, graphitic quartz muscovite schists which are often barium-enriched (>0.4%) and may contain disseminated sulphides ('unit B'). Dolomitic quartz mica schists, containing biotite and/or chlorite and variably enriched in barium ('unit C') occur at this stratigraphic level in one area presently of limited extent, represented by a southerly, upfaulted part of the mineralized zone in western Foss East. Similar calc mica schists are widespread at the top of the mineralized zone and form a lower division of the Ben Lawers Schist. The bulk of this formation is comprised of porphyroblastic garnet- and hornblende-bearing calc mica schists ('unit D').

#### 2.5.1.2 Mineralized horizons and composite beds.

Stratiform mineralized beds were deposited from a number of discrete exhalative events of varying magnitude, reflected in their variable extent and Ba, Zn + Pb contents. These beds comprise one or several of the principal components, namely barite rock, massive sulphide rock, sulphide-bearing quartz and carbonate rocks, quartz celsian 'cherts' and celsian-bearing schists. Seven correlatable mineralized horizons (M1-M7) are recognized in Foss East, and three in Foss West (M3 and probably M4-M5). The two earliest mineralized horizons (M1 and M2) are the most restricted in thickness (<0.7m) and lateral extent (~400m of strike-length and within 100m of the surface in central Foss East). M3 can be widely correlated throughout the Foss area by its unique association with a thin, underlying

metabasite bed (<1m and often <0.1m thick) of probable eruptive (pyroclastic) origin. This mineralized bed contains the largest proportion of barite and base metal reserves in Foss East, where it attains thicknesses of 9-12m near the surface in two areas; at Creagan Loch (BH3), and in the vicinity of the Frenich Burn (DHs 203, 105 and 106). A lenticular bed of barite rock is locally ~4m thick (>2m in DH 406) in the M3 horizon NE of Meall Tairneachan in Foss West. However, in this area the bulk of the barite reserves are in the upper horizon, or in a single, composite mineralized bed which is found in both deep and shallow intersections (eg. BH2) east of Creagan Chanaich and in progressively deeper intersections further west.

In shallow intersections in the Frenich Burn area, the metabasite marker bed underlies a single barite bed, up to 20m thick, which splits laterally into four units separated by wedges of metasediment varying in thickness from a few centimetres to tens of metres. Intraformational breccias in both barite rock and in the intervening metasediments, and possible unconformities in the sequence, suggest sedimentary reworking during and between the successive exhalative events which produced a thick, composite mineralized bed. From the presence of the metabasite marker below the single mineralized bed in several eastern and deeper intersections in Foss West, and from some evidence that this is also a composite unit, it is inferred that sediments were also not deposited between the two exhalative events in these areas. Thus the depositional history in the Frenich Burn area of Foss East is comparable to that in the eastern/down-dip sector of Foss West (fig. 10.5). It is further suggested that the main, upper mineralized horizon in Foss West is stratigraphically equivalent to the most laterally persistent of the upper horizons in Foss East (M5).

#### 2.5.1.3 Thickness variations in the host metasediments.

The interval of unit B metasediments stratigraphically beneath the M3 horizon varies in thickness from 4.5m to 27m (excluding the aforementioned area where unit C lithologies underlie M3). This interval exceeds 12m in two sections comprising 15-20% of the explored volume of the deposit; between Creagan Chanaich and the Frenich Burn Fault, and N of Creagan Loch (figs. 2.16a and 2.30). In the west-central part of Foss West where two mineralized beds are

present, the thickness of unit B metasediments between these horizons varies from 1.5m (DH 427) to at least 26m (BH9 and DH 404). The equivalent interval in Foss East (between M3 and M5) which locally includes some unit A and unit C lithologies, also varies widely in thickness from <3m (DH 203) to 75m (DH 505, at Creagan Loch). Unit B lithologies up to 10m thick also occur above the upper mineralized horizon in much of Foss West (fig. 2.16a), and in some parts of Foss East. Here, up to three closely-spaced mineralized beds occur towards the top of the mineralized zone.

#### 2.5.1.4 Basinal model.

During the formation of the Foss deposit, rapid lateral thickness and facies changes in the sedimentary succession accompanied both diffusive and pulsatory exhalative hydrothermal activity, which generated anomalous barium enrichment in the host metasediments and at least seven mineralized horizons (of which two are laterally extensive). The thickness of metasedimentary rock in the mineralized zone ranges from 10m to over 100m in the explored 2.2km strike-length of the deposit, and may reach 200m on the northern limb of the Creagan na h-Iolaire Anticline. These dramatic thickness changes are attributed to variations in the rates of sediment input and basinal down-warping, probably related to synsedimentary faulting. In stable areas which were proximal to exhalative vents and received (or retained) little or no sedimentary input, the chemical precipitates (chiefly barite) from successive hydrothermal emanations were stacked to form a single, locally thick mineralized bed. In other areas, the distribution of which changed with time, large amounts of sediment accumulated during the same period and some or all of the mineralized horizons are widely spaced (fig. 10.5).

Direct links between contemporaneous faulting and basinal development, and the emanation of hydrothermal fluids, are observed in the Creagan Loch area. Here, a possible sulphide mound and other evidence for proximity to an exhalative site during formation of the M3 horizon, are associated with rapid variations in the thickness of both the mineralization and the host metasediments. Further east, sedimentary material is incorporated into the lower part of the same mineralized bed, possibly due to slumping associated with the start of hydrothermal activity. A volcanic eruption which deposited the

thin, laterally extensive metabasite marker bed, coincident with the onset of this exhalative event, also suggests a direct association between tectonic and hydrothermal activity. Subsequently, basaltic magmas were emplaced as lenticular sills, up to ~10m thick, within the mineralized zone in central Foss West and eastern Foss East. Geochemical characteristics, described in chapter 5, suggest that this magma emplacement probably occurred at a shallow level during deposition of the mineralized zone or shortly after the onset of Ben Lawers Schist sedimentation.

## 2.5.2 Deformational history.

### 2.5.2.1 Folding.

By virtue of the well-exposed Creag an Chanaich section, the scale and style of folding in the Foss West area was appreciated by previous authors (Coats et al., 1978, 1981). Extensive drilling and underground exploration in this area have confirmed the continuity of these WSW-plunging fold structures at depth, but have shown that folding about horizontal axes is unusually prominent in eastern Foss West. This phase of folding is superimposed on the earlier fold structures which have near-vertical axial planes, generating 30-60m amplitude, box-shaped corrugations of the mineralized zone lying within a fold envelope which dips south at 50-60° (figs. 2.12 - 2.14). The barite rock is variably attenuated on the limbs of these folds, and may be thickened in tight fold noses (e.g. near BH2). Drillhole intersections and more limited exposures in Foss East indicate that a contrasting style and scale of folding is developed here, with open to isoclinal, asymmetrical folds which also plunge at 20-25° to the west, but seldom have short limbs of amplitude >10m. Here, the overall dip of the mineralized zone is approximately vertical, but locally varies from 55° N to 65° S (figs. 2.4, 2.24 - 2.27, 2.31 and 2.32).

The relative chronology of fold phases established from major and minor structures is summarised in table 2.2. The development in pelitic rocks of a strong foliation which is generally parallel to lithological boundaries, is associated with F1 isoclinal folding with an approximate E-W axis which formed the Creag na h-Iolaire Anticline. A discrete F2 phase is not recognized in this area, except perhaps to account for deviations in strike such as that west

of the Frenich Burn, and the early deformation may be a composite D<sub>1</sub>-D<sub>2</sub> event. The F3 phase is responsible for the asymmetrical folds with ENE-WSW axes and near-vertical axial planes in both parts of the Foss deposit, and is considered to be synchronous with the formation of the Sron Mhor Syncline. These folds, together with the associated crenulation cleavage in pelitic rocks and rodding lineations in granoblastic rocks, plunge to the west and a regional tilting is attributed to this deformational phase. The folding with sub-horizontal axes referred to above has not been discerned in Foss East, and should be regarded as a late-F3 phase. This probably preceded the final episode of penetrative deformation about NW-SE axes which formed the F4 Ben Eagach Antiform (fig. 1.3), of which there is no evidence at Foss.

#### 2.5.2.2 Faulting.

This account has demonstrated that the effects of faulting on the disposition of the mineralized zone, particularly in Foss East, are much greater than was previously considered. Offsets and discontinuities of stratigraphical horizons observed during mapping and from published geophysical (VLF-EM) surveys, together with sub-surface information from drilling, have led to the recognition of at least six major, N-S to NE-SW trending, post-metamorphic faults in the Foss area, in addition to the Frenich Burn Fault located by Coats et al. (1981). The most major of these, the Creagan Loch Faults, define the eastern limit to the deposit and probably have a large vertical component in addition to the observed sinistral displacement. The same applies to a fault parallel to the Creagan Loch escarpment in the vicinity of DHs 706-707 (fig. 2.7), which coincides with an abrupt change in the lithostratigraphy of the mineralized zone. Other abrupt changes about 200m to the west (near DH 503), and east of the Frenich Burn (near DH 106) may also be due to post-metamorphic, near-vertical displacements.

A new interpretation involving steeply inclined, E- to ENE-trending faults, is presented for the 'upper mineralized zone' which is located to the south of the main mineralized zone in the Frenich Burn area of Foss East. This laterally discontinuous band (up to 30m thick) of alternating quartz celsian cherts, graphitic schists and barium-enriched calcareous mica schists, is correlated with the deeper intersections of the main zone in the same area, and is

considered on lithostratigraphical grounds to be an upfaulted slice of a more distal part of the mineralized zone. The shear zones bounding this slice were intersected in seven drillholes over a lateral distance of over 400m and to a depth of 160m below the surface. This phase of faulting, which may be equated with shearing parallel to the base of the Ben Lawers Schist seen in parts of Foss West (e.g. at BH10A), appears to pre-date the Frenich Burn Fault against which the 'upper mineralized zone' terminates.

**Table 2.1: Frequency of G-series samples\* containing garnet or disseminated pyrite relative to barium content determined by Portable XRF.**  
(See Appendix C).

Counts per second $\times 10^{-3}$ Calibrated wt%Ba (fig. C.1)	background		anomalous		row totals %
	<20.0 0-0.20	20.0-21.9 0.21-0.41	22.0-28.5 0.42-1.11	>28.5 >1.11	
garnetiferous	30	6	0.5\$	0	36
pyritic	3	6	4	5	18
neither of above	17	18	10	1	46
column totals, %	50	30	14	6	100

\* Total of 220 samples, mostly of graphitic schist, located on fig. 2.2.

\$ Sample G13 (filled square symbol on fig. 2.2) is both garnetiferous and anomalously enriched in barium.

**Table 2.2: Deformation history of the Foss deposit: summary of structure and fabric development.**

Episode*	Major structures*	Minor structures and fabric development†
D <sub>1</sub>	Initial folding of the Creag na h-Iolaire Anticline: an overturned, E-W antiform closing to the south.	Strong S <sub>2</sub> foliation in schistose lithologies, generally parallel to bedding. Metamorphic fabric largely overprinted during D <sub>3</sub> : minor D <sub>1-2</sub> structures not recognized.
D <sub>2</sub>	Loch Tummel Fold: no major structures in the vicinity of the Foss deposit.	
D <sub>3</sub>	Modification of earlier structures by ESE-trending, open to isoclinal folds with near-vertical axial planes; formation of the Sron Mhor Syncline; regional tilt to the west. Late D <sub>3</sub> folding about horizontal axes in the Creag an Chanaich area.	Open to isoclinal folding on hand specimen scale; tectonic breccias; minor boudinage and fault drag. S <sub>3</sub> crenulation cleavage in pelites and in cymrite rocks; rodding fabric parallel to F <sub>3</sub> fold axes in barite rock and in some breccias. Syntectonic garnet growth.
D <sub>4</sub>	Ben Eagach Antiform, NE of Foss area: no major folds but possible NNW-SSE flexures of mineralized bed.	No minor structures recognized. Static, post-D <sub>3</sub> growth of hornblende garbenschiefer and garnet overgrowths; annealing; replacement of cymrite by celsian.
D <sub>5</sub>	Major, E-W trending, sub-vertical faulting emplaces the 'upper mineralized zone' at Frenich Burn.	Shearing of similar orientation to major structures. Brecciation. Local retrogressive alteration and late-stage veining. Pyrite replacing pyrrhotite.
D <sub>6</sub>	N-S to NE-SW sinistral faults, commonly downthrow to the E, associated with the Loch Tay Fault system - the Frenich Burn and Creag Loch Faults.	

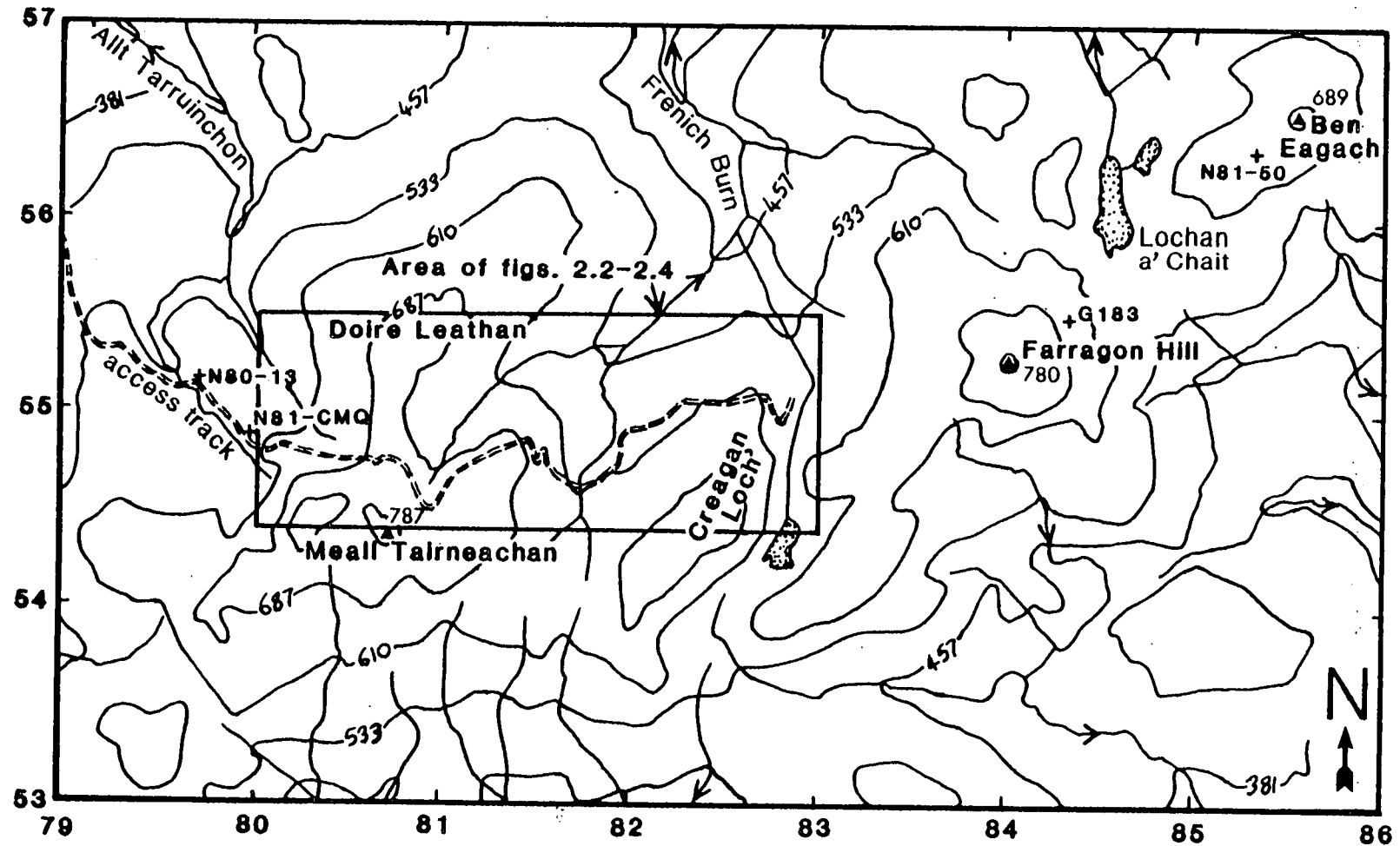
\* Deformation phases according to Roberts & Treagus (1979).

\* See fig. 1.6.

† Described in greater detail in Ch. 8.

Fig. 2.1: Location map of the Foss deposit area and of samples from outwith the area

Kilometre grid (area NN): contours from O.S. sheet 52



Rectangle shows area covered by figs. 2.2 - 2.4, which are located in the back pocket



Fig. 2.5: Generalized lithostratigraphical column of formations, units & marker horizons in the Foss deposit

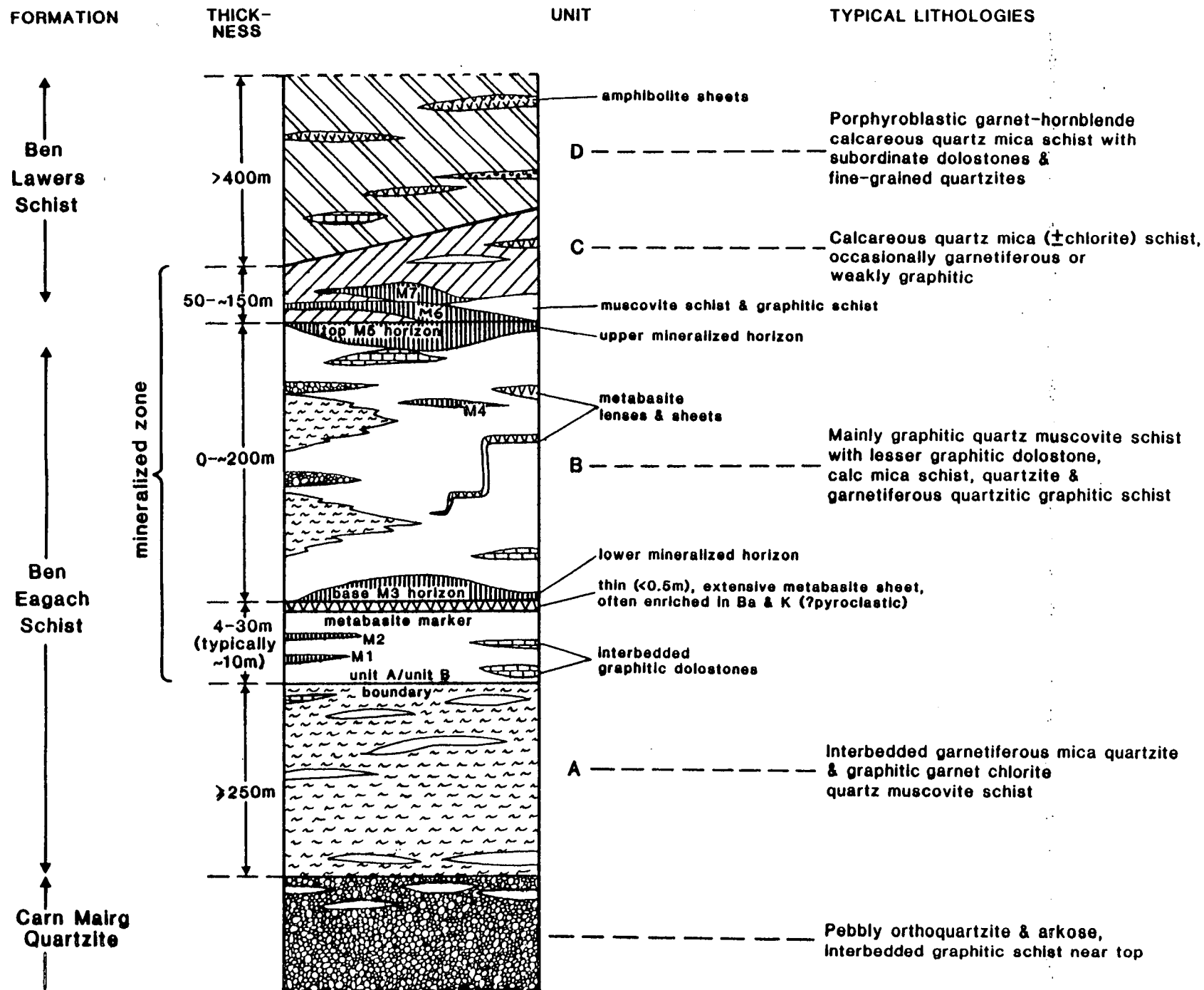
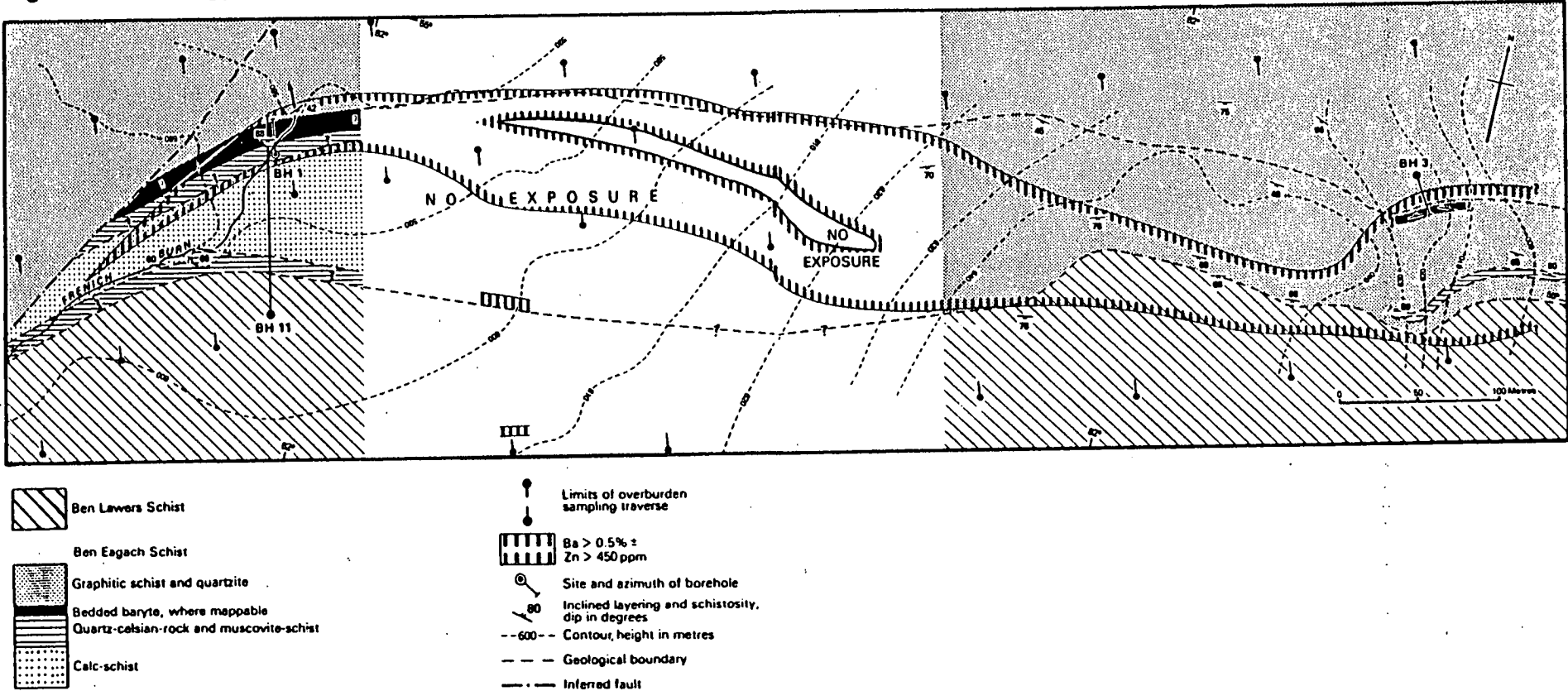


Fig. 2.6: Geology and barium distribution in deep overburden samples, Foss East: from Coats et al., 1981





Common boundary with right margin of Fig. 2.8

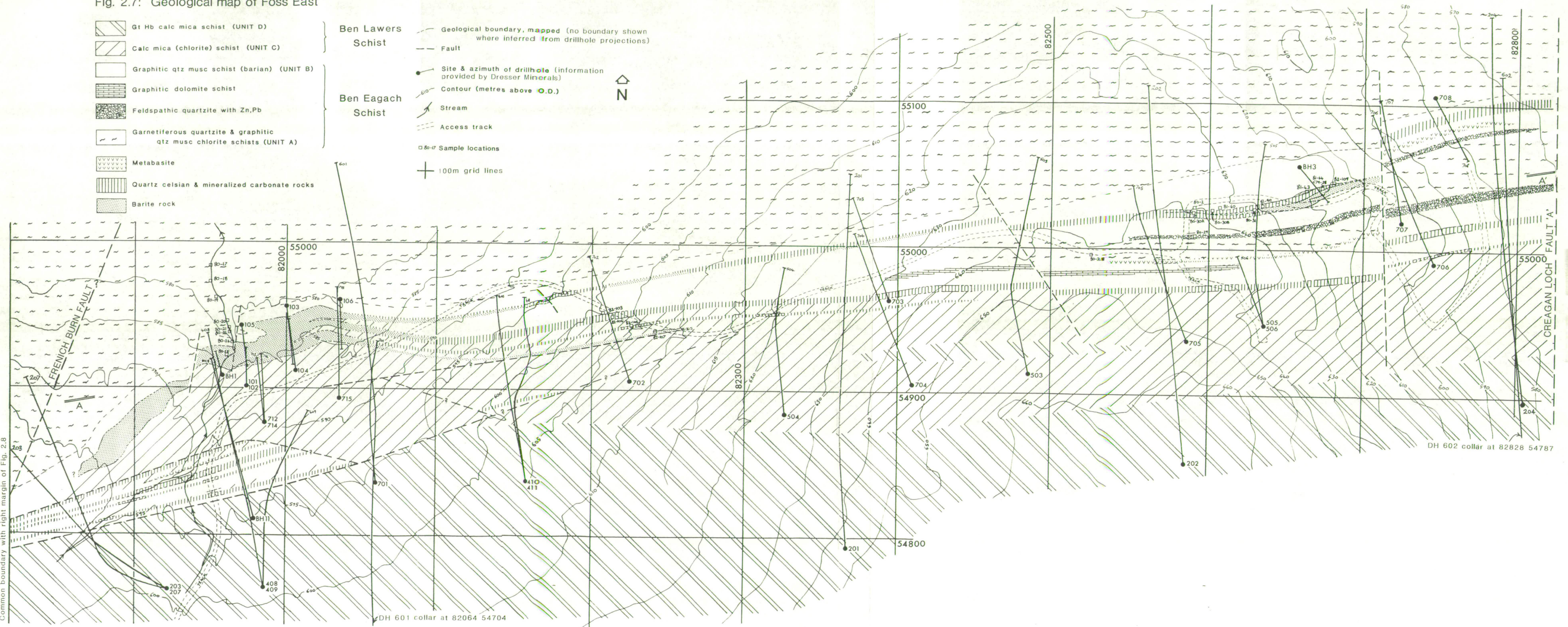




Fig. 2.8: Geological map of Foss West Drillhole locations provided by Dresser Minerals

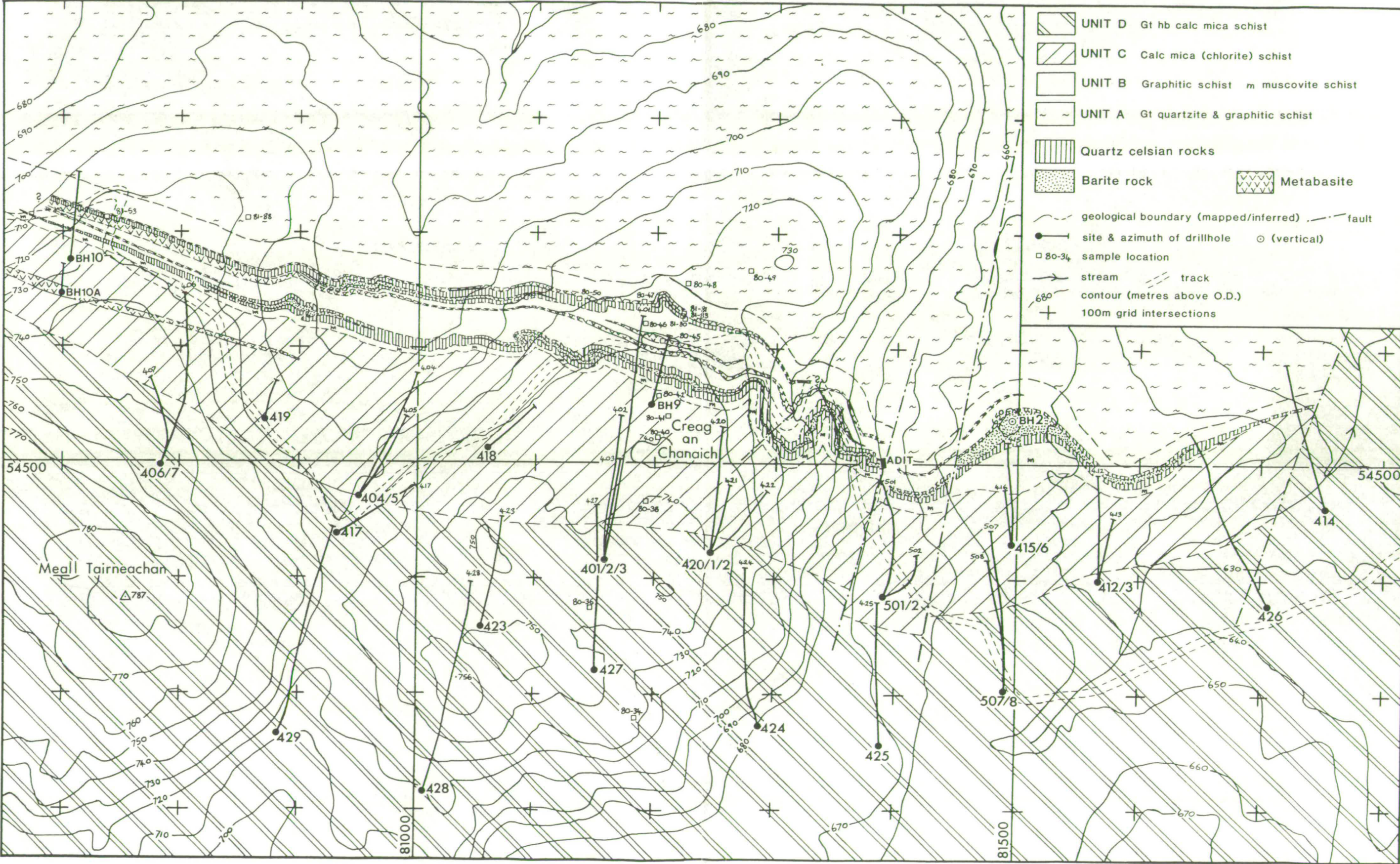




Fig. 2.9: T.V.D. stratigraphical profiles of mineralized zone intersections in I.G.S. boreholes 10, 9, & 2, with barium contents (data from Coats et al., 1981)

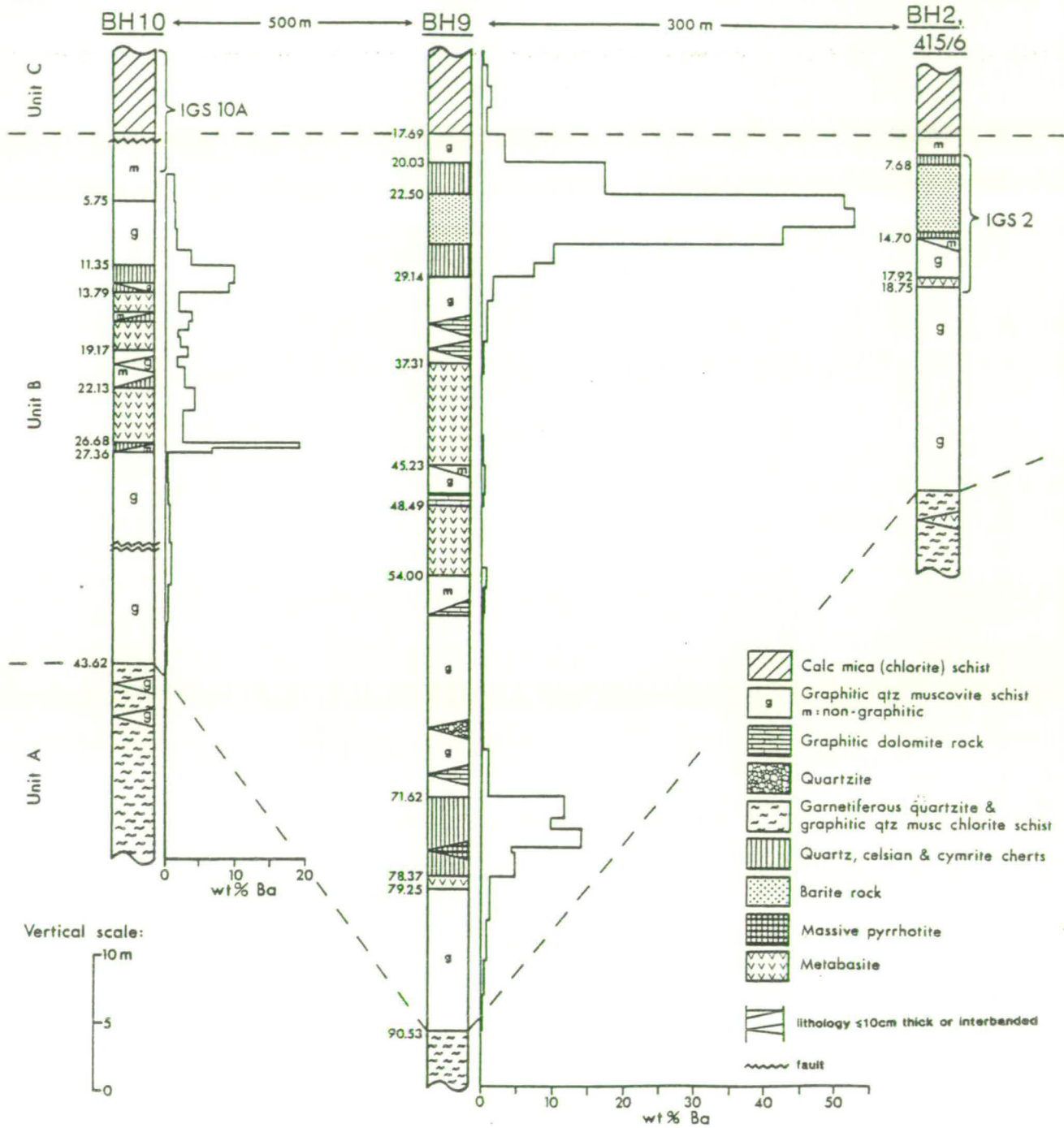


FIG. 2.10: FOSS WEST DRILLHOLES: Vertical projection

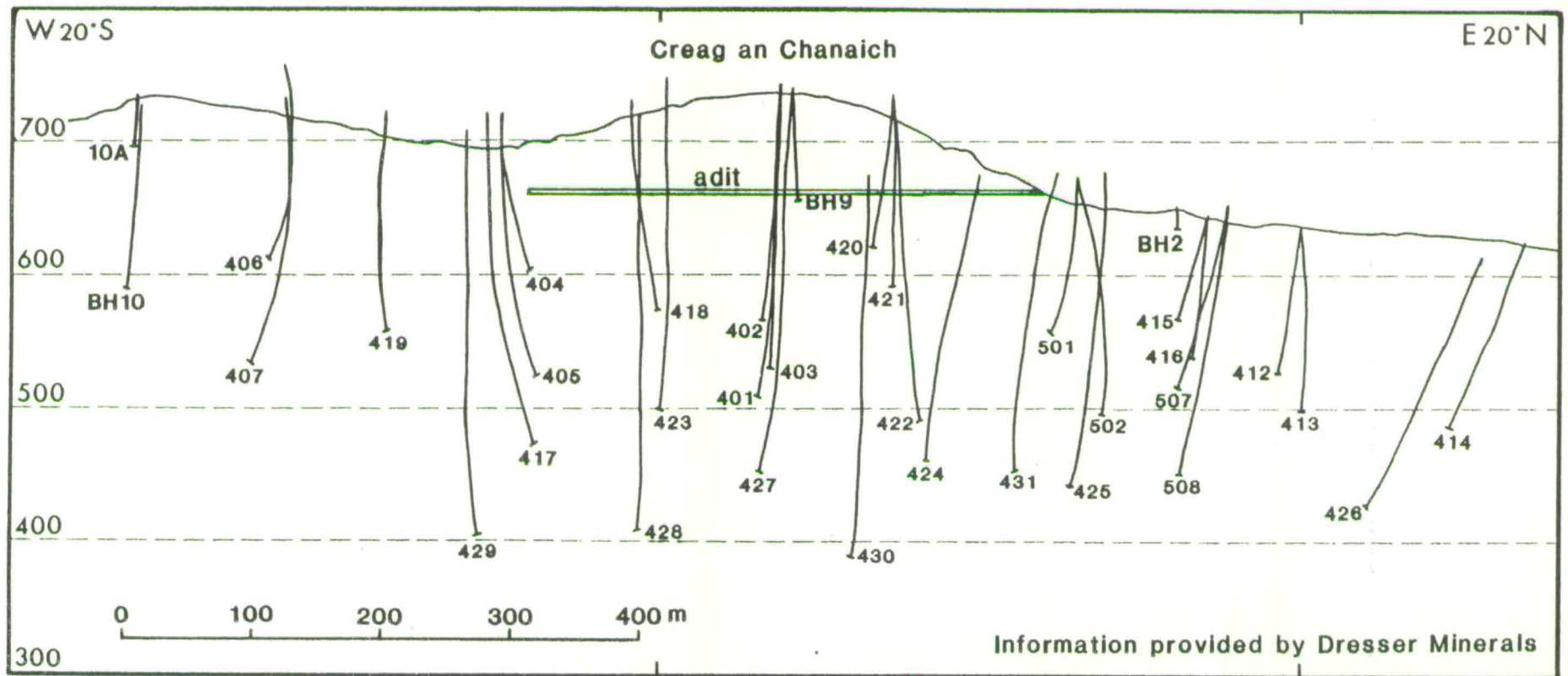


Fig. 2.11: Geological cross-section through DHs 406 &amp; 407, Meall Tairneachan

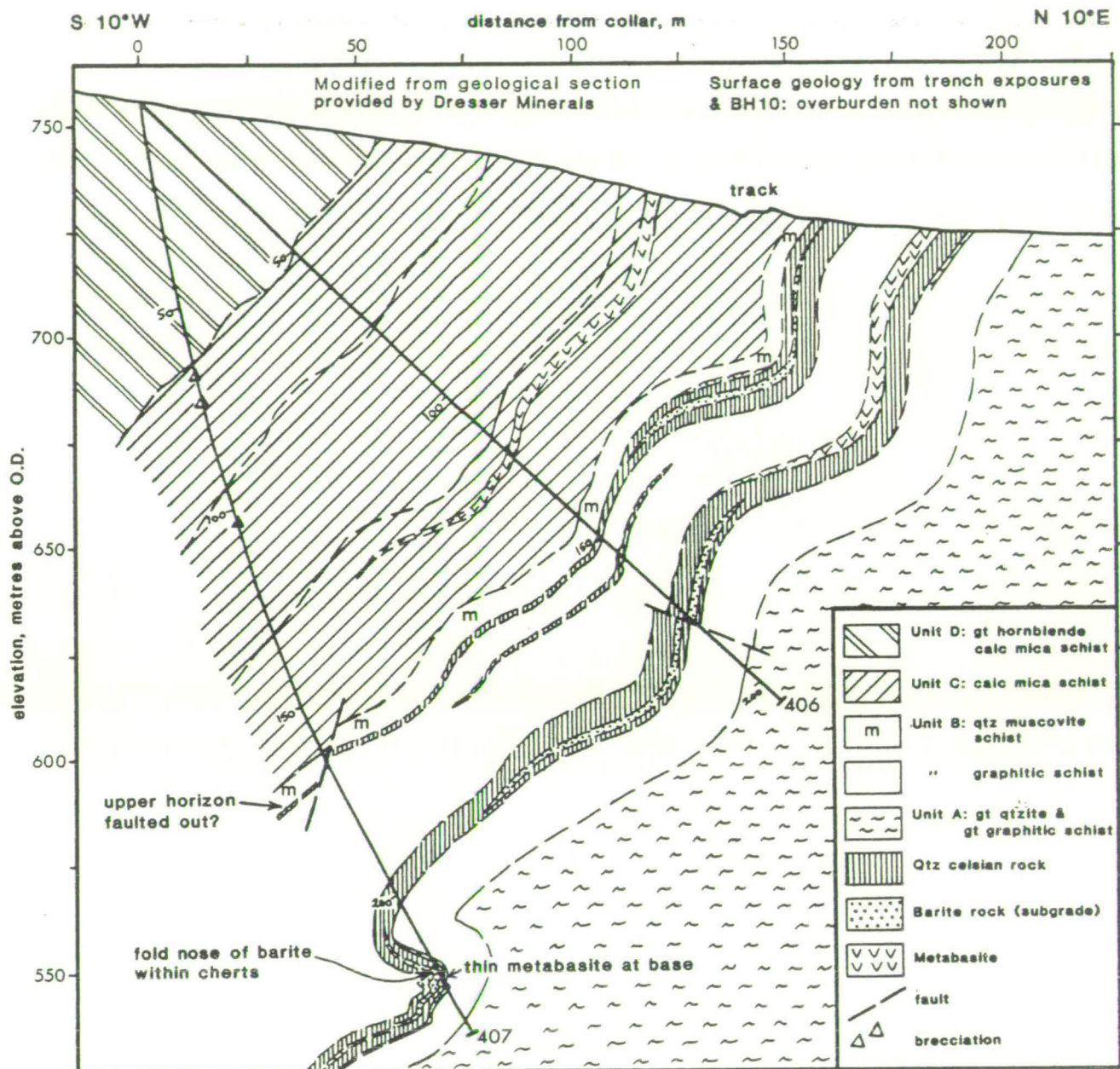




Fig. 2.12: Geological cross-section through DHs 404, 405, 417 & 429, E of Meall Tairneachan

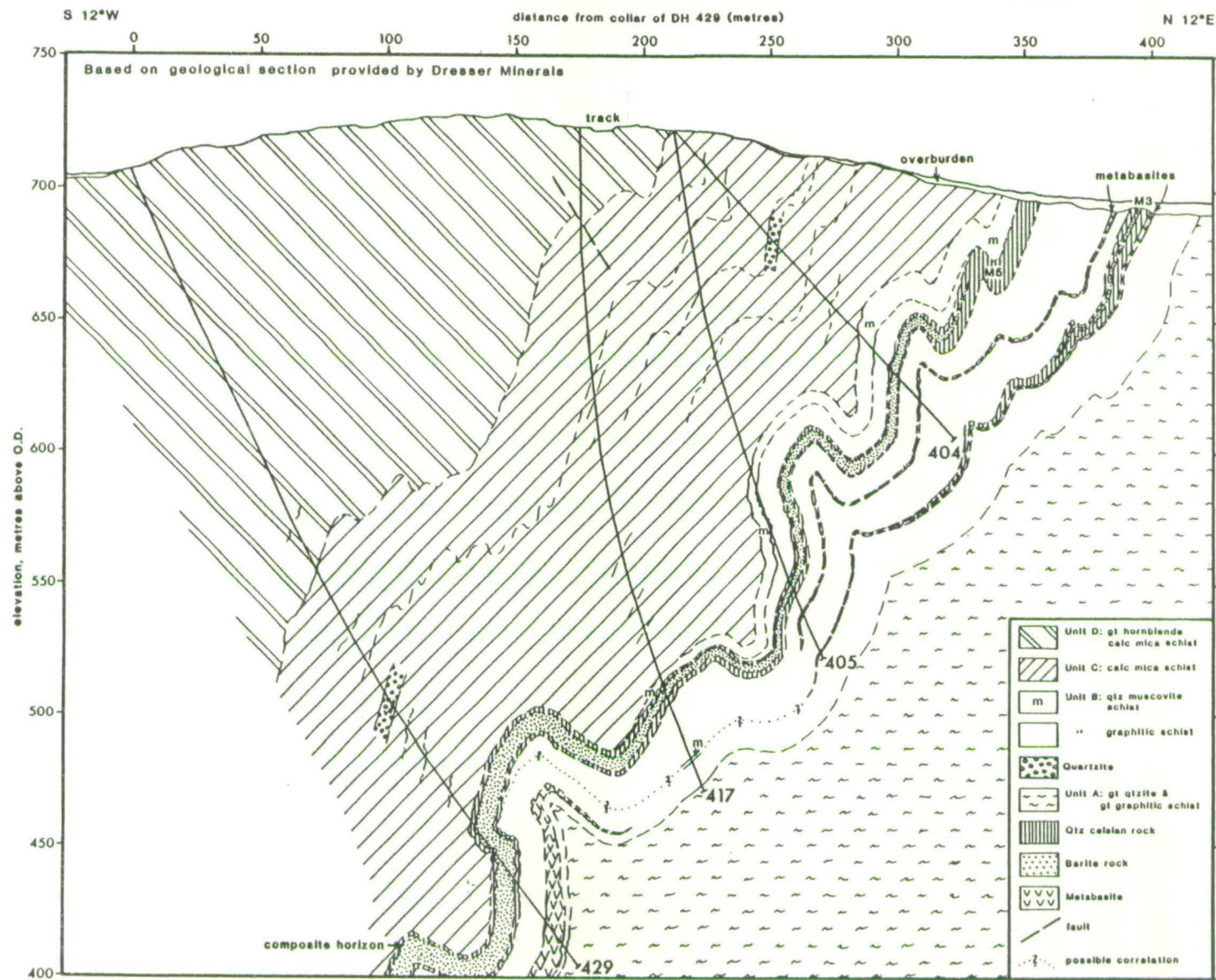
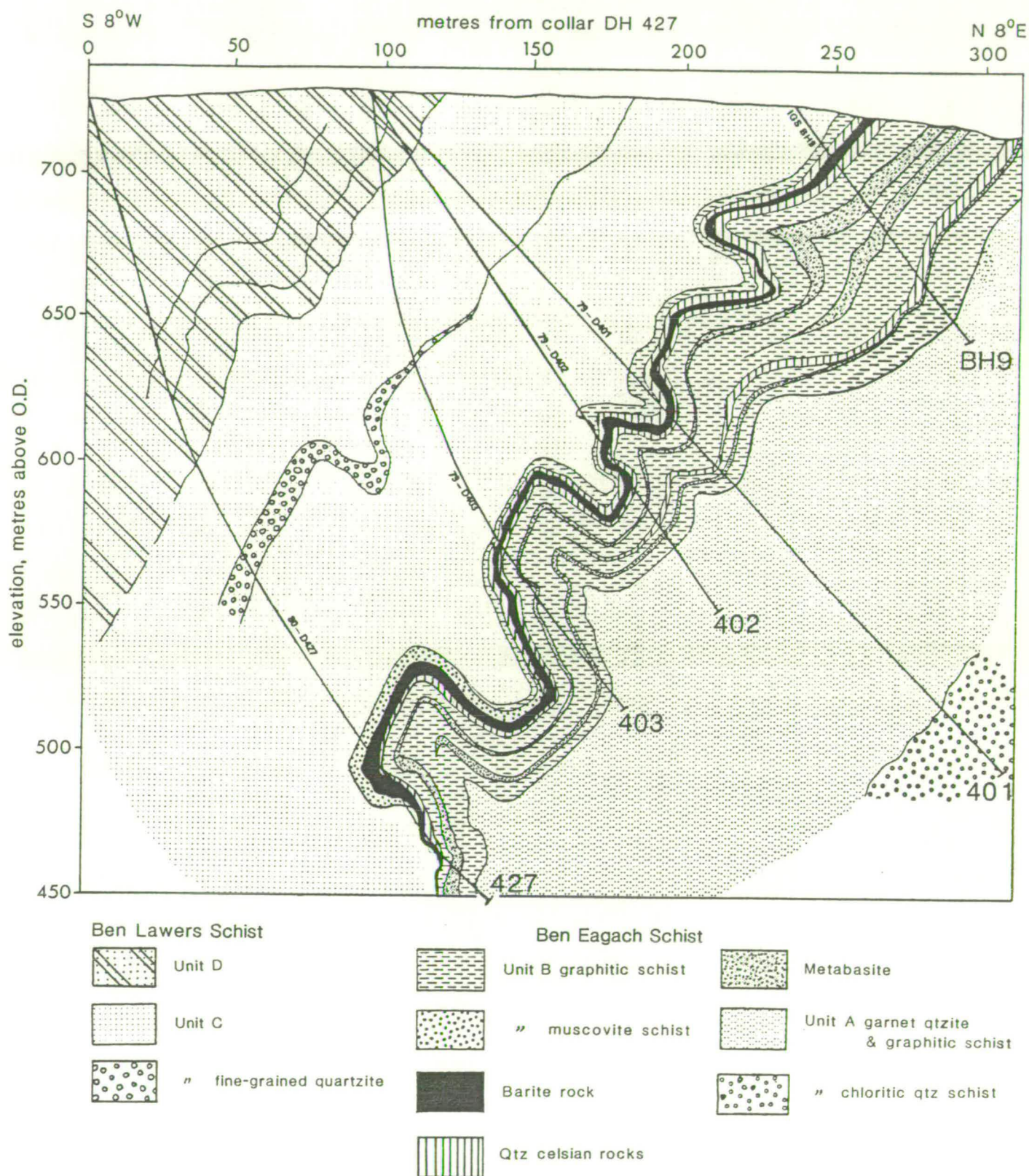




Fig. 2.13a: Geological cross-section through BH9, DHs 401/2/3 &amp; 427, Creag an Chanaid



Modified from a diagram published by Smith  
information made available by Dresser Minerals

(1981) & Gallagher (1983),



Fig. 2.13b: Alternative structural/stratigraphical interpretation of mineralized zone intersections in DHs 403 & 427

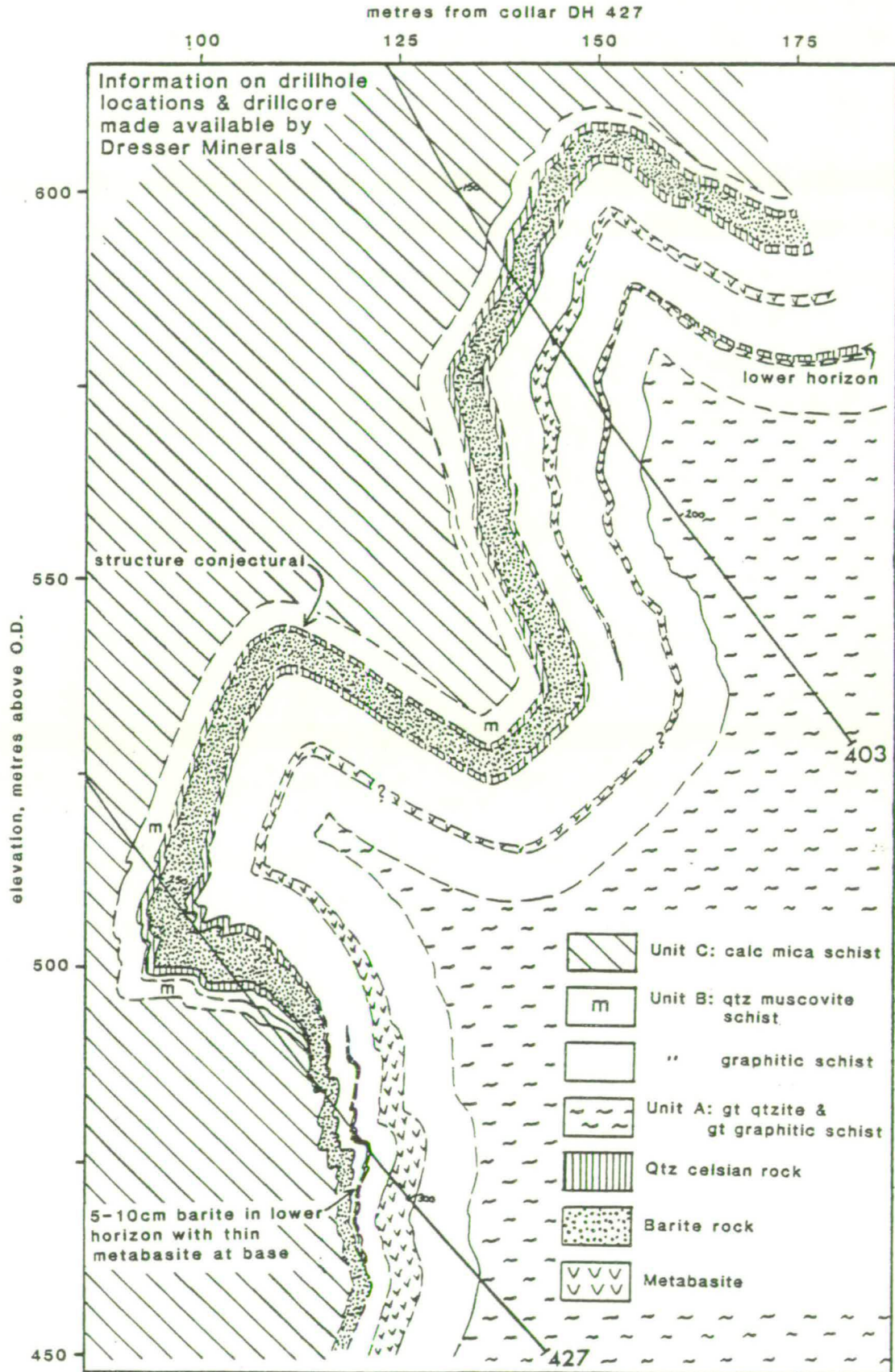


Fig. 2.14: Geological cross-section through BH2 and DHs 415, 416, 507 & 508, east of Creag an Chanaich

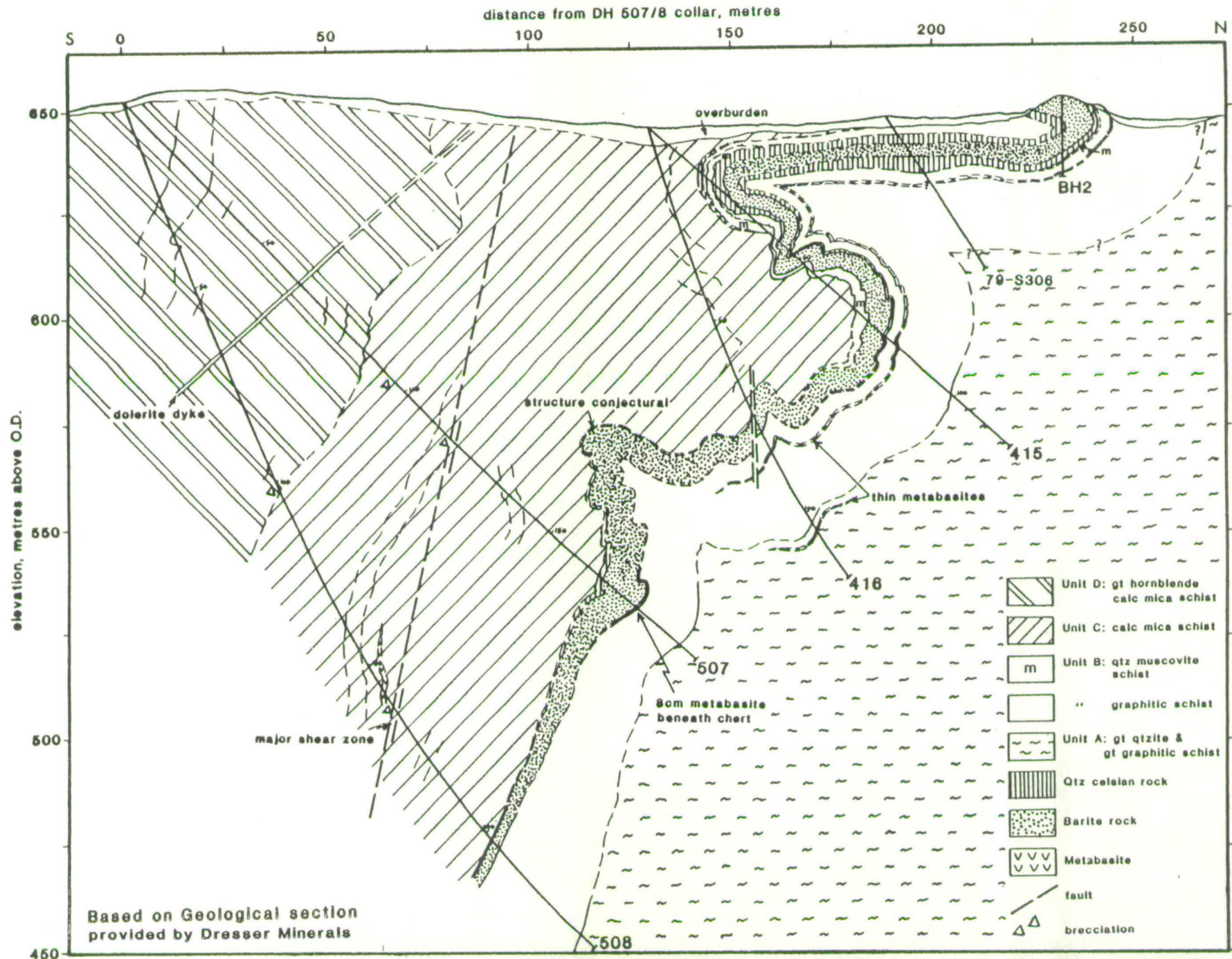




Fig. 2.15: T.V.D. profiles of the mineralized zone in deeper intersections, Foss West

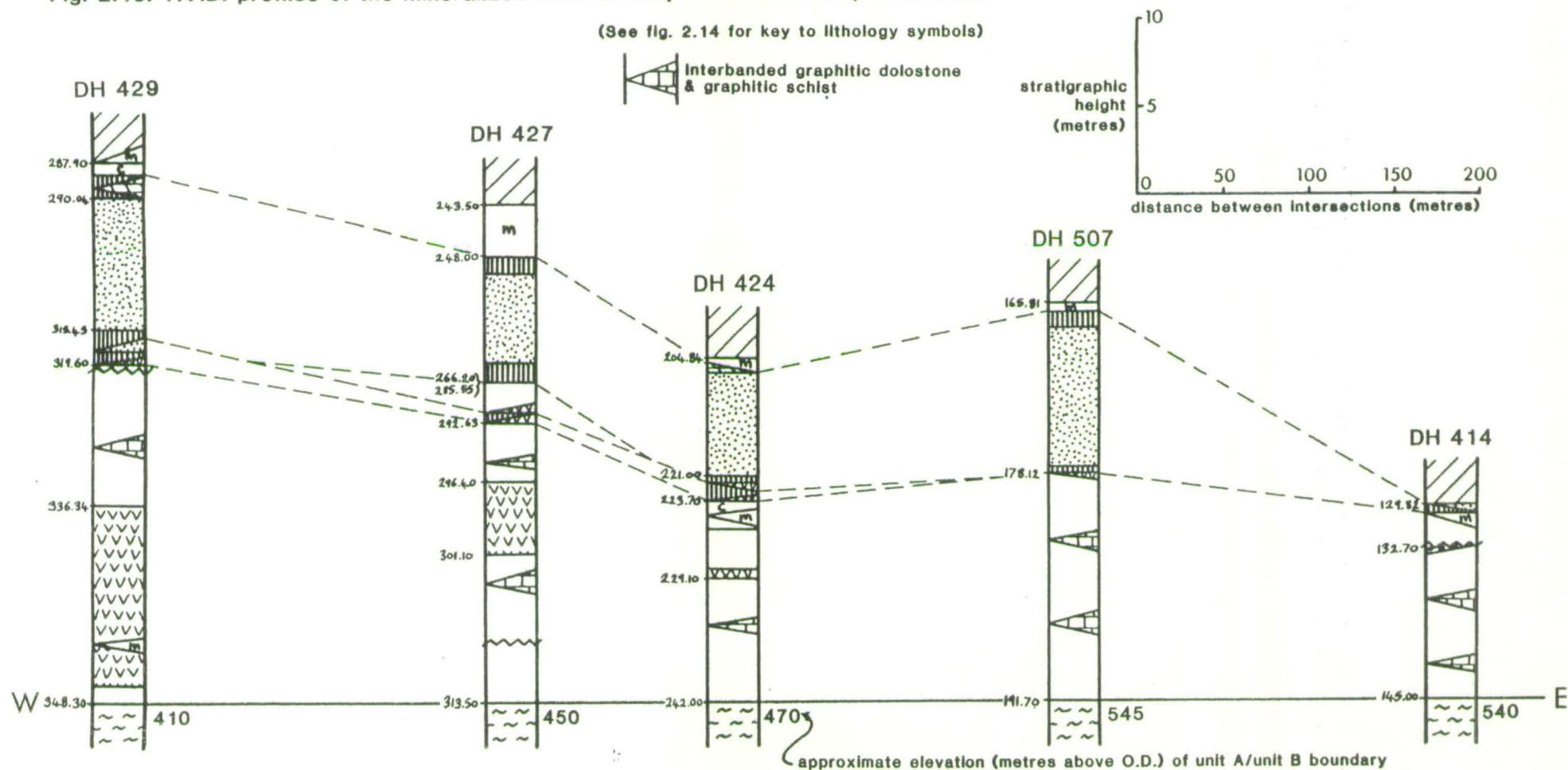


Fig. 2.16: Vertical projection of Foss West drillholes with isopachs of (a) unit B metasediment thickness, (b) metabasite thickness & intersections of the metabasite marker bed

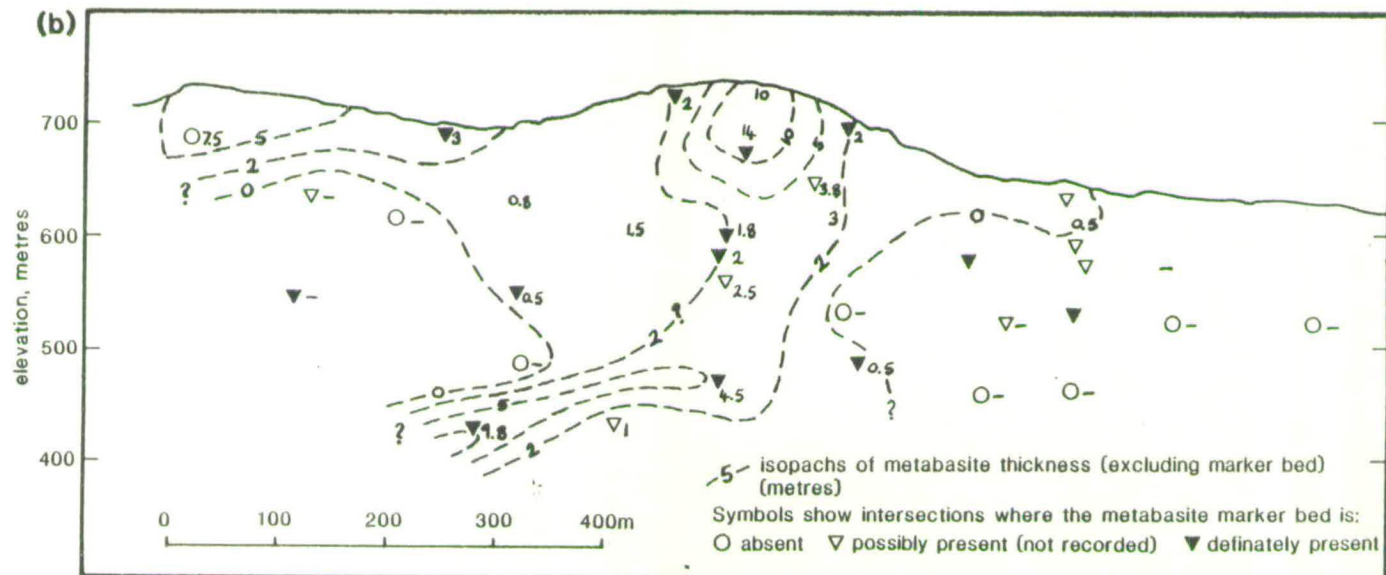
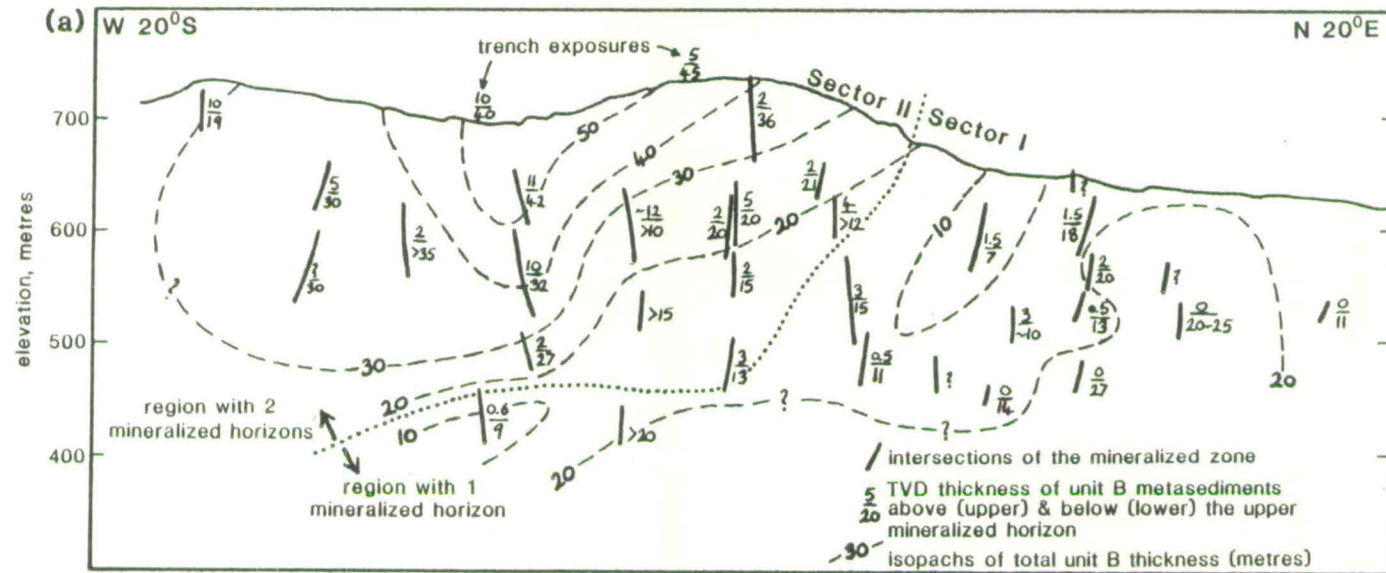
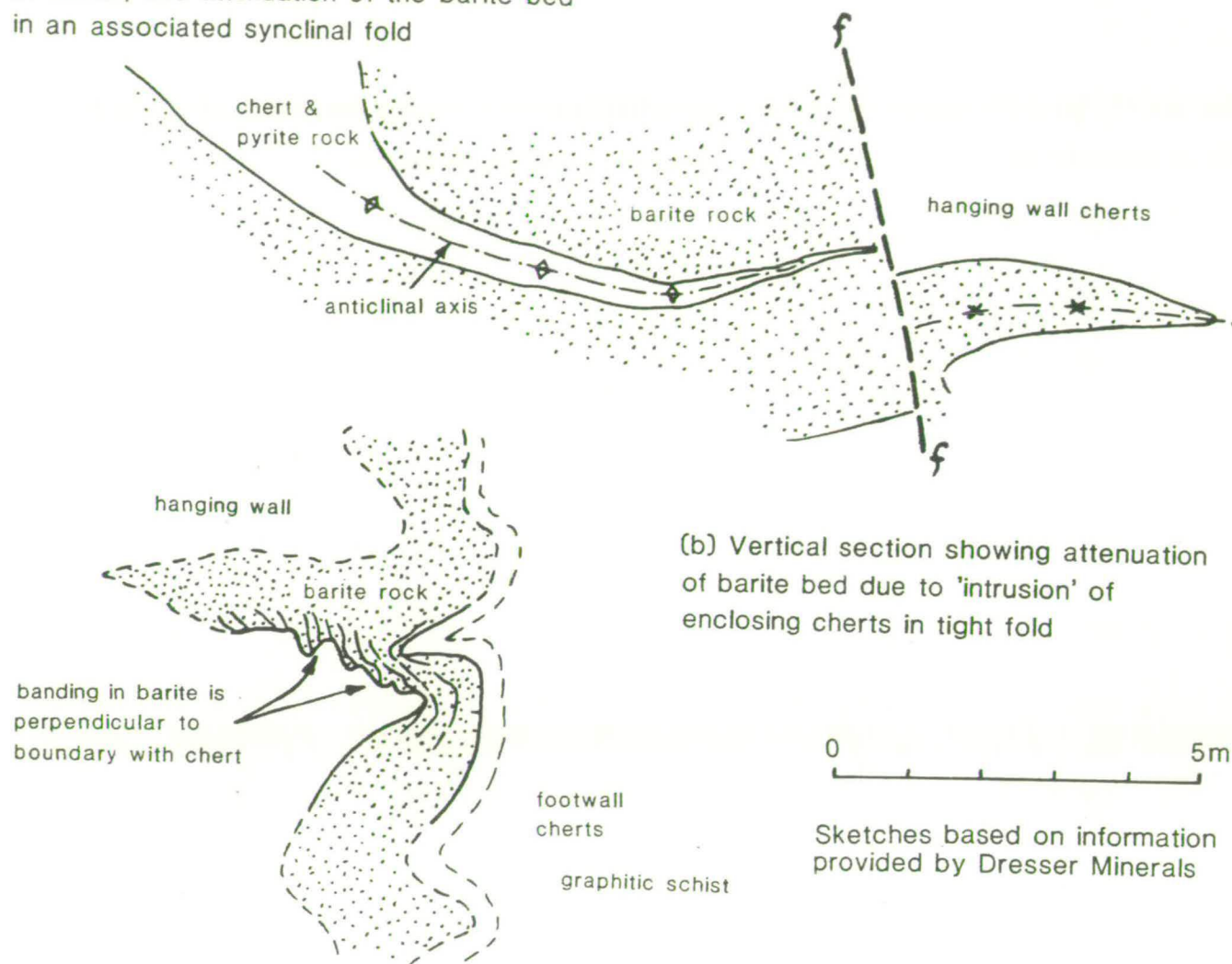


Fig. 2.17: Sketches of structural features observed in the Foss adit and in the basal part of the mineralized bed intersected in DH 102, Frenich Burn

(a) Plan view showing extreme attenuation of footwall pyrite bed in isoclinal fold closure of barite, and attenuation of the barite bed in an associated synclinal fold



(c) Highly complex folding of chert/metabasite underlying parallel-banded barite rock, DH 102 (drawing after A.R. Burns, Sept. 1982)

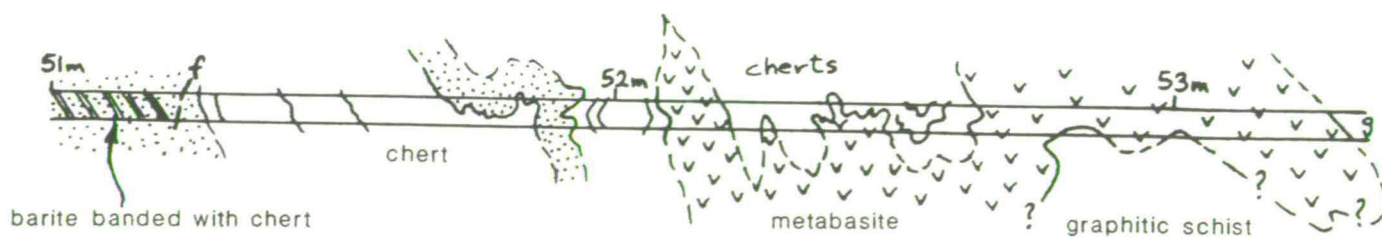


FIG. 2.18: FOSS EAST DRILLHOLES: Vertical projection showing sectors A-F

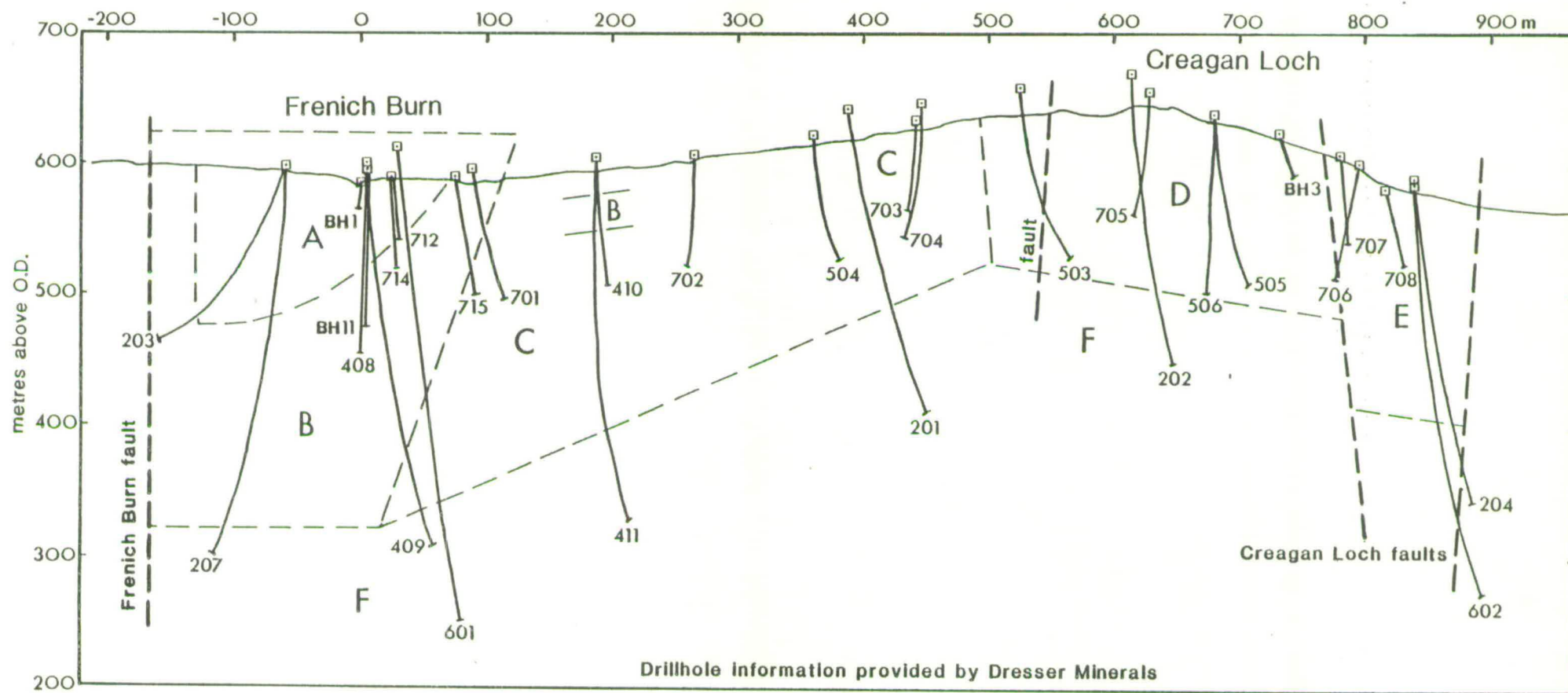


Fig. 2.19 is located in the back pocket



Fig. 2.20: Geological cross-section, DHs 101, 102 & 105, French Burn

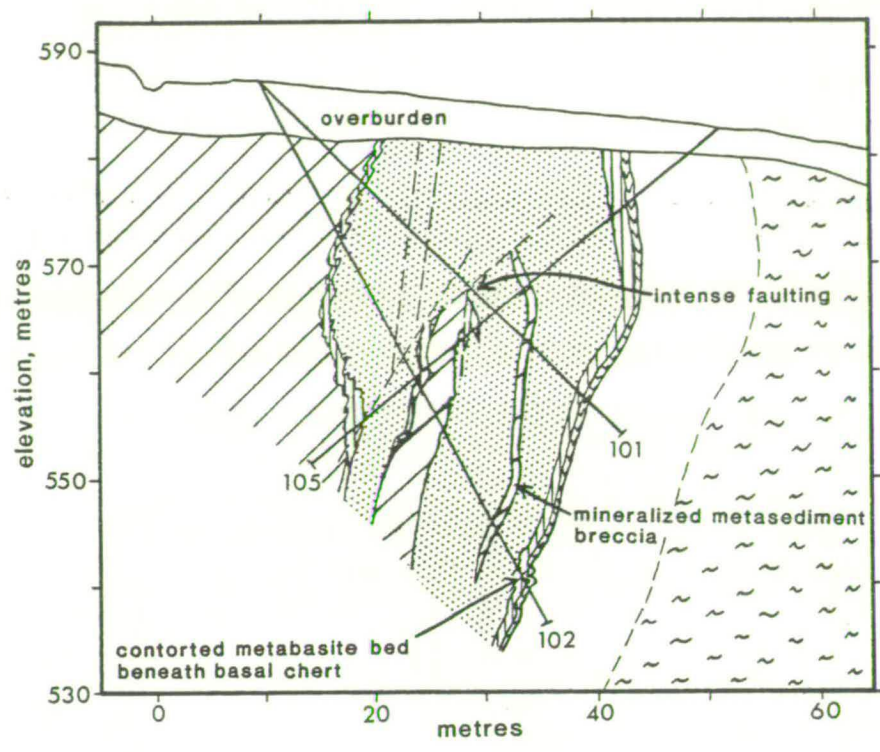


Fig. 2.21: Geological cross-section, DHs 712 & 714, French Burn  
Geology between 712 and surface projected from DHs 101-105

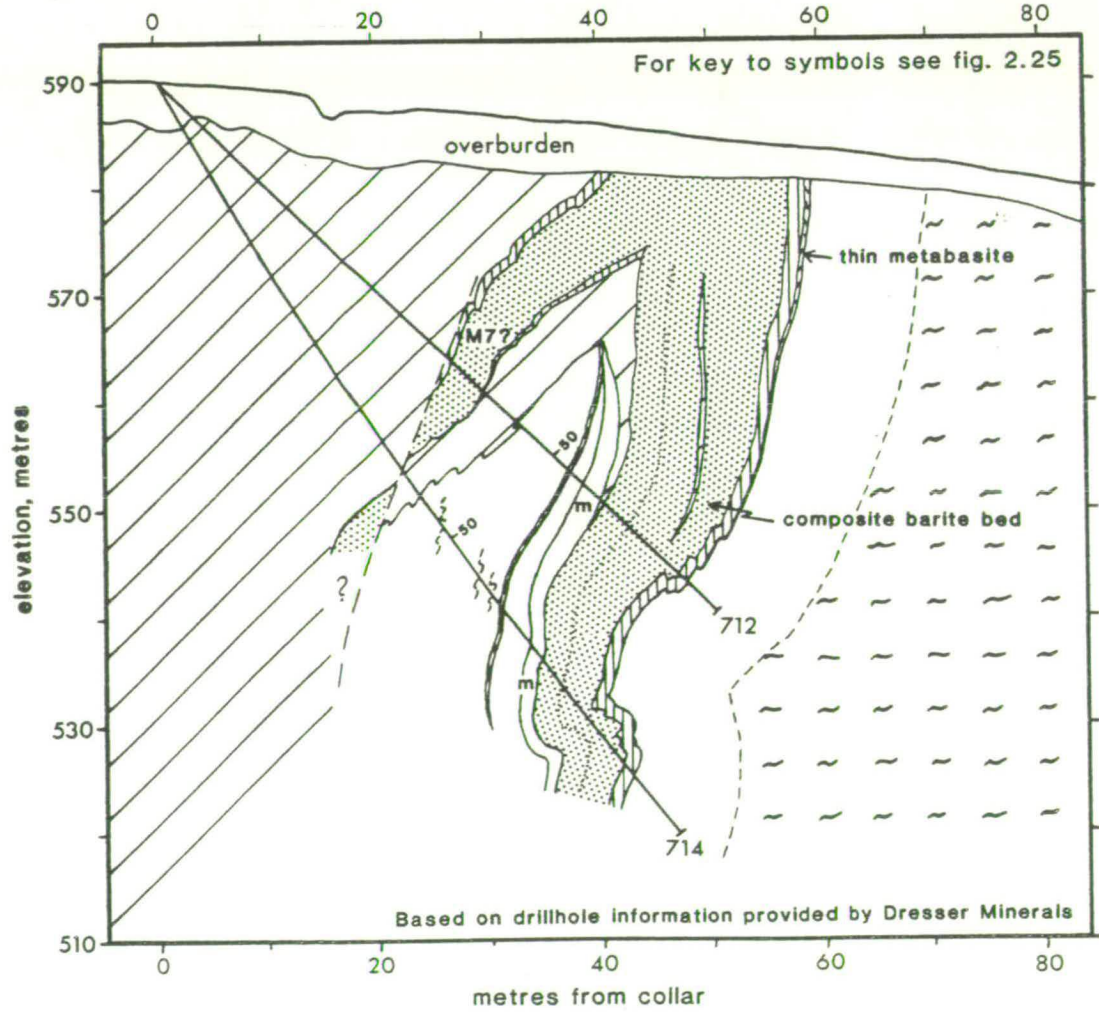




Fig. 2.22: T.V.D. profiles of mineralized intersections in DHs 104 & 105, French Burn

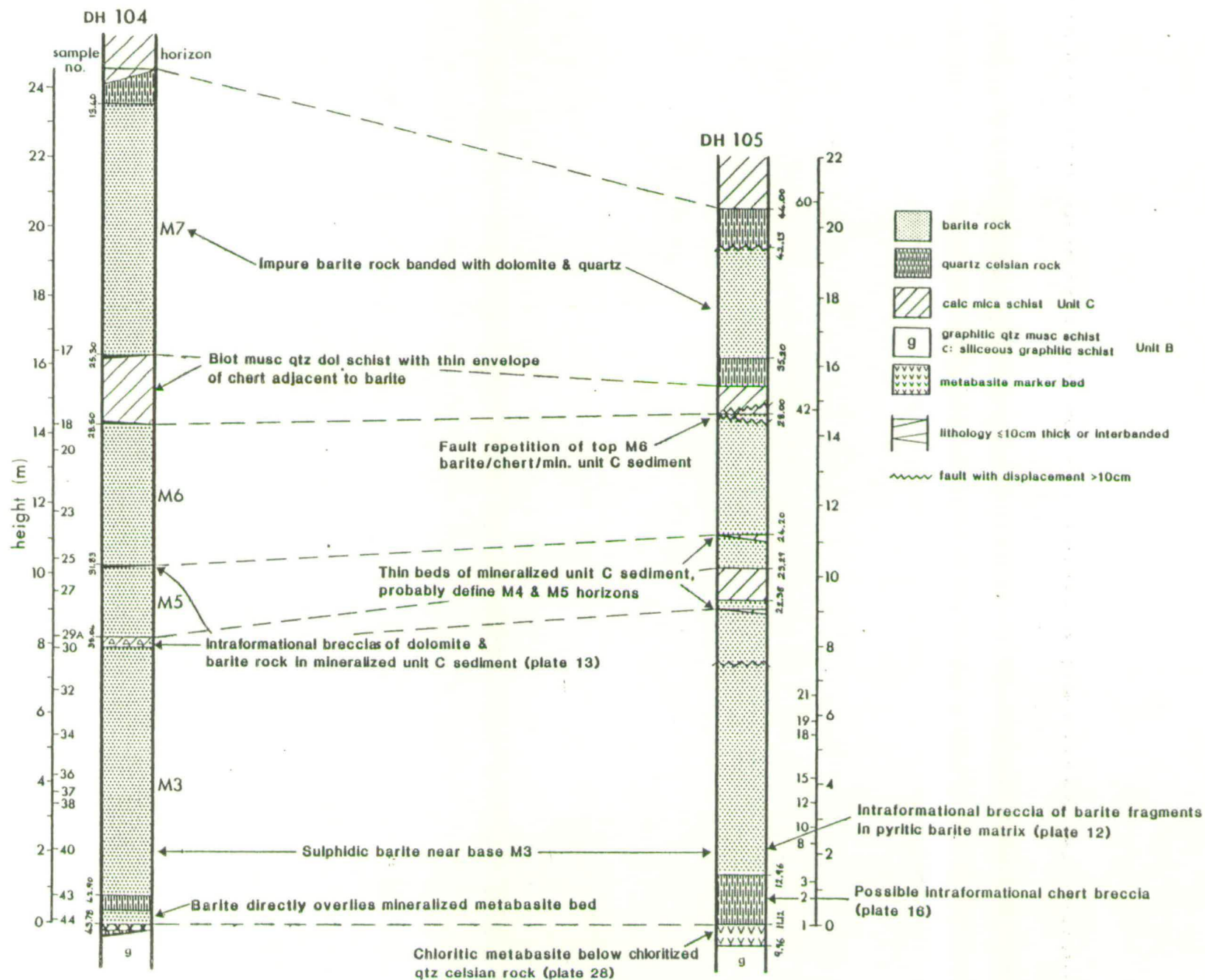


Fig. 2.23: T.V.D. stratigraphical profiles of upper and lower mineralized zone intersections in DHs 207, 203, 408 & BH11, French Burr

Assay data from DHs 207, 203 & 408 provided by Dresser Minerals; data from BH11 is from Coats et al., 1981

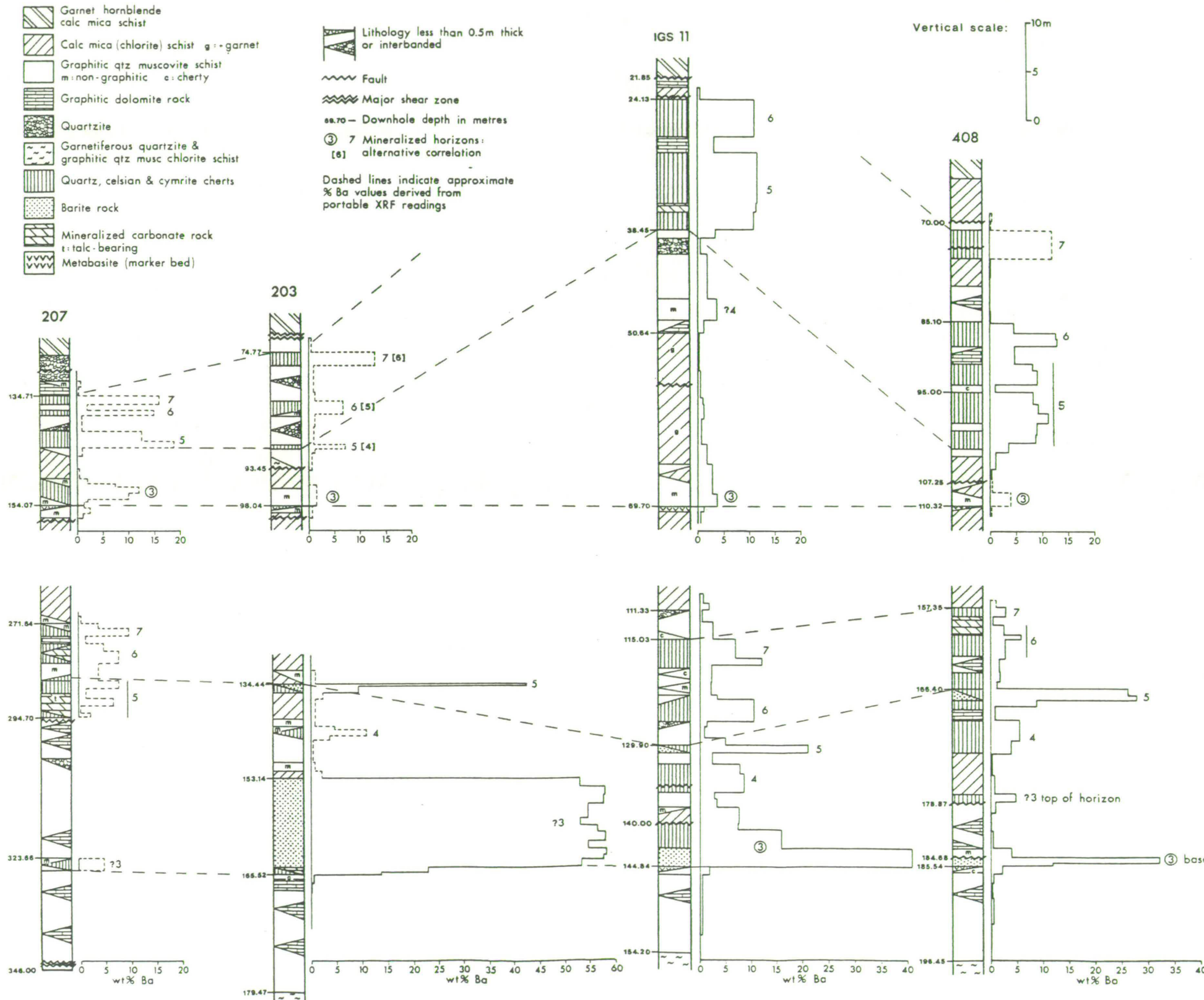




Fig. 2.24: Geological cross-section through BHs 1 & 11 and DHs 408 & 409, French Burn

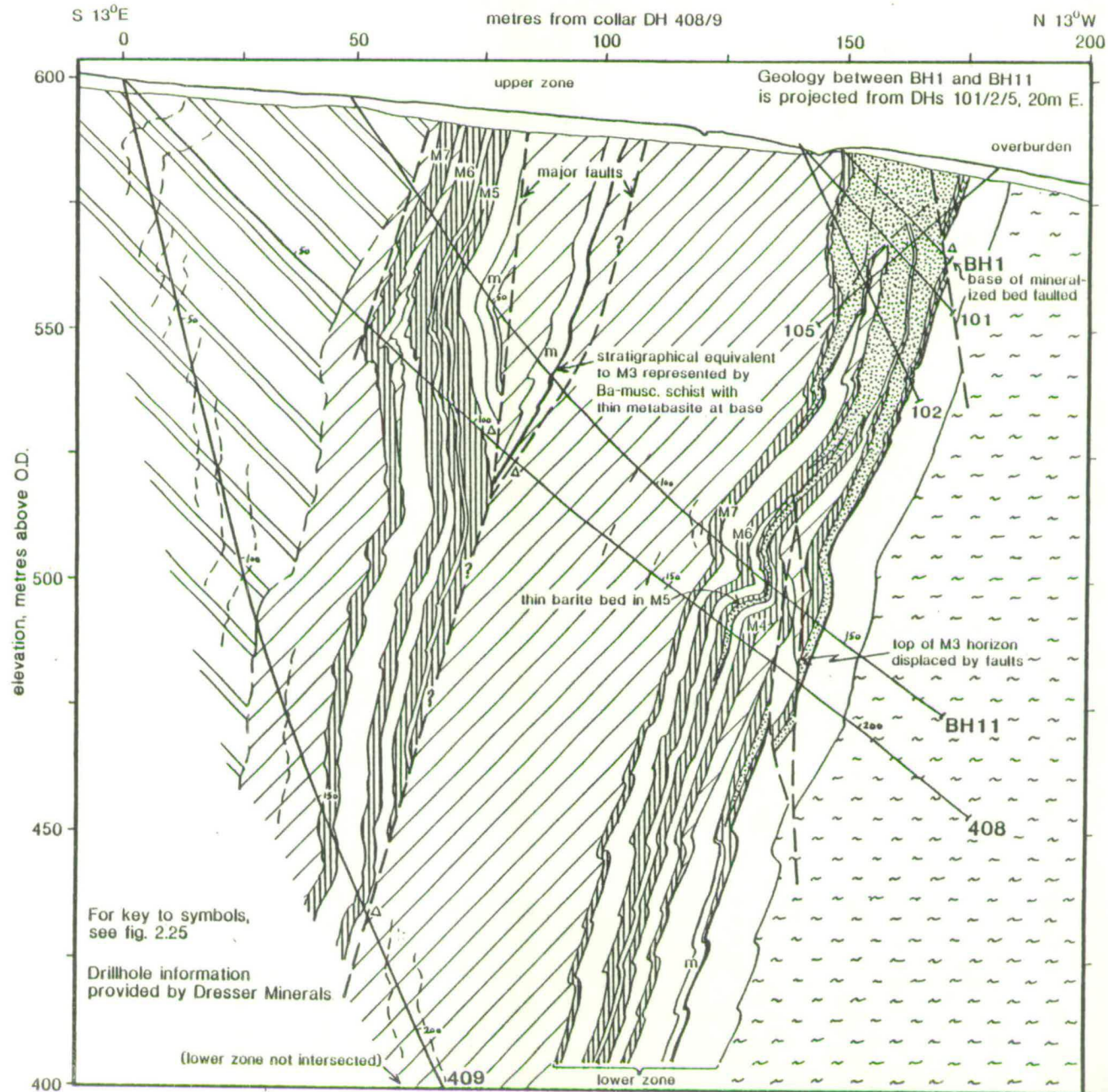


Fig. 2.25: Geological cross-section through DHs 106, 715, 701 &amp; 601, French Burn area

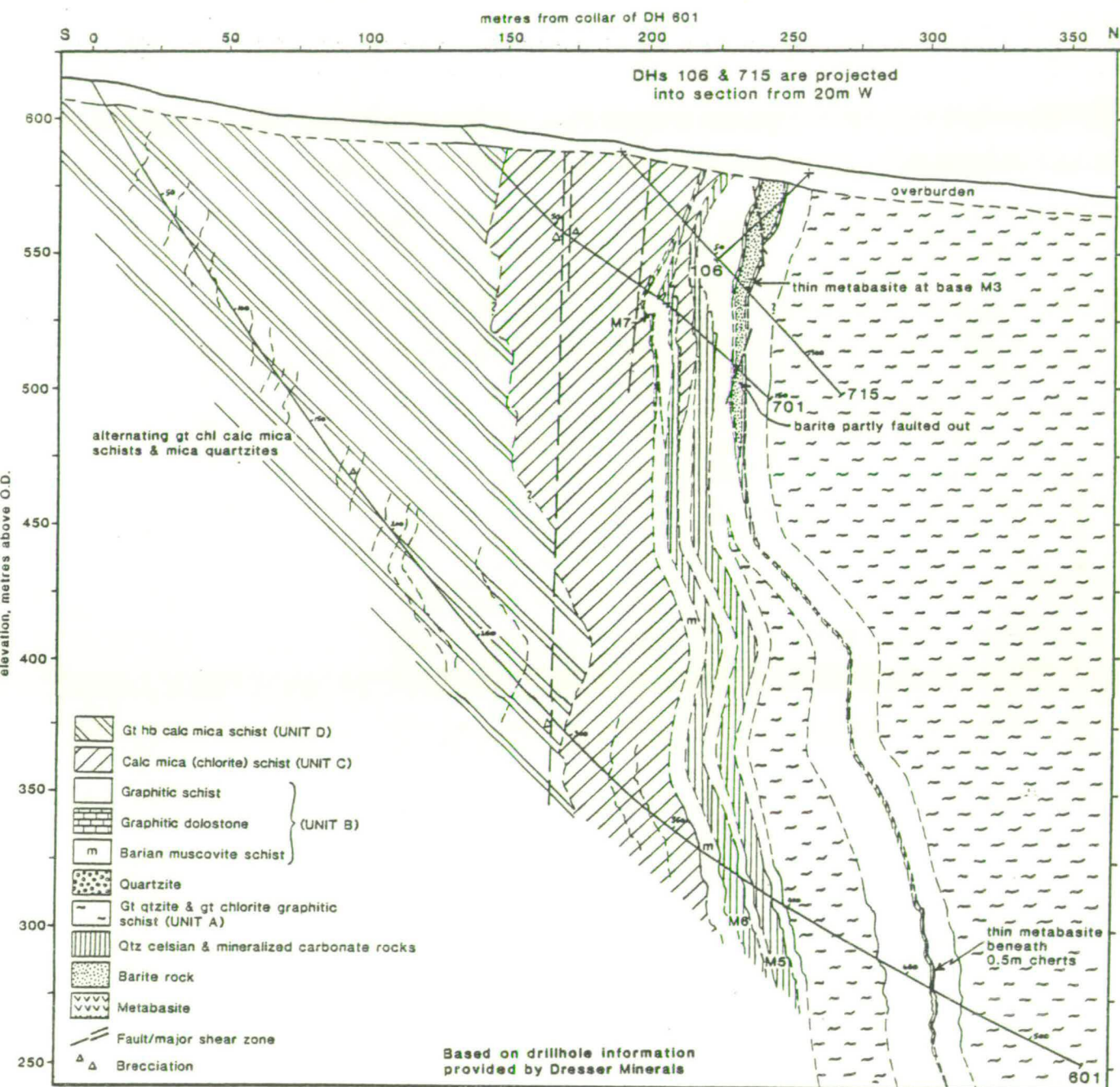
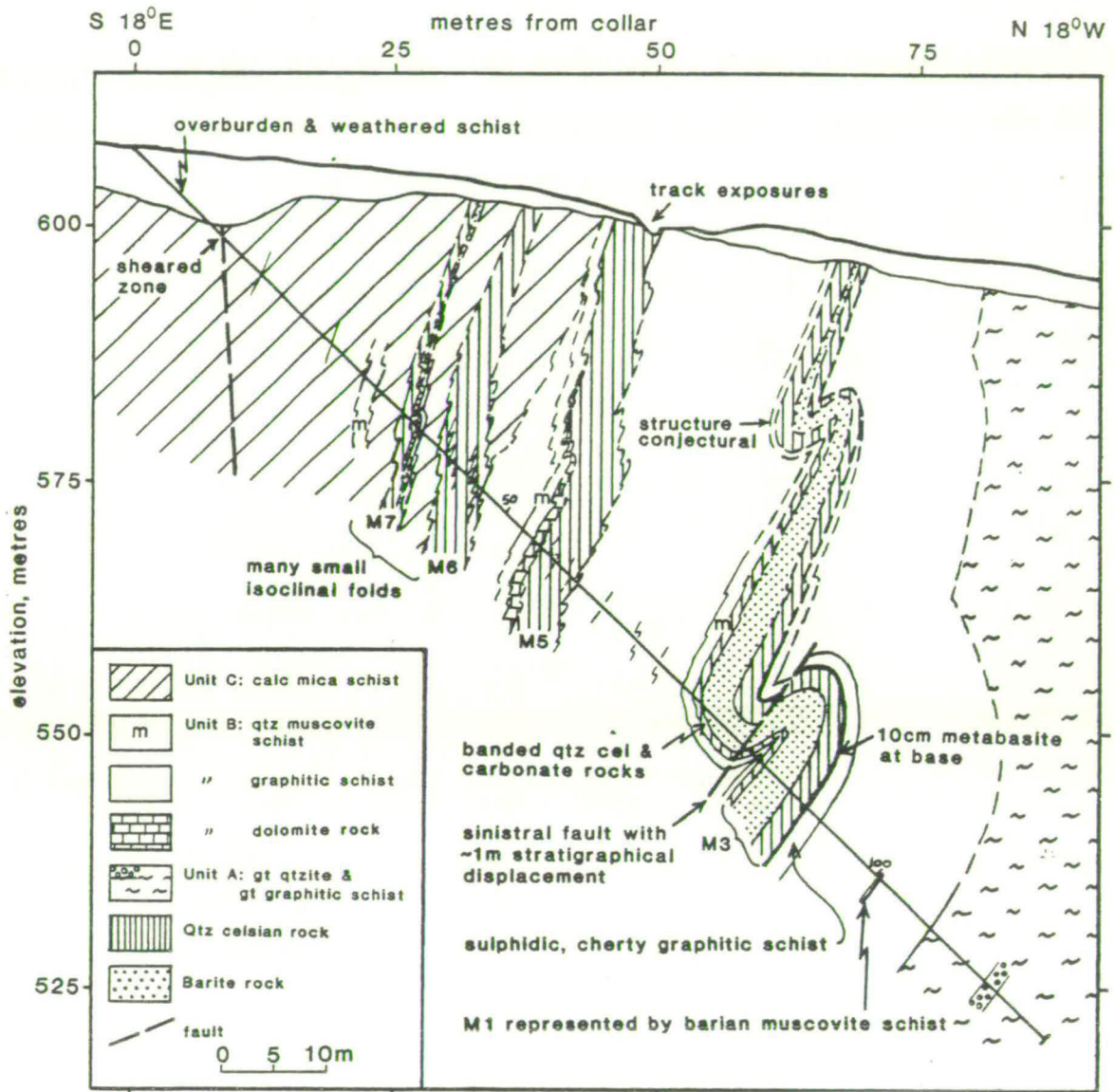




Fig. 2.26: Geological cross-section through DH 702, Foss East



Drillcore made available by Dresser Minerals

Fig. 2.27: Geological cross-section through DHs 703, 704 & 201, central Foss East

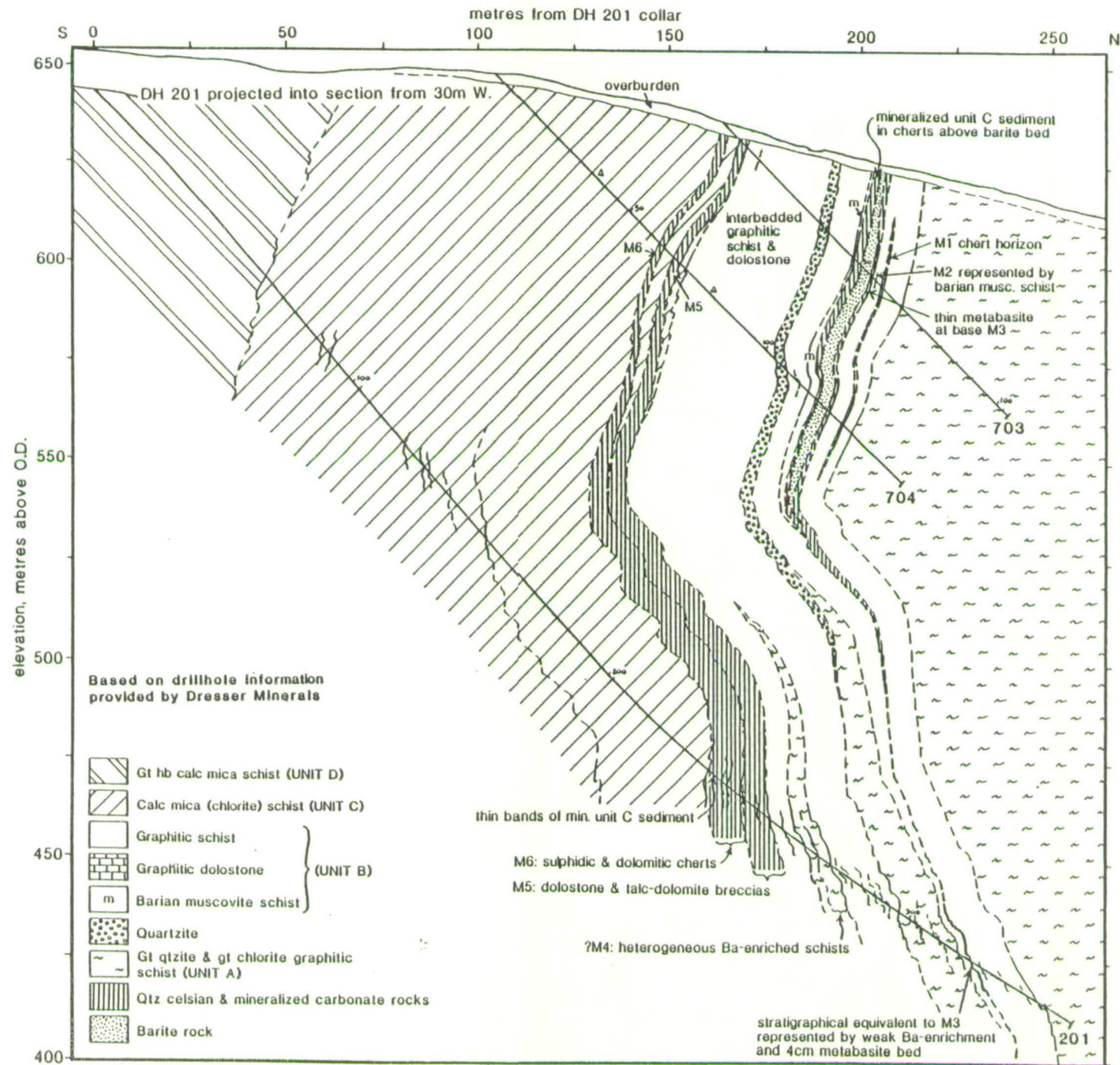


Fig. 2.28: T.V.D. profiles of mineralized zone intersections in central Foss East, with Ba contents determined by Portable XRF.

Refer to fig. 2.27 for key to lithologies  metabasite  3 mineralized horizon  fault

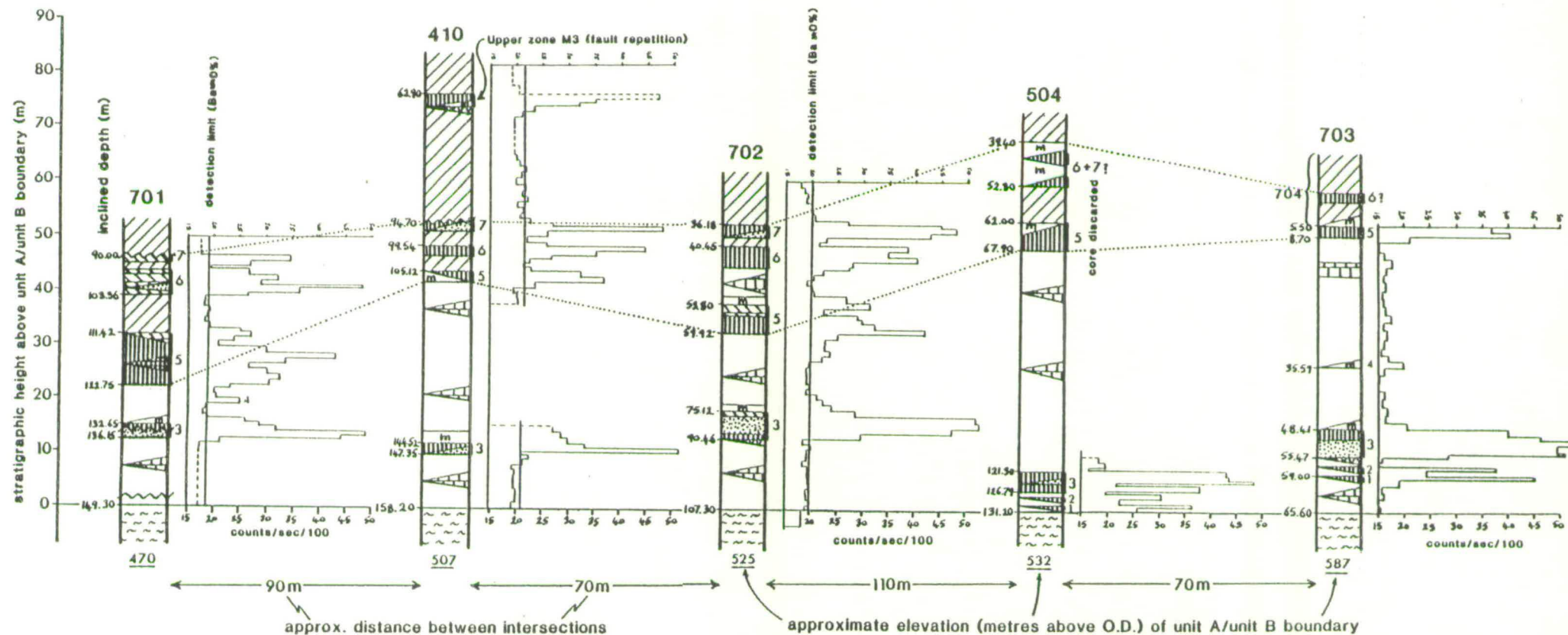




Fig. 2.29: T.V.D. stratigraphical profiles of M3 intersections in Foss East, with Zn&Pb contents of analysed intervals (page 1 of 2)

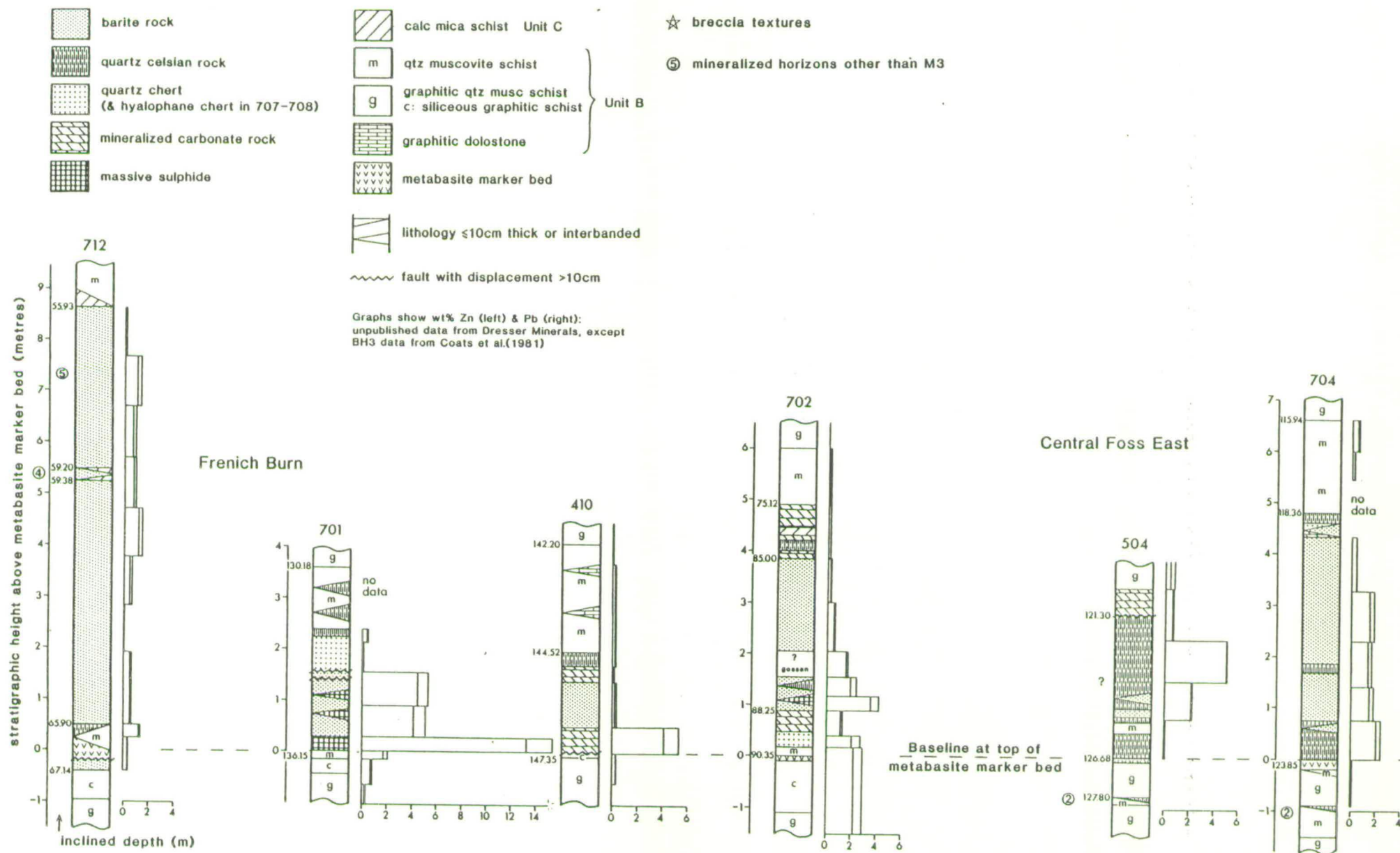




Fig. 2.29 (continued)

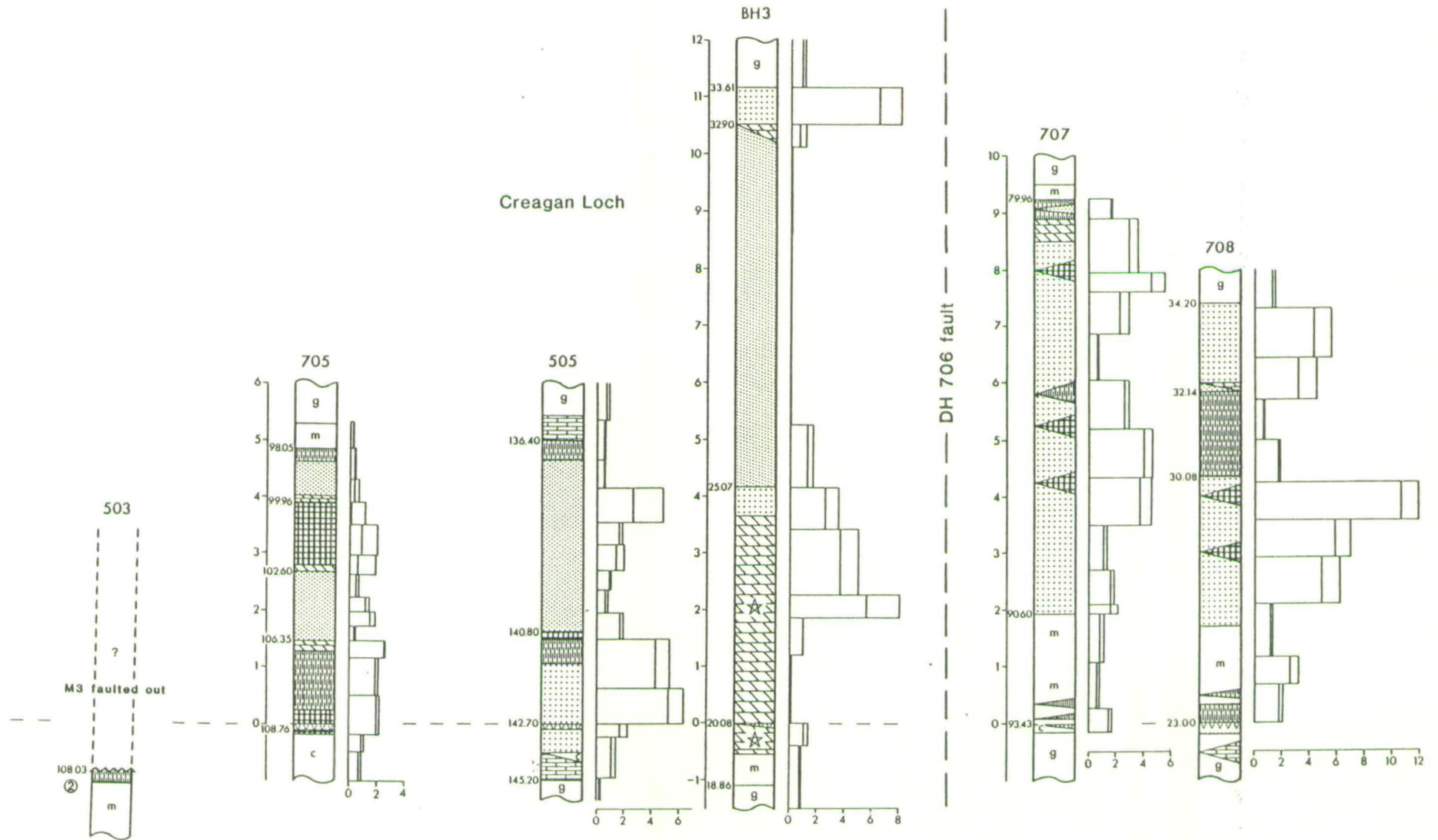


Fig. 2.30: T.V.D. profiles of mineralized zone intersections in the Creagan Loch area  
with Ba content determined by Portable XRF

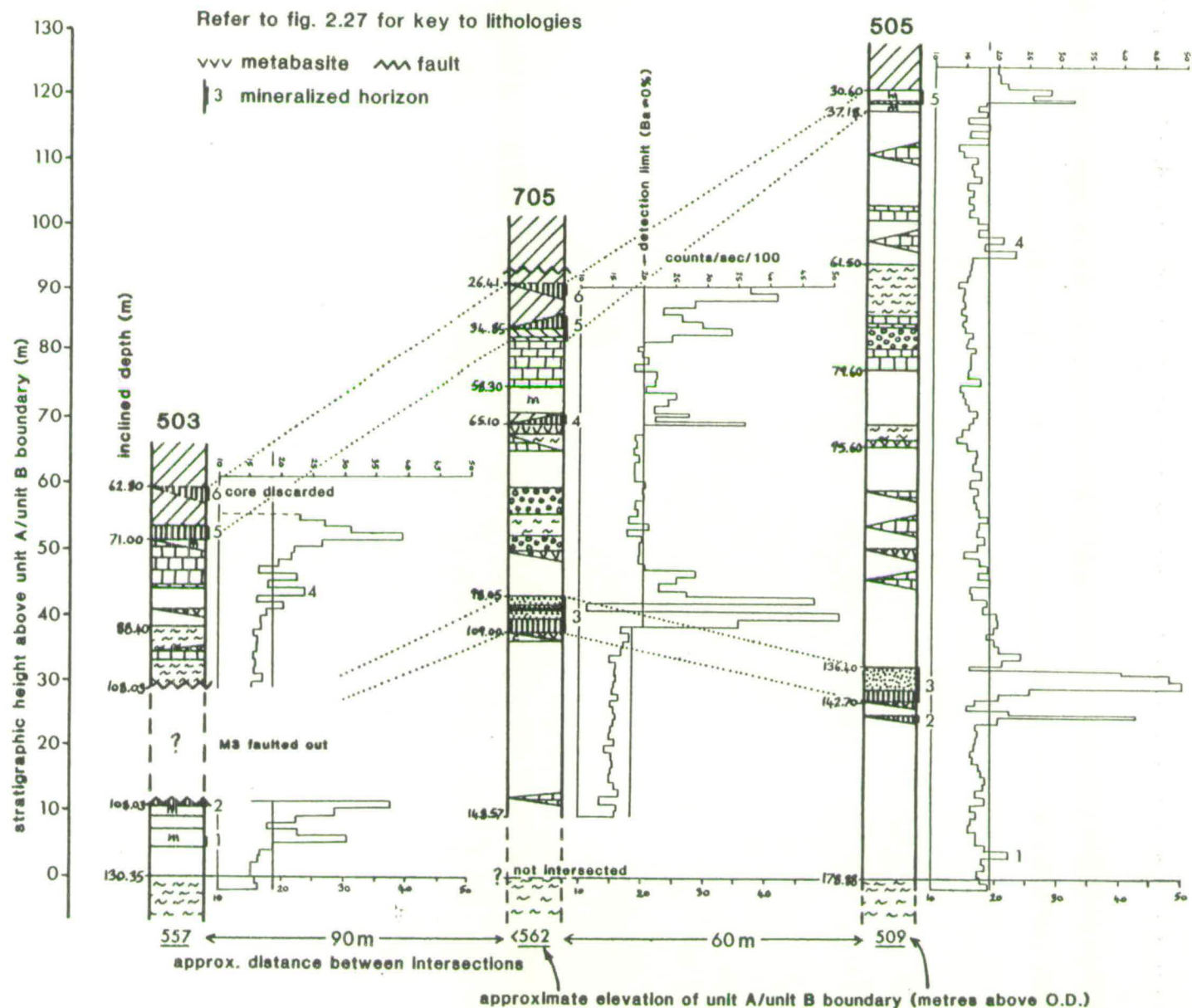


Fig. 2.31: Geological cross-section through DHs 705 & 202, Creagan Loch

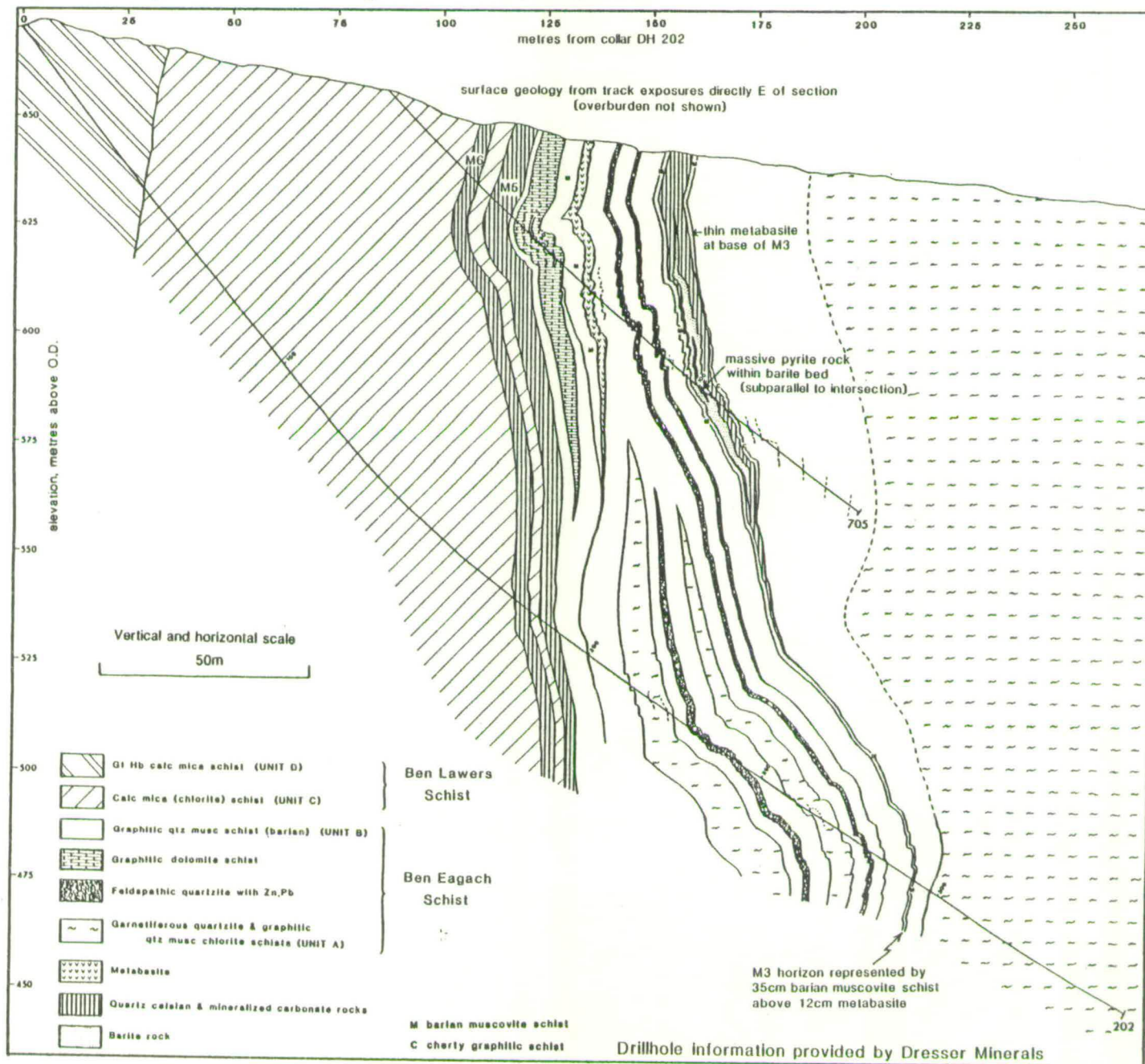




Fig. 2.32: Geological cross-section through DHs 706/7/8, 204 & 602, east of Creagan Loch

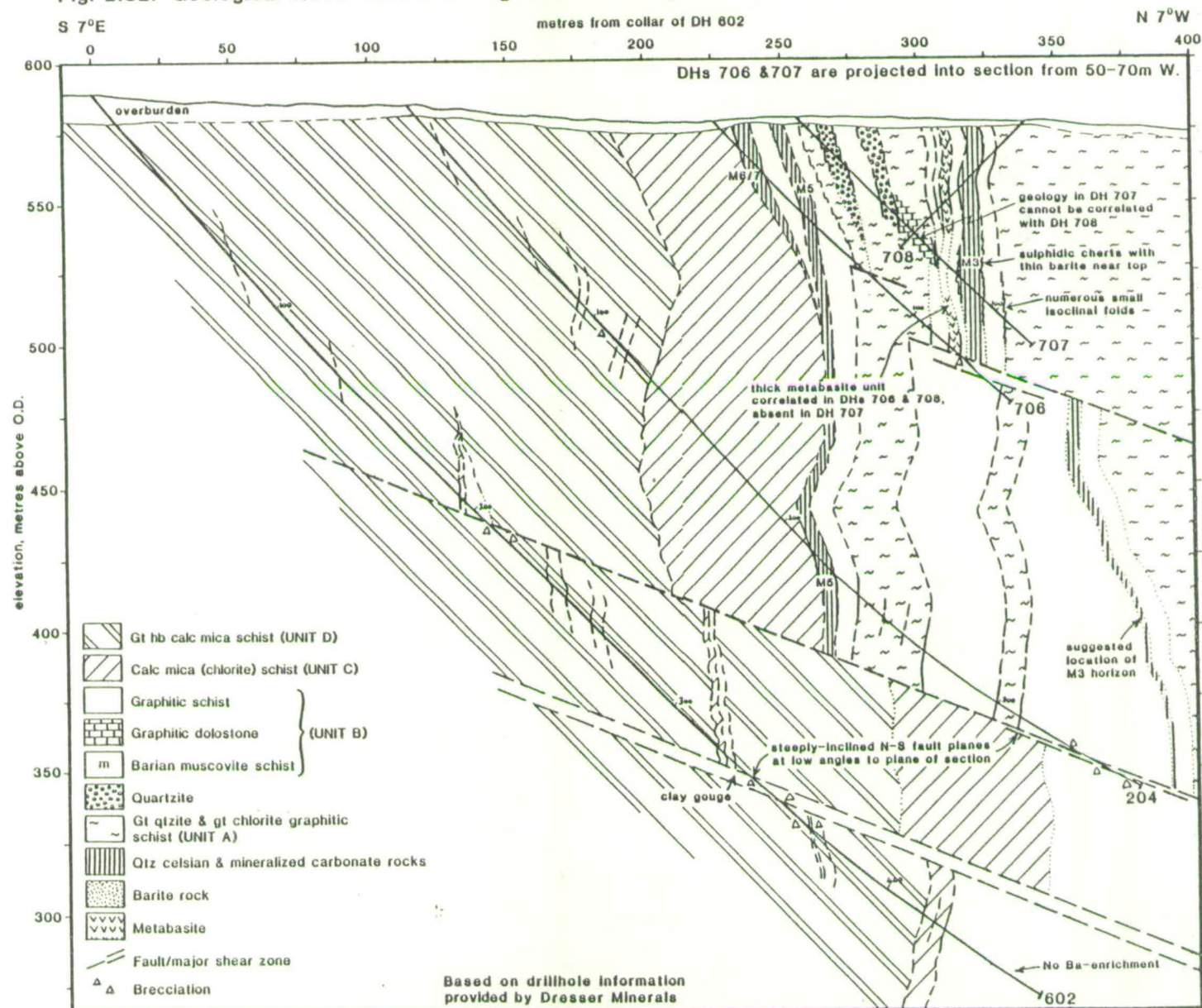


Fig. 2.33: T.V.D. profiles of the mineralized zone in deep intersections in Foss East with Ba contents determined by Portable XRF

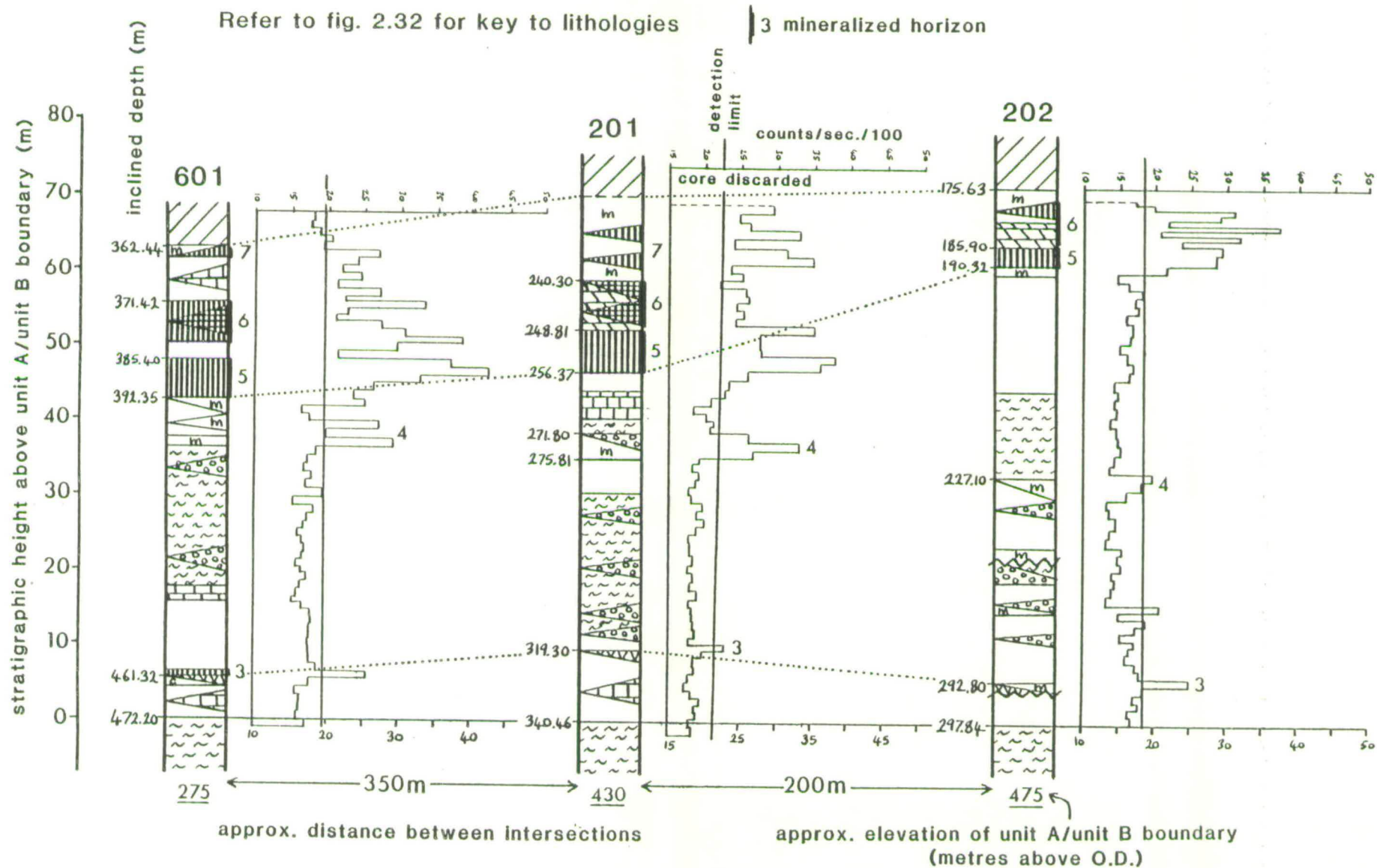
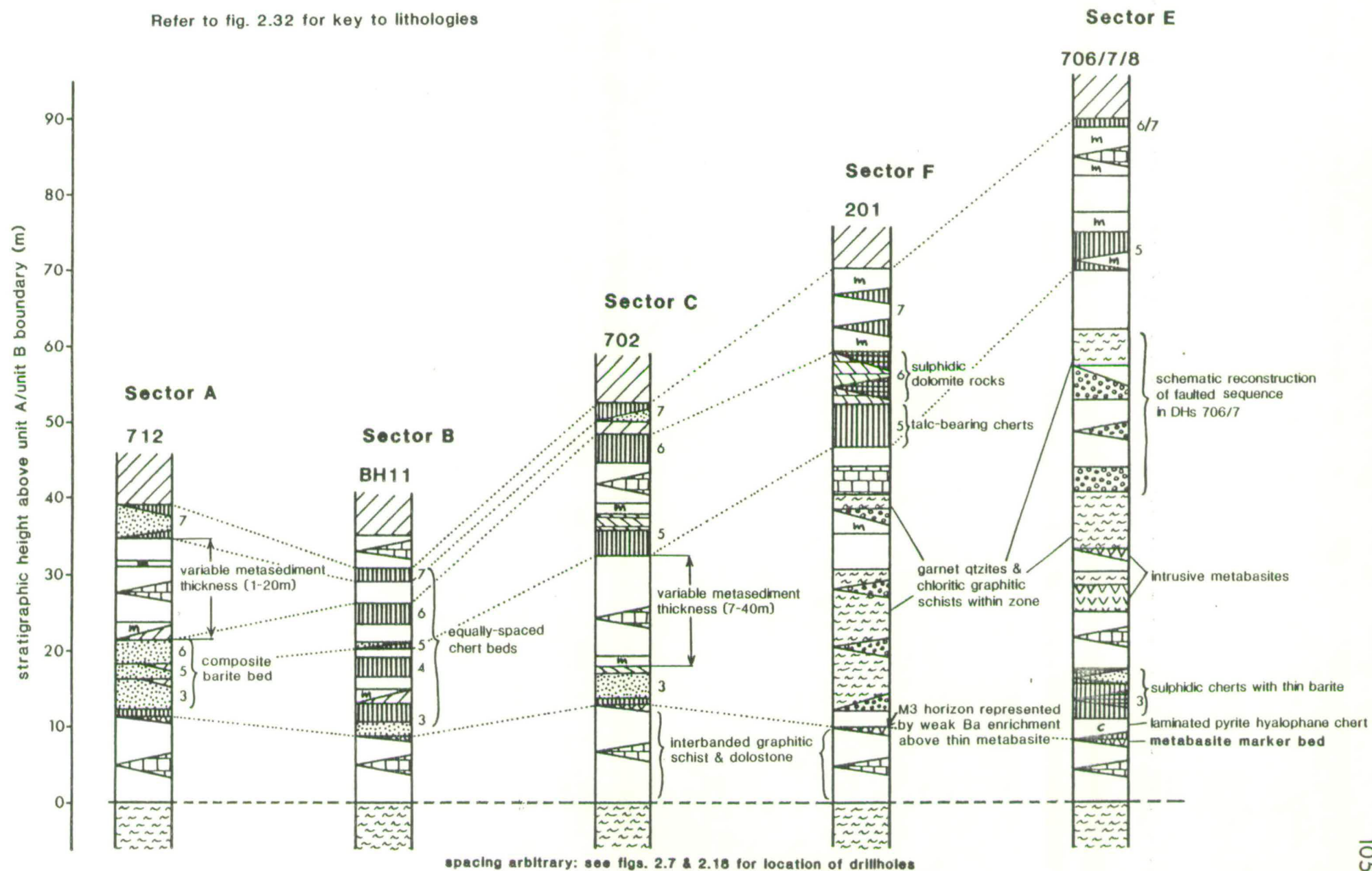


Fig. 2.34: Representative T.V.D. profiles of the mineralized zone in five lithostratigraphical sectors of Foss East

Refer to fig. 2.32 for key to lithologies





## CHAPTER 3: Petrography and geochemistry of the mineralized strata.

### 3.1 Introduction.

This chapter describes the petrography and chemical composition of lithologies which constitute the stratiform mineralized horizons (the 'mineralized strata') at Foss. These rocks consist largely of barite, sulphides, carbonates, barium feldspars and quartz, but generally contain volumetrically minor amounts (<10%) of plagioclase, micas and other ferromagnesian silicates. Metasedimentary and metabasic lithologies (which are generally rich in ferromagnesian silicates) are described in chapters 4 and 5 respectively. However, some rocks which are associated with the stratiform mineralization contain major amounts of both barium feldspars and micas and/or plagioclase. These rocks are also described in this chapter, and geochemical evidence is presented which suggests that they represent mixtures of sedimentary or basaltic material and components of hydrothermal origin. The rock type classification adopted in this study is illustrated in fig. 3.6.

Although mineralized rocks in the deposit exhibit a wide range of textures and modal compositions, they may be classified into four 'end-member' groups in which the predominant components are respectively barite, sulphides, carbonates and barium feldspars. Petrographic features observed in each of these groups are described in section 3.2, with particular reference to distinguishing textural and structural features of depositional origin from those of metamorphic origin. Textural evidence for diagenetic and metamorphic reactions which have affected the mineralogy of some mineralized rocks, including the replacement of diagenetic sulphate crystals by barium feldspars and the decomposition of barium carbonates, are described in section 3.3. Previous geochemical studies of the mineralized strata are reviewed in section 3.4, and the results from XRF analyses of a small number of samples examined in this project are discussed with particular reference to identifying the mode of formation of unusual mineralized rocks which incorporate sedimentary or basaltic material. In section 3.5, spatial variations in the chemical composition of the mineralized strata are examined with an

appraisal of the evidence for metal zonation in the deposit, which may be related to the proximity of exhalative vents.

### 3.2 Petrography.

#### 3.2.1 Barite rock.

##### Textural variation and banding.

Massive barite rock is white or grey coloured and consists largely of a granoblastic matrix of polygonal or irregular barite grains (typical size range, 0.1-0.5mm), which frequently exceed 90% by volume. Some barite rocks are coarser grained (up to 2mm) and in such cases a tectonic fabric may be visible in hand specimen as a dimensional preferred orientation of elongate barite grains. In the Foss adit, this prolate fabric is orientated parallel to the westward-plunging  $F_3$  fold axes and rodding lineations. A tectonic fabric is occasionally visible in thin section, particularly in barite rocks which also contain platy minerals such as micas and cymrite (plate 45).

Parallel banding on scales ranging from 1-2mm to 1-2cm is very common, and barite rock observed in the Foss adit often has a 'zebra' appearance due to alternating white and dark-coloured layers (plates 4 and 5). Less frequently, a lenticular banding is seen with elongate, diffuse lenses of white barite in a darker barite matrix (plate 6), somewhat similar to lenticular-banded barite rock described by Zimmerman (1970) in the Meggen deposit, Germany. At Foss, the banding is defined by varying amounts of coloured impurities, which are principally pyrite and magnetite, with occasionally fuchsite, phlogopite and barian biotite. Very finely dispersed pyrite inclusions account for the grey colouring, and minor and occasionally major amounts of sphalerite (up to 30% in some bands) impart an orange or pink colour to some barite in the M3 horizon in Foss East (plates 26 and 47). However, the red colour of barite in outcrops near BH2 (plate 1) and at Creagan Loch, is due to hematite staining associated with the weathering of enclosed sulphides and/or ferroan carbonates.

Bands of quartz chert and of granular-textured dolomite rock, typically 1-5cm thick, are common in barite rock in the French Burn composite bed (part 2.4.1) and elsewhere. These bands are occasionally boudinaged (plate 9), suggesting differences in



structural competency during metamorphism. Examples of brittle deformation of banded barite rock, subsequently annealed during metamorphism, are illustrated in plates 5 and 10.

#### Mineralogy.

Coats et al. (1981) noted an antipathetic relationship between the presence of magnetite and that of sulphides in barite rock. In some intersections, such as BH3 and DH 705, there is an abrupt change from pyrite- to magnetite-bearing barite rock with increasing stratigraphic height, but elsewhere these varieties alternate through the barite bed (e.g. in M3 intersected in DH 203: Appendix A.6). Coexisting magnetite and sulphides (pyrite, pyrrhotite and sphalerite: plates 97, 98) have been observed in six of about eighty barite samples examined in this study<sup>(see fig. 3.2)</sup>. Dolomite is more common than calcite in barite rocks, except in the Creagan Loch area where sulphide- and calcite-banded barite is comparatively common. Cathodoluminescence and microprobe studies have shown that barium carbonates occur as relict grains in calcareous barite rocks (see part 7.5.3 and plate 48), and much of the calcite, dolomite and barite in these rocks may be decomposition products of barium carbonate precursors (part 3.3.2).

#### Remobilized barite.

Dilational, cross-cutting or conformable barite veinlets are occasionally found in rocks adjacent to barite beds, particularly in areas affected by late-metamorphic faulting. The barite in these veinlets may be coarsely crystalline, or have a bladed appearance with crystal boundaries perpendicular to the vein orientation (plate 112). Open space growth of barite crystals on fault planes was observed in the Foss adit and in a track exposure in central Foss East (plate 44). Coarse barite veinlets are occasionally seen within granoblastic barite rocks. One sample from outcrop has a mottled, clouded appearance with rosette-like growths, and evidently represents post-metamorphic, remobilized barite.

#### 3.2.2 Sulphide rocks.

In the present context, "sulphide rocks" are defined as rocks in which the sulphide forms over half of the volume, and includes units comprised largely of pyrite, pyrrhotite or sphalerite, or of a combination of these phases. Galena and chalcopyrite usually occur

in trace or minor amounts. Rocks in which pyrite, pyrrhotite and sphalerite are the principal constituents are described in turn.

Pyrite is the most abundant sulphide mineral at Foss and typically forms subhedral to euhedral crystals which vary in grain size from microscopic to 5mm or more, often within the same sample (cf. plate 35). Very coarse-grained pyrite rock (1-2cm crystals), in some parts monomineralic, forms a bed about a metre thick in the M3 horizon intersected in DH 705 (fig. 2.29 and plate 25). However, this occurrence is unique at Foss and massive bands and lenses of sulphide-rich rock are usually 5-10cm thick. Coarsely granular pyrite rocks (plate 7), with minor sphalerite, occur near the base of the M3 horizon in several Foss East intersections (DHs 701, 702, 505 and 705: fig. 2.29 and plate 27) and at the base of the M5 barite bed in the Foss adit (part 2.3.3).

More commonly, pyrite crystals are set in a matrix of sphalerite, barite, celsian, quartz or carbonates. Pyrite also occurs as concordant or cross-cutting veinlets, and in many metasediments and some mineralized rocks, textural features indicate that some or all of the pyrite has replaced pre-existing pyrrhotite. Often the porous structure or 'bird's-eye' texture of this secondary pyrite (cf. Ramdohr, 1980: see plates 101, 102) enable it to be distinguished from pre-existing, well-crystallized pyrite. The skeletal nature of replacement pyrite, or other evidence of volume reduction (plate 99) suggest that the pyrrhotite-pyrite reaction may have been accompanied by a loss of iron. Traces of marcasite, distinguished by its green anisotropism, often occur along the interfaces between pyrrhotite and replacement pyrite. Occasionally concentric growth zoning is seen in pyrite crystals which probably grew during the retrograde stages of metamorphism (plate 100).

Pyrrhotite is absent from most sulphidic rocks in the M3 horizon but forms massive bands in some of the upper mineralized horizons in Foss East, notably those intersected in DH 207 (plate 31). In one sample (207-14), a 5cm band of 80% pyrrhotite with interstitial rutile, quartz and calcite adjoins a biotite-rich quartz schist containing about 20% pyrrhotite. Within 10m of drillcore (Appendix A) are several other massive pyrrhotite units, some of which have breccia textures with irregularly-shaped inclusions (up to 1.5cm in size) of coarse quartz and dolomite in a

matrix of pyrrhotite, chlorite, phlogopite and cymrite (partially replaced by celsian: see part 3.2.4). The texture of this pyrrhotite rock, and of similar rocks in other intersections (e.g. DH 505), resembles the "durchbewegung" texture developed by solid state deformation of pyrrhotite during metamorphism, which is commonly found in the Caledonian massive sulphide deposits of Scandinavia (Vokes, 1969).

Sphalerite-rich massive sulphide rocks are particularly common in the M3 horizon intersected in DHs 707 and 708 (fig. 2.29), where sulphides also vein cherty quartz rocks producing "pseudobreccias" (plate 30) which are clearly due to tectonic remobilization. In the sulphide band represented by sample 708-7, euhedral pyrite crystals up to  $1\text{mm}^3$  and constituting 25% of the rock, occur in a matrix of coarse, red sphalerite (grains up to 2mm) which has a modal abundance of 60%. Galena forms ~5% of this sulphide rock and the remaining constituents are porphyroblastic celsian and interstitial quartz, barite and apatite. Other sulphidic rocks are rich in dolomite and/or calcite (e.g. samples 505-18, 705-21 and 708-6), and trace amounts of barium carbonates have been found as small inclusions in the sulphides in many samples (part 7.5.3).

### 3.2.3 Mineralized carbonate rocks.

A wide variety of carbonate-rich rocks occur in the mineralized zone, and these appear to be of both hydrothermal-exhalative and sedimentary origin (metabasic rocks in the mineralized zone also have a large carbonate content: see section 5.2). Four principal types may be distinguished: (1) graphitic dolostones; (2) dolomite-celsian rocks, including talc- and sulphide-bearing varieties; (3) coarsely crystalline dolomite rocks, often rich in sulphides; and (4) calcite rocks.

#### Graphitic dolostones.

These occur as mid- to dark-grey, massive beds, typically decimetric but locally several metres thick, within the Ben Eagach Schist. They often contain sulphide laminae but are seldom enriched in barium, and are regarded as diagenetically altered limestones which may be allochthonous components of the sedimentary sequence. These are described in part 4.2.3. However, gradational lithologies are found since in some intersections of mineralized strata (e.g. M5

in DH 702; Appendix A), barium-enriched dolostones are dark-coloured due to traces of carbonaceous material.

#### Non-carbonaceous dolostones and dolomite-celsian schists.

Cream, pale grey, or beige-coloured, fine-grained dolostones which are similar to the above except for the absence of carbonaceous material and sulphides, are common in parts of the Ben Lawers Schist. Similar lithologies are found in association with the upper mineralized horizons (M5-M7) intersected in many Foss East drill-holes (e.g. DHs 201 and 202; Appendix A), where the dolostones are generally interbedded with quartz celsian rocks rather than pelitic rocks, and may therefore be components of the mineralized strata. This is supported by the presence of minor celsian within these dolostones, which grade into laminated or schistose celsian dolomite rocks (plate 52) and, with decreasing dolomite content, into quartz dolomite celsian schists (cf. plate 51).

Talc is associated with massive, sulphide-poor dolostone beds in many of the Foss East upper mineralized horizon intersections. In one interval (sample 201-6, plates 23 and 47) finely granular dolomite and recrystallized dolomite and quartz form rounded pods several centimetres across in a highly schistose matrix of talc, dolomite and celsian. (The celsian appears to have pseudomorphed foliated cymrite: see part 3.2.4). This is regarded as a tectonic breccia, although the rock has a macroscopic appearance similar to the "chicken-wire texture" seen in evaporite deposits. Reaction textures between dolomite, quartz and talc are absent. The talc may be a primary component of the mineralization or could be a breakdown product of a magnesite-bearing precipitate (part 6.4.2).

#### Coarsely crystalline, sulphidic dolomite rocks.

Mineralized carbonate rocks consisting largely of coarse-grained dolomite with varying amounts of quartz, celsian and sulphides, are common in the M3 horizon in Foss East, and attain their thickest development (~4m) in BH3 at Creagan Loch (fig. 2.29). These often exhibit a breccia texture in which sulphides are abundant in the matrix. Cathodoluminescence observations (for operating conditions, see page preceding plate 45) reveal highly complex textures in these coarse dolomite rocks (e.g. plates 49 and 50), which appear to have undergone several episodes of dissolution and partial recrystallization. Centimetre-sized, euhedral crystals

of celsian, rutile, sphalerite and galena occur in a coarse, ferroan dolomite rock exposed at the roadside about 100m west of BH3 (plate 43). This appears to be a post-tectonic, recrystallized equivalent of a schistose celsian-dolomite rock which outcrops nearby (sample N81-308; plate 52). The rock is beige or tan coloured when fresh, but weathers at outcrop to a friable, dark brown gossan reflecting the high iron (and manganese) content of the carbonate.

#### Calcite rocks.

Calcite and dolomite, readily distinguished under cathodoluminescence by their orange and red colours, respectively, occur together in many mineralized carbonate rocks. These phases may be coarsely or finely intergrown, segregated into bands, or present in composite, growth-zoned crystals. Carbonate rocks consisting entirely of calcite are comparatively rare at Foss, and are closely associated with barite rock. White calcite rock containing minor sulphide (often galena) was noted as thin (usually <10cm) beds in several intersections of M3 in central Foss East and in DH 429.

Coats et al. (1981) found a coarse-grained, manganoan calcite-quartz-sulphide rock underlying the barite rock intersected in BH2 (fig. 2.8). A banded lithology with the same components (and similarly rich in Zn and Pb) occurs above and below a bed of massive pyrite rock in DH 705 (samples 705-18 and 19: fig. 2.29 and plates 24 and 25). A coarsely granular, manganoan calcite rock containing sphalerite bands outcrops on Ben Eagach (sample N81-50: table 7.7). In a shallow borehole nearby (BH4), two intersections of a similar lithology are separated by a zone of brecciated calcite and dolomite rocks. Sulphidic carbonate rocks in BHs 2 and 4 are notably rich in silver (up to 85ppm measured by Coats et al., 1981), and this lithology may be spatially associated with hydrothermal vents (see section 3.5).

#### 3.2.4 Quartz celsian and cymrite rocks.

##### Macroscopic appearance.

Lithologies referred to as quartz celsian rocks are extremely variable in appearance. They range from massive, grey-coloured cherts, which are often banded with varying proportions of the mineral constituents or contain parallel laminae of sulphides (plate 20), to strongly foliated and contorted schistose varieties which

may have white, cream, beige, pale green or purple hues (plates 32-34). Fine grained, celsian-bearing quartz rocks (referred to as cherts to distinguish them from quartzites of detrital origin) are locally common, for example underlying the barite bed in the Foss adit (plate 20), in the 'upper zone' intersections in the Frenich Burn area, and in the M3 horizon intersected in DHs 707 and 708 (fig. 2.29 and plate 30).

Breccia-textured, poikiloblastic quartz celsian rocks containing quartz chert fragments, occurring in the Foss adit and at the base of the Frenich Burn barite bed, were referred in parts 2.3.5 and 2.4.1 (plates 11, 16 - 18). These were originally interpreted as syn-depositional, intra-formational chert breccias. However, cross-sections through two samples from the adit occurrences show that the quartz chert fragments are very elongated with long dimensions up to ten times their width (see plate 18). This structure, together with the presence of what appear to be disrupted fragments of white vein quartz in one sample, suggests that the brecciation may be tectonic rather than syn-depositional in origin. Vokes (1983) has noted that a pronounced elongation of 'clasts' in deformed stratabound orebodies is generally indicative of a tectonic origin. This hypothesis seems more reasonable for the adit occurrences when mineralogical changes during metamorphism, namely the replacement of cymrite by celsian, are taken into account. Textural evidence for this replacement is described below.

#### Microscopic appearance.

In thin section, celsian-bearing rocks often exhibit relict foliated textures in which a mosaic of coarse, skeletal celsian crystals (typically 0.5-1.0mm diameter) appear to have replaced aggregates of a strongly foliated and crenulated phase (plates 52-55). Although coexisting celsian and muscovite are occasionally observed (plate 54), muscovite schists lacking celsian often adjoin quartz celsian schists lacking muscovite and a large-scale, selective replacement of muscovite by celsian seems unlikely. However, many samples of schistose celsian rock examined in this study contain cymrite as inclusions in quartz or pyrite, or relict areas of foliated cymrite in which incipient nucleation of celsian is occasionally seen (plate 51). Cymrite is a widespread although volumetrically minor component of the mineralized strata and, as



noted by Fortey and Beddoe-Stephens (1982), celsian and cymrite are very similar in chemical composition and the replacement of cymrite by celsian merely involves dehydration (part 6.2.3).

Rocks which have a cherty appearance, such as those common in the upper zone in the Frenich Burn area, contain thinly distributed bladed celsian and cymrite in a granular quartz matrix (e.g. plate 57). In a somewhat coarser grained variety illustrated in fig. 2a of Moles (1985), both cymrite and celsian form platy crystals and the textures suggest the replacement of individual or grouped cymrite crystals by single crystals of celsian. In rocks or bands in which celsian is the principal constituent, it forms either an irregular mosaic of small interlocking grains (plate 60b), or more commonly, coarse, subhedral and twinned crystals (plates 52-55). A poikiloblastic texture is occasionally developed with zoned and twinned patches of feldspar enclosing fine-grained quartz (plate 56). A folded or crenulated internal foliation, consisting of trails of quartz, mica, rutile or sulphide inclusions, is often seen within the coarse celsian mosaic (plate 58). This relic fabric is considered to mark original cymrite grain boundaries, a supposition supported by observations of partial replacement of foliated cymrite by coarser-grained celsian in several samples (e.g. plate 51). Celsian pseudomorphs after cymrite have rarely suffered penetrative deformation, which also indicates that celsian growth was post-D3. However, in one sample examined which shows signs of brittle deformation and veining, coarse celsian grains are partially replaced by aggregates of cymrite (101-2, plate 59). This suggests that the stability field of cymrite was re-entered during post-metamorphic uplift, although celsian replacement by cymrite was very localized (see section 8.4 and Moles, 1985).

#### Other mineral constituents of quartz celsian and cymrite rocks.

Carbonates, muscovite and sulphides are commonly present as minor components of quartz celsian rocks, and with increasing modal abundance, these grade into carbonate rocks and quartz muscovite schists (in which hyalophane is more common than celsian, as discussed below). Biotite, phlogopite, fuchsite and talc occur in trace or minor amounts in some schistose quartz celsian rocks. Rutile is a common accessory phase (<1% modal) which occasionally forms coarse crystals or sprays (plate 68), but is usually finely

dispersed within celsian crystals and may be sufficiently abundant to impart a mauve or purple colour to the rock or to rutilated patches (plates 17, 60). Cathodoluminescence observations reveal the widespread presence of apatite as a trace constituent in quartz celsian rocks and mineralized carbonate rocks (section 7.6).

Although Coats et al. (1981) noted that the coexistence of barite and celsian is rare in thin sections, celsian-bearing rocks frequently adjoin barite rock and interbanded quartz celsian chert and barite are common in some Foss East intersections (e.g. DH 504: fig. 2.29 and plate 58). Barite occasionally occurs as thin lamellae within quartz celsian rocks (e.g. N80-30A, see fig. 4a of Moles, 1983), but more frequently barite is present only as syn- or post-metamorphic veinlets.

### 3.2.5 Hyalophane rocks.

Several barium-enriched rocks described in drillcore logs (Appendix A) as 'graphitic chert' were found by microprobe and cathodoluminescence examination to contain hyalophane as a major constituent (modal abundance up to 65%). Typically, quartz and hyalophane form a fine-grained granular matrix containing evenly-dispersed graphitic granules and laminae of coarser pyrite and sphalerite. Coarser-grained quartz and hyalophane are often associated with the sulphides and quartz may form pressure fringes (cf. plates 65, 75). Sulphidic hyalophane cherts are characteristic of the lower part of M3 intersected in DH 708 (plate 29, samples 5a, 5b). Bladed "porphyroblasts", consisting of composite grains of hyalophane and potassic celsian, occur in a few quartz muscovite and hyalophane rocks, previously described by Fortey and Beddoe-Stephens (1982). These provide textural evidence for reaction between barite and barium feldspar and are discussed in detail in the following section.

Hyalophane is also a major constituent of several rock samples which from geochemical studies (described in part 3.4.2) are considered to have been mineralized basic igneous or sedimentary material. The hyalophane in these lithologies forms a coarse-grained matrix or is dispersed in a matrix of quartz, albite, micas and dolomite (plates 78, 84). Unlike celsian, the hyalophane shows no textural evidence for replacement of a foliated precursor such as

cymrite. However, in some samples of quartz muscovite hyalophane schist, hyalophane forms ovoid porphyroblasts which retain an internal  $D_{1-2}$  fabric of fine-grained quartz and muscovite inclusions, which is oblique to the  $D_3$  foliation defined by alignment of coarser muscovite in the matrix (plate 79). In other rocks with a similar mineralogy, a finely foliated muscovite fabric is partially replaced by irregular patches of hyalophane, which may coexist with celsian and cymrite (plate 81). These three phases also coexist in some sulphide rocks (plate 57) in which hyalophane and potassic celsian form complex zoned crystals.

### 3.3 Post-depositional changes in mineralogy and texture.

Petrographical features suggest that some of the barium feldspar at Foss may be a product of diagenetic and metamorphic reactions between sulphate and silicate phases. Although textural evidence of such reactions in feldspathic rocks is rare, their petrogenesis bears upon diagenetic processes which may have had a more widespread influence on rock compositions. Encapsulated grains of barium carbonate minerals, which have been found in trace amounts in the mineralization (described in detail in Ch. 7), may be relicts of a more common, pre-metamorphic component of these rocks. It is argued here (part 3.3.2) that these carbonates are also probably of diagenetic origin. Other petrographical evidence for the diagenetic/metamorphic redistribution of sulphur is discussed in part 3.3.3.

#### 3.3.1 Hyalophane pseudomorphs of probable diagenetic sulphate crystals.

##### Description.

Textural evidence for reaction between barite and barium feldspar is seen in certain uncommon quartz muscovite and hyalophane schists, which contain composite, bladed "porphyroblasts" of hyalophane with internal quartz, barite and kaolinite inclusions. An example from BH9 (inclined depth, 28.6m) was previously illustrated by Fortey and Beddoe-Stephens (1982): another sample from the same intersection (09-06) was examined in this study (Appendix B). This rock is cherty and carbonaceous, and contains white-coloured tabular structures up to 5mm in length and 0.2mm in breadth, which are mostly aligned subparallel to the bedding and foliation, although

some are at oblique angles (plates 61, 62). These structures appear to pre-date the metamorphic fabric as they show signs of disruption by transverse cleavage planes, and some have quartz-filled pressure fringes which are elongated in the direction of the S1-S2 cleavage. Cathodoluminescence observations also show that hyalophane is a major component of the matrix in this rock, which is unusually rich in apatite (up to ~8% in dark, carbonaceous laminae; plate 62b).

A sample of muscovitic "quartzite" examined by Coats et al. (1981) from outcrops in the Creagan Loch area (CYR6: Appendix B.3), contains similar hyalophane structures which appear dark in transmitted light due to enclosed clay material (fig. 3.1). Again, these tabular structures have a bow-tie arrangement of fine quartz inclusions and are variably dismembered by the development of micaceous folia. In this study, a third example of these structures was observed in a graphite-free, quartz mica hyalophane schist occurring adjacent to the M3 horizon in outcrops on Creag an Chanaich (N81-80: fig. 2.8). In this sample, hyalophane forms some 60% of the matrix and also occurs as discrete tabular, platy and radiating structures which contain a clouded mixture of barite, quartz and kaolinite (fig. 3.1 and plate 63). Several of these objects are oblique to a weak foliation defined by the alignment of micas in the matrix, which abuts against and wraps around the tabular structures (fig. 3.1).

A graphitic quartz hyalophane chert from the lower zone intersection of M6 in BH11 (Frenich Burn area; fig. 2.23) also contains randomly orientated, light-coloured tabular structures of similar size. However, on detailed examination (plate 65), the tabular structures in this sample (11-01) are found to consist of composite, fine-grained hyalophane cores mantled by coarse-grained quartz reminiscent of pressure fringes to pyrite (cf. plate 75). Although the hyalophane structures in this rock do not contain barite, quartz or kaolinite inclusions, they may be related to the features described in previous samples and are also regarded as pre-deformational in origin.

Probable pre-metamorphic structures were also noted in a sample of finely laminated, pyritic quartz chert from the equivalent to the M3 horizon on the northern limb of the Creag na h-Iolaire Anticline in Foss West (G114: plate 35). In this rock, potassic celsian forms

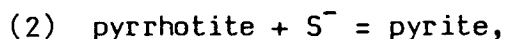
complex, lensoid and tabular structures with frayed or serrated terminations, which appear to have both replaced and displaced the laminated quartz-pyrite matrix (plate 66). The celsian is variably clouded with barite, quartz and clay minerals, which in this case appear to pseudomorph the celsian and are regarded as weathering products. Partial oxidation of coarser-grained pyrite in this sample, which was from float material immersed in peat, also indicates surface weathering.

#### Interpretation.

The textures in samples 09-06, CYR6, and N81-80 suggest that hyalophane formed at the expense of barite under reducing conditions during diagenesis or early metamorphism, an explanation also put forward by Fortey and Beddoe-Stephens (1982). The diagenetic replacement of authigenic barite by hyalophane, quartz, calcite and pyrite in Lower Ordovician shales in the Oslo Graben has been described by Bjorlykke and Griffin (1973). A reaction such as:



concomitant with the incorporation of sulphur into iron sulphides:



is consistent with the observed mineral assemblages in both the Foss and Oslo Graben occurrences. (Sulphur isotope evidence for this reaction at Foss is discussed in part 9.5.2). The necessity of a reducing agent to promote reaction between barite and kaolinite to form barium feldspar has been demonstrated in sintering experiments by Segnit and Gelb (1970). The incomplete replacement of barite in CYR6 and N81-80 may be due to the consumption of all available carbonaceous matter and/or the shielding of relict barite and kaolinite by the reaction envelope of hyalophane. The present day replacement of potassic celsian in G114 by barite, quartz and clay minerals, under oxidizing conditions with high sulphur concentrations, is in effect the reverse of the above reaction.

The curved and serrated barite-hyalophane structures in N81-80, and the celsian pseudomorphs in G114, bear a morphological resemblance to diagenetic gypsum and anhydrite occurring in Recent and ancient evaporite deposits, especially those described from the Proterozoic McArthur Group (Walker et al., 1977) and from the stratigraphically equivalent Urquhart Shales at Mount Isa (McClay

and Carlile, 1978). Barite and quartz pseudomorphs after gypsum have also been described from Barberton Mountain Land, South Africa (Heinrichs and Reiner, 1977) and from the North Pole deposits, Pilbara, W. Australia (Lambert et al., 1978), both of which are early Archean.

Lath-like anhydrite pseudomorphs of gypsum in the Zechstein evaporite deposits at Billingham, Co. Durham, have an hourglass or bow-tie pattern of dolomite inclusions (F.H. Stewart, pers. comm. 1983) (plate 64), which resemble the inclusion patterns in the tabular structures in samples from Foss (09-06 and CYR6: fig. 3.1). Since similar structures have not been illustrated in sedimentary barite crystals, it is possible that the hyalophane-kaolinite-barite and celsian pseudomorphs described above were originally formed as calcium sulphate crystals. These may have formed from highly saline pore waters (salinity >11.6wt%: Russell, 1978) in the sediments shortly after their deposition and before infiltration by the barium-rich hydrothermal fluids which replaced Ca by Ba in the sulphate crystals. The pseudomorphs have survived metamorphism because of the siliceous nature of these rocks, whereas evidence for possible diagenetic sulphate formation in shaly sediments would have been destroyed by penetrative deformation.

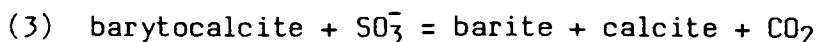
This occurrence of possible pseudomorphs after gypsum is not unique in the Middle Dalradian, since pseudomorphs of similar morphology (consisting of ferroan calcite, quartz and 'opaques') are described by Anderton (1975) from the stratigraphically equivalent Craginish phyllites, and by Barraclough (referenced in Willan, 1983) from the Crinan Grit, in the SW Highlands (fig. 1.4). Quartz-dolomite-pyrrhotite pseudomorphs after gypsum have also been described from the Lower Dalradian, Ballachulish Slate in Argyll (Hall, 1982).

### 3.3.2 Formation and decomposition of barium carbonates.

The barium carbonates, witherite ( $\text{BaCO}_3$ ), norsethite ( $\text{BaMg}(\text{CO}_3)_2$ ), barytocalcite ( $\text{CaBa}(\text{CO}_3)_2$ ) and possibly benstonite ( $\text{MgCa}_6\text{Ba}_6(\text{CO}_3)_{13}$ ), occur in trace amounts as small inclusions in pyrite and quartz crystals (plate 48) in about twenty samples of massive sulphide, barite and carbonate rocks examined (see part 7.5.3). The restricted occurrence as inclusions, and the presence in



the rock martrix of probable reaction products from the decomposition of barium carbonates (barite, dolomite and calcite), suggest that the barium carbonates were a more abundant (although still minor) component of the mineralization before metamorphism. Decomposition of the carbonates would have involved the introduction of sulphite and release of carbon dioxide, for example:



or, alternatively, closed-system reactions could have occurred e.g.:



Lydon et al. (1979) have discussed the genetic significance of coexisting barite and witherite with respect to the formation of bedded barite + sulphide deposits in the Selwyn Basin. Using published thermodynamic data, they demonstrate that the coeval precipitation of a barite-calcite-witherite assemblage would require the mineralizing solution to be far removed in composition from normal ocean water (fig. 3.3). Further investigations by Lydon et al. (op. cit.) failed to confirm the presence of witherite (initially reported by Carne, 1976) in the Tea barite deposit, which they therefore consider to have been deposited from only slightly modified (barium-enriched) seawater. Large (1981a) used solubility product data to argue for a high activity of  $\text{CO}_3^{2-}$  in the pore waters during the diagenetic precipitation of barium carbonates in the Tom deposit (which is located about 18km to the NE of Tea in the same stratigraphic formation). He also suggests that the prevailing activity of  $\text{SO}_4^{2-}$  in the pore water may have been decreased as a result of both the formation of barite and the reducing nature of the pore waters.

Unfortunately, textural evidence of a possible diagenetic origin for the barium carbonates in the Foss deposit has been erased by metamorphic recrystallization and the limited preservation of these phases. It can only be asserted that the barium carbonates were formed before the growth of metablastic pyrites in which they are usually encapsulated. However, from the above discussion, it seems likely that the barium carbonates were precipitated from alkaline, reducing and sulphate-depleted pore waters within the mineralized beds, after their deposition and before the expulsion of pore waters associated with deep burial. The pore waters may have

been a mixture of basinal, alkaline brines (see part 10.3.2) and trapped hydrothermal solutions.

### 3.3.3 Post-depositional mobility of sulphur and metals.

#### Chemical mobility.

Lambert (1973) suggests that a wide variety of secondary textures and structures in sedimentary sulphide deposits (which ~~have~~ *not* been subjected to regional metamorphism) may be attributed to the post-depositional mobility of sulphur and metals. Sulphur species may be made available by the degradation of organic matter, the formation of pyrrhotite from pyrite, and the continuing bacterial reduction of sulphate in the pore waters, while metals may also be released from organic matter and clay minerals. Two comparatively uncommon features of the mineralization at Foss described above, namely the replacement of diagenetic sulphate crystals by barium feldspars and the probable breakdown of barium carbonates to form matrix barite and Ca-Mg carbonates, indicate some movement of aqueous sulphur species during diagenesis or early metamorphism.

Other textural evidence for sulphur mobility within the stratiform mineralization is limited to the localized, late metamorphic to supergene replacement of pyrrhotite by pyrite, which is a widespread phenomenon in the metasedimentary host rocks (see part 7.3.1 and Moles, 1983). Massive pyrrhotite bands (described in section 3.2.2) within the mineralization are very likely to be primary features, as they are in most other stratiform base metal deposits (Plimer and Finlow-Bates, 1978), and no textural evidence of pyrrhotite replacing pyrite is observed (as noted by Willan, 1980 and Willan & Hall, 1980 in samples from McPhun's Cairn, Argyll). However, the presence of pyrrhotite as an essential minor phase in the sub-M3 metabasite bed which is now a quartz dolomite muscovite schist (part 5.2.4), is attributed to hydrothermal and/or metamorphic sulphidation of ferromagnesian silicates (see section 7.7). Disseminated and banded base metal sulphides occurring in coarse-grained, detrital quartzites and in carbonaceous dolostones within the Ben Eagach Schist (see part 4.2.1) are considered to be of diagenetic origin and to have derived both their metal and sulphur contents from the enclosing pelitic sediments.

### Physical mobility.

The physical mobilization of sulphides into veins and segregations during metamorphism is generally minor and localized in extent, except in some mineralized carbonate and cherty quartz rocks where 'pseudobreccias' are developed (part 3.2.2; plates 22, 23 and 30). This contrasts with more extensively deformed sulphide deposits such as those of the Scandinavian and Appalachian Caledonides (e.g. Volkes, 1976; Whelan et al., 1984) and Mount Isa (McClay, 1982), which commonly contain breccias formed by the disruption of banded sulphides and intervening metasediment beds. Breccias of tectonic origin are in some cases difficult to distinguish from synsedimentary breccias in which a mineralized matrix encloses barren chert or carbonate clasts. The sometimes spectacular open-space growth zonation revealed by cathodoluminescence observations of mineralized carbonate rocks, suggests that carbonate breccias such as those intersected in BHs 3 and 4 are more likely to be metamorphic than depositional in origin. Retrograde metamorphic and post-metamorphic veinlets of pyrite, barite, calcite and quartz, are widespread but usually inconspicuous features of the mineralized lithologies.

## 3.4 Geochemistry and rock type classification.

### 3.4.1 Previous work: I.G.S. drillcore analyses.

Coats et al. (1981) provide XRF data for about 100 core intervals of typically 1-2m length from BHs 1-5 (major elements except  $\text{Na}_2\text{O}$ ,  $\text{H}_2\text{O}$  and  $\text{CO}_2$ , plus 12 trace elements), and for a further 370 core intervals from BHs 6-11 (partial analyses). They note that a cumulative frequency distribution of barium shows several distinct populations corresponding to barite rock (>30% Ba; mean = 51% Ba), quartz celsian rock (5-25% Ba), barium-enriched mica schist (0.1-4% Ba) and a background population of non-mineralized lithologies. There is some gradation between celsian rocks and muscovite-hyalophane schists with a lower Ba content. Statistical methods of discerning chemical groupings (cluster and factor analyses) in the more complete data set from BHs 1-5, revealed four stable groupings of mineralized lithologies, namely barite rock, quartz celsian rock,

sulphidic carbonate rock and Ba-Zn-enriched mica schist. Table 3.1 reproduces the average compositions of these groups calculated by Coats et al. (op. cit.).

A trivariate plot of  $\text{Al}_2\text{O}_3$  -  $\text{BaO}$  -  $\text{SiO}_2$  for drillcore samples from BHs 1-5 (fig. 3.4) separates the sample groups of barite rock, quartz celsian rock and Ba-enriched muscovite schist described above. Coats et al. (1981) observed a clear divide running from the  $\text{SiO}_2$  apex between the barium-enriched quartz mica schists and the quartz celsian rocks, which they interpreted as a limiting Ba:Al ratio below which barium is present in mica and above which barium is contained principally in celsian or hyalophane. Much of the scatter on this diagram is due to carbonate- and sulphide-rich rocks which contain minor amounts of barium silicates, or to core intervals in which barite is interbanded with quartz celsian cherts or mineralized sediments. Note that the smaller, homogeneous samples of mineralized rocks analysed in this study (described in subsequent sections) cluster near to the celsian-quartz join.

#### Metabasites, and Ti as a geochemical discriminant.

From the cluster analysis, Coats et al. (op. cit.) noted a fifth group of rocks characterized by high Ti, Ni, Fe and Ca contents which they found to include all rocks recognised as metabasic (i.e. amphibolites, 'epidiorites', and lamprophyres), together with several mica schist intervals (from BHs 5, 10 and 11) which were not obviously meta-igneous in character. The samples from BHs 10 and 11, variously described as calcareous quartz biotite or muscovite schists, are significantly enriched in barium (up to 4.7% BaO) but are otherwise chemically similar to the epidiorites and amphibolites (see tables 5.1 and 5.4). Analogous features indicate a basaltic component in thin bands of biotite quartz celsian schist (plate 67) intercalated with barite rock in BH5 north of Creag an Fhithich, despite the very high barium content (18-27% BaO) of this lithology. Coats et al. (op. cit.) suggested that these rocks formed as volcanic tuffs or thin lavas which were metasomatically altered by infiltrating hydrothermal or diagenetic solutions rich in barium.

The most characteristic feature of the metabasic lithologies is their high  $\text{TiO}_2$  content (>1.2wt% and up to 1.7wt%) compared with the metasedimentary rocks. A cumulative frequency diagram of titanium

in IGS drillcore samples (fig. 3.5a) enables three sample populations to be distinguished: (1) samples with  $<0.5\%$   $\text{TiO}_2$  (28% of the population, chiefly comprising mineralized rocks), (2) samples with  $0.5\text{--}1.0\%$   $\text{TiO}_2$  (67% of the population, the majority of metasediments) and (3) metabasic rocks with  $>1.2\%$   $\text{TiO}_2$  (5% of the population). A clear separation between the latter two groups is also shown by a frequency histogram of wt%  $\text{TiO}_2$  content in samples analysed in this study (fig. 3.5b). However, one sample of 'metabasite' which is similar petrographically and with respect to other major elements to the Foss metabasites, is exceptionally poor in titanium (G183, from Farragon Hill; see part 5.4.2), and three samples placed in the category of 'mineralization' have similar  $\text{TiO}_2$  contents to the majority of metabasites (samples 03-MB, 104-45A and N82-109; table 5.2). The latter are discussed in part 3.4.3, following an introduction to the rock type classification scheme adopted in this study and the selection of material for geochemical analysis.

### 3.4.2 Rock type classification and selection of material for analysis.

#### Rock type classification.

Previous geochemical studies support the initial classification of rock types by mode of formation, namely hydrothermal-exhalative (designated H), sedimentary (S) and basic igneous (B), but also indicate that some overlap occurs between the first group and the second two groups. This may be due to hydrothermal or possibly metasomatic alteration of sedimentary and basaltic material adjoining the mineralized strata, or to the simultaneous deposition of these materials together with chemical precipitates from hydrothermal-exhalative fluids. Note that the simultaneous deposition of sedimentary and basaltic material (derived from pyroclastic eruptions or by sedimentary reworking) may also have occurred, but volcanoclastic rocks of this nature have not been recognized in the Foss deposit area.

Fig. 3.6 presents a rock type classification scheme in which the three 'primary' components are represented by circles with areas approximately proportional to their volumetric abundance in the drillcore examined, and rocks of dual parentage are represented by overlaps between these fields (designated HS and HB). The metased-

iments are subdivided by type (SQ = quartzites, SP = pelites, SC = dolostones) and lithostratigraphical unit (letters A-D following an open bracket) (see chapter 4), and the metabasites are classified by petrographical type (B1-B4; see chapter 5). Barium-enriched metasediments ( $\text{BaO} > 1\text{wt}\%$ ) are indicated by an arc-shaped field bordering the circle representing the mineralized strata, and are distinguished by a letter b (or B) in the rock type code. Similarly, the letter s (or S) identifies sulphide-rich metasediments (Appendix B). This hierarchical coding scheme was developed to facilitate computer data handling and graph plotting, and is sufficiently flexible to classify most rock types examined. Note that the various rock types comprising the mineralized strata (section 3.2) have not been subdivided since comparatively few samples were analysed and codings would merely duplicate the descriptive nomenclature.

As mentioned in the previous section, most samples of mineralized lithologies analysed in this study cluster near the celsian-quartz join on a trivariate plot of  $\text{Al}_2\text{O}_3$ -BaO-SiO<sub>2</sub> (fig 3.4), but several samples plot between this group and that of the barium-enriched metasediments. These rocks are either rich in hyalophane (G119A and ~~408-4~~) or contain both celsian and micas (503-3, 705-A, 705-B, 708-4 and 201-6) (Appendix B). Solely for purposes of classification, an arbitrary division between 'mineralized strata' and 'barium-enriched metasediment' has been taken at a wt% BaO: $\text{Al}_2\text{O}_3$  ratio of 2:1. This is equivalent to a hyalophane composition containing 50% each of celsian and orthoclase molecules (fig. 3.4 and part 6.2.2). Only one sample analysed in this study plots above the celsian-quartz join in fig. 3.4, and this lies close to the SiO<sub>2</sub> apex. This sample, 705-H, consists largely of carbonate, sulphides and quartz, and the hypothesis that some barium is contained in the carbonate is supported by microprobe analyses (cf. sample 705-19: part 7.5.2 and table 7.7).

#### Analytical work.

The majority of the 105 rock samples selected for XRF analysis in this study (part 1.4.2) are readily classified on the basis of hand specimen appearance, supplemented with petrographical information on modal abundances. Other rocks were specifically selected for geochemical analysis in order to clarify their mode of form-



ation, in particular micaceous and celsian-bearing lithologies which were suspected on stratigraphical grounds to have been of basic igneous origin but which are closely associated with the mineralization (part 3.4.3). Geochemical features which allow rocks of uncertain mode of formation to be categorized were sought using the readily classified samples as a reference set. It should be noted that no attempt was made to analyse a volumetrically representative suite of samples from the mineralized strata (see part 1.4.2), although individual samples were chosen as representative of particular rock types.

Details of the analytical methods used are described in Appendix D. Note that sulphur and  $\text{CO}_2$  were not determined, and that all samples were ignited before fusing into glass discs for major element analysis. Therefore all iron is expressed as  $\text{Fe}_2\text{O}_3$  and the major element oxides (including  $\text{BaO}$ ) are adjusted to total 100%. Trace element data is adjusted to correspond with the volatile-free major element data using loss-on-ignition values (which, however, do not accurately represent volatile contents in  $\text{Fe}^{2+}$ -rich samples). The analyses are presented in tables 3.2 (mineralized rocks), 4.2 (metasediments) and 5.2 (metabasites).

### 3.4.3 Mineralized basic igneous and sedimentary material.

#### 'Mineralized basalt'.

Calcareous biotite and muscovite schists with characteristically high Ti, Fe and Ca contents, similar to the metabasites described from BH10 by Coats et al. (1981) (table 5.3), were found in this study throughout the Foss area at the stratigraphic base to the M3 mineralized horizon (chapter 2). Analyses of eight samples from this metabasite bed (table 5.2) indicate a variable enrichment in  $\text{K}_2\text{O}$  (up to 5.7% on a volatile-free basis) in addition to  $\text{BaO}$  (up to 3%), but a uniform content of most other elements. This is discussed further in chapter 5.

Rutile-bearing, biotite quartz dolomite celsian rocks, previously logged in drillhole intersections as chert, were collected from the BH10 intersection (plate 68) and at an equivalent stratigraphic horizon to the sub-M3 metabasite bed in two restricted areas in Foss East and in one drillhole intersection in Foss West (DH 424; sample 424-8, Appendix B). Two samples of this lithology have been

analysed (104-45A and N82-109: Appendix B and table 5.2) plus a rock consisting of quartz, dolomite, celsian, pyrrhotite and rutile from the footwall to the M3 intersection in BH3 (sample 03-MB). Geochemically, these rocks resemble the mineralized basic rock which is intercalated with barite in BH5, and in particular they have characteristically high  $\text{TiO}_2$  contents despite some dilution due to the large amount of barium present (these are the three samples of 'mineralization' with  $>1.5$  wt%  $\text{TiO}_2$  on fig. 3.5b).

It is of interest to estimate the approximate proportion and composition of the 'mineralized' component and of the 'basaltic' component in these rocks using the major element data. Several assumptions are necessary to achieve this. These are: (a) that the original basaltic material had a low barium content and a composition similar to the least altered Foss metabasites; (b) that  $\text{TiO}_2$  has been immobile during hydrothermal and/or metasomatic alteration of the basaltic material (this is argued in part 5.4.2); and (c) that no additional  $\text{TiO}_2$  was contributed by the mineralizing solutions, which is a reasonable approximation considering the low  $\text{TiO}_2$  content of mineralized strata (other than barium-enriched metasedimentary lithologies discussed below) (see part 3.4.1 and fig. 3.5b). By projecting straight lines from the oxide wt% values of 'average' Foss metabasite through values obtained for sample N82-109 (fig. 3.7), it is seen that  $\text{SiO}_2$  and  $\text{Al}_2\text{O}_3$  tie-lines pass close to the origin (at wt%  $\text{TiO}_2 = 0$ ) whereas the tie-lines for  $\text{CaO}$  and  $\text{MgO}$  intersect the abscissa, and those for  $\text{Fe}_2\text{O}_3$  and  $\text{MnO}$  intersect the ordinate. This suggests that sample N82-109 is enriched not only in barium, but also in iron and manganese (and possibly potassium), but is depleted in calcium and magnesium to a greater extent than would be expected by dilution alone. Perhaps the most significant feature is the absence of an enrichment in aluminium relative to a diluted basaltic composition, despite the high modal proportion of celsian in this rock (table 5.1).

Selective removal and addition of components has approximately balanced in 03-MB, so that the immobile elements Ti and P are present in similar amounts to the average unaltered metabasite (tables 5.2, 5.4). Silica and alumina may have been incorporated with excess barium to form celsian in the sulphidic dolomite rock which encloses this rock. However, the 45cm interval of core which

includes this sample interval also has a high  $\text{TiO}_2$  content (about 1%: Coats et al. 1981, Appendix II), which suggests that the volume of incorporated basaltic material is larger than the 6cm interval represented by sample 03-MB.

The compositions of these mineralized metabasites do not indicate the simple addition to a basaltic material of a component corresponding in composition to celsian (i.e.  $\text{SiO}_2$ ,  $\text{Al}_2\text{O}_3$  and  $\text{BaO}$  in the wt% ratio of 32:27:41) since the estimated increases in  $\text{BaO}$  and  $\text{SiO}_2$  greatly exceed the increase in  $\text{Al}_2\text{O}_3$  content (if any). In the case of 03-MB (table 5.2), Ca, Sr, Zn, Pb, S and  $\text{CO}_2$  have also been introduced into the basaltic material during the hydrothermal alteration.

#### Mineralized sedimentary material.

Quartz dolomite biotite celsian rocks, which petrographically resemble the mineralized metabasites described above, occur as thin ( $\leq 30\text{cm}$ ), laterally discontinuous beds within or adjoining the upper mineralized horizons (M5 and M7) in several Foss East intersections (section 2.4). Analyses of four samples of this unusual lithology (201-I, 201-G, 408-M and 410-11B: Appendix B, table 3.2) indicate that it is geochemically distinct from the mineralized basaltic rocks described above. In particular, these four samples have much lower  $\text{TiO}_2$  contents (0.15 - 0.33wt%). The similarity in other major and trace element contents between these biotite-celsian rocks and unit C schists (when allowances are made for dilution due to the high  $\text{BaO}$  content), suggests that these rocks represent mineralized Ben Lawers Schist-type sediments. These analyses are discussed further in sections 4.4 and 4.5.

A micaceous quartz celsian schist which constitutes the M1 horizon intersected in DH 704 (sample 704-B), is similarly regarded as mineralized Ben Eagach Schist sediment. The comparatively high  $\text{TiO}_2$  contents of the mineralized rocks 705-B, 708-4 and 601-6 (table 3.2, cf. fig. 3.5) may also be attributed to the interbanding or incorporation of normal sedimentary material with the products of exhalative hydrothermal solutions. This inference accords with the conclusion from stratigraphical studies (section 2.4) that the exhalative activity which produced the M1 and M2 horizons was of low intensity and limited lateral extent.

### Other mineralized rocks analysed.

The remaining eleven mineralized rocks of which XRF analyses were obtained (table 3.2) are diverse in composition but share several geochemical characteristics, notably low contents (<0.5%) of  $\text{TiO}_2$ ,  $\text{Na}_2\text{O}$  and  $\text{K}_2\text{O}$  and also low Sc, Rb and Zr contents, but generally high levels of BaO, Zn and Pb. Iron contents (expressed as  $\text{Fe}_2\text{O}_3$ ) are also high in many of these samples due to the abundance of iron sulphides. High CaO, MgO, MnO and Sr contents are characteristic of the carbonate-rich rocks, samples 201-6, 201-7 and 705-H.

### 3.5 Proximity to exhalative centres and metal zonation.

#### 3.5.1 Distribution of mineralized metabasite and sulphidic carbonate rocks.

In chapter 2, the distribution of mineralized strata in the Foss deposit was described and areas in which the greatest thickness (and grade) are attained were tentatively related to syndepositional faulting and the loci of exhalative centres (such as near BH3 at Creagan Loch). The restricted occurrence of mineralized basaltic rock in the sub-M3 marker bed at Foss in areas where the overlying mineralized strata attain their thickest development (12m at Creagan Loch, 22m at Frenich Burn, 6.5m in the vicinity of DH 424: fig. 2.15), suggests that the hydrothermal fluids may have interacted with ('mineralized') the underlying tuffaceous material only in areas proximal to the exhalative vents (see fig. 10.5). In these areas, sulphidic and cherty graphitic schists (part 4.2.3) also occur beneath the M3 bed, but this ~~is~~ cannot be considered as a reliable indicator of proximity to exhalative centres since footwall silica- and sulphide-enrichment also occurs in some areas where the overlying mineralized strata is thin or of low grade (e.g. in outcrops on the northern limb of the Creagan h-Iolaire Anticline), and also occurs above the upper mineralized horizon in the Creagan Chanaich area.

Russell et al. (1984) postulate that acid, hydrothermal Ca- and  $\text{CO}_2$ -bearing solutions mixed with alkaline, basinal brines at the points of exhalation, to form the footwall carbonate horizon (at Creagan Loch). In support of a proximal location of these carbonate rocks, they note the high silver contents reported by Coats et al.

(1981) (see below). High carbonate contents have been observed in the stockwork mineralization associated with several sedimentary exhalative deposits such as Rosh Pinah (Page and Watson, 1976) and Tom (Carne, 1979), and the silica-dolomite at Mount Isa could be a comparable feature (Finlow-Bates and Stumpfl, 1979).

#### Isotopic evidence.

Carbonates precipitated in the feeder zones or close to the exhalative vent presumably utilise  $\text{CO}_2$  of hydrothermal origin, and therefore should be isotopically distinct from those in the normal marine sediments (e.g. Boast et al., 1981). However, no significant differences between carbonates of hydrothermal-exhalative, sedimentary and metamorphic origin at Foss were found in a reconnaissance isotopic study, the results of which are presented in Appendix F. This indicates that while compositional differences between mineralized and metasedimentary carbonates (such as higher Mn and Sr contents in mineralized carbonate rocks - see table 7.7) have been retained through metamorphism, isotopic equilibration has taken place on a large (at least decimetric) scale. Comparable isotopic results have been obtained from the Mount Isa Pb-Zn-Ag deposit and surrounding black shales examined by Smith et al. (1978), who also found that primary isotopic variations had been obliterated during lower greenschist facies metamorphism.

Sulphur isotope data obtained from Foss (described in chapter 9) also cannot be used to characterize regions of the mineralized horizons considered to be proximal with respect to the exhalative centres, although the M3 horizon in the eastern block at Creagan Loch appears to be isotopically distinctive (part 9.6.1). This is interpreted as evidence for a uniform, hydrothermal source for the sulphur incorporated into the mineralization regardless of distance from the emanative centres.

### 3.5.2 Pb/Zn and Ag/Pb ratios.

#### Previous studies.

Metal zonation is commonly recognised in both volcanogenic and sedimentary-exhalative ore deposits, which often have a copper-rich core, more widely dispersed zinc and lead, and peripheral barite (R. Large, 1977; D. Large, 1980; Finlow-Bates, 1980). In lateral zonation sequences, zinc is more widespread than lead (e.g. Mount

Isa, McArthur River, Tom), whereas in vertically-zoned deposits the usual sequence of upwards zonation is Cu-Zn-Pb-Ba (e.g. Rammelsberg). The lateral zonation pattern probably reflects the sequential deposition of galena and sphalerite, according to their solubilities (Anderson, 1973), in response to a progressive temperature decrease in the mineralizing fluids as they flowed outward from the exhalative vents. Taylor and Andrew (1978) and Taylor (1984) have illustrated the close spatial relationships between the channelways for ascending ore solutions (which are related to major fault zones), and high Pb/Zn ratios and Ag contents in the Silvermines deposit, Ireland.

Coats et al. (1981) noted that simple calculations of average metal contents in the Ben Eagach Schist, based on core analyses from BHs 7-11, appeared to show higher concentrations of Pb + Zn in graphitic schists from the Foss deposit than from the Ben Eagach deposit. However, statistical tests failed to support the hypothesis that large-scale mineral zonation of this type exists in the host rocks to the deposits. Nevertheless, analyses published by Coats et al. (op. cit.) indicate differing metal contents and ratios in BHs 3 and 4 (in the Foss and Ben Eagach deposits, respectively), and suggest that the higher base metal content of the mineralization intersected in BH4 is associated with higher Pb/Zn and Ag/Pb ratios (see part 7.3.3.1 and fig. 7.5).

#### Data obtained by Dresser Minerals.

Assay data made available by Dresser Minerals for the closely-spaced drillhole intersections of the Foss deposit, allow a more critical appraisal of metal zoning. Fig. 3.8 illustrates Pb/Pb+Zn ratios in eleven intersections of the M3 horizon (above 500m elevation) in Foss East (located on fig. 2.19; see also fig. 2.29). Values for this ratio of >0.5 are only shown by mineralization in DH 705, where a value of 0.94 is calculated from assay data for a section of the unusual massive pyrite rock found in the upper part of the M3 horizon. Galena-bearing, calcareous barite rock occurring in the upper part of the DH 505 intersection appears to correlate with this feature which, however, is absent from BH3 and intersections west of DH 705.

The unusual massive pyrite rock and spatially associated high Pb/Zn ratio in the DH 705 profile suggests that this area was



proximal to an exhalative vent (indeed, the pyrite rock could have been a hydrothermal mound), and this deduction is supported by other evidence such as the presence of manganoan carbonate rock and footwall silicification. The correlated Pb/Zn 'anomaly' in DH 705 and DH 505, but its absence in BH3 suggests that the perturbation in metal ratios associated with the vent is very localized (perhaps <100m in diameter; fig. 2.19), a feature also seen at Silvermines (Taylor, 1984).

The other profiles of the M3 horizon in Foss East do not show systematic vertical or lateral variations in Pb/Pb+Zn ratios, except perhaps for a central zone of low values in DHs 707 and 708, east of BH3. Complete assay data for silver is available only for the DH 708 intersection, where the Ag/Pb ratio is fairly constant with stratigraphic height and varying base metal content (fig. 2.29). However, on average this ratio is considerably lower than in BH3 (fig. 7.5), which has Ag/Pb ratios similar to those in Dresser drillhole intersections further west. This evidence (albeit incomplete) supports the contention that the eastern block at Creagan Loch intersected by DHs 707 and 708 was not originally contiguous with that further west (including BH3: part 2.4.6), and that the mineralized facies in this block represent the products of a brine pool which was distal from the exhalative vents. Supporting evidence is also derived from studies of sphalerite composition (part 7.3.2) and sulphur isotope ratios (mentioned above).

### 3.6 Summary.

Principal components of the mineralized strata are barite, sulphides (pyrite, pyrrhotite and sphalerite), carbonates (mainly dolomite, lesser calcite), quartz and celsian. Hyalophane and micas are major constituents of some cherty rocks but are normally associated with hydrothermally-altered sedimentary (or rarely, basaltic) material. Although commonly interbanded, celsian and barite seldom coexist as major components in homogeneous rocks. Some of the celsian is finely intergrown with quartz, but much is coarsely crystalline with a relict platy or foliated fabric which suggests that the celsian has replaced the platy mineral, cymrite, after the D<sub>3</sub> phase of deformation. Plastic deformation, and locally brecciation, occurred during metamorphism in some sulphide, carb-

onate and cymrite-rich rocks. Metamorphic textures have been modified by late- or post-metamorphic recrystallization in other sulphide and carbonate rocks.

A few cherty rocks contain pre-metamorphic tabular structures consisting of hyalophane with inclusions of quartz, barite and kaolinite. These are interpreted as probable diagenetic sulphate (?gypsum) pseudomorphs. Traces of barium carbonate minerals, probably also of diagenetic origin, have survived decomposition reactions as grains encapsulated in pyrite crystals.

Geochemical studies support a tripartite rock type classification but suggest that some rocks represent mixtures of hydrothermal precipitates and sedimentary or basic igneous material. Metabasites and hydrothermally or metasomatically altered materials of basaltic origin are characterized by comparatively high  $\text{TiO}_2$  contents ( $>1.5$  wt%  $\text{TiO}_2$ ). Although 'mineralized metabasites' contain major amounts of barium (up to 18 wt%  $\text{BaO}$ ) and have a large modal feldspar content (30-45%), geochemical analyses show no significant enrichment in alumina relative to a diluted basaltic composition. Occurrences of these rocks beneath the M3 horizon at Foss may be spatially associated with exhalative centres. Proximity to a hydrothermal vent is also suggested by a zone with unusually high  $\text{Pb}/(\text{Pb}+\text{Zn})$  ratios ( $>0.5$ ) associated with massive pyrite and sulphidic carbonate and barite rocks in the M3 bed at Creagan Loch (Dhs 705, 505). Lower  $\text{Ag}/\text{Pb}$  ratios in the sulphide- and chert-dominated intersections of M3 east of BH3 (DHS 707, 708), support other evidence which suggests that this area was not originally a contiguous part of the deposit.

Table 3.1: Average compositions of major components of the mineralized zone, based on cluster groupings of core sample analyses from boreholes 1-5\*.

	Barite rock	Sulphidic carbonate rock	Quartz celsian rock	Mica schist
No. analyses	36	16	21	24
%				
SiO <sub>2</sub>	6.2	18.7	48.6	52.8
TiO <sub>2</sub> <sup>x</sup>	0.20	0.07	0.53	0.58
Al <sub>2</sub> O <sub>3</sub>	0.03	1.36	8.7	15.2
Fe <sub>2</sub> O <sub>3</sub> <sup>t</sup>	0.83	8.53	3.66	6.75
MnO	0.01	0.83	0.16	0.53
MgO	0.59	5.99	2.68	4.20
CaO	1.50	16.42	3.75	6.15
K <sub>2</sub> O	0.04	0.14	3.20	5.35
BaO	57.1	8.0	16.1	0.98
SrO	0.54	0.24	0.11	0.02
Pb	0.11	2.12	0.10	0.07
Zn	0.24	5.65	0.31	0.31
S <sup>\$</sup>		12.9	2.6	0.93
SO <sub>3</sub> <sup>\$</sup>	31.2			
Total	98.6	81.0	90.5	93.87

\* From Coats et al. (1981; table 5). Elements determined by XRF except for Pb, Zn (by AAS using hot HNO<sub>3</sub> attack). Analysts: D.J. Bland and M.E. Stuart.

<sup>x</sup> Metabasite intervals CYD 16, 30, 95 and 97 are excluded in TiO<sub>2</sub> averages.

<sup>t</sup> Total iron as Fe<sub>2</sub>O<sub>3</sub>.

<sup>\$</sup> Total sulphur as S, except in barite rock where total sulphur as SO<sub>3</sub>.

TABLE 3.2: XRF ANALYSES OF MINERALISED ROCKS<sup>☆</sup> (TOTALS → 100%).

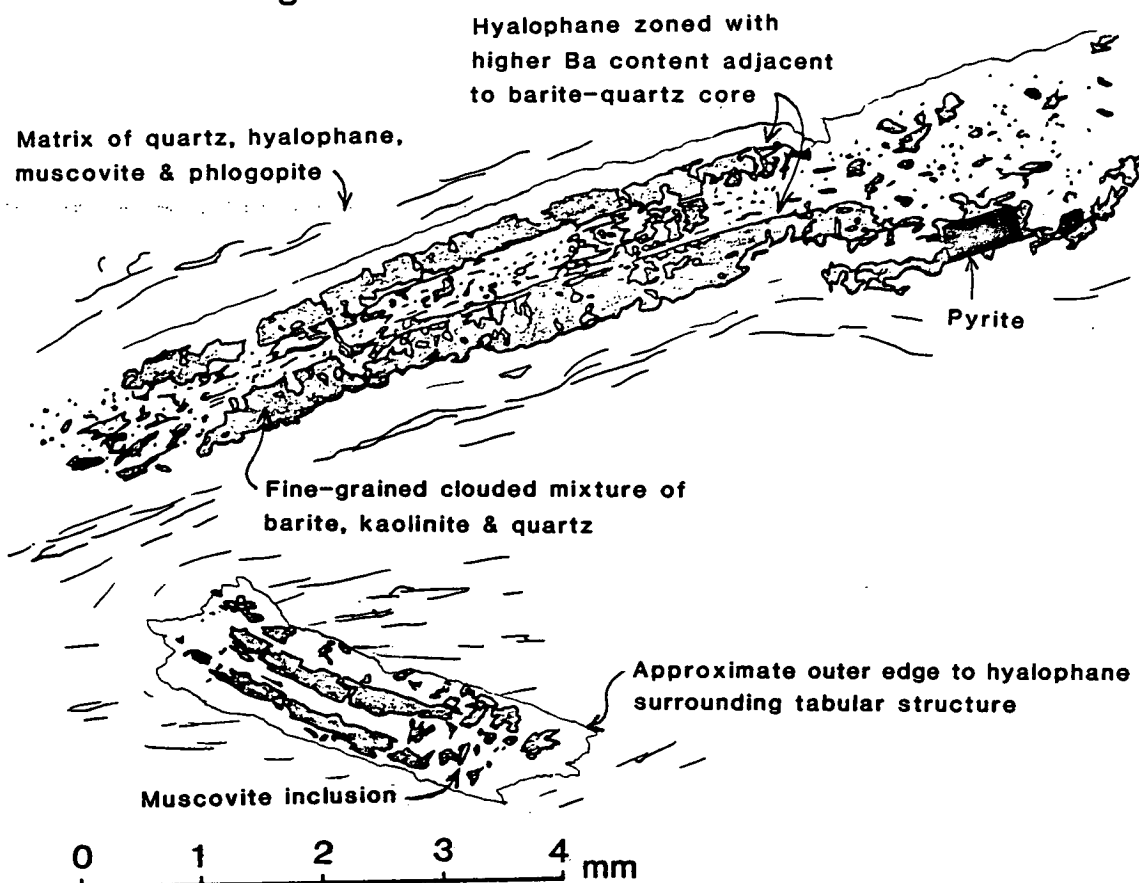
	HS(B)				HS(C)				H	
	601-6	704-8	705-8	708-4	408-M	201-I	201-G	410-118	201-7	705-H
SiO <sub>2</sub>	33.51	50.25	67.78	75.71	47.92	52.84	52.88	51.27	16.11	32.86
TiO <sub>2</sub>	0.19	0.56	0.19	0.23	0.60	0.56	0.55	0.53	0.17	0.03
Al <sub>2</sub> O <sub>3</sub>	5.73	13.39	5.10	6.51	15.35	16.59	16.07	14.68	3.77	0.32
Fe <sub>2</sub> O <sub>3</sub>	25.62	8.94	9.19	10.88	8.01	4.60	4.65	4.92	9.76	18.10
MnO	2.13	0.27	0.15	0.03	0.16	0.03	0.04	0.13	1.60	4.40
MgO	6.79	2.95	4.70	0.64	6.68	4.71	4.56	4.33	25.28	7.18
CaO	20.12	4.00	5.87	0.37	5.27	0.37	0.91	4.20	37.34	35.20
Na <sub>2</sub> O	0.63	0.04	0.15	0.55	0.17	nd	nd	0.03	nd	0.46
K <sub>2</sub> O	0.87	0.77	1.42	1.19	2.98	3.05	2.14	1.65	0.05	nd
P <sub>2</sub> O <sub>5</sub>	0.07	0.09	0.14	0.13	0.18	0.14	0.14	0.15	0.20	0.06
BaO	4.34	18.74	5.31	3.78	12.68	17.12	18.07	18.09	5.71	1.40
total=	100.00	100.00	100.00	100.00	100.00	100.00	100.00	100.00	100.00	100.00
Ni	26	50	31	43	39	33	34	42	19	7
Cr	83	174	113	78	172	174	174	178	80	23
V	75	132	265	62	156	166	147	195	114	31
Sc	-	18	9	8	20	20	21	22	-	-
Cu	184	73	138	227	44	26	36	36	44	13
Zn	660	246	1348	23000	242	217	198	213	372	21020
Sr	916	341	94	132	268	164	61	202	1958	849
Rb	22	47	81	-	95	90	85	69	13	-
Zr	43	132	51	42	88	82	76	66	94	-
Nb	4	11	4	-	7	11	12	9	9	-
Pb	60	106	1280	5605	94	108	122	100	686	23640
La	11	29	10	12	29	41	69	36	5	-
Ce	13	43	19	41	50	69	70	58	16	54
Nd	-	-	-	-	6	5	-	-	-	-
Y	18	20	8	-	27	19	24	23	22	-
ZF/FM	77.25	73.15	63.78	93.90	51.89	46.81	47.86	50.55	25.79	69.40
K/RB	330.19	135.66	145.44	***	260.68	280.88	208.72	198.65	31.93	-

	H								
	201-6	708-3	705-17C	705-F	N80-55	705-J	705-21C	G100E	201-12
SiO <sub>2</sub>	38.39	47.96	58.70	62.04	68.36	72.61	75.59	77.18	83.01
TiO <sub>2</sub>	0.07	0.49	0.48	0.43	0.32	0.14	0.24	0.10	0.19
Al <sub>2</sub> O <sub>3</sub>	7.59	13.82	14.23	12.53	8.80	4.59	5.65	2.52	5.28
Fe <sub>2</sub> O <sub>3</sub>	5.55	7.00	2.92	3.37	8.84	13.37	8.64	15.97	2.51
MnO	1.42	0.42	0.11	0.14	0.02	0.11	0.02	0.01	0.03
MgO	18.62	4.18	0.63	0.61	0.03	0.36	0.03	0.02	0.70
CaO	17.37	6.38	1.00	1.04	0.06	0.86	0.43	nd	0.18
Na <sub>2</sub> O	0.10	0.18	0.30	0.34	0.10	0.57	0.27	0.06	0.05
K <sub>2</sub> O	0.11	0.58	0.41	0.45	0.32	0.13	0.12	0.10	0.09
P <sub>2</sub> O <sub>5</sub>	0.02	0.11	0.11	0.11	0.08	0.18	0.31	0.02	0.03
BaO	10.76	18.88	21.11	18.93	13.09	7.09	8.72	4.02	7.94
total=	100.00	100.00	100.00	100.00	100.00	100.00	100.00	100.00	100.00
Ni	17	33	32	35	31	23	24	23	15
Cr	117	164	113	159	132	90	106	75	115
V	102	123	118	115	98	69	70	135	138
Sc	3	17	14	14	11	6	5	3	10
Cu	21	60	32	37	20	29	23	19	15
Zn	615	188	985	2566	185	26220	9500	939	644
Sr	678	547	72	105	57	58	40	34	26
Rb	28	43	37	44	36	1	13	6	26
Zr	64	109	82	70	85	39	51	39	54
Nb	5	9	4	6	7	1	3	3	6
Pb	194	288	1590	870	250	4058	1780	1007	278
La	1	28	6	13	11	5	7	9	20
Ce	2	37	32	29	27	21	16	11	27
Nd	-	-	-	14	-	-	-	-	4
Y	18	16	9	12	19	-	7	5	12
ZF/FM	21.14	60.13	80.69	83.24	99.61	97.09	99.64	99.85	76.31
K/RB	31.73	112.75	91.55	85.28	74.72	1046	79.19	131.45	27.46

<sup>☆</sup> Except for mineralised basic rocks (3 samples labelled HB, table 5.2)

Refer to Appendix B for sample descriptions & locations.

## N81-80 Creag an Chanaich



## CYR6 Creagan Loch

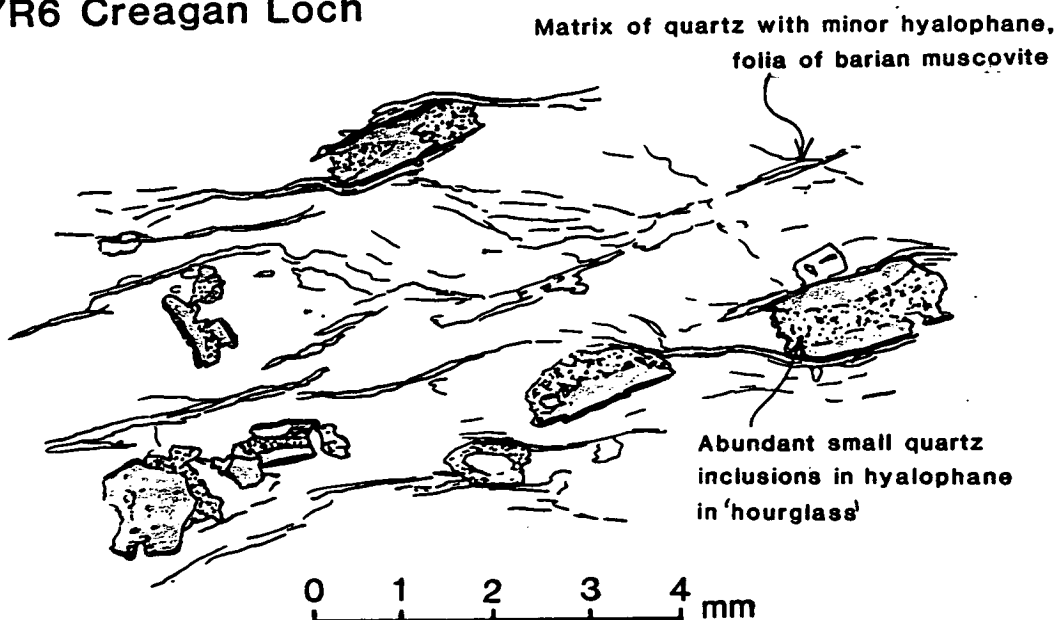


**Fig. 3.1:** Sketches from thin sections (in transmitted light) of tabular structures consisting of hyalophane, quartz, barite and kaolinite, occurring in two samples of mica hyalophane quartz schist (see part 3.3.1 and plate 63).

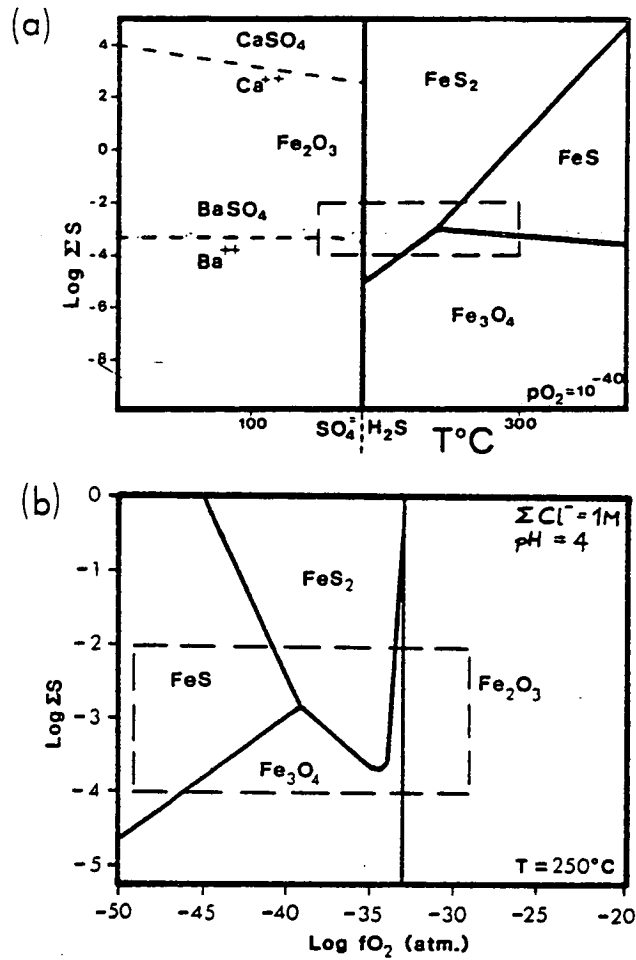


**Fig. 3.2:** Diagrams of log total sulphur concentration against (a) temperature, and (b) log oxygen fugacity, to illustrate location of the equilibrium assemblage pyrite-pyrrhotite-magnetite, from Finlow-Bates (1980) and Large (1981b).

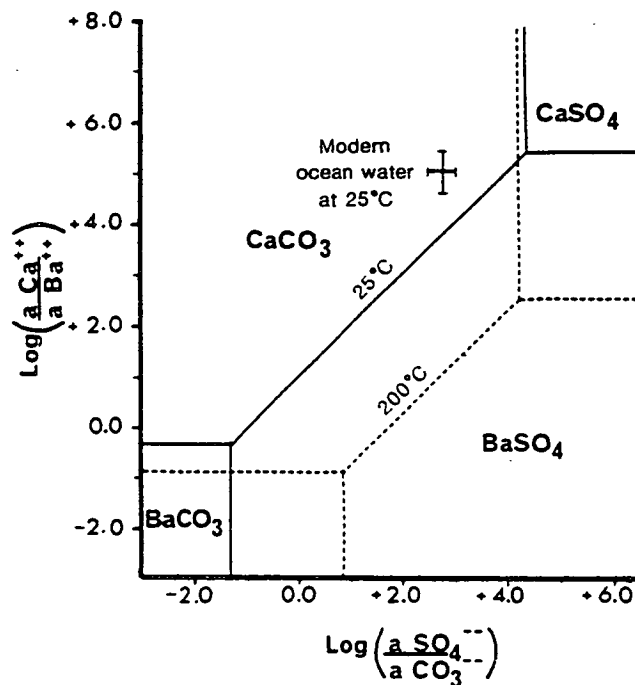


**Fig. 3.3:** Activity diagram of the  $CaO-BaO-H_2O-CO_2-H_2SO_4$  system from Lydon et al. (1979), to illustrate the relationships between witherite, calcite, barite and gypsum, and the composition of normal seawater. Note that barytocalcite ( $BaCa(CO_3)_2$ ) would occupy a field (not delineated) between witherite and calcite.



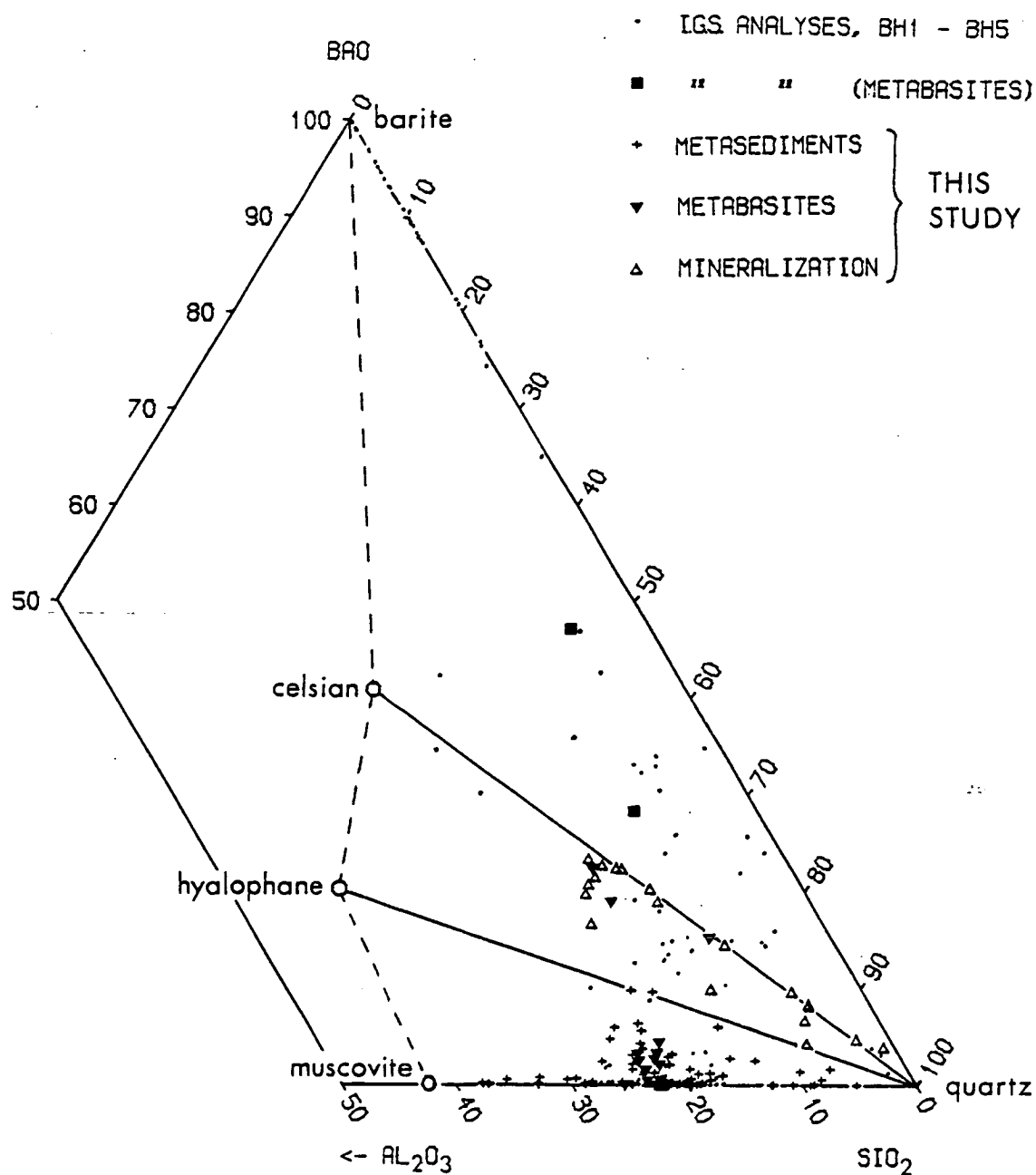


**Fig. 3.4:** Trivariate diagram of  $Al_2O_3$ - $BaO$ - $SiO_2$  (weight %) showing projection of I.G.S. drillcore analyses (BHs 1-5; from Coats et al., 1981) and of samples analysed in this study. Tie-lines join quartz apex with theoretical compositions of celsian, hyalophane of 1:1 orthoclase:celsian composition, and non-barian muscovite.

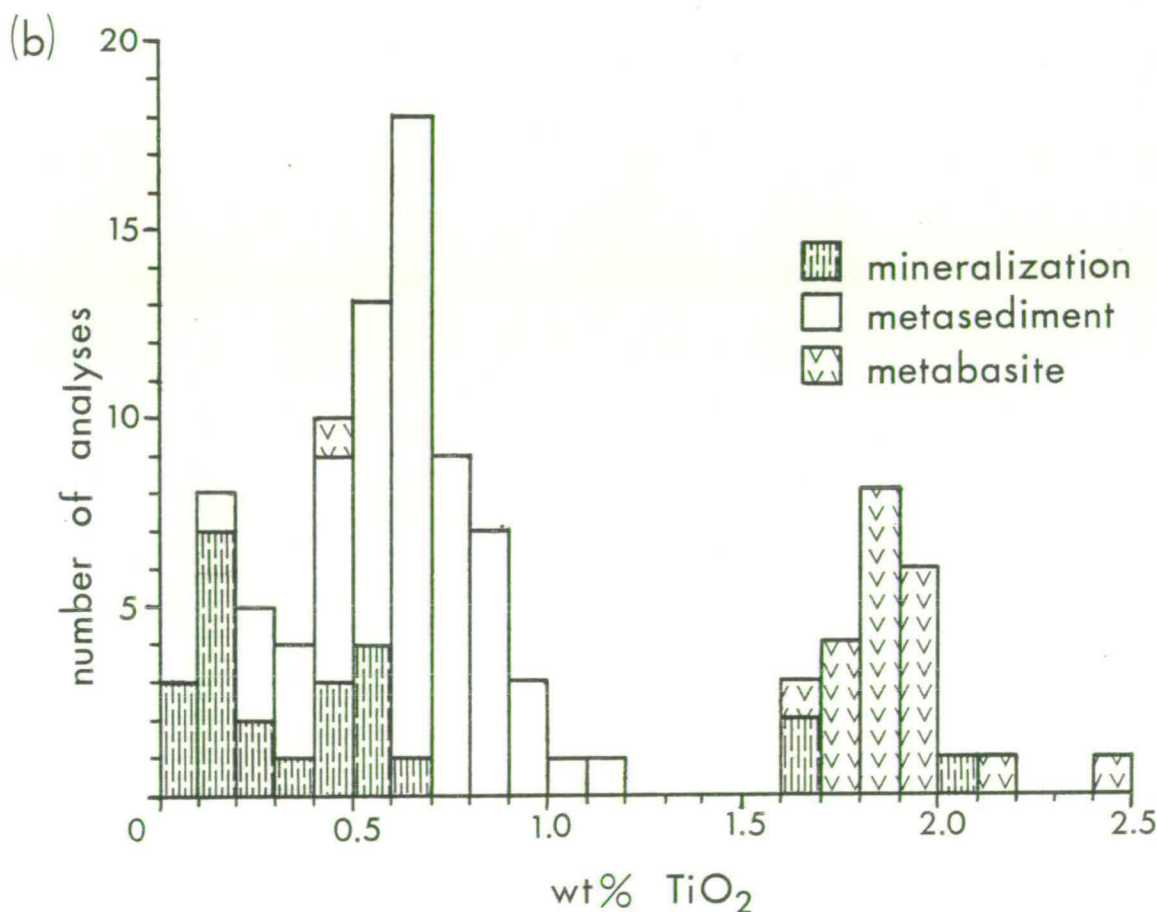
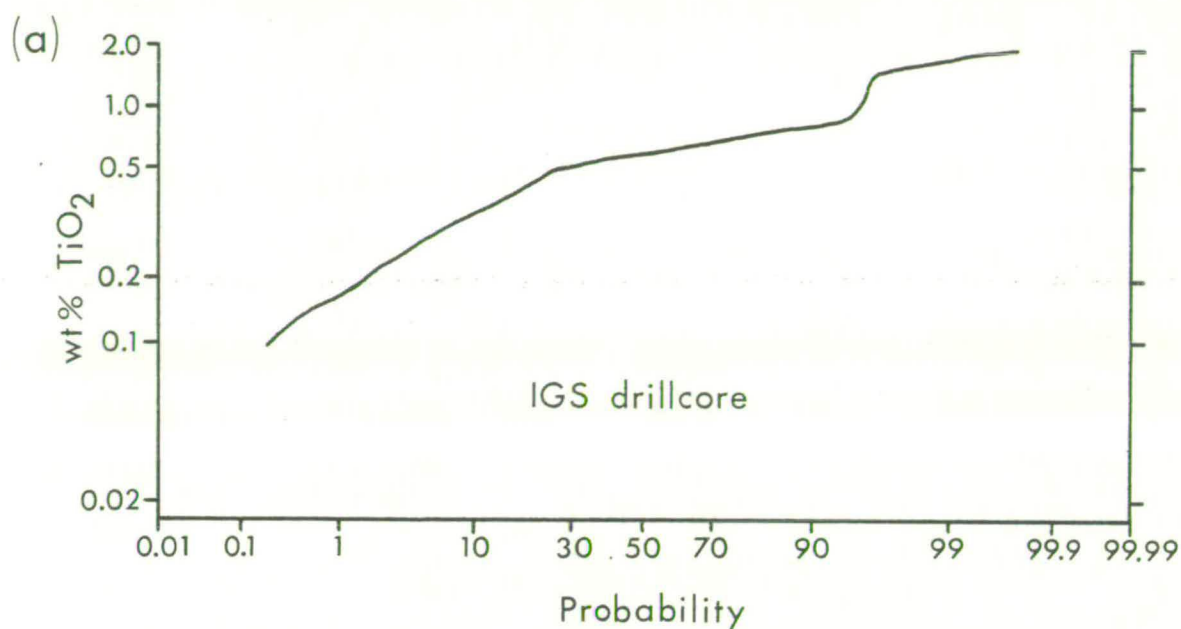


**Fig. 3.5:** (a) Cumulative frequency diagram of titanium content in I.G.S. drillcore analyses ( $n = 470$ ), adapted from Coats et al. (1981). Titanium is expressed as wt% oxide and plotted on a logarithmic scale. Note absence of samples with 1.0–1.5 wt%  $\text{TiO}_2$ . (b) Histogram of  $\text{TiO}_2$  contents (total oxides normalised to 100%) in samples analysed in this study, classified by rock type. Not shown are metabasite samples G225 (3.2%) and N82-A20 (2.8%).

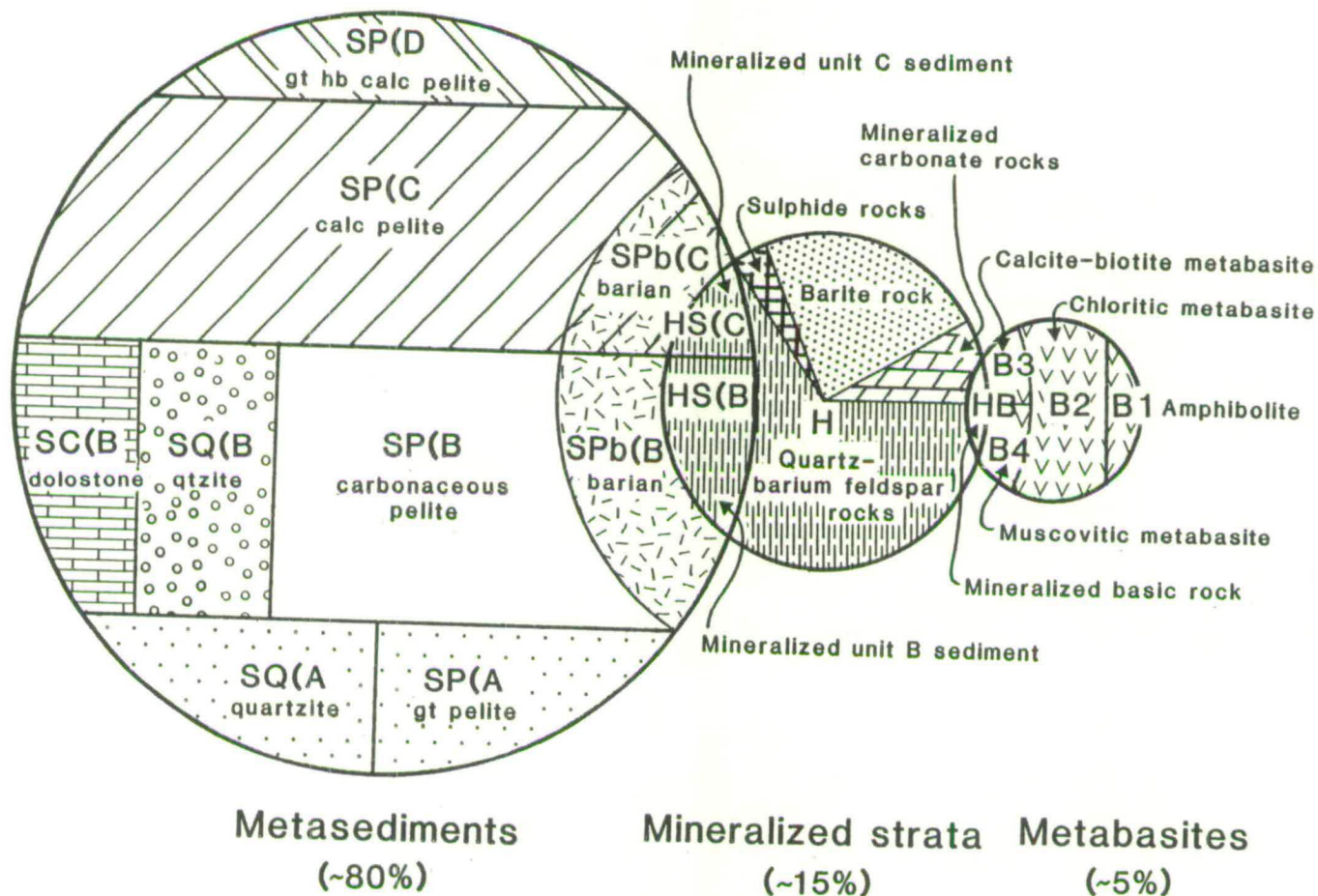


**Fig. 3.6:** Classification scheme for rock types associated with the Foss deposit, with areas approximately proportional to volumetric abundance in the drillcore examined. The metasediment subdivisions are shown in general stratigraphical sequence with unit A [designated (A)] at the base. Note the absence of overlap between metasediments and metabasites.

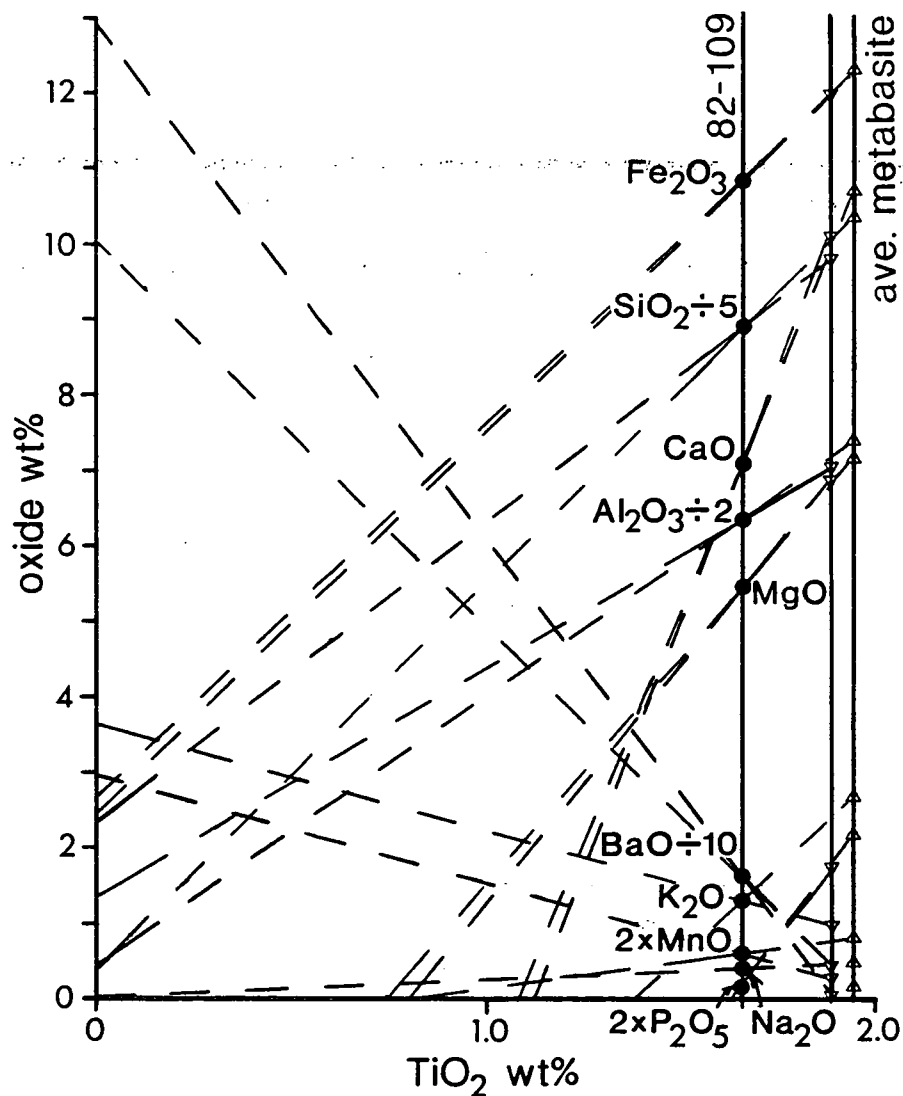


**Fig. 3.7:** Graphic estimation of the 'mineralized component' in sample N82-109, a mineralized basaltic rock from the base of M3 at Creagan Loch, based on  $\text{TiO}_2$  as a fixed component (see part 3.4.2). The two vertical lines at right represent the mean composition (plus and minus one std. dev.) of chloritic metabasites from Foss; the line marked 82-109 represents the composition of this sample (all values normalised to total oxides = 100%).

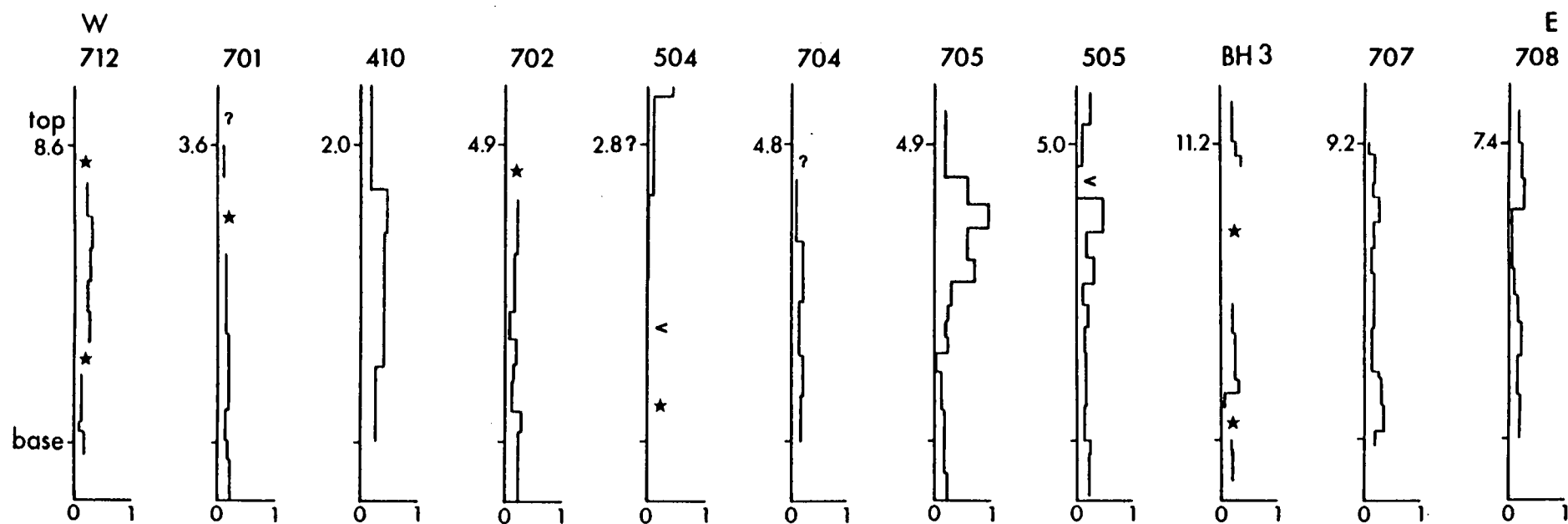
Fig. 3.8: Pb / Pb+Zn ratios in drillhole intersections of the M3 horizon, Foss East.

Vertical scale not constant: figures against vertical bar represent stratigraphic thickness (in metres)

< Ratio less than 0.02

★ Less than 0.2% Pb+Zn

? No assay data



## CHAPTER 4: Petrography and geochemistry of the metasediments.

### 4.1 Introduction.

The general characteristics of the metasedimentary rocks which surround the stratiform mineralization at Foss were described in parts 1.3.1 and 2.2.1. The presence of a complete gradation between rocks of sedimentary and of hydrothermal-exhalative origin, which necessitates an arbitrary division for descriptive purposes, was discussed in section 3.4. In this chapter, the petrography of the metasediments in each lithostratigraphical division are described in more detail to emphasise their textural and mineralogical characteristics (section 4.2), as a prelude to both geochemical studies (this chapter) and to mineralogical and thermobarometric studies (Chs. 6, 7 and 8). Previous lithogeochemical data on the metasedimentary rocks hosting the Aberfeldy deposits, and the selection of rock samples for further analyses, are reviewed in section 4.3. The new results are initially assessed (in section 4.4) by statistical methods to discern sample group and inter-element correlations. In section 4.5, significant geochemical differences between each lithostratigraphical division are evaluated, and bulk compositions are compared with other Dalradian pelites and 'average' shales. Finally, in section 4.6, features diagnostic of the depositional environment are discussed, and geochemical evidence for alkali element mobility during diagenesis and metamorphism is examined.

### 4.2 Petrography.

Petrographical features of the metasedimentary lithologies in each of the four lithostratigraphical divisions (units A-D; section 2.5) of the Ben Eagach and Ben Lawers Schist formations are described in turn. Note that lithologies characteristic of units A and C are locally interbedded with unit B schists within the Ben Eagach Schist formation. Quartzites which are petrographically similar to the underlying Carn Mairg Quartzite also occur in the upper part of the Ben Eagach Schist in some parts of Foss area, and these are described first. Mineral assemblages recorded in representative samples from each unit are summarised in table 4.1 (see also Appendix B), and textural features are illustrated in plates 69 to



86. Opaque phases (principally pyrrhotite and pyrite) were identified in polished thin sections by reflected light microscopy, and the carbonates (calcite and dolomite) were in most cases distinguished by their cathodoluminescence.

#### 4.2.1 Carn Mairg Quartzite and similar quartzites in the Ben Eagach Schist.

Samples of the Carn Mairg Quartzite exposed in two parts of the Foss area were examined. The upper part of this formation immediately underlying the Ben Eagach Schist, in outcrops beside the access road to the west of Meall Tairneachan (sample 81-CMQ; fig. 2.1), consists of pebbly orthoquartzites in which sutured, ovoid grains of quartz, typically 1-2mm in diameter but up to 1.5cm in some beds, are set in a grain-packed matrix of finer quartz grains with minor muscovite (2-3%) (plate 69). Other minor constituents include albite, zircon, rutile and pyrite, and the rock has a dark appearance due to fine grained carbonaceous material, which is largely concentrated into muscovite and along quartz grain boundaries. In contrast, the quartzite which crops out between Creag na h-Iolaire and Creagan Loch (fig. 2.4) is white in hand specimen and contains dispersed detrital grains of blue-coloured quartz and white-weathering feldspars in a granular quartz matrix (cf. plate 36). In thin section the feldspars are observed as variably albitized alkali feldspars (replacement perthite), and multiple-twinned albite grains are also common (3-4%) in the matrix (plate 70). Aligned muscovite flakes constitute about 5% of the rock and carbonate (calcite) is an additional minor phase to those cited above.

Saha (1985) has noted the widespread occurrence of blue quartz grains in late Precambrian and lower Palaeozoic formations in Scotland and Ireland, which may be related to extensive outcrops of Scourian granulites in areas of positive relief to the north and west of the Dalradian basin.

Feldspathic quartzites similar to the second type described above occur in several drillhole intersections of the Ben Eagach Schist at Creagan Loch (e.g. DHs 705 and 202: see fig. 2.31) and crop out in the same area (sample N80-29: fig. 2.7). A thick bed of feldspathic quartzite was also mapped in the western headwater of the French Burn in Foss West (e.g. sample G59: section 2.2.2 and

fig. 2.2). Some of the quartzite in each of these locations contains folded lamellae of sphalerite, galena and iron sulphides (plate 37). In a sulphidic quartzite bed approximately 0.5m thick which was repeatedly intersected in DH 202, thin sulphide laminae can be traced over lateral distances of several metres despite the coarse nature of the sediment. This bed contains about 6% combined Zn + Pb (sample 202-3; table 4.2). A probable diagenetic origin for this stratabound sulphide enrichment is discussed in section 4.6.1.

Other siliceous rocks occurring in the Ben Eagach Schist which contain garnet or major amounts of carbonates and micas, are petrographically distinct from the Carn Mairg Quartzite. These are described in the following section.

#### 4.2.2 Unit A lithologies.

This lower division of the Ben Eagach Schist consists of interbedded micaceous, chloritic quartzitic and graphitic schist, both of which contain garnet but little or no sulphides. The more siliceous lithologies tend to predominate in outcrop, but in drillcore intersections this unit is often characterized by an irregular alternation (on centimetric and metric scales) of micaceous (pelitic) and quartzitic varieties (plate 38). The pelitic component usually has a chaotic fabric and small-scale bedding or laminations are not preserved. Quartz segregations, which vary from centimetre-sized lenses to decimetric veins, are locally common.

Quartzitic schists. Sample 202-P (table 4.1 and plate 72) is a typical unit A quartzitic schist, which consists of about 65% quartz and roughly equal quantities of plagioclase, muscovite, biotite, chlorite and dolomite. A folded schistosity is defined by partly orientated micas and chlorite, and the abundance of chlorite in D<sub>3</sub> crenulation folia and as scattered 1-2mm knots which may contain relict garnet, suggests that retrograde fluid interactions have occurred. Some skeletal garnet porphyroblasts have escaped chloritization; these have curved inclusion trails indicative of syn-tectonic growth (plate 72). Accessory phases in this rock are pyrrhotite, rutile, tourmaline, apatite and zircon.

Chlorite and biotite are absent from other unit A quartzites, such as sample 708-22 (table 4.1). This is a homogeneous, medium-grained rock containing about 70% modal quartz and 8-9% each of dolomite, muscovite and albite. Garnet (<2%) forms scattered 1-2mm

crystals which are skeletal or net-like in appearance because of enclosed quartz grains. Bedding is defined by widely spaced (2cm) lamellae of pyrrhotite (<1%) which are oblique to the D<sub>3</sub> mica folia. Some unit A lithologies are enriched in carbonates, such as sample 505-C (table 4.1) which contains about 18% calcite and 10% dolomite, but in others, carbonate may be completely absent. Frequently, as in sample 503-32, carbonate is largely confined to lenticular quartz-carbonate segregations. Dark grey coloured, graphitic dolostones occur rarely in this unit and are petrographically similar to dolostones in unit B, which are described below.

Graphitic schists. Unit A pelitic schists contain up to 75% muscovite (e.g. samples G8A, G38) and vary in chlorite content from 0-25% (table 4.1). They vary in colour from pale green (or orange-brown due to oxidation) to dark grey, reflecting variations in the graphite content (which probably seldom exceeds 0.5 wt%: table 4.2). Carbonaceous material, referred to as graphite although it is probably amorphous (Coats et al., 1981, p. 30), forms dispersed microgranules in muscovite and is concentrated into secondary cleavage planes. Both plagioclase and garnet occur as porphyroblasts which are typically 0.5-2mm in diameter and each may constitute up to 50% of the rock in certain bands. The plagioclase is usually albite (section 6.2) and forms rounded or ovoid grains which have grown within the muscovite fabric either during or subsequent to deformation (see plate 74). Early syntectonic (pre-D<sub>3</sub>) garnet growth is indicated by helicoidal inclusion trails and discontinuities between internal and external fabrics, which are related to post-garnet growth deformation (D<sub>3</sub> or post-D<sub>3</sub>; see section 2.5 and chapter 8). Some samples contain garnet with static overgrowths which are free of quartz inclusions (cf. plates 85, 86 and 90), and garnets often have parallel microjoints which Sturt and Harris (1961) equated with an episode of post-D<sub>3</sub> brittle strain.

Other post-tectonic fabric developments include the annealing of deformed quartz and sheet silicate grains (as undulose extinction in quartz and kinked micas are absent), and the growth of secondary chlorite as cross-cutting flakes and sprays. Occasionally muscovite also forms cross-cutting crystals, which are larger and less elongate than those defining the foliation. Evidence of retrograde alteration is widespread and include the replacements of garnet by

chlorite or calcite; of biotite by hydrobiotite (section 6.3.4) or chlorite; and of pyrrhotite by pyrite and marcasite (section 7.3).

#### 4.2.3 Unit B lithologies.

Graphitic quartz muscovite schist. Volumetrically, the most abundant lithology in unit B is a mid-grey to black, well-foliated and often laminated, carbonaceous quartz muscovite schist (plate 38). This lithology, which may contain variable amounts of carbonate and sulphides but is free of garnet, is referred to as graphitic schist, although graphite is often the least abundant constituent (normally <0.7: table 4.6). Some samples contain trace or minor amounts of plagioclase, biotite and chlorite, and as noted in part 2.2.2, a gradation is found between assemblages and textures typical of units A and B (e.g. samples G172, G222; table 4.1). With increasing dolomite or quartz contents, graphitic schists grade into graphitic dolomite rocks and siliceous graphitic schists. These are described below.

Graphitic dolostone. Mid-grey to dark grey, compact and fine-grained rocks which exhibit little or no foliation are occasionally interbanded with the graphitic schists (plate 39). These consist largely of ferroan dolomite with a variable admixture of quartz and muscovite, and are described here as graphitic dolomite rock or graphitic dolostone, in preference to the terms 'black limestone' or marble used by Coats et al. (1980, 1981). Graphitic dolostone beds range from 1cm to over 1m in thickness (~2m intersected in DH 705) but are typically around 10cm thick. This lithology often contains sphalerite, associated with pyrrhotite and minor galena, as thin lamellae or bands 2-6mm thick, which may be folded and contorted with the host dolomite rock (e.g. sample 503-23: plate 76) and are clearly pre-metamorphic in origin. Coarse dolomite segregations, which appear as elongate, ovoid or contorted white patches in hand specimen, are often present in the dolostone (plates 39, 76). Growth of zoned dolomite in these lenticular segregations (plate 77) suggests that they are of post-tectonic origin, and may be dilatational features associated with the early phase of relatively rapid uplift following peak metamorphism (section 8.4).

Graphitic 'cherts'. Fine-grained, highly siliceous graphitic rocks, which superficially resemble graphitic dolostones in appearance, are locally found adjacent to mineralized horizons in the mineralized

zone. This lithology is normally rich in pyrite and pyrrhotite, which together with variations in graphite content, often preserve a fine sedimentary banding (plate 75). Muscovite typically forms 10-25% of these rocks, which with increasing muscovite content grade into normal graphitic schists. Hyalophane is present in trace or minor amounts in some samples (such as 705-23; table 4.1), but is the principal constituent of others (e.g. 708-5A, G119A, and 11-01: table 4.1) (discussed in part 3.4.3). Much of the feldspar in these graphitic hyalophane rocks is fine-grained and darkened by carbonaceous micro-granules (cf. plate 61), but hyalophane may also form inclusion-free, cross-cutting tabular or lensoid complexes which may represent sulphate pseudomorphs (described in part 3.3.1: plates 61, 62 and 65).

Cymrite-bearing quartz muscovite schists. Unlike hyalophane, celsian has not been observed in rocks containing graphite. However, celsian and hyalophane occur together with cymrite (see part 6.2.3 for a description of optical characteristics), in graphite-free, quartz mica schists (plate 81). These are common in the 'distal' (low-grade) equivalents of the upper mineralized horizons (M5 - M7) in Foss East (e.g. DHs 503, 705: part 2.4.3). A sample examined in detail, 503-3 (table 4.1), contains patches of fine-grained, well-foliated and strongly crenulated aggregates of barian muscovite with minor cymrite (plate 81), set in a decussate-granoblastic matrix of quartz with minor pyrrhotite, phlogopite and celsian. Hyalophane occurs as irregularly-zoned grains marginal to welts of muscovite, which the hyalophane appears to have partially replaced during or after fabric development (plate 81). In a coarse-grained rock of similar mineralogy but contrasting textures, sample 705-17A (plate 79), hyalophane forms irregular or ovoid porphyroblasts containing muscovite inclusions which preserve an earlier (pre-D<sub>3</sub>) fabric orientation. One unit B muscovite quartz schist sample was found to contain coexisting hyalophane and albite in a granoblastic quartzofeldspathic matrix (N80-2: table 4.1 and plate 78) (see section 6.2). (Coexisting albite + hyalophane are more common in barium-enriched unit C lithologies, described below).

Coarse-grained muscovite schists. Of more widespread occurrence in the Aberfeldy deposits are pale green or beige-coloured quartz muscovite schists, which are usually coarse-grained, fissile and

crenulated (plate 80). This lithology contains variable amounts of carbonate (chiefly dolomite) and sulphides (usually pyrrhotite, less frequently pyrite and sphalerite), but is characterized by the absence of graphite and feldspars (table 4.1). These muscovite schists frequently overlie mineralized horizons and are usually (but not invariably) enriched in barium compared to adjoining or interbedded graphitic schists (see figs. 2.23, 2.28). The light green colouration appears to be related to the presence of barian muscovite, which as shown in section 6.3, has a significant phengitic component. Similar muscovite schists occurring in unit C are distinguished by the presence of biotite and/or chlorite, both of which are rare in unit B, although some gradational lithologies were encountered. Rutile, apatite and trace zircon are ubiquitous as accessory phases in both graphitic schists and muscovite schists (table 4.1), and tourmaline is occasionally present.

#### 4.2.4 Unit C lithologies.

This a lithologically heterogeneous group of non-graphitic and usually carbonate-rich, muscovite-biotite or muscovite-chlorite schists, which form the lower part of the Ben Lawers Schist formation and are also locally interbedded with unit B schists and mineralized strata (part 2.4.2). The absence of garnet, hornblende and epidote distinguishes unit C lithologies from those of unit D. Quartz contents have a limited range of 40-50% (except in volumetrically minor quartzites and dolostones), and plagioclase is an essential minor component (typically 5-10%). Sulphides are often absent, but where present they consist largely of pyrrhotite and the base metal sulphides are present only in rocks adjoining the stratiform mineralization. Calcite is absent or subordinate to ferroan dolomite, which typically forms 15-30% of unit C schists. Trace amounts of tourmaline and apatite are seen in most samples examined (table 4.1).

Outcrops of unit C lithologies are of limited extent, probably because of the rapid weathering of the carbonate. In drillcore, the rock is normally homogeneous and varies in structure from massive with a contorted foliation (typical of chlorite-rich varieties; plate 40) to highly fissile with tight, chevron folding (seen in some biotite-rich varieties). In the first type, muscovite often forms fine-grained, foliated welts set in a coarser matrix of



quartz, plagioclase, dolomite, chlorite and micas (e.g. sample G169; see plate 82). Plagioclase occasionally forms rounded grains replacing the muscovite fabric, which is also crossed by post-tectonic muscovite and chlorite crystals.

Barium-enriched unit C lithologies. Unit C rocks may be variably enriched in barium, a feature which led Coats et al. (1981) to assign these rocks to the Ben Eagach Schist although they may be petrographically indistinguishable from barium-poor Ben Lawers Schist lithologies (part 2.2.2). Barium is accommodated by muscovite and biotite when the whole rock BaO content is less than about 2.5 wt% (e.g. samples 706-B and 203-7B; tables 4.1, 4.3 and 4.4). At higher BaO concentrations, hyalophane appears as a minor constituent and coexists with albite, which is also more abundant in the mineralized unit C schists (e.g. ~12% of sample 702-8A: table 4.1 and plate 84). Cymrite, celsian and hyalophane occur together with biotite, dolomite, albite and quartz in samples of unit C metasediments interbedded with barite in the Frenich Burn area (e.g. sample 101-1). Mineralized unit C sediments which are rich in celsian have been described in parts 3.2.4 and 3.4.2.

#### 4.2.5 Unit D lithologies.

The most characteristic lithology of unit D is a calcareous and chloritic, quartz plagioclase muscovite schist containing porphyroblasts of garnet and hornblende (e.g. samples N80-36 and 429-5; table 4.1 and plates 85, 86). Garnets form red coloured rhombododecahedra, which are typically 3-7mm in diameter and exhibit sigmoidal inclusion trails of quartz, rutile and ilmenite. Hornblende occurs as dark-coloured (green in thin section), stumpy or elongate prisms which are often 1-3cm in length and typically form radiating sprays of 'garbenschiefer' which cut across the crenulated micaceous fabric (plate 41). The hornblende contains oxide inclusion trails which are generally continuous with the matrix, and is often partially replaced or pseudomorphed by chlorite, biotite and carbonates. Calcite and dolomite coexist in the matrix and additional minor phases are biotite, zoisite and tourmaline. Carbonaceous matter is invariably absent.

However, of equal or greater abundance in unit D are chloritic, calcareous and epidote-bearing mica schists which are free of garnet and hornblende. Representative samples of this lithology (table

4.1) include N80-33, in which chlorite is the dominant ferromagnesian silicate; 429-3, which contains equal amounts of chlorite, biotite and carbonate with about 10% zoisite; and 602-2, which consists largely of zoisite, quartz and carbonates. Epidote forms elongate crystals up to 2mm long with a lozenge-shaped cross-section (plate 87) (epidote compositions and nomenclature are discussed in part 6.5.3). The lithology often has a chaotic structure with fine-grained, foliated aggregates of micas and of quartz and plagioclase set in a recrystallized matrix of quartz, dolomite and chlorite. Dolomite forms coarse, lenticular segregations in some rocks (e.g. sample 429-1; C & O isotope analyses in Appendix F). Less chloritic and micaceous varieties may preserve sedimentary banding, and structurally competent, fine-grained quartzites and dolostones are occasionally interbedded with the calcareous pelites.

#### 4.3 Geochemistry: previous studies and sampling rationale.

##### 4.3.1 Previous work.

Coats et al. (1981) presented about 100 near-complete geochemical analyses and 350 partial analyses of core-lengths from BHs 1-5 and 6-11 respectively. Some aspects of this data set (Ba and Ti distributions) were discussed in part 3.4.1. The data for metasediment intervals intersected in BHs 2, 3, 9, 10 and 11 (total core-length, 321m) has been assigned to the lithostratigraphical units (A, B and C) adopted in this study, on the basis of petrographical descriptions given by Coats et al. (1981) and partial relogging of this drillcore. Mean compositions for each unit in these intersections (given in table 4.3) are used in this study as bulk samples for comparative purposes.

Willan (1981) analysed approximately one hundred samples of the Ben Eagach Schist and Carn Mairg Quartzite from along- and across-strike transects between the Loch Tay Fault and Loch Faskally (fig. 1.3), to identify anomalous levels of major and trace elements in these rocks and determine the vertical and lateral dispersion of anomalies related to the mineralization. He found that the Ben Eagach Schist is similar in major element content to average shales and pelites, except for relatively high  $\text{Al}_2\text{O}_3$  and  $\text{K}_2\text{O}$  contents which reflected a dominantly illitic composition for the original sediment. Of the trace elements, Ba, Zn, Pb, Cr and Rb were found

in higher concentrations than in average shales. An anomalous subpopulation of graphitic schist samples that were enriched in Ba, Zn and Pb, were also found to be relatively enriched in  $K_2O$ , Cu and Co (but not in Mn or Cr) when compared with the background subpopulation. Willan (op. cit.) found weakly anomalous values up to 4km west of the mineralization outcropping at Meall Tairneachan, and throughout the thickness of the Ben Eagach Schist in the Creag an Fhithich-Ben Eagach area. He suggested that the absence of a Mn halo around the Aberfeldy deposits is due to the reducing conditions which prevailed during deposition.

#### 4.3.2 This study: objectives and sample selection.

The objectives of further lithogeochemical investigations of the metasedimentary host rocks to the Foss deposit (outlined in part 1.4.2), were to: (1) define the geochemical characteristics of the several lithostratigraphical subdivisions of the Ben Eagach and Ben Lawers Schists, which were based on mineralogical/petrographical criteria; (2) deduce the chemistry of the sedimentary environment, and the contribution from hydrothermal sources, during deposition of these lithofacies; and (3) seek evidence for diagenetic and/or metamorphic modification of the primary sediment composition.

A total of sixty-two metasedimentary rock samples were analysed by XRF for twenty seven elements in three batches (see Appendix D). The initial reconnaissance batch comprised sixteen core intervals of 0.6-2.0m length (some sequential) from DH 705 in Foss East (samples 705-A, 705-B, etc.). As these were analysed for barium on the trace element program, six barium-rich samples were subsequently re-analysed with barium incorporated as a major element. The second batch of metasediment analyses included twenty 'G-series' outcrop samples collected during geological and lithogeochemical mapping (section 2.2), together with several more drillcore samples. The final batch consisted mainly of small drillcore samples (mostly 10-30cm long) from many Foss East intersections, representing a wide range of unusual as well as common lithologies.

The total number of samples analysed from each lithostratigraphical unit are as follows: Carn Mairg Quartzite (CMQ)-type lithologies, three; unit A, fourteen; unit B, twenty-nine; unit C, twelve; and unit D, four. This reflects the greater attention given to the host rocks of the mineralization, which are predominantly

unit B of the Ben Eagach Schist, and it should be noted that a high proportion (55%) of unit B and C samples analysed contain  $>1\%$  BaO. Another inherent sample bias in the data set may be in the relative proportions of pelitic, quartzitic and calcareous lithologies, particularly within units A and B. The proportions of samples from each unit, subdivided by rock type and barium content, are shown in fig. 4.1a.

Reduction of the data set to a manageable number of mean rock compositions is desirable to facilitate comparisons of the major lithostratigraphic units, and also comparisons with published data on average pelite and shale compositions (section 4.5). However, the limited number of analyses of a wide range of bulk compositions (table 4.2) may render calculated average compositions meaningless because of a disproportionate number of particular rock types within any one group. This problem, which was recognised at the outset, is highlighted by comparing the mean compositions of all samples from unit B which were collected from outcrop ( $n = 11$ ) and from drillcore intersections ( $n = 18$ ) (table 4.4). Outcrop samples have, on average, considerably less Fe, Mn, Mg and Ca, and more Al, Ti, Na and K than the average of drillcore samples. This is readily explained by sampling bias since carbonate-rich rocks are comparatively scarce at outcrop due to preferential weathering and erosion, but are easily sampled in drillcore as they tend to shatter less than mica-rich schists during drilling.

Both the outcrop and the drillcore material sampled in this study is significantly more siliceous (and barian) than a weighted average of 20.4m of unit B lithologies intersected by IGS boreholes 2 and 3 (table 4.4, column 4). This bulk sample has a correspondingly higher carbonate and mica content (represented by the higher Fe, Mn, Mg, Ca, Sr, Rb and K in the IGS average; see following section). Comparisons of bulk compositional differences between the lithostratigraphic units, using IGS drillcore analyses (of Coats et al., 1981; fig. 4.1b) and data obtained in this study, are discussed in section 4.5.

#### 4.4 Element associations and mineralogical components.

##### 4.4.1 Multivariate analysis.

An initial appraisal of the geochemical data for seventy metasediments and mineralized sediment samples employed two methods

of multivariate analysis. Cluster analysis was used to discern geochemical groupings of the sample analyses, and both cluster analysis and R-mode factor analyses (Lawley and Maxwell, 1963) were also employed to evaluate inter-element correlations. Computer programs used for cluster and factor analysis were modified from those given by Davis (1973) to produce graphic output (program compilation by Stephen Rainey, University of Edinburgh, 1983).

#### Cluster analysis.

Significant sample groupings shown by cluster analysis include: CMQ-type quartzites; unit A quartzites; calcareous graphitic schists and dolostones; barian pelites from unit B; and calc mica schists of units C and D. However, outcrop and drillcore samples of unit B graphitic schists are placed in separate groups, with the former group incorporating several unit A pelites. Thirteen sample groups are distinguished with intra-group correlation coefficients of  $>0.5$ , and thirty-two sample groups with coefficients of  $>0.75$ . Of the latter, sixteen comprise single samples. This emphasizes the diversity in rock compositions represented in the data set, and suggests that the equal weighting given to each element in cluster analysis is inappropriate to a geochemical classification of the rock types represented.

Cluster analysis also reveals several significant element groupings in the data set, which represent common mineralogical components of the metasediments. Element groupings with correlation coefficients greater than  $+0.75$  are: (a) Al-K-Ti-Sc-Rb, which represents the mica component; (b) Fe-Mg-Ca-Mn which characterizes the carbonate component; (c) La-Ce-Nd, which are probably concentrated in apatite and rare-earth phosphates (section 7.6); and (d) Pb-Zn, which represents the close association of galena and sphalerite. Silica is not correlated with the mica component because of dilution by variable amounts of quartz. Significantly, neither Na nor Ba are closely associated with other major elements, although Ba is weakly correlated with V and Cr.

#### Factor analysis and interpretation.

More information on inter-element covariance is obtained by factor analysis. By representing variables as vectors and using matrix manipulation, 'factors' are extracted which represent the independent co-ordinates of the space enclosing a particular set of correlations. Six factors were found to account for 80% of the

variation in 26 elements determined in the total data set of metasediment analyses. (Th was omitted because of an interference problem: Appendix D.4). Factor loadings are shown graphically in fig. 4.2.

The first factor accounts for nearly one third of the total variation and has high positive loadings ( $>0.5$ ) of Al, K, Ti, Sc, Rb, and Nb, associated with significant loadings ( $>0.25$ ) of V, Zr, Nb and Cr. This factor clearly reflects the abundance of mica, chiefly muscovite, in the metasediment samples. The trace element association could be accounted for by the scavenging action of clay mineral precursors to the mica component. Coats et al. (1980, 1981) consider these precursors to have incorporated Ba, Mn, Zn and Pb during deposition and diagenesis, resulting in the cryptic mineralization detected near the stratiform mineralization. However, the negative loadings of Ba (together with Cu, Zn and Pb and several other elements) in factor I suggests a complex distribution of these elements, which is not simply related to the original clay mineral content. Barium has the strongest positive loading in factor III in which Ba is associated with V, Sr and Cr and shows a negative correlation with Si, Zr and Nd. This factor accounts for 12% of the total variation and may indicate V and Cr enrichment in rocks containing barian micas (although none of the samples contain fuchsite: see section 6.3). These rocks appear to be relatively depleted in the resistate fraction represented by Si (quartz) and Zr (zircon).

Both quartz and carbonate effectively dilute the concentration of the mica component in the metasediments and their antipathetic relationship is illustrated by factor II (fig. 4.2) which has a strong positive loading Si and negative loadings of Fe, Mg, Ca, Mn and Sr. Factor IV has high positive loadings of P, La, Y, Nb, Ce and Nd, all of which occur principally in apatite and rare-earth phosphates. The poor correlation between these elements and Ca may be explained by the much larger influence of carbonates on the calcium distribution. The base metal sulphide component is represented by strong loadings of Zn and Pb, associated with weak loadings of Cu and Fe, in factor V. If the number of factors is increased, Fe and Cu are prominent in factor VIII which illustrates the association of copper with iron sulphides rather than with base

metal sulphides in the metasediments, a feature also noted by Coats et al. (1981).

Sodium, which receives no significant loadings in previous factors, becomes dominant in factor VI in which sodium is associated with Sr, Y, Zr and Nd. The apparently anomalous behaviour of both sodium and barium is resolved by applying factor analysis to subsets of the total group of metasediment samples. In the sub-group of unit B samples which are anomalously enriched in barium ( $>0.5\%$  BaO), sodium has a strong loading in factor I in association with the mica component. However, in the remaining Ben Eagach Schist samples, barium takes the place of sodium in factor I. This accords with the observation by Willan (1981) that Ba is strongly correlated with Al and K in a background population of Ben Eagach Schist samples which are not barium enriched, indicating the incorporation of Ba in clays, micas and possibly potassic feldspars in the normal sedimentary environment. In the sub-group of unit C samples, Na, Ba and Zn are strongly correlated. Petrographical examination of the mineralized members of this sample group showed the presence of co-existing albite and hyalophane (part 4.2.4).

#### 4.4.2 Alkali element associations.

A bivariate plot of BaO and Na<sub>2</sub>O (fig. 4.3) illustrates the contrasting association of these elements in the different lithostratigraphic units sampled. Most samples from the lower division of the Ben Eagach Schist, unit A, contain  $<0.5\%$  BaO and 1-3% Na<sub>2</sub>O, whereas samples from unit B generally contain  $<1\%$  Na<sub>2</sub>O but are variably enriched in BaO. Dilution of the pelitic component by excess SiO<sub>2</sub> and CaO + MgO in quartzites and carbonate-rich rocks respectively, results in some overlap of the fields of unit A and unit B samples. This overlap is largely resolved on a triangular plot of Na<sub>2</sub>O-BaO-K<sub>2</sub>O (fig. 4.4). However, as in the previous figure, the field of Ben Lawers Schist samples overlaps with the fields of unit A and unit B samples, but mineralized unit C metasediments show a loose positive correlation between Na<sub>2</sub>O and BaO, as anticipated from petrographical observations and factor analysis.

There are several notable exceptions to the 'normal' distribution of alkaline elements in samples assigned to units A and B (using the petrographical/mineralogical criteria defined in section 2.2). Sample G13, which resembles other garnetiferous unit A



pelites in appearance and composition, is significantly enriched in barium (table 4.2), and plots close to a unit B sample, G219, which has a higher than average sodium content. One garnet-rich graphitic schist, sample 706-5, is poor in plagioclase and plots close to the  $K_2O$  apex together with unit B samples. The core interval represented by sample 201-K (table 4.2, p. 171) is the only occurrence found of a barium-enriched lithology containing garnet (see part 2.4.5), and this plots with other unit B samples in fig. 4.4. One of the two graphitic dolostone samples analysed (705-11) is affiliated with unit A lithologies by its alkaline element distribution, although it is enclosed by unit B graphitic schists (Appendix A and fig. 2.31).

The dominant influence of albite and muscovite contents on the alkaline element distribution in unit A and unit B lithologies is illustrated by fig. 4.5, in which rock compositions cluster about the mixing line which joins these components. Unit B samples cluster near to the muscovite end-member reflecting the absence or low modal abundance of plagioclase, but a group of these samples plot at lower values of  $K_2O/Al_2O_3$ . This is accounted for by the substitution of Ba for K in barian muscovite. In the remaining samples, scatter to either side of the muscovite-albite line can be explained by: (a) the presence of minerals other than muscovite containing  $K_2O$  and/or  $Al_2O_3$  such as biotite, chlorite, hornblende, clinozoisite and garnet; (b) substitution of Ca for Na in plagioclase; and (c) the variable presence of Na in micas and hornblende.

Figure 4.6 shows bulk metasediment compositions plotted on a modified A'KF diagram. This diagram differs from that introduced by Eskola (see Turner, 1968, p. 175-6) in that BaO has been substituted for CaO in the A' component, and all oxide components are calculated as molecular percent rather than weight percent. Except for one sample (G119A, which is rich in hyalophane), the metasediment compositions occupy a wedge-shaped field between typical mineral compositions of muscovite, biotite and chlorite, extending towards the F apex where the alkali-free phases including garnet, carbonates and sulphides, plot on this diagram.

## 4.5 Comparative lithogeochemistry.

### 4.5.1 Bulk compositional characteristics of the lithostratigraphical units.

As noted in section 4.3, the limited number of samples analysed in the study and a disproportionate representation of particular rock types, may restrict the use of this data set in establishing significant compositional differences between the lithostratigraphic units (other than the alkali element associations discussed above). There<sup>fore</sup>, bulk rock compositions have also been calculated from geochemical data published by Coats et al. (1981) for IGS borehole intersections at Foss. Full major element analyses (for all elements except Na) are only available for unit B graphitic schists intersected in BHs 2 and 3, and the combined mean composition of these is given in table 4.4. Partial analyses of the much greater intervals of metasediment intersected in boreholes 9, 10 and 11 (totalling nearly 300m: table 4.3) allow geochemical comparisons of the lithostratigraphical units to be made with more confidence.

From the intersection-weighted mean analyses, it is apparent that the unit B lithologies represented in boreholes 2 and 3 (table 4.3, columns 4 & 5) have a higher average carbonate component (high CaO, MnO) than the corresponding lithostratigraphic unit represented in BHs 9, 10 and 11. The average CaO content of unit A and unit C lithologies also shows considerable variation between these boreholes. Nevertheless, average CaO values progressively increase from unit A through to unit C, in which the Ca/Mn ratio is substantially higher than in the Ben Eagach Schist. Fe<sub>2</sub>O<sub>3</sub>, TiO<sub>2</sub> and Ni contents remain fairly constant throughout, but as expected the amounts of Ba, Cu, Zn and Pb are highest in unit B which hosts the stratiform mineralization. Significantly, barium levels are higher in unit C (calc mica schist) than in unit A whereas the converse applies to the distribution of lead and zinc. The ratio of Pb to Pb+Zn, which averages 0.30 in the Ben Eagach Schist, decreases to 0.12 in unit C.

Despite shortcomings due to the small number of samples and sampling bias discussed above, average compositions calculated for sample groups analysed in the present study (fig. 4.7) show a general similarity in chemical features to those of the bulk samples represented by IGS borehole analyses. Note that in generating the data shown in fig. 4.7, analyses with >70% SiO<sub>2</sub> have been excluded,

and analyses of unit B and unit C schists with >1% BaO have been averaged separately (coded SPb(B and SPb(C respectively). This treatment of the data shows that in the unit B pelites analysed, barium enrichment may be linked with slightly higher average concentrations of SiO<sub>2</sub>, Fe<sub>2</sub>O<sub>3</sub> and Sr, significantly lower concentrations of Al<sub>2</sub>O<sub>3</sub>, TiO<sub>2</sub>, Na<sub>2</sub>O, K<sub>2</sub>O and Rb (fig. 4.7; Rb not plotted). Barium enrichment in unit C lithologies is associated with increased average Fe<sub>2</sub>O<sub>3</sub>, Na<sub>2</sub>O, Sr and possibly Zn, Cr contents, but decreased CaO contents relative to barium-poor unit C pelites. Unit D garnet hornblende calc mica schists are very similar to the calc mica schists of unit C except for the lower BaO and Zn content and higher F/FM ratio of the garnet- and hornblende-bearing samples.

Significant geochemical features which characterise the four lithostratigraphical subdivisions of the Ben Eagach and Ben Lawers Schist formations at Foss are summarized below:

- Unit A: Lowest Ca and (La + Ce + Nd) of all units. Lower Mn, Ba, Zn and Pb but higher Na (plus Sc, Zr?) than unit B.
- Unit B: Lowest Na of all groups; highest Ba, Zn and Pb. Al and K contents similar to, or lower than, unit A.
- Unit C: Higher Mg, Ca, Sr, Y and Ca/Mn ratio than units A and B; lower Al, K, F/FM ratio and (except in the barian group) Zn, Pb contents.
- Unit D: Compositionally similar to unit C except for lower average Ba and Zn and higher F/FM ratio.

Geochemical data for the Ben Eagach Schist presented by Willan (1981a) and summarized above in section 4.3, are in good agreement with the results of the present study. Willan does not state his average wt% values for SiO<sub>2</sub> and CaO, however the averages of other elements (19.2% Al<sub>2</sub>O<sub>3</sub>, 4.25% K<sub>2</sub>O, 152ppm Rb and 0.08% MnO in seventy eight samples) suggest that Willan's outcrop sampling may have been biased towards the more siliceous and less calcareous lithologies in the same manner as in the present study. Willan used the ratio of K<sub>2</sub>O to Na<sub>2</sub>O to argue for potassium enrichment in the 'anomalous population' of twenty-four graphitic schist samples with >0.4% Ba. In this group, the ratio is significantly higher than the background population (~9 compared with ~4). Similar K<sub>2</sub>O/Na<sub>2</sub>O ratios were found for unit B and unit A respectively, in the present study. However, as discussed in part 4.6.2, sodium depletion rather than

potassium enrichment is regarded as the chief cause of differences in alkali content between the background (equivalent to unit A?) and anomalous (equivalent to unit B?) populations of Ben Eagach Schist samples.

#### 4.5.2 Comparison of the Ben Eagach Schist with other Dalradian metasediments and average shales.

Bearing in mind the uncertainty attached to average values because of sampling bias and the small size of the data set, it is of interest to compare the Ben Eagach Schist data with published average Dalradian pelite compositions and "world average" pelite and shale (table 4.5). The published major element averages have been adjusted to total 100% (volatile-free), and comparisons are facilitated by the reasonably similar  $\text{SiO}_2$  contents ( $60 \pm 4$  wt%) in all data sets. Compared with other Dalradian pelites, the Ben Eagach Schist pelites analysed in this study are on average relatively poor in  $\text{Fe}_2\text{O}_3$ , Ni, Sr and Zr, but are relatively enriched in  $\text{K}_2\text{O}$ , BaO, Rb, Zn and Pb. These differences are also observed in comparing the bulk sample (incorporating quartzites and carbonate rocks) provided by IGS boreholes (tables 4.3 and 4.4) with other Dalradian pelites and "world average" pelites and shales (table 4.5). Apart from the barium, zinc and lead enrichment, the most significant difference between unit B pelites and the other data sets is the low sodium content of the unit B samples. Possible explanations for this are discussed in section 4.6.

'Black shales' such as the Middle Cambrian Alum Shale of Scandinavia (Bjorlykke and Englund, 1979), the upper part of the Devonian-Mississippian Canol Formation which overlies the Tom barite-Pb-Zn deposit in Yukon (Large, 1981c), and the Permian Kupferschiefer of Northern Europe (Hutchison, 1983, p. 93), are generally enriched in Ti, P, Cr, V, Cu and Ni compared with normal shales. It is significant that none of these elements are enriched in the Ben Eagach Schist pelites, in which Ni may actually be depleted relative to average shales.

'Black shales' are also characterized by high vanadium/chromium ratios ( $>4$ ), high sulphur contents, and carbon contents greater than 2% (cf. Vine and Tourtelot, 1970). In the Ben Eagach Schist samples analysed, the V/Cr ratio ranges from 0.7 to 1.6, and

on average is close to 1. The ratio may have been reduced by the addition of Cr associated with barium enrichment (see part 4.4.1) but there is no evidence that such a mechanism counterbalanced originally high V/Cr ratios. The reduced carbon contents of six samples of graphitic schist analysed in this study (table 4.6) do not exceed 1%, although Willan (pers. comm. 1984) has recorded over 2 wt% carbon in this lithology. However, much of the original carbon content may have been oxidized during metamorphism, as suggested by the extensive carbonation of metabasites interbedded with the graphitic schists, and by stable isotope analyses of the carbonates (Appendix F) (see also Graham et al., 1983). Complete oxidation of the carbonaceous material in metasediments adjacent to mineralized horizons may account for the presence of at least some non-graphitic quartz muscovite schists in the mineralized zone.

In conclusion, the geochemical data suggest that the Ben Eagach graphitic schist represents a metamorphosed shale but not a 'black shale', in the sense reserved for the sapropelic muds formed in sediment-starved euxinic conditions typical of transgressive seas.

#### 4.6 The nature of the sedimentary environment and post-depositional changes.

##### 4.6.1 Composition of the sedimentary material.

As noted by Willan (1981a), the high K<sub>2</sub>O content of the Ben Eagach Schist may be explained by a predominantly illitic precursor sediment, perhaps with some admixture of hydromuscovite and kaolin-ite. When recalculated to a volatile-free total, an average illite composition closely resembles that of the unit B pelites (tables 4.5, 4.7). Many studies have demonstrated the transformation of montmorillonitic and kaolinitic clays to illite by a process of interlayer potassium fixation (e.g. Perry and Hower, 1972), and further adsorption of potassium accompanies the conversion of illite to muscovite. From geochemical studies of an undisturbed stratigraphic pile, Hower et al. (1976) concluded that during burial metamorphism shales act as closed systems for all components except H<sub>2</sub>O, CO<sub>2</sub>, CaO and Na<sub>2</sub>O, which decrease in abundance. However, they observed a progressive increase in the aluminium and potassium content of the clay fraction with burial diagenesis. This was

attributed to the breakdown of detrital potassic feldspar and micas, concomitant with the conversion of smectite to illite and an increase in the chlorite content of the argillaceous sediment.

Kaolinite and illite (or hydromuscovite) may also form by crystallization from an aluminosilicate gel, or directly from hydrothermal solutions such as those which formed the Kuroko deposits (Sato, 1977; Urabe, 1974b; Iijima, 1974). Fine-grained, potassic white mica is commonly associated with sulphides in stratiform ore deposits (McLeod and Stanton, 1984), and neoformed muscovite has been observed in hydrothermal sediments of the Galapagos rift (Hekinian et al., 1980). Although the barium incorporated into muscovite in schists associated with the Aberfeldy deposits is undoubtedly of hydrothermal origin, these rocks are otherwise geochemically similar to the bulk of the graphitic quartz muscovite schists of unit B. Therefore, a direct hydrothermal origin for volumetrically significant amounts of the muscovite in the host rocks seems unlikely.

Russell et al. (1984) have drawn attention to the temporal and spatial relationships between the Aberfeldy deposits and the Early Cambrian, Fucoid Beds of NW Scotland, which are dolomitic argillites rich in potassic feldspar. Swett (1968) suggested that K-feldspar in the Fucoid Beds formed after deposition of the argillites, during dolomitization of the overlying illitic limestones (the Durness Limestone). However, Russell and co-authors consider the K-feldspar to be an authigenic mineral (cf. Břuyce and Friedman, 1975), which was deposited in a shallow shelf sea made intermittently alkaline and aluminous by an admixture of continental run-off and groundwater. They suggest that saline and aluminous brines flowed into the adjacent, developing Middle Dalradian basins, into which turbidity currents also carried potassic argillite. The alkaline brines then interacted with acid, metalliferous, hydrothermal solutions to precipitate the ore assemblage and the unusually abundant barium silicates of the Aberfeldy deposits (section 10.3.2). This model could also account for the unusually potassic and aluminous sediments associated with the deposits, which may have been derived directly from the sediment influx or by the incorporation of aqueous species into neoformed, authigenic clay minerals.

In an early account of the Fucoid Beds and their economic potential, Bowie et al. (1966) drew attention to a generally

observed, worldwide maximum in the potassium content of shales deposited in the late Precambrian and Cambrian. Conway (1945) suggested that this over-return of potassium to sediments from ocean water could be related to a high organic content of the ocean at this time. Recent geochemical studies (e.g. Bjorlykke and Englund, 1979) appear to confirm unusually high potassium levels in Cambrian shales, but no recent worldwide compilation of data appears to be available. A worldwide stagnant ocean episode in the late Proterozoic-Early Cambrian, which may have favoured the formation of kaolinitic sediments, has been suggested by Berry and Wilde (1978) and Keith (1982), on the basis of several lines of evidence including the marine isotopic record (see chapter 9) and stratigraphical abundances of black shales and stratabound ore deposits formed at this time.

The sedimentary environment which prevailed during deposition of the calc pelites of units C and D (i.e. the Ben Lawers Schist and similar lithologies within the Ben Eagach Schist), was probably oxidizing because of the abundance of carbonate and absence of sulphides, reflected in the low Zn, Pb contents of non-mineralized unit C sediments. The absence of reduced carbon, although probably also a primary feature, is in itself an unreliable indicator of an oxidizing sedimentary environment because of possible oxidation during metamorphism. The high Ca, Mg and Sr contents reflect the major dolomite component, and the precursor sediment is likely to have been a calcareous siltstone or marl.

#### 4.6.2 Diagenetic and epigenetic changes in the metasediments.

##### Hydrothermal silicification.

Highly siliceous (and often pyritic) graphitic schists, described in section 4.2.3, occur in the footwall to the M3 horizon in parts of Foss East, and at several locations in Foss West (such as in the adit: part 2.3.3). Geochemically, this lithology is heterogeneous (samples coded SQb(B, table 4.2) but resembles other unit B graphitic schists apart from the dilution by  $\text{SiO}_2$ . The excess silica relative to normal graphitic schists (which commonly contain 50-70%  $\text{SiO}_2$ ) is considered to be of hydrothermal origin, and is attributed to siliceous brines which infiltrated the sediment subsequent to its deposition. The presence of this silicification below mineralized horizons is one of several features associated



with areas proximal to exhalative vents (parts 2.4.6 and 3.5.2), although the extensive occurrences on the northern limb of the Creag na h-Iolaine Anticline in Foss West do not appear to be spatially related to emanative centres. Graphitic hyalophane rocks which are also found in this area (such as G119A; table 4.2), are considered to be barium-enriched carbonaceous metasediments (see part 3.4.2).

#### Epigenetic Zn-Pb mineralization in arenites.

Mineralized siliceous rocks which are clearly of detrital origin also occur within the Ben Eagach Schist. These petrographically resemble the Carn Mairg Quartzite (section 4.2.1), except that they contain bands of sphalerite and galena. This lithology is not enriched in barium (samples 202-3, 202-7 and 705-7; table 4.2), and the petrographical and isotopic evidence (section 9.5.2) is compatible with a process of diagenetic/epigenetic mineralization of permeable, sandy strata within a thick sequence of shaly sediments enriched in Pb and Zn. Sphalerite bands within graphitic dolostones (particularly in unit B) probably have a similar origin. This implies that base metals and sulphur were mobile during diagenesis and dewatering of the sediment pile. This is discussed further with reference to sulphur isotope studies in chapter 9.

#### Dolomitisation.

Dolomite is not normally precipitated under marine conditions but forms by the diagenetic or metasomatic alteration of limestones. Some of the magnesium required for this process may be derived from a primary carbonate (high-Mg calcite) or from associated argillaceous sediments containing montmorillonite or chlorite. However, many studies have indicated that the bulk of the Mg is supplied from percolating saline solutions during diagenesis, and dolomitisation by the incorporation of external Mg is favoured in the case of Ben Lawers Schist metasediments since the Ca/Mg ratio is fairly constant and close to unity. Porosity enhancement during dolomitisation of calcareous turbidites may account for the common occurrence of sphalerite laminae in graphitic dolostones in unit B; this mineralization is also regarded as diagenetic/epigenetic in origin.

#### 4.6.3 Alkaline element mobility during metamorphism.

The mineralogy and composition of metabasic rocks within the Ben Eagach Schist at Foss (chapter 5) provides evidence for the extensive movement of potassium, and to a lesser extent, sodium and

barium, during diagenesis and/or metamorphism of the rock pile. Lenticular metabasite bodies up to 10m thick have been carbonated, hydrated and enriched in  $K_2O$  (typically forming >1 wt% of chloritic metabasites: see fig. 5.4). Adjacent to mineralized horizons, metabasites are also enriched in barium (such as those intersected in BH10: Coats et al., 1981). Sodium depletion accompanies mineralogical changes associated with further K and Ba enrichment in altered metabasites (see section 5.3).

Geochemical evidence for the loss of sodium from calcareous metamorphic rocks in which albite, or the sodic component of plagioclase, was destroyed by prograde mineral reactions involving an inter-granular fluid phase, has been presented by Tanner and Millar (1980), and by Ferry (1983b). Watkins (1983) has demonstrated that a metamorphic redistribution of sodium, without appreciable sodium input or loss, can account for the origin of albite porphyroblast schists which are located in the crests of regional F3 antiforms in the SW Scottish and NE Irish Dalradian. Retrograde fluid infiltration and hydrogen metasomatism is suggested as the causative process for the redistribution of albite from quartz-albite bands into micaceous bands, concomitant with the growth of chlorite and magnetite and the formation of quartz segregations. In unit A pelites at Foss, much of the plagioclase occurs as porphyroblasts replacing muscovite (part 4.2.2), and a similar process of albite redistribution during metamorphism may have occurred.

It may be speculated that a larger scale redistribution of sodium occurred in the unit B graphitic schists, whereby sodium was removed with the permeating metamorphic fluid. Some of this sodium may have reacted with detrital alkali feldspars in quartzites interbedded with the Ben Eagach Schist, to form replacement perthites and albite (see part 4.2.1 and note the comparatively high  $Na_2O$  contents of samples 505-C, 202-P, 708-22 and 202-C, table 4.2). A diagenetic or metamorphic process of sodium depletion in the unit B pelites might be analogous to that which affected the enclosed, relatively thin (<0.5m) metabasite beds, which have stable mineralogies devoid of plagioclase and chlorite (section 5.2). To this extent, it is suggested that the development of stable mineralogies during metamorphism involved changes in bulk rock composition (cf. Leake, 1972), and therefore the low sodium content of unit B pelites

may not be a primary feature of the sedimentary precursor. However, aside from the absence of garnet and common presence of pyrite in unit B lithologies (table 4.1), there is little to indicate the cause of such a pronounced difference in response between unit A and unit B rocks to infiltrating metamorphic fluids. It is therefore suggested that sodium depletion during diagenesis and/or metamorphism may have enhanced geochemical differences between these units, but is unlikely to have been the primary cause of such differences.

#### 4.7 Metasediment geochemistry: a summary.

The sixty-two metasediment samples analysed cover a wide range of petrographical types and compositions, and mineralized sediments are disproportionally represented in the data set. Sampling bias is also seen in comparing outcrop and drillcore samples of one lithostratigraphical unit. Therefore, bulk compositions derived from IGS drillcore analyses (Coats et al., 1981) were also used in comparing the geochemical characteristics of these units.

Mineralogical components of the metasediments are expressed by inter-element covariances. Important components are: micas (Al-K-Ti-Sc-Rb-V-Cr), quartz (Si), carbonates (Fe-Mg-Ca-Mn-Sr), phosphates (P-La-Y-Nb-Ce-Nd) and sulphides (Zn-Pb and Fe-Cu). Sodium and barium are poorly correlated with other elements in the total metasediment group since they are each present in different components (feldspars and micas) in different lithological types.

The relative proportions of the alkaline oxides, Na<sub>2</sub>O, K<sub>2</sub>O and BaO, provide a geochemical discriminant between samples of the three lithostratigraphical units (A, B and C). Unit A metasediments contain <0.5% BaO and 1-3% Na<sub>2</sub>O, whereas unit B rocks generally have less sodium and are variably enriched in barium. Average K<sub>2</sub>O levels are similar in pelites from both of these units but are lower in unit C metasediments, in which BaO and Na<sub>2</sub>O contents show a positive correlation. Other significant geochemical differences between these units include the low Ca content of unit A, the generally high Zn, Pb and Mn levels in unit B, and the higher Mg, Ca, Sr and Y contents and Ca/Mn ratios in unit C. Unit C lithologies also have lower Al contents and F/FM ratios, and (except in the barium-enriched group) lower Zn, Pb contents than units A and B. Garnet-

and hornblende-bearing schists of unit D are compositionally similar to unit C calc mica schists except for lower Ba contents and higher F/FM ratios in the former.

Compared with mean compositions published for other Dalradian pelites and 'world average' pelites and shales, the Ben Eagach Schist is enriched in K, Rb, Ba, Zn and Pb and depleted in Fe, Ni, Sr and Zr. The formation lacks the geochemical characteristics of sapropelic black shales (namely: high P, Ti, Cr, V, Ni, Cu and organic carbon contents). The Ba, Zn and Pb are considered to be largely of hydrothermal origin, and exhalative brines may also have contributed some potassium. The deposition of a potassic, aluminous sediment may be temporally and genetically related to the formation of authigenic K-feldspar in the Lower Cambrian shelf sediments of NW Scotland (Russell et al., 1984). Previous authors have also noted a worldwide increase in the potassium content of late Precambrian-lower Cambrian shales, which may be related to a stagnant ocean episode. The Ben Lawers Schist, and similar lithologies within the Ben Eagach Schist, was probably deposited in an oxidizing environment characterized by an abundance of carbonate and a scarcity of sulphides, reflected in low Zn+Pb contents. The precursor sediment is likely to have been a calcareous siltstone or marl, which incorporated magnesium during dolomitization.

Silicification of hydrothermal fluids infiltrating the surface layers of the sea floor sediment, is proposed to account for the high silica content of certain barium enriched graphitic rocks adjacent to mineralized horizons. Replacement of detrital potassic feldspar by sodic feldspar in quartzites interbedded with the pelites is attributed to reactions with saline pore waters during diagenesis. Pore waters expelled from the base metal enriched shales and channelled through interbedded permeable sandstones, may have been responsible for stratabound Pb-Zn mineralization in some quartzites and graphitic dolostones (dolomitised calc turbidites) within unit B of the Ben Eagach Schist. Alkali metasomatism of metabasic rocks within the Ben Eagach Schist suggests that potassium was redistributed by extensive fluid infiltration during diagenesis and/or metamorphism, while sodium may have been flushed from the unit B pelites which are devoid of plagioclase.

TABLE 4.1: Metasediment mineral assemblages.

Sample	Unit	Code	Qz	Pl	Mu	Bi	Chl	Gt	Hyal	Cel	Rut	Ilm	Po	Py	BMe	Cal	Dol	To	Ap	
202-3	A	SQS	X	X	M	-	RM	-	-	-	T	-	M	RM	M	T	M	-	-	
705-7	A	SQ	X	M	M	T	RM	-	-	-	T	-	-	T	T	T	M	-	-	
708-22	A	SQ	X	M	M	-	T	T	-	-	T	-	T	T	-	-	M	-	-	
202-P	A	SQ	X	M	M	M	M	T	-	-	T	-	T	T	-	-	M	-	-	
505-C	A	SQ	X	M	X	-	RM	M	-	-	T	-	RM	T	M	X	T	T	-	
503-32	A	SP	g	X	M	X	T	M	M	-	M	-	-	T	-	-	T	T	-	
G13	A	SP	g	X	M	X	T	RM	M	-	T	-	-	-	-	-	M	T	T	
G48	A	SP	g	X	M	X	M	RM	M	-	T	T	-	-	-	-	-	T	-	
G218	A	SP	g	X	M	X	M	RM	T	-	-	-	-	-	-	-	-	T	-	
N81-88	A	S	g	X	M	M	T	RM	M	-	T	-	T	-	T	-	-	T	T	
202-Q	A	SP	g	X	M	X	T	RX	T	-	-	-	T	T	-	-	-	T	-	
202-5	A	SPS	g	X	M	X	M	M	-	-	T	-	T	RM	T	T	M	T	T	
G22	B	SQ	g	X	-	X	-	-	-	-	T	-	-	M	T	-	-	-	T	
G61	B	SPB	g	X	-	X	-	-	-	-	T	-	-	M	-	-	-	-	-	
G172	B	SPB	g	X	M	X	M	RM	-	-	-	T	-	-	-	-	M	-	-	
G222	B	SP	g	X	M	X	M	RM	-	-	-	T	-	-	-	-	-	T	T	
705-4	B	SP	g	X	T	X	T	RT	-	-	-	T	-	M	T	T	X	T	T	
705-11	B	SC	g	X	T	M	T	-	-	-	-	T	-	T	T	M	T	-	-	
503-23	B	SC	g	M	-	T	T	RT	-	-	-	T	-	M	T	M	T	-	-	
705-23	B	SQB	g	X	-	M	-	-	-	-	T	-	-	T	M	M	T	-	-	
708-5A	B	SQB	g	X	-	M	T	-	-	-	T	-	-	M	M	M	-	-	-	
N80-52	B	SQB	g	X	-	M	-	-	-	-	X	-	-	M	M	M	-	-	-	
G119A	B	SPB	g	X	-	M	-	-	-	-	X	-	-	M	M	T	M	-	-	
503-3	B	SPB	X	-	X	M	-	-	-	-	M	-	-	M	T	-	-	-	-	
705-17A	B	HS	X	-	X	-	-	-	-	-	X	-	-	M	T	-	-	-	-	
708-4	B	HS	X	-	X	-	-	-	-	-	X	-	-	M	T	M	-	-	-	
N80-2	B	SPB	X	M	X	T	RM	-	-	-	X	-	-	T	M	M	-	-	-	
10-08	B	SPB	X	-	X	-	-	-	-	-	T	-	-	M	RM	T	-	-	-	
202-R	B	SPB	X	-	X	-	RT	-	-	-	-	-	-	M	T	M	-	-	-	
503-20	B	SPB	X	-	X	-	-	-	-	-	-	-	-	M	-	T	X	T	M	
505-9	B	SPB	X	-	X	-	-	-	-	-	T	-	-	M	-	T	X	-	T	
G169	C	SP	X	M	X	M	M	-	-	-	T	-	T	-	-	T	X	T	-	
705-2	C	SP	X	M	X	M	M	-	-	-	T	-	-	-	-	T	M	-	-	
705-3	C	SPB	X	M	X	X	T	-	-	-	T	-	T	-	-	-	-	-	-	
706-B	C	SPB	X	M	X	X	-	-	-	-	T	-	M	-	-	-	X	-	-	
702-8A	C	SPB	X	M	X	M	-	-	-	-	T	-	M	RT	-	-	X	-	-	
105-42	C	SPB	X	X	-	X	-	-	-	-	T	-	-	T	-	-	X	-	T	
Sample		Code	Qz	Pl	Mu	Bi	Chl	Gt	Hb	Ep	Se	Rut	Ilm	Po	Py	BMe	Cal	Dol	-To	Ap
N80-36	D	SP	X	X	X	M	M	M	M	-	T	T	T	-	-	-	M	X	-	T
429-5	D	SP	X	X	X	M	M	M	M	T	-	-	T	-	T	-	M	X	T	T
N80-33	D	SP	X	M	X	T	X	-	-	M	-	T	T	-	-	-	-	M	T	T
429-3	D	SP	X	M	M	X	X	-	-	M	-	-	-	-	-	-	-	M	-	-
602-2	D	SC	X	X	M	M	T	-	-	X	-	T	-	-	-	-	X	M	-	-

Code : see fig. 3 for explanation

X = major (&gt;10%); M = minor (1-10%); T = trace (&lt;1%); R = retrograde; BMe = sphalerite, galena; g = graphitic.

Qz, quartz; Pl, plagioclase; Mu, muscovite; Bi, biotite; Chl, chlorite; Gt, garnet; Hyal, hyalophane; Cel, celsian; Rut, rutile; Ilm, ilmenite; Po, pyrrhotite; Py, pyrite; BMe, sphalerite and/or galena; Cal, calcite; Dol, dolomite; To, tourmaline; Ap, apatite.

TABLE 4.2: XRF ANALYSES OF METASEDIMENTS (TOTALS -&gt; 100%).

SP(A)									
	G10	G8A	G13	G48	705-6	202-Q	G217	706-5	202-5
SiO <sub>2</sub>	50.11	50.28	53.16	54.52	55.18	57.47	61.92	63.60	65.65
TiO <sub>2</sub>	0.96	0.89	1.10	0.91	0.85	0.86	0.76	0.81	0.69
Al <sub>2</sub> O <sub>3</sub>	29.60	30.35	29.30	26.71	19.49	22.60	25.17	18.86	15.22
Fe <sub>2</sub> O <sub>3</sub>	6.96	6.04	3.93	6.16	7.30	7.16	1.95	7.36	6.62
MnO	0.08	0.07	0.07	0.12	0.24	0.10	0.01	0.17	0.24
MgO	3.62	3.16	3.01	3.37	4.85	3.05	1.41	2.65	3.04
CaO	0.40	0.14	0.14	0.36	5.10	1.38	0.13	0.83	3.24
Na <sub>2</sub> O	1.26	1.30	1.08	1.69	1.38	1.67	1.54	0.41	2.00
K <sub>2</sub> O	6.73	7.42	7.57	5.92	4.72	5.30	6.74	5.09	3.07
P <sub>2</sub> O <sub>5</sub>	0.16	0.11	0.13	0.08	0.15	0.11	0.14	0.16	0.09
BaO	0.12	0.23	0.51	0.17	0.73	0.31	0.22	0.07	0.13
total=	100.00	100.00	100.00	100.00	100.00	100.00	100.00	100.00	100.00
Ni	18	7	4	8	39	31	3	34	29
Cr	170	164	180	172	145	149	133	111	98
V	185	157	177	165	186	136	124	100	84
Sc	29	29	31	31	24	27	27	20	16
Cu	1	1	1	1	29	32	-	9	42
Zn	179	145	92	176	82	103	44	35	640
Sr	64	74	69	104	136	77	112	41	102
Rb	256	266	277	231	170	191	240	158	116
Zr	157	129	209	143	127	206	109	196	262
Nb	13	15	20	15	12	13	15	13	11
Pb	45	75	54	71	18	26	29	13	36
Th	35	22	36	33	21	11	23	20	15
La	28	11	5	15	44	44	38	44	41
Ce	63	11	9	32	91	85	81	84	84
Nd	23	4	9	14	39	39	35	35	38
Y	22	14	19	24	25	24	24	30	22
XF/FM	63.38	63.21	54.04	62.19	57.55	67.87	55.52	71.38	66.20
K/RB	217.93	232.02	227.12	212.87	230.55	230.93	233.61	266.79	218.82

	SP(A)		SQ(A)		SQs(A)			
	6218	G16	505-C	202-P	708-22	202-3	202-7	705-7
SiO2	65.98	66.96	70.51	71.39	75.45	77.44	80.29	87.63
TiO2	0.70	0.70	0.43	0.46	0.36	0.31	0.22	0.24
Al2O3	17.93	17.73	10.12	10.43	9.20	7.95	7.84	4.88
Fe2O3	6.90	5.96	4.26	6.64	3.83	7.51	5.11	2.63
MnO	0.08	0.11	0.37	0.19	0.39	0.07	0.09	0.08
MgO	1.92	2.98	2.43	3.57	2.20	0.96	0.90	0.83
CaO	0.30	0.36	7.73	3.20	4.86	1.44	2.60	2.05
Na2O	1.65	0.90	2.56	3.10	1.80	3.02	0.51	0.43
K2O	4.22	3.93	1.48	0.92	1.75	1.20	2.16	1.11
P2O5	0.07	0.30	0.05	0.06	0.06	0.05	0.14	0.03
BaO	0.24	0.06	0.06	0.04	0.09	0.05	0.16	0.09
total=	100.00	100.00	100.00	100.00	100.00	100.00	100.00	100.00
Ni	132	13	13	19	10	30	30	9
Cr	104	128	58	60	44	20	31	18
V	92	104	45	52	33	17	22	14
Sc	17	21	7	8	6	1	5	2
Cu	72	13	28	23	20	74	41	15
Zn	386	165	39	111	68	52800	15400	1241
Sr	56	35	170	70	85	-	35	41
Rb	155	156	54	66	64	-	49	36
Zr	257	194	193	239	233	83	103	169
Nb	12	10	7	8	7	-	2	5
Pb	52	39	68	16	20	7745	1765	440
Th	21	21	7	7	16	-	10	4
La	43	15	21	23	16	13	12	24
Ce	92	28	39	39	31	62	30	56
Nd	47	12	18	17	17	13	13	24
Y	16	15	15	13	11	-	8	8
ZF/FM	76.34	64.33	61.17	62.61	61.03	87.56	83.68	73.98
K/RB	226.31	209.84	230.44	115.15	227.82	***	363.06	259.32

TABLE 4.2 (cont.)

	SP(B)								
	G219	705-10	705-8	G221	G222	705-4	705-9	705-L	G7
SiO <sub>2</sub>	56.17	56.79	58.07	59.72	60.29	62.83	62.85	65.26	67.36
TiO <sub>2</sub>	0.89	0.74	0.86	1.03	0.94	0.55	0.54	0.60	0.70
Al <sub>2</sub> O <sub>3</sub>	27.22	18.74	19.93	25.97	25.28	14.48	14.43	15.80	19.24
Fe <sub>2</sub> O <sub>3</sub>	4.59	9.27	5.90	3.02	3.16	4.43	4.82	5.32	2.83
MnO	0.02	0.28	0.31	0.01	0.03	0.27	0.43	0.29	0.07
MgO	1.84	3.40	3.67	1.24	1.35	4.84	4.61	2.80	1.78
CaO	0.07	4.64	4.74	0.03	0.15	7.01	7.32	4.13	1.07
Na <sub>2</sub> O	0.97	0.19	0.40	0.56	0.67	0.42	0.26	0.15	0.34
K <sub>2</sub> O	7.36	5.60	5.64	7.68	7.26	4.09	4.30	4.93	5.97
P <sub>2</sub> O <sub>5</sub>	0.15	0.20	0.17	0.19	0.21	0.17	0.25	0.15	0.22
BaO	0.71	0.12	0.32	0.54	0.64	0.93	0.21	0.56	0.42
total=	100.00	100.00	100.00	100.00	100.00	100.00	100.00	100.00	100.00
Ni	5	57	30	5	6	25	22	27	20
Cr	157	123	132	150	151	103	77	96	116
V	151	99	118	147	149	76	61	74	90
Sc	29	22	22	27	26	14	13	15	20
Cu	3	77	69	3	1	24	35	55	23
Zn	102	142	1118	16	23	3333	2910	2120	780
Sr	76	86	157	66	93	114	96	99	69
Rb	221	210	182	254	231	140	121	163	215
Zr	165	174	182	241	218	135	131	154	143
Nb	17	12	11	21	18	8	5	9	12
Pb	54	86	1338	35	42	137	4288	913	395
Th	35	14	14	38	41	20	10	15	32
La	42	65	52	54	46	22	48	33	62
Ce	87	129	108	122	97	47	101	69	102
Nd	38	53	44	53	46	30	41	35	53
Y	26	26	18	35	32	16	-	13	21
%F/FM	69.19	71.03	59.15	68.74	67.85	45.18	48.49	63.09	58.88
K/RB	276.60	221.12	256.62	251.09	260.96	242.77	295.66	251.51	230.81

	SQ(B)				SPb(B)				
	G22	G60	503-20	705-5	G172	202-R	705-D	705-E	G119A
SiO <sub>2</sub>	72.82	74.58	57.95	58.51	58.95	60.04	60.98	61.69	61.81
TiO <sub>2</sub>	0.55	0.71	0.76	0.76	0.61	0.55	0.70	0.13	0.65
Al <sub>2</sub> O <sub>3</sub>	14.61	16.22	19.95	21.53	15.68	14.37	18.68	18.50	17.76
Fe <sub>2</sub> O <sub>3</sub>	5.00	1.27	5.98	7.76	7.16	6.53	4.40	6.01	4.37
MnO	0.02	0.01	0.13	0.05	0.18	0.41	0.21	0.01	0.03
MgO	0.80	1.65	2.32	2.99	4.78	5.19	3.32	2.20	0.89
CaO	0.34	0.06	3.07	0.48	6.31	7.25	4.68	2.35	nd
Na <sub>2</sub> O	0.17	0.35	0.19	0.51	0.60	0.08	0.29	0.09	0.46
K <sub>2</sub> O	4.49	4.55	5.14	5.21	3.91	4.15	5.34	5.22	5.32
P <sub>2</sub> O <sub>5</sub>	0.30	0.08	0.60	0.17	0.15	0.17	0.26	0.15	0.04
BaO	0.90	0.51	3.93	2.03	1.66	1.27	1.14	3.65	8.67
total=	100.00	100.00	100.00	100.00	100.00	100.00	100.00	100.00	100.00
Ni	91	3	38	36	30	29	38	35	29
Cr	87	94	158	142	90	90	118	128	162
V	65	89	120	157	115	71	89	97	110
Sc	12	16	23	24	16	13	19	20	18
Cu	81	1	68	46	42	42	30	72	27
Zn	1152	44	142	110	75	1974	232	731	140
Sr	38	50	192	57	169	175	129	205	624
Rb	123	158	157	172	121	141	183	156	112
Zr	192	235	165	178	135	141	192	165	118
Nb	9	14	11	13	15	9	13	11	10
Pb	378	65	158	63	52	547	200	356	148
Th	28	30	-	-	-	-	-	-	-
La	18	12	62	53	46	40	49	42	33
Ce	36	18	110	103	83	71	102	85	64
Nd	18	14	39	45	38	30	44	32	11
Y	21	27	29	28	23	17	23	20	15
%F/FM	84.90	40.98	69.90	70.02	57.41	53.08	54.43	71.04	81.54
K/RB	302.99	239.54	271.53	251.62	268.48	244.29	242.30	277.90	394.72



TABLE 4.2 (cont.)

	SPb(B)					SQb(B)			
	503-3	N80-2	704-C	705-A	661	201-K	G30	701-21B	705-K
SiO <sub>2</sub>	63.09	63.61	63.82	65.53	69.40	71.05	75.77	75.93	83.02
TiO <sub>2</sub>	0.59	0.79	0.49	0.44	0.63	0.45	0.58	0.30	0.21
Al <sub>2</sub> O <sub>3</sub>	16.15	21.09	11.70	11.95	18.37	10.87	16.32	8.19	6.08
Fe <sub>2</sub> O <sub>3</sub>	5.62	1.80	7.52	5.48	2.17	6.85	0.44	9.65	6.35
MnO	0.02	0.03	0.50	0.15	0.02	0.17	0.01	0.07	0.02
MgO	2.06	1.61	3.98	3.57	1.33	3.25	0.87	1.02	0.67
CaO	0.06	0.08	6.55	4.72	nd	2.65	nd	0.99	0.45
Na <sub>2</sub> O	0.19	0.32	0.21	0.16	0.21	0.05	0.31	0.36	0.12
K <sub>2</sub> O	3.68	5.16	2.97	2.85	5.17	2.45	4.46	2.11	1.55
P <sub>2</sub> O <sub>5</sub>	0.08	0.10	0.08	0.14	0.01	0.07	0.04	0.12	0.07
BaO	8.45	5.40	2.19	5.03	2.69	2.15	1.20	1.26	1.47
total=	100.00	100.00	100.00	100.00	100.00	100.00	100.00	100.00	100.00
Ni	29	58	21	32	11	24	2	26	21
Cr	159	162	78	123	124	77	108	58	51
V	150	115	57	122	94	73	89	55	72
Sc	19	22	8	15	17	9	17	7	7
Cu	36	29	71	50	5	32	-	132	84
Zn	167	2316	6500	602	43	142	15	18000	2265
Sr	58	65	109	166	80	48	76	31	21
Rb	104	145	90	84	163	111	139	53	37
Zr	179	156	157	111	170	213	114	56	42
Nb	10	11	7	8	10	8	10	5	5
Pb	373	560	770	260	114	31	296	3395	1014
Th	-	-	-	-	-	-	-	-	14
La	22	39	20	29	6	35	21	23	16
Ce	50	85	37	58	9	65	51	39	30
Nd	15	28	16	20	4	26	25	13	13
Y	18	16	10	17	14	17	9	5	5
%F/FM	71.03	50.02	62.98	57.99	59.47	65.48	31.01	89.52	89.51
K/RB	294.08	295.32	273.60	281.18	263.17	183.09	266.62	330.20	346.89

	SC(B)		SP(C)				SPb(C)	
	705-11	705-C	G168	705-2	G77	G169	G76	706-8
SiO <sub>2</sub>	19.49	51.85	55.30	57.26	57.52	58.99	61.68	49.79
TiO <sub>2</sub>	0.18	0.17	0.58	0.69	0.56	0.63	0.66	0.45
Al <sub>2</sub> O <sub>3</sub>	4.76	4.56	14.40	17.77	14.26	15.94	18.00	15.75
Fe <sub>2</sub> O <sub>3</sub>	13.33	4.00	5.98	6.67	5.95	6.22	4.64	8.53
MnO	2.09	0.58	0.12	0.10	0.14	0.10	0.10	0.19
MgO	21.04	14.35	7.05	6.37	6.70	6.45	3.15	10.01
CaO	37.28	22.57	10.95	4.76	9.70	6.38	4.62	8.52
Na <sub>2</sub> O	0.27	0.09	2.54	1.20	1.32	1.53	1.33	0.68
K <sub>2</sub> O	1.29	1.26	2.76	4.15	3.32	3.36	4.61	3.85
P <sub>2</sub> O <sub>5</sub>	0.24	0.20	0.16	0.17	0.14	0.16	0.17	0.08
BaO	0.04	0.36	0.16	0.86	0.38	0.24	1.06	2.14
total=	100.00	100.00	100.00	100.00	100.00	100.00	100.00	100.00
Ni	18	14	30	27	30	36	27	208
Cr	35	38	83	96	86	95	93	360
V	27	70	103	124	104	12	314	122
Sc	-	-	14	22	15	18	19	24
Cu	34	7	68	12	2	5	16	65
Zn	11120	1847	40	64	45	125	33	163
Sr	302	405	332	196	239	296	160	220
Rb	33	40	90	146	123	131	151	128
Zr	126	51	145	158	115	144	155	76
Nb	1	3	15	18	12	13	16	6
Pb	2213	436	8	26	16	18	36	64
Th	7	4	18	28	15	20	30	-
La	-	3	56	60	53	59	73	50
Ce	17	18	105	115	104	110	139	41
Nd	6	13	48	53	50	51	62	19
Y	12	10	31	35	28	28	34	21
%F/FM	36.31	20.05	43.29	48.50	44.41	46.44	56.97	43.41
K/RB	327.51	258.95	254.04	235.98	224.11	213.55	253.29	249.77

TABLE 4.2 (cont.)

	SPb(C)					SC(D)	SP(D)		
	203-78	101-1	706-A	702-8A	705-3	602-2	429-5	429-1	N80-36
SiO <sub>2</sub>	53.49	55.48	58.04	60.65	62.47	54.40	58.02	58.42	62.06
TiO <sub>2</sub>	0.62	0.86	0.69	0.63	0.73	0.59	0.64	0.77	0.62
Al <sub>2</sub> O <sub>3</sub>	15.96	16.28	18.59	15.60	20.16	15.07	16.40	19.24	14.73
Fe <sub>2</sub> O <sub>3</sub>	6.70	8.50	6.27	4.71	4.90	5.74	6.62	7.66	7.34
MnO	0.16	0.07	0.06	0.12	0.02	0.19	0.10	0.17	0.19
MgO	6.44	4.81	6.32	4.52	2.49	4.90	7.21	4.39	4.54
CaO	8.16	1.66	2.16	4.09	0.25	15.17	5.92	3.73	5.97
Na <sub>2</sub> O	2.01	4.37	0.69	3.40	2.46	2.60	1.61	1.99	1.84
K <sub>2</sub> O	3.54	2.84	5.26	3.64	4.96	1.16	3.16	3.38	2.45
P <sub>2</sub> O <sub>5</sub>	0.18	0.23	0.17	0.07	0.16	0.18	0.15	0.16	0.18
BaO	2.75	4.91	1.75	2.56	1.41	nd	0.17	0.10	0.07
total=	100.00	100.00	100.00	100.00	100.00	100.00	100.00	100.00	100.00
Ni	44	54	25	35	27	43	46	45	42
Cr	131	118	121	108	131	71	92	103	79
V	120	86	133	62	127	67	135	96	99
Sc	19	20	23	18	22	8	22	16	12
Cu	30	10	15	55	17	6	48	-	4
Zn	150	272	134	295	44	46	138	150	113
Sr	467	465	134	332	120	646	324	182	233
Rb	128	89	205	136	172	36	132	119	101
Zr	129	272	124	213	164	126	176	132	145
Nb	13	18	13	12	13	14	20	14	12
Pb	38	56	28	34	53	30	39	13	5
Th	-	-	-	-	-	11	19	14	9
La	54	46	23	37	43	50	77	51	50
Ce	101	90	142	66	88	105	157	93	101
Nd	41	33	61	28	38	47	66	42	46
Y	29	47	36	27	26	53	42	29	31
%F/FM	48.34	61.40	47.18	48.41	63.95	51.31	45.25	61.08	59.28
K/RB	229.67	264.45	212.98	222.38	239.31	266.72	199.13	235.14	201.02

TABLE 4.3: AVERAGE PARTIAL ANALYSES OF METASEDIMENT UNITS IN IGS BOREHOLES.

	1	2	3	4	5	6	7	8	9	10
Length*	10.00	92.80	22.10	3.10	17.20	38.60	27.90	34.30	14.20	60.70
TiO2	0.65	0.53	0.70	0.63	0.57	0.57	0.63	0.49	0.69	0.61
Fe2O3	8.74	5.56	8.52	5.58	6.36	5.27	6.05	5.04	7.19	6.80
MnO	0.17	0.14	0.10	0.32	0.61	0.23	0.19	0.17	0.15	0.10
CaO	2.14	1.66	0.94	5.36	6.15	3.23	1.94	3.94	7.85	5.06
BaO	0.11	0.12	0.23	0.93	0.48	0.67	1.17	1.93	0.73	0.76
Ni	29	25	33	28	24	27	31	20	34	29
Cu	39	30	48	74	52	43	52	51	32	47
Zn	446	650	134	5240	3440	2460	423	1890	68	65
Pb	88	292	27	1300	910	1033	296	1108	4	10
Ca/Mn	11.62	10.94	8.67	15.46	9.30	12.96	9.42	21.39	48.29	46.69
Pb/Pb+Zn	0.16	0.31	0.17	0.20	0.21	0.30	0.41	0.37	0.06	0.13
1 Unit A, BH9                      4 Unit B, BH2                      7 Unit B, BH10                      9 Unit C, BH9 2 Unit A, BH10                      5 Unit B, BH3                      8 Unit B, BH11                      10 Unit C, BH11 3 Unit A, BH11                      6 Unit B, BH9										
	A	B	C							
Length*	124.90	121.10	74.90							
TiO2	0.57	0.56	0.62							
Fe2O3	6.34	5.55	6.87							
MnO	0.14	0.26	0.11							
CaO	1.57	3.60	5.59							
BaO	0.14	1.12	0.75							
Ni	27	26	30							
Cu	34	49	44							
Zn	540	2040	66							
Pb	230	875	9							
Ca/Mn	10.35	12.78	46.89							
Pb/Pb+Zn	0.30	0.30	0.12							
A Total unit A (mean of 3) B Total unit B (mean of 5) C Total unit C (mean of 2)										

\* Length of intersection in metres.

Data in each column calculated as the intersection-weighted mean of all analyses of the respective lithostratigraphic unit, from analyses given by Coats et al. (1981). Unit designation based on petrographical descriptions given by Coats et al. and partial relogging of drillcore.

Table 4.4:

MEAN COMPOSITIONS OF OUTCROP AND BOREHOLE SAMPLES OF UNIT B

	<u>1.mean</u>	<u>1.sdev</u>	<u>2.mean</u>	<u>2.sdev</u>	<u>3.mean</u>	<u>3.sdev</u>	<u>4.mean</u>
SiO <sub>2</sub>	65.52	6.83	63.75	7.31	64.42	7.06	58.20
TiO <sub>2</sub>	0.70	0.18	0.47	0.24	0.56	0.24	0.60
Al <sub>2</sub> O <sub>3</sub>	19.80	4.47	13.95	5.34	16.17	5.73	16.60
Fe <sub>2</sub> O <sub>3</sub>	3.26	1.92	6.39	1.70	5.20	2.34	6.70
MnO	0.04	0.05	0.23	0.17	0.15	0.17	0.60
MgO	1.65	1.10	3.83	2.91	3.00	2.59	4.00
CaO	0.74	1.87	4.97	5.00	3.37	4.56	6.50
Na <sub>2</sub> O	0.45	0.24	0.21	0.14	0.30	0.21	nd
K <sub>2</sub> O	5.58	1.31	3.77	1.53	4.46	1.69	6.20
P <sub>2</sub> O <sub>5</sub>	0.13	0.09	0.18	0.12	0.16	0.11	nd
BaO	2.12	2.62	2.25	2.23	2.20	2.35	0.60
total=	100.00	20.69	100.00	26.68	100.00	27.04	100.00
<hr/>							
Ni	24	28	30	9	27	19	24
Cr	130	32	107	37	116	36	nd
V	110	29	103	52	106	44	nd
Sc	19	6	13	7	15	7	nd
Cu	20	25	59	34	44	36	55
Zn	433	732	2199	3190	1529	2670	3700
Sr	128	168	125	89	126	122	172
Rb	171	50	124	52	142	55	187
Zr	171	45	138	54	150	52	167
Nb	13	4	8	3	10	4	10
Pb	194	182	869	1166	613	974	965
Th	39	12	29	17	32	16	nd
La	34	18	35	18	35	18	nd
Ce	68	36	69	34	69	34	nd
Nd	30	17	28	15	29	15	nd
Y	22	8	16	8	18	8	19
<hr/>							

1 = Outcrop samples: mean & std. deviation of 11 analyses.

2 = Borehole samples: mean & std. deviation of 18 analyses.

3 = Combined: mean & std. deviation of 29 analyses.

4 = I.G.S. boreholes 1+3: intersection weighted mean  
of 16 analyses (total, 20.4m of drillcore).

nd = not determined.

TABLE 4.5: AVERAGE COMPOSITIONS OF DALRADIAN &amp; WORLD PELITES

	<u>1</u>	<u>2</u>	<u>3</u>	<u>4</u>	<u>5</u>	<u>6</u>	<u>7</u>	<u>8</u>
n=	10	9	38	85	104	44	155	
SiO <sub>2</sub>	59.0	61.0	60.1	56.8	61.3	59.4	64.2	*
TiO <sub>2</sub>	0.8	0.8	1.0	1.2	0.7	1.3	0.9	0.8
Al <sub>2</sub> O <sub>3</sub>	23.4	20.1	20.4	21.3	21.8	19.6	17.7	15.9
Fe <sub>2</sub> O <sub>3</sub>	5.9	4.8	8.9	10.2	7.0	9.6	7.2	7.1
MnO	0.11	0.19	0.10	0.15	0.02	0.12	*	0.12
MgO	2.8	2.8	2.9	3.0	3.0	2.6	2.6	2.6
CaO	0.7	3.2	1.2	1.4	1.1	1.1	1.8	3.3
Na <sub>2</sub> O	1.4	0.4	1.9	1.9	1.3	2.0	1.9	1.4
K <sub>2</sub> O	5.6	5.9	3.5	3.7	3.6	4.1	3.6	3.4
P <sub>2</sub> O <sub>5</sub>	0.13	0.19	*	0.30	0.10	0.20	*	0.17
BaO	0.20	0.49	*	0.09	0.07	0.09	*	0.07
total=	100.0	100.0	100.0	100.0	100.0	100.0	100.0	34.9
<hr/>								
Ni	28	22	*	86	20	54	64	68
Cr	141	123	*	102	126	101	110	90
V	132	107	*	*	*	*	120	130
Sc	25	21	*	*	*	*	14	13
Cu	17	32	*	47	29	29	18	45
Zn	196	1172	*	134	80	118	*	95
Sr	73	95	*	196	150	177	710	300
Rb	204	193	*	160	141	139	*	140
Zr	186	171	*	230	205	271	200	160
Nb	14	12	*	22	14	*	*	11
Pb	44	810	*	41	18	17	24	20
Th	24	24	*	19	14	*	*	12
La	28	47	*	42	43	*	*	92
Ce	57	96	*	81	76	94	*	59
Nd	26	44	*	42	*	32	*	24
Y	21	21	*	39	21	*	45	26
<hr/>								
F/FM	65	60	73	75	68	77	71	
K/RB	227	253		192	212	245		202
CA/SR	71	244		51	52	44	18	79
CA/MN	6	16	11	9	51	8		25
<hr/>								

1 = Ben Eagach Schist pelites - unit A, Foss.

2 = Ben Eagach Schist pelites - unit B (with <1% BaO), Foss.

3 = Middle Dalradian pelites: Atherton & Brotherton, 1982.

4 = N. Connemara pelites: Senior & Leake, 1978.

5 = Appin Group slates from Argyll: Hickman & Wright, 1983.

6 = Upper Dalradian pelites from Glen Esk, Angus: Mohamid, 1980.

7 = Average pelites. Major elements from Shaw, 1956; trace elements for 63 rocks of the Devonian Littleton Formation from Shaw, 1954.

8 = Average shales: Turekian & Wedepohl, 1961. Major elements converted to oxides and increased by an arbitrary factor of 5% to allow for volatile content. Compilation of data from several sources.

\* = not determined

TABLE 4.6: Reduced carbon and volatile contents of Ben Eagach schist samples.

Sample	Unit	XRF wt%			C-N analyser wt%			LOI%
		SiO <sub>2</sub>	BaO	CaO	N	C	H <sub>2</sub> O <sup>◆</sup>	
G48	A	51.5	0.16	0.34	0.25	0.28	9.4	5.9
G217	A	59.3	0.21	0.12	0.08	0.28	7.6	4.2
G61	B	66.3	2.57	-	0.03	0.58	4.5	4.5
G30	B	73.0	1.16	-	0.04	0.69	3.8	3.6
705-K	B	80.2	1.42	0.43	0.06	0.58*	1.8	3.4
207-25	B	nd	nd	nd	0.07	0.90	9.9	nd

Sample locations and descriptions: see Appendix B. 207-25 is a highly fissile, black quartz muscovite schist (no XRF analysis obtained).

\* Measured value of 0.68 adjusted for carbonate content, based on XRF value for CaO. Note that the other samples analysed do not contain carbonate.

◆ Water content = H<sub>2</sub>O<sup>-</sup> + H<sub>2</sub>O<sup>+</sup> calculated from measured H content.

LOI = loss on ignition: differences from H<sub>2</sub>O content due to (1) volatilization of CO<sub>2</sub> and sulphide-S in 705-K, (2) oxidation of FeO to Fe<sub>2</sub>O<sub>3</sub>.

Samples combusted for 200 seconds at 920°C. Standard: acetanilide. Estimated accuracy +0.3%; precision (reproducibility) <2% of values.

TABLE 4.7: Major element composition of clay minerals expressed on a volatile-free basis\*.

	Kaolinite	Illite	Hydro- muscovite	Mont- morillonite	Chamosite
SiO <sub>2</sub>	52.8	62.8	49.8	66.7	29.0
TiO <sub>2</sub>	-	0.9	0.2	-	-
Al <sub>2</sub> O <sub>3</sub>	45.6	20.4	38.9	25.8	20.0
Fe <sub>2</sub> O <sub>3</sub>	0.9	5.8	1.2	1.1	37.8
MgO	0.2	2.3	0.5	4.2	12.4
CaO	0.5	1.8	0.2	2.1	0.5
Na <sub>2</sub> O	-	0.5	0.5	0.1	0.2
K <sub>2</sub> O	<0.1	5.6	8.6	<0.1	0.2

\*Calculated from analyses given by Deer et al. (1962a).

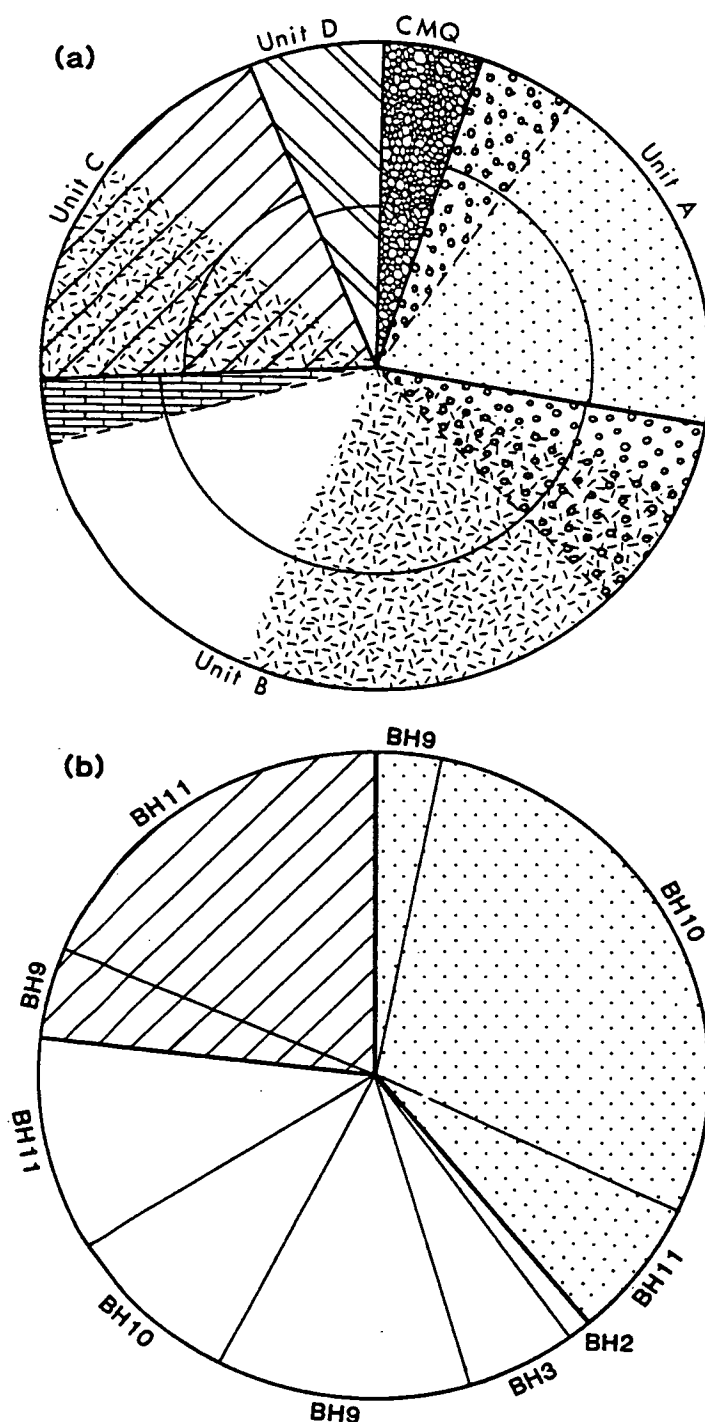


**Fig. 4.1:** Pie diagrams to illustrate (a) the proportions of samples analysed in this study from each lithostratigraphical unit, subdivided by main rock type/barium content, and (b) the relative lengths of drillcore analysed from Foss boreholes by Coats et al. (1981), subdivided by lithostratigraphical unit and borehole number. For key to lithologies see fig. 3.1. CMQ = quartzites petrographically similar to the Carn Mairg Quartzite occurring within the Ben Eagach Schist formation.

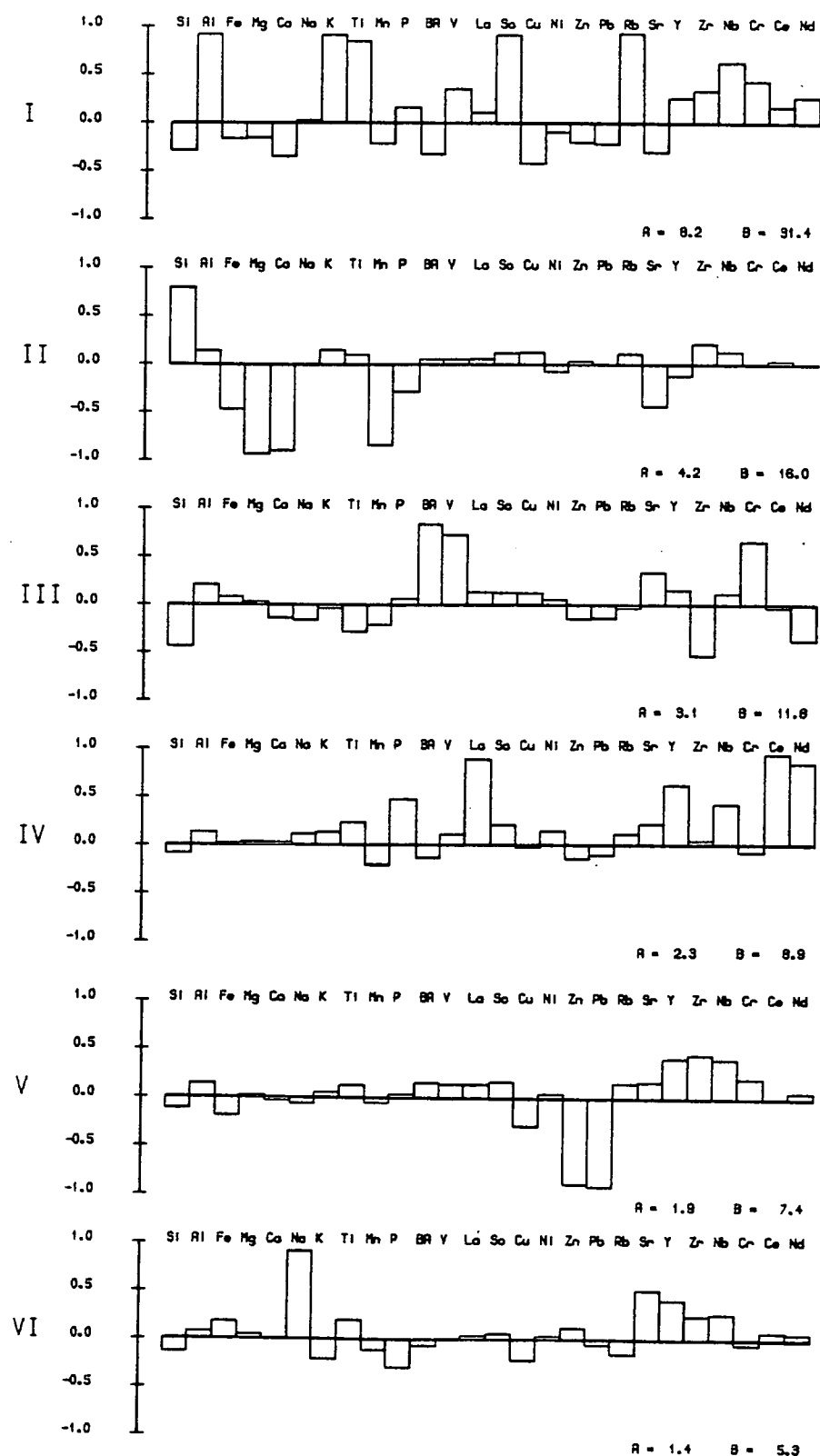
Fig. 4.2:

## METASEDIMENTS AND MINERALIZED SEDIMENTS

## R-MODE FACTOR ANALYSIS - varimax rotated factor loadings

A - eigenvalue B - percent contribution

FACTOR





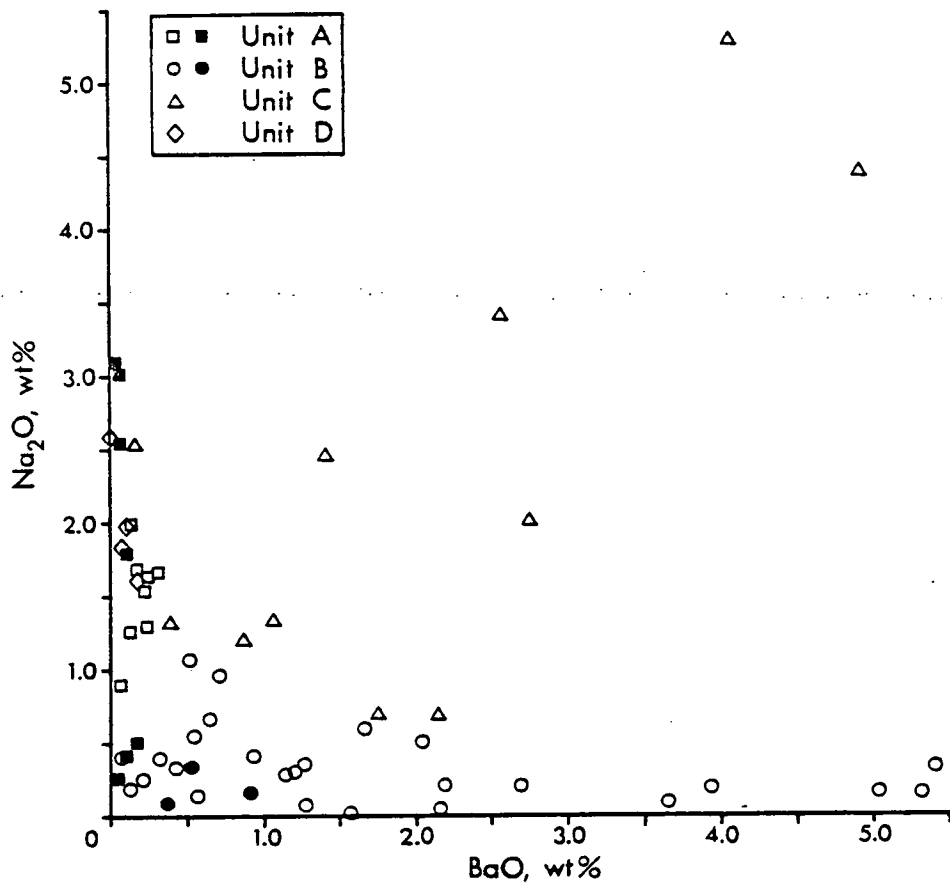


Fig. 4.3: Plot of Na<sub>2</sub>O vs. BaO contents (total oxides = 100%) for meta-sediment samples analysed in this study, subdivided by lithostratigraphical unit and silica content (solid symbols indicate SiO<sub>2</sub> > 70%).

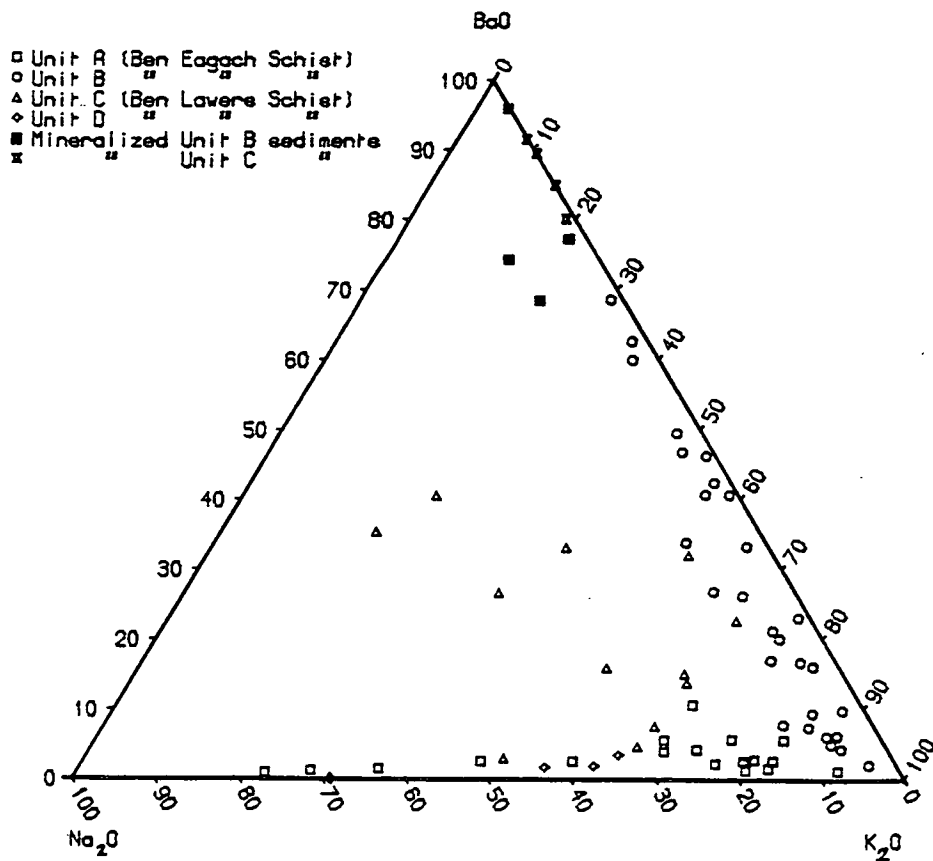


Fig. 4.4: Weight% Na<sub>2</sub>O-BaO-K<sub>2</sub>O diagram of metasediment and mineralized sediment samples from Foss analysed in this study.

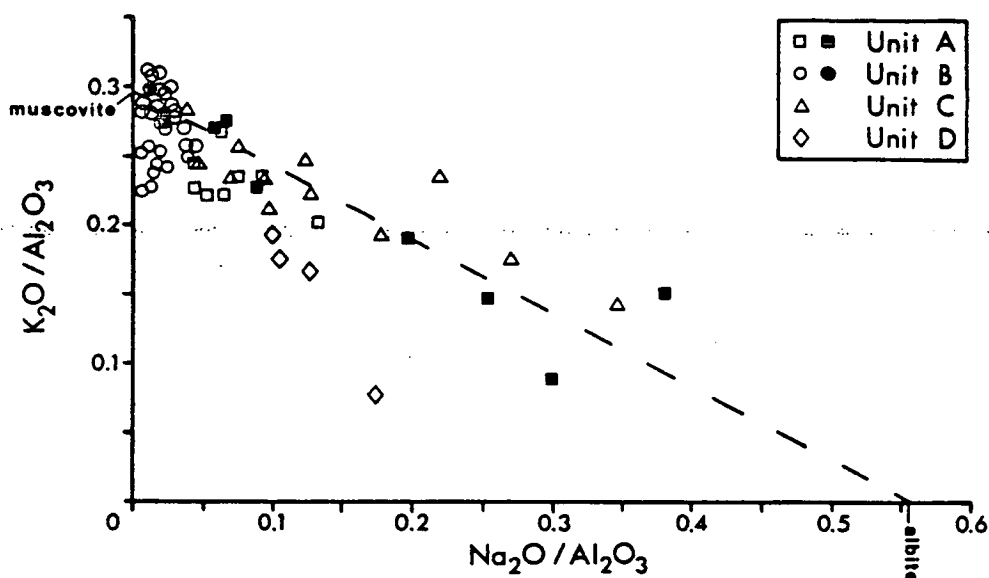


Fig. 4.5: Diagram of  $K_2O$  vs.  $Na_2O$ , both ratioed to  $Al_2O_3$ , for Foss metasediments subdivided by lithostratigraphical unit and silica content (solid symbols indicate  $SiO_2 > 70\%$ ). Dashed line joins compositions of pure albite and muscovite.

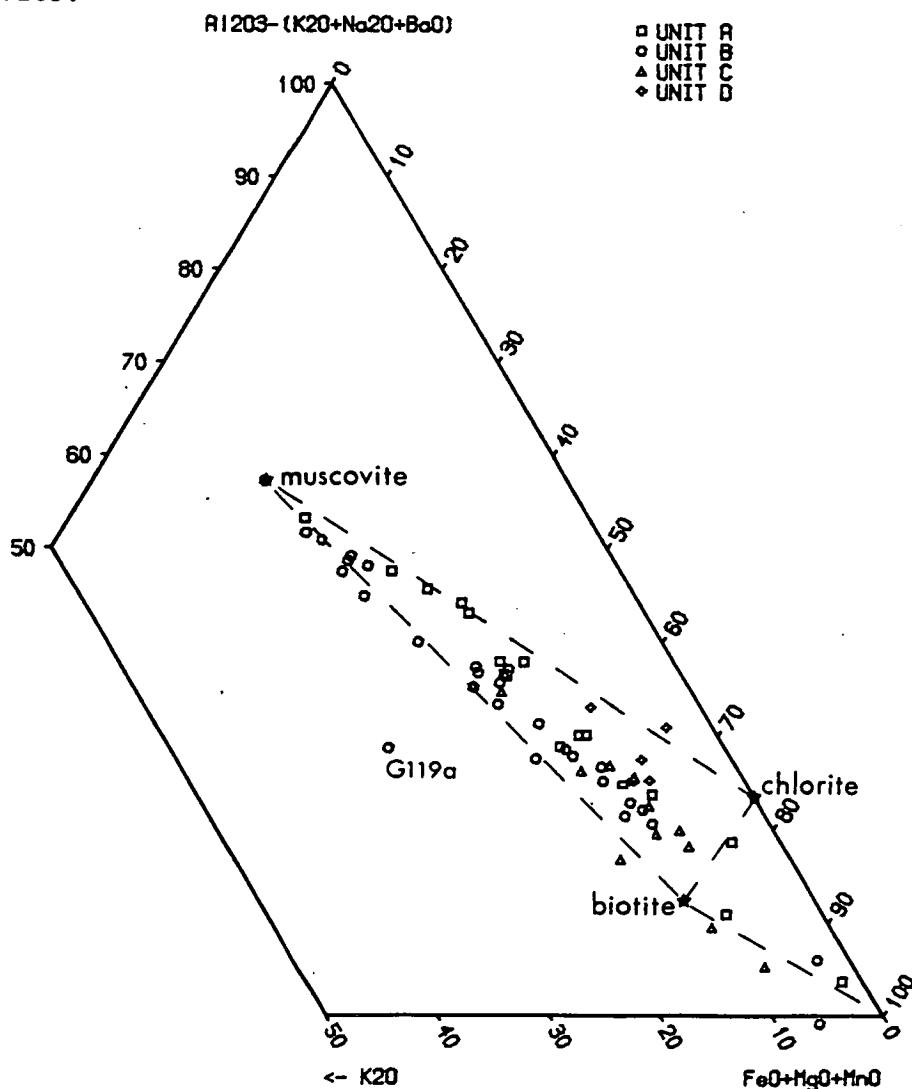
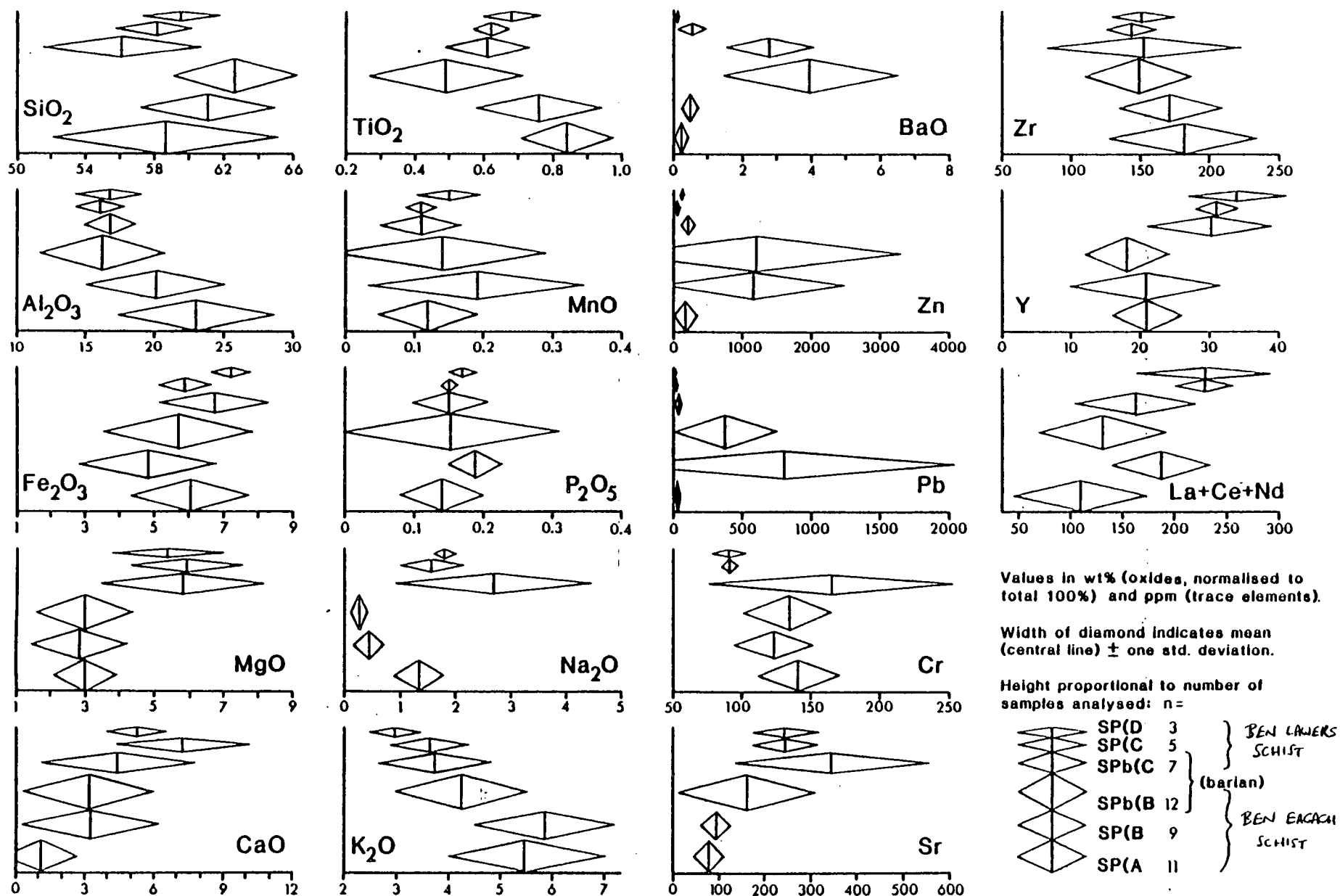


Fig. 4.6: Modified A'KF projection of Foss metasediments in which barium is taken into account in calculating A'. Samples are subdivided by lithostratigraphical unit (symbols as in fig. 4.5: quartzites not distinguished). Tie-lines join typical phyllosilicate compositions obtained from microprobe analyses (chapter 6). Sample G119a is a graphitic quartz hyalophane rock.

**Fig. 4.7: Comparative major & selected trace element distributions of metasediment groups**  
(averaged by lithostratigraphical unit and barium content)



## CHAPTER 5 : Petrography and geochemistry of the metabasites.

### 5.1 Introduction.

The identification of rocks of basaltic origin which are associated with the Foss deposit was described in section 3.3. Although they constitute a small proportion of the host rocks to the deposit (less than 5% by volume of unit B), the metabasites are significant to an understanding of both the tectonic setting of the mineralization, and the nature of the diagenetic and metamorphic processes which have influenced the mineralogy and composition of the host rocks (part 1.4.2).

Twenty seven metabasite samples collected in this study were analysed by the XRF technique for 27 elements (Appendix D, tables 3.2 and 5.2). Most of these samples are from the immediate vicinity of the Foss deposit (including three mineralized basic rocks previously described in part 3.3.2), but the set includes two amphibolites from the overlying Ben Lawers Schist and two metabasites in the Ben Eagach Schist some distance from the deposit. Data on a larger suite of samples (analysed by Roulston, 1981) from the Ben Vrackie intrusive complex (emplaced at the top of the Ben Eagach Schist 15km NE of Foss) and the volcanoclastic and extrusive Farragon Beds (which overlie the Ben Lawers Schist), is presented for comparative purposes.

Metabasic rocks within the Ben Eagach Schist are notably variable in their petrography (section 5.2). The dominance of hydrous and carbonate phases suggests a considerable volatile enrichment relative to a basaltic precursor, and the presence of often large amounts of biotite and muscovite indicates that the original basaltic material may have been metasomatically enriched in potassium. Some metabasic units are also known to be enriched in barium. Therefore, it is necessary to consider the nature and extent of element mobility during diagenetic and/or metamorphic alteration of the basaltic material (section 5.3), before examining compositional variations which relate to primary magmatic processes (section 5.4). Stratigraphical and geochemical features pertaining to the mode of emplacement of the metabasites at Foss are then evaluated. Finally (in section 5.5), the petrochemistry of other Middle Dalradian metabasaltic suites are compared with the Foss

metabasites and inferences on their respective tectonic settings are discussed.

## 5.2 Petrography.

The metabasites occurring at Foss may be categorized into four petrological types, which are described with reference to representative samples for which both whole rock and mineral analyses have been obtained. It should be noted, however, that gradations between most of these types are present, due to wide variations in modal mineralogy. Modal proportions of phases in all metabasite samples examined are presented in table 5.1. Photomicrographs 88-92 (in Vol. II) illustrate textural features.

### 5.2.1 Amphibolites (type B1).

Amphibolites of basaltic composition occur within the Ben Lawers Schist in the vicinity of the Aberfeldy deposits. Four samples examined in this study (table 5.1) all contain coarse grained hornblende with quartz and variable amounts of plagioclase, biotite, chlorite, epidote and calcite. Accessory phases are ilmenite, rutile or sphene, apatite and sulphides. In N80-13, pyrite occurs as scattered, 1-2mm euhedral crystals and hornblende has a patchy distribution through the rock, forming cm-sized pods enveloped by a more schistose, chloritic matrix (plate 88). Within 2cm of the margins of a 16cm thick metabasite layer represented by sample 204-1, hornblende is absent and biotite plus chlorite are the principal Fe-Mg silicates, suggesting some infiltration by CO<sub>2</sub>-bearing fluids (fig. 5.1). The micaceous margins to this amphibolite bed are finer grained (<2mm) than the central part, in which interlocking hornblende crystals reach 1cm in size. The amphibolite is enclosed by hornblendic calc mica schists.

Amphibolites are also major constituents of the Ben Vrackie metabasite complex, which lies on the boundary between the Ben Eagach and Ben Lawers Schist formations to the east of Pitlochry, and of the Farragon Beds which stratigraphically overlie the Ben Lawers Schist in central Perthshire (fig. 1.3). The petrography of these metabasites has been described by Pantin (1956) and Bradbury (1979), and in an unpublished report by Roulston (1981).

### 5.2.2 Chloritic metabasites (type B2).

The descriptive term "chloritic" is used here to identify dark

green, calcareous and dolomitic schists which are the principal metabasaltic rock type within the Ben Eagach Schist at Foss. However, petrographically similar rocks also occur in the Ben Lawers Schist, and N80-13 may be regarded as transitional in character between amphibolite and chloritic metabasite. These metabasites are usually massive, homogeneous rocks with a distinctive appearance due to the presence of equant or ovoid, orange-weathering dolomite grains set in a crudely schistose matrix of chlorite, biotite, plagioclase and quartz (plates 28 and 90). A more pronounced schistosity, often accompanied by a finer or more uniform grain size, is generally observed towards the margins of thicker metabasite units and throughout thinner (<0.5m) metabasite beds.

Chlorite may exceed 30% of the mode in this lithology, but is usually accompanied by variable amounts of biotite and muscovite (table 5.1). While ferroan dolomite is usually the principal carbonate phase, calcite is common in minor amounts and predominates in some samples. Sample 505-B is exceptional in that this chloritic metabasite is rich in calcite and muscovite but contains very little dolomite and biotite, and also contains sphene instead of ilmenite as the principal Ti-bearing phase (cf. fig. 5.1). These features suggest relatively oxidising conditions during metamorphism, which are in accord with the absence of carbonaceous matter in the enclosing quartzites. Other minor phases usually present in the chloritic metabasites are epidote (<5%), rutile, apatite and trace amounts of sulphides. Garnet is restricted in occurrence to metabasites adjoining or incorporating pelitic or quartzitic meta-sediments (e.g. 503-10 and 706-4B, table 5.1 and plate 90).

Due to their fine grain size, the modal proportions of plagioclase and quartz are not easily estimated using the petrological microscope, but plagioclase may be readily identified by its characteristic cathodoluminescence (plate 113). The cathodoluminoscope also reveals chemical zonation in both plagioclase and carbonates. Bright orange-luminescent calcite commonly forms patches adjacent to, or enclosed within, dull red-luminescent dolomite, and variations in the intensity of luminescence reflect the variable iron contents of both phases. In N80-45, compositional zoning in apatite grains has also been observed with cathodoluminescence (section 7.6).

### 5.2.3 Calcite biotite schists (type B3 metabasite).

Using geochemical criteria discussed in section 3.3, Coats et al. (1981) identified the calcareous quartz biotite schists interbedded with quartz felsic rocks in BH10 as metabasaltic rocks which have been enriched in barium. A sample from this borehole examined in this study (10-02, Appendix B) contains the same assemblage as the chloritic metabasites described above, but the dominant ferromagnesian phase is biotite. A similar lithology, consisting principally of biotite, calcite and quartz but with minor plagioclase, muscovite, chlorite and dolomite, was intersected by several drillholes through the 'upper mineralized zone' in the Frenich Burn area (samples 207-5 and 410-4B; tables 5.1, 5.2 and plate 89). Here, the biotitic metabasite forms a thin bed enclosed by unit C metasediments which have a similar mineralogy.

A quartz-calcite-biotite schist, which stratigraphically underlies the M3 horizon, forms a small, lenticular outcrop near the collar to BH3 at Creagan Loch (N81-43; fig. 2.7 and plate 42). This rock does not contain any chlorite, dolomite, or plagioclase. The absence of plagioclase was confirmed by XRD and cathodoluminescope examination, and is manifested by a low Na<sub>2</sub>O content in the XRF analysis (table 5.2; see also Appendix D, table D.5). Biotite in N81-43 is strongly pleochroic (from pale tan to dark chestnut brown) and forms coarse (2-5mm) poikiloblastic plates, the alignment of which defines the moderately well developed schistosity (plate 91). Muscovite grains of similar size are patchily distributed through this rock and muscovite also occurs in cross-cutting veinlets. Both the muscovite and biotite are barium-enriched (section 6.3). Dark clots in the calcite matrix, observed in transmitted light, are due to limonitic inclusions: the affected calcite appears to be depleted in iron and consequently produces a brighter cathodoluminescence. This feature is significant to the interpretation of carbon-oxygen isotope data (Appendix F) which suggest that  $\delta^{18}\text{O}$  values have been affected by interaction with meteoric water.

### 5.2.4 Dolomite muscovite schists (metabasite type B4).

Certain quartz dolomite muscovite schists, which contain about 10% pyrrhotite, 2-3% rutile, and accessory apatite (but no chlorite, biotite, plagioclase or calcite: table 5.1), were suspected to be metabasic in origin because of their stratigraphic occurrence



directly beneath the M3 horizon in many Foss East and in some Foss West drillhole intersections (section 2.4 and part 2.3.4). This inference was substantiated by XRF analyses of three samples from this bed (202-C, 401-13 and 703-10: table 5.2), which reveal the characteristic geochemical features (high Ti, Fe, Mg, Ca, Ni, and Cr contents) of the previously recognised metabasaltic rocks. As with the biotitic metabasites, the muscovitic metabasites are enriched in barium and potassium compared with the chloritic metabasites. Unlike metasedimentary rocks which commonly have the same mineral assemblage, the dolomite muscovite metabasites are characteristically homogeneous with little variation in the modal proportions of constituent phases within or between intersections. However, they show some variation in grain size and fissility, and coarser varieties show a textural similarity to the chloritic metabasites in that ovoid dolomite crystals are set in a schistose matrix (plate 92).

Figure 5.1 shows that the diverse mineral assemblages developed in metabasites in the vicinity of the Foss deposit can be accounted for by varying partial pressures of  $\text{CO}_2$  in the metamorphic fluid. The development of the type B4 assemblage only in relatively thin metabasite beds (<0.5m), or occasionally at the margins of thicker, chloritic metabasite beds, is consistent with comparatively high partial pressures of  $\text{CO}_2$  and extensive fluid infiltration. Fluid-buffered assemblages containing both reactants and products of the equilibrium, biotite + chlorite + calcite = muscovite + dolomite + quartz (type B2) are widespread in both metabasites and metasediments in the mineralized zone.

### **5.3 Element mobility and the diagenetic/metamorphic alteration of metabasite compositions.**

#### **5.3.1 Previous studies.**

In the literature on basaltic geochemistry, considerable attention is given to the recognition of element contents, ratios or patterns which may be used to characterize the magmatic type and tectonic affinity of basic igneous rocks and their hydrothermally altered or metamorphosed equivalents. Ideally, this characterization can be based on geochemical patterns, without recourse to primary petrographical features and information on structural settings, both of which are often obscured by metamorphism. Pearce

and Cann (1973), Floyd and Winchester (1975), Pearce and Norry (1979) and others have demonstrated that the petrochemical affinities of basic igneous rocks may be characterized by the relative concentrations of the incompatible elements, chiefly Ti, P, Zr, Y and Nb. These elements have a high field strength (charge/radius ratio) and as a result are not usually transported in aqueous fluids; furthermore they tend to be concentrated in minerals such as rutile, ilmenite, apatite and zircon which have a wide P-T stability range.

Several studies have specifically examined the nature of element mobility subsequent to the emplacement of basaltic igneous rocks. For example, Macdonald et al. (1981) found evidence for the mobility of Mg, Ca, Na, K, Ba, Cs, Rb, Zn and Pb during various types of low temperature alteration (sericitization, albitization, hydration and carbonation) of the late Palaeozoic quartz dolerite dykes in Scotland. Floyd and Winchester (1983) have described planar sequences of biotite garnet schists, interpreted as synmetamorphic shear zones, within the Ben Hope amphibolite sills of NW Scotland. These mafic schists are enriched in K, Rb and Ba, considered to have been introduced from the external metasediments by hydrous fluids, which also caused some redistribution of Ca, Mg, Mn, Na and Sr within and adjacent to the shear zones.

High potash contents (5 to 13% K<sub>2</sub>O) are a common feature of water-lain tuff beds (referred to as tuffites when interbedded or mixed with clastic sediments) and also of some bentonites. The potassium enrichment can be attributed to the formation of zeolites, K-feldspar and illite by reactions between the original glass shards and potassic, saline pore waters during diagenesis (Iijima and Hay, 1968) and/or burial metamorphism (Altaner et al., 1984). Potassic tuffites have been described from several sediment-hosted stratabound Ba-Zn-Pb deposits such as Mount Isa (Croxford, 1964), Rammelsberg (Hannak, 1981) and Meggen (Krebs, 1981), and are considered to be a characteristic feature of such deposits (Large, 1980). This raises the possibility that diagenetic alteration, rather than metamorphic processes, may have been responsible for some of the chemical (and mineralogical) changes in the less thick metabasite beds observed at Foss.

Another secondary process which can change the composition of basaltic rocks is spilitic alteration. This occurs under

hydrothermal or burial metamorphic conditions, and involves the redistribution of chemical components of basaltic rocks to form complimentary domains enriched in Na (albite) and Ca (epidote) (Smith, <sup>K</sup>1968; Hughes, 1972). Graham (1976a) recognised extensive spilitic alteration of the Dalradian metabasaltic suite in the SW Highlands, and epidotites which are petrographically and geochemically similar to those described by Graham are found in the Ben Vrackie metabasite complex (Roulston, 1981).

### 5.3.2 Volatile and alkaline element enrichment in the Foss metabasites.

The general similarity in composition of the metabasic rocks sampled from the Ben Eagach Schist in the immediate vicinity of the Foss deposit (i.e. excluding G183 and G225 which are from Farragon Hill and Doire Leathan), was mentioned in section 3.3 and is evident from table 5.2. However, fig. 5.2 shows that the contents of  $K_2O$ ,  $Na_2O$ ,  $BaO$ , Rb, Sr, Zn and Pb are much more variable than the other elements. Of particular interest are the ranges in  $K_2O$  and  $BaO$  content, respectively 0.7–5.7% and 0.03–3.0% (on a volatile-free basis).  $K_2O$  contents closely correspond to the modal proportions of micas in the samples, and the calc biotite and muscovitic metabasites are relatively enriched in  $K_2O$ ,  $BaO$  and Rb (table 5.3).

A plot of Rb against  $K_2O$  (fig. 5.3) shows the strong correlation between these elements in both metasediments and metabasites from Foss. Although the K/Rb ratio is similar in both groups (metasediments average 249, s.d. 44; metabasites average 196, s.d. 46), the slightly lower ratio for the metabasites may indicate a greater affinity of Rb for biotite than for muscovite (contrast N81–43 and 401–13, fig. 5.3). Strontium shows a loose positive correlation with CaO (fig. 5.4) but Ca/Sr ratios are highly variable in both the metabasites and metasediments, perhaps due to variable initial concentrations and hydrothermal enrichment (e.g. 03-MB), and the partitioning of Sr into several phases (section 4.4) during metamorphism. Clearly, the elements K, Ba, Rb and to a lesser extent Sr, have been mobile during diagenesis and/or metamorphism and therefore cannot be used in characterizing the original chemistry of the metabasaltic suite. These elements were presumably transported into the metabasites from the surrounding sediments and mineralization, along with a considerable influx of  $H_2O$  and  $CO_2$

(loss on ignition values are typically 10-12 wt%: table 5.5). Carbon isotopic evidence from sample N81-43 which supports this source for the  $\text{CO}_2$  is discussed in Appendix F.

Although no single sequence of samples from the edge to the centre of a metabasite bed were analysed in this study, a loose negative correlation between metabasite thickness and  $\text{K}_2\text{O}$  content may be seen (fig. 5.5). The low  $\text{K}_2\text{O}$  content of sample 204-1, and mineralogical zonation observed in this thin amphibolite bed (part 5.2.1), illustrates the limited extent of hydrous alteration and potassic metasomatism of metabasites in the Ben Lawers Schist. In contrast, most of the eight samples from the metabasite marker bed underlying M3 (or its distal stratigraphic equivalent), show a greater  $\text{K}_2\text{O}$  enrichment than other metabasite beds of comparable thickness within the Ben Eagach Schist. The sub-M3 metabasite samples (designated [I on table 5.1) also have the highest barium contents. The significance of these features are discussed in part 5.4.3.

### 5.3.3 Sodium depletion and enrichment.

Figures 5.2 and 5.6 show the markedly lower sodium contents of most muscovitic, biotitic and 'mineralized' metabasites compared with the chloritic metabasites and amphibolites examined, reflecting the absence of plagioclase from all samples of petrographical types B3, B4 and HB (except 207-5, discussed below). This could be interpreted in two ways: either (i) sodium was removed during hydrothermal/diagenetic alteration of the basaltic material, and consequently plagioclase did not develop during metamorphism of these rocks, or (ii) sodium was released into the metamorphic fluid during reactions in which plagioclase (of magmatic or metamorphic origin) was consumed to form micas. Geochemical evidence for the loss of sodium from calcareous metamorphic rocks in which albite, or the sodic component of plagioclase, was destroyed by prograde mineral reactions involving an intergranular fluid phase, has been presented by Tanner and Millar (1980) and Ferry (1983a,b). An analogous process may be invoked for the metasomatic alteration of the Foss metabasites, most of which are associated with the calcium- and sodium-poor unit B pelites (section 4.5), from which sodium may also have been removed during metamorphism (part 4.6.2). Sodium loss may therefore have been enhanced by local chemical potential

gradients during metamorphism, but could also reflect the development of diagenetic mineral assemblages devoid of sodic feldspar.

Sample 207-5 is exceptional in that this biotitic metabasite has a sodium content which is twice that of the chloritic metabasite average (tables 5.2, 5.3). Petrographic examination shows that plagioclase forms 12-18% (by volume) of the chloritic metabasites and 8-10% of sample 207-5 (table 5.1). Mineralized unit C lithologies (celsian-bearing quartz dolomite mica schists) enclose the 10cm metabasite bed represented by this sample, and the sodium enrichment could be related to the mineralization since a positive correlation between BaO and Na<sub>2</sub>O contents is observed in mineralized unit C sediments (part 4.4.2). However, another biotitic metabasite from the same structural/stratigraphic horizon (sample 410-4B) and also enclosed by barium-enriched unit C metasediments (although celsian is absent), is strongly depleted in sodium.

A possible alternative explanation for the sodium enrichment in 207-5 is spilitic alteration of the original basaltic composition. On a plot of Na<sub>2</sub>O against CaO (fig. 5.7), 207-5 lies just above the dividing line placed by Graham (1976a) between Dalradian metabasites enriched in sodium (spilites) and metabasites with a normal sodium content. The additional data on fig. 5.7 are for 69 metabasite samples from the Ben Vrackie complex and Farragon Beds (discussed in the following section), of which ten plot in together with 207-5 in the high-Na<sub>2</sub>O field. Four Ben Vrackie metabasite samples are comparatively depleted in Na<sub>2</sub>O (<2 wt%) and enriched in CaO (>14 wt%). These rocks contain epidote as a major component (Roulston, 1981). Sample 505-B (a muscovitic metabasite enclosed by garnet mica quartzite) is comparatively enriched in CaO and may also have undergone spilitic alteration, although the metamorphic mineral assemblage does not include epidote (table 5.1). Calcium enrichment in sample 03-MB (a 6cm band of highly altered and mineralized metabasite intersected in BH3) is attributed to dilution by carbonate of hydrothermal-exhalative origin (part 3.4.2).

#### 5.3.4 Silica depletion.

One metabasite analysis (N82-A20: table 5.2) has not been plotted or used in calculating average metabasite compositions because of an unusual type of alteration. This sample contains 15% less SiO<sub>2</sub> (35.5 wt% on a volatile-free basis) than the average

chloritic metabasite, which it resembles in hand specimen appearance. It is correspondingly enriched in most other major and trace elements, compared with both the Foss group average and sample N82-A21, which is from the margin of this metabasite bed at the same locality (table 3.2). By recasting the N82-A20 analysis with an  $\text{SiO}_2$  value equal to the average of least altered metabasites, other relative changes in composition are seen, notably an increase in  $\text{Al}_2\text{O}_3$ ,  $\text{MgO}$  and  $\text{TiO}_2$ , and a decrease in  $\text{CaO}$ . An alternative method of recasting the analysis which assumes  $\text{TiO}_2$  to have been immobile, results in a high residual for  $\text{SiO}_2$  and lower  $\text{Al}_2\text{O}_3$ ,  $\text{Fe}_2\text{O}_3$  and  $\text{CaO}$  contents than the Foss average.

A possible explanation for the selective removal of silica and calcium from this metabasite might be dissolution by acid metamorphic fluids. These fluids may have redeposited the  $\text{SiO}_2$  and  $\text{CaCO}_3$  as quartz veins and quartz-dolomite segregations which are often associated with the metabasite beds in the Ben Eagach Schist (although not observed at this particular locality).

#### **5.4 Immobile element chemistry of Foss and other Middle Dalradian metabasites.**

##### **5.4.1 The Ben Vrackie and Farragon Beds suite.**

The metabasites occurring within the Ben Eagach and Ben Lawers Schist formations at Foss are at a comparable stratigraphic level to the Ben Vrackie metabasite complex NE of Pitlochry (fig. 1.3). Basaltic igneous activity in the Middle Dalradian of central Perthshire culminated in the formation of the volcanic and volcanoclastic Farragon Beds which overlie the Ben Lawers Schist. Subsequently, a major episode of basaltic volcanism and sill emplacement occurred in the SW Highlands where the meta-igneous suite comprises about 5km of the Dalradian succession (Graham, 1976a; Wilson and Leake, 1972). From a detailed petrochemical study of the lower part of the Tayvallich Volcanic Group (Upper Dalradian) in Knapdale, Graham (op. cit.) recognized an extensive differentiation history involving fractionation both at depth and within the thicker sills following emplacement. He concluded that the metabasites are transitional in character between continental and oceanic tholeiites. A strongly tholeiitic chemistry typical of accreting plate margins was also noted by Graham and Bradbury (1981) for meta-

dolerite sills within and stratigraphically above the Loch Tay Limestone (Upper Dalradian Group) in Perthshire.

Analyses obtained by Roulston (1981) of about 70 samples from the Ben Vrackie metabasite complex and the Farragon Beds ('FB') cropping out east of Pitlochry, confirm the view expressed by previous authors that the Ben Vrackie metabasites are pre-metamorphic intrusive bodies which were comagmatic with the basaltic eruptives and volcanoclastic sediments forming the Farragon Beds (e.g. Bradbury, 1979). The metabasaltic suite is tholeiitic in chemistry with a broad range of magmatic evolution marked by trends of enrichment in Fe, Ti, P, Zr, Y, and V and depletion in Mg, Ni and Cr with increasing differentiation, probably due to the precipitation of olivine and clinopyroxene. Of the two main intrusive bodies, the stratigraphically higher Meall an Daimh sill ('MD') consists of more evolved basaltic compositions than are represented by the bulk of samples from the main Ben Vrackie sill ('BV'), which was emplaced along the Ben Eagach Schist-Ben Lawers Schist boundary. The analytical results obtained by Roulston (presented in table 5.5) provide a broad data base with which analyses of the Foss metabasites may be compared (figs. 5.8 a-f and 5.9, table 5.4).

The average major and trace element compositions of metabasites from the Ben Vrackie (BV and MD) intrusives and from the Farragon Beds nearby (table 5.4), are similar to a typical ocean ridge olivine dolerite (Thompson, 1973). Thirty-two 'epidiorites' (metabasite sills) from the Upper Dalradian Green Beds of SW and central Scotland (Van de Kamp, 1970) and thirty-one Tayvallich area epidiorites (Wilson and Leake, 1972) have similar average compositions, but show an enrichment in Ti and P which according to Graham (1976b) is a reflection of sampling bias. Higher averages for Si, K, Rb, Zr and Ba, and a lower average Ca in greenstones (volcanoclastic sediments) analysed by Van de Kamp (op. cit.) (table 5.4), can be attributed to slight contamination from associated clastic sediments.

#### 5.4.2 Metabasites from Foss and Ben Eagach.

The average major element and normative compositions of chloritic metabasite samples from the vicinity of the Foss deposit (designated B2[I: tables 5.1 and 5.4) are similar to other Dalradian metabasites and clearly indicate a tholeiitic chemistry influenced by potassium metasomatism. More apparent are differences in trace



element content (other than those previously mentioned as having been mobile or introduced, ie. Ba, Rb, Sr, Zn and Pb). Foss metabasites have higher concentrations of Cr and the rare earth elements (REE) La, Ce and Nd, and lower concentrations of Sc, V, Ni and Y than the averages of Ben Vrackie, Farragon Beds, and Upper Dalradian metabasites. These differences can also be seen in the minor and trace element variation diagrams (figs. 5.9 a-f), on which most of the Foss metabasite analyses form a tight cluster of points marginal to, or outwith the broader field of Ben Vrackie and Farragon Beds metabasite analyses.

Four of the metabasite samples analysed in this study (N80-13, 204-1, G183 and G225) scatter widely on the minor and trace element variation diagrams. This dispersion is far greater than that attributed to element mobility during metasomatism, diagenesis or mineralization of a primary basaltic composition equivalent to 'B2[I]' (table 5.4), and these four samples were clearly different in original composition to the remainder. Samples N80-13 and 204-1 are of amphibolite beds occurring within the Ben Lawers Schist at the western and eastern extremities of the field area (figs. 2.1, 2.18). Both are enriched in Ti and depleted in Cr, and N80-13 is notably enriched in P and Ni (figs. 5.9 b,f) in comparison with the majority of Foss and Ben Vrackie metabasites. Similar characteristics, in particular a pronounced enrichment in P and Zr, are observed in G225 which is from an isolated metabasite outcrop within the Ben Eagach Schist in poorly exposed ground at Doire Leathan (fig. 2.2). Sample G183, taken from a small metabasite body occurring at the Ben Eagach Schist-Ben Lawers Schist boundary on Farragon Hill (fig. 2.1), is geochemically distinct from all other metabasites analysed. Exceptionally low levels of Ti, P, Y and V and high levels of Cr and Ni in G183 are consistent with the very low index of differentiation (fig. 5.9), and this metabasite is considered to approximate to a 'primitive' basaltic composition.

A high nickel content is also characteristic of metabasites from the Ben Eagach deposit, for which six partial analyses are available (table 5.3). Rocks inferred by Coats et al. (1981) to have been of basaltic origin because of their high Fe, Ca and Ti contents ( $\text{TiO}_2 > 1.2\%$ ), which were intersected in IGS boreholes 5, 6 and 7, contain 84-145 ppm Ni. Similar rocks intersected in BHs 2, 9, 10 and 11 in the Foss deposit contain 28-51 ppm Ni (cf. average

of my data, 48 ppm Ni: table 5.4). Further sampling and analytical data for elements such as V and Cr would be necessary to confirm the impression, gained from the distribution of nickel, that metabasites associated with the Ben Eagach deposit (perhaps including G183 from Farragon Hill) represent a less evolved magmatic suite than the metabasites associated with the Foss deposit.

#### 5.4.3 Stratigraphical and geochemical constraints on the time and mode of basalt emplacement.

The geochemical evidence presented above favours the comagmatic and probably contemporaneous formation of the Ben Vrackie sill complex with the eruptive and volcanoclastic Farragon Beds, which has been suggested by previous authors on the basis of their relative stratigraphic positions. However, geochemical and stratigraphical evidence for the mode of emplacement of metabasites occurring in the vicinity of the Foss deposit do not allow such a straightforward interpretation. This evidence, derived from (1) lithostratigraphy, (2) alteration and mineralization of the Foss metabasites, and (3) their immobile element compositions, is reviewed below.

(1) Excellent stratigraphic continuity of the thin (typically 10-20 cm) metabasite bed which directly underlies the M3 horizon throughout Foss, contrasts with the more variable thickness (up to 10m) and localized occurrence of other metabasite bodies in the area, which are also occasionally observed to transgress stratigraphic markers (part 2.3.2). The 'sub-M3' metabasite bed has been correlated at an equivalent stratigraphic position where the mineralized horizon is marked by only weakly barium-enriched metasediments (e.g. DHs 201, 202 in Foss East), and where different metasediment facies are developed (in the upper mineralized zone at Frenich Burn) (section 2.4). With a single exception, represented by sample 416-MB (fig. 2.14), the basaltic beds other than the sub-M3 bed occur at a higher stratigraphical level than this horizon (between M3 and M5). These relationships suggest that the sub-M3 metabasite may have been deposited as a basaltic tuff from a pyroclastic eruption which immediately preceded the exhalation of metalliferous fluids forming M3, whereas the other metabasite lenses were subsequently intruded into, and possibly extruded onto, the

sediments which accumulated to form the remainder of the Ben Eagach Schist.

(2) Metabasite samples from the sub-M3 bed have generally higher  $K_2O$  and  $BaO$  contents than the other metabasite bodies, with the exception of those interlayered with the mineralized strata in BH10 (fig. 2.9). Even where the M3 horizon consists only of weak barium enrichment in metasediments (e.g. 202-R; table 4.2), the underlying metabasite bed is significantly enriched in  $BaO$  and  $K_2O$  (cf. 202-C; table 5.2) compared with other metabasite beds of similar thickness (fig. 5.5). It is suggested that this may be evidence of a greater extent of diagenetic alteration in a basaltic ash deposit than in basalt sills of comparable thickness. At two localities which were probably proximal to exhalative centres, the sub-M3 metabasite is diluted by major amounts of barium which combined with silica and alumina in the basaltic material to form barium feldspar (part 3.4.2). The alternative hypothesis, namely that this metabasite was intruded as a thin sill beneath the mineralized strata, and that localized and chemically selective mobilisation of this mineralization then occurred, seems implausible considering the general lack of evidence for metasomatic reactions between Ba-bearing lithologies in the Aberfeldy deposits (part 3.3.3).

(3) The immobile element chemistry of the sub-M3 metabasite is indistinguishable from that of the other (probably intrusive) metabasite bodies in the mineralized zone at Foss (fig. 5.9). This similarity in primary composition contrasts with the markedly different extents of magmatic differentiation evident in other intrusive bodies at similar stratigraphic levels in the Aberfeldy area, and suggests that the Foss metabasites were the product of a single episode of magmatic activity. However, this conflicts with the evidence presented in (1) and (2) which support the contention that the sub-M3 metabasite bed was deposited by a pyroclastic eruption which preceded the intrusion of sills (or extrusion of lavas) by a sufficiently long period for the deposition of a column of sediments now represented by typically 40m of graphitic schists.

These conflicting lines of evidence appear to indicate that a reservoir of moderately evolved basaltic magma (at some unknown depth beneath the Foss deposit) was repeatedly tapped to form the pyroclastic bed and subsequent basaltic sills, during which time no

significant differentiation of this magma took place. This model requires a rapid accumulation of sediments and their intrusion by sills at a very shallow level, since a long period between the eruptive and intrusive/extrusive events would have resulted in further differentiation of the magma at depth.

## 5.5 Petrogenetic affiliations and their tectonic significance.

### 5.5.1 Trace element discrimination diagrams.

A plot of V against Ti (fig. 5.10) clearly separates the Foss metabasites from the Ben Vrackie and Farragon Beds amphibolites. The amphibolites plot in an elongate field of positive slope which clusters about the average Ti/V ratio of 25, with the exception of three samples (N81-21, JR-B4 and JR-M2) which have much lower V and higher Ti contents (table 5.5). Least altered members of the Foss metabasite group form a tight cluster at a Ti/V ratio of 39, with a tail to lower V and Ti contents which may be accounted for by dilution associated with progressive alkali enrichment.

Servais (1982) demonstrated that modern basalts from several tectonic settings could be discriminated using their distribution on the Ti/V plot. Island arc tholeiites have Ti/V ratios generally lower than 20, whereas ocean island and alkali basalts have ratios largely in the range 50 to 100. Intermediate ratios (Ti/V = 20-50), such as those found for the Dalradian metabasites, are characteristic of mid ocean ridge basalts, back arc basin basalts, and continental flood basalts, which cannot be distinguished on this plot (Servais, op. cit.).

Chondrite-normalized plots of the immobile element distributions (generally referred to as spidergrams) facilitate comparisons between the Dalradian metabasite suites and modern basalts of well-established petrogenetic affiliations. Of the elements normally plotted on such diagrams (eg. Thompson et al., 1983), Ba, K, Rb, Th and Sr have been omitted here because of their mobility during diagenesis and metamorphism. The resulting diagram (fig. 5.11) serves to emphasize the similarity between the Farragon Beds and Ben Vrackie amphibolites, average compositions of which plot as sub-parallel curves falling off to the left except for a marked increase with the chondrite-normalized Nb concentration. Differences between the Meall an Daimh and Ben Vrackie (sensu stricto) intrusives, which

relate to the degree of magmatic differentiation, are reflected in changes in the position of the curves but not of their shape. However, the curve corresponding to the Foss group metabasite is quite different in shape, with a comparatively flat chondrite-normalized distribution apart from the depletion in yttrium. A similar shaped curve for sample G225, displaced to much higher concentrations, supports the view that this rock was formed from an analogous, but considerably more differentiated, magma type to the Foss group metabasites. Samples N80-13 and 204-1 also have immobile element distributions similar to the Foss group average, and in particular show a similar decrease towards Y. The erratic curve for G183, which as noted above has the lowest index of differentiation encountered, does not resemble either the Foss or the Ben Vrackie metabasite suites.

On a triangular diagram of Ti-Zr-Y (fig. 5.12), a clear separation is again observed between the fields occupied by the majority of Foss metabasites and the Ben Vrackie - Farragon Beds suite. Following the classification scheme of Pearce and Cann (1973), all except three of the Foss metabasite samples (204-1, G183 and 104-45A) plot in the field of "within-plate" (including continental) basalts, whereas the Farragon Beds amphibolites and all but the three anomalous Ben Vrackie amphibolites plot in the field of ocean floor basalts. IGS samples CYD 16 and 97 (from BHs 2 and 5), for which the requisite trace element data were obtained (table 5.3; abstracted from Coats et al., 1981), also plot in the field of "within-plate" basalts.

The principal difference between Foss and Ben Vrackie-Farragon Beds metabasites in terms of the Ti-Zr-Y classification scheme, is the lower Y content and higher Zr/Y ratio of the Foss metabasite group. These features, according to Pearce and Norry (1979), are indicative of a within-plate source for the basaltic magma. A reasonable explanation for the low Y content, suggested by these and other authors, would be preferential partitioning of Y into a residual phase such as garnet during partial melting in the mantle source region. This interpretation is supported by the comparatively low scandium content of the Foss metabasites (the low variance of which suggests immobile behaviour, at least in type B2), since Sc is also strongly partitioned into garnet from basaltic melts

(Henderson, 1982). Garnet is not stable in the comparatively shallower (less than 30km depth) mantle source regions from which oceanic basalt magmas are derived. Therefore, Y (and Sc) depletion may be used as an indicator of a deep, subcontinental source for the Foss magma.

Significantly higher concentrations of REE (La, Ce and Nd) in the Foss metabasite relative to the Ben Vrackie suite (fig. 5.8 and table 5.4), may also indicate a comparatively enriched ('fertile') mantle source region (in the sense used by Sun et al., 1979) for the former. The chondrite-normalized immobile element pattern for the Foss metabasite is comparable to that for enriched mid ocean ridge basalt (MORB), whereas the pattern for the Ben Vrackie - Farragon Beds suite represents a source region strongly depleted in the incompatible elements, particularly Ce and La (Norry and Fitton, 1983). Niobium appears to be anomalous in behaviour, although according to Thompson et al. (1983), Nb enrichment should be a characteristic feature of subcontinental mantle which has not previously undergone partial melting and basalt extraction.

#### 5.5.2 The tectonic significance of metabasites at Foss and Ben Vrackie.

Graham (1976a) and Graham and Bradbury (1981) have reviewed the tectonic significance of the Dalradian metabasaltic suite, and note that igneous activity accompanied several episodes of basin deepening and rifting during Middle and Upper Dalradian sedimentation. The strong affinity of the Dalradian metabasites with tholeiites of accreting plate margins is considered by these authors to reflect continental distention and incipient opening of a proto-Atlantic ocean (Iapetus) in Lower Cambrian times, possibly analogous to the development of the present day Gulf of California (Graham and Borradaile, 1984).

Amphibolites which occur within the Killiecrankie Schist in the Loch Tummel area (table 1.1, fig. 1.3) represent metadolerite sills and possibly metamorphosed tuffs (Harris, 1963; Harris and Pitcher, 1975). Apart from these amphibolites, the basic volcanic activity represented by the pyroclastic metabasite marker horizon and apparently comagmatic sill intrusions (part 5.4.3) in the Ben Eagach Schist at Foss, are the earliest recognized expression of magmatism in the Middle Dalradian of Perthshire. Although the Ben Vrackie

sill (or laccolith) was emplaced at a similar stratigraphic level, it is clearly comagmatic and probably contemporaneous with the lava flows, tuffs and volcanoclastic sediments which form the Farragon Beds. This formation attains its greatest thickness east of Ben Vrackie but extends over the Aberfeldy area (fig. 1.3). Since the Farragon Beds stratigraphically overlie the Ben Lawers Schist, which ranges in (present) thickness from 250m to over 500m in the Ben Eagach - Ben Vrackie area (and may attain 4km in the SW Highlands: Harris and Pitcher, 1975), a substantial interval of time may have elapsed between the two periods of volcanic and intrusive activity. During this time, the subcontinental lithosphere was presumably stretched and thinned, allowing partial melting of the upper mantle at depths analogous to modern mid ocean ridges. The within-plate characteristics of the Foss metabasites are therefore consistent with the model of Graham and Bradbury (1981), in which a transition from continental to oceanic magma types is to be expected during the initial stages of rifting and igneous activity.

This interpretation of the tectonic setting of the basaltic igneous activity is supported by other features of the upper Middle - Upper Dalradian sequence, not least of which are the Aberfeldy stratiform Ba-Zn-Pb deposits. Russell, Willan et al. (1981, 1984) in applying the "downward-penetrating" convection cell hypothesis to the Aberfeldy deposits, emphasize the importance of extensional tectonics in allowing the access of seawater to the underlying, heated sedimentary pile. An equally important factor for the formation of the deposits is the favourable depositional environment (a carbonaceous shale basin, now the Ben Eagach Schist) generated by fault related basin subsidence. Graham and Borradaile (1984) have suggested that the Gulf of California provides a good modern analogy with the Middle Dalradian of the SW Highlands in terms of both rapid sedimentation rates and the style of magma intrusion. In the Guaymas Basin (central in the Gulf of California), sill intrusion into soft sediments results in large-scale expulsion of heated pore waters, alteration of intruded dolerites, mobilisation of elements such as K, Ca, Mg and Si, and the establishment of hydrothermal convection systems (Einsele et al., 1980; Lonsdale et al., 1980). The relationship between magmatic activity and mineralization in the formation of the Aberfeldy deposits is discussed further in chapter 10 (part 10.3.1).



### 5.6 Metabasite geochemistry: a summary.

Amphibole is absent from rocks of basaltic composition occurring in the Ben Eagach Schist, which are predominantly composed of chlorite, biotite, dolomite, plagioclase and quartz, but in some instances are rich in muscovite or calcite. Geochemically these metabasites are comparable to unaltered basalts except for a high volatile content ( $\sim 11$  wt%  $H_2O + CO_2$ ) and a variable enrichment in K, Ba and Rb. Depletion in sodium accompanies the disappearance of plagioclase and chlorite with further potassic enrichment in some thin ( $<0.5$ m) metabasite beds, although one example of sodium enrichment is described. These chemical and mineralogical changes may have been initiated by hydrothermal, diagenetic and spilitic alteration during burial, and were completed by alkali metasomatism during prograde metamorphism.

Despite broad variations in volatile and alkali content, metabasites in the Ben Eagach Schist at Foss have similar concentrations of the relatively immobile elements such as Ti, P, Cr, V, Ni, Sc, Zr, Y and the REE. This contrasts with the range in compositions, characteristic of a tholeiitic suite of variable differentiation, shown by amphibolites from the Ben Vrackie metabasite complex and the Farragon Beds east of Pitlochry. Compared with this suite, Foss metabasites have higher levels of Cr, La, Ce and Nd and lower levels of Sc, V, Ni and Y. The compositions of several metabasites which occur peripheral to the Foss deposit are clearly different from the majority of those analysed, as are volumetrically minor metabasites associated with the Ben Eagach deposit.

Throughout the Foss deposit, an exceptionally persistent and thin (typically 10-20 cm) metabasite bed underlies the lower mineralized horizon (M3) or its stratigraphical equivalent. This metabasite has undergone a greater enrichment in  $K_2O$  and BaO than other metabasite beds of similar thickness, and has been locally impregnated with barium to form lithologies rich in barium feldspar. This evidence suggests that the sub-M3 metabasite bed was deposited from a pyroclastic eruption which immediately preceded the first major hydrothermal-exhalative event. Other metabasite beds at Foss vary greatly in thickness and lateral continuity but are usually not enriched in barium, and are considered to have been intrusive in

origin. The immobile element chemistry of these metabasites is indistinguishable from the sub-M3 metabasite. This similarity in original compositions strongly suggests that the Foss metabasites were formed in a single episode of magmatic activity. However, the intrusion of basaltic sills must have followed the pyroclastic eruption which deposited the sub-M3 metabasite bed by a sufficiently long interval for the remainder of the Ben Eagach Schist to be deposited. Therefore it is argued that geochemically identical magmas were emplaced twice in the vicinity of the Foss deposit, but that these events were separated by a comparatively short interval of time, indirectly indicating high sedimentation rates.

Chondrite-normalized immobile element distributions and the Ti-Zr-Y discrimination diagram clearly indicate a 'within-plate' basalt affinity for the Foss metabasites which are distinct from the 'ocean floor' basalt type represented by 95% of the Ben Vrackie - Farragon Beds suite. The lower Y content and higher REE contents of the Foss metabasites suggest a comparatively deep (subcontinental) and 'fertile' mantle source region in which Y was partitioned into garnet during partial melting.

From the stratigraphical and geochemical evidence it is concluded that although the Foss metabasites occur at a similar stratigraphic level to the Ben Vrackie sill complex, both the Ben Vrackie complex and the comagmatic Farragon Beds are substantially younger than the metabasites in the Foss area. An upward transition from the 'within-plate' characteristics of the Foss metabasites to the 'oceanic' characteristics of the Ben Vrackie - Farragon Beds suite, is consistent with previous tectonic models which consider the Dalradian metabasaltic suite to have formed during continental distension and incipient opening of a proto-Atlantic ocean (Iapetus) in Lower Cambrian times. This interpretation of the tectonic setting is supported by the occurrence and chemistry of stratabound mineralization in the Easdale subgroup of the Middle Dalradian.

TABLE 5.1: Metabasite mineral assemblages and estimated\* modal proportions of phases.

Sample	Type <sup>▽</sup>	Data	Qz	Pl	Mu	Bi	Chl	Gt	Hb	Ep	Se	Rut	Ilm	Po	Py	Cpy	Cal	Dol	Ap
4323	1	R	9	7	-	4	6	-	65	-	3	-	t	-	1	t	4	-	1
204-1	1	R	14	-	1	11	2	-	52	10	-	3	1	-	3	t	2	-	1
N82-116	1		20	8	-	22	7	-	12	18	-	2	1	t	5	t	3	1	1
N80-13	1/2	R M	17	14	-	6	24	-	10	12	-	2	t	-	2	t	10	2	1
N80-45	2	R M	15	14	4	6	16	-	-	1	1	-	2	1	-	t	9	30	1
N80-47	2	R	18	12	3	16	20	-	-	-	2	t	2	-	t	t	20	6	1
N81-81	2/3	R	16	17	8	24	15	-	-	-	1	-	2	-	-	t	13	3	1
G31C	2	R	17	15	9	3	34	-	-	t	2	t	1	-	1	-	16	1	1
G81	2	R	20	16	14	2	13	-	-	t	1	-	3	t	1	-	3	26	1
G225	2	R	24	8	17	8	12	-	-	-	1	-	4	1	-	-	-	22	3
N82-A21	2	R M	20	17	4	9	11	-	-	-	-	2	-	-	1	t	4	31	1
09-02	2	R	18	16	6	2	28	-	-	t	2	-	2	-	t	t	10	15	1
10-02	2/3	R	16	14	7	21	9	-	-	t	1	-	3	1	t	t	4	22	1
416-MB	2	R	20	13	17	4	10	-	-	-	-	t	3	2	-	-	2	28	1
429-11	2	R M	18	17	3	5	22	-	-	1	1	t	4	1	1	t	8	20	1
503-10	2	M	26	13	5	9	14	2	-	-	-	1	1	1	1	t	3	23	1
505-B	2	R	23	10	15	t	18	-	-	-	3	-	2	t	1	-	2	25	1
706-4B	2	M	13	18	4	8	17	12	-	t	t	t	3	t	1	t	7	16	1
708-16	2	R	16	18	4	1	30	-	-	1	1	-	2	1	-	-	8	18	t
207-5	3	R M	24	9	1	30	7	-	-	-	-	1	-	-	4	t	18	5	1
410-4B	3	R	26	-	19	17	3	-	-	-	-	2	-	2	1	-	17	12	1
N81-43	3	R M	20	-	14	45	-	-	-	-	-	-	-	1	-	t	20	-	t
09-05	4	M	23	-	34	-	-	-	-	-	-	3	-	9	-	-	-	31	t
202-C	4	R	28	-	37	-	-	-	-	-	-	2	-	8	-	-	-	25	t
424-9	4	M	30	-	32	-	-	-	-	-	-	1	-	7	1	-	-	29	t
703-10	4	R	26	-	34	-	-	-	-	-	-	2	-	7	1	-	-	30	t
705-22B	4	M	25	-	30	-	-	-	-	-	-	2	-	9	-	t	t	33	1
					BF														
03-MB	5	R	36	11	-	-	-	-	-	-	-	2	-	7	1	1	1	40	1
05-C	5	R M	18	23	-	16	3*	-	-	-	-	2	-	-	12	t	-	24	2
10-06	5	M	14	32	1	8	t	-	-	-	-	3	1	5	t	t	-	35	1
82-109	5	R	35	28	-	5	-	-	-	-	-	2	t	t	6	t	3	19	1
104-45A	5	R	21	43	-	2	-	-	-	-	-	1	-	3	2	-	t	28	t
424-8	5	M	20	36	t	6	-	-	-	-	-	3	-	t	4	t	2	28	1

\* Modal proportions (volume %) estimated visually, accuracy about  $\pm 10\%$  of value given.

t = trace (<1%).

▽ Refers to petrographical classification (section 5.2).

R = rock analysis (Table 5.2), M = mineral analyses.

BF = barium feldspar (celsian or hyalophane) or cymrite (in 05-C, 10-06).

\* Talc in 05-C.

TABLE 5.2: XRF ANALYSES OF METABASITE SAMPLES (TOTALS -&gt; 100%).

	B1(I)		B2(O)		B2(I)					
	N80-13	204-1	G225	G183	N80-45	09-02	429-11	G31C	G81	708-16
SiO <sub>2</sub>	47.68	49.40	49.97	49.39	50.54	50.60	50.82	50.92	51.04	51.21
TiO <sub>2</sub>	2.16	2.41	3.23	0.41	1.91	1.94	1.91	1.93	1.87	1.87
Al <sub>2</sub> O <sub>3</sub>	16.26	14.32	15.32	17.97	14.06	14.30	14.28	14.31	14.00	14.49
Fe <sub>2</sub> O <sub>3</sub>	12.46	14.27	11.57	10.35	12.25	12.26	12.14	12.18	11.78	12.19
MnO	0.16	0.17	0.48	0.14	0.19	0.20	0.21	0.20	0.26	0.19
MgO	9.04	6.73	5.23	10.13	6.92	6.95	6.94	7.04	6.74	7.11
CaO	8.06	10.46	8.70	7.98	10.34	10.36	10.30	10.69	10.14	9.90
Na <sub>2</sub> O	2.91	1.20	0.92	2.56	2.05	2.14	1.90	1.49	1.89	2.02
K <sub>2</sub> O	0.93	0.77	3.61	0.90	1.48	0.98	1.21	0.99	2.02	0.75
P <sub>2</sub> O <sub>5</sub>	0.33	0.25	0.64	0.03	0.21	0.21	0.24	0.21	0.20	0.19
BaO	0.02	0.02	0.31	0.15	0.05	0.06	0.05	0.04	0.06	0.08
total=	100.00	100.00	100.00	100.00	100.00	100.00	100.00	100.00	100.00	100.00
Ni	192	52	28	134	56	47	53	46	42	52
Cr	110	76	109	407	310	317	332	342	313	341
V	225	436	290	136	283	300	291	314	285	294
Sc	25	47	31	40	40	42	41	43	40	42
Cu	58	457	7	77	31	35	33	20	30	54
Zn	169	167	89	111	243	195	141	372	282	239
Sr	441	276	245	221	405	389	426	281	297	341
Rb	36	29	130	25	71	49	69	48	100	32
Zr	161	164	373	40	111	120	113	116	115	114
Nb	13	12	34	4	9	10	9	9	9	9
Pb	57	33	22	20	39	39	37	38	46	85
Th	-	-	3	5	-	1	-	7	6	2
La	10	9	27	5	9	7	9	10	6	8
Ce	25	18	62	3	17	17	13	17	17	13
Nd	15	14	37	5	13	14	9	13	12	11
Y	24	39	38	11	22	22	21	22	22	19
X/FM	55.37	65.61	66.57	47.92	61.43	61.35	61.16	60.88	61.13	60.65
K/RB	213.55	217.89	229.83	303.95	173.53	166.72	144.72	170.53	168.12	197.73

	B2(I)				B2(T)			B3(T)		
	416-MB	N82-A21	G233	10-02	N80-47	N81-81	505-B	410-4B	207-5	N81-43
SiO <sub>2</sub>	47.84	50.73	50.12	47.39	49.90	49.51	50.13	49.41	48.13	48.68
TiO <sub>2</sub>	1.88	1.89	1.90	1.98	1.85	1.82	1.97	1.73	1.68	1.74
Al <sub>2</sub> O <sub>3</sub>	14.68	14.10	13.96	14.39	14.03	13.87	14.53	15.15	14.88	13.87
Fe <sub>2</sub> O <sub>3</sub>	12.31	11.92	12.14	12.07	12.20	11.63	11.16	11.20	10.59	11.66
MnO	0.62	0.19	0.17	0.23	0.20	0.18	0.39	0.16	0.13	0.17
MgO	7.18	7.10	6.84	6.73	6.74	6.63	5.92	7.11	6.96	6.47
CaO	10.75	9.84	10.59	10.57	10.06	9.42	12.44	8.43	8.44	9.69
Na <sub>2</sub> O	1.71	2.11	1.64	2.02	2.09	1.77	0.69	0.10	3.88	0.13
K <sub>2</sub> O	2.80	1.71	2.19	3.42	1.31	2.83	2.47	4.23	3.47	5.67
P <sub>2</sub> O <sub>5</sub>	0.20	0.20	0.21	0.21	0.21	0.21	0.22	0.20	0.18	0.19
BaO	0.03	0.20	0.24	1.00	1.40	2.13	0.08	2.28	1.66	1.73
total=	100.00	100.00	100.00	100.00	100.00	100.00	100.00	100.00	100.00	100.00
Ni	42	46	50	49	54	45	46	58	75	51
Cr	352	295	312	304	304	278	322	283	264	324
V	279	287	302	285	286	267	293	241	214	256
Sc	40	41	40	39	39	36	38	32	28	37
Cu	41	30	32	54	29	30	51	55	15	37
Zn	139	392	118	124	168	190	265	108	125	158
Sr	120	406	410	741	574	439	219	214	389	251
Rb	120	116	100	148	53	112	113	175	163	281
Zr	107	111	118	129	115	107	112	113	115	103
Nb	8	9	9	10	9	9	8	8	9	8
Pb	17	37	16	26	36	42	42	19	28	11
Th	3	-	-	8	4	14	3	11	9	2
La	11	7	11	9	8	8	10	10	8	10
Ce	18	13	16	19	14	12	15	22	17	20
Nd	12	12	15	17	15	9	12	14	11	13
Y	20	22	23	23	23	21	23	25	24	23
X/FM	60.68	60.18	61.49	61.73	61.93	61.23	62.90	58.65	57.81	61.84
K/RB	193.85	122.49	182.26	191.73	205.67	210.00	181.88	200.62	176.89	167.40

TABLE 5.2 (cont.)

	B4(T)			HB(T)			XB2(I)
	202-C	703-10	401-13	03-MB	N82-109	104-45A	N82-A20
SiO <sub>2</sub>	50.13	50.61	49.61	44.26	44.25	44.97	35.45
TiO <sub>2</sub>	1.87	1.75	1.73	2.00	1.65	1.62	2.77
Al <sub>2</sub> O <sub>3</sub>	14.19	14.18	13.41	6.36	12.65	12.16	19.51
Fe <sub>2</sub> O <sub>3</sub>	11.40	11.40	10.69	13.63	10.68	10.04	15.48
MnO	0.30	0.23	0.31	0.88	0.29	0.23	0.26
MgO	6.80	6.72	6.34	9.01	5.40	5.81	10.14
CaO	10.36	10.38	10.96	14.35	7.04	9.35	11.85
Na <sub>2</sub> O	0.13	0.32	nd	nd	0.16	0.13	2.26
K <sub>2</sub> O	4.12	3.66	3.78	0.20	1.26	2.11	1.88
P <sub>2</sub> O <sub>5</sub>	0.20	0.19	0.19	0.21	0.19	0.16	0.16
BaO	0.48	0.57	2.97	9.09	16.43	13.44	0.25
total=	100.00	100.00	100.00	100.00	100.00	100.00	100.00
Ni	39	47	39	35	41	47	62
Cr	249	279	254	218	262	265	397
V	224	220	227	298	309	287	351
Sc	32	35	31	17	38	38	52
Cu	61	84	72	275	102	60	72
Zn	138	1562	138	608	289	199	497
Sr	224	456	432	820	499	702	440
Rb	147	124	92	18	50	54	70
Zr	104	94	88	88	110	72	158
Nb	9	7	7	11	9	7	12
Pb	20	28	24	165	37	52	40
Th	5	4	12	19	18	22	2
La	7	5	13	8	3	3	6
Ce	14	14	24	21	10	14	16
Nd	15	13	11	-	10	-	12
Y	21	17	22	22	18	23	24
XF/FM	60.13	60.43	60.28	57.64	64.03	60.85	57.88
K/RB	232.63	244.78	340.92	92.24	208.38	324.09	223.13

TABLE 5.3: Analyses of metabasites intersected in IGS boreholes (from data given by Coats et al., 1981).

BH	FOSS										BEN EAGACH					
	2	9			10					11	5		6		7	
CYD number	16	587	588	591	635	637	639	643	644	766	95	97	807	831	553	562
Intersection (metres)	0.83	4.62	2.44	4.96	1.95	0.42	1.52	1.97	2.58	0.55	0.43	0.70	1.73	3.69	3.39	3.51
SiO <sub>2</sub> (%)	45.60										26.10	38.30				
TiO <sub>2</sub>	1.49	1.60	1.48	1.72	1.54	1.57	1.50	1.49	1.59	1.43	1.23	1.69	1.41	1.50	1.17	1.42
Al <sub>2</sub> O <sub>3</sub>	11.30										3.98	6.81				
Fe <sub>2</sub> O <sub>3</sub>	12.4	12.21	9.52	12.87	11.08	10.78	10.58	9.57	11.15	10.21	4.2	6.7	10.12	10.38	9.48	11.74
MnO	0.3	0.18	0.31	0.17	0.17	0.20	0.17	0.20	0.16	0.14	0.3	0.2	0.14	0.16	0.10	0.15
MgO	5.5										5.8	6.3				
CaO	10.70	8.48	8.37	8.52	7.70	7.13	8.24	7.53	7.39	6.51	6.67	5.74	7.61	5.93	4.95	6.80
K <sub>2</sub> O	2.55										1.28					
BaO	0.08	0.05	0.21	0.07	2.10	3.49	2.27	4.71	2.77	1.33	26.8	17.9	0.30	0.94	0.20	0.05
S	0.42										5.09	1.58				
Sum	90.3										81.5	87.5				
Ni (ppm)	39	39	31	41	43	41	38	36	46	51	107	145	115	128	84	94
Cu	90	33	40	52	38	80	40	39	38	84	180	285	77	58	32	69
Zn	1200	154	115	180	173	256	174	159	139	71	1800	1750	122	186	75	188
Sr	260										3350	2020				
Rb	99										58	103				
Zr	113										203	209				
Nb	7										10	12				
Y	18										22	22				
Pb	230	31	28	45	12	19	17	21	15	17	230	50	18	22	5	56
100.F/FM*	67										39	49				

Other CYD samples which are probably metabasite-metasediment mixtures include 592 (dolomite muscovite schist, BH9), 605 (muscovite schist, BH9), and 638 (muscovite quartz schist, BH10). CYD 30 (sulphide-rich dolomite rock, BH3) includes the mineralized metabasite 03-MB: the 45cm CYD interval contains 1.0 wt% TiO<sub>2</sub>.

\*Where F/FM = FeO/(FeO+MgO); total Fe expressed as FeO.

Table 5.4: Average compositions of Dalradian metabasites and MORB.

	FOSS(12)	BV(36)	MD(19)	FB(14)	VK(32)	VK(64)	WL(31)	MORB
SiO <sub>2</sub>	50.05	49.24	47.80	48.27	49.90	54.30	47.40	48.40
TiO <sub>2</sub>	1.90	1.64	2.11	1.66	3.00	1.20	2.40	2.70
Al <sub>2</sub> O <sub>3</sub>	14.21	14.28	14.06	14.86	14.10	14.30	15.10	14.20
Fe <sub>2</sub> O <sub>3</sub>	12.09	13.20	14.92	13.54	2.90	3.60	4.30	4.40
FeO	nd	nd	nd	nd	11.60	8.70	10.40	9.30
MnO	0.24	0.21	0.22	0.23	0.27	0.19	0.23	0.21
MgO	6.91	7.82	6.97	8.11	5.70	6.70	5.70	6.30
CaO	10.25	10.89	11.16	10.17	8.70	6.60	9.70	11.00
Na <sub>2</sub> O	1.90	2.34	2.32	2.75	2.70	2.50	3.50	2.60
K <sub>2</sub> O	1.81	0.24	0.23	0.25	0.60	1.20	0.60	0.20
P <sub>2</sub> O <sub>5</sub>	0.21	0.14	0.21	0.14	0.52	0.11	0.64	0.24
BaO	0.44	nd	nd	nd	nd	nd	nd	nd
total=	100.00	100.00	100.00	100.00	100.00	99.40	100.0	99.55
Ni	48	72	63	80	-	107	-	60
Cr	317	269	139	263	113	182	-	100
V	289	394	482	396	380	556	-	310
Sc	40	60	59	60	-	-	-	-
Cu	35	32	37	28	157	126	-	240
Zn	217	118	122	164	-	159	-	-
Sr	402	209	467	226	498	236	-	320
Rb	85	7	5	7	4	43	-	-
Zr	115	104	145	105	131	183	-	200
Nb	9	6	8	6	-	6	-	-
Ba	-	87	50	116	331	365	-	65
Pb	38	12	16	10	12	21	-	-
Th	4	1	2	1	4	7	-	-
La	8	3	3	2	7	13	-	-
Ce	15	5	10	3	-	56	-	-
Nd	13	6	9	4	-	-	-	-
Y	22	33	43	35	34	29	-	41
qtz	1.07	0.22	-	-	3.98	7.28	-	0.65
en	11.22	13.30	10.53	8.07	11.14	14.96	1.93	9.72
fs	6.76	8.16	7.91	4.92	9.90	11.39	1.85	7.34
cen	5.99	6.18	6.05	5.37	3.06	1.73	3.97	5.97
cfs	3.61	3.79	4.54	3.27	2.71	1.32	3.80	4.51
cwo	10.10	10.48	11.00	9.10	5.93	3.16	7.94	10.88
fo	-	-	0.54	4.74	-	-	5.81	-
fa	-	-	0.45	3.18	-	-	6.14	-
or	10.69	1.41	1.34	1.48	3.55	7.09	3.55	1.18
an	24.88	27.76	27.27	27.44	24.58	24.25	23.72	26.48
ab	16.09	19.77	19.65	23.30	22.85	21.15	29.62	22.00
mag	4.04	4.42	4.99	4.53	5.28	4.44	5.31	4.93
ilm	3.60	3.12	4.01	3.16	5.70	2.28	4.56	5.13
ap	0.62	0.42	0.63	0.43	1.56	0.33	1.91	0.72
[ Fe <sub>2</sub> O <sub>3</sub> / (FeO + Fe <sub>2</sub> O <sub>3</sub> ) = 0.25 ]								

FOSS = Chloritic metabasites in the vicinity of the Foss deposit

BV = Ben Vrackie sill (s.s.)

MD = Meall an Daimh sill

FB = Farragon Beds amphibolites

VKa = Upper Dalradian epidiorites analysed by Van de Kamp, 1970

VKb = " " Green Beds " " " " " "

WL = Tayvallich epidiorites analysed by Wilson &amp; Leake, 1972

MORB = Olivine dolerite 'A150-8-TR' from the Mid-Atlantic ridge; Thompson, 1973

(Numbers in parentheses indicate number of analyses averaged.)

TABLE 5.5 : XRF ANALYSES OF BEN VRACKIE & FARRAGON BEDS METABASITES<sup>★</sup>.

## (a) Ben Vrackie sill

	BV93A	BV127	B42,BV	B46(1)	C6,BV	L40,BV	CN22	CN53	1062	1030
SiO <sub>2</sub>	49.38	49.02	50.23	48.97	47.24	50.37	50.21	47.44	48.63	49.00
TiO <sub>2</sub>	1.77	1.64	1.23	1.75	1.51	1.90	1.61	1.66	1.80	1.92
Al <sub>2</sub> O <sub>3</sub>	14.31	14.80	15.16	14.51	15.67	13.47	13.95	15.42	15.00	14.32
Fe <sub>2</sub> O <sub>3</sub>	12.76	13.30	11.24	13.03	12.74	14.67	13.42	13.31	12.99	13.95
MnO	0.26	0.19	0.18	0.20	0.19	0.21	0.19	0.23	0.21	0.22
MgO	7.07	8.33	7.69	7.20	5.42	6.47	6.96	9.04	5.94	7.33
CaO	11.94	9.18	11.29	10.92	15.53	10.73	10.85	8.94	12.67	8.30
Na <sub>2</sub> O	2.02	3.10	2.71	3.18	1.58	1.95	2.40	2.94	2.49	4.62
K <sub>2</sub> O	0.34	0.29	0.18	0.11	0.02	0.07	0.25	0.89	0.10	0.17
P <sub>2</sub> O <sub>5</sub>	0.16	0.14	0.08	0.13	0.11	0.17	0.17	0.13	0.18	0.17
total=	100.00	100.00	100.00	100.00	100.00	100.00	100.00	100.00	100.00	100.00
Ni	56	101	90	69	55	58	52	101	66	94
Cr	152	306	437	108	134	123	118	147	160	267
V	439	376	363	440	463	448	389	367	376	414
Sc	63	55	66	68	60	57	57	57	47	60
Cu	13	2	10	4	198	70	52	19	26	6
Zn	140	163	91	93	65	135	79	121	131	102
Sr	252	143	172	282	797	795	143	215	412	269
Rb	9	7	6	2	1	2	3	5	3	3
Zr	116	108	71	113	87	127	102	157	130	116
Nb	6	7	3	6	4	6	9	7	11	6
Ba	31	84	71	31	6	20	26	24	61	60
Pb	11	9	9	7	19	86	8	5	9	13
Th	-	-	-	1	-	1	3	1	4	-
La	1	3	2	1	-	4	4	6	9	2
Ce	6	2	-	3	-	4	7	13	24	2
Nd	7	5	3	5	2	7	6	11	12	6
Y	47	34	28	37	33	41	32	45	34	39
F/FM	61.9	59.0	56.8	62.0	67.9	67.1	63.4	57.0	66.3	63.1

	77-21	77-23	77-24	77-25	N81-16	N81-17	N81-18	N81-20	N81-21	N81-21A
SiO <sub>2</sub>	48.90	49.46	49.14	49.49	51.06	49.60	49.32	50.65	45.60	49.51
TiO <sub>2</sub>	1.47	1.61	1.50	1.47	1.75	1.55	1.48	1.45	2.43	1.35
Al <sub>2</sub> O <sub>3</sub>	14.25	13.07	14.26	14.28	14.20	14.41	14.63	14.29	13.26	14.99
Fe <sub>2</sub> O <sub>3</sub>	13.56	14.48	12.74	13.01	15.16	13.76	12.52	13.23	14.47	12.12
MnO	0.24	0.22	0.18	0.20	0.30	0.23	0.19	0.29	0.22	0.18
MgO	7.83	7.07	8.01	7.58	7.23	7.90	8.30	8.60	9.69	8.28
CaO	10.51	11.41	12.20	12.15	7.98	10.27	11.02	9.00	11.93	10.07
Na <sub>2</sub> O	3.06	2.48	1.54	1.47	1.65	1.84	2.27	2.06	1.99	3.28
K <sub>2</sub> O	0.10	0.07	0.32	0.26	0.54	0.33	0.15	0.32	0.14	0.11
P <sub>2</sub> O <sub>5</sub>	0.09	0.12	0.10	0.10	0.12	0.13	0.11	0.10	0.27	0.10
total=	100.00	100.00	100.00	100.00	100.00	100.00	100.00	100.00	100.00	100.00
Ni	50	47	58	63	63	83	67	74	145	59
Cr	114	215	266	268	125	205	221	347	484	454
V	397	434	391	370	448	412	390	382	285	380
Sc	66	67	57	56	63	61	64	61	36	61
Cu	2	4	36	-	12	4	33	48	18	27
Zn	112	107	95	90	123	120	98	100	121	91
Sr	159	196	212	284	61	88	143	78	58	159
Rb	3	1	16	5	50	6	2	12	1	1
Zr	87	94	79	81	104	94	84	80	182	77
Nb	5	4	4	4	5	4	4	4	14	3
Ba	138	43	246	155	187	162	80	122	150	97
Pb	9	8	9	13	5	9	7	8	6	7
Th	2	1	1	-	1	-	1	-	1	-
La	1	2	2	-	4	3	1	2	6	3
Ce	-	-	-	-	3	-	-	-	18	-
Nd	2	2	2	2	5	5	4	1	12	2
Y	32	36	32	32	38	37	32	31	24	30
F/FM	60.9	64.8	58.9	60.7	65.4	61.0	57.6	58.0	57.3	56.8

★ Analyses recast to 100% on a volatile-free basis.  
F/FM = 100x FeO/(FeO+MgO) where all Fe expressed as FeO.



TABLE 5.5 (cont.): XRF ANALYSES OF BEN VRACKIE &amp; FARRAGON BEDS METABASITES .

## Ben Vrackie sill (continued)

	N81-23	N81-24	N81-25A	N81-25B	N81-30	N81-31	N81-32	JR-405B	JR-81	JR-82
SiO <sub>2</sub>	49.87	49.30	50.10	51.36	49.96	48.15	52.00	46.46	49.93	51.45
TiO <sub>2</sub>	1.26	1.37	1.95	1.44	1.78	1.34	1.19	1.03	1.56	1.98
Al <sub>2</sub> O <sub>3</sub>	14.97	14.74	14.04	14.09	14.49	14.92	12.85	13.90	14.23	12.21
Fe <sub>2</sub> O <sub>3</sub>	11.70	12.31	13.75	12.15	12.42	12.66	11.23	12.66	14.03	12.00
MnO	0.19	0.20	0.20	0.20	0.21	0.21	0.18	0.27	0.27	0.23
MgO	8.18	8.01	7.48	8.28	7.03	8.28	8.55	11.06	7.39	9.23
CaO	11.15	11.99	8.52	8.79	11.71	12.00	12.47	12.49	11.79	8.92
Na <sub>2</sub> O	2.44	1.92	3.66	3.40	2.13	2.17	1.37	1.44	0.60	3.74
K <sub>2</sub> O	0.18	0.06	0.10	0.18	0.12	0.18	0.09	0.65	0.07	0.07
P <sub>2</sub> O <sub>5</sub>	0.06	0.10	0.19	0.10	0.15	0.09	0.07	0.05	0.12	0.16
total=	100.00	100.00	100.00	100.00	100.00	100.00	100.00	100.00	100.00	100.00
Ni	70	66	53	56	61	69	98	108	75	94
Cr	450	379	171	270	236	434	638	241	188	306
V	348	376	402	375	419	371	312	402	403	358
Sc	61	61	57	68	59	61	61	61	54	64
Cu	28	61	18	14	9	18	4	67	11	4
Zn	85	88	113	109	99	115	82	359	116	177
Sr	154	120	144	67	235	126	93	167	161	160
Rb	9	-	-	1	2	2	2	15	4	2
Zr	69	80	129	85	115	74	64	55	100	129
Nb	3	3	11	4	6	3	3	4	4	6
Ba	85	27	37	43	17	59	33	320	67	35
Pb	10	9	9	8	8	9	7	9	10	9
Th	1	1	3	1	1	-	2	-	-	1
La	-	-	4	2	-	2	1	-	-	3
Ce	-	1	11	-	2	-	-	1	4	9
Nd	1	2	9	3	6	1	-	4	6	8
Y	29	30	32	31	37	27	26	28	35	37
F/FM	56.3	58.0	62.3	56.9	61.4	57.9	54.2	50.7	63.1	53.9

	JR-83	JR-84	JR-85	JR-86	JR-87-3	JR-87-4
SiO <sub>2</sub>	49.44	48.53	49.22	49.43	48.38	45.74
TiO <sub>2</sub>	1.46	3.94	2.14	1.14	1.27	1.44
Al <sub>2</sub> O <sub>3</sub>	13.28	14.51	12.76	14.60	14.54	15.56
Fe <sub>2</sub> O <sub>3</sub>	13.66	15.20	15.04	11.24	13.33	15.28
MnO	0.24	0.15	0.24	0.19	0.21	0.23
MgO	7.76	5.57	7.19	8.41	8.20	9.02
CaO	12.48	8.47	10.21	13.06	11.24	10.03
Na <sub>2</sub> O	1.50	1.40	2.84	1.77	2.63	2.43
K <sub>2</sub> O	0.06	1.51	0.14	0.07	0.11	0.26
P <sub>2</sub> O <sub>5</sub>	0.11	0.72	0.23	0.07	0.09	0.01
total=	100.00	100.00	100.00	100.00	100.00	100.00
Ni	57	69	74	80	63	51
Cr	300	81	188	415	374	371
V	393	333	445	341	377	551
Sc	62	29	60	64	63	80
Cu	20	229	14	76	4	6
Zn	109	174	127	82	107	124
Sr	166	177	407	111	186	122
Rb	1	67	2	1	2	4
Zr	87	345	106	66	75	85
Nb	4	30	6	4	3	6
Ba	56	322	23	58	71	79
Pb	11	13	27	7	9	14
Th	2	-	1	1	1	2
La	-	24	1	-	-	-
Ce	6	59	6	-	-	1
Nd	5	38	8	3	4	3
Y	32	45	39	26	28	26
F/FM	61.3	71.1	65.3	54.6	59.4	60.4

TABLE 5.5 (cont.): XRF ANALYSES OF BEN VRACKIE &amp; FARRAGON BEDS METABASITES .

## (b) Meall an Daimh sill

	1048	1045	N81-28	N81-29	JR-M1	JR-M2	JR-M3	JR-M4	JR-M5A	JR-M5B
S102	48.41	48.05	48.19	49.34	48.20	48.62	49.98	47.24	45.30	45.84
Ti02	2.04	2.72	2.11	2.37	1.71	2.37	1.88	2.05	2.52	1.76
Al2O3	14.36	13.23	13.83	12.94	14.45	14.91	14.15	15.20	12.98	14.94
Fe2O3	13.93	16.62	13.48	15.56	14.04	12.42	13.66	15.73	16.02	14.68
MnO	0.21	0.22	0.23	0.23	0.19	0.13	0.21	0.23	0.27	0.23
MgO	6.65	6.02	6.93	6.94	8.23	9.31	6.83	5.77	9.94	7.67
CaO	9.78	9.07	11.54	8.55	10.31	10.03	11.11	11.73	10.29	12.26
Na2O	4.16	3.70	3.27	3.69	2.34	1.40	1.87	1.66	2.12	2.11
K2O	0.29	0.13	0.22	0.18	0.40	0.44	0.12	0.22	0.31	0.37
P2O5	0.17	0.24	0.19	0.19	0.12	0.36	0.18	0.17	0.25	0.15
total=	100.00	100.00	100.00	100.00	100.00	100.00	100.00	100.00	100.00	100.00
Ni	60	48	46	49	65	242	62	43	52	53
Cr	91	42	88	43	229	411	172	95	165	227
V	490	528	470	547	428	209	398	564	438	438
Sc	64	64	64	68	62	33	53	65	70	64
Cu	44	21	58	29	68	32	72	99	14	31
Zn	115	114	106	122	133	256	118	93	159	110
Sr	421	302	195	159	349	48	783	1129	40	213
Rb	8	2	4	6	7	9	1	2	5	5
Zr	124	194	144	141	106	174	136	138	176	117
Nb	7	10	8	8	4	12	9	6	10	6
Ba	62	28	55	33	82	60	15	53	49	76
Pb	14	14	8	9	13	15	72	13	6	10
Th	2	-	-	2	1	3	3	-	2	2
La	2	6	5	4	2	9	3	3	3	1
Ce	6	13	11	11	7	28	18	8	16	5
Nd	7	13	11	9	5	19	11	8	12	5
Y	41	54	45	44	36	28	37	45	43	42
F/FM	65.3	71.3	63.7	66.8	60.6	54.5	64.3	71.0	59.2	63.3

	JR-M5C	JR-M5D	JR-M6	JR-M7	JR-M8	BV6, MD	BV50	BV56	1040
S102	48.77	49.35	48.45	49.19	49.14	48.07	45.64	45.76	44.77
Ti02	2.30	1.90	2.04	2.04	1.96	3.00	1.81	2.02	1.51
Al2O3	13.53	14.04	13.77	13.43	13.82	12.81	16.10	13.31	15.33
Fe2O3	14.85	14.19	15.64	15.64	14.96	19.00	14.33	14.76	13.90
MnO	0.23	0.23	0.25	0.24	0.23	0.20	0.19	0.24	0.23
MgO	6.55	7.41	6.63	8.24	6.57	4.27	4.85	7.70	5.91
CaO	11.56	9.95	10.80	7.51	11.25	9.45	15.41	13.95	17.51
Na2O	1.61	2.47	2.12	3.43	1.75	2.74	1.28	1.75	0.64
K2O	0.41	0.30	0.13	0.12	0.16	0.10	0.10	0.29	0.03
P2O5	0.20	0.17	0.18	0.16	0.17	0.35	0.31	0.21	0.19
total=	100.00	100.00	100.00	100.00	100.00	100.00	100.00	100.00	100.00
Ni	39	80	31	47	27	40	47	84	79
Cr	104	261	58	77	80	13	49	163	274
V	505	491	522	499	512	578	614	502	420
Sc	63	66	59	65	61	54	51	56	46
Cu	35	23	10	4	21	85	56	-	4
Zn	120	133	111	140	103	92	79	112	104
Sr	207	148	624	194	689	493	1679	196	1005
Rb	12	9	3	1	3	1	3	10	2
Zr	149	149	138	130	129	265	115	126	99
Nb	8	6	8	6	6	11	10	7	5
Ba	60	101	44	35	47	34	34	69	18
Pb	11	8	7	18	11	19	8	13	43
Th	2	3	2	1	3	1	3	-	2
La	3	2	2	3	2	11	4	2	-
Ce	13	7	10	7	5	23	1	4	2
Nd	10	8	9	6	6	20	6	5	5
Y	49	45	45	42	40	73	41	44	34
F/FM	67.1	63.3	68.0	63.1	67.2	80.0	72.7	63.3	67.9

TABLE 5.5 (cont.): XRF ANALYSES OF BEN VRACKIE &amp; FARRAGON BEDS METABASITES .

## (c) Farragon Beds, NE of Pitlochry

	B25,FB	T32,FB	V35,FB	N81-2	N81-9A	N81-10	N81-11	N81-13	N81-14
SiO2	47.80	51.15	49.02	48.83	50.02	42.67	48.83	46.90	47.00
TiO2	1.76	1.78	1.35	2.02	2.05	1.73	1.53	1.47	1.48
Al2O3	16.49	12.16	14.77	14.60	14.10	14.79	13.72	13.72	15.04
Fe2O3	12.56	13.67	13.09	14.90	10.79	19.10	14.04	14.84	14.02
MnO	0.19	0.19	0.21	0.20	0.24	0.31	0.22	0.28	0.27
MgO	7.89	8.73	7.89	7.28	7.47	9.47	7.60	8.60	8.74
CaO	8.85	8.73	10.62	8.26	11.51	9.98	11.67	11.97	10.60
Na2O	4.03	3.24	2.81	3.51	3.32	1.57	2.13	1.88	2.25
K2O	0.27	0.13	0.14	0.21	0.33	0.23	0.13	0.25	0.47
P2O5	0.17	0.22	0.09	0.18	0.17	0.14	0.12	0.11	0.12
total=	100.00	100.00	100.00	100.00	100.00	100.00	100.00	100.00	100.00
Ni	131	89	88	63	34	98	47	70	84
Cr	266	284	240	164	46	314	109	297	481
V	363	409	379	432	426	468	418	411	359
Sc	53	59	65	60	57	70	63	80	58
Cu	37	28	48	-	12	73	49	20	-
Zn	131	215	169	180	233	172	102	174	188
Sr	475	212	188	155	267	98	102	146	153
Rb	4	16	2	6	6	2	2	6	20
Zr	118	102	80	140	104	104	88	85	95
Nb	6	5	5	6	7	5	4	5	4
Ba	42	840	79	41	161	86	34	50	79
Pb	11	7	11	14	10	6	7	7	8
Th	-	-	1	2	-	1	-	1	2
La	1	2	1	6	3	3	-	2	1
Ce	4	-	-	11	5	-	-	-	-
Nd	6	4	1	11	6	-	3	1	2
Y	36	31	32	43	40	33	34	30	32
F/FM	58.9	58.5	59.9	64.8	56.5	64.5	62.4	60.8	59.1

## 385,FB 385C 936,FB 954,FB 810/810

48.42	46.88	50.48	48.91	48.93
1.39	1.54	1.70	1.59	1.90
15.90	15.19	17.18	15.07	15.28
12.91	14.15	9.64	12.31	13.56
0.26	0.29	0.20	0.18	0.19
8.59	8.35	8.52	7.68	6.75
9.25	11.57	8.09	11.57	9.72
2.93	1.62	3.80	2.22	3.23
0.23	0.26	0.26	0.32	0.25
0.12	0.14	0.12	0.15	0.19

100.00 100.00 100.00 100.00 100.00

102	92	17	128	81
259	272	366	286	301
331	394	410	350	396
51	60	65	49	55
32	6	3	51	33
213	187	112	108	118
224	244	96	514	285
5	6	6	7	3
97	106	97	108	153
6	6	4	5	10
68	23	39	33	42
8	12	10	16	16
-	3	-	1	1
-	2	1	1	4
-	4	-	2	8
1	5	-	4	6
33	37	29	34	42

57.5 60.4 50.4 59.1 64.4

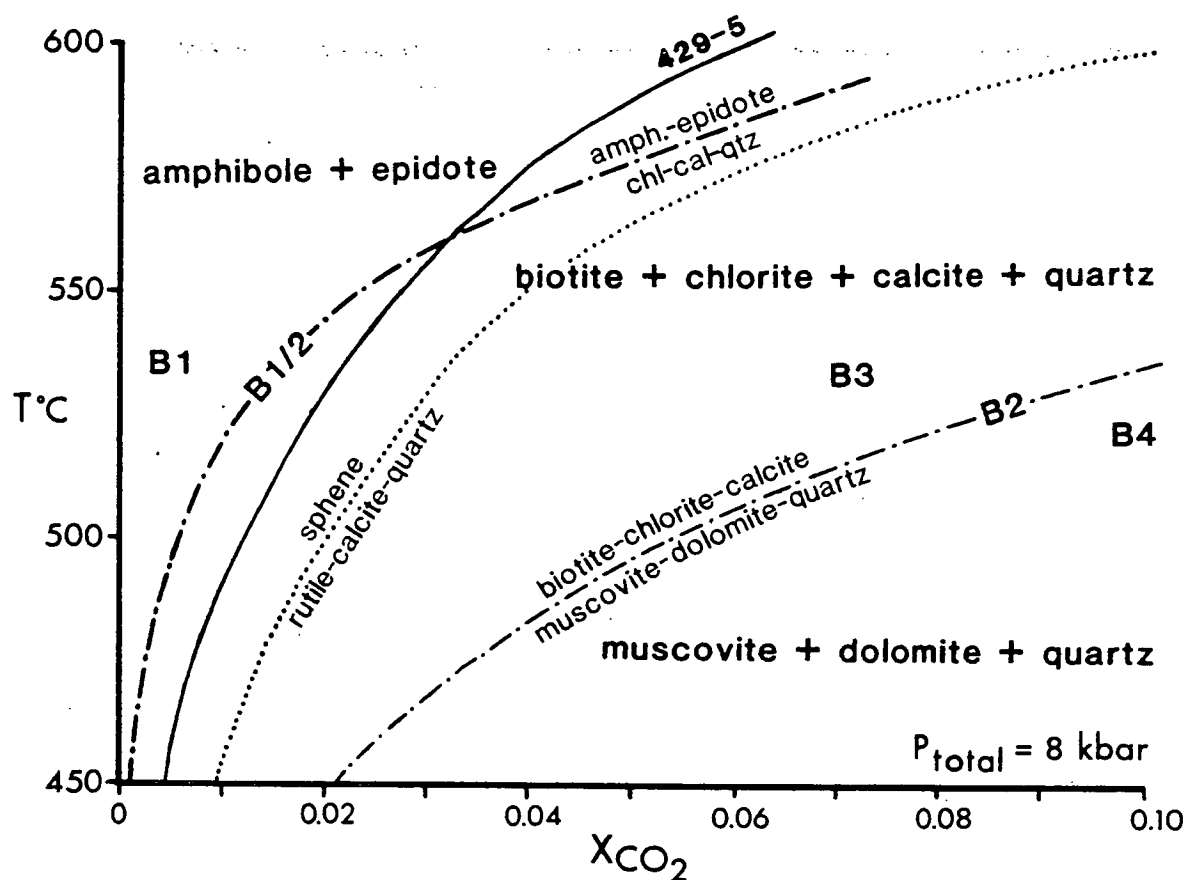


**Fig. 5.1:**  $T - X_{\text{CO}_2}$  section at 8kbar with approximate locations of key reactions which relate to metabasite mineral assemblages, adapted from Graham et al. (1983). Heavy and light dash-dot curves are calculated locations of the equilibria, respectively; chlorite + calcite + quartz = amphibole + epidote + fluid, and biotite + chlorite + calcite = muscovite + dolomite + quartz, in greenschist facies metabasites of the SW Highlands (Graham et al., 1983). Dotted curve is calculated location of the equilibrium, sphene +  $\text{CO}_2$  = rutile + calcite + quartz, at 8kbar. Solid curve labelled 429-5 is the location of the equilibrium, biotite + chlorite + calcite = muscovite + dolomite + quartz, calculated using actual mineral compositions in a garnet hornblende calc pelite (sample 429-5; see Moles, 1985). B1 - B4 represent metabasite types; note very common occurrence of fluid-buffered assemblages corresponding to type B2, whereas type B1 is absent from the Ben Eagach Schist formation at Foss.

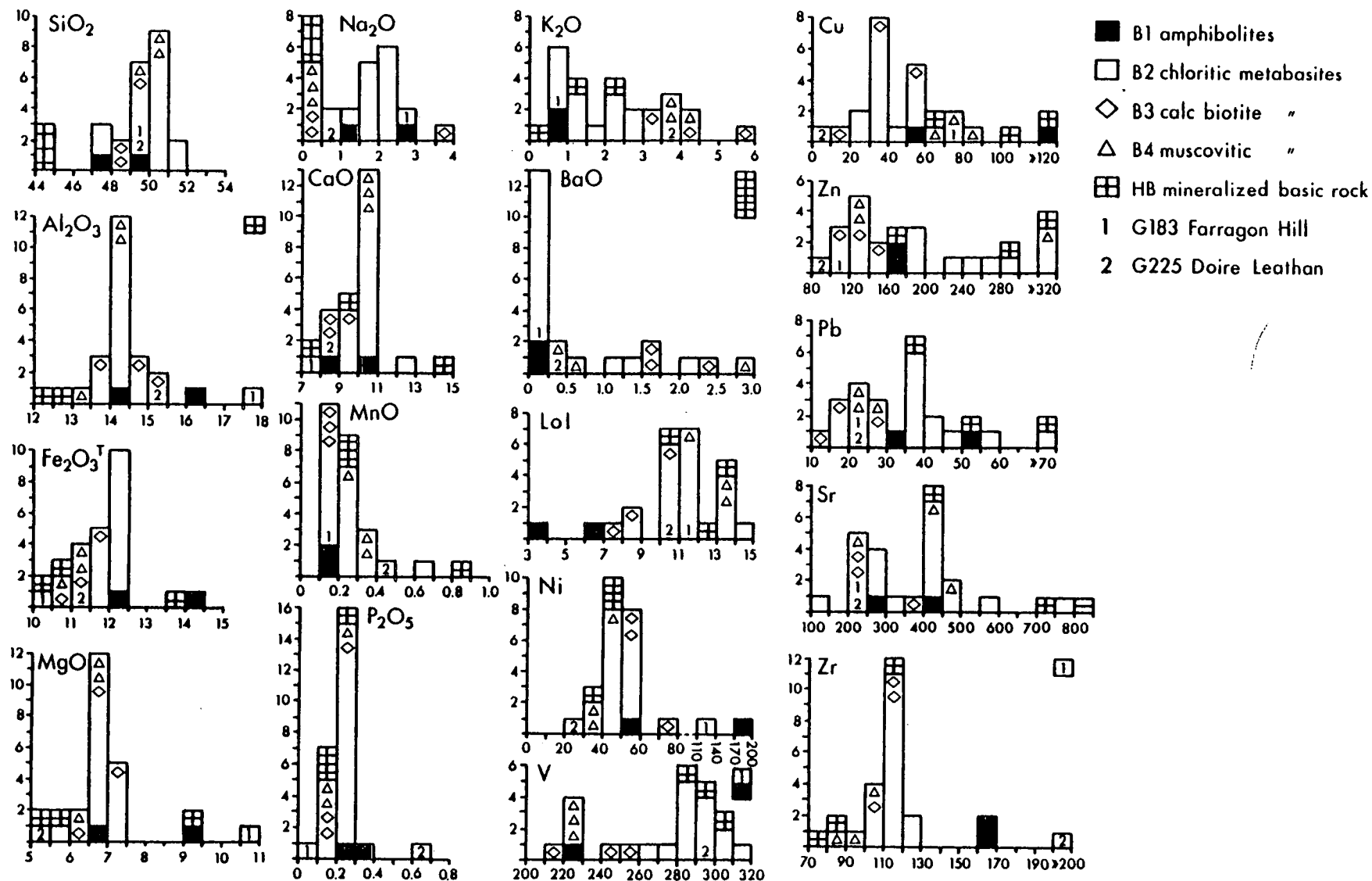


Fig. 5.2: Histograms of major and selected trace element distributions in metabasites from Foss analysed in this study ( $n = 27$ ; N82-A20 excluded, see text). Samples which would plot outside range are shown at top right corner of  $\text{Al}_2\text{O}_3$ ,  $\text{BaO}$ , V and Zr histograms. Values for oxides and LoI (loss on ignition) are in weight percent, trace elements in parts per million. Note breaks in scale on Ni, Cu, Zn, Pb and Zr histograms.

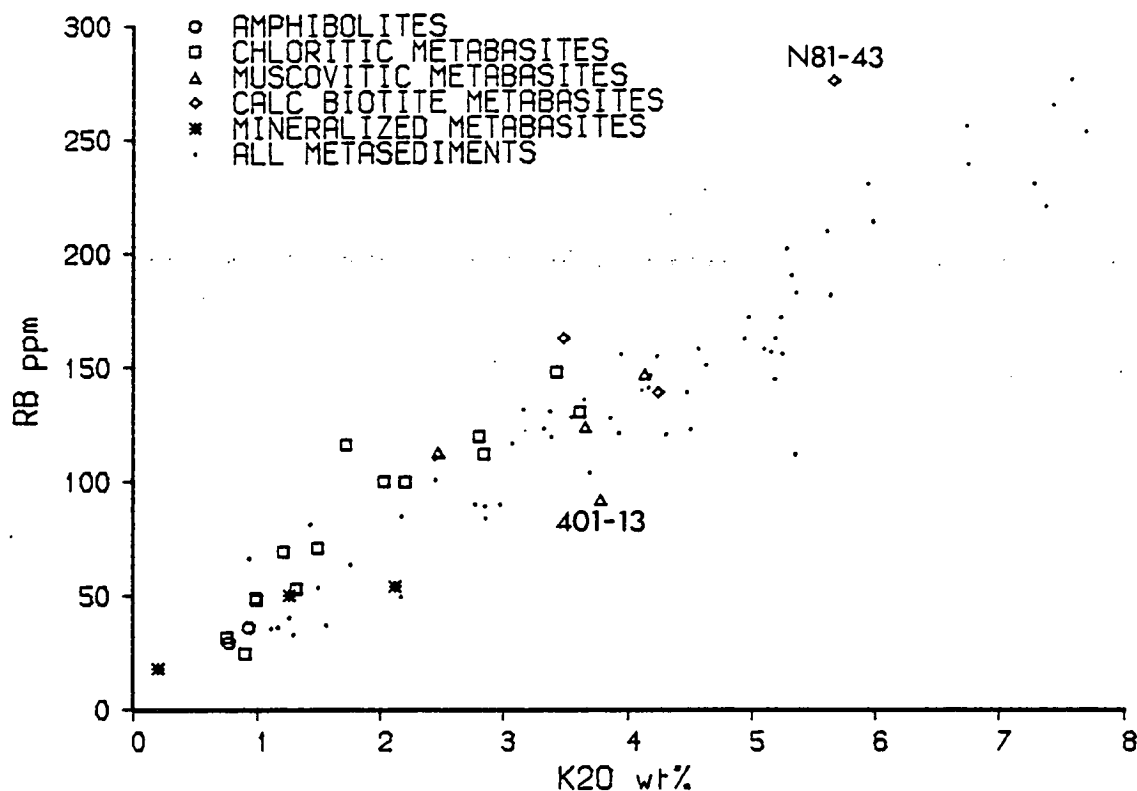


Fig. 5.3: Rb vs. K<sub>2</sub>O in metasediments and metabasites from Foss. Note good correlation and similar Rb/K<sub>2</sub>O ratios in samples of both rock types.

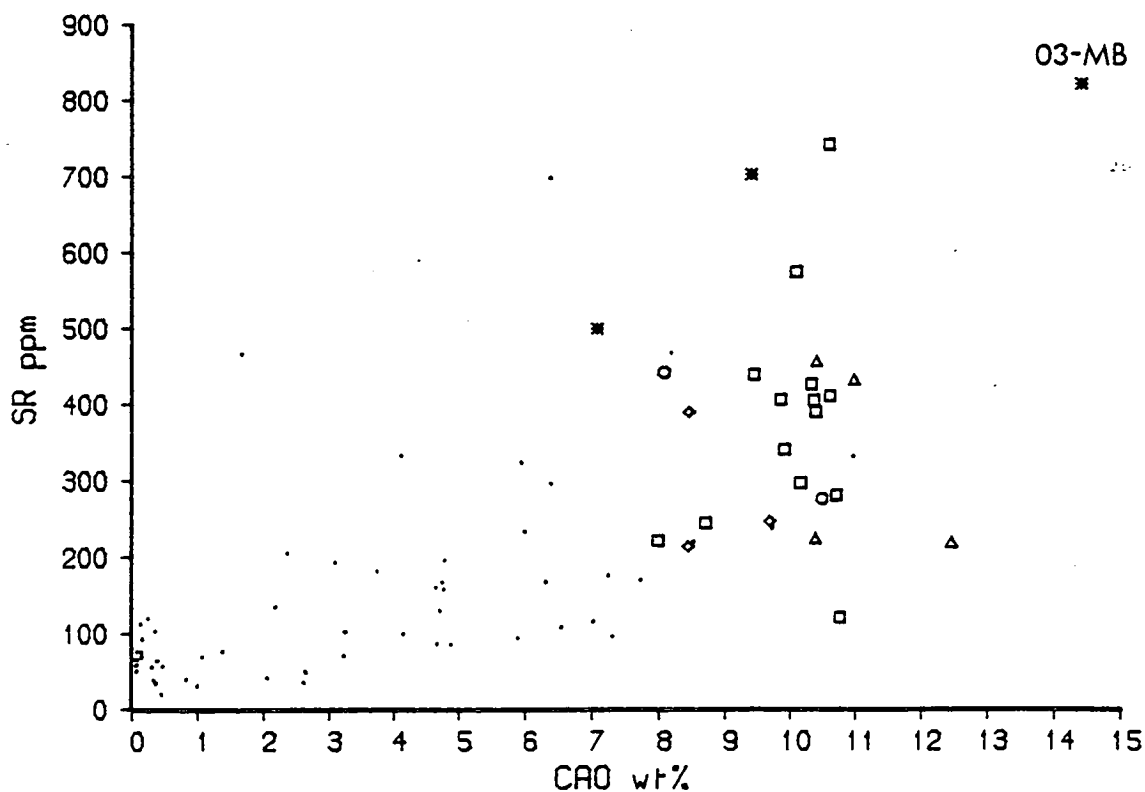
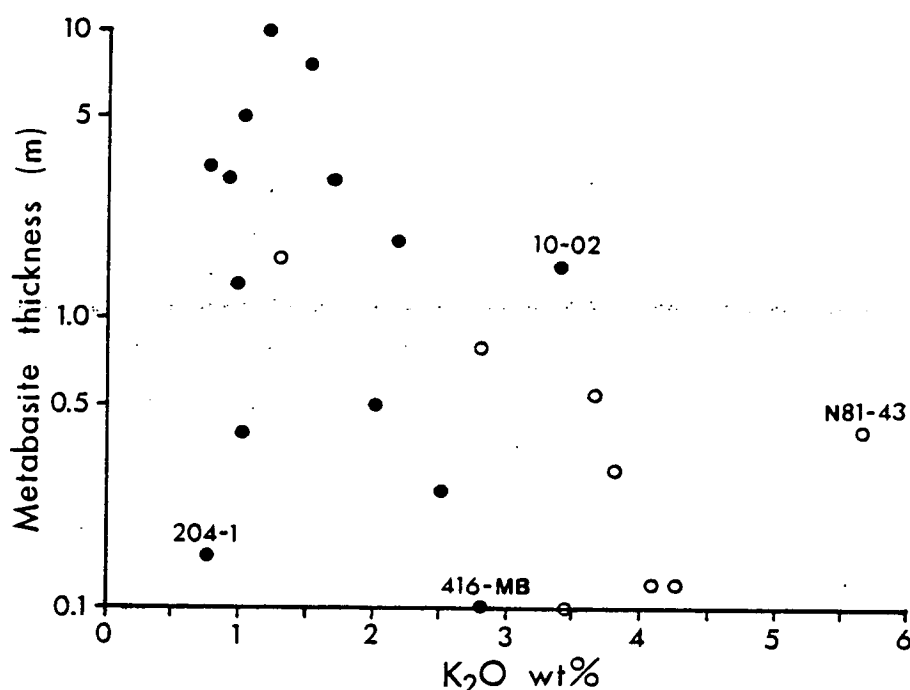
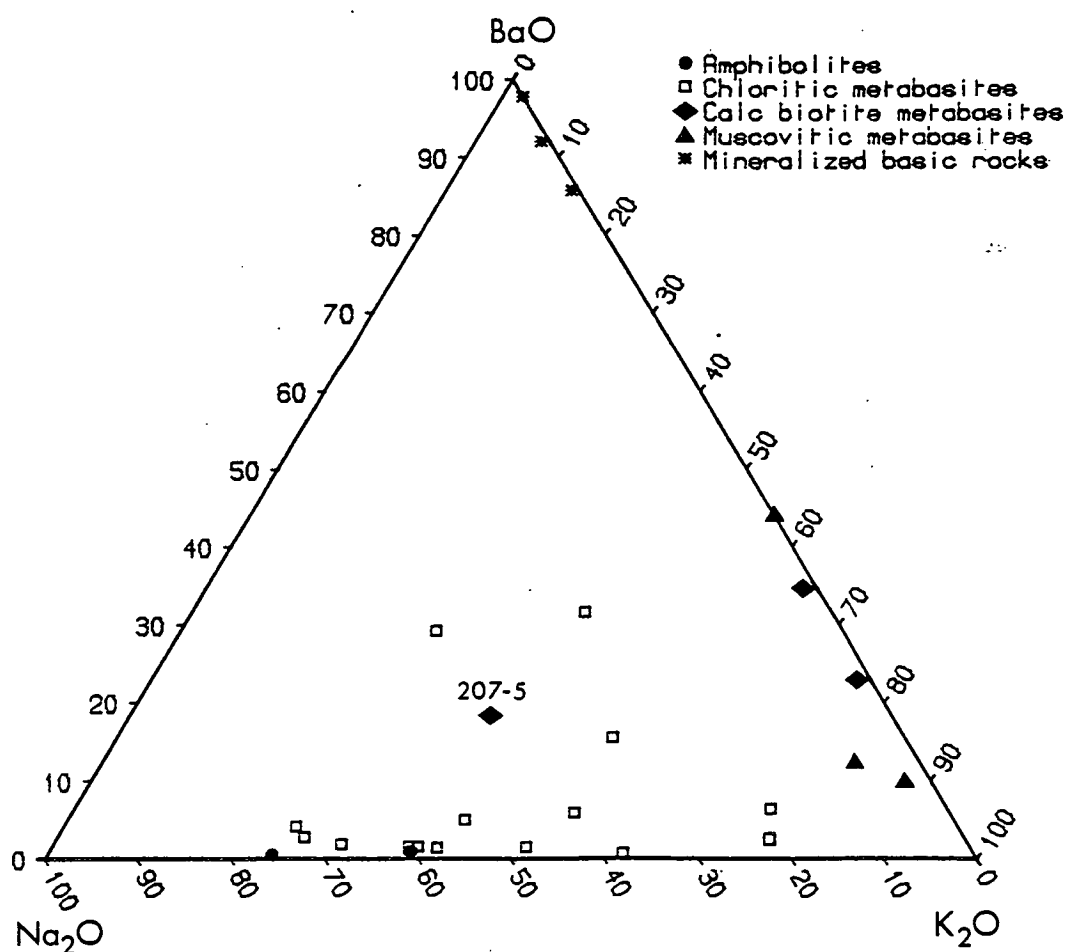


Fig. 5.4: Sr vs. CaO in metasediments and metabasites from Foss. Note weak correlation but broad scatter in Sr content of metabasites. Hydrothermal Ca and Sr enrichment in mineralized basic rock, 03-MB.

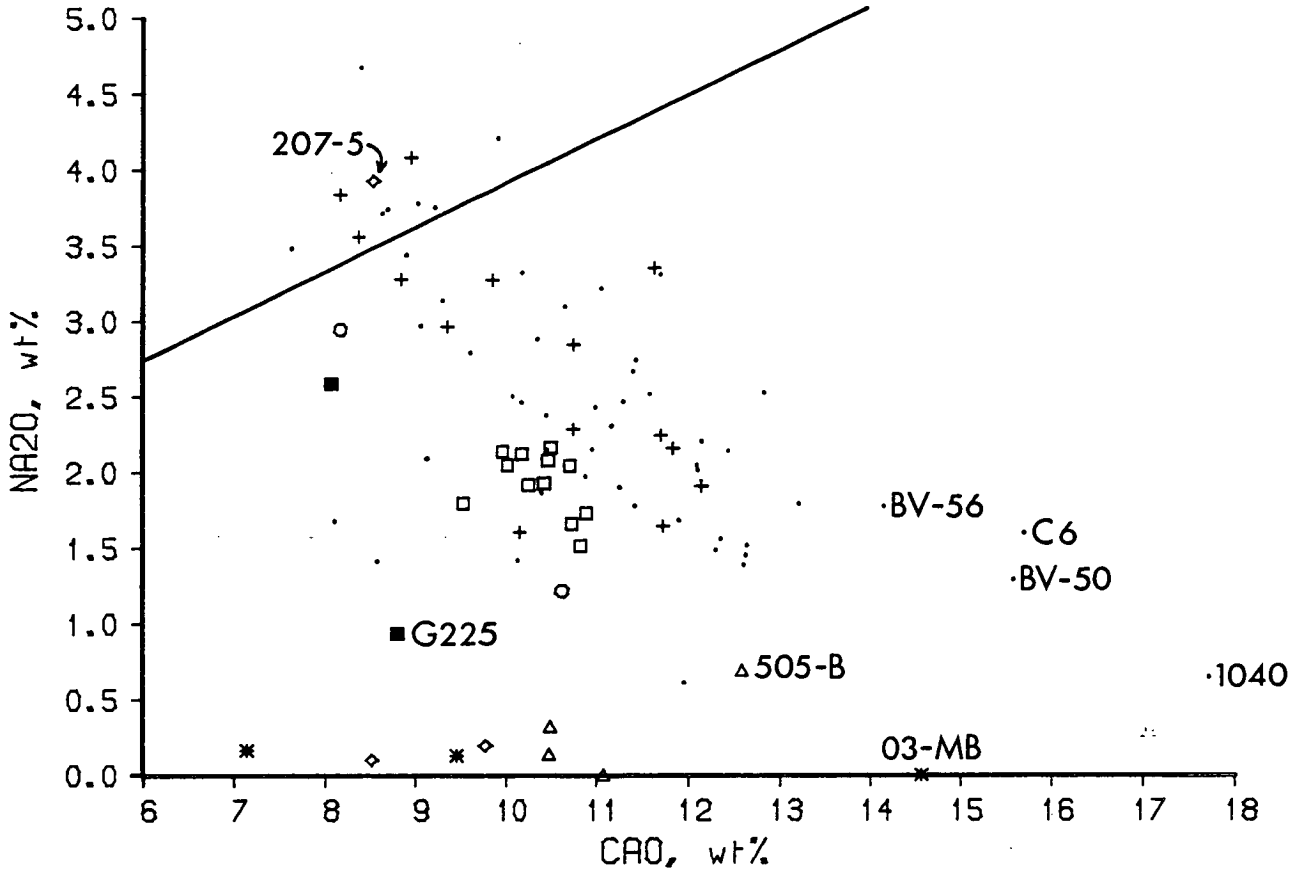


**Fig. 5.5:** Relationship between metabasite bed thickness and K<sub>2</sub>O content of analysed samples. Estimated stratigraphical thickness is plotted on a logarithmic scale: sample G225 omitted (thickness not known). Open circles indicate samples from the sub-M3 metabasite marker bed (see text). K<sub>2</sub>O content based on volatile-free totals = 100%.



**Fig. 5.6:** Na<sub>2</sub>O-BaO-K<sub>2</sub>O diagram of Foss metabasites, to illustrate sodium depletion associated with potassium enrichment in calc biotite metabasites (except 207-5) and muscovitic metabasites, and with barium enrichment in mineralized basic rocks.

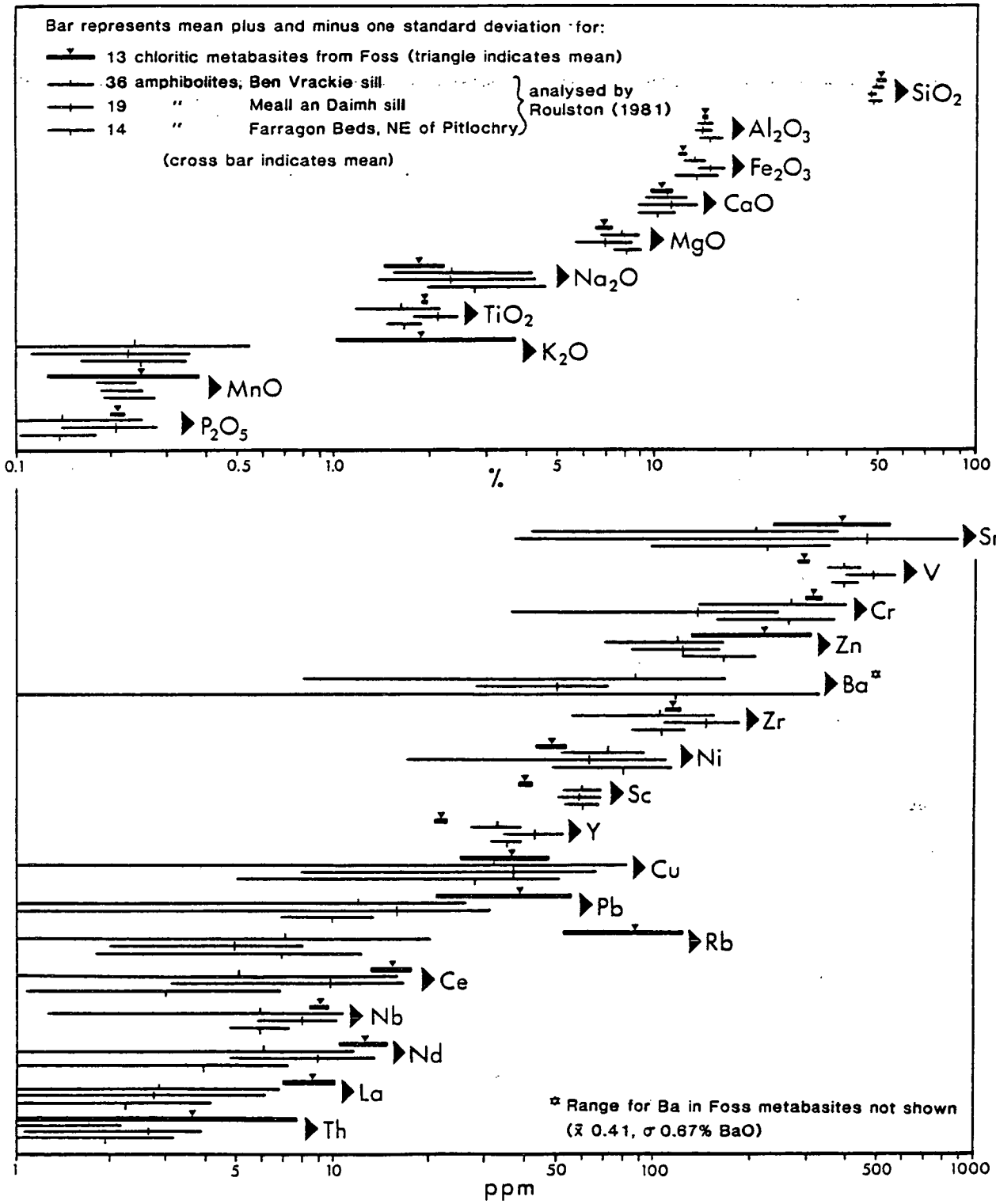
- Ben Vrackie amphibolites
- + Farragon Beds
- Foss amphibolites
- chloritic metabasites
- △ muscovitic
- ◇ calc biotite
- \* mineralized



**Fig. 5.7:** Plot of Na<sub>2</sub>O vs. CaO (expressed on a volatile-free basis) for metabasites from Ben Vrackie, Farragon Beds and Foss. Diagonal line separating high-Na<sub>2</sub>O group of spilitic compositions (including 207-5) from normal metabasites, taken from Graham, 1976. With the exception of 03-MB, metabasites containing >14 wt% CaO are rich in epidote (see text, and Roulston, 1981).



Fig. 5.8: Compositional ranges of Foss and Ben Vrackie metabasite suites.



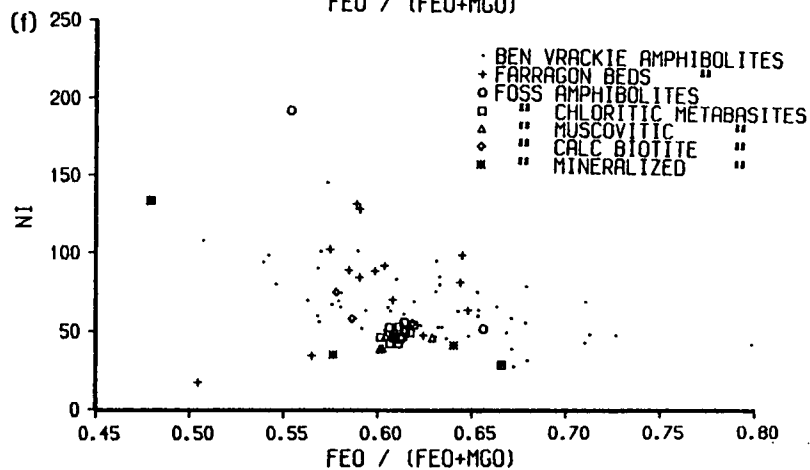
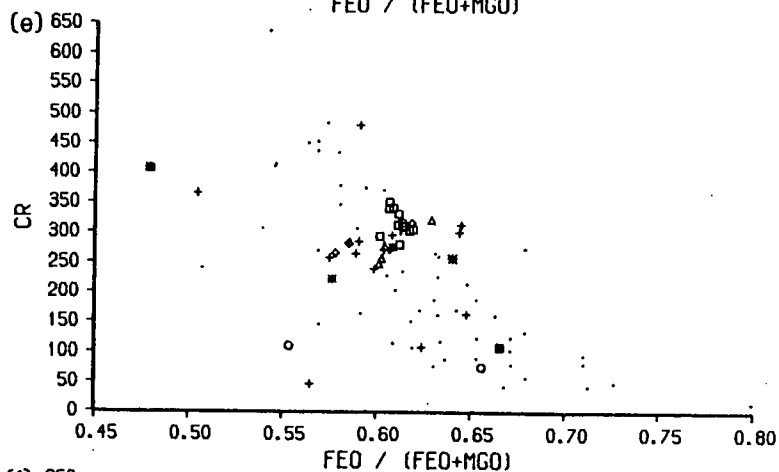
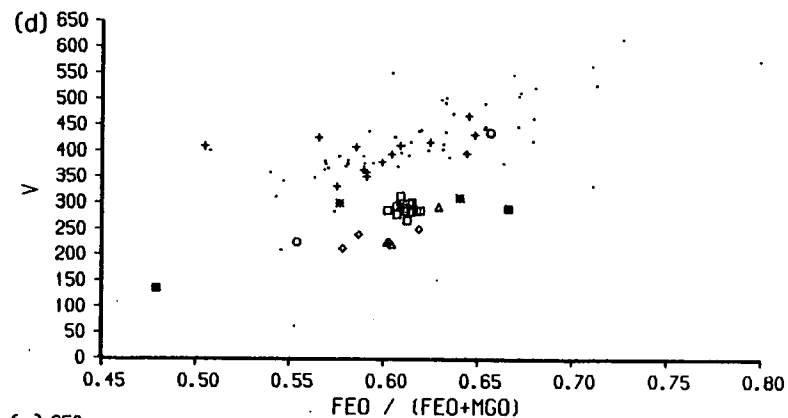
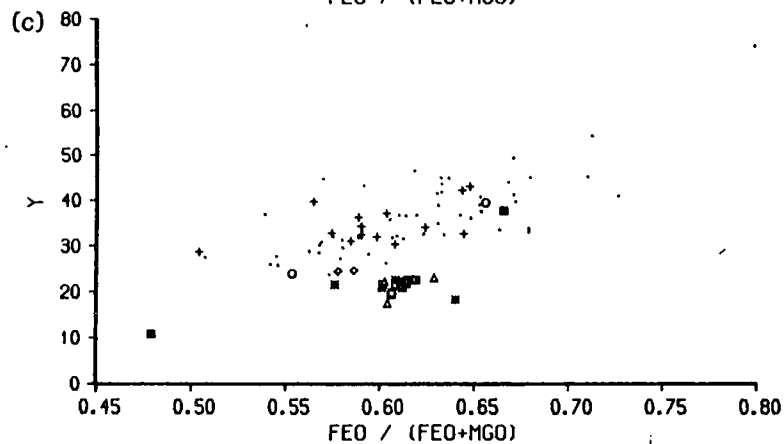
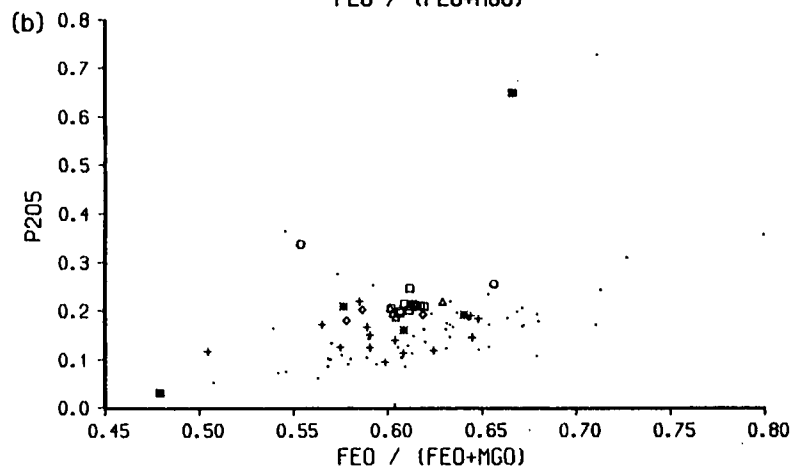
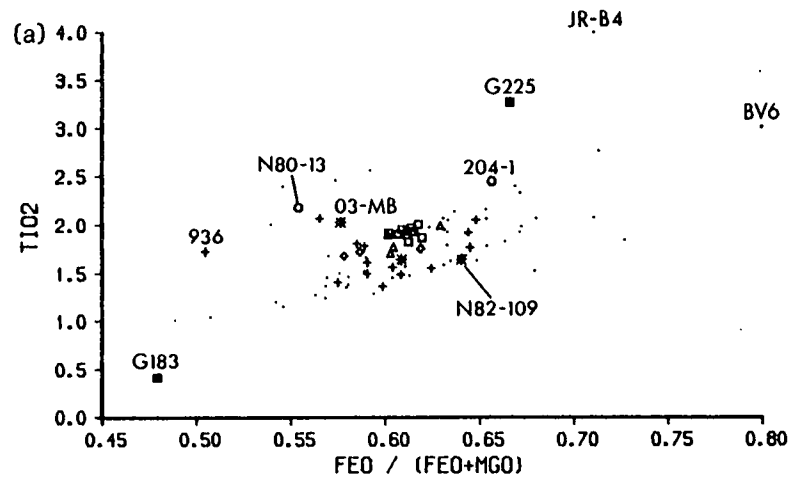
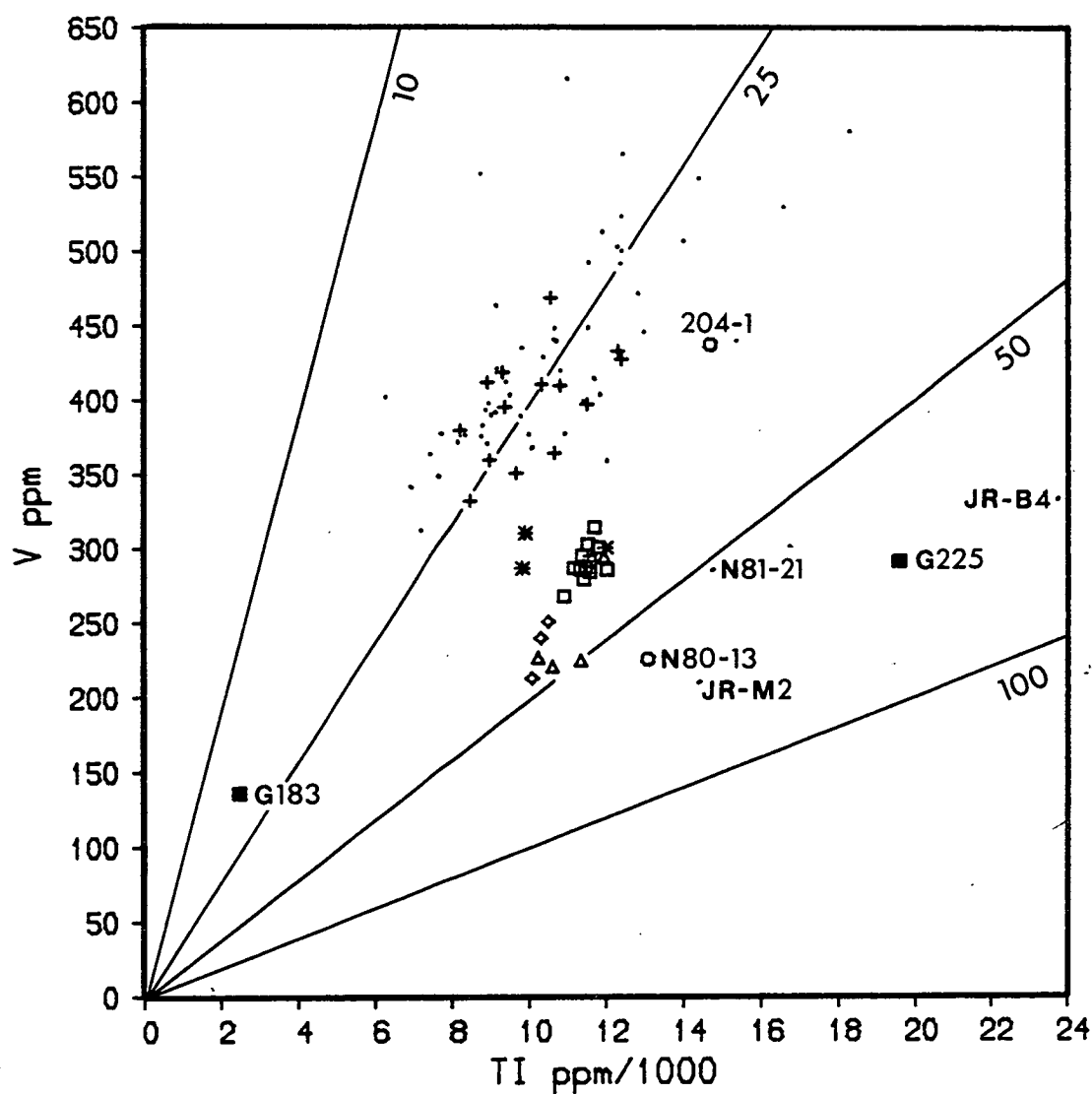
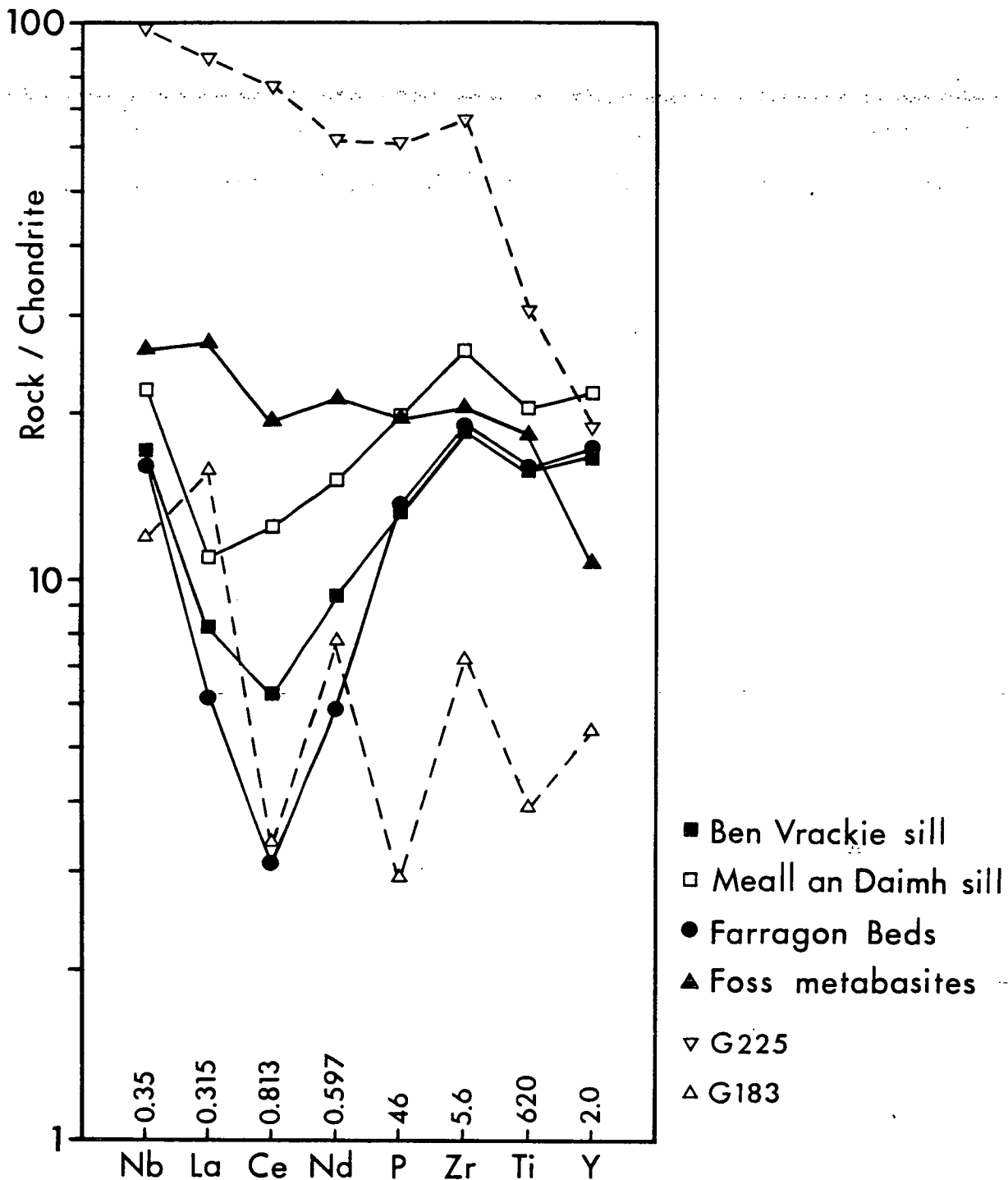


Fig. 5.9 (a)-(f): Variation diagrams for TiO<sub>2</sub>, P2O<sub>5</sub> and trace elements vs. differentiation index, for metabasites from Ben Vrackie (dots), Farragon Beds (crosses) and Foss (other symbols: key on Fig. 5.9f). FeO/(FeO+MgO) expressed as weight percent ratio; Fe total calculated as FeO.

· BEN VRACKIE AMPHIBOLITES  
 + FARRAGON BEDS  
 ○ FOSS AMPHIBOLITES  
 □ " CHLORITIC METABASITES  
 △ " MUSCOVITIC  
 ◇ " CALC BIOTITE  
 ■ " MINERALIZED



**Fig. 5.10:** Vanadium vs. titanium plot of Ben Vrackie, Farragon Beds and Foss metabasites. Trend lines of constant Ti/V ratios = 10, 25, 50 and 100, are shown for reference (see text). Ti ppm/1000 calculated as  $5.995 \times \text{TiO}_2$  (wt%).



**Fig. 5.11:** 'Spidergram' of chondrite-normalized, immobile trace and minor element distributions (note logarithmic scale). Continuous lines and solid symbols: averages of Ben Vrackie sills, Farragon Beds, and Foss metabasites (B2[I group]; dashed lines and open symbols: samples G225 (Doire Leathan) and G183 (Farragon Hill). Numbers above elements are normalizing factors employed (from Sun et. al., 1979). See text.

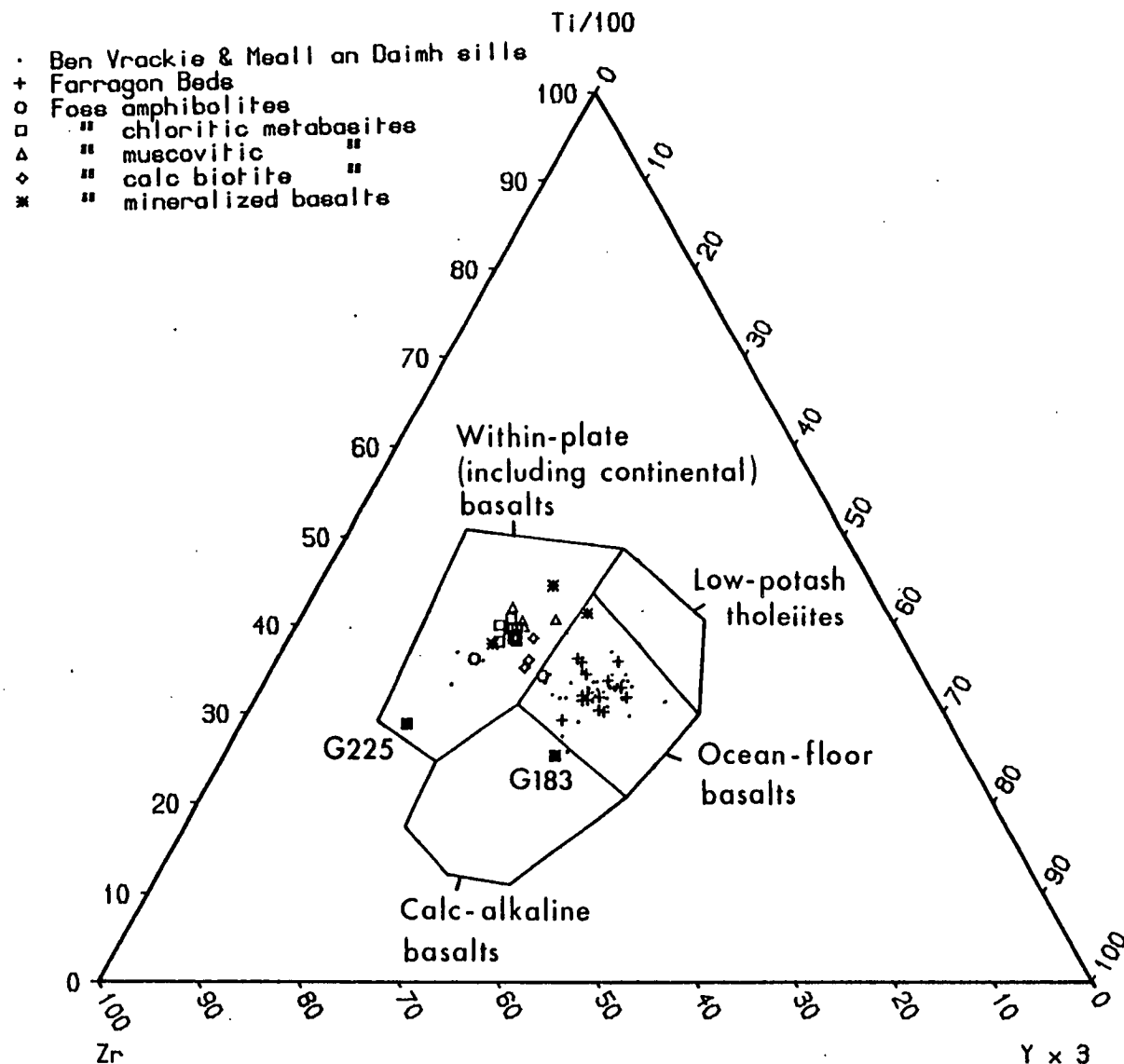


**Fig. 5.12:** Zr-Ti( $\times 10^{-2}$ )-Y( $\times 3$ ) diagram of Ben Vrackie, Farragon Beds and Foss metabasites, after Pearce and Cann (1973). Note that only four Ben Vrackie metabasites plot in the 'within-plate' basalt field, in which all but three of the Foss metabasites plot.

## CHAPTER 6: Silicate mineral chemistry.

### 6.1 Introduction.

This chapter presents the results of a mineralogical and microprobe examination of silicate minerals in over 150 thin sections representing a wide range of rock types from the Foss deposit and its host rocks. Data on oxide, sulphide, sulphate, carbonate and phosphate compositions in the same sample suite are the subject of Chapter 7, the last section of which reviews compositional relationships between coexisting silicate and non-silicate phases. The objectives of mineralogical studies, as outlined in part 1.4.3, were threefold: (1) to characterise the mineral phases present and to establish their compositional ranges; (2) to identify compositional features related to the mode of formation of the various minerals and to the conditions of metamorphism; and (3) to assess compositional inter-relationships between coexisting phases which may reflect either bulk rock compositions or metamorphic element partitioning. The application of mineralogical and compositional data to quantify the conditions and P-T history of metamorphism is discussed in Chapter 8.

Feldspars and micas occurring in the vicinity of the deposit are of particular interest because of the volumetric abundance of barium-rich varieties. These minerals, together with the hydrous barium aluminosilicate, cymrite, were previously described by Coats et al. (1981) and Fortey and Beddoe-Stephens (1982). Their work is reviewed and a large number of new analyses are evaluated in sections 6.2 (which incorporates plagioclase, barium feldspars and cymrite) and 6.3 (muscovites and biotites). Section 6.4 concerns the mineral chemistry of the other ferromagnesian silicates examined (chlorite, talc, garnet, hornblende, epidote group minerals, and tourmaline), and minor silicate phases (sphene, and baoite; a newly described occurrence at Foss). The results are summarized in section 6.5. Details of the analytical technique are described in Appendix E, and representative analyses of each silicate phase appear in tables 6.1-6.13.

## 6.2 Plagioclase, barium-potassium feldspars and cymrite.

The feldspar group may be divided into alkali feldspars, plagioclase feldspars and barium feldspars. Perthitic alkali feldspar, variably replaced by albite (plate 70), has been observed in Carn Mairg Quartzite-type psammitic lithologies which were not examined by microprobe in this study. However, potassic feldspar is rare in the mineralized zone at Foss, and since it is only found in intimate association with the barium-potassium feldspar series (celsian and hyalophane), these are described together in section 6.2.2. Cymrite, although structurally not a feldspar, is similar in composition to celsian and is dealt with in section 6.2.3. Plagioclase occurring in the vicinity of the Foss deposit contains insignificant amounts of K and Ba, and this mineral is considered first.

### 6.2.1 Plagioclase.

Since plagioclase examined in this study generally contains  $<0.1$  wt%  $K_2O$  ( $<0.5\%$  orthoclase 'molecule'), compositions may be adequately represented by the molecular percentage of the anorthite end-member (=  $An_{100}$ ). Seventy-eight analyses were obtained of plagioclase occurring in thirty-eight samples, and these cover the range  $An_{0.1}$  (nearly pure albite) to  $An_{22.7}$  (oligoclase). These data are summarized in fig. 6.1 and representative analyses are presented in table 6.1.

In rocks from Foss, plagioclase occurs in three distinct associations: (1) as a major component of the quartzo-feldspathic groundmass in chloritic metabasites and amphibolites, and in calcareous pelites of units C and D (plates 82, 113); (2) as rounded porphyroblasts replacing muscovite in graphitic pelites of unit A (and less frequently, unit B) (plate 74); and (3) as matrix grains and as replacement of relict detrital (alkali?) feldspar grains in quartzites constituting the Carn Mairg Quartzite formation and in similar rocks in unit B (plates 37 and 70). However, these associations do not correspond to distinct compositions of plagioclase, although oligoclase with  $An_{>14}$  was not found in samples of Ben Eagach Schist (fig. 6.1). Furthermore, the compositions of plagioclase coexisting with other calcic phases, namely garnet and/or epidote group minerals and/or carbonates, appear to be indistinguishable from plagioclase compositions in rocks which lack some or all of these phases. In two samples examined which contain

both plagioclase and hyalophane, N80-2 (a unit B muscovite quartz schist; plate 78) and 105-42 (a unit C mineralized pelite similar to that in plate 84), the plagioclase was found to be nearly pure albite ( $An_{<1}$ ) with no detectable Ba.

Within individual samples, plagioclase compositions frequently vary by several %An from grain to grain. Concentric zonation in plagioclase porphyroblasts, observed as variations in extinction position under crossed polars, is generally due to more calcic core compositions. However, in some thin sections both 'normal' zoning and 'reverse' zoning (ie. cores more sodic than rims) were observed in different grains of plagioclase (e.g. IGS 4321: see Coats et al., 1981, Appendix III). Coexisting albite ( $An_{<2}$ ) and oligoclase ( $An_{18-23}$ ) were found in one sample of unit D calcareous pelite, 429-5 (plate 86), in which the albite occurs predominantly in fine-grained quartzo-feldspathic domains and the oligoclase in mica-chlorite-carbonate domains.

These compositions ( $An_{<2}$ ,  $An_{>18}$ ) outline the peristerite solvus (Crawford, 1966; Goldsmith, 1982) which has been described from several regional metamorphic terrains (e.g. Marayama et al., 1982; Grapes and Masayuki, 1983). Marayama et al. (op. cit.) have shown that the An content of albite in coexisting albite-oligoclase pairs provides a relative geobarometer, since the peristerite solvus shifts towards pure albite and higher temperatures with increasing pressure (fig. 6.2). The feldspar compositions in sample 429-5 are similar to those recorded in metabasites from the garnet isograd located 12 km due S of the Foss area (Graham, 1973, and reported in Fettes et al., 1976), and could indicate equilibration at pressures of 7-10 kbar (cf. Marayama et al., op. cit.). Coexisting albite-oligoclase pairs are also recorded by Brown (1969) in a garnet psammite from near Crianlarich, 45km to the WSW. However, the absence of oligoclase in garnet zone rocks of the SW Highlands (cf. Fig. 5.10 of Graham, 1973) was attributed by Fettes et al. (op. cit.) to significantly higher metamorphic pressures in this area than in the central Highlands.

The apparent scarcity of coexisting albite plus oligoclase (present in possibly two of over fifty plagioclase-bearing samples examined), and the abundance of plagioclase with intermediate compositions (i.e.  $An_{2-15}$ ) at Foss, appears to be not unusual in the Scottish Caledonides (Dempster, 1983 and C.M. Graham, pers. comm., 1984), although more regular variations are observed in other metamorphic terrains. This could be explained by postulating that



plagioclase recrystallized in different rocks over a considerable range of load pressures during and subsequent to the metamorphic climax (see part 8.3.5 and section 8.4).

#### 6.2.2 Celsian, hyalophane and orthoclase.

Petrographical features of the mineralized lithologies containing barium feldspars were described in parts 3.2.2 and 4.3.3, and the formation of these feldspars was discussed in part 3.4.2. It was noted that celsian is common in mineralized strata but is uncommon in barium-enriched metasediments (and is absent from carbonaceous lithologies). The converse holds for hyalophane, which as noted above, coexists with albite in some mineralized metasediments (particularly those geochemically affiliated with unit C; part 4.4.2). Celsian, hyalophane and cymrite coexist with barian micas in several samples examined, notably from the upper mineralized horizons in central-eastern Foss East. Orthoclase was identified by microprobe examination of four mineralized rocks in which it forms veinlets and thin overgrowths on barium feldspars.

#### Previous studies of barium feldspar compositions.

Fortey and Beddoe-Stephens (1982) present twenty-two analyses of celsian and nine analyses of hyalophane, the majority of which are from BH7 samples (Ben Eagach deposit). These were found to plot close to a line of constant K/Na ratio on a Ba-K-Na diagram (discussed below), although ternary (Ba,K,Na)-feldspars from locations other than Aberfeldy scatter widely on this diagram. The authors noted the absence of compositions midway between celsian and hyalophane and suggested that this supports the existence of a compositional gap in the low-T structural state of the series  $\text{KAlSi}_3\text{O}_8$ - $\text{BaAl}_2\text{Si}_2\text{O}_8$ , as previously suggested by Gay and Roy (1968). However, zoning in the potassium content of some celsian crystals, related to growth and replacement phenomena, is illustrated by microprobe traverses presented by Fortey and Beddoe-Stephens (op. cit.). Some substitution of Na+K for Ba in cymrite was also observed by these authors, and in the sample examined, cymrite was found to be compositionally similar to the coexisting celsian.

#### This study.

Two hundred and fifty analyses of barium feldspars in sixty samples from the Foss and Ben Eagach deposits were obtained, a selection of which are presented in table 6.2 (see Appendix E.2). The data show a complete range of compositions (fig. 6.3) between

nearly pure celsian ( $Cn_{<97}$ , where  $Cn_{100} = 100 \text{ mol\% BaAl}_2\text{Si}_2\text{O}_8$ ) and hyalophane ( $Cn_{>25}$ ), and a range of K/Na ratios between 2 and 11. For descriptive purposes, feldspars in the range  $Cn_{25-70}$  are referred to here as 'hyalophane' and those in the range  $Cn_{70-90}$  are termed 'potassic celsian'. No feldspars with 13-25% Cn were found, but the potassic feldspar overgrowths mentioned above have 1-13% Cn.

Within individual samples, zoned hyalophane and potassic celsian crystals have generally constant K/Na ratios (fig. 6.4), which are often similar in samples from the same small area or interval of drillcore. The data presented by Fortey and Beddoe-Stephens (1982) show that barium feldspars in several samples from BH7 have similar K/Na ratios ( $\sim 4.3$ ) whereas this ratio is lower ( $\sim 3$ ) in a sample from BH9. Particularly high K/Na ratios (8-11) are found in three samples of hyalophane-bearing sulphidic breccia rocks from BH4 which were examined in this study (PTS 3917, 3920 and 3924: for locations see Coats et al., 1981). At the other extreme, exceptionally sodic hyalophane ( $K/Na \approx 2$ ) coexists with albite in a sample of mineralized calc biotite schist interbedded with barite (105-42), although average K/Na ratios (3-6) were observed in hyalophane in a muscovite quartz schist containing minor albite (N80-2: fig. 6.4 and plate 78). Comparatively high sodium contents were also observed in K-celsian in a sample of pyritic quartz chert, G114A (Appendix B; plates 35 & 66), which also contains relatively Na-rich barian muscovite (part 6.3.1).

The constancy of feldspar K/Na ratios within samples and beds up to several metres across (BH4 samples are from a 3m core interval) suggests that original compositional inhomogeneities (with respect to K/Na ratios) may have been smoothed out by equilibration with an infiltrating metamorphic fluid phase which was buffered by the average bulk rock composition. Complex zoning in barium feldspars, described by Fortey and Beddoe-Stephens (1982) and in part 3.2.4, often appear to be due to the marginal replacement and veining of celsian and hyalophane crystals by potassic celsian with intermediate compositions (plate 57). The extent of this replacement may be spatially related to post-tectonic fractures and cross-cutting veinlets, which supports the fluid infiltration hypothesis. Evidence for late-metamorphic fluid interactions in some samples is provided by the occurrence of patches of potassic celsian in celsian pseudomorphs of a foliated cymrite fabric (cf. plate 54 and part 8.3.4).

The sodium-poor, barian orthoclase identified as forming thin (<100 $\mu$ m), optically distinct rims to celsian and hyalophane crystals, occurs in three massive sulphide rocks and one barite rock. The latter (sample G171) is traversed by a fine-grained micaceous zone which may represent an annealed fault. In the other samples, almost pure orthoclase partially surrounds coarse celsian crystals set in a sulphide matrix (plate 93), and seems to have infilled cracks probably caused by differential thermal contraction or expansion during cooling and uplift. However, a sodium-poor hyalophane (28% Cn, K/Na = 88) was found in sample 705-30 in a similar location to the barian orthoclase rims mantling celsian crystals elsewhere in the same thin section. The textural and chemical evidence suggests that these feldspars of unusual composition were post-metamorphic in origin and did not form in equilibrium with the earlier-formed crystals.

The absence of hyalophane compositions of <Cn<sub>25</sub> (except for the orthoclase described above), suggests the presence of a solvus in the orthoclase-hyalophane series under the metamorphic P,T conditions experienced by the rock mass at Foss. However, a solvus in this position has not been described previously (Gay and Roy, 1968), although Vermaas (1953) has discussed XRD evidence for two isomorphous series, Cn<sub>0-40</sub> and Cn<sub>45-100</sub>, in barium feldspars from the Otjosundu manganese deposit, S.W. Africa. More recently, Viswanathan and Kielhorn (1983) have examined the composition and lattice dimensions of (Ba,K,Na)-feldspars from Otjosundu, and report submicroscopic intergrowths of the compositions Cn<sub>45</sub> and Cn<sub>95</sub>. Further elucidation of the subsolidus relationships of barium potassium feldspars occurring in the Aberfeldy deposits requires a similar detailed structural study.

### 6.2.3 Cymrite.

Cymrite is a uniaxial-negative, colourless mineral of moderate relief and low birefringence. It may be distinguished from celsian in thin section by the somewhat higher refractive index of cymrite, and its pronounced cleavage parallel to (001) and a less well developed cleavage perpendicular to this. According to Drits et al. (1975), it has a sheeted, mica-like structure. The correct formula for cymrite, BaAl<sub>2</sub>Si<sub>2</sub>O<sub>8</sub>.H<sub>2</sub>O, was established by Carron et al. (1964) who showed from infra-red data that the water content (~4.6 wt%) is held as H<sub>2</sub>O and not as OH (confirmed by Fortey and Beddoe-Stephens,

1982). Cymrite was first reported from the Benallt manganese mine (Smith et al., 1949) and has since been described from stratabound sulphide and barite deposits (Froehlich and Sandrea, 1973; Large, 1981b), black shales (Soong and Olivecrona, 1975), and Ba-rich rocks which have undergone low to medium grade metamorphism (Runnells, 1964; Essene, 1967; Reinecke, 1982).

Cymrite was positively identified in only two of >200 specimens examined by Coats et al. (1981) and Fortey and Beddoe-Stephens (1982), but was identified in many thin sections examined in this study. Textural evidence for the partial or complete replacement of cymrite by coarser celsian crystals is widespread (see part 3.2.4 and plates 51-55, 58). Very occasionally, evidence is also seen for the localized replacement of celsian by secondary cymrite (part 8.3.4 and plate 59). Cymrite is most common in the quartz mica cymrite celsian schists which form the upper mineralized horizons in the central-eastern Foss East area (part 2.4.3), and in similar schists and cymrite-bearing quartzose cherts within the upper mineralized zone in the Frenich Burn area. Cymrite is also commonly a trace component of quartz celsian rocks and massive sulphide rocks, where it occurs as small inclusions in pyrite crystals (cf. plate 67). As with celsian, cymrite is absent from carbonaceous metasediments at Foss.

Thirty-six microprobe analyses of cymrite (of which ten are presented in table 6.3) were obtained in this study, and together with analyses given by Fortey and Beddoe-Stephens (1982), show that K and Na are minor but essential components of this phase. The K/Na atomic ratio varies from 2 to 9 and the majority of analysed crystals contain 94-97 mol% of the cymrite end-member (fig. 6.5). As with celsian, other cations such as Ti, Fe, Mg and Mn are generally below detection limit in reliable analyses, but cymrite is more prone to chloritic alteration than celsian and this can account for the higher Fe and Mg values in some analyses, several of which had to be discarded because of contamination. The significance of the restricted compositional range of cymrite compared with the chemically analogous barium feldspars, is discussed with reference to experimental studies of cymrite-celsian equilibria, in part 8.3.4 and Appendix G.

### 6.3 Micas.

A general formula which describes the composition of micas (Deer et al., 1962a) is  $X_2Y_{4-6}(Si,Al)_8O_{20}(OH,F)_4$ , where X is mainly K, Na, Ca or Ba, and Y is mainly Al, Mg or  $Fe^{2+}$  but can also include Mn, Ti, Cr and V.  $Fe^{3+}$  and other trivalent cations may substitute for (Si,Al) in the tetrahedral site, and vacant sites may also exist in mica structures. Micas are subdivided into di-octahedral and tri-octahedral classes in which the ideal number of Y ions is four and six respectively. While in the broadest sense all di-octahedral micas examined in this study are muscovite, for descriptive purposes two further subgroups are distinguished, namely barian muscovite and fuchsite. 'Barian muscovite' is arbitrarily defined as muscovite containing  $>0.20$  Ba cations per formula unit (equal to approximately 3.5 wt% BaO). Following the convention suggested by Deer et al. (op. cit.), the name 'fuchsite' is used here to describe muscovites with  $>0.12$  cations Cr per formula unit (equal to about 1.0 wt%  $Cr_2O_3$ ), regardless of their Ba content. Muscovites containing 0.2-1.0 wt%  $Cr_2O_3$  are referred to as 'chromium-bearing'.

The tri-octahedral micas are similarly divided into biotites and barian biotites, in which Ba cations account for  $>0.20$  of the formula unit (based on 22 oxygens). An arbitrary division is also placed between biotite and the more magnesian phlogopite, at an  $Fe/(Fe+Mg)$  atomic ratio of 0.3. This value was chosen in preference to the Mg:Fe ratio of 2:1 employed by Deer et al. (1962a) because it more closely follows a natural break in the analytical data set (fig. 6.13).

#### 6.3.1 Muscovite and barian muscovite.

##### Occurrence and compositional range.

Muscovite is abundant in the metasediments enclosing the mineralization, and is also found in major quantities in many mineralized sedimentary rocks and in the metabasite marker bed beneath M3 (part 5.2.4). Minor or trace amounts of muscovite are also seen in the mineralization, although here, iron-poor tri-octahedral micas are of similar abundance. Muscovite is observed to coexist with most other silicate phases (except talc) and also with graphite, sulphides and carbonates, but only Cr-bearing varieties of muscovite coexist with barite.

Approximately 170 microprobe analyses of muscovite and barian muscovite (in roughly equal proportions) were obtained from about

sixty rock samples representing a wide range of parageneses. A representative selection of these analyses appear in table 6.4. After calculating molecular formulae and eliminating analyses showing evidence of contamination, inter-element variations in the data set were evaluated by means of divariate and trivariate plots (figs. 6.7-6.18). The range in muscovite compositions and between-phase relationships are discussed before considering lattice substitutions suggested by these inter-element variations.

Within individual thin sections, muscovite grains are usually similar in composition, although large variations in Ba, Na, Ti, Al, Fe and Mg contents are evident in the data set as a whole. Within-section (<1cm) heterogeneity was observed in three situations: (1) In disseminated or encapsulated muscovite in quartz hyalophane schists with zoned hyalophane pseudomorphs of sulphate crystals (samples 4330 and N81-80: plate 63 and fig. 6.14). (2) In muscovite associated with cross-cutting calcite-pyrite veinlets of retrograde origin, for example in a biotitic metabasite, sample 207-5 (plate 89). (3) In two samples of micaceous quartz celsian rock, G100d and 705-22 (table 6.4), individual muscovite grains show zonation in Ba content whereby a central zone (elongated parallel to the muscovite cleavage) is relatively poor in Ba and is sandwiched by Ba-rich muscovite with no break in optical continuity. Comparable zoning in a barian phengite has been described by Chopin and Maluski (1980), who attributed the zoning to localized retrogressive metasomatism. A similar explanation is suggested here for zoned and vein-associated muscovites at Foss.

Fortey and Beddoe-Stephens (1982) reported up to 8.3 wt% BaO in barian muscovite, of which eleven analyses from Aberfeldy deposit samples were presented. However, in muscovite coexisting with barium feldspar, the BaO content was consistently found to be about 6 wt%. The authors suggested that this could represent an effective saturation level in muscovite in equilibrium with barium feldspar under the metamorphic conditions attained. In the muscovites analysed in this study, BaO contents range from nearly zero to 10.6 wt%, but show a bimodal distribution with peaks corresponding to 0-0.10 and 0.30-0.45 Ba cations per formula unit (fig. 6.6). The hypothesis of Fortey and Beddoe-Stephens (op. cit.) is clearly not substantiated, since in at least twelve samples examined, barian muscovite containing >0.40 Ba cations (>7 wt% BaO) coexists with celsian or hyalophane. In addition, fuchsite containing 0.67 Ba cations (11.5 wt% BaO) coexists with celsian in two samples studied

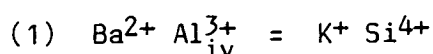
(G114A and 703-9, section 6.3.3).

The Na<sub>2</sub>O content of Foss muscovite ranges from 0.1 wt% to 1.2 wt% (0.02-0.30 Na cations per formula unit), but calcium was found to be generally at or below the detection limit ( $\leq 0.02$  wt% CaO). On the Ba-K-Na diagram (fig. 6.7), the spread of barium-poor muscovite compositions parallel to the K-Na join indicates a solid solution with between  $\sim 7$  and  $\sim 16$  mol% of the paragonite end-member, Na<sub>2</sub>Al<sub>4</sub>(Si,Al)<sub>8</sub>O<sub>20</sub>(OH)<sub>4</sub>. Although paragonite has not been identified as a separate species in samples from Foss, this extent of muscovite-paragonite solid solution is consistent with Na saturation at metamorphic temperatures of 400-560°C (cf. Chatterjee and Froese, 1975). Only two samples examined contain barian muscovite with a comparable paragonite content (N81-43 and G114A: table 6.4). The remaining barian muscovites (plus those analysed by Fortey and Beddoe-Stephens) contain 1-7 mol% paragonite, but within this range, sodium content generally increases with increasing barium content (fig. 6.7). K/Na ratios in muscovite are lower than in coexisting barium feldspar, but are generally higher than in the tri-octahedral micas (fig. 6.7 inset) (see part 6.3.4).

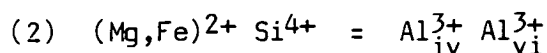
A notable feature of the majority of muscovite analyses is a deficiency in X-site occupancy. This is illustrated by a plot of Na+K cations against Ba cations (fig. 6.8) in which many muscovites, including all those poor in barium, fall significantly below the line representing (Na+K+Ba) = 2. The presence of additional trace elements such as Rb, estimated from XRF data (fig. 5.3) to constitute about 300ppm of Ba-poor muscovite, is unlikely to account for this deficiency in X-site cations which is inferred to be due to site vacancies or to the presence of (H<sub>3</sub>O)<sup>+</sup> ions (cf. Deer et al., 1962a).

#### Substitution mechanisms.

Inspection of the molecular formula (table 6.4) and figs. 6.8-6.10 indicates that the substitution of divalent Ba ions for K+Na ions in the X-site is charge-balanced by a coupled substitution of Al<sup>3+</sup> for Si<sup>4+</sup> in the tetrahedral site:



Fortey and Beddoe-Stephens (1982) consider that this substitution is independent of the common phengitic ('tschermakitic') substitution:



Note that barian muscovites have higher (Mg,Fe) contents than Ba-poor muscovites with a similar total Al content (fig. 6.12), and

that the operation of both substitution mechanisms in muscovites from the Aberfeldy deposits accounts for the absence of simple relationships between Ba, Si,  $Al^{iv}$  and (Mg,Fe) contents. The range of phengitic substitution is comparable to muscovites from other areas which attained similar metamorphic grades (e.g. Butler, 1967). Lower total Al and higher (Mg,Fe) and Si contents indicate a greater degree of phengitic substitution in some barian muscovites (in samples 4314, G100a and G100d), whereas considerably less phengitic substitution is apparent in another group of aluminous barian muscovites (samples 4330 and G114A) in which substitution scheme (1) predominates. The spread of points on either side of the ideal substitution lines (figs. 6.9, 6.12) may be related to other substitutions and to the incomplete X-site occupancy which, as noted above, is characteristic of barium-poor muscovites from Foss.

The relative proportions of Mg and Fe also vary considerably, and lower Fe/(Fe+Mg) ratios are characteristic of most barian muscovites (fig. 6.14). The variation in this ratio in muscovite is analogous to that in biotite, and the explanation for this and also Mg-Fe partitioning between coexisting micas, is discussed in parts 6.3.3 and 6.3.4. Barian muscovites also generally have higher  $TiO_2$  contents (up to 1.8 wt%) than barium-poor muscovites (fig. 6.15).

### 6.3.2 Chromium and vanadium muscovites.

Although Coats et al. (1980, 1981) reported the occurrence of fuchsite in several rocks from the Ben Eagach and Foss deposits, this mineral was not characterised by microprobe analyses. Some of these occurrences have since been discredited because the dark green flakes referred to as fuchsite are actually barian biotite or altered biotite (see section 6.3.4). However, twenty-two analyses have been obtained of chromium-rich, barian muscovites occurring in eight samples from Foss examined in this study (table 6.5). These samples are mostly of sulphidic quartzose cherts (part 3.2.1) but include two sulphidic barite rocks (410-31 and 705-28). Although occasionally present in sufficient quantity to impart a distinctive green colour to the rocks, fuchsite is invariably a minor or trace constituent and its presence does not indicate high bulk Cr contents (e.g. 75ppm Cr in sample G100e: table 3.2). Presumably, chromium is concentrated into the small amount of mica present because other suitable receptor phases (e.g. chromite) are absent.

Within individual thin sections, fuchsite grains vary in their depth of colour from very pale to vivid emerald green (plate 46),



corresponding to variations in Cr content. A striking feature of most fuchsites analysed is their high barium content (up to 15.7 wt% BaO), which generally increases with increasing chromium content (up to 9.3 wt% Cr<sub>2</sub>O<sub>3</sub>) (fig. 6.13). However, ten of the analyses are suspect because they have oxide totals of <90%, and have markedly lower Al contents and somewhat lower Si, Na and F contents than the remaining fuchsites. 'Altered' fuchsites in the barite rock samples 505-14 and 705-28 have the highest measured Cr contents and are rich in iron compared with fuchsite in most other samples (which have lower Fe/(Fe+Mg) ratios). This might suggest an affinity with the tri-octahedral micas, but fig. 6.12 shows that the altered fuchsites lie near to the trend of phengitic substitution (Mg+Fe for Al) in normal muscovites. A similar style of alteration is observed in biotites, with the exception that barium is also depleted (part 6.3.4).

A vanadium-rich, barian fuchsite was discovered in one sample of sulphidic barite rock, 410-31. This mineral occurs as irregular grains and flakes enclosed by barite and pyrite crystals, and varies in body colour from a murky olive-brown to translucent pale green, the latter variety being strongly pleochroic (colourless, viridian green, mid brown). Three analyses of this mica (table 6.5; see Appendix E.3) show that it contains 3.4-4.3% Cr<sub>2</sub>O<sub>3</sub> and 9.3-10.8% V<sub>2</sub>O<sub>3</sub> (assuming that Cr and V are entirely trivalent), in addition to considerable amounts of FeO and MgO (total, 11-14%) and 9.9-12.3% BaO. Considering these features, plus the similarity in SiO<sub>2</sub> and Al<sub>2</sub>O<sub>3</sub> content to barian biotites, this mica was initially considered to be a member of the tri-octahedral group. However, the octahedral-site cations total just over four, and the oxide totals of 94-95 wt% do not allow for large site vacancies. It is therefore suggested that V<sup>3+</sup> and Cr<sup>3+</sup> have largely substituted for Al<sup>3+</sup> in the octahedral site of the muscovite lattice, coupled with an increase in tetrahedral Al and decrease in Si due to increased Ba and tschermakitic substitution. This is essentially an extension of the substitution reaction observed above in the Cr-Ba muscovites.

Vanadium-rich barian micas ('roscoelite') containing 6-18 wt% V<sub>2</sub>O<sub>3</sub> and 7% BaO, have been reported by Kultiassov and Dubinkina (1946: see Heinrich and Levinson, 1955). Snetsinger (1966) has described a Ba-V muscovite containing 3.2% equivalent V<sub>2</sub>O<sub>3</sub> and 2-4% BaO from a graphitic quartz schist pendant in a Californian granite intrusion. Chromian muscovites are comparatively common (their compositions and occurrences have been reviewed by Whitmore et al.,

1946 and Heinrich, 1965), but Ba-Cr varieties are rare. Barium-free chromian phengite containing up to 16.25%  $\text{Cr}_2\text{O}_3$  was found by Mevel and Kienast (1980) in a high pressure metamorphosed gabbro. Matthews (1967) presents an analysis of fuchsite containing 1.07% BaO and 3.09%  $\text{Cr}_2\text{O}_3$  from zoned ultramafic pods on Skye, and a hydromuscovite containing 1.32% BaO and 0.46%  $\text{Cr}_2\text{O}_3$  was described by Neiva (1978). However, Dymek et al. (1983) have recently described green micas from pyritic metasediments of Archaean age in southern West Greenland, which range from nearly pure muscovite to types with up to ~8% BaO and ~17%  $\text{Cr}_2\text{O}_3$ . A compositional discontinuity (not evident in this study) was observed between micas with 0.4-0.9 and 1.6-1.9 cations Cr per formula unit (based on 22 oxygens). These enrichments are coupled with high Mg, Fe and Ti contents (up to 2-3% each), and the authors describe coupled substitution mechanisms similar to those inferred in this study.

### 6.3.3 Biotite, phlogopite and barian biotite.

#### Occurrence.

Biotite is widespread in metasediments of units A, C and D and in metabasites at Foss, but is seldom a major constituent (>10%) except in some unit C calc mica schists (table 4.1) and in biotitic metabasites (e.g. sample N81-43: table 5.1 and plates 42, 91). Biotite (sensu stricto) seldom coexists with more than trace amounts of iron sulphides, and is largely absent from the sulphidic graphitic schists of unit B. Pale brown coloured phlogopite occurs as a minor constituent of graphitic dolostone rocks (plate 76), of mineralized metasediments, and of some sulphidic quartz celsian rocks. A few occurrences of pyrrhotite-rich quartz phlogopite schist were noted in the upper mineralized horizons in Foss East. Strongly pleochroic, brown-green biotite was found as disseminated flakes or lamellae in several barite rocks examined (plate 94).

The low iron content of both muscovites and biotites occurring in graphitic dolostones and in many mineralized lithologies (in which other ferromagnesian silicates are usually absent), may be attributed to low effective  $\text{Fe}/(\text{Fe}+\text{Mg})$  ratios due to the partitioning of iron into sulphides during metamorphic mineral neoformation or recrystallization (cf. Mohr and Newton, 1983) (section 7.7). Iron-poor phlogopites and muscovites are characteristic of lithologies in which the abundance of iron sulphide is similar to, or greater than that of the micas. However, minor or trace amounts of

iron sulphides coexist with relatively Fe-rich micas in micaceous rocks. Micas in grain contact with iron sulphides are generally similar in composition to micas elsewhere in the same thin section, indicating the attainment of equilibrium on this scale with respect to Fe-partitioning.

#### Compositional range.

Ninety analyses were obtained of tri-octahedral micas occurring in over forty samples. This includes twenty analyses of barian biotite (with  $\geq 0.20$  Ba cations per formula unit) and an equal proportion of biotite and phlogopite analyses (with  $< 0.20$  Ba cations) (table 6.6). Tri-octahedral micas were analysed in twenty-five samples from which analyses of coexisting muscovite (or barian muscovite) were also obtained. In a number of cases, phlogopite with a low iron content (0.5–1.5 wt% FeO) was misidentified as muscovite before microprobe analyses were obtained. Note that in all analyses the total iron content is expressed as wt% FeO, but that some trivalent iron is probably present in biotite, and particularly in the green-pleochroic barian biotites associated with barite.

In all but three of the sixteen samples in which phlogopites were analysed, this mineral was found to be enriched in barium (1.7–3.4 wt% BaO). Barian biotites form a compositionally distinct group in which Fe/(Fe+Mg) ratios generally range from 0.3 to 0.5 and BaO contents range from 3.1 to 5.5 wt%. To this extent, the iron and barium contents of barium-enriched tri-octahedral micas are inter-related. Phlogopites also contain less aluminium (in both octahedral and tetrahedral sites) than Ba-poor biotites, but barian biotites have a broad range in Al content (figs. 6.14, 6.18). The significance of these relationships to substitution mechanisms in these micas are discussed below.

Unlike the di-octahedral micas, the tri-octahedral micas do not show any correlation between barium and titanium, but TiO<sub>2</sub> contents (up to 3.4 wt%) generally increase with increasing Fe/(Fe+Mg) ratio (fig. 6.15) and Al<sup>iv</sup> content (fig. 6.18). These relationships between Ti, Fe, Mg and Al<sup>iv</sup> in tri-octahedral micas are recorded in several previous studies (e.g. Robert, 1976b; Guidotti et al., 1977) and are attributed to crystallochemical factors. Relatively high Ti contents are characteristic of biotites occurring in metabasic rocks such as N81-43 and 424-8, but barian biotites found in barite rock are relatively poor in titanium (samples 3963 and G171; fig. 6.15). This indicates that the partitioning of Ti into tri-octahedral micas

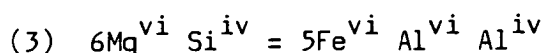
is partly controlled by bulk rock composition. This also applies to manganese and chromium: MnO contents are usually <0.2 wt%, but 0.5-0.7 wt% MnO occurs in phlogopite in sample 429-18, which also contains Mn-calcite; and 0.1-0.3 wt% Cr<sub>2</sub>O<sub>3</sub> was detected in phlogopite coexisting with fuchsite in 708-10 (table 6.6).

Other notable features of the tri-octahedral micas from Foss are their low sodium contents compared with muscovite (fig. 6.7). Both groups of micas have low calcium contents and a general deficiency in X-site occupancy (see section 6.3.2 and fig. 6.8), but the tri-octahedral micas generally contain relatively more fluorine (fig. 6.16). Fluorine substitutes for (OH)<sup>-</sup> in the interlayer site, and as commonly observed by previous authors, F contents of the tri-octahedral micas are inversely proportional to the Fe/(Fe+Mg) ratio (up to ~3.6 wt% F in phlogopite in sample 708-5B; fig. 6.16). An explanation for this phenomenon, termed 'Fe-F' avoidance (cf. Munoz, 1984), has been provided by nuclear magnetic resonance studies (Sanz, 1979). These studies indicate that OH groups are in direct coordination with Fe<sup>2+</sup> in phlogopites, whereas F ions probably form homogeneous domains and are coordinated with Mg<sup>2+</sup> ions.

#### Substitution mechanisms.

The incorporation of barium into tri-octahedral micas is by a mechanism similar to that described above (reactions 1&2) for muscovite. Barian biotites and phlogopites at Foss generally contain less Al (in both sites) and more Fe+Mg than Ba-poor biotites (fig. 6.12), and therefore differ from most phlogopites described from igneous rocks, in which higher Ba contents are correlated with increases in Al content. Natural phlogopites containing up to 20 wt% BaO and 14 wt% TiO<sub>2</sub> have been described by Mansker et al. (1979), and Ba-rich, Al-poor phlogopite is quite common in nephelinites and other undersaturated basic eruptive rocks (e.g. Velde, 1979) and in carbonatites (Gaspar and Wyllie, 1982).

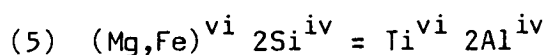
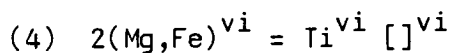
Variation in the Al content of Ba-poor tri-octahedral micas from Foss may be largely accounted for by limited solid solution between the phlogopite and siderophyllite end-members (fig. 6.14) by means of the substitution reaction:



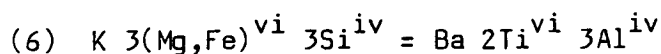
An excess of Al in most phlogopites and barium-poor biotites, which plot to the right of the phlogopite-siderophyllite line on fig. 6.14, could be explained by a greater component of the eastonitic

(tschermakitic) substitution reaction (2). Barium incorporation by substitution reaction (1) in effect counterbalances the siderophyllite substitution in barian biotites, but not to the extent that the sum of Al + Si cations falls below eight per formula unit.

Titanium solubility and substitution mechanisms in phlogopites have been investigated experimentally by Robert (1976b), and in natural occurrences by Arima and Edgar (1981). Forbes and Flower (1974) and Robert (1976a) suggest that titanium is incorporated by two substitution reactions, respectively:



Crude positive correlations between Ti content and both octahedral site cation deficiency (fig. 6.17) and  $\text{Al}^{\text{iv}}$  contents (fig. 6.18) suggest that both reactions may partly explain Ti substitution in tri-octahedral micas from Foss. Several authors (Wendlandt, 1977; Velde, 1979 and Mansker et al., 1979) have found that a combination of reactions (1), (4) and (5), such as:



(Mansker et al., op. cit.) could account for coupled variations in the chemistry of barian phlogopites. However, this scheme fails to account for the incorporation of barium and titanium into tri-octahedral micas from Foss, probably because these contain an excess of aluminium to that required to fill the tetrahedral site.

#### Altered biotites.

Dark micas in several samples examined with the microprobe were found to yield unusually low oxide totals (84-94 wt%), although these biotites are optically indistinguishable from normal biotites. This is due principally to depletion in the alkaline oxides (table 6.7). All stages are observed from the onset of alteration marked by X-site cation totals falling below 1.8, to the complete loss of K, Na and Ba from the mica structure. The loss of alkaline elements (probably replaced by  $[\text{H}_3\text{O}]^+$  ions) is generally accompanied by increases in iron content and Fe/(Fe+Mg) ratio, coupled with decreases in Al and Ti content. Dempster (1984) has observed similar chemical changes associated with the formation of hydrobiotites in paragonite-bearing schists of the Appin Group in Central Perthshire. This alteration is distinct from that which formed secondary chlorite (see part 6.4.1), and probably occurred late in metamorphism or during weathering.

The dark green coloured mica flakes, described as fuchsite by Coats et al. (1981), which occur in several samples of barite rock from BHs 1 and 2, appear to be altered barian biotites. A similar pattern of alteration (loss of K, Na, Al and Si) was noted in fuchsite (section 6.3.3).

#### 6.3.4 Compositional variations in coexisting micas.

As noted above, wide ranges in Fe:Mg ratios are found in both the di-octahedral and tri-octahedral micas examined in this study, but coexisting micas within individual samples have similar Fe/(Fe+Mg) ratios (fig. 6.14). An exception to this is sample N81-80 (see part 3.3.2), in which muscovites have highly variable Fe and Mg contents, whereas phlogopites are essentially uniform in composition. In the remaining samples examined which do not contain other ferromagnesian silicates, coexisting muscovite and biotite (or phlogopite) have Fe-Mg partition coefficients (cf. Butler, 1967) close to unity (fig. 6.19). However, in rocks containing garnet, chlorite and/or hornblende, biotites generally have higher Fe/(Fe+Mg) ratios than coexisting muscovites, and partition coefficients range from 1.3 to 1.5. This evidence for equilibration between coexisting ferromagnesian silicates at Foss is relevant to the application of Fe-Mg exchange geothermometers and barometers (Chapter 8), and supports the contention that effective bulk Fe/(Fe+Mg) ratios are controlled primarily by the partitioning of iron between sulphide and silicate phases.

Butler (1967), Guidotti (1969), Wenk (1970) and other authors have observed a general increase in the Al contents of both muscovite and biotite with increasing metamorphic grade. Wenk found that the partition coefficient,  $K_D = Al_{\text{musc}}^{\text{vi}} / Al_{\text{biot}}^{\text{vi}}$ , decreased from 14 to 3 in passing from the biotite zone into the staurolite zone in the central Alps. The similar range of  $K_D$  found in coexisting micas as Foss (fig. 6.20) clearly cannot be related to variation in the metamorphic grade. This systematic relationship is a function of the similar extents of tschermakitic substitution in coexisting micas with similar Ba contents and Fe:Mg ratios, and therefore indirectly reflects a bulk compositional control. Scatter on either side of the trend line in fig. 6.20 may be due to disequilibrium: for example, some of the muscovite in sample 207-5 is enriched in barium and is spatially associated with late metamorphic veinlets (see section 6.3.2 and plate 89).

## 6.4 Other ferromagnesian silicates and minor phases.

### 6.4.1 Chlorite.

The chemical distinction between altered biotites and chlorite,  $(\text{MgFeAl})_{12}(\text{SiAl})_8\text{O}_{20}(\text{OH})_{16}$ , has been made in the previous section. This is illustrated by a diagram of  $\text{Fe}/(\text{Fe}+\text{Mg})$  against Si cations (fig. 6.21), which is similar to that used by Hey (1954) to classify the variations in chlorite chemistry. Although the  $\text{Fe}^{3+}$  contents of chlorites have not been determined, their optical properties (green colour, anomalous birefringence colours) and paragenesis (often associated with pyrrhotite and graphite) suggest that iron is predominantly in the divalent state. The majority of the thirty chlorite grains analysed in this study, mostly in samples of chloritic metabasite and pelites from units A and D (table 6.8), are very similar in composition and lie within the ripidolite field (fig. 6.21).

Several chlorites with somewhat lower than average  $\text{Fe}/(\text{Fe}+\text{Mg})$  ratios ( $<0.4$ ) and higher Si contents (e.g. in 207-5), appear to have formed as a result of late metamorphic alteration. In general, chlorites exhibiting a variety of habits and associations (replacing garnet and hornblende, coaxial with or replacing biotite, or as coarse flakes and sprays) are compositionally uniform. This suggests that chlorites, whether primary or secondary in origin (i.e. syn- or post-metamorphic maximum), equilibrated during retrograde metamorphism. This observation is significant to the application of the biotite-muscovite-chlorite-quartz geobarometer of Powell and Evans (1983), which is discussed in part 8.3.2.

### 6.4.2 Talc.

The occurrence of talc,  $\text{Mg}_3\text{Si}_2\text{O}_5(\text{OH})_2$ , in the Foss deposit was first confirmed by XRD and microprobe analyses of samples of sulphidic and dolomitic breccia rocks from DHs 201 and 601 (part 3.2.2). Talc was subsequently identified as a minor constituent in about ten samples of various mineralized lithologies, including barite rock and quartz celsian chert, from other locations at Foss. Although some samples contain chlorite and biotite, talc was not observed in association with muscovite. Talc was also found to coexist with phlogopite, celsian and pyrite in a sample of the mineralized metabasite interlayered with barite in BH5 (Ben Eagach deposit; plate 57).

No evidence of reaction textures between quartz and dolomite were seen in talc-bearing rocks, and talc is not directly associated with calcite or apatite (cf. Thompson, 1975). It is therefore tentatively regarded as a primary constituent of these mineralized lithologies. Talc is currently precipitating at ocean-floor hydrothermal sites in the Guaymas Basin and East Pacific Rise (Lonsdale et al., 1980; Haymon and Kastner, 1981), and talc is also a common constituent of ancient massive sulphide deposits (Costa et al., 1980; Costa et al., 1983; McLeod and Stanton, 1984).

Two microprobe analyses obtained from each of four samples, show that the principal variation in talc composition is due to the partial substitution of Fe (1.6–9.7 wt% FeO) for Mg, although Mn is present in small amounts (table 6.9). The alkali oxides total <0.1 wt% in all analyses and similar amounts of  $\text{Al}_2\text{O}_3$  were also found. The oxide totals suggest that the talc contains 6.5–7.0 wt%  $\text{H}_2\text{O}$  (plus minor F). This exceeds the theoretical  $\text{H}_2\text{O}^+$  content of ~4.7 wt% and presumably indicates the presence of adsorbed water (Deer et al., 1962a, p. 227–8).

#### 6.4.3 Garnet.

Garnet is uncommon in the mineralized zone at Foss but is widespread in pelitic and quartzitic schists of units A and D (plates 72, 73, 85 & 86). It also occurs near to the margins of some chloritic metabasite beds in the Creagan Loch area (plates 30 & 90; part 5.2.2). The antipathetic relationship between the occurrence of garnet and of iron sulphides (in other than trace amounts) in the metasedimentary rocks adjacent to the deposit, was noted at early stage (part 2.2.1). This is attributed to the decrease in both effective bulk  $\text{Fe}/(\text{Fe}+\text{Mg})$  and  $f\text{O}_2$  in iron sulphide-bearing rocks, which are detrimental to the stability of garnets. Although garnet and sphalerite coexist in some detrital quartzites within unit B, lithologies of hydrothermal-exhalative origin at Foss do not contain garnet, unlike those in some high-grade metamorphosed stratabound deposits such as Gamsberg (Rozendaal, 1980), Broken Hill and Mount Misery (Stanton, 1976 and 1982).

About forty EDS analyses and one hundred WDS analyses were obtained of garnet,  $(\text{Fe},\text{Mg},\text{Mn},\text{Ca})\text{Al}_2\text{Si}_3\text{O}_{12}$ , occurring in twenty samples examined. Systematic profiles (fig. 6.23) and in one case, a compositional map (fig. 6.24), were produced for garnets in six samples. Although all garnets examined are Fe-rich (almandine), they show considerable ranges in Mn (spessartine) and Ca (grossular)



content (fig. 6.22). The total ranges of mol% end-members observed at Foss are: almandine, 50-71%; pyrope, 4.3-10.8%; spessartine, 3.9-25.1%; and grossular, 9.5-27.1%. In some samples of unit A schists individual zoned garnets exhibit almost the same range of compositions as are observed in the entire data set (e.g. N81-88: see fig. 6.22 and table 6.10). The nature of this zoning is described below.

Despite this large compositional range, garnets from the vicinity of the Foss deposit have significantly higher Mn and Ca contents than the majority of those from the Aberfeldy-Grandtully-Pitlochry areas described by Sivaprakash (1981b) (fig. 6.22 inset) and Dempster (1983). In the garnets described by these authors, Mn contents approach zero in the rims. This regional difference in rim compositions seems unlikely to reflect variations in bulk rock composition, since the average Mn contents of unit A and D pelites analysed in this study are similar to other Dalradian pelites (part 4.5.2). Higher spessartine contents in garnet have been related to formation under conditions of high  $fO_2$  (e.g. Hsu, 1968), but significant differences between metamorphic fluid compositions in unit A graphitic schists and unit D calcareous pelites are not manifested by significant differences in garnet rim composition (fig. 6.22). Therefore an adequate explanation for this areal variation in garnet rim Mn-content remains to be found.

All garnets examined have a normal (growth) zonation with relatively Mn-rich cores and (Fe+Mg)-rich rims, and Fe:Mg ratios are generally constant or decrease slightly from core to rim. Following Hollister (1966) and others, the characteristic bell-shaped Mn profiles are attributed to the strong partitioning of Mn into garnet and the corresponding depletion of Mn in the matrix during garnet growth. Garnets in the unit A pelites examined (e.g. 503-27, N81-88) have lower Ca contents, and have higher garnet-core Mn contents than are observed in garnets within unit D calcareous pelite (e.g. 429-5, N80-36: fig. 6.23). A chloritic metabasite containing a large (1cm diameter) garnet which shows static, post-D3 overgrowths on a sigmoidal garnet nucleus (sample 706-4B, plate 90), is exceptional in that the garnet is weakly zoned, although this could be due to an off-centre cross-section.

Rim compositions of garnets within individual samples were often found to show little variation on the thin section scale, which indicates that garnet rims were in equilibrium with the ferromagnesian phases in the matrix at the cessation of garnet

growth. However, exceptions to this were noted in samples N81-88 and 708-15, in which some crystal promontories were found to have lower than average rim values for Mn (fig. 6.22), perhaps due to continued garnet growth at these restricted points. Another exception is IGS 4685, in which the zonation is reversed within 100 $\mu$ m of the garnet rim (fig. 6.23c). In previous studies of metamorphic garnets (e.g. Grant and Weiblen, 1971; de Bethune et al., 1975), reverse zonation at garnet rims has been attributed to retrograde resorption. However, the garnets in 4685 have euhedral outlines and show no sign of resorption in the thin section examined. Retrograde, garnet-matrix cation exchange (such as suggested by Yardley, 1977) may therefore explain this reverse zonation. Three analyses of garnet rims in sample 503-10 have a range of Fe:Mg ratios which gives rise to an L-shaped trend on fig. 6.22. The replacement of garnet by chlorite observed in this sample suggests that this trend could be explained by the retrograde formation of a more Fe-rich garnet due to the growth of the more Mg-rich chlorite (Tracy, 1982).

The grossular content of the garnets examined does not show a consistent core to rim pattern (fig. 6.24), although more often than not, garnets have more calcic cores (e.g. 503-27 and 4685). In other samples, the intermediate zones of garnet are relatively poor in Ca (706-48), or Ca contents are markedly irregular (e.g. unit D samples, 429-5 and N80-36). All rocks containing garnet also contain plagioclase, and with the exception of some unit A pelites (e.g. N81-88), also contain dolomite and/or calcite (table 4.1). Fluctuations in the uptake of calcium by growing garnet crystals may therefore be related to variations in the composition of coexisting plagioclase (cf. Crawford, 1974 and 1977) or possibly to silicate-carbonate reactions. As noted in part 6.2.1, coexisting albite and oligoclase, outlining the peristerite gap, were found in 429-5 and probably also occur in N80-36. The Ca zonation patterns in garnets in these two samples are similar and presumably reflect identical growth and reaction histories possibly involving discontinuous changes in plagioclase composition (cf. Crawford, 1974 and Sivaprakash, 1981b).

Sivaprakash (1981b), Tracy (1982) and others have used information on the distribution and composition of mineral inclusions in zoned garnets to elucidate the prograde and retrograde reactions involving garnet. The compositions of garnet inclusions were not examined in detail in this study, but petrographic observations

relevant to garnet-forming reactions are summarized here. Whereas ilmenite is very common as inclusions in garnet (plate 90), rutile and sphene are rare, although these phases may occur together with ilmenite in the matrix of calcareous pelites and metabasites. In some rocks ilmenite is present only as inclusions in garnet and is absent from the matrix (e.g. sample 503-27). Chlorite, muscovite and plagioclase were not observed as inclusions in garnet, although biotite inclusions are occasionally seen (plate 86). In the metabasite 706-48 (plate 90), calcite and dolomite are abundant in the matrix but only dolomite is present within the garnet porphyroblast. Quartz and apatite inclusions are ubiquitous in garnet and are generally finer grained than in the matrix.

Continuous reactions involving the growth of garnet which are consistent with these observations have been described by Sivaprakash (1981b). These have chlorite, muscovite and quartz as reactants (plus ilmenite or plagioclase), and have garnet, biotite and  $H_2O$  as products (plus rutile or a plagioclase of a more albitic composition). A fourth reaction might include calcite as an additional component in the reactants, with  $CO_2$  as an additional product, i.e.  $chlorite + muscovite + quartz + calcite = garnet + biotite + dolomite + H_2O + CO_2$ .

#### 6.4.4 Hornblende.

Core and rim compositions of hornblende crystals were analysed in three samples of unit D calcareous pelite and in one chloritic amphibolite (N80-13) (table 6.11). In each case the hornblende is weakly zoned with relatively ferroan and aluminous cores, but rim compositions adjacent to ferromagnesian phases in the matrix are similar within individual samples and between the three unit D samples. Hornblende in the metabasite is somewhat more magnesian and less aluminous than hornblende in the metasediments, but both contain similar amounts of Ti, Mn, Na and K. In terms of end-member classification, the hornblendes lie near to pargasite,  $NaCa_2(Fe,Mg)_4Al_3Si_6O_{22}(OH)_2$ , but have a significant amount (20-30%) of the tschermakite end-member  $Ca_2(Fe,Mg)_3Al_4Si_6O_{22}(OH)_2$  (Deer et al., 1966). As such, the hornblendes are typical of the garnet zone of the Scottish Dalradian (Graham, 1974).

#### 6.4.5 Epidote group minerals.

Several EDS and WDS analyses were obtained of clinozoisite-epidote group minerals occurring in three unit D calcareous mica schist samples and in two metabasite samples (table 6.12). The name 'clinozoisite' is used for the monoclinic, optically positive and iron-poor members of the series  $\text{Ca}_2\text{Al}_3\text{Si}_3\text{O}_{12}(\text{OH})$  -  $\text{Ca}_2\text{Fe}^{3+}\text{Al}_2\text{Si}_3\text{O}_{12}(\text{OH})$ . The epidote group minerals in two of the unit D samples examined (N80-36 and 4685) have optical properties which are characteristic of clinozoisite (including anomalous blue interference colours), but nevertheless contain appreciable amounts of iron (8-10 wt%  $\text{Fe}_2\text{O}_3$ , assuming all Fe to be trivalent). These analyses also indicate a significant MnO content (typically 0.3 wt%). In the third unit D sample (602-1A; plate 87) and in the metabasites (N80-45 and N80-13; plate 88), the pale yellow-green colour and negative optic sign of the epidote group minerals, together with their higher iron content (11-12.5 wt%  $\text{Fe}_2\text{O}_3$ ), indicates that the name 'epidote' is appropriate in these cases (Deer et al., 1962c). Core and rim analyses confirm that the zoning in birefringence colours, observed in clinozoisite and epidote prisms in all samples examined, is due to an outward decrease in iron content (typically of 0.6%  $\text{Fe}_2\text{O}_3$ ).

A 5mm diameter, yellow-brown coloured crystal with a central twin plane and opaque dendritic inclusions, which occurs in a sulphide-banded quartzite (sample G59A; Appendix B), was identified as allanite by microprobe analysis (table 6.12). It contains unusually large amounts of lanthanum, neodymium and praseodymium in addition to cerium, and these trivalent ions together with some magnesium substitute for calcium in the epidote structure. The absence or very low concentration of radioactive components such as Th and U is suggested by the lack of metamict alteration of the allanite crystal. Although recrystallized during metamorphism, this is presumably a detrital mineral which ultimately derives from a granitic source.

#### 6.4.6 Tourmaline and sphene.

The borosilicate tourmaline is a widespread but usually very minor phase in metasedimentary rocks at Foss. It is considered to be a metamorphic mineral stabilized by boron released from clay minerals (cf. Reynolds, 1965), or in some instances may be recrystallized detrital tourmaline. Stratabound tourmaline such as that associated with several massive sulphide deposits in the

Appalachian-Caledonian belt (Slack, 1982), is not developed in the Aberfeldy deposits.

Partial analyses of tourmaline (by EDS and WDS techniques) in ten samples indicate that its compositional variation is largely due to varying proportions of the Fe and Mg end-members, schorl and dravite respectively (table 6.13). The molecular proportion of dravite in Foss tourmaline is typically 70% but the range observed is 56-81%. Tourmaline in a sample of unit A semi-pelite, N81-88, has a high dravite content and is also comparatively rich in Ti (~1 wt%  $\text{TiO}_2$ ) and Ca (1.3-1.5 wt%  $\text{CaO}$ , compared with 0.3-0.7% in other analyses). This variation is presumably due to element partitioning between tourmaline and other phases such as plagioclase, micas, garnet and titanium oxides. Typically, tourmalines are zoned with more magnesian cores than rims, and abrupt compositional changes are indicated by concentric colour changes (pale green to green-brown). Similar features have been noted in other metamorphic tourmalines by Tracy (1982).

Sphene, ideal composition  $\text{CaTiSiO}_4(0,0\text{H},\text{F})$ , occurs as an accessory phase in some Ben Lawers Schists and metabasites (tables 4.1, 5.1). It was analysed in two samples, C79-34 and N80-36 (table 6.13 and Appendix B). It contains 2.8-3.4 wt%  $\text{Al}_2\text{O}_3$  and 0.5-1.1 wt%  $\text{Fe}_2\text{O}_3$  (recalculated assuming all Fe is trivalent), and therefore may be the variety 'grothite' referred to by Deer et al. (1962c). The iron content is consistent with the light to dark brown colour of the sphene. The analyses also show the presence of some fluorine (0.4-0.6%).

#### 6.4.7 Baoite.

This mineral, the composition of which closely approximates to  $\text{Ba}(\text{Ti},\text{Fe})_2\text{SiO}_7(\text{Cl},\text{F})$ , was discovered as two tiny inclusions (about 10 by 15  $\mu\text{m}$ , and less than the thickness of the polished rock slice) in coarse pyrite crystals in a sample of sulphidic barite rock, 203-18 (table 6.14). The high  $\text{BaO}$  and  $\text{TiO}_2$  contents (each about 40 wt%) of the phase necessitated the use of collimator slits to increase spectrometer resolution, and the absorption coefficients of Theisen and Vollath (1967) were used in preference to those of Heinrich (1966) (see Appendix E). Al, Cr, Mn, Ca, K, S and the rare earth elements were looked for but not found, and very small amounts of Mg and Na were detected in each of the grains respectively.

The mineral formula, based on seven oxygens, is similar to that of the niobium-bearing Ba-Ti silicate named Pao-T'ou-K'uang or

baoite. This rare mineral is unusual in having a metasilicate ring,  $\text{Si}_4\text{O}_{12}$  (Fleischer, 1961). It has been observed in a sulphidic quartz vein in Outer Mongolia (Fleischer and Chao, 1960) and in a carbonate vein containing barite, in Montana, U.S.A. (Heinrich et al., 1962) (analysis reproduced in table 6.14). The occurrence at Foss, albeit as minute inclusions which are probably too small to characterize by XRD, is a new mineral species for the British Isles and may represent the titanium end-member of a Ti-Nb substitution series in baoite.

## 6.5 Summary.

### Feldspars and cymrite.

In the samples studied, plagioclase and ternary Ba-K-Na feldspars form discrete and occasionally coexisting phases, with no detectable Ba in the former or Ca in the latter. Continuous solid solution is indicated by the range of compositions in both series ( $\text{An}_{0.1}$  -  $\text{An}_{23}$ ,  $\text{Cn}_{25}$  -  $\text{Cn}_{97}$ ), although some samples contain coexisting albite and oligoclase (defining the peristerite solvus), and others contain both celsian and hyalophane (plates 57 and 81). Variations in plagioclase composition are not clearly related to differences in bulk composition or mineral assemblages. However, K/Na ratios in the barium feldspars (range, 2-11) are generally constant on a decimetric scale and may reflect the averaging of bulk compositional heterogeneity by infiltrating metamorphic fluids, which have produced complex zoning in some hyalophane crystals. Cymrite, which is more widespread than previously recognized at Foss, also contains K and Na as minor but essential components. K/Na ratios vary from 2-9 and reliable analyses indicate that cymrite contains 94-97 mol% of the  $\text{BaAl}_2\text{Si}_2\text{O}_8 \cdot \text{H}_2\text{O}$  end-member.

### Micas.

Within individual sections, muscovite and/or biotite grains each show little variation in composition, although large compositional variations are evident between different lithologies. Barium-poor muscovite generally contains 7-16 mol% of the paragonite end-member. Barian muscovites commonly contain less sodium than Ba-poor muscovites, but show a broader range of phengitic substitution and typically have higher Mg:Fe ratios and Ti contents. Muscovite coexisting with barium feldspar contains up to 10.6 wt% BaO. Chromium-rich barian muscovites, analysed in seven samples,

contain up to 15.7% BaO and 9.3% Cr<sub>2</sub>O<sub>3</sub>, and one sample of barite rock contains a di-octahedral Cr-V-Ba mica with up to 10.8% V<sub>2</sub>O<sub>3</sub>. Many of the barian fuchsites, including those with the highest Cr and Ba contents, are depleted in Al (plus Si, Na and F) and appear to have been altered since crystallization. Similar alteration has affected biotites in several barite rocks examined.

Phlogopite, a common minor constituent of sulphidic lithologies, contains 1.7 - 3.4 wt% BaO, whereas up to 5.5% BaO (and 3.4% TiO<sub>2</sub>) occurs in barian biotites which are found in several sulphide-poor mineralized lithologies. Both phlogopite and barian biotite are generally less aluminous than the Ba-poor biotites which occur in pelitic and metabasic lithologies. Barium substitution in the interlayer site is charge-compensated by tschermakitic substitution, resulting in higher Fe+Mg contents. Ti contents are dependant on bulk composition, but the saturation level increases with increasing Fe content. Titanium substitution is coupled with increases in both Al<sup>iv</sup> content and octahedral site cation deficiencies. Except in samples with textural evidence of disequilibrium, coexisting muscovite and biotite have closely correlated Al<sup>vi</sup> contents and similar Fe/(Fe+Mg) ratios, although consistently higher values for this ratio are observed in biotite in rocks containing additional ferromagnesian silicates such as chlorite.

#### Other silicates.

Chlorite is common in a variety of lithologies and textural associations, but has a restricted compositional range within the ripidolite field. This suggests that chlorite of both primary and secondary origin re-equilibrated during retrograde metamorphism. However, chlorites formed during late-metamorphic reactions have lower Fe:Mg and Al:Si ratios. Several lithologies in the mineralized strata at Foss contain major or minor amounts of talc, which is regarded as a primary constituent. It contains up to 10 wt% FeO.

Garnets which occur in metasediments and in some metabasites at Foss are generally almandine-rich, but have notably higher spessartine and grossular contents than most garnets previously described from central Perthshire. The garnets are zoned with typical bell-shaped Mn profiles, but garnets in unit A lithologies are generally smaller in size and have higher Mn and lower Ca contents than those in unit D lithologies. Radial fluctuations in Ca contents in some unit D garnets may be related to the development of the peristerite solvus in coexisting plagioclase. Garnet rim compositions often show little variation within samples, but

exceptions may be attributed to localized extensions of garnet growth or to retrograde cation exchange with other ferromagnesian silicates. The mineralogy of inclusions in garnets are consistent with prograde garnet-forming reactions involving chlorite, muscovite, quartz,  $\pm$  ilmenite  $\pm$  plagioclase  $\pm$  carbonates.

Hornblende in an amphibolite sample is slightly more magnesian and less aluminous than hornblende porphyroblasts in the calcareous pelites examined. The hornblendes are pargasitic with a significant tschermakite content and are weakly zoned with Fe- and Al-enriched cores. Clinozoisite with 8-10 wt%  $\text{Fe}_2\text{O}_3$  occurs in unit D schists, but higher iron contents and optical properties justify using the name epidote for this phase occurring in some metabasites and in one epidote-rich schist examined. One quartzite sample contains a 5mm crystal of allanite, which is presumably of detrital origin. Tourmaline is widespread as an accessory phase (<1%) in Foss metasediments: it is dravite (Mg)-rich and zoned with more ferroan rims. Sphene analysed in two samples of Ben Lawers Schist was found to be enriched in Al and Fe.

Baoite,  $\text{Ba}(\text{Ti},\text{Fe})_2\text{SiO}_7(\text{Cl},\text{F})$ , was discovered as tiny inclusions in one sample (203-18) of sulphidic barite rock. The Foss occurrence may represent the Ti end-member of a Ti-Nb substitution series in this very rare mineral.



Abbreviations in tables of microprobe analyses.

The analysis number (or occasionally, letter) follows the sample name and is separated from it by a comma (,); sample locations and brief descriptions are tabulated in Appendix B. Following the analysis number, C indicates grain core, R grain rim, and I an intermediate location. Several analyses obtained from individual grains may be labelled A1, A2, B1, B2, etc. Text following the analysis name provides a brief description of the phase type, location or textural association (adj, adjacent to; enc, enclosed within; ex, external to; nr, near to).

Elements not detected and elements not determined are both indicated by nd; refer to table E.1 for list of elements normally looked for in each phase. All analyses were obtained by wavelength-dispersive spectrometry, except for talc analyses headed E in table 6.9 which were obtained by the energy-dispersive technique (Appendix E.1).

Cation ratios:

Y-site =  $(Al^{VI} + Fe + Mg + Mn + Ti + Cr + V)$

X-site =  $(Ca + Na + K + Ba)$

F/FM =  $Fe / (Fe + Mg)$

Others are explained on the relevant tables.

TABLE 6.1: SELECTED PLAGIOCLASE ANALYSES.

	1	2	3	4	5	6	7	8
SiO2	67.33	69.68	64.08	65.54	68.63	63.88	62.79	64.79
Al2O3	20.74	19.69	21.89	20.98	19.50	22.51	22.74	22.03
FeO	0.02	nd	nd	0.01	0.08	nd	0.09	nd
MgO	0.01	0.02	nd	nd	0.01	nd	0.01	0.02
CaO	1.50	0.04	2.92	1.71	0.14	3.39	4.07	3.05
Na2O	11.21	11.85	10.34	11.05	11.92	9.82	9.36	9.90
K2O	0.08	0.08	0.07	0.07	0.06	0.10	0.08	0.09
BaO	nd	0.05	0.02	0.01	0.06	nd	nd	nd
total=	100.89	101.41	99.32	99.37	100.40	99.70	99.14	99.88
Si	11.72	12.00	11.39	11.60	11.96	11.31	11.20	11.42
Al	4.25	4.00	4.58	4.38	4.01	4.70	4.78	4.58
Fe2	-	-	-	-	0.01	-	0.01	-
Ca	0.28	-	0.56	0.32	0.03	0.64	0.78	0.58
Na	3.78	3.96	3.56	3.79	4.03	3.37	3.24	3.38
K	0.02	0.02	0.02	0.02	0.01	0.02	0.02	0.02
total=	20.06	19.99	20.11	20.11	20.06	20.04	20.03	19.99
oxygens=	[32]	[32]	[32]	[32]	[32]	[32]	[32]	[32]
An%	6.86	0.19	13.45	7.85	0.64	15.93	19.29	14.47
1 N81-88,1 ALB REPL MU								
2 N80-2,1 ALB								
3 G13,AC OLIG CORE								
4 G13,AR ALBITE RIM								
5 207-5,1 ALB								
6 429-11,1 OLIGO								
7 N82-A21,1 CALCIC CORE ZONED OLIGO								
8 G59A,1 OLIGO LEAST ALTERED								
	9	10	11	12				
SiO2	67.38	62.14	62.86	66.60				
Al2O3	20.38	24.10	22.94	19.87				
FeO	0.04	0.10	0.07	0.09				
MgO	0.01	nd	0.02	nd				
CaO	0.40	4.85	3.78	0.92				
Na2O	11.55	9.04	9.56	11.47				
K2O	0.07	0.09	0.06	0.05				
BaO	nd	0.02	nd	nd				
total=	99.83	100.34	99.29	99.00				
Si	11.81	10.99	11.19	11.80				
Al	4.21	5.02	4.81	4.15				
Fe2	-	0.01	0.01	0.01				
Ca	0.08	0.92	0.72	0.17				
Na	3.93	3.10	3.30	3.94				
K	0.02	0.02	0.01	0.01				
total=	20.05	20.06	20.06	20.10				
oxygens=	[32]	[32]	[32]	[32]				
An%	1.87	22.75	17.87	4.23				
9 429-5,3 ALBITE+QTZ PATCH								
10 429-5,5 OLIGO ADJ ALB+MUSC+BIOT								
11 4685,2 OLIGO CORE								
12 N80-13,2 ALB ADJ CC								

$$\text{An\%} = 100 \cdot \text{Na} / (\text{Ca} + \text{Na} + \text{K})$$

TABLE 6.2: SELECTED BARIUM-POTASSIUM FELDSPAR ANALYSES.

	1	2	3	4	5	6	7	8	9	10
SiO <sub>2</sub>	59.30	47.29	40.84	31.98	51.93	49.37	46.87	49.77	38.62	46.41
Al <sub>2</sub> O <sub>3</sub>	19.75	23.43	25.41	27.76	22.42	23.16	23.50	22.39	25.42	23.43
FeO	0.02	0.01	0.02	0.16	nd	nd	nd	0.01	0.09	0.09
MgO	0.02	0.02	0.02	0.04	0.03	0.04	0.04	0.04	0.06	0.04
CaO	nd	nd	nd	0.02	nd	nd	nd	nd	0.04	nd
Na <sub>2</sub> O	0.06	0.56	0.39	0.12	1.57	1.27	1.10	1.52	0.66	1.38
K <sub>2</sub> O	13.46	7.30	4.25	0.35	7.63	6.67	6.08	7.20	2.72	5.94
BaO	5.77	22.01	30.93	41.34	17.95	21.64	24.04	18.92	32.75	23.18
total=	98.38	100.63	101.88	101.77	101.53	102.14	101.63	99.86	100.36	100.48
Si	11.54	10.10	9.21	7.89	10.59	10.28	10.02	10.43	8.98	10.00
Al	4.53	5.90	6.76	8.07	5.39	5.68	5.92	5.53	6.97	5.95
Fe <sub>2</sub>	-	-	-	0.03	-	-	-	-	0.02	0.02
Mg	-	-	-	0.01	0.01	0.01	0.01	0.01	0.02	0.01
Na	0.02	0.23	0.17	0.06	0.62	0.51	0.46	0.62	0.30	0.58
K	3.34	1.99	1.22	0.11	1.98	1.77	1.66	1.93	0.81	1.63
Ba	0.44	1.84	2.73	3.99	1.43	1.76	2.01	1.55	2.98	1.96
total=	19.88	20.06	20.11	20.17	20.02	20.02	20.08	20.07	20.08	20.14
oxygen=	[32]	[32]	[32]	[32]	[32]	[32]	[32]	[32]	[32]	[32]
Y-site	8.076	8.003	7.979	7.999	7.984	7.974	7.952	7.977	7.989	7.970
X-site	3.803	4.062	4.129	4.167	4.038	4.047	4.126	4.098	4.095	4.166
K/Na	140.33	8.549	7.081	1.920	3.205	3.468	3.645	3.111	2.727	2.830
Cn	0.116	0.453	0.662	0.958	0.355	0.436	0.488	0.379	0.729	0.469
1	3917, 2R Ba-orthoclase			5	N81-80, G3 Hyalophane			9	4330, 5C K-cel core	
2	3917, 2C Hyalophane			6	N81-80, G4 Hyalophane			10	4330, 5R Hyal rim	
3	3917, 4CI Hyalophane			7	N81-80, H1 Hyalophane					
4	3917, 6C Celsian			8	4330, 4 Hyalophane					
	11	12	13	14	15	16	17	18	19	20
SiO <sub>2</sub>	33.60	53.41	39.04	35.49	50.29	42.43	33.35	45.74	51.53	32.51
Al <sub>2</sub> O <sub>3</sub>	26.65	21.94	25.44	26.32	22.74	24.55	26.68	23.58	22.13	26.74
FeO	nd	0.03	nd	0.13	0.06	0.20	0.24	0.02	0.05	0.23
MgO	0.02	0.02	0.01	0.02	0.02	0.04	0.02	nd	0.02	0.02
CaO	0.00	nd	nd	0.03	0.03	0.01	nd	nd	nd	0.03
Na <sub>2</sub> O	0.24	1.60	0.67	0.39	1.69	0.33	0.11	1.02	1.28	0.17
K <sub>2</sub> O	0.90	8.63	2.81	1.43	6.99	4.48	0.33	5.99	8.40	0.61
BaO	38.75	15.34	32.82	37.15	18.76	30.44	40.79	23.82	17.25	40.88
total=	100.16	100.98	100.79	100.95	100.59	102.48	101.50	100.17	100.66	101.18
Si	8.25	10.77	9.03	8.51	10.43	9.46	8.19	9.93	10.60	8.06
Al	7.71	5.21	6.93	7.43	5.56	6.45	7.72	6.04	5.36	7.81
Fe <sub>2</sub>	-	-	-	0.03	0.01	0.04	0.05	-	-	0.05
Mg	-	-	-	-	-	0.01	-	-	-	-
Na	0.11	0.63	0.30	0.18	0.68	0.14	0.05	0.43	0.51	0.08
K	0.28	2.22	0.83	0.44	1.85	1.27	0.10	1.66	2.20	0.19
Ba	3.73	1.21	2.97	3.49	1.52	2.66	3.92	2.03	1.39	3.97
total=	20.09	20.05	20.07	20.09	20.06	20.03	20.03	20.09	20.08	20.17
oxygen=	[32]	[32]	[32]	[32]	[32]	[32]	[32]	[32]	[32]	[32]
Y-site	7.968	7.992	7.967	7.975	7.999	7.953	7.957	7.976	7.975	7.921
X-site	4.125	4.058	4.102	4.110	4.062	4.075	4.075	4.115	4.101	4.253
K/Na	2.489	3.546	2.772	2.432	2.715	8.816	1.986	3.857	4.330	2.350
Cn	0.903	0.298	0.725	0.849	0.375	0.652	0.962	0.492	0.339	0.933
11	4080, 1R Celsian			16	3920, C1 Hyal rim					
12	N80-2, 3 Hyalophane			17	3920, C2 Celsian core					
13	C79-30, D1 K-celsian			18	3966, B1 Hyal rim					
14	705-17A, B1 K-celsian core			19	3966, O2 Hyal rim					
15	705-17A, B2 Hyal rim			20	429-18, B Celsian					

$$Cn = Ba / (Na + K + Ba)$$

TABLE 6.2 (continued): SELECTED BARIUM-POTASSIUM FELDSPAR ANALYSES.

	21	22	23	24	25	26	27	28	29	30
SiO <sub>2</sub>	51.80	41.37	39.05	37.37	37.15	35.29	49.48	48.77	52.36	33.21
Al <sub>2</sub> O <sub>3</sub>	21.58	24.37	25.15	25.74	25.43	26.80	23.51	23.38	22.24	27.59
FeO	0.01	0.02	nd	nd	0.12	nd	nd	0.02	0.06	0.02
MgO	nd	0.01	0.02	0.02	0.03	0.03	0.03	nd	0.02	0.05
CaO	nd	nd	0.01	0.02	nd	0.01	nd	0.02	0.01	nd
Na <sub>2</sub> O	0.83	0.49	1.10	0.90	0.49	0.34	1.17	1.59	1.73	0.21
K <sub>2</sub> O	9.10	4.46	2.54	1.96	2.36	1.06	6.23	6.52	7.98	0.65
BaO	16.48	30.05	31.81	33.97	34.32	39.03	22.80	20.43	15.73	39.51
total=	99.81	100.78	99.67	99.98	99.89	102.55	103.22	100.74	100.12	101.24
Si	10.71	9.39	9.07	8.81	8.82	8.41	10.24	10.23	10.67	8.09
Al	5.26	6.52	6.89	7.15	7.11	7.53	5.73	5.78	5.34	7.92
Fe <sub>2</sub>	-	-	-	-	0.02	-	-	-	0.01	-
Mg	-	-	-	-	-	-	-	-	-	0.02
Na	0.33	0.22	0.50	0.41	0.23	0.16	0.47	0.65	0.68	0.10
K	2.40	1.29	0.75	0.59	0.71	0.32	1.64	1.74	2.07	0.20
Ba	1.33	2.67	2.90	3.14	3.19	3.64	1.85	1.68	1.26	3.77
total=	20.03	20.10	20.11	20.11	20.09	20.07	19.95	20.08	20.04	20.10
oxygen=	[32]	[32]	[32]	[32]	[32]	[32]	[32]	[32]	[32]	[32]
Y-site	7.964	7.920	7.964	7.970	7.965	7.944	7.985	8.008	8.025	8.032
X-site	4.068	4.182	4.146	4.144	4.129	4.123	3.964	4.073	4.016	4.070
K/Na	7.182	5.945	1.520	1.428	3.171	2.071	3.501	2.691	3.029	2.018
Cn	0.328	0.639	0.698	0.757	0.773	0.883	0.466	0.412	0.313	0.926
21	429-18,01 Hyal core				26	G1000,2C K-cel core				
22	429-18,02 Hyal rim				27	G1000,2R Hyal sheath				
23	G114A,1 K-cel core				28	G119A,3 Large hyal				
24	G114A,2 K-cel rim				29	G119A,4 Small hyal				
25	705-20,3 K-celsian				30	702-3,2 Cel replacing cymrite				

	31	32	33	34	35	36	37	38	39	40
SiO <sub>2</sub>	48.34	39.04	54.08	49.19	32.76	47.34	32.93	50.68	47.54	34.96
Al <sub>2</sub> O <sub>3</sub>	22.83	25.18	20.92	22.40	26.74	23.19	26.84	22.98	23.65	27.30
FeO	nd	0.02	0.04	0.11	0.04	0.02	0.12	nd	0.02	nd
MgO	0.02	0.02	0.01	0.02	0.04	0.02	0.01	0.01	0.02	0.04
CaO	nd	nd	nd	0.01	nd	nd	0.01	nd	0.02	0.01
Na <sub>2</sub> O	1.33	0.73	1.62	1.41	0.19	1.34	0.30	0.84	0.76	0.17
K <sub>2</sub> O	6.82	2.77	9.49	7.25	0.40	6.09	0.53	8.35	6.88	0.83
BaO	20.68	32.68	12.96	19.13	40.14	21.93	39.66	18.52	22.20	39.00
total=	100.02	100.43	99.11	99.52	100.31	99.92	100.41	101.38	101.09	102.31
Si	10.26	9.06	10.96	10.38	8.12	10.13	8.13	10.44	10.09	8.34
Al	5.71	6.89	5.00	5.57	7.82	5.85	7.81	5.58	5.92	7.67
Fe <sub>2</sub>	-	-	-	0.02	-	-	0.03	-	-	-
Mg	-	-	-	-	0.01	-	-	-	-	0.01
Na	0.55	0.33	0.64	0.58	0.09	0.56	0.14	0.34	0.31	0.08
K	1.85	0.82	2.45	1.95	0.13	1.66	0.17	2.19	1.86	0.25
Ba	1.72	2.97	1.03	1.58	3.90	1.84	3.84	1.49	1.85	3.64
total=	20.08	20.07	20.08	20.10	20.08	20.05	20.12	20.04	20.04	19.99
oxygen=	[32]	[32]	[32]	[32]	[32]	[32]	[32]	[32]	[32]	[32]
Y-site	7.973	7.953	7.968	7.982	7.962	7.992	7.970	8.016	8.014	8.021
X-site	4.112	4.119	4.116	4.114	4.113	4.060	4.148	4.023	4.025	3.973
K/Na	3.370	2.502	3.862	3.374	1.402	2.990	1.180	6.533	5.979	3.324
Cn	0.418	0.721	0.250	0.384	0.948	0.453	0.925	0.371	0.459	0.916
31	505-19,4C Hyal core				36	708-4,2C Hyalophane				
32	505-19,4R K-cel rim				37	708-4,3C Cel replacing cymrite				
33	424-8,1C Hyal core				38	708-10,1C Hyal core				
34	424-8,1R Hyal rim				39	708-10,1R Hyal rim				
35	504-8,4 Celsian				40	708-10,3C Cel core with hyal rim				



TABLE 6.3: SELECTED CYMRITE ANALYSES.

	1	2	3	4	5	6	7	8	9	10
SiO <sub>2</sub>	30.69	31.43	31.51	30.57	31.00	30.99	30.97	31.65	31.01	31.49
Al <sub>2</sub> O <sub>3</sub>	25.55	25.47	26.07	25.24	25.89	25.10	25.51	25.87	25.70	25.99
FeO	0.14	0.31	0.16	0.17	0.47	0.78	0.16	0.24	nd	nd
MgO	0.04	0.05	0.06	0.04	0.02	0.02	nd	0.09	0.05	nd
CaO	0.01	nd	0.04	0.01	0.02	nd	nd	nd	0.01	0.04
Na <sub>2</sub> O	0.13	0.11	0.08	0.11	0.09	0.08	0.07	0.10	0.12	0.10
K <sub>2</sub> O	0.24	0.55	0.34	0.21	0.32	0.39	0.37	0.49	0.39	0.23
BaO	38.69	38.31	38.49	38.15	38.73	37.90	38.15	38.53	38.09	39.22
total=	95.50	96.23	96.75	94.51	96.55	95.27	95.23	96.96	95.36	97.08
Si	8.04	8.13	8.08	8.07	8.02	8.11	8.09	8.11	8.08	8.09
Al	7.89	7.77	7.88	7.86	7.90	7.75	7.86	7.81	7.89	7.87
Fe <sub>2</sub>	0.03	0.07	0.03	0.04	0.10	0.17	0.03	0.05	-	-
Mg	0.02	0.02	0.02	0.02	-	-	-	0.03	0.02	-
Ca	-	-	0.01	-	-	-	-	-	-	0.01
Na	0.06	0.06	0.04	0.06	0.05	0.04	0.04	0.05	0.06	0.05
K	0.08	0.18	0.11	0.07	0.11	0.13	0.12	0.16	0.13	0.08
Ba	3.97	3.88	3.87	3.95	3.92	3.89	3.91	3.87	3.89	3.95
total=	20.09	20.10	20.05	20.06	20.11	20.10	20.06	20.09	20.07	20.04
oxygen=	[32]	[32]	[32]	[32]	[32]	[32]	[32]	[32]	[32]	[32]
Y-site	7.973	7.983	8.023	7.984	8.025	8.040	7.989	8.011	7.991	7.957
X-site	4.117	4.121	4.027	4.079	4.083	4.059	4.066	4.075	4.080	4.084
K/Na	1.243	3.242	2.851	1.234	2.231	3.078	3.381	3.344	2.191	1.556
Cn	0.964	0.942	0.960	0.968	0.961	0.958	0.961	0.949	0.953	0.966
1	504-8,1 Cymrite			6 3917,82 Cymrite						
2	504-8,3 Cymrite enc pyrite			7 410-27,5 Cymrite						
3	504-5,2 Cymrite			8 705-22A,2 Cymrite						
4	N80-30A,2 Cymrite			9 503-3,C Cymrite						
5	3920,2 Cymrite			10 705-27,4 Cymrite						

$$Cn = Ba / (Na + K + Ba)$$









TABLE 6.5: BA-CR- AND BA-V-CR MUSCOVITES.

	1	2	3	4	5	6	7	8	9
SiO <sub>2</sub>	40.53	33.94	42.42	37.29	45.35	36.66	46.39	40.79	42.90
TiO <sub>2</sub>	1.28	1.32	1.45	0.75	0.88	0.70	1.10	1.12	1.07
Al <sub>2</sub> O <sub>3</sub>	26.30	18.42	27.21	16.41	31.13	16.59	27.95	27.74	30.86
Cr <sub>2</sub> O <sub>3</sub>	4.19	4.60	0.45	9.27	0.63	5.15	0.98	3.39	0.50
FeO	0.38	0.25	0.35	3.09	0.47	2.30	0.51	0.37	0.36
MnO	0.07	0.08	0.04	0.16	0.04	0.04	0.02	0.06	nd
MgO	2.62	2.14	3.31	1.44	2.11	1.55	3.82	2.64	3.11
Na <sub>2</sub> O	0.25	0.15	0.24	0.09	0.31	0.10	0.11	0.33	0.39
K <sub>2</sub> O	5.82	4.78	7.86	6.42	9.43	6.10	8.73	5.89	6.70
BaO	11.48	15.70	8.34	11.02	3.50	11.13	6.27	11.55	9.97
total=	92.92	81.38	91.67	85.94	93.85	80.32	95.88	93.88	95.86
F	0.05	nd	0.23	0.07	0.14	nd	0.22	0.10	0.20
Si	6.06	6.19	6.25	6.36	6.27	6.59	6.41	6.01	6.05
Ti	0.14	0.18	0.16	0.10	0.09	0.09	0.11	0.12	0.11
Al	4.63	3.96	4.72	3.30	5.07	3.51	4.55	4.82	5.13
Cr	0.50	0.66	0.05	1.25	0.07	0.73	0.11	0.40	0.06
Fe <sub>2</sub>	0.05	0.04	0.04	0.44	0.05	0.35	0.06	0.05	0.04
Mn	-	0.01	-	0.02	-	-	-	-	-
Mg	0.58	0.58	0.73	0.37	0.43	0.42	0.79	0.58	0.65
Na	0.07	0.05	0.07	0.03	0.08	0.03	0.03	0.09	0.11
K	1.11	1.11	1.48	1.40	1.66	1.40	1.54	1.11	1.20
Ba	0.67	1.12	0.48	0.74	0.19	0.78	0.34	0.67	0.55
total=	13.82	13.90	13.98	13.99	13.94	13.91	13.93	13.86	13.90
oxygens=	[22]	[22]	[22]	[22]	[22]	[22]	[22]	[22]	[22]
Y-site	3.971	3.619	3.954	3.827	4.001	3.695	4.027	3.986	4.040
X-site	1.854	2.285	2.026	2.161	1.936	2.216	1.907	1.869	1.862
F/FM	0.075	0.062	0.056	0.546	0.111	0.454	0.070	0.073	0.061
1 G114A,5 FUCHSITE					6 705-28,1 ALTERED BA-FUCHSITE				
2 G100E,1 DK GREEN FUCHSITE					7 708-10,2 FUCHSITE				
3 G100E,2 SMALL PALE GREEN FUCHSITE					8 703-9,1 GREEN FUCHSITE				
4 505-14,1 DK GREEN FUCHSITE					9 703-9,2 CLEAR CENTRE OF SAME				
5 N81-FU,2 FUCHSITE									

	10	11	12
SiO <sub>2</sub>	34.28	36.40	34.77
TiO <sub>2</sub>	2.36	1.49	1.80
Al <sub>2</sub> O <sub>3</sub>	13.76	13.67	13.77
Cr <sub>2</sub> O <sub>3</sub>	3.43	4.25	3.48
FeO	11.24	7.52	10.25
MnO	0.10	0.04	0.08
MgO	2.60	3.30	2.13
Na <sub>2</sub> O	0.08	0.09	0.05
K <sub>2</sub> O	5.86	6.64	5.83
V <sub>2</sub> O <sub>3</sub>	9.35	10.82	10.07
BaO	10.85	9.86	12.33
ZnO	0.12	0.06	0.03
total=	94.03	94.14	94.59
F	0.04	0.10	nd
Si	5.66	5.86	5.74
Ti	0.29	0.18	0.22
Al	2.68	2.59	2.68
Cr	0.45	0.54	0.45
Fe <sub>2</sub>	1.55	1.01	1.42
Mn	0.01	-	0.01
Mg	0.64	0.79	0.52
Na	0.03	0.03	0.02
K	1.23	1.36	1.23
V	1.24	1.40	1.33
Ba	0.70	0.62	0.80
Zn	0.01	-	-
total=	14.50	14.39	14.43
oxygens=	[22]	[22]	[22]
Y-site	3.283	2.979	3.047
X-site	1.961	2.012	2.041
F/FM	0.708	0.561	0.730

10 410-31,A1 BROWN BA-V-FUCHSITE WITH EX V-CR-FE OX  
 11 410-31,A2 GREEN BA-V-FUCHSITE ENC PY  
 12 410-31,A3 GREEN BA-V-FUCHSITE EX PY





TABLE 6.7: ALTERED BIOTITES.

	1	2	3	4	5	6	7	8
SiO2	37.48	36.59	36.00	34.84	35.39	35.53	33.36	33.54
TiO2	1.69	1.86	1.70	0.06	nd	0.01	1.17	0.03
Al2O3	17.63	18.44	18.00	13.12	12.54	12.42	11.44	11.49
Cr2O3	nd	nd	nd	nd	nd	0.04	nd	0.01
FeO	15.61	16.94	15.48	20.22	22.78	23.45	17.72	17.34
MnO	0.03	0.13	0.09	0.17	0.11	0.19	nd	0.15
MgO	13.23	10.89	9.17	14.44	14.85	14.14	10.84	14.47
CaO	nd	0.01	nd	nd	nd	nd	nd	nd
Na2O	0.22	0.11	0.08	nd	nd	0.14	0.02	0.30
K2O	7.32	6.53	4.59	5.40	3.77	0.41	6.72	1.02
BaO	0.75	nd	nd	2.35	1.24	0.19	3.07	0.33
total=	93.96	91.50	85.11	90.60	90.68	86.52	84.34	78.68
F	0.51	0.72	0.65	0.49	0.50	0.35	0.14	0.11
Si	5.62	5.61	5.82	5.64	5.68	5.82	5.86	5.92
Ti	0.19	0.21	0.21	-	-	-	0.15	-
Al	3.12	3.33	3.43	2.50	2.37	2.40	2.37	2.39
Fe2	1.96	2.17	2.09	2.74	3.06	3.21	2.60	2.56
Mn	-	0.02	0.01	0.02	0.01	0.03	-	0.02
Mg	2.96	2.49	2.21	3.48	3.55	3.45	2.84	3.80
Na	0.06	0.03	0.03	-	-	0.04	-	0.10
K	1.40	1.28	0.95	1.12	0.77	0.09	1.51	0.23
Ba	0.04	-	-	0.15	0.08	0.01	0.21	0.02
total=	15.36	15.16	14.74	15.66	15.52	15.05	15.55	15.05
oxygens=	[22]	[22]	[22]	[22]	[22]	[22]	[22]	[22]
Y-site	5.851	5.846	5.772	6.395	6.672	6.905	5.830	6.696
X-site	1.509	1.311	0.972	1.264	0.849	0.142	1.725	0.355
F/FM	0.398	0.466	0.486	0.440	0.463	0.482	0.478	0.402

1 G172,2

2 G16,A

3 G48,A ALTERED

4 4085,1R BA-BIOT: CHLORITIZED

5 4085,C ALTERED IN BAR

6 4085,D ALTERED IN BAR

7 702-15,1 GREEN ALTERED BA-BIOT

8 4084,1 ALTERED

TABLE 6.8: SELECTED CHLORITE ANALYSES.

	1	2	3	4	5	6	7	8
SiO <sub>2</sub>	23.66	24.21	26.90	24.71	25.07	24.93	25.46	25.60
TiO <sub>2</sub>	0.08	0.12	0.07	0.06	0.07	0.09	0.04	0.09
Al <sub>2</sub> O <sub>3</sub>	21.60	21.86	20.85	21.92	21.87	22.01	21.32	20.77
FeO	22.93	23.52	16.68	24.42	23.33	23.49	21.59	18.97
MnO	0.25	0.29	0.11	0.28	0.13	0.09	0.10	0.12
MgO	15.08	15.08	22.15	15.95	16.02	15.76	17.49	20.15
CaO	0.02	0.05	nd	nd	nd	0.02	nd	nd
Na <sub>2</sub> O	0.01	0.03	nd	0.01	0.05	0.02	nd	0.02
K <sub>2</sub> O	0.01	0.08	0.03	nd	0.04	0.03	0.02	0.02
total=	83.64	85.24	86.79	87.35	86.58	86.44	86.02	85.74
Si	5.19	5.22	5.46	5.21	5.30	5.28	5.36	5.35
Ti	0.01	0.02	0.01	-	0.01	0.01	-	0.01
Al	5.59	5.56	4.99	5.45	5.45	5.50	5.29	5.11
Fe <sub>2</sub>	4.21	4.24	2.83	4.31	4.12	4.16	3.80	3.31
Mn	0.05	0.05	0.02	0.05	0.02	0.02	0.02	0.02
Mg	4.94	4.85	6.71	5.02	5.05	4.98	5.49	6.27
Ca	-	0.01	-	-	-	-	-	-
Na	-	0.01	-	-	0.02	-	-	-
K	-	0.02	-	-	0.01	-	-	-
total=	20.00	19.99	20.03	20.05	19.98	19.97	19.98	20.09
oxygens=	[28]	[28]	[28]	[28]	[28]	[28]	[28]	[28]
100xF/FM	46.04	46.67	29.70	46.21	44.97	45.54	40.92	34.56
1 N81-88,1 RADIATING 2 G48,A REPL. GARNET 3 207-5,1 RETROGRADE? 4 503-10,2 RETROGRADE?								
5 429-11,3 SPRAY 6 N80-45,2 CHL COAXIAL BIOT 7 N80-36,2 BIG SPRAY, GREEN 8 N80-13,1 X-CUT BY BI								

TABLE 6.9: SELECTED TALC ANALYSES.

	1 E	2 E	3 W	4 W
SiO <sub>2</sub>	62.09	62.15	60.04	59.68
TiO <sub>2</sub>	nd	0.02	nd	0.02
Al <sub>2</sub> O <sub>3</sub>	nd	0.08	0.04	0.09
FeO	2.44	1.57	9.73	5.56
MnO	0.27	0.10	0.23	0.03
MgO	29.46	30.47	24.43	27.22
Na <sub>2</sub> O	nd	0.02	0.04	0.03
K <sub>2</sub> O	nd	0.01	0.04	0.03
BaO	nd	0.01	nd	0.02
total=	94.26	94.43	94.55	92.68
Si	8.02	7.98	8.01	7.96
Al	-	0.01	-	0.01
Fe <sub>2</sub>	0.26	0.17	1.09	0.62
Mn	0.03	0.01	0.03	-
Mg	5.67	5.83	4.86	5.41
Na	-	-	0.01	-
total=	13.98	14.01	14.00	14.03
oxygens=	[22]	[22]	[22]	[22]
1 201-6,1 TALC 2 201-7B TALC 3 703-7,2 TALC FLAKE IN BAR 4 05-C,1 TALC				



TABLE 6.11: SELECTED HORNBLLENDE ANALYSES.

	1	2	3	4
SiO2	42.60	42.36	42.88	43.87
TiO2	0.43	0.36	0.44	0.44
Al2O3	15.54	16.83	15.65	13.71
FeO	16.36	17.11	15.80	15.27
MnO	0.13	0.21	0.22	0.17
MgO	8.78	7.76	8.86	10.02
CaO	9.93	9.98	9.90	9.98
Na2O	2.11	2.18	2.43	2.23
K2O	0.34	0.40	0.43	0.48
total=	96.22	97.19	96.61	96.17
Si	6.40	6.32	6.41	6.57
Ti	0.05	0.04	0.05	0.05
Al	2.75	2.96	2.76	2.42
Fe2	2.06	2.14	1.97	1.91
Mn	0.02	0.03	0.03	0.02
Mg	1.97	1.73	1.97	2.24
Ca	1.60	1.60	1.58	1.60
Na	0.61	0.63	0.70	0.65
K	0.07	0.08	0.08	0.09
total=	15.52	15.51	15.56	15.54
oxygen=	[23]	[23]	[23]	[23]
100xF/FM	51.11	55.30	50.01	46.09

- 1 429-5,1 FRESH RIM  
 2 429-5,3 CORE  
 3 4685,4 RIM ADJ QTZ  
 4 N80-13,2 RIM ADJ DOL

TABLE 6.12: EPIDOTE GROUP MINERALS.

	1	2	3	4	5
SiO2	37.77	37.24	37.36	37.52	31.98
TiO2	0.13	0.14	0.05	0.10	0.10
Al2O3	26.35	26.79	24.23	24.55	20.51
Fe2O3	9.52	8.88	12.23	11.57	10.62
MnO	0.34	0.28	0.03	0.09	0.34
MgO	0.04	0.05	0.06	0.05	0.48
CaO	22.44	22.44	23.37	23.20	10.86
Na2O	0.03	0.03	nd	nd	0.10
La2O3	nd	nd	nd	nd	5.19
Ce2O3	nd	nd	nd	nd	12.46
Pr2O3	nd	nd	nd	nd	1.24
Nd2O3	nd	nd	nd	nd	4.24
total=	96.62	95.85	97.33	97.08	98.12
Si	3.17	3.15	3.17	3.18	3.09
Al	2.61	2.67	2.43	2.45	2.33
Fe3	0.67	0.63	0.87	0.82	0.86
Mn	0.02	0.02	-	-	0.03
Mg	-	-	-	-	0.07
Ca	2.02	2.03	2.13	2.11	1.12
Na	-	-	-	-	0.02
La	-	-	-	-	0.18
Ce	-	-	-	-	0.44
Pr	-	-	-	-	0.04
Nd	-	-	-	-	0.15
total=	8.52	8.51	8.61	8.58	8.34
oxygen=	[13]	[13]	[13]	[13]	[13]
%Ps	20.40	19.04	26.37	25.06	26.87

- 1 4685,1 CLINOZOISITE CORE  
 2 4685,2 RIM OF SAME  
 3 N80-13,1C EPIDOTE CORE  
 4 N80-13,1R RIM OF SAME  
 5 G59A,1 ALLANITE

%Ps =  $100 \cdot \text{Fe} / (\text{Fe} + \text{Al})$ : total Fe calculated as  $\text{Fe}^{3+}$



TABLE 6.13: TOURMALINE &amp; SPHENE.

	1	2	3	4
SiO <sub>2</sub>	35.56	36.23	30.86	31.03
TiO <sub>2</sub>	0.58	0.97	34.82	36.18
Al <sub>2</sub> O <sub>3</sub>	31.30	30.90	3.36	2.81
FeO	6.18	3.84	1.01	0.56
MnO	nd	0.05	nd	nd
MgO	8.03	9.48	nd	nd
CaO	0.58	1.30	27.50	27.09
Na <sub>2</sub> O	2.55	2.09	nd	nd
K <sub>2</sub> O	0.01	0.07	nd	nd
total=	84.79	84.93	97.55	97.67
F	0.36	0.25	0.49	0.38
Si	4.82	4.85	4.11	4.11
Ti	0.06	0.10	3.48	3.61
Al	5.00	4.88	0.53	0.44
Fe <sub>2</sub>	0.70	0.43	0.11	0.06
Mg	1.62	1.89	-	-
Ca	0.08	0.19	3.92	3.85
Na	0.67	0.54	-	-
K	-	0.01	-	-
total=	12.96	12.89	12.15	12.06
oxygens=	[20]	[20]	[20]	[20]
100xF/FM	30.16	18.52	-	-

1 4688,2 TOURMALINE CORE  
 2 N81-88,1 TOURMALINE CORE  
 3 N80-36,1 SPHENE IN QTZ-ALB  
 4 N80-36,2 SPHENE RHOMB IN MUSC

TABLE 6.14: BAOITE.

	1	2
SiO <sub>2</sub>	14.17	15.32
TiO <sub>2</sub>	29.33	39.91
Fe <sub>2</sub> O <sub>3</sub>	3.07	0.96
MgO	nd	0.02
CaO	nd	0.02
Na <sub>2</sub> O	nd	0.09
BaO	37.55	39.98
Nb <sub>2</sub> O <sub>5</sub>	11.50	nd
total=	95.62	96.31
F	nd	0.20
Cl	2.01	1.79
-O=Cl	0.45	0.40
total=	97.18	97.80
Si	0.96	1.00
Ti	1.49	1.95
Fe <sub>3</sub>	0.16	0.05
Na	-	0.01
Ba	0.99	1.02
Nb	0.35	-
total=	3.95	4.03
oxygens=	[7]	[7]

1 Pao-t ou-k uang (baoite): Fleischer & Chao, 1960  
 2 Ti-baoite(?), sample 203-18, Foss: ave of 2 analyses

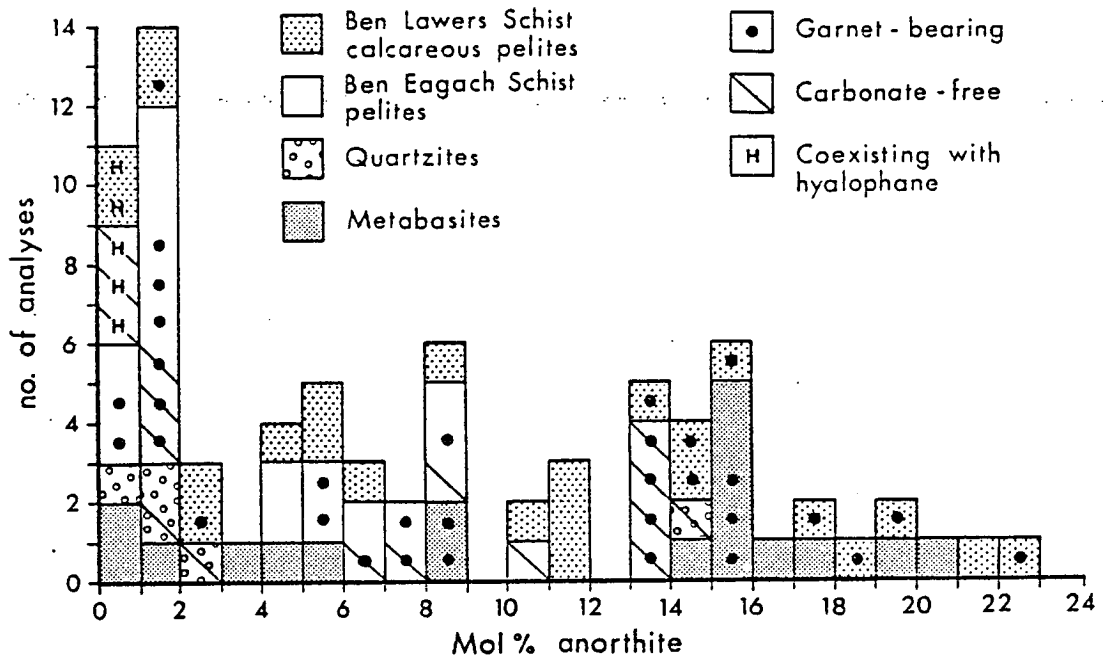


**Fig. 6.1:** Histogram of mol% anorthite content of plagioclase (in 78 analyses from 38 samples) from a variety of rock types and mineralogical associations.

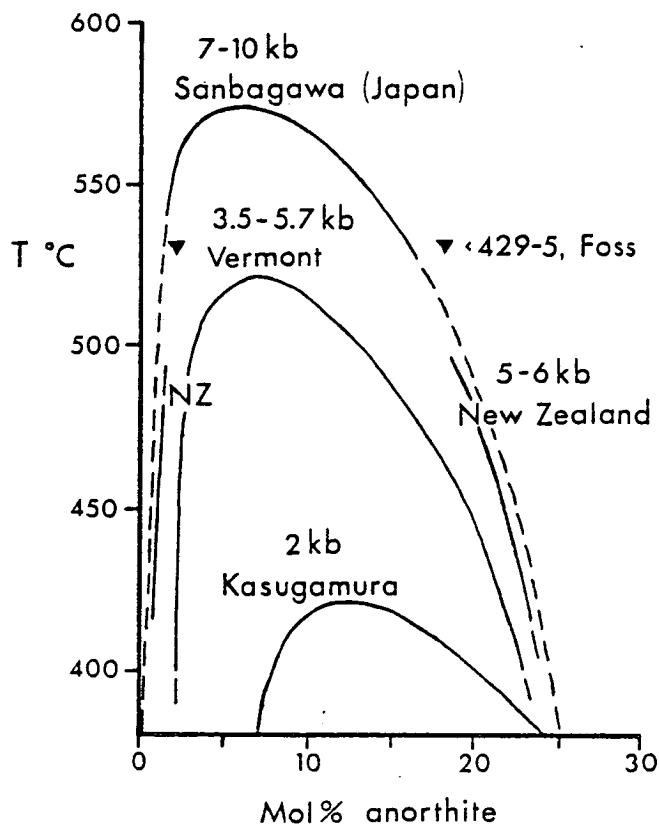


**Fig. 6.2:**  $T - X_{An}$  diagram of peristerite gap for different pressures, compiled from previous studies and new data from the Kasugamura Granite aureole, Japan, by Maruyama et al., 1982. Triangles indicate feldspar compositions in sample 429-5 plotted at estimated peak metamorphic temperature at Foss.

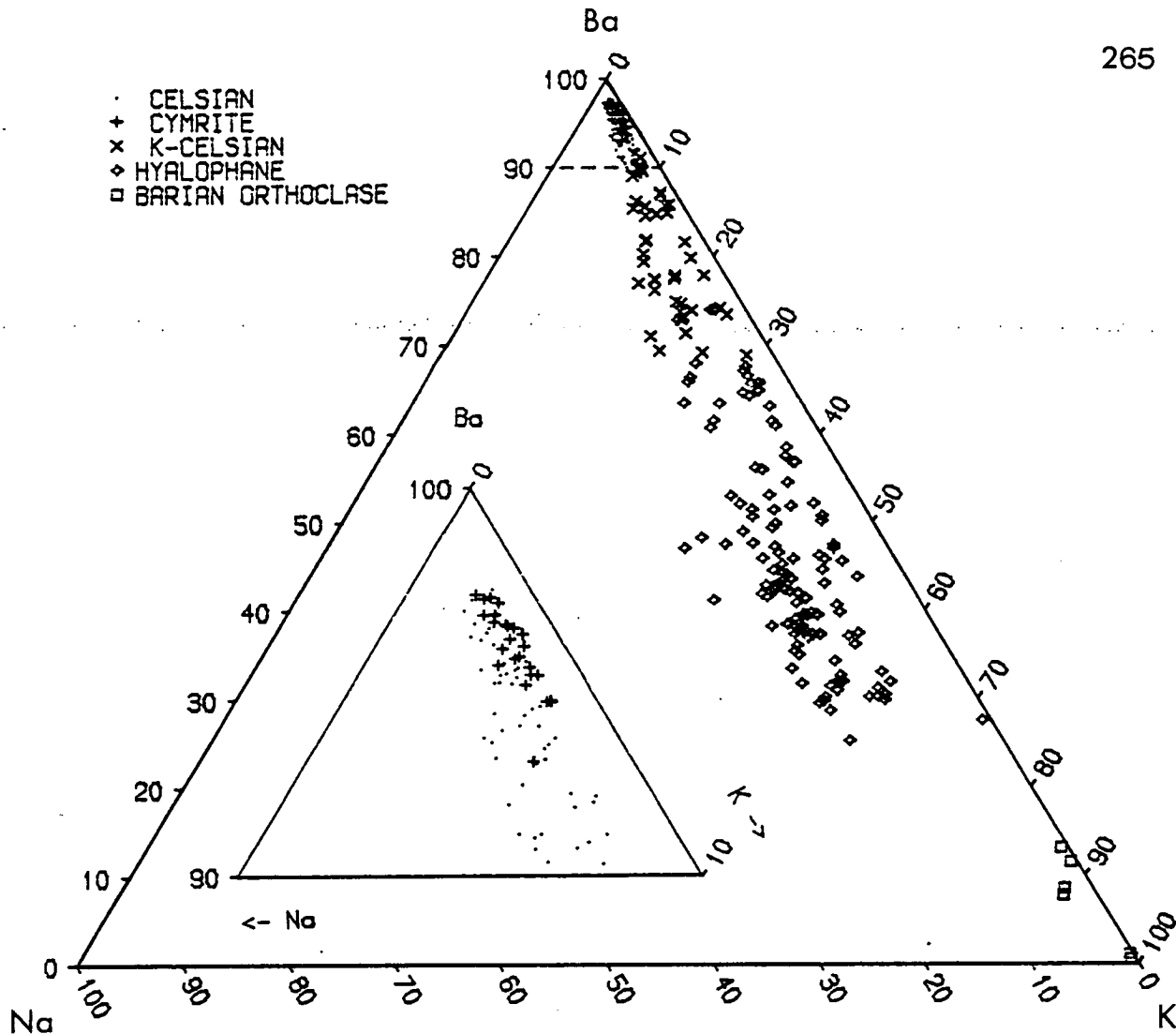


**Fig. 6.3:** Molecular Na-Ba-K diagram showing the distribution of all barium-potassium feldspar compositions analysed. Inset: enlargement of top corner showing celsian and cymrite compositions. Note that plagioclase feldspars from Foss contain insignificant Ba and K and would plot at the Na apex.

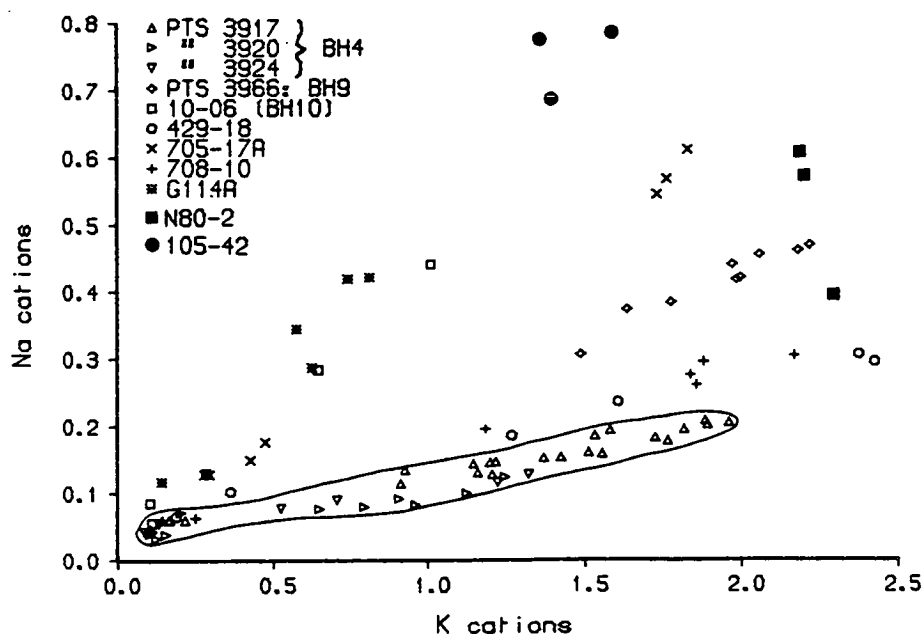


**Fig. 6.4:** Diagram of Na versus K cations (32 oxygens) for barium-potassium feldspars in selected samples, to illustrate the wide range of K/Na ratios which, however, are uniform in individual samples and in samples from restricted areas or drillcore intervals, such as BH4.

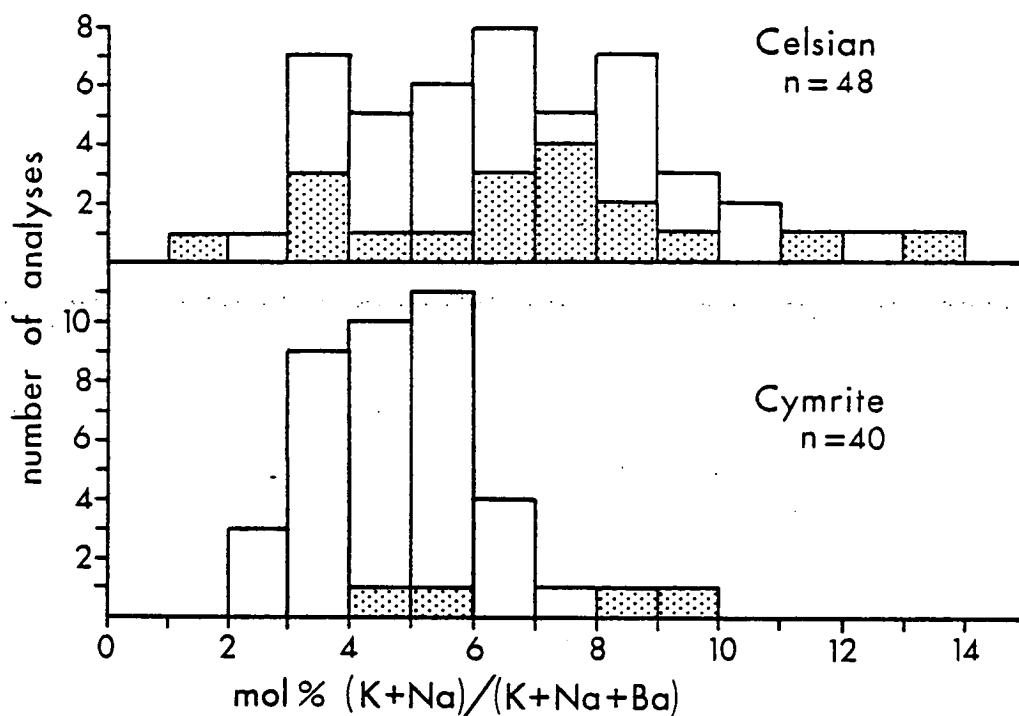


Fig. 6.5: Histograms of mol% orthoclase + albite component in celsian, and of mol% (sanidine + albite)-hydrate component in cymrite in analysed samples from the Aberfeldy deposits. Stippled: data published by Fortey & Beddoe-Stephens (1982).

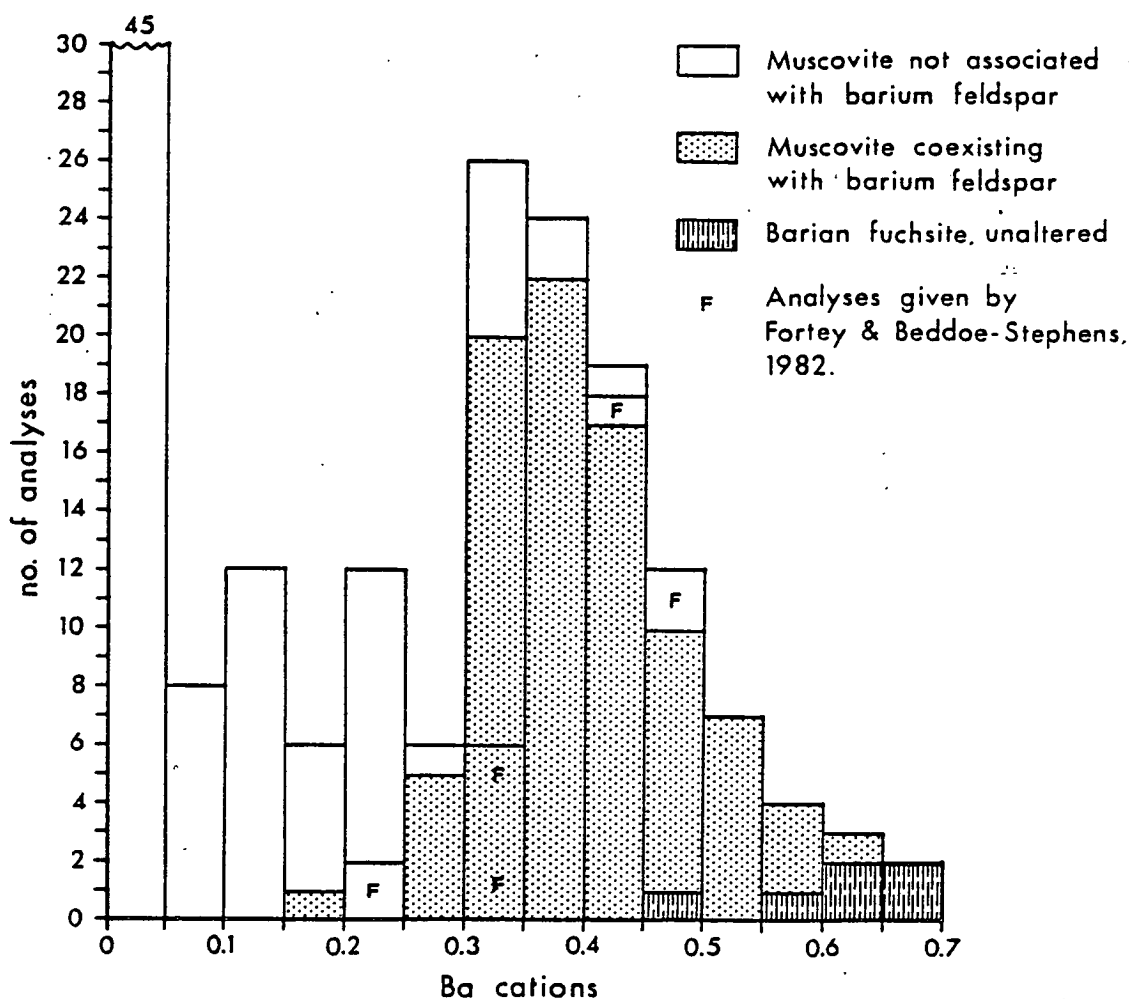
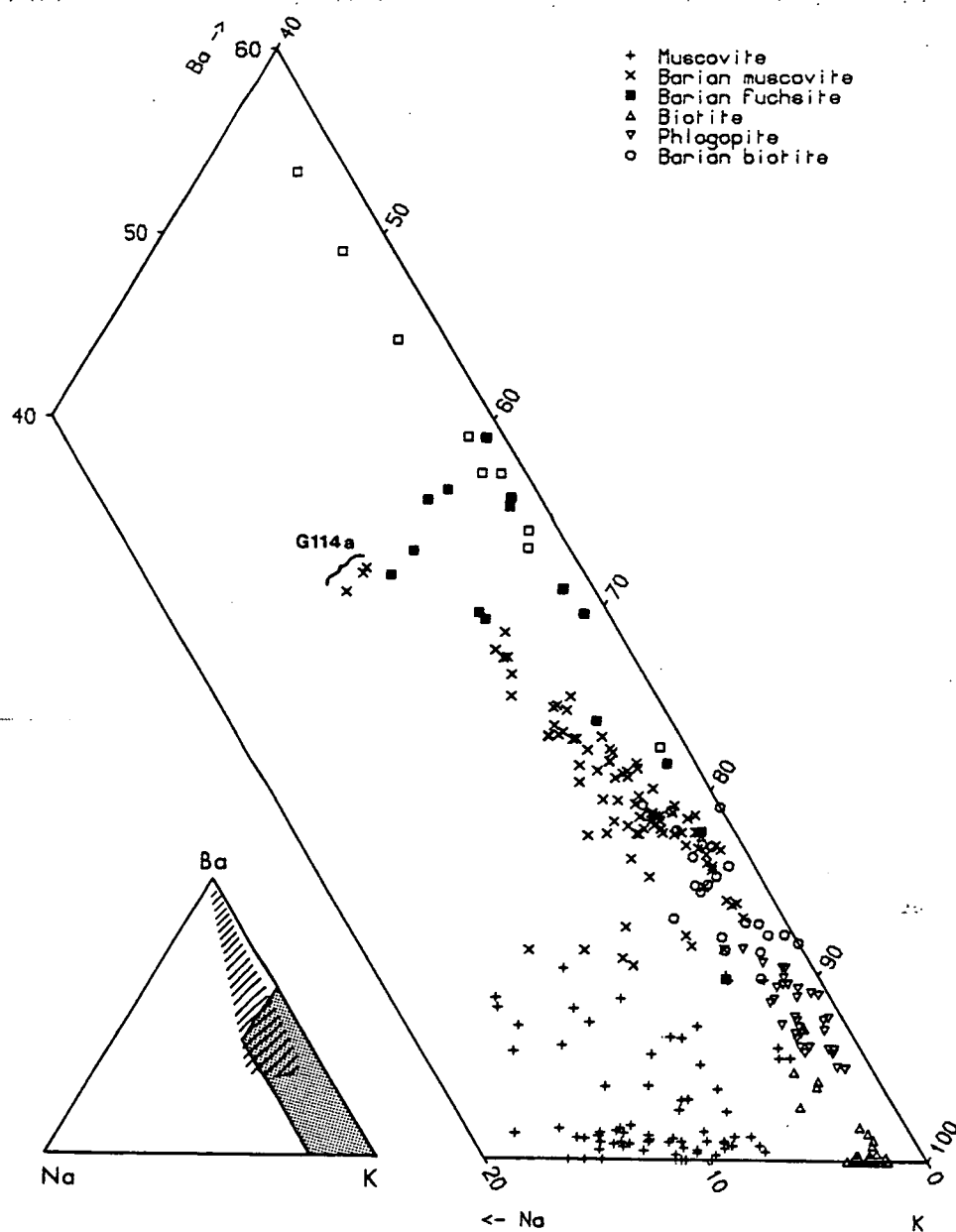


Fig. 6.6: Histogram of Ba cations (22 oxygens) in 186 analyses of dioctahedral micas from Foss, including 11 analyses published by Fortey & Beddoe-Stephens (1982) (Foss and Ben Eagach deposits). Note that several analyses of altered, barian-rich fuchsite have been excluded (see Fig. 6.17).



**Fig. 6.7:** Na-Ba-K diagram of micas in analysed samples from Foss. Inset shows location of the larger figure (shaded polygon) and field of barium feldspar compositions (diagonal stripes: see fig. 6.3). Open squares represent altered Ba-Cr micas and Ba-V-Cr micas.

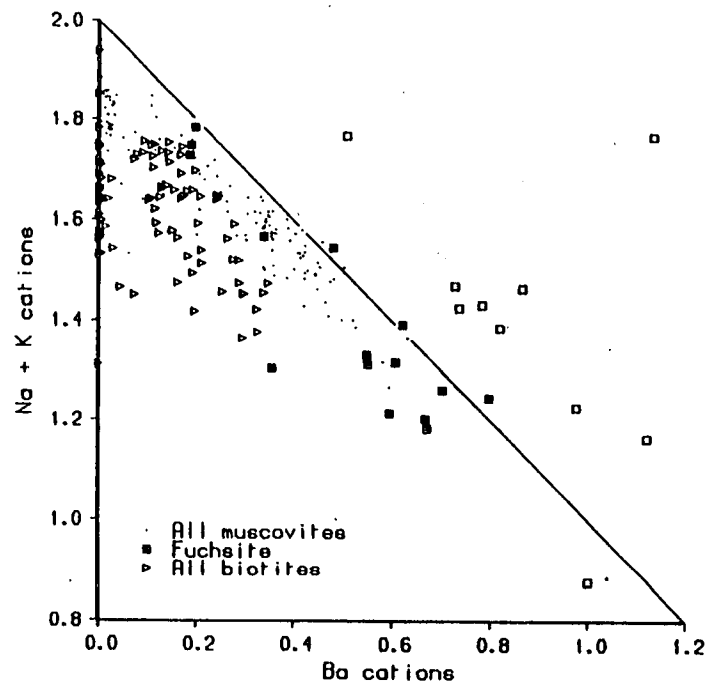


Fig. 6.8: Na plus K cations vs. Ba cations in all mica analyses. Open squares represent altered fuchsites. Line indicates ideal X-site occupancy ( $\text{Na} + \text{K} + \text{Ba} = 2$ ).

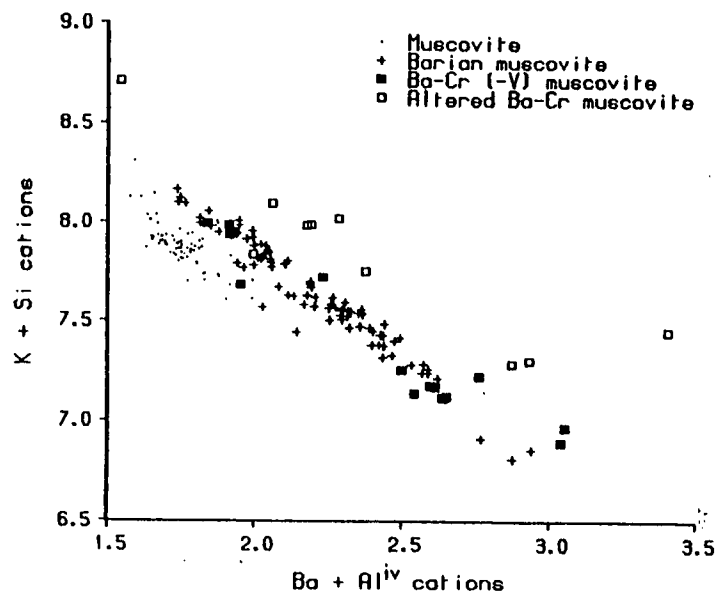


Fig. 6.9: K plus Si cations vs. Ba plus  $\text{Al}^{\text{IV}}$  cations (22 oxygens) in di-octahedral micas from Foss, illustrating the coupled substitution scheme (see text). Open squares represent altered fuchsites.

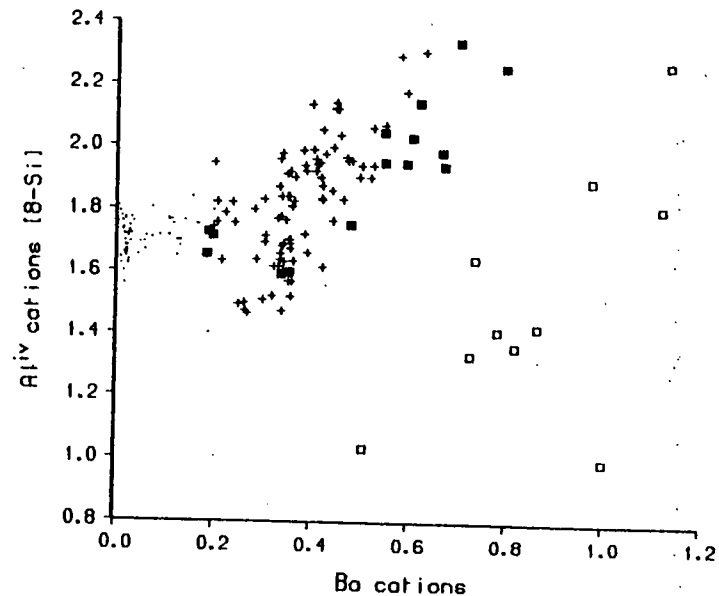


Fig. 6.10: Tetrahedral Al vs. Ba cations (22 oxygens) in di-octahedral micas, to illustrate the higher  $\text{Al}^{\text{IV}}$  content of micas with  $>0.4$  Ba cations, but lack of correlation at lower Ba contents. Symbols as in fig. 6.11.

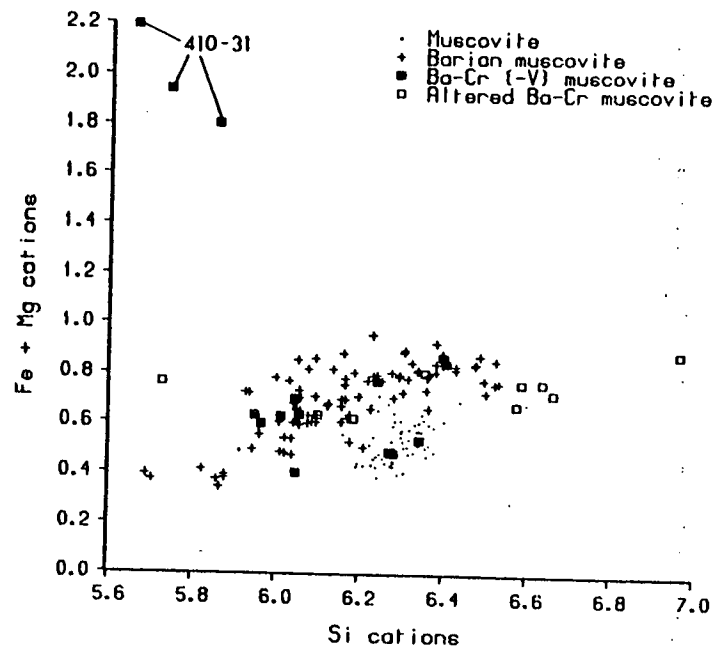


Fig. 6.11: Fe plus Mg cations vs. Si cations in di-octahedral micas, to illustrate the greater degree of phengitic substitution in barian muscovite than in Ba-poor muscovite. Note high Fe+Mg content of Ba-V-Cr mica in 410-31.

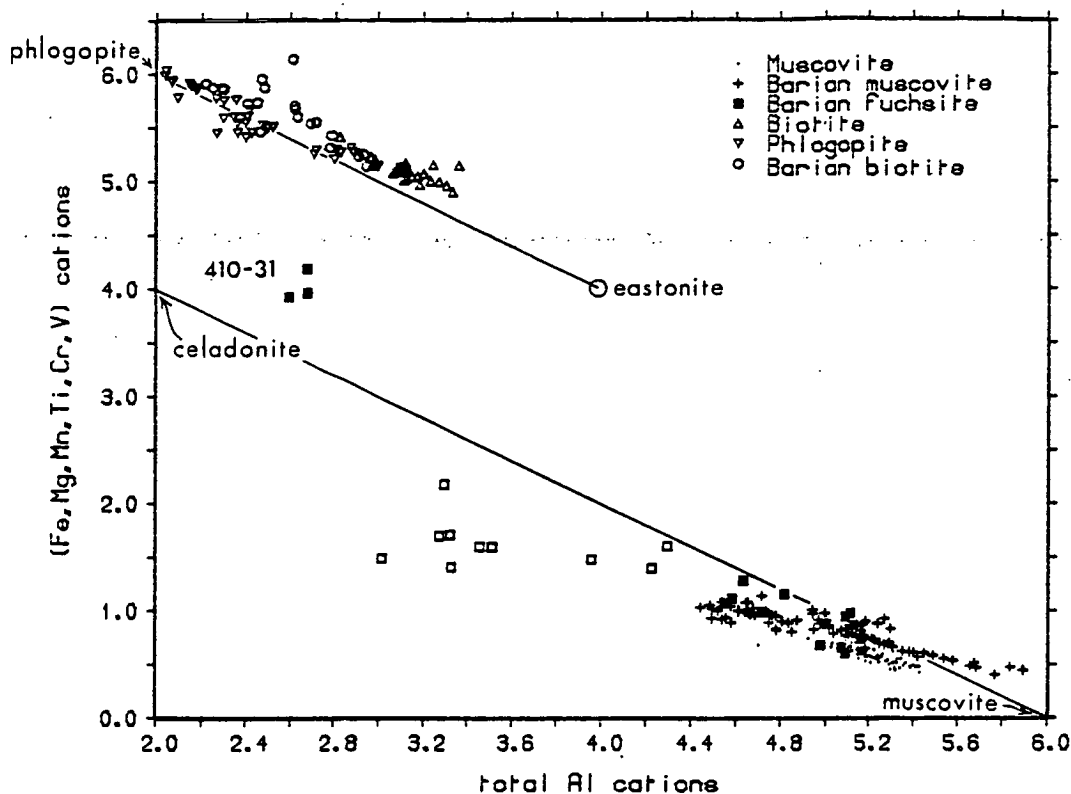


Fig. 6.12: Total of Y-site cations excluding Al, versus total Al cations in all mica analyses. Lines indicate ideal  $Al^{IV}$  substitution trends in di-octahedral micas (lower right) and tri-octahedral micas (upper left). Open squares represent altered fuchsites. Three Ba-V-Cr mica analyses from sample 410-31 indicated by sample number.

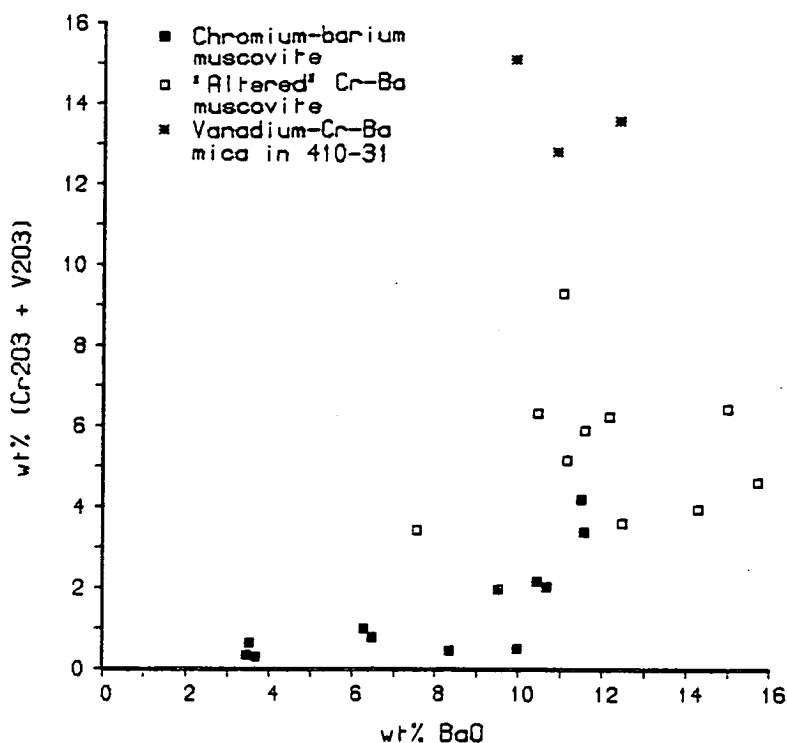


Fig. 6.13: Weight percent  $Cr_2O_3$  (plus  $V_2O_3$  in 410-31 micas) vs. weight percent  $BaO$ , to illustrate the higher barium contents of chromium-rich muscovites (cf. fig. 6.6).

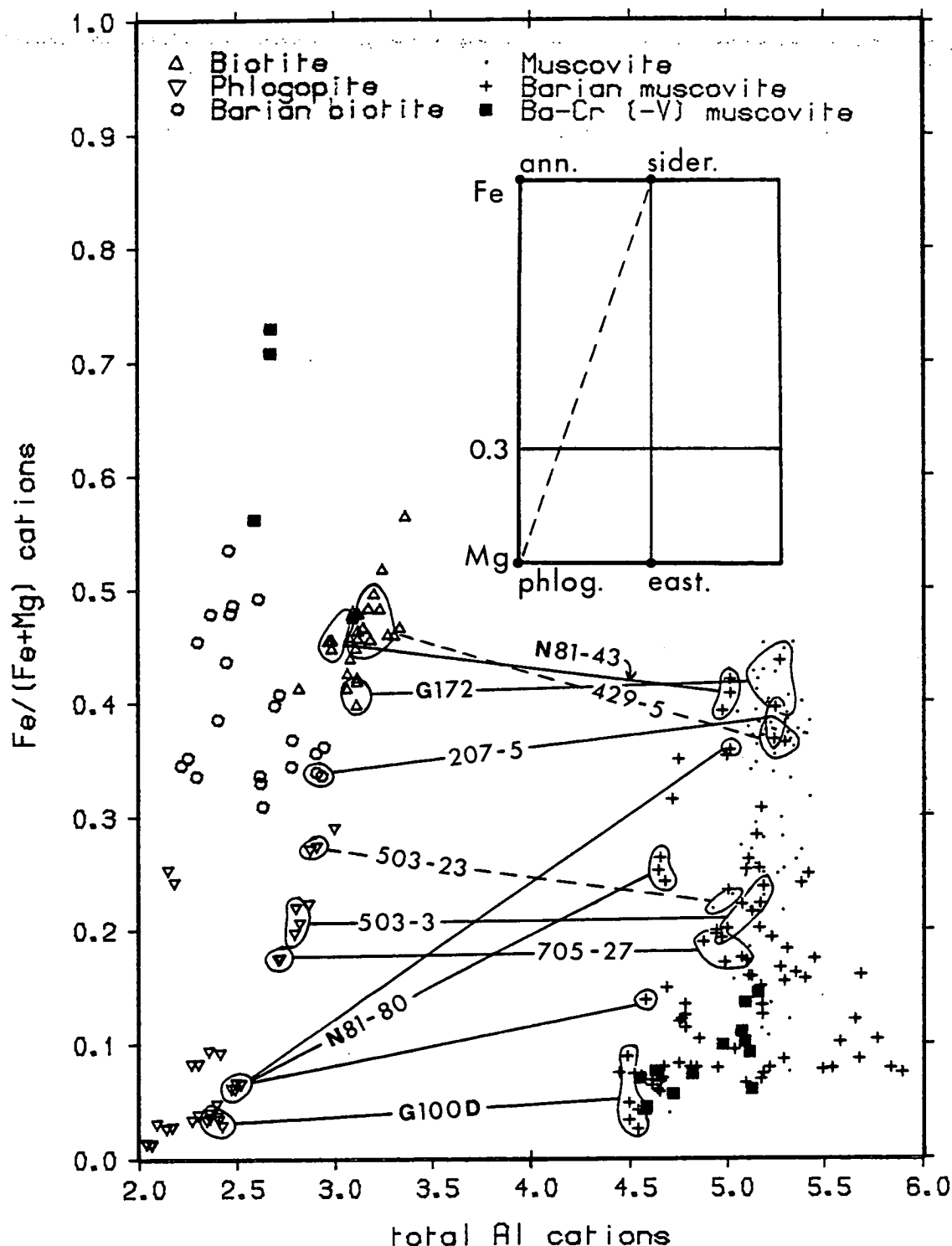


Fig. 6.14: Molecular ratio of Fe/(Fe+Mg) vs. total Al cations (22 oxygens) in all mica analyses (except altered fuchsites, not plotted). Inset shows locations of end-member compositions. Tie-lines connect coexisting biotite and muscovite compositions within selected samples: dashed tie-lines indicate that sample also contains other ferromagnesian silicates (e.g. garnet). Note wide range of Fe:Mg ratios shown by muscovite in N81-80 (see text).



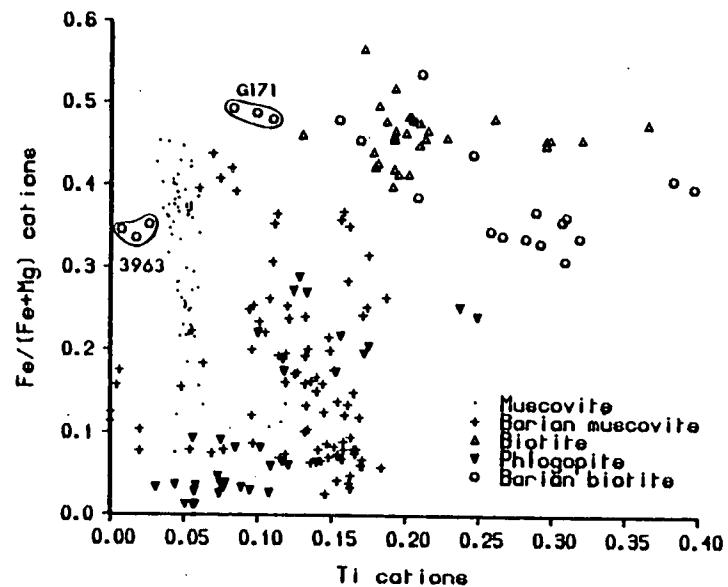


Fig. 6.15: Molecular ratio of Fe/(Fe+Mg) vs. Ti cations in all micas. Note higher Ti content of most barian muscovites relative to Ba-poor muscovites, and increase in maximum Ti content with increasing Fe in the tri-octahedral micas. Samples 3963 and G171 are barite rocks (see text).

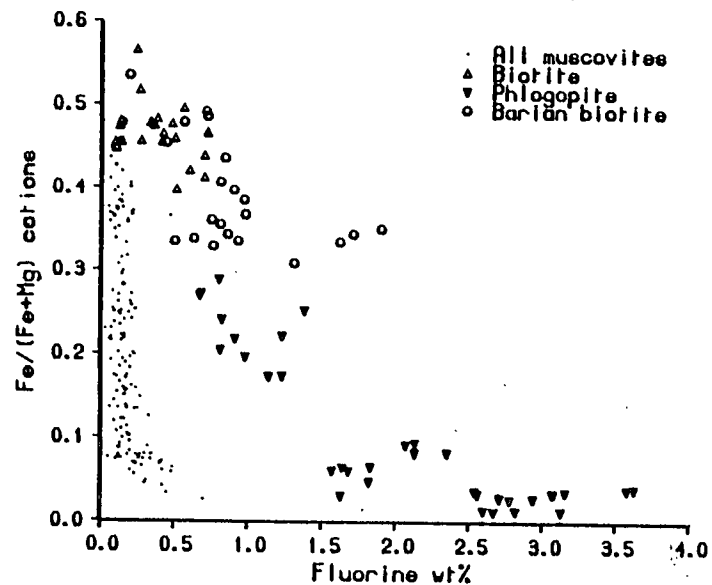


Fig. 6.16: Molecular ratio of Fe/(Fe+Mg) vs. weight percent fluorine in all micas. See text.

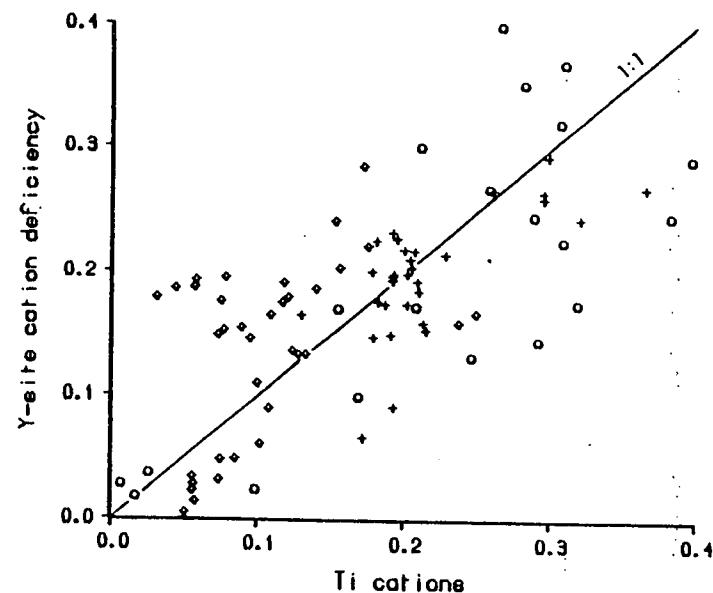


Fig. 6.17: Octahedral cation site deficiency vs. Ti cations in tri-octahedral micas from Foss (symbols as in fig. 6.18). Y-site deficiency calculated as  $6 - (\text{Fe} + \text{Mg} + \text{Mn} + \text{Ti} + \text{Cr})$  cations (22 oxygens); line shows 1:1 relationship between site vacancy and Ti content.

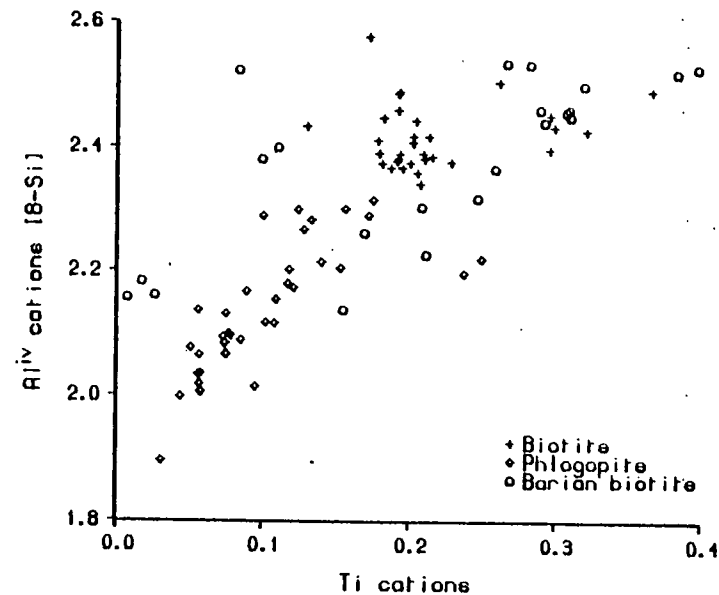


Fig. 6.18: Tetrahedral Al cations vs. Ti cations in tri-octahedral micas from Foss. Note loose positive correlation (see text).

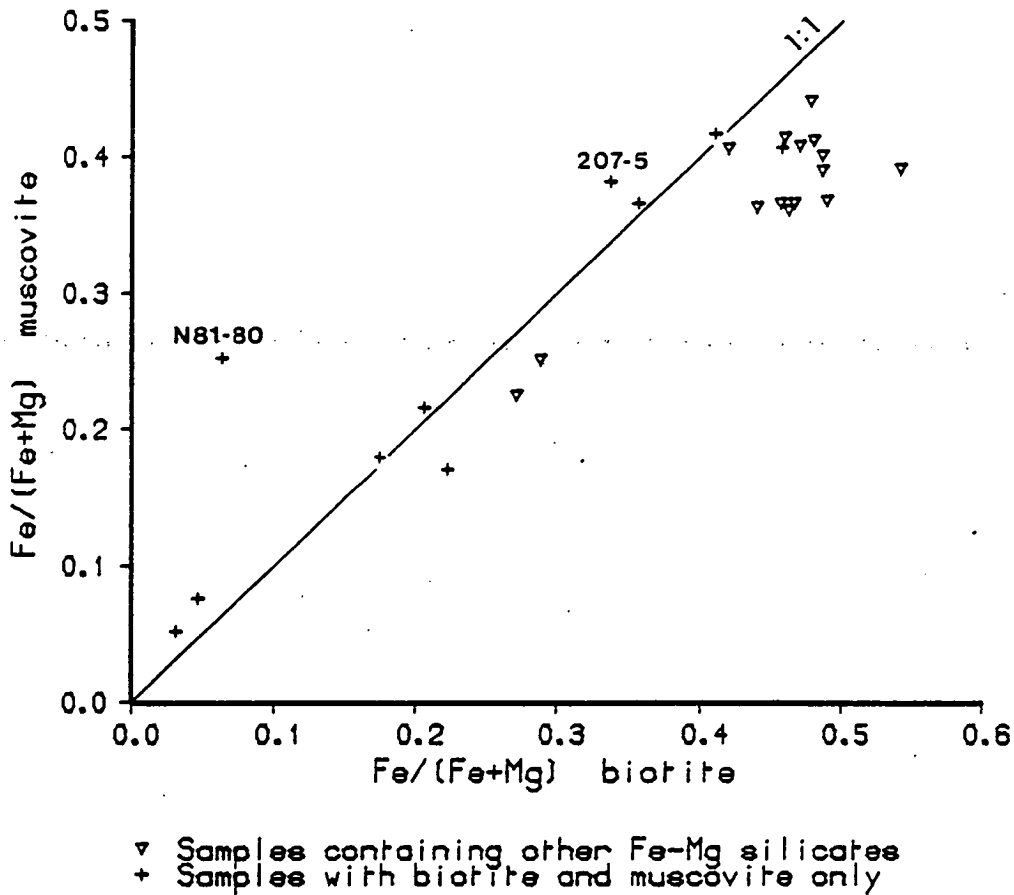


Fig. 6.19: Molecular ratios of  $\text{Fe}/(\text{Fe}+\text{Mg})$  of muscovite versus coexisting biotite in samples from Foss containing both micas. See text.

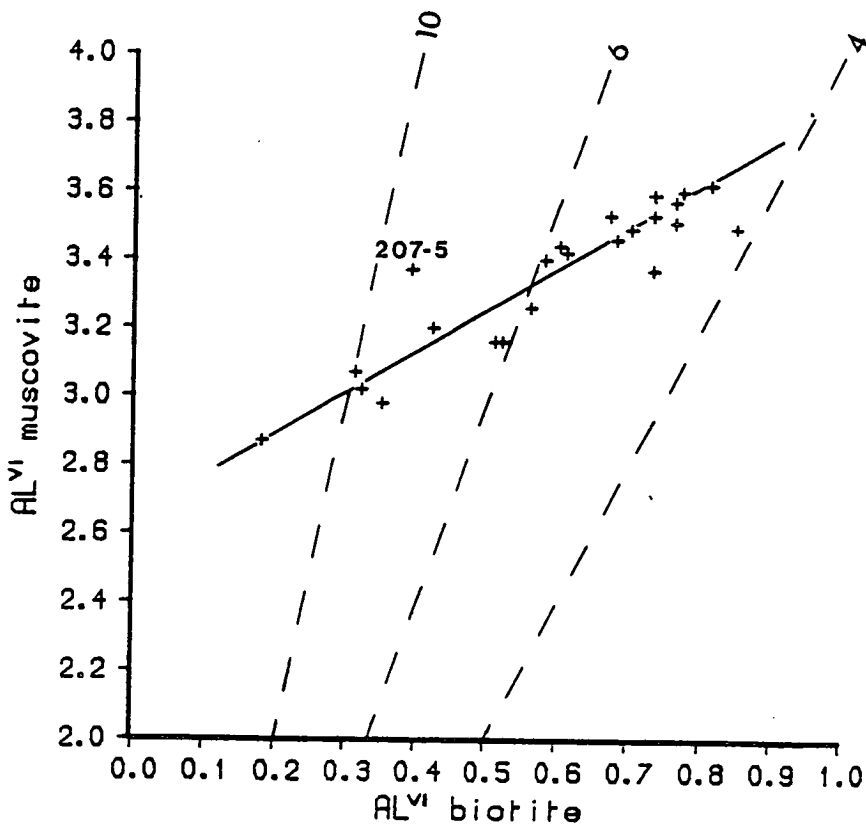
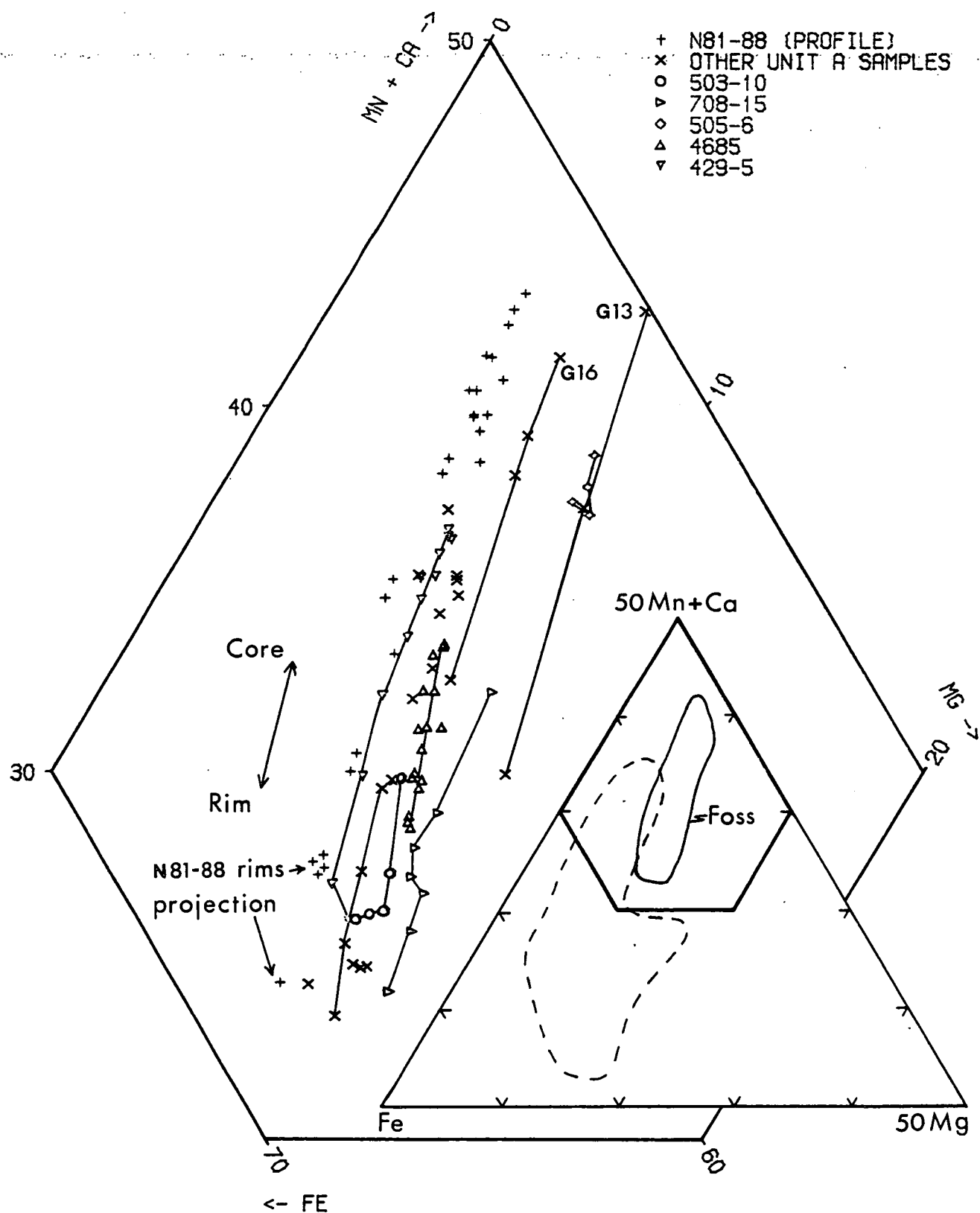
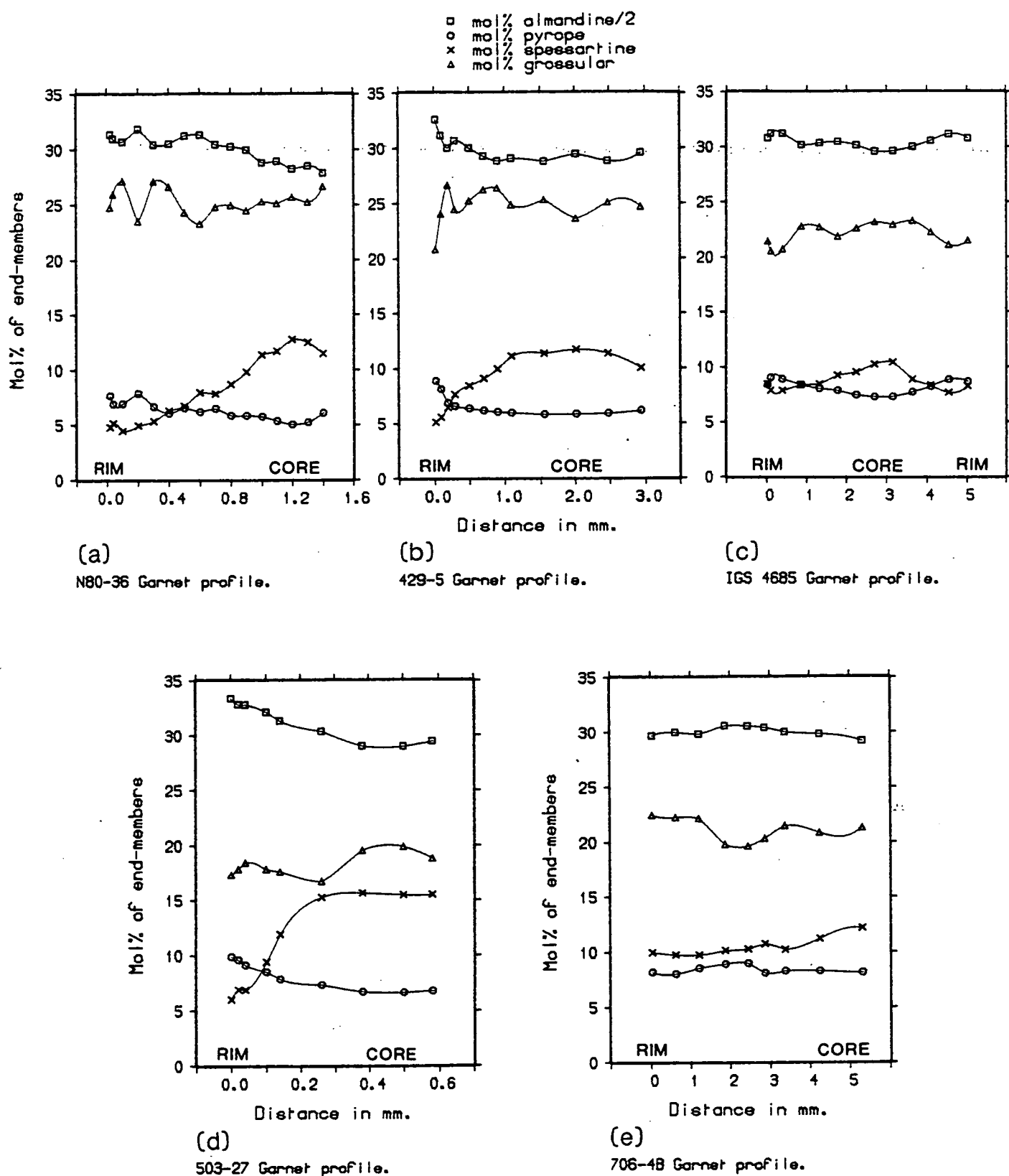


Fig. 6.20: Octahedral Al cations in muscovite, versus octahedral Al cations in coexisting biotite, in samples from Foss containing both micas. Plotted points represent average  $\text{Al}^{\text{VI}}$  contents where more than one analysis was obtained. Solid line fitted through data points by classical linear regression. Dashed lines represent loci of constant  $K_D$  (values indicated by numbers 4, 6, 10) (see text).





**Fig. 6.22:** Triangular diagram of (Mn+Ca)-Mg-Fe showing distribution of garnet compositions in samples from Foss. Inset shows location of the larger figure and compares the compositional field of garnets analysed in this study (solid outline) with that of garnets analysed by Sivapakash (1981) from the Aberfeldy-Grandtully-Pitlochry area (dashed outline).



**Fig. 6.23a-e:** Compositional profiles (expressed as mol% of end-members) of zoned garnet crystals in five samples from Foss. In all cases, the left side represents a garnet rim (taken as zero distance), and in 6.23c, both ends of the profile are rims. In the remaining profiles, the right side represents the geometrical centre of the garnet section. Curves are fitted to the data points by spline interpolation. Note that 50% of mol% almandine shown.

### N81-88 Garnet section

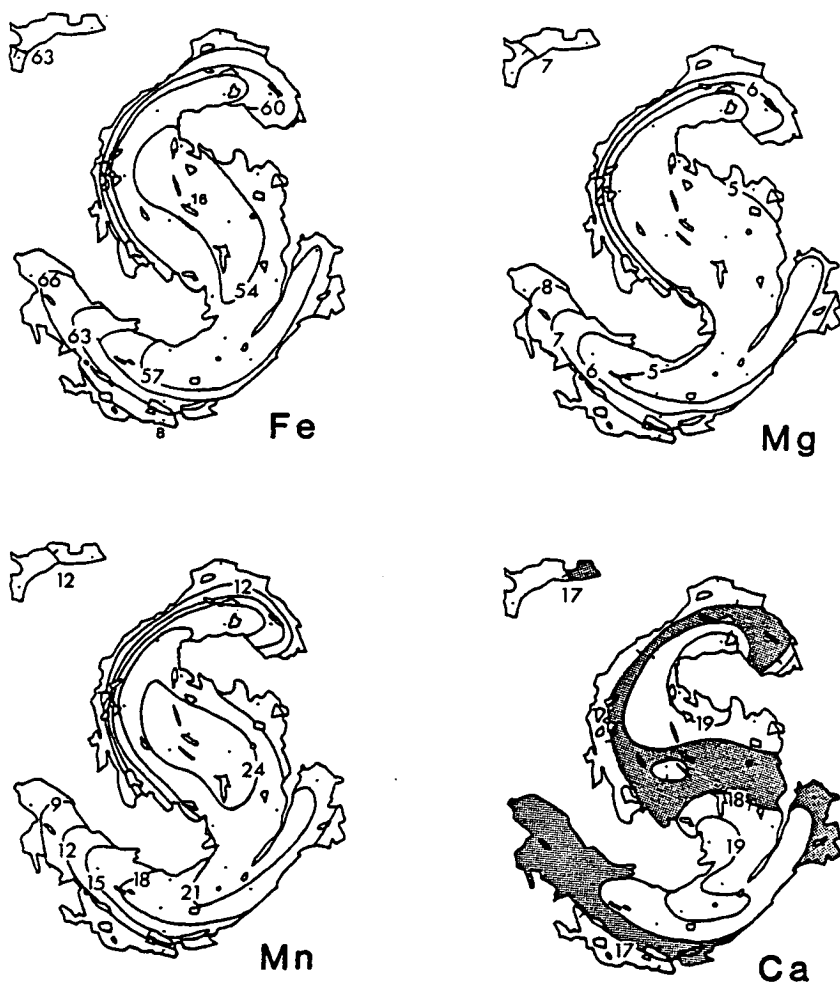


**Fig. 6.24:** Compositional map based on 25 microprobe analyses (located by dots) of almandine, pyrope, spessartine and grossular contents (expressed as mol%) of a spiral-shaped garnet crystal section in sample N81-88 (a unit A micaceous quartzite). Small numbers 8 and 16 (top left figure) locate rim and core analyses given in table 6.10. The area of garnet section in which mol% grossular = 17-18 is shaded to clarify the map.

## CHAPTER 7: Non-silicate mineral chemistry.

### 7.1 Introduction.

This chapter deals with the mineralogy and composition of non-silicate minerals found in association with the Foss deposit. These belong to five major groups, namely oxides, sulphides, sulphate, carbonates and phosphates, and are described in this order in sections 7.2 - 7.6. As in the previous chapter, emphasis is placed on defining the compositional range of each phase and on discerning features which relate to the primary conditions of formation or to metamorphic processes. Particular attention is given to sphalerite, which has preserved a detailed compositional record of depositional and metamorphic processes, and to several unusual minerals including Ti-V-Ba oxides and barium carbonates which have not previously been described from the Aberfeldy deposits. The concluding section (7.7) reviews the influence of metamorphism on the primary mineralogy, and discusses evidence for element partitioning and equilibration between the various silicate and non-silicate minerals examined.

Analytical methods and estimates of accuracy and precision in routine microprobe analyses are given in Appendix E, and representative analyses appear in tables 7.1-7.9.

### 7.2 Oxides.

Rutile is a widespread but minor component of all rock types at Foss, and ilmenite occurs in many metabasites and also in unit D schists. Magnetite is restricted in occurrence to some barite and sulphidic quartz barite rocks (part 3.2.1), and is absent from the host rocks to the Aberfeldy deposits. Hematite occurs as a weathering product of iron sulphides (and carbonates?) in outcrops of barite rock, giving the barite a red colouration (see plate 1). Other oxides described in this section, namely cassiterite and two crichtonite-like minerals, have only been identified in a few thin sections but are sufficiently unusual to merit some discussion of their composition and origin.

### 7.2.1 Magnetite.

This mineral is regarded as a primary component of the stratiform mineralization. It typically forms rounded grains up to 2mm in diameter and is either disseminated or concentrated into laminae within barite rocks (modal concentration <5%). However, magnetite has occasionally been observed as massive, granular bands over 1cm thick. Magnetite grains occasionally have embayed outlines or appear to be partly replaced by pyrite, and magnetite sometimes forms fine grained aggregates. Magnetite often coexists with pyrite and sphalerite (plate 95), and also coexists with pyrrhotite in several samples examined (e.g. I.G.S. 4084; 702-7: plate 96).

Microprobe analyses of magnetite in five samples of barite rock from Foss show that it is nearly pure  $\text{Fe}_3\text{O}_4$ , although oxide totals below that expected from the stoichiometric formula may indicate an excess of  $\text{Fe}^{3+}$  (i.e.  $\text{Fe}^{3+}:\text{Fe}^{2+} > 2:1$ ). Impurities are generally near or below detection limits but some analyses of magnetite indicate trace amounts of  $\text{Al}_2\text{O}_3$  (<0.05 wt%),  $\text{TiO}_2$  (<0.06%),  $\text{Cr}_2\text{O}_3$  (<0.02%) and  $\text{MnO}$  (<0.09%). A positive relationship between the Mn contents of coexisting magnetite and sphalerite is suggested by the limited data from two samples in which both phases were analysed (702-9, 702-11: see table 7.4).

### 7.2.2 Rutile and ilmenite.

In thin section, rutile ( $\text{TiO}_2$ ) varies in colour from golden yellow (plate 68) to reddish brown, ruby red and black (cf. plate 43). Opaque rutile occurring in several mineralized rocks was initially mistaken for ilmenite, and microprobe analyses indicate a significant chromium content (0.6-1.1wt%  $\text{Cr}_2\text{O}_3$ : table 7.1). One sample in which Cr-rutile was analysed (G100E) also contains Ba-Cr muscovite (see table 6.5). Low oxide totals for these analyses could indicate the presence of other impurities such as vanadium and rare earth elements, which were not determined. The iron contents of chromian rutiles are low, but more  $\text{FeO}$  (generally 0.5-0.9wt% and up to 1.5wt%) is found in the yellow-brown coloured rutile which commonly occurs in both metasedimentary and metabasaltic rocks at Foss. Other elements which appear in some analyses, but which are normally at or below the detection limit, are Si, Al, Mg and Mn (table 7.1).



Ilmenite ( $\text{Fe}^{2+}\text{Ti}^{4+}\text{O}_3$ ) was analysed by the E.D.S. technique in three chloritic metabasites and two unit D pelites (plates 86, 90). It contains significant amounts of  $\text{SiO}_2$  (0.15–0.3wt%),  $\text{MnO}$  (0.4–1.4%) and  $\text{MgO}$  (0–0.6%). Consistently low oxide totals of 99.3% may indicate the presence of ~5%  $\text{Fe}_2\text{O}_3$  in solid solution or as submicroscopic hematite exsolution (cf. Deer et al., 1962b).

### 7.2.3 Cassiterite and crichtonite-group minerals.

One small (~0.2mm), rounded grain of a mineral similar in appearance to rutile, occurring in a sample of barite rock banded with quartz and clay minerals (IGS 4679: BH9, 25.1m), was found to be cassiterite. Two microprobe analyses gave  $\text{SnO}_2 \approx 100\%$ , with very minor Fe, Ti and Mn impurities. Cassiterite is usually found in acid igneous rocks, pegmatites, high-temperature hydrothermal veins, and derived detrital sediments. The occurrence at Foss is therefore unusual, but since tin is seldom accommodated into other mineral lattices, the presence of cassiterite need not indicate a significant tin enrichment. However, unpublished geochemical data obtained by Dresser Minerals does suggest slightly higher Sn contents in the upper mineralized horizons (10–20ppm) than in the M3 horizon (<10ppm) at Foss, which possibly reflects a change in composition of the mineralizing fluids.

Titanium-rich minerals examined with the microprobe in two samples from Foss are probably members of the crichtonite group of rare, complex oxides of general formula  $\text{AB}_2\text{O}_{38}$ , the best known of which is davidite  $[(\text{La},\text{Ce})(\text{Y},\text{U},\text{Fe}^{2+})(\text{Ti},\text{Fe}^{3+})_{20}(\text{O},\text{OH})_{38}]$  (Hayton, 1960; Grey et al., 1976; Gatehouse et al., 1979). Compared with published analyses of members of the group, the Foss occurrences are notably rich in Cr, V and Ba (table 7.2). Both samples, N81-90 and 703-8, are from the M3 horizon in Foss East (Appendix B). They consist of sulphidic quartz celsian rock and sulphide-banded barite rock respectively.

In N80-90, the mineral is prominent in thin section as a ~0.3 by 0.6mm, isotropic opaque grain with medium grey reflectance, in a matrix of chloritized celsian and quartz. Most of the grain is homogeneous but it has an optically distinct, incomplete rim which is richer in iron but has less V, Mn, U and Sr than the central part. Uranium oxide constitutes at least 5% of the central part of

the mineral, and the associated lead oxide (1.8%) may be radiogenic. E.D.S. examination also confirms the presence of scandium (in the percent range), but K and Na were not detected. A formula calculated on the basis of thirty-eight oxygens gives a cation total of 22.5 (table 7.2). This slight excess may be attributed to analytical uncertainties or to the presence of valencies other than those assumed, or to both factors.

A similar mineral found as several (at least six) 10-20  $\mu\text{m}$  inclusions in pyrite crystals in 703-8 (plate 97), contains no U, Pb, Mg, Sc or Sr. Four grains analysed have 0.2%  $\text{Al}_2\text{O}_3$ ; 1.0-1.4% FeO, 3-6%  $\text{Cr}_2\text{O}_3$ , about 17-20%  $\text{V}_2\text{O}_3$ , 51-53%  $\text{TiO}_2$  and 20-21% BaO. This yields a formula close to  $(\text{Ti,V,Cr,Ba,Fe})_{22}\text{O}_{38}$ , but the high barium content has no previously described analog in the crichtonite group. Reliable analysis of this mineral requires the resolution of wavelength interference problems in the determination of vanadium in a Ti-rich matrix (Appendix E.3), and complete characterization may require XRD studies.

### 7.3 Sulphides.

A dozen sulphide minerals have been identified in rocks from the Foss and Ben Eagach deposits, but of these only pyrite, pyrrhotite, sphalerite and galena are common. Chalcopyrite is widespread but is usually present in very small amounts. Chalcocite and bornite of probable supergene origin (replacing chalcopyrite) were recognised in two samples, and covellite was recorded by Coats et al. (1981). Pentlandite and marcasite are associated with pyrrhotite in a few samples from Foss, and individual occurrences of arsenopyrite and tennantite are reported here for the first time.

Coats et al. (1981) present six microprobe analyses of sphalerite plus four of galena, and sulphide compositions in the Aberfeldy deposits have also been examined in detail by Willan (1981b, 1983). Sphalerite ( $\text{ZnS}$ ) has received more attention than the other sulphide phases as it is comparatively refractory and variable in minor element (Fe, Mn) content, and has retained compositional records of both metamorphic conditions and the primary processes of sulphide deposition. A published paper included in this volume (Moles, 1983) describes the textural and compositional relationships of

sphalerite and associated minerals in representative samples from Foss, and discusses both sphalerite geobarometry (see also Moles, 1985 and sections 8.4.3 & 8.5) and the interpretation of primary variations in sphalerite composition (discussed further in this chapter).

### 7.3.1 Iron and copper sulphides.

#### 7.3.1.1 Pyrite.

The petrographical characteristics of pyrite occurring in mineralized strata at Foss were described in part 3.2.2, and part 3.3.3 discussed the evidence for partial or complete post-metamorphic replacement of pyrrhotite by pyrite in some lithologies. During the course of routine microprobe examination, pyrite grains were analysed in a selection of mineralized, metasedimentary and metabasic lithologies (Appendix B). The average S content of pyrite (53.06 wt%,  $\sigma = 0.37$ ) derived from twenty-two pyrite analyses using the W.D.S. technique, is slightly below the theoretical value (53.45 wt%) for  $\text{FeS}_2$ , and the average Fe content (47.07 wt%) is correspondingly in excess. Considering the small number of determinations and analytical uncertainty (Appendix E.1), these discrepancies are probably insignificant, although some authors have discussed the replacement of some S by Fe in the pyrite structure (cf. Deer et al., 1962b).

Minor elements detected in most of the pyrites are Cu ( $<0.07\%$ ), Ni ( $<0.12\%$ ) and Co (0.02–0.21%), but 2.0% Co was measured in one of several small, isolated pyrite grains in a sample of celsian dolomite rock (504-5). Pyrite in two metabasite samples (424-8, 424-9) contains equal amounts of Ni and Co (both  $<0.08\%$ ), but in the mineralized and metasedimentary rocks examined, pyrite contains more Co than Ni and Co/Ni ratios range from 2–10. Similar variations in the Co and Ni contents of pyrite were noted by Willan (1983) and may indicate a limited extent of equilibration during metamorphism. Willan also found no clear distinction between the trace element contents of pyrite associated with base metal sulphide mineralization and pyrite in otherwise unmineralized metasediments. The generally low Co, Ni contents and high Co/Ni ratios of pyrites from the Aberfeldy deposit, and from other stratiform and disseminated mineralization in the Scottish Dalradian, suggests a sedimentary

affiliation with some hydrothermal/volcanogenic influence (Willan and Hall, 1980; Willan, 1983).

#### 7.3.1.2 Pyrrhotite.

The occurrence of pyrrhotite at Foss was described in part 3.2.2. Tests with magnetic colloid and XRD tracings show that in all samples from Foss examined, the pyrrhotite is monoclinic. This is supported by the mean  $(\text{Fe}+\text{Cu}+\text{Ni}+\text{Co})/\text{S}$  atomic ratio of  $0.895 \pm 0.007$  (cf. Vaughan and Craig, 1978), obtained in thirteen microprobe analyses from a selection of lithologies examined. The pyrrhotite contains similar amounts of Cu, Ni and Co to pyrite, and Co/Ni ratios range from 0.8 (in two metabasite samples) to 7 (in a graphitic schist) and average 2.3. No consistent relationships were observed between the minor element contents of coexisting pyrrhotite and pyrite, but within individual thin sections the Co/Ni ratios of pyrrhotite grains are similar although the absolute amounts of both elements may vary.

#### 7.3.1.3 Pentlandite.

This mineral,  $(\text{FeNi})_9\text{S}_8$ , was observed as orientated, fine lamellar intergrowths with pyrrhotite in a sample of barium-enriched unit C pelite, 706-B (plate 98), and also in a massive pyrrhotite-biotite rock (207-22; Appendices A & B). No microprobe analyses were obtained. An XRF analysis of sample 706-B (table 4.2) indicates that it is exceptionally rich in Ni (208ppm) and Cr (365ppm), perhaps due to a volcanic component, although the Ti content is low. Pentlandite is commonly exsolved from monosulphide solid solutions during cooling (Kelly and Vaughan, 1983).

#### 7.3.1.4 Chalcopyrite.

This occurs in many mineralized and metabasaltic rocks, and is often seen as small grains adjoining pyrrhotite. In a few samples, embayed grains of chalcopyrite form clusters several millimetres across (e.g. 708-6) or form monomineralic lamellae (e.g. N82-A4 and 602-1; plate 87). Chalcopyrite is also common (usually in trace amounts) as inclusions in sphalerite. These inclusions are typically equant, are up to  $30\mu\text{m}$  in diameter, and may be randomly dispersed or orientated along crystallographic planes in the host sphalerite (cf. plate 104). Although some chalcopyrite may have been exsolved from sphalerite during cooling (Wiggins and Craig, 1980), the abundance of inclusions suggests that much of the

chalcopyrite originated as a primary two-phase intergrowth which was recrystallized during metamorphism (Hutchison and Scott, 1981; Craig and Vaughan, 1981).

Eight E.D.S. analyses and five uncontaminated W.D.S. analyses of chalcopyrite ( $\text{CuFeS}_2$ ) from Foss, indicate that zinc is commonly present in trace amounts (up to 0.35 wt%). Donnay and Kullerud (1958) suggest that up to 10% ZnS may be soluble in chalcopyrite at high temperatures, but experimental studies by Hutcheon and Scott (1978) indicate that zinc is accommodated in Cu-Fe-S intermediate solid solutions above 350°C and 5 kbar. At this temperature and pressure, chalcopyrite in equilibrium with sphalerite and iron sulphides contains only 0.4 wt% Zn. Therefore, as observed by Boctor (1980), the low Zn content of most natural chalcopyrite (including that at Foss) indicates equilibration to temperatures lower than 350°C.

#### 7.3.1.5 Bornite and chalcocite.

These minerals,  $\text{Cu}_5\text{FeS}_4$  and  $\text{Cu}_2\text{S}$  respectively, occur in two thin sections cut from a sample of banded calcareous and chloritic unit D schist, 602-1, which is rich in epidote (plate 87). In the calcareous part of the rock, bornite has partly or completely replaced trails of small chalcopyrite grains, whereas coarser sulphide in a nearby quartz-chlorite segregation consists of complex intergrowths of bornite and chalcocite set in a matrix of pure chalcocite. Tiny isotropic and bright reflecting inclusions in this chalcocite are probably pyrite, and an even smaller speck ( $<2\mu\text{m}$ ) of gold was also observed within this crystal (identification confirmed by qualitative E.D.S. analysis). It should be noted that this rock is from outwith the mineralized zone in the lower part of the Ben Lawers Schist, and that weak copper and gold enrichments have been reported by <sup>C.G.</sup>Smith et al. (1977) in the upper part of this formation (the laterally extensive Pyrite Horizon).

#### 7.3.2 Sphalerite.

Although sphalerite is widespread in both mineralized rocks and host metasediments at Foss, it is seldom a major constituent. Sphalerite occasionally forms >50% of massive sulphide bands up to 20cm thick within mineralized horizons (cf. plate 30), but it more commonly occurs as disseminated grains or tenuous laminae which are

parallel to the lithological layering (cf. plate 20). Small sphalerite grains are often encapsulated in pyrite crystals, and sphalerite may contain inclusions of pyrite, pyrrhotite or chalcopyrite. Grains of differing colour often occur in the same thin section (plates 47, 105 & 106) and colour zoning in sphalerite is observed less frequently (plate 109). Microprobe analyses confirm that these colour variations reflect variations in the iron content of sphalerite (fig. 7.1). This ranges from the detection limit to 17mol% FeS, corresponding to a range in appearance from colourless, through yellow and orange, to dark red in transmitted light, which allows the abundance of particular compositions (Fe-rich or Fe-poor) to be estimated visually from thin sections. Textural and compositional relationships in sphalerite-bearing assemblages are illustrated by Moles (1983) (in Appendix) with reference to six representative samples from Foss.

#### 7.3.2.1 Compositional range.

Microprobe analyses of a colourless, but orange-yellow fluorescent sphalerite which contains 2.7mol% MnS (IGS 3897, BH2) are presented by Coats et al. (1980, 1981). This manganese content remains the highest encountered in sphalerite from the Foss and Ben Eagach deposits in an extensive microprobe study which involved the examination of >700 sphalerites in approximately one hundred samples. A diagram of mol% MnS against FeS contents in this data set (fig. 7.2) shows the broad range in sphalerite composition and the absence of an overall systematic relationship between these components. Higher Mn contents appear to be more typical of sphalerite with 4-12mol% FeS than of iron-poor sphalerite, and the composition of the manganoan sphalerite in BH2 is exceptional. Contrary to the impression gained by Coats et al. (1981) that Mn-rich sphalerite is associated with barite rock, the twelve samples encountered in this study with sphalerite containing >1mol% MnS are quartz, celsian and calcite rich rocks with only minor barite.

Other minor elements detected in many sphalerites are copper and cadmium, but antimony is generally below the microprobe detection limit (c. 0.06wt% in routine use: table E.2). The highest reliable value for Cu is 0.20wt% (equivalent to 0.30mol% CuS: sample 505-19), measured in a colourless sphalerite grain which gives a

distinct green cathodoluminescence (plate 108) (cf. Goni and Remond, 1969). Comparable levels of Cu were found in non-luminescent, iron-rich sphalerites in samples G191A, 705-30 and 708-10. Higher Cu values in several other analyses can be attributed to interference from adjoining chalcopyrite, or to microscopic chalcopyrite inclusions which may give sphalerite grains a speckled or darkened appearance.

Cadmium contents of sphalerite (0-0.44 wt%) are also unrelated to iron content in the data set as a whole, but in some samples (specifically 705-19AB: table 7.4) variations in Cd and Fe or Mn are inter-related. An average Cd content of ca. 0.25 wt% in sphalerite from Foss, derived from the microprobe data, is also obtained by extrapolation from unpublished bulk assay data obtained by Dresser Minerals, which show a good correlation between Zn and Cd ( $r = 0.976$  for twenty-four analyses).

Evidence for the non-stoichiometry of zinc sulphides has been reviewed by Craig and Scott (1974), who refer to several studies which demonstrate that the hexagonal (Zn,Fe)S polymorph, wurtzite, is slightly deficient in sulphur whereas dark-coloured sphalerites may be metal-deficient. A spread in the wt% S values (31.7-33.7) in the Foss data set is attributed to analytical uncertainties (largely due to temperature-related peak shifts: Appendix E.1), and reliable determinations suggest that the sphalerite is stoichiometric within the limits of analytical precision ( $\pm 0.3\%$  of the amount present for sulphur). Therefore, only metal wt% values were used in calculating molecular percent sulphide components, normalized to total 100% (Appendix 7.1, table 7.4).

#### 7.3.2.2 Metamorphic modification of primary sphalerite compositions.

Several processes which have erased or modified original sphalerite compositions during metamorphism were distinguished by Moles (1983) and are reviewed here. These processes, summarised in fig. 7.3, are: (a) buffering of the iron content of sphalerite coexisting with pyrrhotite + pyrite; (b) homogenization of individual grains or of massive bands of sphalerite by intra-crystalline diffusion; (c) partitioning of iron and manganese between sphalerite and carbonate or possibly other sulphide phases; and (d) exsolution and retrograde alteration of sphalerite assemblages. The FeS content of sphalerite in equilibrium with pyrite and hexagonal pyrrhotite is

a function only of pressure in the temperature range 254–550°C, and has been calibrated as a geobarometer to 10 kbar by Scott (1973), Lusk and Ford (1978), and Hutchison and Scott (1981). The application of the sphalerite geobarometer at Foss, and evidence for retrograde equilibration in sphalerite-iron sulphide assemblages, are discussed by Moles (1983) and in part 8.3.3.

Disseminated sphalerites of contrasting composition frequently coexist within individual samples from the Aberfeldy mineralization, and in at least one instance (sample 701-19), small, homogeneous sphalerite grains of markedly different FeS-content are in mutual contact (table 7.4). Clearly, equilibrium domains have been minute or disequilibrium has been maintained in many rocks despite having undergone regional metamorphism, and at least some of the observed variation in sphalerite composition appears to have been inherited from the time of deposition.

However, sphalerite is invariably red-coloured and ferroan (>10mol% FeS) when it is in grain contact or in close association with pyrrhotite (or pyrite pseudomorphs of pyrrhotite). This is interpreted as evidence for localized equilibration of sphalerite compositions during metamorphism, in response to high activities of FeS in the immediate vicinity of pyrrhotite grains. An interstitial fluid phase is suggested to have been the transport medium for enrichment in the iron content of the affected sphalerite. Rock volumes within which disseminated sphalerite has been buffered by fluids in equilibrium with pyrrhotite grains range from much less than 1mm<sup>3</sup> (e.g. samples N80-30A, 702-15: plate 105) to at least the size of a hand specimen, and may be pervasive in schistose lithologies. In well-banded rocks, buffered equilibrium domains may be planar in shape, particularly where banding is defined by variations in mica content (cf. plate 106). In some rocks, the distribution of sphalerite with equilibrated compositions is spatially related to cross-cutting veinlets.

Depositional growth zoning in sphalerite, characterized by abrupt and often oscillatory variations in minor element content (e.g. McLimans et al., 1980; Oehler & Logan, 1977), is absent from Foss sphalerite. It is inferred that such growth zoning, if originally present in the sphalerite, has been erased by recrystallization and intracrystalline diffusion during prograde metamorphism



(cf. Barton, 1970; Goble et al., 1979). The presence of encapsulated sphalerites of variable composition may provide evidence for the homogenization of the matrix sphalerite in massive sulphide rocks. In rocks containing disseminated sphalerite with a bimodal distribution of compositions, some sphalerite grains of intermediate composition (fig. 7.1, plate 47) may have formed by the coalescence of several grains of 'end-member' composition. Coalescence during grain coarsening may account for the scarcity of mutual grain contacts between sphalerites of contrasting composition, noted above (fig. 7.3).

Small sphalerite grains which are encapsulated in pyrite are often Fe- and Mn-rich compared to the bulk of sphalerite in the matrix, but detailed studies have shown that these differences are not systematic, and may be related to primary processes rather than to inter-phase element partitioning during metamorphism. However, marginal decreases in the iron and manganese contents of sphalerite within coarsely recrystallized carbonate rocks (e.g. sample 705-21, illustrated in Moles, 1983), are attributed to retrograde matrix-partitioning and diffusion processes. This gradational, continuous zonation may be regarded as a frozen diffusion profile produced during loss of Fe and Mn from the sphalerite into the carbonate matrix. In some carbonate rocks (e.g. sample 203-19, plate 109), individual sphalerite grains appear to have homogenized after marginal depletion in Fe and Mn, resulting in a positive correlation between grain size and minor element content. In such cases only the cores of coarser ( $\geq 1\text{mm}$ ) sphalerite crystals of grains encapsulated by pyrite may preserve the pre-metamorphic sphalerite composition. 'Reverse' zonation in sphalerite with the development of iron-rich rims, has been observed in only one sample (IGS 4145, BH5). These sphalerite grains are near a post-tectonic barite-hyalophane vein, and the iron enrichment may be due to interaction with late metamorphic, circulating fluids.

Criteria which allow the selection of primary sphalerite compositions least likely to have been modified during metamorphism, are summarised in fig. 7.3. These criteria are most frequently satisfied in barite rocks containing disseminated sulphides, but primary sphalerites have been recognized in other mineralized lithologies such as quartz celsian cherts, and also in a few

metasedimentary rocks such as sample 705-14 (Appendix B; table 7.4). It should be stated that variable degrees of uncertainty must inevitably accompany any interpretation of 'original' sphalerite compositions because of the diverse nature of metamorphic and probably diagenetic processes which have affected sulphide assemblages. However, the recognition of systematic spatial variations in the composition of least altered sphalerites strengthens the argument that these have retained primary compositions.

### 7.3.2.3 Spatial variations in primary sphalerite compositions.

Within many thin sections, a bimodal distribution of sphalerite compositions is observed with the Fe-poor fraction usually predominating (e.g. 705-20: plate 47 and fig. 7.1). Primary iron-rich sphalerites are commonly finer grained (maximum diameter  $\sim 200\mu\text{m}$ ), more equant in shape and more often encapsulated in pyrite than the Fe-poor sphalerite occurring in the same rock (plate 47). These textural features suggest that the ferroan sphalerite may have been precipitated earlier than both the Fe-poor sphalerite and much of the pyrite. Moles (1983) suggested that iron-rich sphalerite was precipitated during the expulsion of relatively hot, weakly acidic, and perhaps sulphur-poor metalliferous fluids at the exhalative vents, and was transported in the laterally flowing brine to the site of ore deposition, where more sphalerite with a lower iron content was precipitated in situ. This scenario suggests that (i) primary Fe-rich sphalerite should be most prominent close to the exhalative vents, and (ii) the iron content of the Fe-poor sphalerite fraction should decrease with distance from the vent area, but the composition of the Fe-rich fraction should be unrelated to this parameter.

In order to test this model, an extensive study was undertaken of sphalerites occurring in the M3 horizon in Foss East, which shows pronounced lateral facies variations related in part to the proximity of exhalative vents (part 2.4.6). The mol% FeS contents of about 300 sphalerites which are considered to have retained primary compositions, are plotted against stratigraphic height in nine intersections of this mineralized horizon (fig. 7.4). However, a simple east to west pattern does not emerge because of the wide range of sphalerite composition within each intersection, and often within individual samples. Furthermore, both relatively iron-rich

and iron-poor sphalerite fractions (where clearly distinguished) are highly variable in composition between samples, and where the matrix sphalerite contains <3mol% FeS, the coexisting more iron-rich sphalerite contains only 4-6mol% FeS. This may reflect episodic variations in the sulphur content or rate of discharge of the hydrothermal fluids, or in the oxygen fugacity of the entrained basinal seawater (see part 10.3.2). (The source of the sulphide sulphur in the Foss deposit is discussed with reference to isotopic studies in chapter 9.)

Systematic variations in sphalerite iron content with stratigraphic height can be discerned in two of the profiles (figs. 7.4a, i). Primary sphalerite becomes progressively Fe-poor with height in DH 708, which is the easternmost intersection in Foss East. The lowest iron contents occur in a short barite interval (~10cm) near the top of the 7.5m profile, but rise abruptly in the overlying cherts. A contrasting trend of increasing iron content in sphalerite with increasing stratigraphic height is seen in DH 105, which intersects the thick, stacked barite beds in the vicinity of the Frenich Burn headwater (part 2.4.1). Here, the composition of the Fe-rich sphalerite fraction in samples near the base of the profile is similar to the bulk of sphalerite occurring higher in the barite bed, where sulphides are subordinate in quantity to quartz and magnetite impurities.

A decrease in the iron content of sphalerite with stratigraphic height in the Kuroko deposits (Urabe, 1974a; Urabe & Sato, 1978) is attributed largely to a decline in temperature of the ore forming fluids. However, this trend may also be related to increases in total sulphur concentration and oxygen fugacity in the brines (Finlow-Bates, 1980), which also favour the formation of barite. The physico-chemical changes may have occurred in the eastern Foss East area as a brine pool, ponded in a seafloor depression, mixed with the overlying seawater (parts 2.4.4 and 2.5.1). The contrasting trend in sphalerite compositions in the Frenich Burn area is consistent with a decrease in sulphur concentration due to the restriction of bacterial activity in a relatively shallow, oxidizing environment which is also suggested by the thick accumulation of barite and evidence of syndepositional erosion of the intervening metasediments in this area (part 2.4.1).

Stratigraphical and geochemical evidence, presented in section 2.4, indicates that an exhalative vent may have existed close to the DH 705 intersection of the M3 horizon, in which a metre-thick bed of massive pyrite rock is sandwiched by sulphidic carbonate and barite rock. The carbonate and barite rocks contain a comparatively high proportion (20-50%) of the Fe-rich sphalerite fraction (samples 705-19 and 20: figs. 7.1, 7.4g and plates 24-26 & 47), which is consistent with the model to account for coexisting sphalerites of contrasting composition (see above). However, in contrast to all other intersections examined, bimodal sphalerite populations are absent from the DH 708 profile in eastern Foss East (fig. 7.4i). This could be explained by ore deposition in a stagnant brine pool perhaps some distance from the exhalative centre in the area of DH 705, which may be additional evidence for a major post-depositional fault displacement between the eastern and western blocks at Creagan Loch (part 2.4.6 and fig. 2.35).

### 7.3.3 Galena, tennantite and arsenopyrite.

#### 7.3.3.1 Galena.

Galena is a widespread minor constituent of mineralized rocks in the Aberfeldy deposits and also occurs together with sphalerite in some metasediments (parts 3.3.3, 4.2.1). Except in recrystallized carbonate and massive sulphide rocks, it seldom forms crystals larger than 1mm, and typically occurs as irregularly shaped grains interstitial to, or enclosed within, other sulphides.

Coats et al. (1981) present five microprobe analyses of galena from BHs 4 and 7 in the Ben Eagach deposit, and demonstrate that it contains minor amounts of silver and antimony (both  $\leq 0.15\text{wt}\%$ ). In fourteen samples from Foss examined in this study, lower Ag levels of 0-0.08wt%, were found except in one sample from the M5 horizon (701-11) in which galena contains 0.13-0.45% Ag (two analyses) (table 7.5). Assay data published by Coats et al. (1981) and also obtained by Dresser Minerals, show good correlations between Pb and Ag contents in bulk samples from individual drillhole intersections (fig. 7.5). Extrapolation of these trends allows the average Ag content of galena in these intersections to be estimated, assuming that all the Ag resides in galena. The results indicate that silver levels are significantly lower in the M3 horizon within the eastern

block at Creagan Loch (DHs 707, 708), than in other parts of Foss East (M3 intersected in BH3 and M5-M7 in Frenich Burn area drill-holes) and in the Ben Eagach deposit (BH4). Although insufficient information is presently available for a detailed spatial and stratigraphical analysis of Ag/Pb ratios (since only a few Foss drillhole samples were assayed for Ag by Dresser Minerals), the data shown in fig. 7.5 provide further support to the contention that the eastern block at Creagan Loch was not contiguous with the rest of the Foss deposit during deposition (parts 2.4.6 and 7.3.2.3).

#### 7.3.3.2 Tennantite.

This mineral, the arsenic-rich member of the tetrahedrite group (general formula,  $\text{Cu}_3(\text{As}, \text{Sb}, \text{Zn}, \text{Fe}, \text{Ag})_2\text{S}_4$ ), was discovered in one sample of barite rock from Foss (429-14). It occurs as small ( $<50\mu\text{m}$  diameter), anhedral grains which coexist with pyrite, sphalerite and galena. Three microprobe analyses (table 7.5) show little variation in the As/Sb atomic ratio ( $\sim 5$ ) but show an antipathetic relationship between the Zn and Fe content (5.0-6.5wt% and 3.4-1.9wt% respectively). The tennantite contains 0.66-0.85wt% Ag and trace amounts of Co and Cd. Tennantite is often a minor or trace constituent of sedimentary exhalative ore deposits (Large, 1981a) and its very limited occurrence at Foss presumably reflects the low As and Sb content of the mineralizing fluids.

#### 7.3.3.3 Arsenopyrite.

Arsenopyrite,  $\text{Fe}(\text{As}, \text{S})_2$ , was recognized by its optical properties and distinctive triangular shape (plate 111) in another sample of sulphidic barite rock (705-28). The only crystal found is  $10\mu\text{m}$  across and appears to be totally enclosed by pyrite and galena. A microprobe analysis (table 7.5) was obtained with difficulty because of the small size of the crystal and may not be reliable because of possible interference. This analysis suggests that the arsenopyrite is sulphur-rich (35.0 atomic% S) and correspondingly poor in arsenic ( $\sim 31.3$  atomic% As), which may indicate equilibration with pyrite and vapour at roughly  $400-430^\circ\text{C}$  (Scott, 1983). However, arsenic-bearing buffering phases are absent from the assemblage and sphalerite in this sample retains a range of primary compositions with  $<10\text{mol}\%$  FeS (fig. 7.4g). The arsenopyrite is therefore not in equilibrium with the coexisting sphalerite (cf. Scott, 1983).

#### 7.4 Sulphate (barite).

Barite often occurs as a minor constituent of sulphidic carbonate and quartz celsian rocks, in addition to forming the principal constituent of granoblastic barite rock (section 3.2). Remobilized barite occurs in syn- or post-metamorphic veinlets and has been found as euhedral crystals encrusting fracture surfaces in fault zones (plates 112, 44). Minor amounts of barite appear to have formed from the breakdown of barium carbonates (section 7.5.3), and from surface weathering of barium feldspar (plate 66). Textural evidence in some hyalophane-bearing rocks indicates that barite has reacted with clay minerals to form feldspar (part 3.3.1), perhaps concomitant with the formation of pyrite (isotopic evidence for this is discussed in part 9.5.3).

Drillcore assays and partial analyses of barite concentrates by Coats et al. (1981), indicate that strontium is a minor but ubiquitous constituent of barite rock in the Aberfeldy deposits. The  $\text{SrSO}_4$  content of barite in IGS drillcore ranges from 0.8 to 1.9mol%, and a similar range is observed in the majority of microprobe analyses of barite forming the matrix of barite rocks examined in this study (fig. 7.6 and table 7.6). However, some samples of barite rock have lower  $\text{SrSO}_4$  contents of 0-0.8mol% (e.g. 701-19, 705-28, 708-9), and higher values were observed in two barite rocks which are traversed by fracture zones (G171 and 4085, both from the Frenich Burn area). Sr-poor barite appears to be associated with carbonate-bearing rocks, regardless of the  $\text{SrCO}_3$  content of the coexisting carbonate (part 7.5.2). This suggests a preferential partitioning of Sr into carbonates than into the coexisting barite.

Whereas the composition of barite occurring as a matrix phase varies little within thin sections, barite in cross-cutting veins or in grains encapsulated by sulphide crystals is markedly variable in Sr content (fig. 7.6). The most Sr-rich barite encountered (6.2mol%  $\text{SrSO}_4$  in sample 504-8) is in a small grain enclosed by pyrite, and encapsulated grains of widely differing Sr content have been found within individual thin sections. The restricted range in composition of matrix barites may be due to the coalescence and equilibration of originally heterogeneous barite grains during metamorphism. The analytical data obtained by Coats et al. (1981:

table 14 and Appendix II) do not indicate any systematic spatial variation in the Sr content of barite intersected in BHs 1-5.

## 7.5 Carbonates.

### 7.5.1 Introduction.

Calcite and dolomite are common constituents of both the stratiform mineralization and the metasedimentary and metabasic rocks at Foss and Ben Eagach. Semi-quantitative analyses presented by Coats et al. (1980, 1981) show that a sulphidic 'limestone' occurring at BH4 on Ben Eagach, contains manganoan calcite with about 14mol%  $\text{MnCO}_3$ . Some of the dolomite examined by these authors is iron-rich and should strictly be referred to as ankerite (cf. Deer et al., 1962b). The large range in Ca-Mg-Fe-Mn carbonate compositions, both in the deposits as a whole and within certain samples examined in this study, has been established by >250 microprobe analyses (Appendix E and section 7.5.2). The Mg and Fe contents of calcites were determined in several non-mineralized rocks specifically for application of the calcite-dolomite geothermometer (see part 8.2.3 and Moles, 1985).

In the reconnaissance work reported by Coats et al. (1981), no barium carbonates were found despite the use of staining solutions on drillcore from BHs 3 and 4. However, in this study, trace amounts of witherite ( $\text{BaCO}_3$ ), barytocalcite ( $\text{BaCa}(\text{CO}_3)_2$ ), and norsethite ( $\text{BaMg}(\text{CO}_3)_2$ ) were found in six thin sections from BH4 and also in fifteen samples from Foss. These carbonates, which often occur only as small inclusions in pyrite crystals (see part 3.3.2), were initially located by their distinctive cathodoluminescence (plate 48). Their compositions have been determined by nearly fifty microprobe analyses (section 7.5.3). Iron-, zinc- and manganese-rich carbonates (siderite-smithsonite solid solutions), discovered in four BH4 samples, have also been characterized by microprobe analyses (section 7.5.4).

### 7.5.2 Calcite and dolomite.

The identity of carbonate phases can be difficult to establish with the petrological microscope, except where calcite and dolomite coexist as coarse-grained aggregates (e.g. plate 113). In reconnaissance work, weak hydrochloric acid and XRD patterns were used to

distinguish these carbonates. The intensity and colour of cathodoluminescence in carbonates is sensitive to small variations in composition (e.g. Sommer, 1972), and in addition to facilitating their identification, the luminescope has revealed complex zonation and crystallization histories in carbonates occurring in many mineralized rocks and in some metasediments from Foss (plates 49, 50, 77). Microprobe analyses confirm that the variations in luminescence are usually related to variable Fe and Mn contents. Since iron quenches the luminescence, both ferroan dolomite and Fe-rich calcite appear dull regardless of their Mn content (e.g. the manganoan calcite rock near BH4).

The compositional ranges of analysed Ca-Mg-Fe-Mn carbonates are shown in triangular diagrams (figs. 7.7a-c). These reveal the clear chemical distinction between calcite and the dolomite-ankerite series, both of which contain up to 22mol% of the rhodochrosite ( $\text{MnCO}_3$ ) end-member in solid solution (e.g. samples 3924 and 11-03: table 7.7). Most dolomites contain 48-52 mol%  $\text{CaCO}_3$ , although a few analyses indicate higher calcium contents (maximum, 58 mol%  $\text{CaCO}_3$  in sample 708-8), possibly due to tiny calcite inclusions. Ankeritic dolomites contain up to 21 mol%  $\text{FeCO}_3$ . Calcites coexisting with ferroan dolomite in non-mineralized rocks typically contain 3.4-4.6 mol%  $\text{MgCO}_3$ , 2.9-4.4 mol%  $\text{FeCO}_3$  (fig. 7.8), and 0.6-1.4 mol%  $\text{MnCO}_3$ , whereas calcite in other rocks is more variable in composition with consistently lower Fe contents. Some calcite analyses have >5mol%  $\text{MgCO}_3$ , and up to 12.7mol% was found in red-luminescent grains of magnesian calcite in sample 105-2 (plate 107). In other samples, spuriously high Mg contents may be attributed to interference from adjacent dolomite grains or to fine-grained exsolved dolomite which creates a turbid appearance (plate 46). The Mg content of calcite associated with dolomite is compatible with experimental studies of the  $\text{CaCO}_3$ - $\text{MgCO}_3$  system (Goldsmith, 1959; Goldsmith and Newton, 1969), which suggests that calcite-dolomite equilibration occurred at temperatures of 450-550°C (see part 8.2.3).

Other components detected in calcite and dolomite in some mineralized lithologies are  $\text{SrCO}_3$  (<2.0 mol%),  $\text{BaCO}_3$  (<0.5 mol%) and  $\text{ZnCO}_3$  (<0.2 mol%). The manganoan carbonates occurring in BH4 at Ben Eagach and in BH3 and DHs 410, 702 and 705 at Foss, all contain appreciable amounts of strontium (table 7.7). Lead was looked for,



but not detected, in carbonates in several samples. However, the former presence of some  $\text{PbCO}_3$  in solid solution may be indicated by finely dispersed galena within manganoan calcite crystals in a sample from the Ben Eagach deposit (A2002) submitted for examination by A.M. Boast.

### 7.5.3 Barytocalcite, norsethite and witherite.

#### 7.5.3.1 Barytocalcite.

$(\text{BaCa}(\text{CO}_3)_2)$  was first discovered in the Aberfeldy deposits as lemon-yellow-luminescent grains encapsulated by pyrite (cf. plate 48), in a sample in which manganoan calcite and barite are the principal matrix phases (A2002). A microprobe analysis shows the presence of 6.4 mol%  $\text{MnCO}_3$  in this barytocalcite (table 7.8), which is similar to the Mn content of the matrix calcite. Barytocalcite recognized in other samples produces a bright yellow to dull orange luminescence, reflecting variations in Mn and Fe contents (up to 4 mol%  $\text{FeCO}_3$ ). The yellow luminescence is attributed to a longer wavelength emission activated by  $\text{Mn}^{2+}$  ions within the relatively large  $\text{Ba}^{2+}$  site (Grahame Walker, pers. comm. 1985).

Microprobe analyses of eighteen grains of barytocalcite in nine samples also show considerable variations in  $\text{MgCO}_3$  and  $\text{SrCO}_3$  contents (0-7.3 and 0-6.0 mol% respectively) and a corresponding variation in both  $\text{CaCO}_3$  and  $\text{BaCO}_3$  components. It is therefore possible that some of the grains are of benstonite,  $\text{MgCa}_6\text{Ba}_6(\text{CO}_3)_{13}$  (Lippman, 1962), which is a structurally distinct mineral species. However, the scarcity and small size ( $<100\mu\text{m}$ ) of the 'barytocalcite' inclusions presently precludes their characterization by X-ray studies. An alternative explanation for the dispersion in compositions may be limited solid solution between barytocalcite and both dolomite and norsethite (fig. 7.9).

#### 7.5.3.2 Norsethite.

This carbonate,  $(\text{BaMg}(\text{CO}_3)_2)$ , has previously been described from the Green River Formation (of saline and dolomitic oil shales) in Wyoming (Milton and Eugster, 1959; Mrose et al., 1961) and from the Rosh Pinah mine in SW Africa (Steyn and Watson, 1967; Page and Watson, 1976). Rosh Pinah norsethite contains about 3mol%  $\text{MnCO}_3$ , and from experimental studies, Chang (1964) suggests that a complete solid solution series is possible between norsethite and the

iso-structural compound  $\text{MnBa}(\text{CO}_3)_2$ . Norsethite was synthesized by Chang at  $500^\circ\text{C}$ , but Hood et al. (1974) have precipitated this mineral at room temperature from a wide range of starting solutions.

Norsethite was found in a similar mode to barytocalcite in twelve samples of sulphide, barite and carbonate rocks from the Foss deposit and from BH4. In four of these samples, pyrite crystals contain inclusions of both carbonate phases. Unlike barytocalcite, the norsethite does not have a distinctive luminescence (presumably because  $\text{Mn}^{2+}$  ions are located in the  $\text{Mg}^{2+}$  site, as in dolomite), and therefore may have been overlooked in other samples. Twenty microprobe analyses (of which five are included in table 7.8) reveal a considerable range of substitution for the  $\text{MgCO}_3$  component by  $\text{FeCO}_3$  (0-9.5 mol%) and  $\text{MnCO}_3$  (0-9.0 mol%). More limited ranges are observed for  $\text{CaCO}_3$  (0.4-2.5 mol%) and  $\text{SrCO}_3$  (0-1.2 mol%), which appears to substitute for  $\text{BaCO}_3$  (fig. 7.9). Two analyses which fall outside the compositional fields of barytocalcite and norsethite in fig. 7.9, are probably calcite-norsethite and barytocalcite-norsethite mixtures (samples 408-30A and 3916).

#### 7.5.3.3 Witherite.

Witherite ( $\text{BaCO}_3$ ) has been positively identified in only three samples examined, again occurring as small, weakly luminescent (purple) inclusions in pyrite (IGS 3965, from BH3, and samples 410-29 and 701-19). It is noteworthy that these samples are all barite rocks and that barytocalcite and norsethite have not been found together with witherite in individual samples (although they occur within 1m of drillcore). The witherite in 3965 and 410-29 contains about 3mol%  $\text{SrCO}_3$  in solid solution whereas that in 701-19 is strontium-rich with nearly 10mol%  $\text{SrCO}_3$  (table 7.8). Ca, Mg, and Mn contents are low and  $\text{FeCO}_3$  varies from 0.6-3.3 mol% (although higher Fe values may be partly due to interference from the surrounding pyrite). Gundlach (1959) reports that witherite from Alston in England contains 1.2-1.8 mol%  $\text{SrCO}_3$  and the barytocalcite from the same locality contains 0.3-0.45%  $\text{SrCO}_3$ .

#### 7.5.4 Siderite and siderite-smithsonite solid solutions.

Siderite occurs as a late metamorphic or supergene phase which occupies fissures in a few mineralized rocks examined (e.g. C79-28). Dark brown-coloured siderite analysed in IGS 3906 (BH2) (table 7.9)

contains 3-4 mol% each of  $\text{MgCO}_3$  and  $\text{MnCO}_3$ , but contains very little Ca or Zn.

A soft-polishing and variously coloured (pale to dark green and locally red) carbonate phase occurs in the matrix of four sulphide-rich rock samples from BH4 (IGS 3916, 3920, 3922 and 3924: for location see Coats et al., 1981). This was found to be a Fe, Zn, Mn carbonate containing 13-30 mol%  $\text{ZnCO}_3$  (smithsonite) and 9-25 mol%  $\text{MnCO}_3$  (rhodochrosite) end-members, with subordinate amounts of  $\text{CaCO}_3$  and  $\text{MgCO}_3$  (table 7.9). A Mn-Fe-Zn diagram (fig. 7.10) illustrates the limited range in compositions (which bear no relationship to colour variations) determined in twelve microprobe analyses.

These carbonates, which correspond to Kager's (1980)  $\text{SSm}_1$  subdivision of the siderite-smithsonite solid solution series, are considered to be a product of late metamorphic reactions involving the dissolution of pyrite, sphalerite and pre-existing manganoan dolomite and calcite, relicts of which are enclosed within sulphides in two of these samples. Shikazono (1977) discusses the physico-chemical controls on the Zn-content of siderites in the Miocene Green Tuff region of Japan, which are similar in composition to those occurring in BH4 at Ben Eagach. He concludes that crystallization temperatures were in the range 150-300°C and that the carbonate compositions are most sensitive to variations in  $f\text{O}_2$ . A detailed analysis of the conditions during formation of the siderites occurring in BH4 samples is beyond the scope of the present study, but they are clearly of retrograde metamorphic origin.

## 7.6 Phosphates.

### 7.6.1 Apatite.

This mineral,  $\text{Ca}_5(\text{PO}_4)_3(\text{OH}, \text{F}, \text{Cl})$ , was previously known to be a common minor or trace constituent of many rocks associated with the Aberfeldy deposits (Coats et al., 1981) but the ubiquitous presence of apatite (in all lithologies except barite rock) has been shown by cathodoluminescence observations. In samples from Foss, apatite usually occurs as small (<150µm) disseminated and equant grains which produce a bright whitish-green or yellow-green luminescence (plate 62). In two samples examined, apatites are zoned with pink or purple luminescent cores (N80-45, 203-1) of possible pre-metamorphic origin. Coarser grained apatite often occurs in massive sulphide

and mineralized carbonate rocks, and granular apatite forms folded monomineralic bands several millimetres thick in one dolomite-celsian rock (plate 116). This suggests that some apatite at Foss may be derived from phosphates introduced with the hydrothermal fluids, in addition to phosphate of sedimentary and igneous origin.

A few analyses (mostly E.D.S.) of apatite obtained in this study show that it is the commonest variety, fluorapatite (Deer et al., 1962b), and that it generally contains few detectable impurities. Apatite associated with sphalerite and the rare-earth phosphate monazite (see below) in sample 701-11, contains 0.13 wt%  $\text{Ce}_2\text{O}_3$  in addition to 4.2 wt% F. This sample also contains F-bearing phlogopite (table 6.6). E.D.S. spectra of the zoned apatite in the metabasite sample, N80-45, indicate lower Ce and La contents in the cores of grains than in grain rims.

#### 7.6.2 Monazite.

This phosphate, general formula  $(\text{Ce},\text{La},\text{Y},\text{Th})\text{PO}_4$ , was identified by qualitative microprobe analysis in a few mineralized rocks, in which it occurs as small, apatite-like grains coexisting with apatite. However, monazite was also found as an aggregate of coarse (1-2mm), anisotropic and yellowish brown-coloured crystals with high refractive indices, occurring in a quartz matrix in one sample of banded quartz-carbonate-celsian rock (701-11: plate 115). Partial microprobe analyses indicate that these crystals are slightly zoned and contain approximately 30 wt%  $\text{P}_2\text{O}_5$ , 32 wt%  $\text{Ce}_2\text{O}_3$ , 25 wt%  $\text{La}_2\text{O}_3$ , 5-6 wt%  $\text{Nd}_2\text{O}_3$  and 1.6 wt%  $\text{Pr}_2\text{O}_3$  (no calcium was detected). In addition, 0.6-0.9 wt% F was determined in this monazite, and low oxide totals may be due to the presence of several percent  $\text{ThO}_2$  which was not determined. The presence of radioactive elements in the monazite is also suggested by a luminiscent halo in the surrounding quartz (although the monazite itself does not respond to cathodoluminescence) (cf. Smith and Stenstrom, 1965).

Unlike the allanite described in part 6.4.5, a detrital origin for this monazite is unlikely because of its location within the stratiform mineralization. The occurrence at Foss is very unusual, particularly when the quantity of monazite in sample 701-11 is considered. However, the association may not be unique, as Plimer and Lovering (quoted in Plimer, 1984) have recorded monazite in Mn-silicate - barite "exhalites" of Wilkes Land, Antarctica.

## 7.7 Primary mineralogy, element partitioning and metamorphic equilibration.

Over forty mineral species and compositionally distinct sub-species have been described from the vicinity of the Foss deposit, of which about a dozen were not previously identified (table 7.10). Except for the barium carbonates (found in trace amounts in a significant proportion of barite rocks examined), the newly described non-silicate minerals were found in single specimens or a few samples and must be considered as volumetrically insignificant. These phases, which include cassiterite, chromian rutile, Ti-V-Ba oxide and a uraniferous complex oxide probably belonging to the crichtonite group, pentlandite, tennantite, arsenopyrite and monazite, are interesting because of their unusual compositions and parageneses. Together with other mineral constituents such as fuchsite, these may indicate the presence of trace amounts of elements such as Ti, V, Cr, Ni, As, Sn, rare earths, Th and U in the hydrothermal fluids.

### 7.7.1 Primary compositions and the effects of metamorphism.

The occurrence and composition of all the mineral groups examined reflect to varying degrees both the primary chemical composition of the sedimentary, igneous and hydrothermal lithologies, and the influence of metamorphic processes. Refractory minerals which may have retained their primary compositions are largely absent from the metasediments and metabasites, in which most of the silicate and carbonate minerals were neoformed during metamorphism from detrital, authigenic and igneous minerals. However, in the mineralized strata, refractory sulphides such as pyrite and sphalerite have often equilibrated only on a microscopic scale, and spatial variations in sphalerite iron content may be used to deduce primary ore-forming processes and conditions. Less refractory sulphides such as pyrrhotite and chalcopyrite (fig. 7.11) have uniform compositions which indicate continued equilibration to temperatures (and pressures) much lower than the peak metamorphic conditions. Several examples were described in section 3.3 where pre-metamorphic mineral species, such as the barium carbonates and kaolinite, or pre-metamorphic heterogeneities in mineral composition (e.g. in barite), have survived metamorphism because the grains were

encapsulated in non-reactive minerals at an early stage.

Changes in mineralogy and mineral composition during metamorphism may be related to several processes: (1) Reaction or replacement, which usually involved interaction with a fluid phase, and occurred in various situations throughout the depositional and metamorphic history and during minor near-surface alteration. (2) Homogenization by recrystallization, intracrystalline diffusion, or exchange with metamorphic fluids. Compositional variations on a decimetric to metric scale due to the partial 'smoothing out' of primary heterogeneities during metamorphism, are illustrated by observations of K/Na ratios in barian feldspars (part 6.2.2), the Sr content of barite (section 7.4) and possibly the Ag content of galena (part 7.3.3.1). (3) Structural changes, which may result in the exsolution of one phase from another (e.g. pentlandite in pyrrhotite, pyrrhotite in some sphalerite) or the coexistence of two phases which have limited solid solution (e.g. peristerite compositions in plagioclase, calcite-dolomite equilibria). (4) Partitioning of elements between coexisting phases, controlled by partitioning coefficients, the pressure and temperature of metamorphism, and kinetic factors.

#### 7.7.2 Examples of inter-phase element partitioning.

There is no clear evidence for a systematic partitioning of manganese between coexisting calcite and dolomite, although increased Mn contents in both carbonates reflects a bulk compositional control. In all sphalerite- and carbonate-bearing samples examined in which the sphalerite is enriched in manganese (>1mol% MnS), the carbonate is also manganoan, but in other samples, manganoan carbonates coexist with sphalerites of widely variable MnS content. This presumably reflects primary phase disequilibria, whereas the marginal depletion of Fe and Mn in sphalerite within coarsely recrystallized carbonate rocks (Moles, 1983) is attributed to late-metamorphic partitioning between these phases (part 7.3.2). The metamorphic equilibration of sphalerite in the presence of pyrrhotite, also appears to involve a loss of manganese relative to primary (non-buffered) sphalerite compositions in the same sample (see fig. 4b of Moles, 1983). Further work is required to substantiate the possible correlation between Mn contents of coexisting magnetite and sphalerite, noted in part 7.2.1.

Barite occurring as a minor phase in carbonate rocks, or as a major phase in barite-carbonate layers, is generally poor in strontium compared with the barite in carbonate-poor barite rocks. The preferential partitioning of Sr into carbonate is also illustrated by the high  $\text{SrCO}_3$  contents of barytocalcite and witherite inclusions in barite, which were found in several samples (part 7.5.3 and table 7.8).

#### 7.7.3 Partitioning of iron between sulphides and silicates.

Several authors have described a decrease in the iron content of silicate minerals close to metamorphosed massive sulphide deposits, such as Ducktown, Tennessee (Nesbitt, 1982). Systematic relationships between the Fe:Mg ratios of phyllosilicates and the iron contents of coexisting sphalerite and carbonates, have been described by McLeod and Stanton (1984) from the unmetamorphosed stratiform sulphide deposits of southeastern Australia. The authors regard these relationships as primary features of the mineralization, which are principally governed by sulphur fugacity variations during precipitation from the hydrothermal fluids. No systematic correlation between coexisting sphalerite and mica compositions was found in the present study, as both Fe-rich and Fe-poor sphalerite coexist with phlogopite or biotite in a variety of rock types.

The low Fe:Mg ratios in micas coexisting with volumetrically significant amounts of iron sulphides, noted in section 6.3, is attributed to the partitioning of iron into sulphides during diagenesis or metamorphic recrystallization, due to the high sulphur fugacities prevailing in these lithologies. The corresponding increase in effective bulk Fe:Mg ratios, together with low oxygen fugacities, may account for the scarcity of garnet, chlorite and biotite in unit B sulphidic graphitic schists.

Ferry (1981) found a systematic relationship between biotite composition and the identity of iron sulphides in graphitic schists from south-central Maine, such that all rocks with pyrite + pyrrhotite contained phlogopite with measured  $\text{Fe}/(\text{Fe}+\text{Mg})$  ratios of 0.02-0.06, whereas if only pyrrhotite was present, then this ratio varied from 0.16-0.47 in the tri-octahedral micas. Ferry suggested that the unique composition of phlogopite coexisting with pyrite + pyrrhotite may reflect initial crystallization in an invariant

assemblage, and demonstrated that biotite does not participate in desulphidation reactions until pyrite is eliminated from the assemblage. By analogy, the presence of biotite rather than phlogopite in graphitic schists of unit A at Foss may be related to the absence of pyrite (other than as a retrograde replacement of pyrrhotite) in these rocks. Exceptionally variable Fe:Mg ratios in muscovite, but uniform phlogopite compositions in the hyalophane schist sample N81-80 (fig. 6.14), may be related to muscovite-consuming reactions (involving the reduction of barite and formation of hyalophane and pyrite) during burial or regional metamorphism (see part 9.5.3).

Provided increased sulphur fugacities do not exert an overriding control, the equilibrium distribution of Fe and Mg between ferromagnesian silicates is temperature-dependant. Several silicate mineral pairs (including garnet and biotite, garnet and hornblende) have been calibrated as geothermometers, and the following chapter discusses the use of these, and a variety of other mineral equilibria, in estimating the pressure and temperature during metamorphism.



TABLE 7.1: SELECTED RUTILE &amp; ILMENITE ANALYSES.

	1	2	3	4	5	6
SiO2	0.06	0.02	0.05	nd	0.18	0.32
TiO2	98.87	95.91	99.83	91.29	51.56	51.28
Al2O3	0.05	nd	0.05	0.04	nd	nd
Cr2O3	0.06	0.60	0.09	1.12	nd	nd
FeO	0.68	0.35	0.88	0.15	46.44	46.24
MnO	nd	0.01	nd	nd	0.88	1.16
MgO	0.02	0.01	0.02	0.03	0.28	nd
CaO	nd	nd	0.01	0.11	nd	nd
total=	99.74	96.90	100.93	92.74	99.34	99.00
Si	-	-	-	-	-	0.01
Ti	1.99	1.99	1.99	1.98	1.32	1.31
Cr	-	0.01	-	0.03	-	-
Fe2	0.02	-	0.02	-	1.32	1.32
Mn	-	-	-	-	0.03	0.03
Mg	-	-	-	-	0.01	-
total=	2.01	2.01	2.01	2.01	2.68	2.68
oxygens=	[4]	[4]	[4]	[4]	[4]	[4]

1 RU 4685,1 OPAQUE IN MUSC  
 2 RU G100E,2 ENC PY  
 3 RU 503-32,1 MATRIX  
 4 RU N82-A4-4,1 DARK RED  
 5 IL N80-36,1 ENC GARNET  
 6 IL 4683,1 MATRIX

TABLE 7.2: ?CRICHTONITE-GROUP MINERALS.

	1	2	3	4
SiO2	0.02	3.61	nd	nd
TiO2	52.33	53.19	51.93	52.09
Al2O3	0.32	1.12	0.20	0.20
Cr2O3	13.91	12.51	6.59	3.94
FeO	9.65	12.80	1.02	1.19
MnO	1.26	0.29	nd	nd
MgO	0.27	0.06	nd	nd
V2O3	7.10	4.62	18.93	21.67
BaO	4.35	3.93	20.84	21.13
SrO	1.59	0.28	nd	nd
ZnO	0.89	0.21	0.01	nd
Ag2O	0.06	0.09	nd	nd
PbO	1.78	1.11	nd	nd
U2O3	5.32	1.37	nd	nd
total=	98.85	95.19	99.52	100.22
F	nd	nd	0.28	0.19
Si	-	1.11	-	-
Ti	12.51	12.33	12.57	12.54
Al	0.12	0.41	0.08	0.08
Cr	3.50	3.05	1.68	1.00
Fe2	2.57	3.30	0.27	0.32
Mn	0.34	0.08	-	-
Mg	0.13	0.03	-	-
V	1.81	1.14	4.89	5.56
Ba	0.54	0.47	2.63	2.65
Sr	0.29	0.05	-	-
Zn	0.21	0.05	-	-
Ag	-	0.01	-	-
Pb	0.15	0.09	-	-
U	0.39	0.10	-	-
total=	22.58	22.22	22.11	22.14
oxygens=	[38]	[38]	[38]	[38]

1 N81-90,CENTRE  
 2 N81-90,RIM  
 3 703-8,1R ENC PY  
 4 703-8,3 ENC PY

TABLE 7.3: PYRITE, PYRRHOTITE &amp; CHALCOPYRITE.

	1	2	3	4	5	6	7	8	9	10
Fe	47.19	47.05	46.91	47.08	44.85	46.89	60.20	59.93	60.08	60.25
Ni	0.07	0.06	0.01	0.02	nd	nd	0.06	0.10	0.12	0.17
S	52.94	52.49	53.51	52.99	52.74	52.71	39.39	39.18	38.53	38.32
Co	0.13	0.08	0.08	0.08	2.02	0.06	0.17	0.14	0.10	0.12
Cu	0.01	0.06	0.07	0.02	0.02	0.03	0.09	0.16	nd	0.04
Zn	nd	nd	0.41	nd	nd	nd	nd	0.15	nd	nd
total=	100.34	99.74	100.99	100.19	99.63	99.69	99.91	99.66	98.83	98.90
S/Fe	1.007	1.001	1.024	1.010	1.055	1.009	0.587	0.587	0.576	0.571
<hr/>										
	11	12	13	1 202-3,PY2 2 429-8,PY2 3 705-14,PY1 4 504-7,PY2 SMALL 5 504-5,PY1 SMALL IN DOL					6 504-5,PY4 7 202-3,P01 8 705-14,P02 9 424-8,P01 10 504-5,P02	
Fe	30.68	30.59	30.70							
Ni	0.07	0.01	nd							
S	34.45	34.47	34.35							
Co	0.11	0.07	nd							
Cu	34.35	33.86	34.40							
Zn	0.34	0.06	0.12							
Cd	nd	nd	0.13							
total=	100.00	99.06	99.70							
S/Fe	1.008	1.011	1.004							
<hr/>										
11 202-3,CPY1 12 705-14,CPY1 13 N82-A4-3,CPY1 BAND										

TABLE 7.4: SELECTED SPHALERITE ANALYSES.

	1	2	3	4	5	6	7	8	9	10	
Fe	6.72	9.87	7.21	3.34	6.89	3.18	6.84	4.27	8.20	8.66	
Mn	0.02	0.07	0.02	0.68	0.02	0.02	0.01	0.04	0.01	0.31	
S	32.81	33.31	33.65	33.43	33.01	33.23	33.00	32.92	32.86	33.41	
Cu	0.01	0.03	0.03	0.03	0.05	0.06	0.06	0.08	0.18	nd	
Zn	60.76	56.96	60.18	63.75	60.40	64.09	60.79	62.81	58.76	57.52	
Cd	0.22	0.24	nd	nd	0.12	0.11	0.05	0.06	nd	nd	
Sb	nd	nd	nd	0.02	0.03	nd	nd	nd	0.01	0.01	
total=	100.54	100.48	101.09	101.25	100.52	100.69	100.75	100.18	100.02	99.91	
<hr/>											
mol%	FeS	11.44	16.80	12.29	5.71	11.75	5.48	11.62	7.35	14.00	14.90
	MnS	0.04	0.12	0.04	1.18	0.04	0.04	0.02	0.07	0.02	0.54
	CuS	0.02	0.05	0.05	0.05	0.07	0.09	0.09	0.12	0.27	nd
	ZnS	88.33	82.83	87.63	93.05	88.01	94.30	88.23	92.40	85.70	84.55
	CdS	0.19	0.20	nd	nd	0.10	0.09	0.04	0.05	nd	nd
	SbS	nd	nd	nd	0.02	0.02	nd	nd	nd	0.01	0.01
<hr/>											
1	202-3,6 ADJ P0 + PY(SPONGY)				11	3897,2 CLEAR MN-SPH					
2	202-3,P17 DARK RED CORE				12	708-9,1 YELLOW IN BAR					
3	N80-30A,RED2A				13	701-19,68 SAME; NEAREST TO YEL SPH					
4	N80-30A,YEL3				14	701-19,7 ADJOINING YEL SPH					
5	705-14,2 ADJ MARCASITE				15	705-9,6 ADJ P0: COARSE					
6	705-14,5 YELLOW IN DOL				16	705-9,14 CORE OF DARK ISO IN DOL					
7	429-8,2 RED BAND CORE				17	705-19AB,5 DK RED IN CAL+QTZ; CENTRAL					
8	429-8,5 YELLOW BAND				18	705-19AB,9 RIM OF SAME					
9	G191A,2 RED INC PY				19	505-15,1 SMALL CLEAR (GREEN LUM)					
10	429-8,6R RED ENC PY IN YEL BAND				20	505-15,6 ORA IN BAR ISO					
<hr/>											
	11	12	13	14	15	16	17	18	19	20	
Fe	0.02	0.88	4.78	2.24	6.58	7.80	8.01	1.88	0.13	2.96	
Mn	1.53	0.47	0.06	0.07	nd	0.04	0.15	0.15	0.03	nd	
S	32.30	32.44	32.62	32.57	33.08	33.28	32.11	31.68	31.68	31.76	
Cu	0.03	0.06	0.05	0.04	nd	0.03	nd	0.06	0.20	0.01	
Zn	65.24	66.26	61.71	64.72	60.57	59.34	59.37	64.88	67.77	64.57	
Cd	0.07	0.22	0.06	0.15	0.21	0.22	0.16	0.41	0.21	0.09	
Sb	0.01	nd	0.05	0.06	nd	nd	nd	nd	nd	nd	
total=	99.20	100.33	99.33	99.85	100.44	100.71	99.80	99.06	100.02	99.39	
<hr/>											
mol%	FeS	0.04	1.52	8.29	3.88	11.26	13.30	13.59	3.26	0.22	5.09
	MnS	2.71	0.81	0.11	0.12	nd	0.07	0.26	0.26	0.05	nd
	CuS	0.05	0.09	0.08	0.06	nd	0.05	nd	0.09	0.30	0.02
	ZnS	97.14	97.38	91.44	95.76	88.56	86.40	86.02	96.03	99.24	94.82
	CdS	0.06	0.19	0.05	0.13	0.18	0.19	0.13	0.35	0.18	0.08
	SbS	0.01	nd	0.04	0.05	nd	nd	nd	nd	nd	nd

TABLE 7.5: GALENA, TENNANTITE &amp; ARSENOPYRITE.

	1	2	3	4	5	6	7
Fe	0.09	0.03	0.06	0.13	3.11	1.86	35.20
Ni	nd	nd	nd	nd	nd	nd	0.03
S	13.21	12.43	13.18	12.94	27.63	27.63	20.91
Co	nd	nd	nd	nd	0.03	0.04	0.05
Cu	nd	nd	0.09	0.07	41.88	42.34	nd
Zn	0.05	nd	nd	nd	5.02	6.53	nd
As	nd	nd	nd	nd	16.23	16.50	43.75
Ag	0.07	0.12	nd	0.49	0.72	0.66	0.03
Cd	nd	nd	nd	nd	nd	0.03	0.03
Sb	nd	nd	nd	nd	5.59	5.41	nd
Pb	86.36	86.71	85.68	85.63	nd	nd	nd
Bi	0.35	nd	nd	nd	nd	nd	nd
total=	100.12	99.29	99.01	99.26	100.21	101.00	100.00

1 705-30,GAL2

2 A2002,GAL2

3 702-11,GAL2 MATRIX ADJ PY

4 701-11,GAL2 IN DOL

5 429-18,TE1 TENNANTITE

6 429-18,TE3 LARGEST TENNANTITE GRAIN

7 705-28,1 ARSENOPYRITE (ON QTZ&amp;RAP)

TABLE 7.6: SELECTED BARITE ANALYSES.

	1	2	3	4	5	6	7	8	9	10
SiO2	0.03	0.12	0.05	0.05	nd	nd	0.20	nd	nd	nd
FeO	0.09	0.07	nd	nd	0.03	nd	0.17	nd	0.48	0.05
CaO	0.02	0.18	0.02	nd	nd	0.01	0.03	nd	0.03	0.03
SO3	33.77	35.55	32.94	32.46	32.90	33.21	31.37	34.49	34.23	33.92
BaO	65.88	63.25	64.56	63.95	64.87	64.65	61.80	65.81	63.69	65.20
SrO	0.57	0.73	0.89	1.62	0.61	0.72	2.80	0.31	1.87	0.10
total=	100.36	99.90	98.46	98.08	98.41	98.59	96.37	100.61	100.30	99.30
Fe2	-	-	-	-	-	-	-	-	0.02	-
S	0.99	1.01	0.99	0.98	0.99	0.99	0.97	1.00	0.99	1.00
Ba	1.01	0.94	1.01	1.01	1.02	1.01	1.00	1.00	0.96	1.00
Sr	0.01	0.02	0.02	0.04	0.01	0.02	0.07	-	0.04	-
total=	2.02	1.98	2.02	2.03	2.02	2.02	2.05	2.00	2.01	2.00
oxygens=	[4]	[4]	[4]	[4]	[4]	[4]	[4]	[4]	[4]	[4]
mol% SrSO4	1.26	1.66	2.00	3.62	1.37	1.62	6.24	0.69	4.10	0.23

1 4143,2

2 N81-80,2 RELICT

3 705-17A,VEIN1

4 705-17A,VEIN2

5 705-20,2

6 G171,2 BRECCIA

7 504-8,2 ENC LARGE PY

8 708-9,1 ASSOC CARBONATE

9 203-18,1 ENC PY

10 203-18,3 MATRIX



TABLE 7.8: BARIUM CARBONATE ANALYSES.

	1	2	3	4	5	6	7	8
FeO	0.34	0.10	1.54	0.80	0.27	1.21	1.35	0.75
MnO	3.09	0.79	2.25	0.21	0.21	1.63	1.74	4.75
MgO	0.50	0.66	6.34	0.05	1.93	3.53	14.57	11.37
CaO	16.13	15.73	11.85	18.00	17.62	42.48	0.20	1.01
BaO	51.27	45.61	53.90	52.49	44.43	12.78	56.36	55.35
SrO	0.80	9.55	nd	nd	4.24	1.16	0.10	nd
total=	72.13	72.44	75.88	71.55	68.70	62.79	74.32	73.23
mol%	FeCO3	0.69	0.20	2.77	1.64	0.54	1.72	1.41
	MnCO3	6.31	1.59	4.10	0.44	0.42	2.35	9.07
	MgCO3	1.80	2.34	20.34	0.18	6.85	8.94	38.20
	CaCO3	41.67	40.13	27.33	47.31	44.93	77.34	0.46
	BaCO3	48.42	42.54	45.45	50.43	41.42	8.51	47.30
	SrCO3	1.12	13.19	-	-	5.85	1.14	0.12
total=	100.00	100.00	100.00	100.00	100.00	100.00	100.00	100.00
1 A2002,2 BARYTOCALCITE ENC PY								
2 3915,1 SR-BARYTOCALCITE ENC BAR								
3 3916,4 BARYTOCALCITE ENC PY: MIX?								
4 3916,5 BARYTOCALCITE ENC PY								
5 703-8,3 SR-BARYTOCALCITE IN BAR								
6 408-30A,2 CAL-NORS MIX ENC PY								
7 3917,1 NORSETHITE ENC PY								
8 3921,5 BIG NORSETHITE ENC PY								

	9	10	11	12	13	14
SiO2	nd	nd	nd	0.11	nd	nd
FeO	4.92	1.63	4.96	1.21	0.29	0.64
MnO	0.42	2.10	0.76	nd	nd	0.02
MgO	12.97	12.69	11.40	0.07	0.03	0.04
CaO	0.33	0.59	0.20	0.08	0.08	0.17
BaO	55.68	54.77	53.79	72.08	73.73	69.83
SrO	0.10	0.04	0.91	1.52	1.50	5.25
total=	74.42	71.82	72.02	75.07	75.63	75.95
mol%	Si	-	-	0.36	-	-
	FeCO3	8.94	3.09	9.51	0.81	1.72
	MnCO3	0.77	4.03	1.48	-	0.05
	MgCO3	42.00	42.83	38.98	0.34	0.19
	CaCO3	0.77	1.43	0.49	0.28	0.58
	BaCO3	47.39	48.58	48.33	92.46	95.87
total=	100.00	100.00	100.00	99.64	100.00	100.00
9 408-10,5 NORSETHITE ENC PY						
10 408-28,1 NORSETHITE ENC PY						
11 702-9,3 SMALL NORSETHITE IN BAR						
12 3965,1 WITHERITE ENC PY						
13 410-29,3 WITHERITE ENC PY						
14 701-19,3 SR-WITHERITE ENC PY						

TABLE 7.9: SIDERITE ANALYSES.

	1	2	3	4	5	
SiO2	3.28	nd	nd	nd	0.01	
Al2O3	nd	0.04	nd	nd	nd	
FeO	54.11	31.88	30.96	43.20	29.53	
MnO	2.34	10.24	14.73	5.59	8.37	
MgO	0.94	0.22	0.21	0.43	0.16	
CaO	0.12	1.47	4.04	1.93	0.97	
ZnO	0.04	17.53	9.35	9.91	19.54	
total=	60.83	61.38	59.29	61.06	58.58	
mol% {	Si	5.93	-	-	0.02	
	Al	-	0.09	-	-	
	FeCO3	81.75	53.06	51.86	70.99	51.98
	MnCO3	3.58	17.26	24.99	9.30	14.92
	MgCO3	2.53	0.65	0.63	1.26	0.50
	CaCO3	0.23	3.13	8.67	4.06	2.19
	ZnCO3	0.05	25.76	13.83	14.38	30.37
	total=	94.07	99.91	100.00	100.00	99.98
1 3906,1 SIDERITE						
2 3916,1 CLEAR ZN-SIDERITE						
3 3916,8 ZN-SIDERITE MATRIX						
4 3920,6 ZN-SIDERITE GREEN						
5 3922,2 ZN-SIDERITE						

TABLE 7.10: Mineral species identified in the Foss deposit and host rocks

Group	Species/variety	Abundance <sup>1</sup>	Origin <sup>2</sup>	Probe data <sup>3</sup> (WDS)	
Silicates	Quartz	M	PM V	-	
	Plagioclase	M	pM	6.1	48
	K-feldspar	m	P R	6.2	6
	Hyalophane	M	pM	6.2	124
	Celsian, K-celsian	M	p R	6.2	132
	Cymrite	m	pM	6.3	35
	Muscovite	M	pM	6.4	70
	Ba-muscovite	M	pM	6.4	83
	Ba-Cr(-V)-muscovite	t	M	6.5	25
	Biotite, phlogopite	M	pM	6.6	75
	Ba-biotite	t	M	6.6	23
	Hydrobiotite	m	R	6.7	16
	Kaolinite	t	p R	x	
	Chlorite	M	p R	6.8	30
	Talc	t	pM	6.9	4
	Garnet	M	M	6.10	100
	Hornblende	M	M	6.11	11
	Zoisite-epidote	m	M	6.12	6
	Allanite	i	P	6.12	3
	Tourmaline	m	M	6.13	3
	Zircon	m	P	-	
	Sphene	m	M	6.13	5
	Baoite	i	P	6.14	2
Oxides	Magnetite	m	P	x	
	Hematite	t	R	-	
	Ilmenite	M	pM	7.1	4
	Rutile	M	pM	7.1	7
	Cassiterite	i	P	x	
	Crichtonite group	t	Pm	7.2	7
Sulphides	Pyrite	M	PmRV	7.3	22
	Marcasite	t	R	x	
	Pyrrhotite	M	PM	7.3	12
	Pentlandite	t	R	-	
	Chalcopyrite	m	PmR	7.3	3
	Bornite	i	R	x	
	Chalcocite	i	R	x	
	Sphalerite	M	Pm	7.4	738
	Galena	m	P V	7.5	24
	Tennantite	i	P	7.5	3
Sulphates	Arsenopyrite	i	p	7.5	1
	Barite	M	P V	7.6	62
Carbonates	Calcite	M	PM V	7.7	105
	Dolomite	M	PM V	7.7	155
	Witherite	t	P	7.8	4
	Barytocalcite (?Benstonite)	t	P	7.8	18
	Norsethite	t	P	7.8	20
	Siderite-smithsonite	t	R	7.9	13
Phosphates	Apatite	m	pM	x	
	Monazite	t	P	x	
Native elements	'Graphite'	m	Pm	-	
	V-Cr-Fe oxide (410-31)	i	R	x	
	Gold	i	Pm	x	

<sup>1</sup> M = major; m = minor but widespread or locally common; t = trace, several samples; i = trace, one sample.

<sup>2</sup> P = primary or diagenetic (pre-metamorphic); M = metamorphic (prograde); R = retrograde metamorphic or supergene; V = common in veins. Lower case indicates uncertainty.

<sup>3</sup> Refers to Appendix table: x = examined, but analyses not presented. Numbers indicate total no. of WDS analyses obtained.

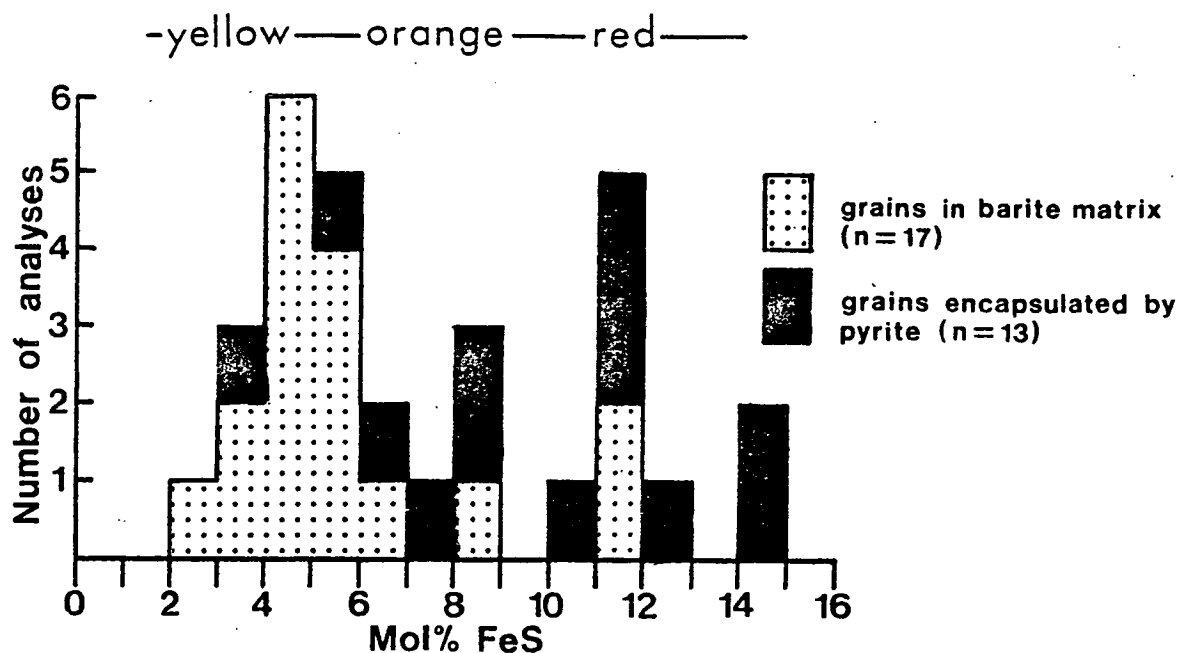


Fig. 7.1: Histogram of mol% FeS contents of thirty sphalerite grains in sample 705-20 (a sulphidic barite rock from the Creagan Loch area), with a qualitative indication of sphalerite colour in transmitted light. Note wider range in FeS-content of encapsulated sphalerite grains than of matrix grains.

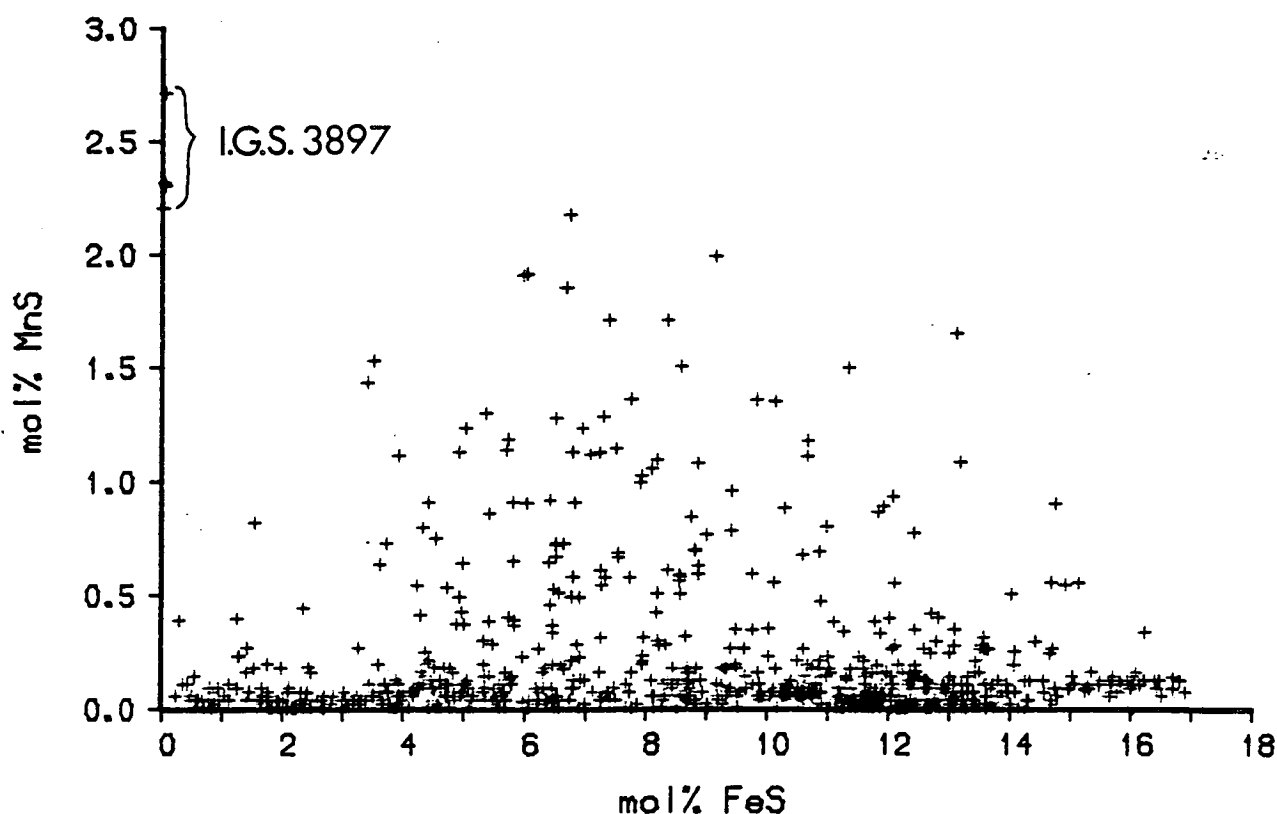


Fig. 7.2: Molecular percent MnS vs. mol% FeS in all sphalerite analyses obtained in this study. Note exceptional composition of sphalerites in sample 3897 (barite rock, BH2).

## Primary textures/compositions

## Secondary textures/compositions

## Deposition &amp; diagenesis

## Prograde metamorphism

## Retrograde metamorphism

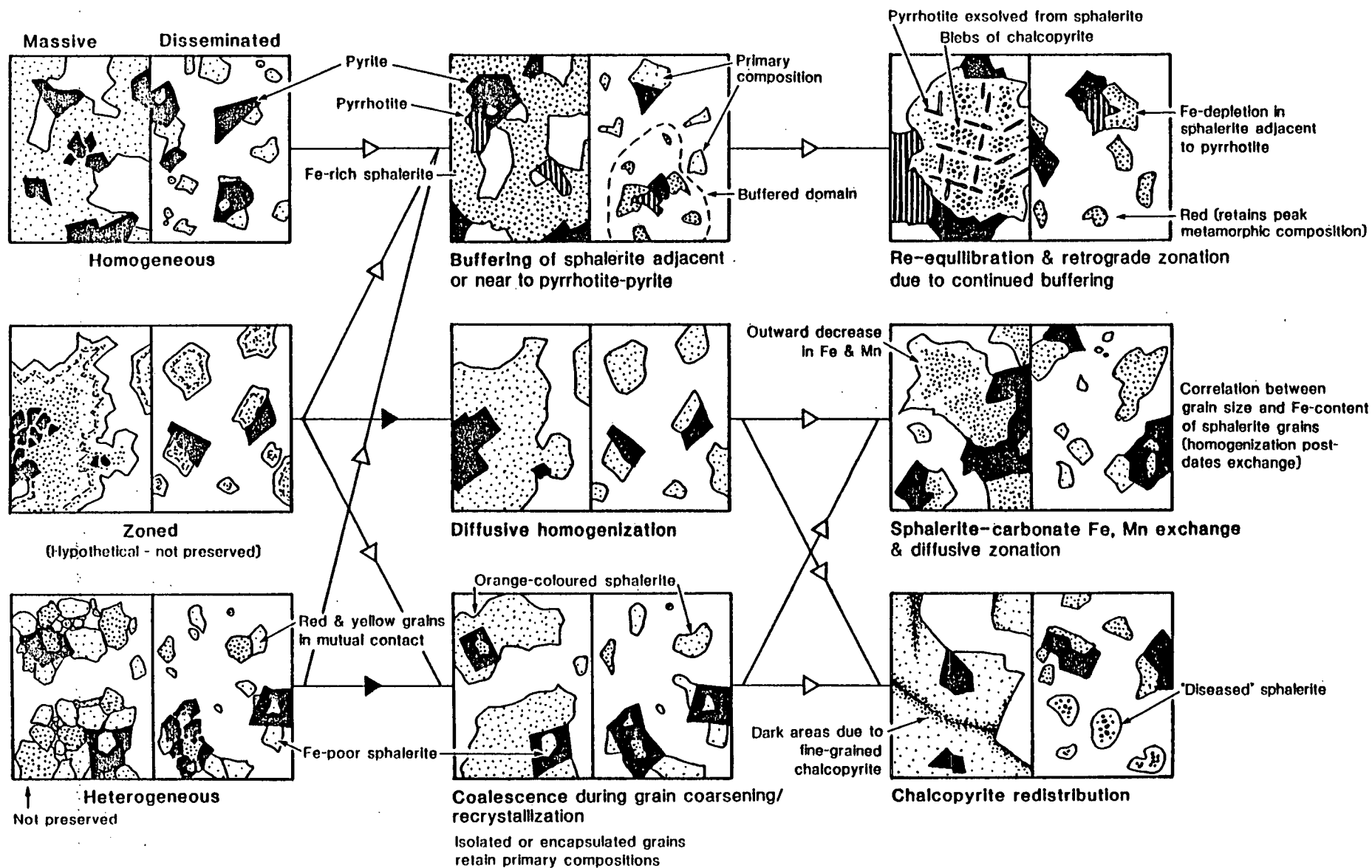


**Fig. 7.3:** Summary of textural/compositional relationships in sphalerite observed in samples from Foss. and of their genetic interpretation in terms of



Fig. 7.4

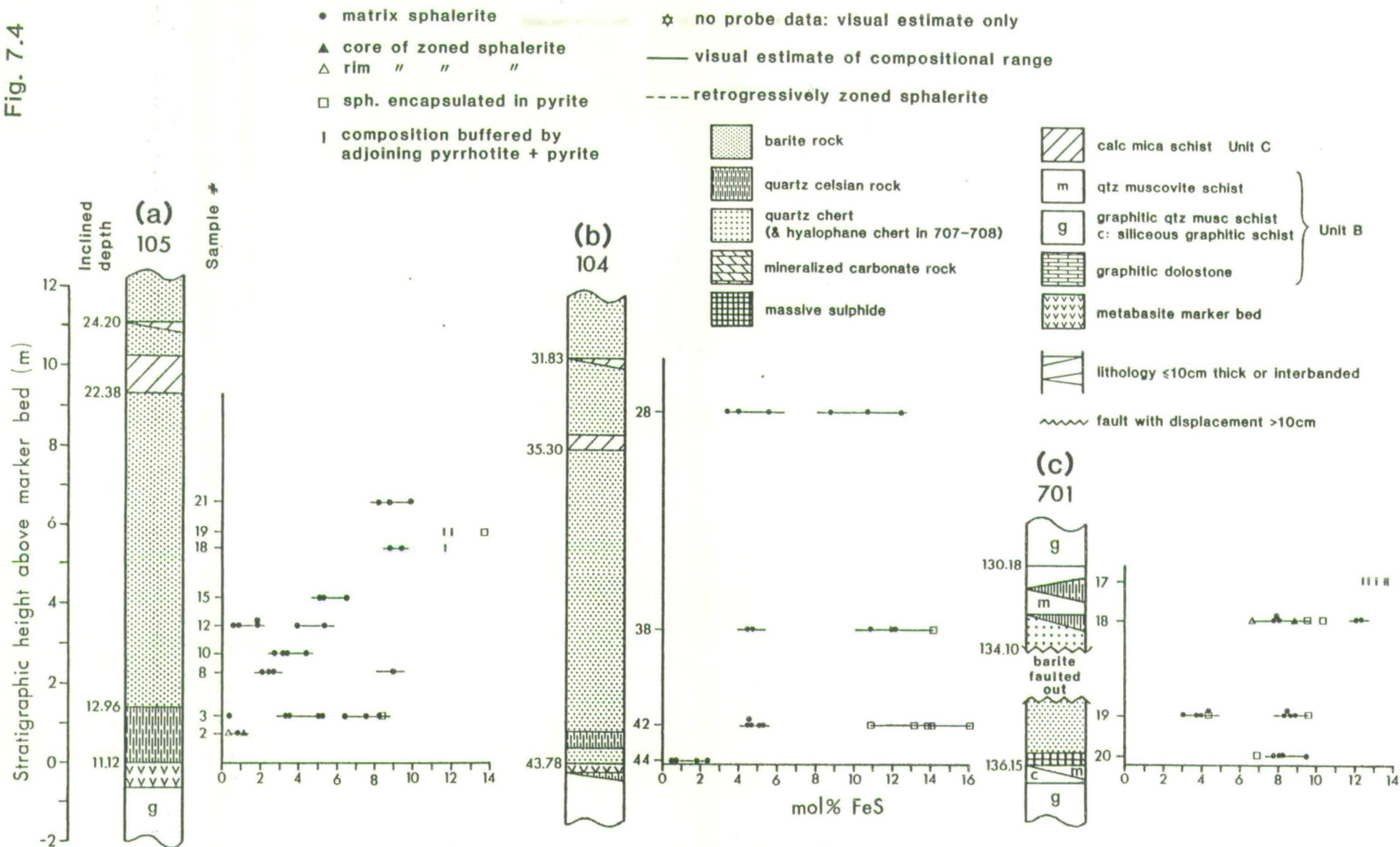


Fig. 7.4a-i: True vertical distance profiles of the M3 horizon intersected in nine Foss East drillholes (located on fig. 2.19), showing mol% FeS contents of sphalerite in samples examined. Apart from sphalerites associated with pyrrhotite and those showing retrograde zonation, compositions are regarded as pre-metamorphic. See text.

Fig. 7.4 (cont.)

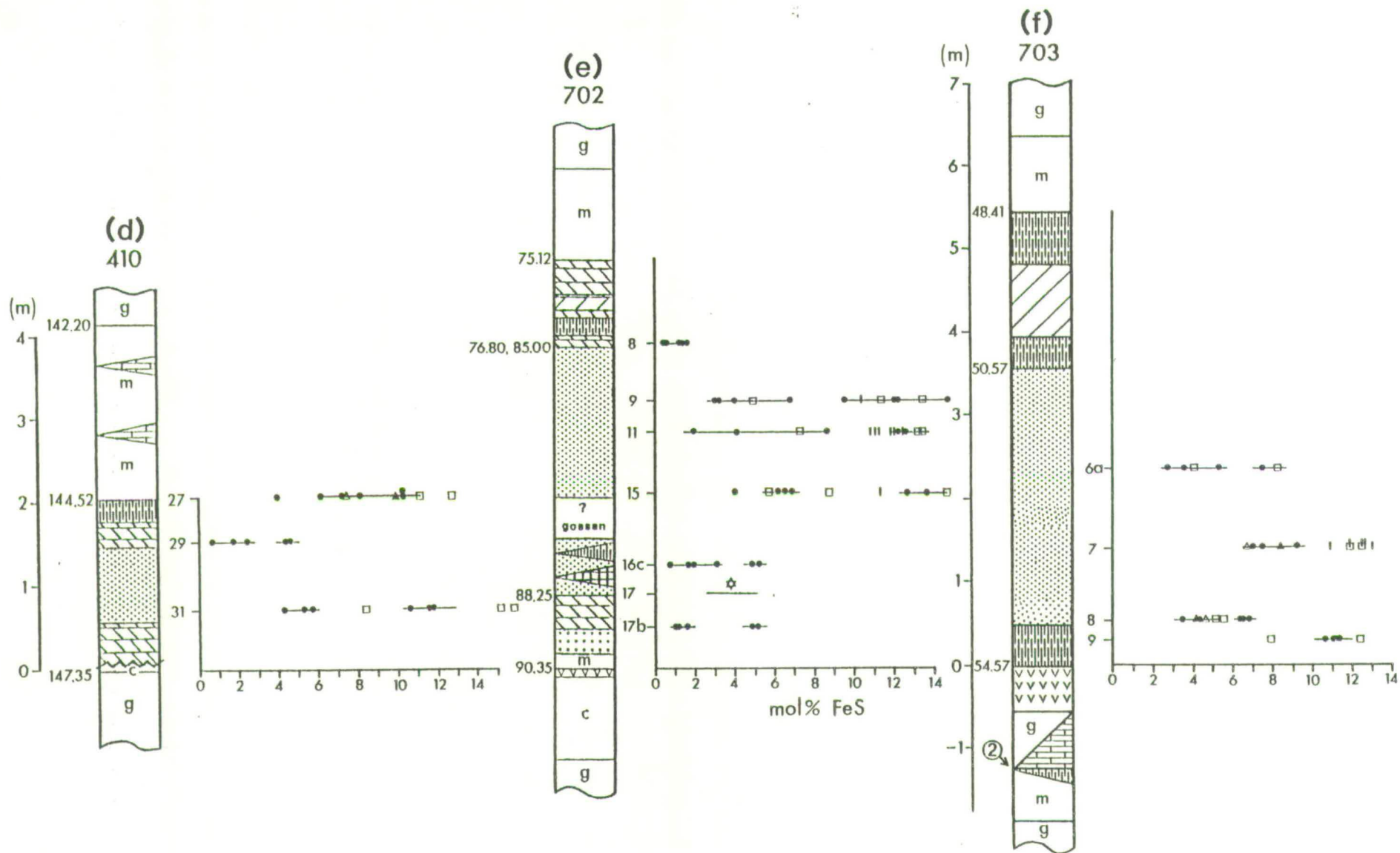
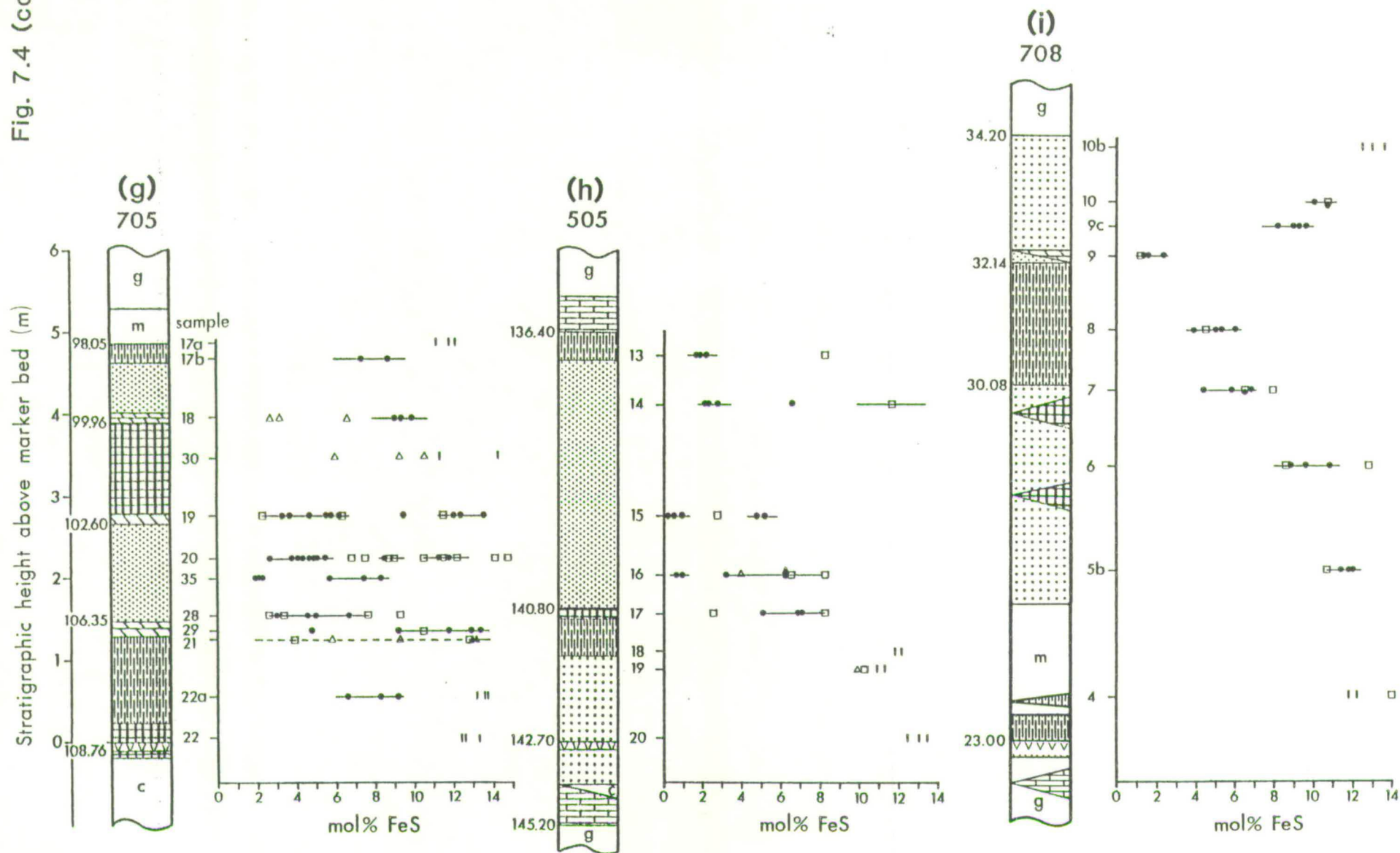
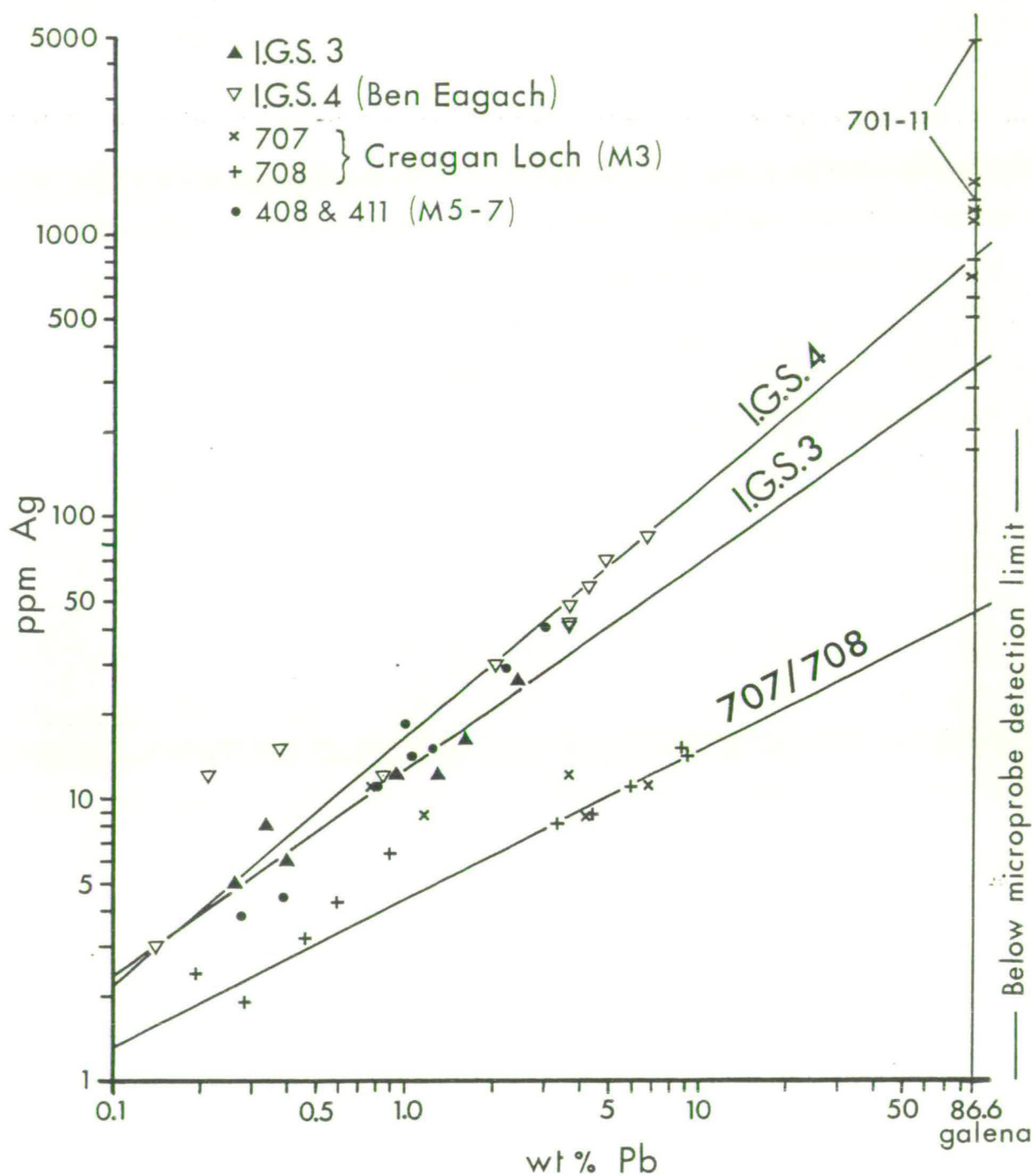


Fig. 7.4 (cont.)





**Fig. 7.5:** Silver vs. lead content of drillcore intervals from Foss East and Ben Eagach (BH4), and silver content of galena determined by microprobe analysis (crosses represent data given by Coats et al., 1981; otherwise this study). Note logarithmic scales. Best-fit lines estimated qualitatively. Assay data for BHs 3 and 4 from Coats et al., 1981; for DHs 707, 708, 408 and 411 from Dresser Minerals (unpublished material).



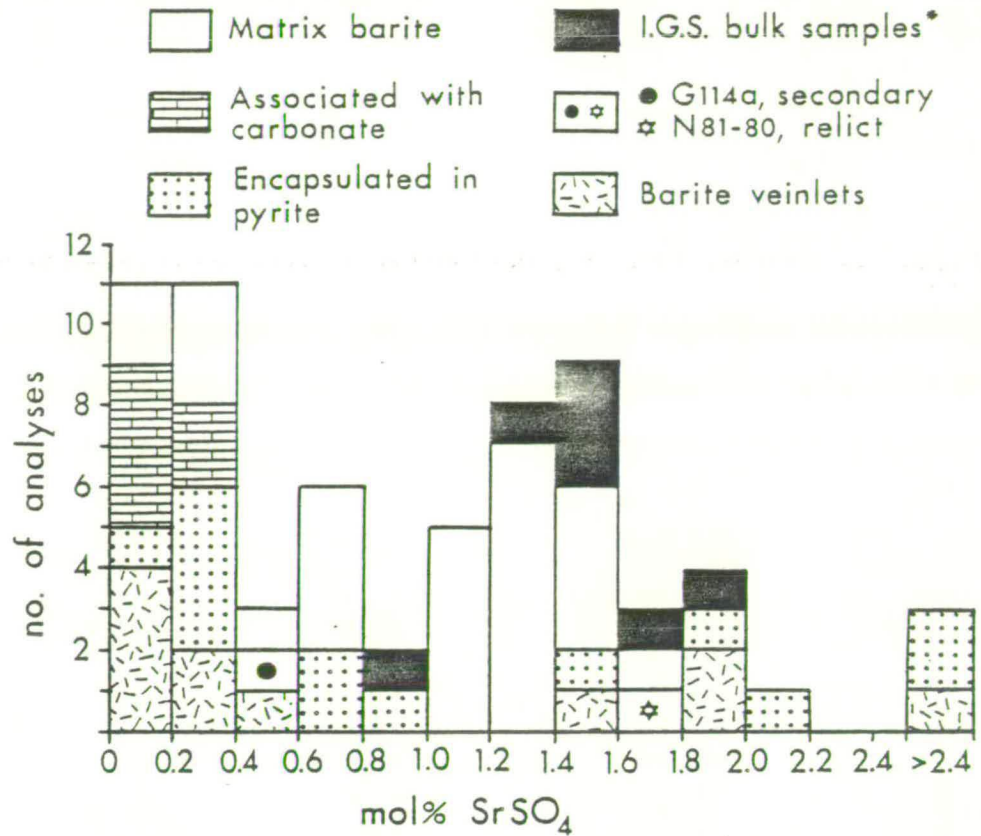


Fig. 7.6: Histogram of mol%  $\text{SrSO}_4$  contents in 59 microprobe analyses of barite from a variety of lithologies at Foss. Also shown are seven bulk samples of barite concentrates from BH2, recalculated to mol%  $\text{SrSO}_4$  in pure barite from data given by Coats et al., 1981.

Fig. 7.7: on following page.

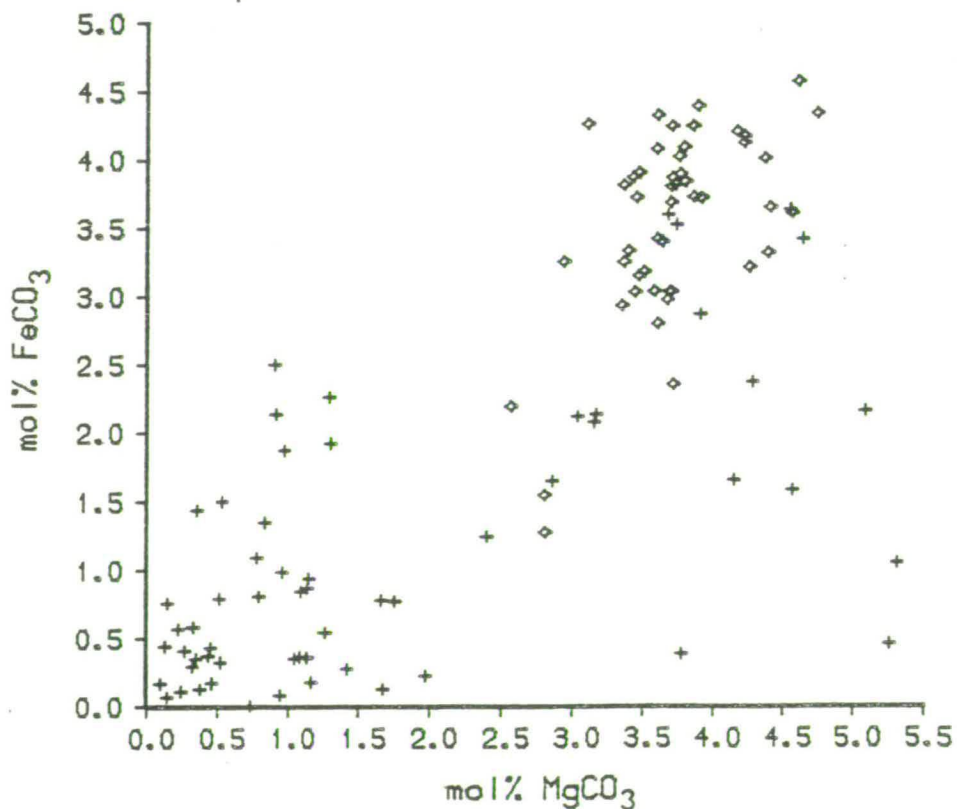


Fig. 7.8: Molecular percent  $\text{FeCO}_3$  vs.  $\text{MgCO}_3$  diagram of analysed calcites to show compositional differences between calcite coexisting with dolomite in non-mineralized rocks ( $\diamond$ ) and calcite in other samples (+).

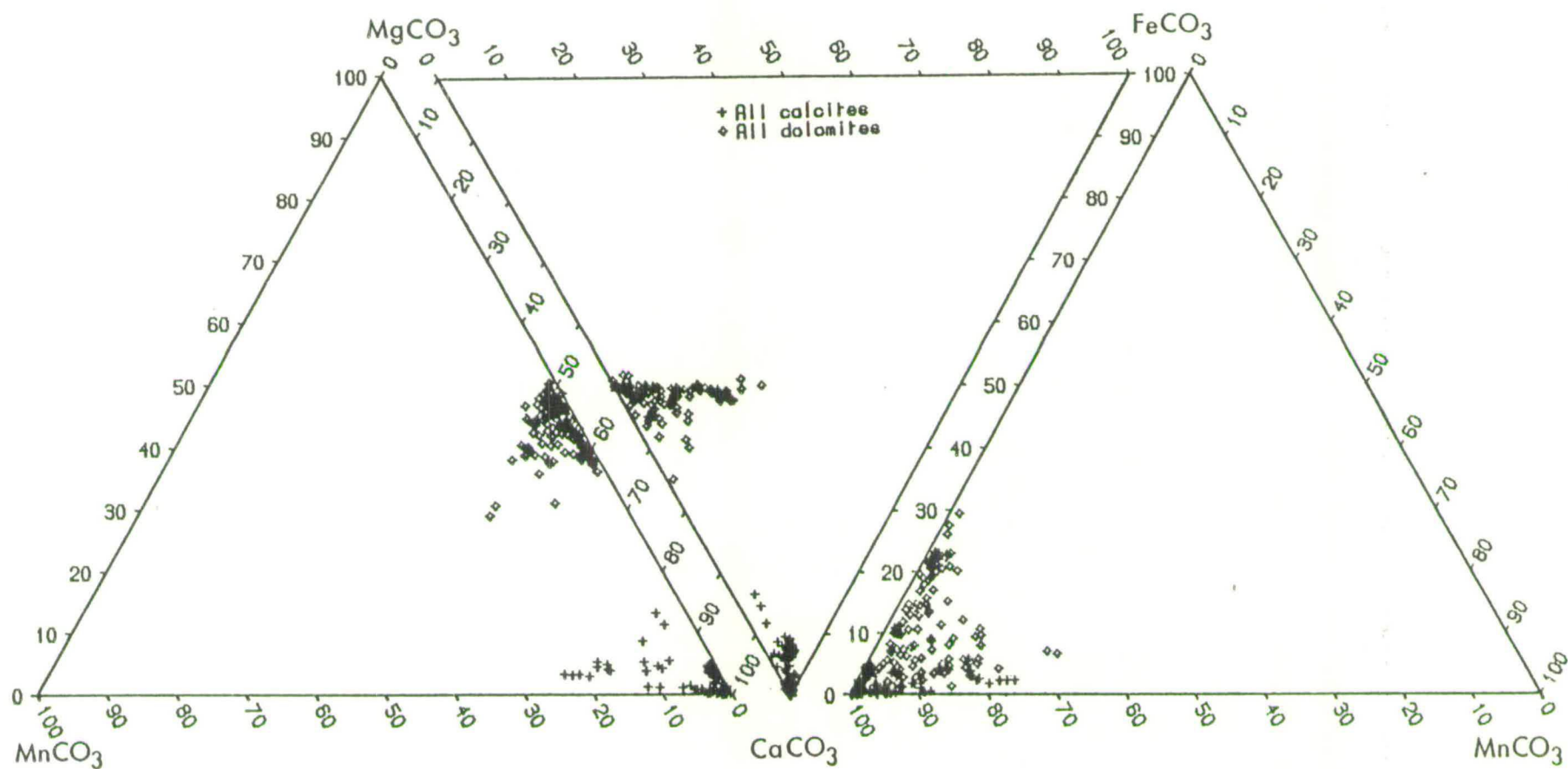


Fig. 7.7: Triangular diagrams of end-member carbonate compositions to illustrate compositional range of all Ca-Mg-Fe-Mn carbonates analysed (excluding members of the siderite-smithsonite series).

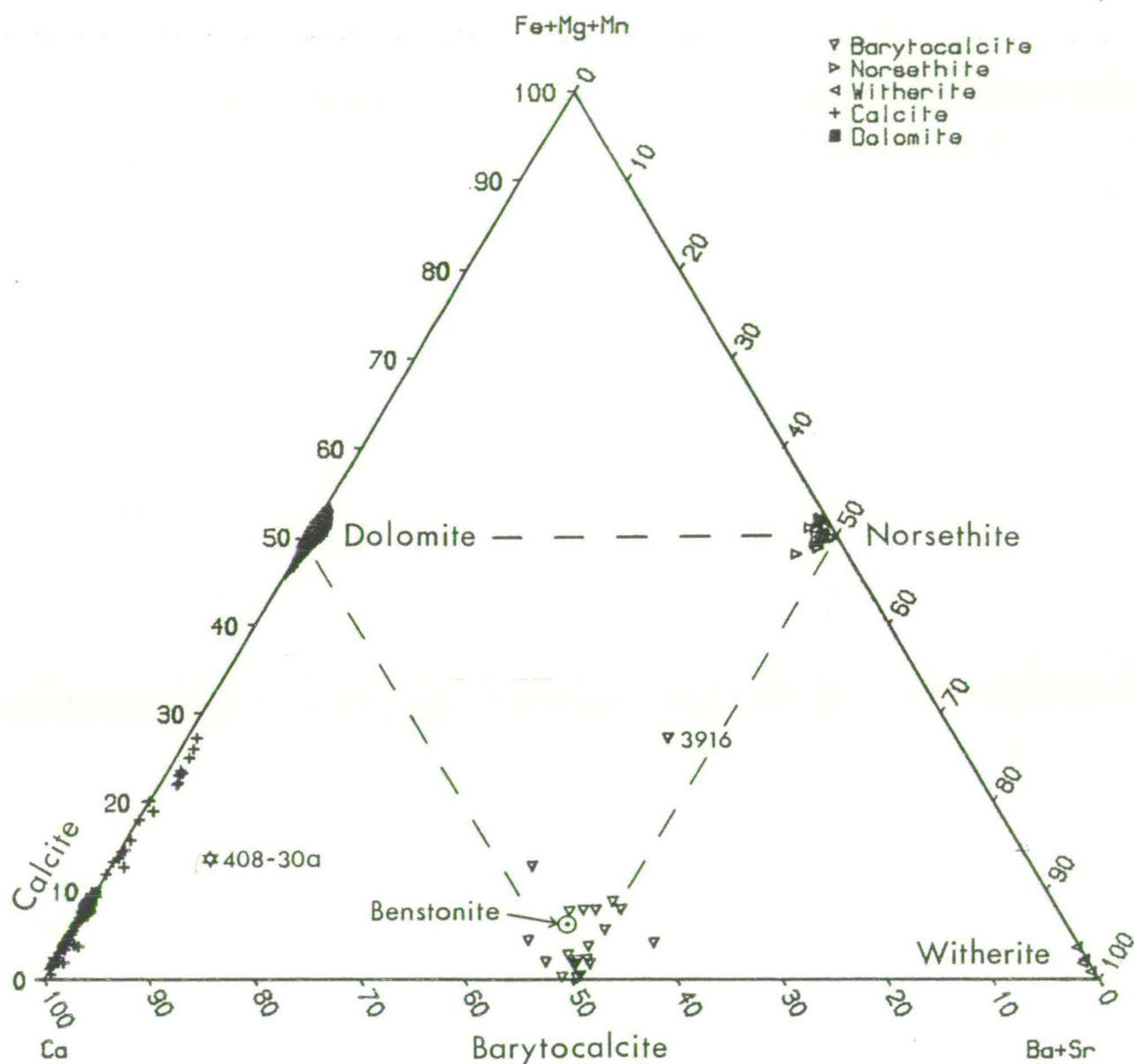
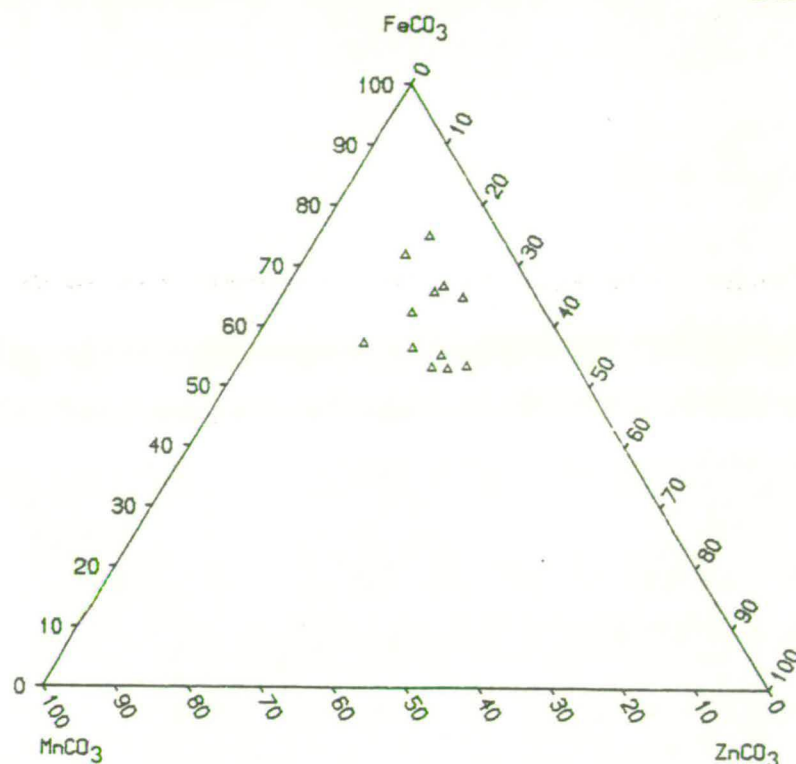
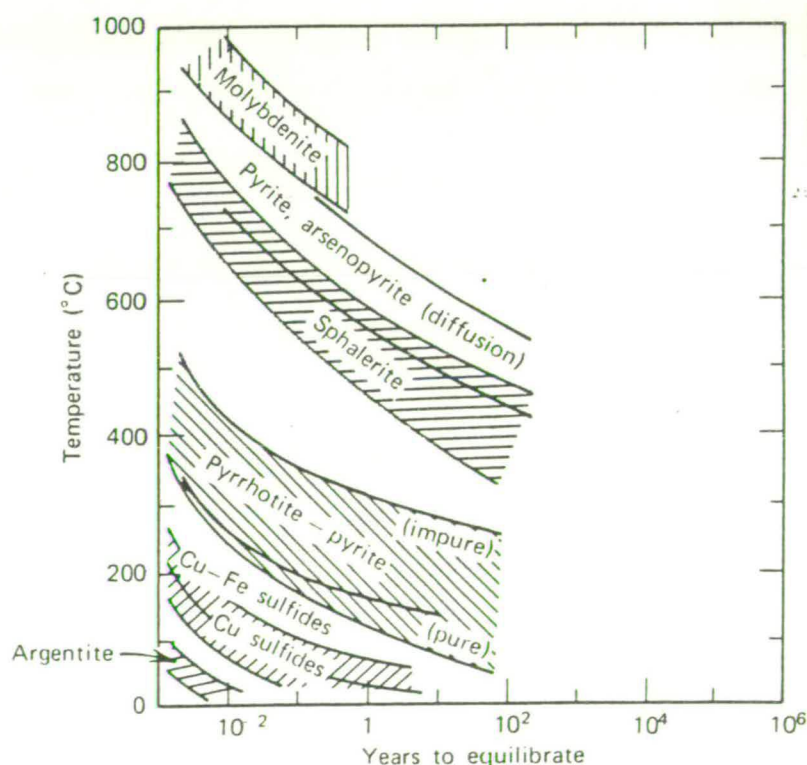


Fig. 7.9: Triangular diagram of molecular proportions of Ca, Fe+Mg+Mn, and Ba+Sr in analysed carbonates (excluding members of the siderite-smithsonite series). Circled dot indicates ideal composition of benstonite (Lippman, 1962). Star labelled 408-30A represents probable calcite-norsethite mixture (see text).



**Fig. 7.10:**  $\text{MnCO}_3$ - $\text{FeCO}_3$ - $\text{ZnCO}_3$  diagram of siderite-smithsonite<sub>s.s.</sub> in samples from BH4, Ben Eagach (see text).



**Fig. 7.11:** Equilibration times for various sulphides involved in solid-state reactions as a function of temperature. Shaded fields represent differing rates depending on particular reactions and on compositional variations (particularly in sphalerite and pyrrhotite), together with experimental uncertainty. (Modified from Craig and Vaughan, 1981; after Barnes, 1979).



## CHAPTER 8: Geothermometry, geobarometry and metamorphic evolution.

### 8.1 Introduction.

Several recent studies have attempted to quantify the peak P-T conditions of Barrovian metamorphism in central Perthshire (e.g. Wells and Richardson, 1979; Willan, 1980; Sivaprakash, 1982; Dempster, 1983 ; Baker, 1985). These authors have derived similar temperature ranges (generally  $550 \pm 50^{\circ}\text{C}$ ), but a much broader range of pressures (6-12 kbar) (see table 8.1), which could represent genuine spatial or temporal pressure variations during metamorphism, or merely reflect the greater uncertainties in the calibration of geobarometers. This chapter describes the application of empirical and experimental calibrations of mineral equilibria appropriate to the mineral assemblages found in the vicinity of the Foss deposit, to determine the peak metamorphic conditions in the area and, if possible, to constrain the subsequent P-T history.

Initial P-T estimates were obtained from sphalerite-pyrite-pyrrhotite geobarometry (part 7.2.3) and calcite-dolomite geothermometry using published calibrations (table 8.2) and microprobe analyses of coexisting mineral grains in textural equilibrium. Mineralized lithologies were found to be unsuitable for calcite-dolomite geothermometry because of the variable and often high  $\text{MnCO}_3$ -content of both phases, low  $\text{MgCO}_3$ -contents of calcite suggesting low-temperature ( $<200^{\circ}\text{C}$ ) equilibration, and textural evidence of zoning or late metamorphic recrystallization (section 7.5.2). Samples of calcareous pelites from units A and D, and of chloritic metabasites from unit B, were found to be most suitable for geothermometric studies using calcite-dolomite, garnet-biotite, and the recently calibrated garnet-hornblende equilibria. In the final phase of analytical work, a large number of analyses of coexisting minerals were obtained from a few selected samples to investigate within-sample variations in mineral composition.

Several key minerals, notably the aluminosilicate polymorphs and staurolite, are absent from the lithologies at Foss which precludes the use of several geobarometers commonly applied in metasedimentary terrains. However, kyanite and staurolite are

recorded by Chinner (1974) and Sivaprakash (1981, 1982) from Grandtully, which is about 10km to the E (fig. 1.3), and kyanite was also found by Wells and Richardson (1979) at Schiehallion, which is about 10km to the W of Foss across the Loch Tay Fault. Chloritoid appears in aluminous, magnesian rocks at Grandtully, but it occurs as inclusions in garnet and is only present as a retrograde phase in the matrix (Atherton and Smith, 1979; Sivaprakash, 1981). The limited development of kyanite and staurolite in the Aberfeldy area has been attributed to the paucity of favourable bulk compositions, in particular the lack of suitably high  $Mg/(Mg+Fe)$  ratios (Atherton and Brotherton, 1972; Atherton, 1977), and to the stabilizing effect of high pressure on garnet-biotite-chlorite assemblages (Dempster, 1983).

Two recently calibrated silicate barometers utilise the assemblages plagioclase-biotite-garnet-muscovite (Ghent and Stout, 1981) and biotite-muscovite-chlorite-quartz (Powell and Evans, 1983), which occur in a wide range of rock compositions. Both geobarometers are tested using samples from the vicinity of the Foss deposit (parts 8.3.1 and 8.3.2), and pressure estimates are compared with information derived from sphalerite geobarometry (part 8.3.3) and from experimentally determined cymrite-celsian equilibria (part 8.3.4 and Appendix G), using samples from the mineralized strata.

## 8.2 Geothermometry.

### 8.2.1 Garnet-hornblende.

The geothermometer of Graham and Powell (1984) is based on the partitioning of Fe and Mg between garnet and hornblende, calibrated using the garnet-clinopyroxene thermometer of Ellis and Green (1979) applied to garnet-clinopyroxene-hornblende rocks. The distribution coefficient is approximately independent of pressure, but requires a correction for the grossular component in garnet (table 8.2). Microprobe analyses of non-retrogressive rim compositions of garnet and hornblende porphyroblasts in three calc mica schist samples from the vicinity of the Foss deposit were used to derive temperature estimates (table 8.3), which are in the range 520-550°C.

As mutual contacts between garnet and hornblende crystals are rare in this lithology, analyses were obtained from unaltered porphyroblast rims separated by only a few millimetres of matrix.



Anomalous temperature estimates might arise if closely associated porphyroblast rims had failed to equilibrate during the post-D3 thermal climax, or had subsequently re-equilibrated with ferromagnesian silicates in the matrix within domains smaller than the distance between porphyroblasts. The preservation of peak metamorphic equilibrium compositions is supported by observations of within-sample homogeneity in hornblende rim compositions, but some dispersion in calculated temperatures is caused by variation in garnet rim compositions (fig. 6.22 and table 8.3). This dispersion is nevertheless no greater than the uncertainty of  $\pm 30^{\circ}\text{C}$  inherent in the calibration of the geothermometer, as estimated by Graham and Powell (1984), and in errors arising from analytical precision (Appendix E.2).

#### 8.2.2 Garnet-biotite.

The variation with temperature of Fe and Mg partitioning between garnet and biotite has been calibrated empirically by Thompson (1976) and other workers, and experimentally by Ferry and Spear (1978). The latter calibration (table 8.2) is applicable to garnets of restricted composition (>80 mol% almandine + pyrope components), and it has generally been found that garnets with a large grossular component, such as are typical of the Scottish Dalradian, yield anomalously low temperatures. Of the samples from Foss examined (table 8.3), only those with  $X_{\text{Ca}} < 0.18$  give temperature estimates using the Ferry and Spear calibration which are in the range indicated by garnet-hornblende thermometry; the remaining Ca-rich garnet-bearing samples appear to indicate much lower temperatures (420–500°C). The correction factor for the grossular component in garnet and the Margules parameters used by Hodges and Spear (1982) (table 8.2) yield garnet-biotite temperatures which are 60–100°C higher and, with the exception of samples 503-27 and 708-15, range from 510° to 590°C. The correction factors for both Ca and Mn substitution in garnet used by Pigage and Greenwood (1982) (table 8.2) appear to give excessively high temperatures (table 8.3) relative to other methods and to petrological prejudices.

Ferry and Spear (1978) suggested a limit to the  $\text{Al}^{\text{VI}} + \text{Ti}$  content of biotite for successful application of their geothermometer, which is exceeded in most samples from Foss (table 8.3). However, any

effects due to this appear to be negligible compared with the variations in temperature estimates caused by high Ca levels in garnet, and by within-sample variation in garnet rim and biotite compositions. This compositional heterogeneity results in a range of calculated temperatures (typically of 25–50°C) for each sample, which may be attributed to partial retrograde re-equilibration among the ferromagnesian silicates, since biotites which are isolated from garnet and chlorite often have relatively lower Mg/Fe ratios (e.g. sample 503-27, table 8.3). Similar variation in biotite compositions has been ascribed to retrogression or disequilibrium in other studies of garnet-biotite thermometry, e.g. Tracy et al. (1976), Ghent et al. (1979), and Dempster (1983).

### 8.2.3 Calcite-dolomite.

The  $\text{MgCO}_3$  content of calcite coexisting with dolomite was experimentally calibrated as a geothermometer by Goldsmith and Newton (1969). Bickle and Powell (1977) incorporated adjustments for iron-bearing carbonates, and their calibration is adopted here since Foss carbonates are iron-rich (tables 8.2 and 7.7). Compositions of forty calcite grains in six samples of unit D calcareous pelites and chloritic metabasites (in which calcite contains <1.5 mol%  $\text{MnCO}_3$ ), plotted in fig. 8.1, suggest that equilibration occurred at temperatures ranging from 470° to 540°C, assuming that pressures of 7–9 kbar prevailed at Foss (justified below). However, an experimental calibration of the iron correction to the calcite-dolomite geothermometer (Powell et al., 1984) indicates that these temperatures may be about ~30°C too high (Powell, pers. comm.).

Several anomalously high values for the  $\text{MgCO}_3$  content of calcite (>4.5 mol%; fig. 8.1) are probably due to overlap of the defocussed microprobe beam (diameter, 10–15  $\mu\text{m}$ ) with adjacent dolomite grains, and low values (<2.5 mol%; see fig. 7.8) may be attributed to retrogressive alteration or to late-metamorphic carbonate growth revealed by cathodoluminescence observations (plate 113). The central areas of coarser ( $\geq 0.5\text{mm}$ ) grains of calcite are enriched in Mg and Fe compared with the rims of these crystals and the whole of smaller grains, both of which yield lower temperature estimates. This dispersion in compositions suggests that partial retrograde equilibration occurred while temperatures were



sufficiently high to allow Mg-Fe exchange between calcite and matrix phases on a  $\sim 0.1$  mm scale. Temperatures derived using the Bickle and Powell (1977) calibration and the maximum Mg and Fe contents of reliable calcite analyses ( $520-540^{\circ}\text{C}$  at pressures of 7-9 kbar), are therefore chosen as representative of peak metamorphic conditions.

Reasonable agreement is therefore shown by the results of garnet-hornblende, garnet-biotite and calcite-dolomite geothermometry (fig. 8.2), provided that care is taken in selecting peak metamorphic equilibrium compositions in zoned minerals and in calcite, and that a correction is incorporated for the high grossular content of garnet in garnet-biotite thermometry. The results indicate the attainment of peak metamorphic temperatures of  $530 \pm 30^{\circ}\text{C}$  during and shortly after the D3 deformation episode in this area.

### 8.3 Geobarometry.

#### 8.3.1 Plagioclase-biotite-garnet-muscovite.

Ghent and Stout (1981) used the garnet-plagioclase- $\text{Al}_2\text{SiO}_5$ -quartz geobarometer (Ghent et al., 1979) in conjunction with garnet-biotite thermometry (Ferry and Spear, 1978) to derive an empirical geobarometer for the assemblage plagioclase - biotite - garnet - muscovite (table 8.2). The resolution of this geobarometer depends on the uncertainty attached to activity-composition relationships and to the garnet-biotite temperature estimate, and on analytical uncertainty in determining garnet, biotite, muscovite and plagioclase compositions (Appendix E.2). In addition, Ghent and Stout (1981) found that samples containing albitic plagioclase yielded higher pressure estimates than nearby samples containing more calcic plagioclase, which they attributed to incomplete correction of strong positive deviations from the ideal molecular mixing model for compositions of  $\text{An}_{<8}$ .

Application of the plagioclase-biotite-garnet-muscovite barometer at Foss is restricted by the low and variable anorthite content of plagioclase (often  $\text{An}_{10}$ ). Pressure estimates of between 7.7 and 8.5 kbar (with a probable uncertainty of  $\pm 0.8$  kbar: Ghent and Stout, 1981) have been obtained from three samples containing oligoclase in the compositional range  $\text{An}_{15-20}$  (table 8.3). As noted in part 6.2.1, coexisting albite ( $\text{An}_{<3}$ ) and oligoclase ( $\text{An}_{18-23}$ ),

defining the peristerite gap, occurs in quartzo-feldspathic domains in samples N80-36 and 429-5. Significantly higher pressure estimates of  $9.6 \pm 0.8$  kbar, obtained from samples 503-10 and G48 (table 8.3), could be due to less calcic plagioclase composition or to the higher temperatures obtained by garnet-biotite thermometry, or to a combination of these factors. Widely variable Ca contents of both plagioclase and coexisting garnet in Dalradian pelites near Spean Bridge, Inverness-shire (Richardson and Powell, 1976), were considered by Ghent and Stout (1981) to be partly responsible for the comparatively lower temperatures and higher pressures for the Spean Bridge area estimated by them using plagioclase-biotite-garnet-muscovite thermobarometry.

Since Ghent and Stout (1981) constructed their geobarometer using temperature estimates from Ferry and Spear's (1978) calibration of Fe-Mg exchange between garnet and biotite, the use of "corrected" garnet-biotite calibrations such as those of Hodges and Spear (1982), leads to inconsistent pressure estimates from the Fe and Mg end-member equations for the plagioclase-biotite-garnet-muscovite geobarometer. Average pressure estimates given by this barometer using temperatures obtained from the Hodges and Spear equation (assuming  $W_{MgMn}=0$ ), are about 0.8 kbar higher than pressure estimates based on the uncorrected garnet-biotite geothermometer (tables 8.2, 8.3 and fig. 8.2).

### 8.3.2 Biotite-muscovite-chlorite-quartz.

This geobarometer, recently formulated by Powell and Evans (1983) (table 8.4), is based on the extent of Mg-Al celadonite substitution in white mica in equilibrium with biotite and chlorite. Activity data for muscovite, celadonite, phlogopite and clinochlore end-members, calculated from representative microprobe analyses of seven samples using the activity formulations of Powell and Evans, are presented in table 8.4. The range in derived equilibrium constants ( $\ln K_D = 4.2$  to  $6.0$ ) for the reaction;

Celadonite + clinochlore = muscovite + phlogopite + quartz + H<sub>2</sub>O  
defines a band of positive slope in P-T space (fig. 8.2) which intersects with the temperature range of 520-580°C at pressures of between 7.8 and 10.7 kbar. Presently unclear is the extent to which the isopleths are displaced to lower temperatures and to higher



pressures by the presence of other components in the fluid phase, particularly  $\text{CO}_2$  as carbonates are present in all samples (although none contain graphite).  $\text{Fe}_2\text{O}_3$  contents of minerals in the samples have not been determined, but Powell and Evans found their barometer to be insensitive to  $\text{Fe}^{2+}/\text{Fe}^{3+}$  ratios.

The barometer is sensitive, however, to within-sample variation in muscovite compositions. Pressure estimates which differ by up to 1 kbar may be obtained by using activity data derived from several muscovite analyses within individual thin sections (eg. N80-45, table 8.4). This variation is presumably due to localized retrogressive equilibration of peak metamorphic equilibrium compositions. Dempster (1983) has shown that in central Perthshire, retrograde alteration of muscovite results in a decrease in the celadonite content, coupled with an increase in the paragonite content of affected grains.

### 8.3.3 Sphalerite-pyrite-pyrrhotite.

Scott and Barnes (1971) have demonstrated that the amount of FeS in solid solution in sphalerite is essentially a function of pressure in the temperature range 254–550°C (at 1 bar pressure; 300–>600°C at higher pressures), provided that the sphalerite is buffered by coexisting pyrite + hexagonal pyrrhotite (part 7.3.2). Under these conditions, the FeS content of sphalerite decreases progressively with increasing pressure, and this has been calibrated experimentally as a geobarometer to 10 kbar by Scott (1973) and Lusk and Ford (1978). Although one of the more refractory sulphides, sphalerite is nevertheless susceptible to retrograde metamorphic and supergene compositional alteration, particularly if it contains chalcopyrite inclusions (eg. Bockor 1980; Craig and Vaughan, 1981). A major pitfall with application of the geobarometer is that the FeS content of sphalerite generated by equilibration with monoclinic pyrrhotite + pyrite at low temperatures (<254°C), are similar to equilibrium compositions retained from buffering with hexagonal pyrrhotite at about 9 kbar (cf. Groves et al., 1975). Therefore evidence of low temperature alteration in metamorphosed sulphide assemblages must be critically examined before application of the geobarometer.

The textural and compositional relationships of sphalerite occurring in the Foss deposit have been discussed in detail in part 7.3.2 and by Moles (1983), and the analytical results presented here (fig. 8.3) are restricted to sphalerites which satisfy established criteria for retention of peak metamorphic equilibrium compositions. These range in FeS content from 10 to 13 mol% with a distinct concentration between 11.0 and 11.7 mol% FeS, from which pressures of 8-9 kbar ( $\pm 0.5$  kbar analytical and calibration uncertainty) are calculated using the equation of Hutchison and Scott (1981) (table 8.2). These estimates, which are significantly higher than earlier results from sphalerite geobarometry at Foss (Willan, 1980 and 1983: table 8.1), are in good agreement with pressures derived from the silicate barometers discussed above.

#### 8.3.4 Cymrite-celsian.

Textural evidence reviewed in part 3.2.4 indicates that cymrite ( $\text{BaAl}_2\text{Si}_2\text{O}_8 \cdot \text{H}_2\text{O}$ ) was a major constituent of the mineralized strata during prograde metamorphism and fabric development, and was largely replaced by celsian ( $\text{BaAl}_2\text{Si}_2\text{O}_8$ ) at some time after  $D_3$ . The location in P-T space of the reaction, cymrite = celsian +  $\text{H}_2\text{O}$  (Essene, 1967), has been determined to 7 kbar in reversed hydrothermal experiments by Nitsch (1980), who confirmed that cymrite is the stable phase under higher pressure/lower temperature conditions (fig. 8.2). In earlier experiments, Seki and Kennedy (1964a,b) used the wrong formula  $\text{BaAlSi}_3\text{O}_8(\text{OH})$  for cymrite and also incorrectly suggested that this phase formed a complete solid solution with hexagonal celsian. Nevertheless, Seki and Kennedy (1964b) surmised that cymrite and sanidine hydrate,  $\text{KAlSi}_3\text{O}_8 \cdot \text{H}_2\text{O}$ , form a complete or partial solid solution series (here designated cym<sub>ss</sub>), and established that the formation of sanidine hydrate from sanidine +  $\text{H}_2\text{O}$  requires very high water pressures (ca. 18kbar at 400°C). Therefore, as suggested by Reinecke (1982), the minimum water pressures for the stability of potassic cymrite should be higher than for pure cymrite. This is supported qualitatively by (a) the restricted compositional range of cymrite occurring in the Aberfeldy deposits, none of which contains >10 mol% sanidine + albite hydrate in solid solution (fig. 6.5), and (b) textural evidence that hyalophane was



stable throughout metamorphism and fabric development (part 3.2.5).

Further hydrothermal experiments with synthetic cymrite-potassic cymrite and celsian-potassic celsian compositions were undertaken at the Experimental Petrology Unit, Edinburgh University, in order to determine: (1) The P-T location of the pure cymrite-celsian equilibrium at 8 kbar (corresponding to the approximate peak metamorphic pressure at Foss, derived from geobarometric studies described above). (2) The displacement of this equilibrium to higher temperatures due to the substitution of (K+Si) for (Ba+Al) in both cymrite and celsian. Appendix G describes the experimental procedures and evaluates the results obtained and their interpretation.

The experiments successfully bracketed the pure cymrite-celsian equilibrium at 8.0 kbar,  $590 \pm 10^\circ\text{C}$ , which is near to the extrapolated position of the reaction line determined by Nitsch (1980) (figs. G.1 and 8.2). Rapid attainment of equilibrium in this system was found by Nitsch and confirmed in the present study, with complete reaction in runs lasting 8-12 hours. However, attempts to locate the reaction lines for potassic compositions were hindered by a marked reduction in reaction rate and the metastable growth and persistence of K-bearing cymrite in the celsian field. These effects were pronounced even with a 5 mol% substitution of the potassic end-members, and may account for the metastable persistence of some  $\text{cym}_{\text{ss}}$  in the Aberfeldy deposits, which had previously seemed difficult to reconcile with observations of rapid reaction in the pure system under experimental conditions. It is therefore significant that 'pure' (K,Na-free) cymrite and celsian are absent in samples from the Aberfeldy deposits (fig. 6.5), and it is postulated that the 4-6 mol% [sanidine + albite]-hydrate component present in the natural cymrite was sufficient, in some lithologies, to retard the replacement by celsian during early retrograde metamorphism.

The experimentally determined reaction line therefore constrains the minimum P, maximum T of metamorphism and indicates that hydrostatic pressures exceeded 7.5 kbar during peak metamorphism at  $550^\circ\text{C}$ , which is in satisfactory agreement with the results of other geobarometers applied in this area. The post-D3 replacement of cymrite by celsian indicates that the stability field of celsian was

entered by decreasing pressure and/or increasing temperature. A pressure decrease at near-constant or declining temperatures at this time is supported by evidence from other geobarometers of higher peak pressures (8-10 kbar), which would otherwise have been erased.

Rare examples have been found of cymrite occurring in late-stage veinlets, and of cymrite replacing celsian (itself retaining the morphology of a cymrite precursor, plate 59) in a rock affected by late (? Loch Tay Fault age) shearing. These suggest that the cymrite stability field may have been re-entered during uplift, possibly about the time of the Loch Tay Fault movements, and that the down-grade P-T evolution (discussed below) probably did not depart substantially from the cymrite-celsian reaction line.

#### 8.3.5 Discussion of peak metamorphic pressure estimates.

Pressures calculated using the plagioclase-biotite-garnet-muscovite geobarometer of Ghent and Stout (1981) are probably imprecise due to calibration uncertainties and between-sample variation in the calcium contents of garnet and plagioclase. Despite these reservations, peak metamorphic pressures indicated by this barometer (7.5 to 10kbar: table 8.3) are in good agreement with results from sphalerite geobarometry applied to sphalerites which satisfy textural criteria for the retention of peak metamorphic buffered compositions (fig. 8.2). Similar or slightly higher pressures are also derived from the temperature-sensitive celadonite geobarometer of Powell and Evans (1983), assuming that the sheet silicates preserve compositions equilibrated close to the peak metamorphic temperatures (fig. 8.2) and that  $P_{H_2O} = P_{total}$ . These assumptions may not be justified because of the presence of carbonates and evidence for retrogressive changes in mica compositions, manifested by a spread in the celadonite content of white micas within thin sections. However, pressures estimated from the celadonite geobarometer assuming equilibration to lower than peak temperatures (eg. 8-9 kbar at 500°C: table 8.4) are incompatible with evidence from the cymrite-celsian 'barometer' which requires that the stability field of celsian was entered by a relatively greater decrease in pressure than in temperature (see above and fig. 8.4). Therefore the celadonite geobarometer is suspected of yielding pressure estimates which are perhaps 1-2 kbar too high at



Foss. Similar conclusions have been reached by other users (C.M. Graham, pers. comm.).

Wells (1979) and Wells and Richardson (1979) estimated pressures of  $12 \pm 1.5$  kbar (at temperatures of up to  $620^{\circ}\text{C}$ ) for the Schiehallion area using plagioclase-garnet-kyanite-quartz geobarometry. Using the same barometer, Sivaprakash derived pressures of 10-11 kbar for the Grandtully area. However, a more recent calibration of the plagioclase-garnet-kyanite-quartz equilibrium by Newton and Haselton (1981) indicates that these pressure estimates may be several ( $\sim 3-4$ ) kilobars too high (Dempster, 1983). Using the plagioclase-biotite-garnet-muscovite barometer of Ghent and Stout (1981), Dempster (op. cit.) has derived pressures of 7 kbar and 9-10 kbar for the Aberfeldy and Loch Tummel areas respectively. These agree with revised pressure estimations from the data of Sivaprakash (1982) and of Wells and Richardson (1979), and with the results of the present work.

#### 8.4 Metamorphic evolution in central Perthshire.

Dempster (1983) and Harte et al. (1983) have discussed evidence for overprinting of pre-D<sub>3</sub>, lower pressure (5-6kbar) chloritoid-biotite assemblages by higher pressure (9-10kbar) assemblages at around the time of D<sub>3</sub> deformation, in the northern part of the Tummel Steep Belt near Blair Atholl (fig. 1.3). They suggest that this syn-D<sub>3</sub> pressure increase could relate to the formation of the Steep Belt, which Bradbury et al. (1979) consider to be a 'deep-seated rotation zone' where movements 'spanned the time of Barrovian metamorphism'.

Although significantly higher peak metamorphic pressures are indicated by mineral barometry for the vicinity of the Foss deposit than for the Aberfeldy - Grandtully area, there is no mineralogical evidence for a syn-D<sub>3</sub> increase of pressure at Foss, which lies to the southern margin of the Steep Belt about 10km SSW of Blair Atholl. If the pre-D<sub>3</sub> conditions postulated by Dempster (1983) and Harte et al. (1983) for the Blair Atholl area ( $\leq 6$ kbar at  $550^{\circ}\text{C}$ ) had prevailed at Foss, celsian rather than cymrite would have been the stable barium silicate (fig. 8.2) and textural evidence might be expected for syn-D<sub>3</sub> replacement of celsian by cymrite (perhaps similar to that described from the island of Andros, Greece, by

Reinecke, 1982). No evidence of prograde replacement of celsian by cymrite has been observed at Foss. However, a more limited increase in pressure (within the stability field of cymrite) during D<sub>3</sub> movements (fig. 8.4), cannot be precluded on the basis of the textural and thermobarometric data available.

The relations of cymrite and celsian in the Foss deposit were mentioned above as evidence for an uplift and cooling path lying close to the cymrite-celsian equilibrium line. The P-T history, so constrained, is very similar to that modelled by Dempster (1983 and 1985) for the area near the River Tay at Aberfeldy (fig. 1.3) using isotopic mineral age data. An interesting feature of Dempster's model P-T path (fig. 8.4) is the period commencing at about 450M.y., during which cooling proceeded without significant uplift, until regional uplift resumed with a major faulting episode between 410 and 390M.y. During this period of tectonic inactivity the P-T path (fig. 8.4) re-entered the stability field of cymrite. Late-stage growth of cymrite is only observed at Foss in some cross-cutting veinlets and in a fault zone where the passage of fluids allowed partial retrogressive hydration of celsian (part 3.2.1.2). Incomplete reaction may be explained by the low temperatures (~250°C) prevailing at the time, which with the resumption of uplift allowed the metastable persistence of this second-generation cymrite. These textural relationships therefore support the episodic nature of post-orogenic uplift advocated by Dempster (1983 and 1985) on the basis of isotopic dating.

The composition of relict Fe-rich areas in coarsely crystalline, retrogressively-zoned sphalerite coexisting with pyrrhotite, pyrite and chalcopyrite in a sample (202-3) of quartzite from Foss, was used by Moles (1983) to define a P-T area through which the rock passed at some time during uplift. This area is constrained by pressures of  $3.1 \pm 0.3$  kbar estimated by extrapolation of the sphalerite geobarometer (calibration of Hutchison and Scott, 1981) and by the temperature of the hexagonal - monoclinic transition in pyrrhotite, estimated to be 260-300°C at this pressure. This P-T area lies close to the uplift and cooling path modelled for Aberfeldy by Dempster (1985) and is also close to the cymrite-celsian reaction line (fig. 8.4). However, its location within the celsian field conflicts with the suggestion that cymrite was stable



at this point in the uplift and cooling history. Possible explanations for this relatively small discrepancy include continued equilibration of the sphalerite with hexagonal pyrrhotite persisting metastably to lower temperatures (e.g. 200-250°C), or the metastable growth of cymrite associated with the late metamorphic brittle deformation and fluid infiltration.

### 8.5 Conclusions.

Temperature and pressure ranges derived from a variety of mineral equilibria in metasedimentary, metabasaltic and mineralized lithologies associated with the Foss deposit, are in reasonable agreement and indicate peak metamorphic conditions of 530  $\pm$  30°C and 9  $\pm$  1 kbar. The post-D3 replacement of cymrite by celsian in the stratiform mineralized rocks is considered to post-date the attainment of peak metamorphic temperatures during a period of decreasing lithostatic pressure. The subsequent P-T evolution probably followed a path close to the cymrite-celsian equilibrium until the cymrite stability field was re-entered during late metamorphic fault movements.

The post-tectonic evolution recorded by mineral equilibria at Foss is in good agreement with that modelled in a recent study of isotopic mineral ages in central Perthshire (Dempster 1983 and 1985). However, the prograde history and peak metamorphic conditions attained at Foss appear to be significantly different from those in areas 10km to the north, where pre-D3, lower pressure (5-6 kbar) assemblages appear to be overprinted by higher pressure equilibria (9-10 kbar), and to the south, where lower pressures (6-7 kbar) were attained.

Table 8.1: Previously published, peak metamorphic temperature and pressure estimates for the Aberfeldy area.

Author	Area	Mineral equilibria*	T, °C	P, kbar
Wells and Richardson (1979)	Schiehallion (Dalradian)	Plag-gt-ky-qtz Garnet-biotite <sup>a</sup>	560 $\pm$ 50	12 $\pm$ 1.5
Wells (1979)	Schiehallion (Moine)	Hb-plag-qtz-gt-ep Garnet-biotite <sup>a</sup> Gt-hornblende	550 $\pm$ 50	11.3 $\pm$ 2
Sivaprakash (1982)	Aberfeldy-Grandtully	Plag-gt-ky-qtz Epid-gt-plag-qtz Garnet-biotite <sup>a</sup> Calcite-dolomite <sup>b</sup>	500-580 420-550	10 $\pm$ 1 8-10
Dempster (1983)	Aberfeldy Loch Tummel	Garnet-biotite <sup>a</sup> Plag-biot-gt-musc <sup>c</sup>	490 $\pm$ 30 530 $\pm$ 30	7.0 $\pm$ 1 9.1 $\pm$ 1
Baker (1985)	Schiehallion	Garnet-biotite <sup>a</sup> Plag-gt-ky-qtz <sup>d</sup>	530-590 $\pm$ 30	9.7-10.1 $\pm$ 1
Willan (1980, 1981)	Foss & Ben Eagach deposits	Sph-py-po		6.8 $\pm$ 0.3 6.1 $\pm$ 0.3

\*See Appendix B for abbreviations. Calibrations used:

<sup>a</sup>: Ferry and Spear, 1978

<sup>b</sup>: Bickle and Powell, 1977

<sup>c</sup>: Ghent and Stout, 1981

<sup>d</sup>: Newton and Haselton, 1981

Table 8.2: Formulations of geothermometers and geobarometers used.

Garnet-hornblende: Graham and Powell, 1984.

$$T(^{\circ}\text{K}) = \frac{2880 + 3280 \cdot X_{\text{Ca}}^{\text{Gt}}}{\ln K_D + 2.426} \quad \text{where } K_D = \frac{\left[ \frac{X_{\text{Fe}}^{\text{Gt}}}{X_{\text{Mg}}^{\text{Gt}}} \right] / \left[ \frac{X_{\text{Fe}}^{\text{Hb}}}{X_{\text{Mg}}^{\text{Hb}}} \right]}{\left[ \frac{X_{\text{Fe}}^{\text{Gt}}}{X_{\text{Mg}}^{\text{Gt}}} \right] / \left[ \frac{X_{\text{Fe}}^{\text{Hb}}}{X_{\text{Mg}}^{\text{Hb}}} \right]}$$

Garnet-biotite:

1. Ferry and Spear, 1978.

$$T(^{\circ}\text{K}) = \frac{12454 + 0.057P \text{ (bars)}}{4.662 - 3RT \cdot \ln K_D} \quad \text{where } K_D = \frac{\left[ \frac{X_{\text{Mg}}^{\text{Gt}}}{X_{\text{Fe}}^{\text{Gt}}} \right] / \left[ \frac{X_{\text{Mg}}^{\text{Bi}}}{X_{\text{Fe}}^{\text{Bi}}} \right]}{\left[ \frac{X_{\text{Mg}}^{\text{Gt}}}{X_{\text{Fe}}^{\text{Gt}}} \right] / \left[ \frac{X_{\text{Mg}}^{\text{Bi}}}{X_{\text{Fe}}^{\text{Bi}}} \right]}$$

2. Hodges and Spear, 1982 ( $K_D$  as above).

$$T(^{\circ}\text{K}) = \frac{12454 + 0.057P \text{ (bars)} + 3 \cdot X_{\text{Ca}}^{\text{Gt}} \cdot (3300 - 1.5T)}{4.662 - 3RT \cdot \ln K_D}$$

3. Pigage and Greenwood, 1982 ( $K_D$  as above).

$$T(^{\circ}\text{K}) = \frac{1586 \cdot X_{\text{Ca}}^{\text{Gt}} + 1308 \cdot X_{\text{Mn}}^{\text{Gt}} + 2089 + 0.00956P \text{ (bars)}}{0.78198 - \ln K_D}$$

Calcite-dolomite: Bickle and Powell, 1977.

An IMP program, PTCALCS, compiled by Andy Walker (1982), was used to calculate temperatures for given calcite compositions and pressures, assuming equilibrium with dolomite. The first equation derives a pure  $X_{\text{Mg}}^{\text{Cal}}$  value given the specified pressure and calcite composition and iterates until the input temperature and calculated temperature coincide. The second equation is the correction term for temperature estimates from iron-bearing calcite:

$$\log X_{\text{Mg}}^{\text{Cal}} = (0.847 - 3091/T) + (P-1)(0.17 \times 10^{-8}T - 0.33 \times 10^{-6})$$

$$T(^{\circ}\text{K}) = \frac{-1560 - (0.032 P)}{R \cdot \log \left[ \frac{X_{\text{Mg}}^{\text{Cal}} - X_{\text{Mg}}^{\text{Cal}}}{X_{\text{Fe}}^{\text{Cal}} + X_{\text{Ca}}^{\text{Cal}}} \right]}$$

Plagioclase-biotite-garnet-muscovite: Ghent and Stout, 1981.

$$P_1(\text{bars}) = \frac{(R \cdot \ln K_{D1} - 16.675) \cdot T - 8888.4}{1.738}$$

$$P_2(\text{bars}) = \frac{(R \cdot \ln K_{D2} - 22.061) \cdot T + 4124.4}{1.802}$$

$$\text{where } K_{D1} = \frac{\left[ \frac{X_{\text{Ca}}^{\text{Pl}} \cdot X_{\text{Mg}}^{\text{Bi}}}{X_{\text{Mg}}^{\text{Gt}} \cdot X_{\text{Ca}}^{\text{Gt}}} \right]^3 \cdot \frac{1}{X_{\text{K}}^{\text{Mu}} \cdot (X_{\text{Alv}}^{\text{Mu}})^2}}{\left[ \frac{X_{\text{Ca}}^{\text{Pl}} \cdot X_{\text{Mg}}^{\text{Bi}}}{X_{\text{Mg}}^{\text{Gt}} \cdot X_{\text{Ca}}^{\text{Gt}}} \right]^3 \cdot \frac{1}{X_{\text{K}}^{\text{Mu}} \cdot (X_{\text{Alv}}^{\text{Mu}})^2}}$$

and  $K_{D2}$  is the same expression but with  $X_{\text{Fe}}^{\text{Gt}}$  and  $X_{\text{Fe}}^{\text{Bi}}$ .  $T(^{\circ}\text{C})$  is derived from garnet-biotite geothermometry using the calibration of Ferry and Spear (1978).

Biotite-muscovite-chlorite-quartz: Powell and Evans, 1983.

See table 8.4 and fig. 8.2. Activity terms calculated by an IMP program, PTCALCS, by Andy Walker, 1982.

Sphalerite-pyrite-pyrrhotite: Hutchison and Scott, 1981.

$$P \text{ (kbar)} = 42.30 - 32.10 \cdot \log(\text{mol\% FeS in sphalerite}).$$

TABLE 8.3: Garnet, hornblende, biotite, plagioclase and muscovite compositions and derived temperature and pressure estimates (published in Moles, 1985)

Sample	(1) rock type	(2) $X_{Ca}^{Gt}$	(3) $X_{Mn}^{Gt}$	Mg/Fe			(4) $X_{(Al^{Vi}+Ti)}^{Bi}$	(5) $X_{Ca}^{Pl}$	(6) $X_K^{Mu}$	(7) $X_{Al^{Vi}}^{Mu}$	Gt-Hb T°C G&P	Gt-Bi T°C (assuming P=8 kbar)			Pl-Bi-Gt-Mu P kbar (G&S) using T from:	
				Gt	Hb	Bi						F&S	H&S	P&G	F&S	H&S
429-5	SP(D	0.208	0.051	0.1362	0.956	1.160	0.212	0.190	0.891	0.855	541	468	542	603	8.0	8.3-9.0
"	"	0.211	0.058	0.1232	"	"	"	"	"	"	525	443	517	579	7.6	7.9-8.6
N80-36	SP(D	0.253	0.046	0.1349	1.209	1.372	0.155	albite			530	425	512	574	na	na
4685	SP(D	0.218	0.077	0.1411	1.000	1.349	0.152	0.179	0.851	0.848	547	440	516	586	7.8	8.1-8.9
706-4B	B2	0.225	0.100	0.1376	-	1.137	0.166	0.156	0.834	0.864	-	475	556	644	8.5	8.9-9.6
503-10	B2	0.158	0.103	0.1496	-	1.016	0.156	0.089	0.844	0.873	-	530	592	672	9.9	10.3-11.0
"	"	"	"	"	-	1.098	0.158	"	"	"	-	507	568	646	9.3	9.6-10.2
708-15	B2	0.166	0.074	0.1660	-	1.047	0.224	0.157	0.873	0.888	-	552	618	693	9.1	9.4-10.0
G16	SP(A	0.260	0.064	0.1337	-	1.146	0.199	albite			-	466	564	635	na	na
"	"	0.208	0.039	0.1523	-	"	"	"			-	501	581	637	"	"
G48	SP(A	0.186	0.056	0.1325	-	1.056	0.254	0.107	0.885	0.885	-	485	556	614	9.6	10.1-10.7
503-27	SP(A	0.173	0.060	0.1486	-	0.9314	0.161	albite			-	554	623	689	na	na

## Notes

- (1): Identified in fig. 3.6: see Appendix B  
 (2):  $Ca/(Ca+Fe+Mg+Mn)$  in garnet rim.  
 (3):  $Mn/(Ca+Fe+Mg+Mn)$  in garnet rim.  
 (4):  $(Al^{Vi}+Ti)/(Al^{Vi}+Ti+Fe+Mg+Mn)$  in biotite.  
 (5):  $Ca/(Ca+K+Na)$  in plagioclase: 'albite' indicates  $<0.03$ .  
 (6):  $K/(K+Na+Ca+Ba)$  in muscovite.  
 (7):  $Al^{Vi}/(Al^{Vi}+Ti+Fe+Mg+Mn)$  in muscovite.

Calibrations of: G&P Graham and Powell, 1984  
 F&S Ferry and Spear, 1978  
 H&S Hodges and Spear, 1982  
 P&G Pigage and Greenwood, 1982  
 G&S Ghent and Stout, 1981

na: Not applicable.



Table 8.4: Activity data\* and pressure estimates from  
biotite-muscovite-chlorite-quartz geobarometry.

Sample	Rock type	$a_{\text{chlorite clinoch.}}$	$a_{\text{biotite phlog.}}$	$a_{\text{white mica celadonite}}$	$a_{\text{white mica muscovite}}$	$\ln K_D$	P kbar at T=	
							520*	580°C
429-5 m	SP(D	0.050	0.063	0.081	0.588	4.22	9.5	10.7
"		0.050	0.075	0.079	0.542	4.77	8.9	10.1
N80-36	SP(D	0.061	0.084	0.080	0.607	4.97	8.7	9.9
C79-31	SP(C	0.091	0.104	0.074	0.528	5.38	8.4	9.5
706-48	B2	0.045	0.060	0.076	0.553	4.38	9.4	10.6
503-10	B2	0.044	0.053	0.060	0.589	5.04	8.7	9.9
N80-45	B2	0.040	0.055	0.063	0.619	5.10	8.6	9.8
"		0.041	0.054	0.049	0.603	6.00	7.8	8.9
429-11	B2	0.042	0.062	0.063	0.582	5.35	8.4	9.5
"		0.042	0.059	0.055	0.609	5.79	8.0	9.1

\* Activity formulations and equilibrium constant for the expression:

$$K_D = \frac{(X_{\text{white mica}}^{\text{muscovite}}) \cdot (X_{\text{biotite}}^{\text{phlogopite}})^3}{(X_{\text{white mica}}^{\text{celadonite}})^4 \cdot (X_{\text{chlorite}}^{\text{clinocllore}})}$$

from Powell and Evans (1983).

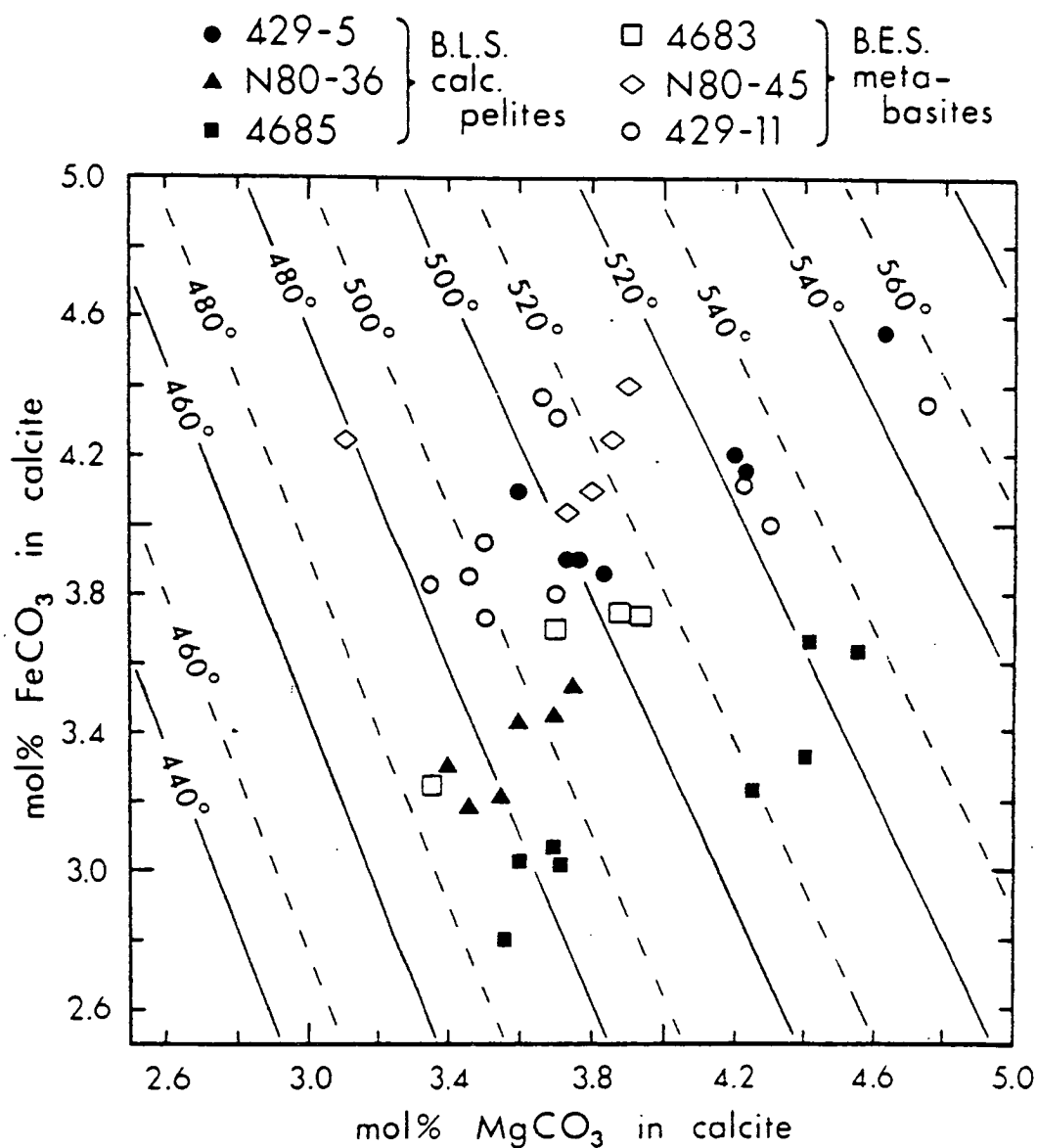


**Fig. 8.1:**  $\text{FeCO}_3$  content plotted against  $\text{MgCO}_3$  content in calcite coexisting with dolomite in six samples from Foss, contoured for temperature in  $^{\circ}\text{C}$  at  $P=9$  kbar (solid lines) and  $P=7$  kbar (dashed lines) (after Bickle and Powell, 1977).

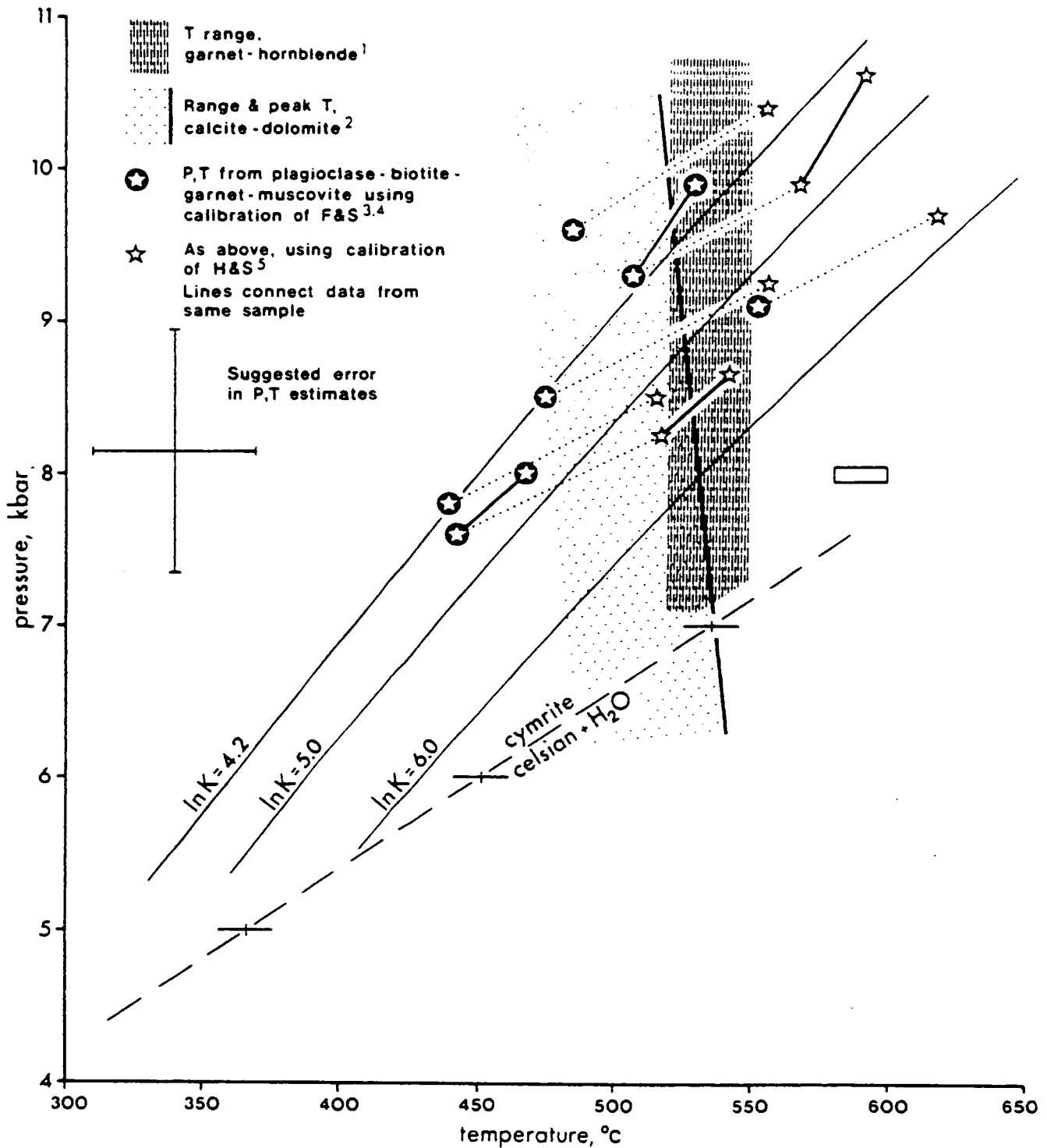


**Fig. 8.2:** P-T diagram showing results from several geothermometers and geobarometers applied at Foss. Calibrations of: 1 Graham & Powell (1984), 2 Bickle & Powell (1977), 3 Ghent & Stout (1981), 4 Ferry & Spear (1978) (star in circle) and 5 Hodges & Spear (1982) (star) (see table 8.3 for details). Curved lines are  $\ln K$  contours from biotite-muscovite-chlorite-quartz geobarometry (Powell & Evans 1983) and represent minimum, mean and maximum values obtained (see table 8.4). Dashed line with error bars for the pure cymrite-celsian reaction from Nitsch (1980): rectangular box locates 8 kbar reversal obtained in this study (see fig. G.1).

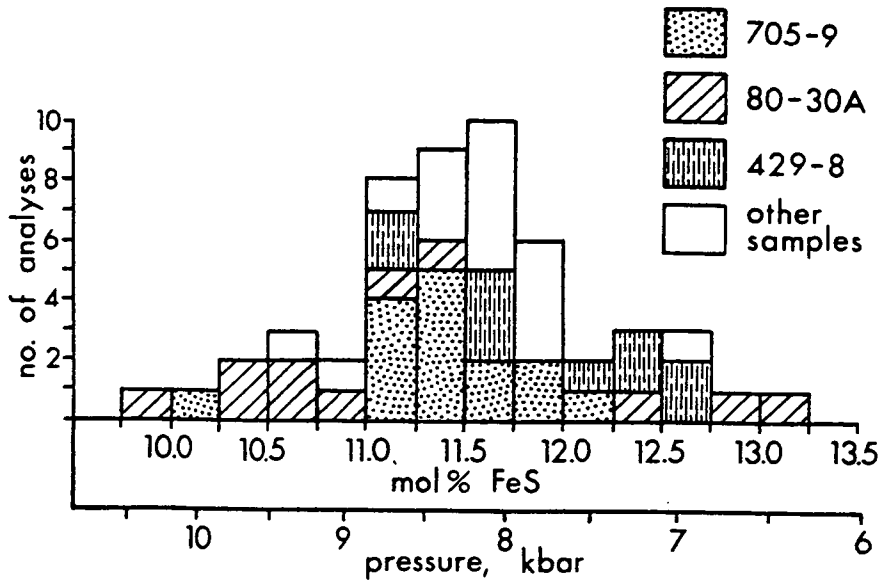


**Fig. 8.3:** Histogram of mol% FeS in 52 analyses of sphalerite from Foss. Sphalerites satisfy textural criteria for retention of peak metamorphic compositions buffered in the assemblage pyrrhotite-pyrite-sphalerite. Textural and compositional data for samples 705-9, 80-30A and 429-8 published in Moles (1983). Pressure calibration of Hutchison and Scott (1981).

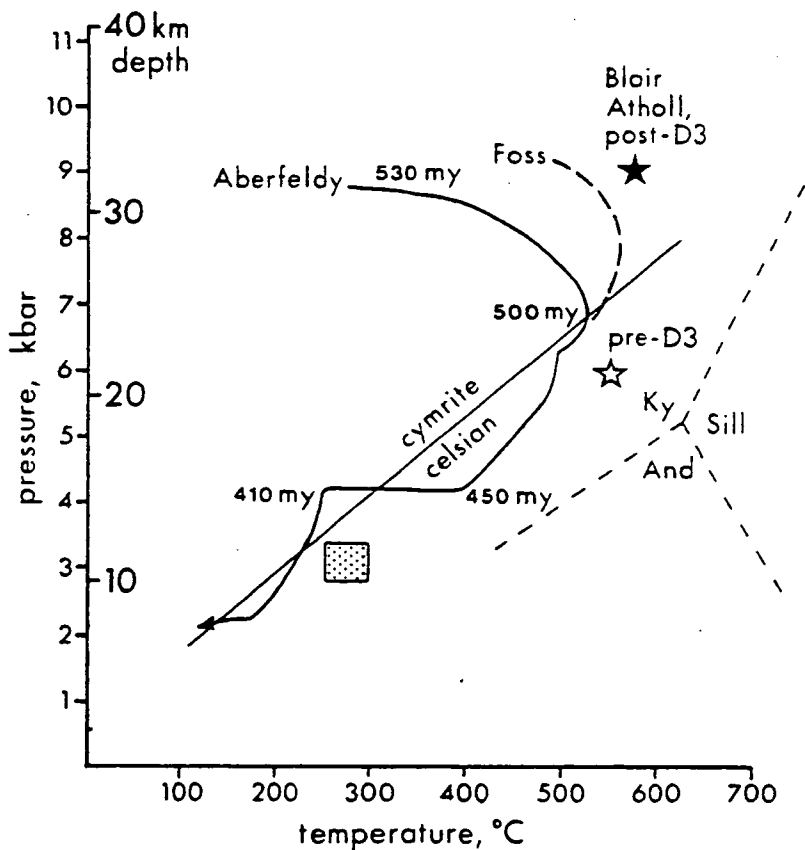


**Fig. 8.4:** Possible P-T conditions during and subsequent to metamorphism in central Perthshire. Heavy curved line: uplift path modelled by Dempster (1985), Aberfeldy area. Heavy dashed line: suggested alternative path for the Foss area (see text). Equilibrium line for the reaction, cymrite = celsian + H<sub>2</sub>O, from Nitsch (1980). Aluminosilicate triple point (light dashed lines) from Richardson et al. (1969). Shaded box represents conditions at Foss deduced from the composition of retrogressively zoned sphalerite in sample 202-3 (Moles, 1983). Stars represent probable pre-D3 conditions indicated by chloritoid-biotite assemblages, and subsequent peak P-T conditions at Blair Atholl, 10km N of Foss (Dempster, 1983).

## CHAPTER 9: Sulphur isotope studies.

### 9.1 Introduction.

This chapter is concerned with the results of sulphur isotope determinations on 49 sulphide and 35 barite separates from Foss, which supplement similar numbers of results (56 and 20 respectively) from the Aberfeldy deposits previously obtained by Willan and Coleman (1981, 1983). Following an introduction to sulphur isotope systematics (section 9.2), the interpretation of the previous isotopic results is summarised (section 9.3), and objectives and sampling methods of the present research are described (section 9.4). Details of sample preparation and analysis, undertaken at the Isotope Geology Unit of the British Geological Survey in London, are described in Appendix H. Section 9.5 is a detailed examination of the evidence concerning isotopic equilibration and sulphur mobility during metamorphism, the evaluation of which is essential to the interpretation of the macroscopic variation in isotope ratios. Stratigraphical and lateral variations in isotopic composition at Foss are described in section 9.6. Inferences on the sources of sulphur and the nature of the depositional environment are presented in section 9.7, with reference to sulphur isotope data from other sedimentary exhalative deposits. The conclusions are summarised in section 9.8.

### 9.2 Sulphur isotope systematics.

Sulphur has four isotopes of which mass 32 accounts for about 95% of the sulphur in average crustal and meteoric rocks, while the heavier isotope,  $^{34}\text{S}$ , accounts for 4.2% of the remainder. The ratio of the abundance of these isotopes in a sample is expressed in the conventional ' $\delta$ ' notation as per mil differences from the Canyon Diablo meteoric troilite standard:

$$\delta^{34}\text{S}_{\text{sample}} = \left[ \frac{^{34}\text{S}/^{32}\text{S}_{\text{sample}}}{^{34}\text{S}/^{32}\text{S}_{\text{standard}}} \right] - 1 \times 1000\text{‰}.$$

The fractionation of sulphur isotopes between two phases, for example barite and pyrite, is approximated as the numerical difference in their respective  $\delta^{34}\text{S}$  values, and is expressed as  $\Delta^{34}\text{S}_{\text{barite-pyrite}}$ .

The following is based on reviews of sulphur isotope systematics by Boast (1978), Claypool et al. (1980), Nielsen (1978), Rye and Ohmoto (1974) and Willan (1983).

### 9.2.1 Sources of sulphur.

The two major terrestrial reservoirs of sulphur are the lithosphere (mantle or homogenised crust) and the ocean (seawater sulphate). Meteoric troilite displays a uniform isotopic composition ( $\delta^{34}\text{S}$  range, -0.1 to +0.6‰, e.g. Jensen, 1967) and it is widely accepted that this is representative of the value for deep-seated terrestrial sulphur. Likewise, present day seawater is uniform in composition with a mean  $\delta^{34}\text{S}$  value of +20.99‰ (Rees et al., 1978). However, the sulphur isotope composition of seawater sulphate has varied considerably with geological time, as recorded by marine evaporite deposits of various ages (fig. 9.1) (Claypool et al., 1980; Holser, 1977). Barite and sulphides in sedimentary ore deposits display a similar  $\delta^{34}\text{S}$  age curve (Sangster, 1968). The most positive isotopic ratios attained by oceanic sulphate (~33‰) are recorded by evaporites and barite of both uppermost Devonian and latest Precambrian-Lower Cambrian ages (Goodfellow and Jonasson, 1984; Viezer et al., 1980).

This variation in the  $\delta^{34}\text{S}$  of seawater sulphate (which is adequately known only for the Phanerozoic) has been attributed to an imbalance between the fixation of isotopically light sulphur in sedimentary sulphides, which results in a corresponding enrichment in  $^{34}\text{S}$  of the ocean sulphate reservoir, and the influx of light sulphate derived from the erosion of older marine sediments (Holser and Kaplan, 1966). Holser (1977) envisages the accumulation of isotopically heavy sulphate as evaporitic deposits in enclosed, Mediterranean-type basins, the destruction of which resulted in sudden increases in the  $^{34}\text{S}$  content of open ocean sulphate. This hypothesis is supported by detailed studies of  $\delta^{34}\text{S}$  secular trends in barite and sulphides of Palaeozoic age in the Selwyn Basin, Yukon (Goodfellow and Jonasson, op. cit.).

### 9.2.2 Fractionation.

The wide spectrum of observed  $\delta^{34}\text{S}$  values, which range from about -40‰ to +40‰ in 98% of determinations (Nielsen, 1978), may be attributed to two processes which act upon the major sulphur reservoirs. These are (i) equilibrium fractionation, involving the partitioning of the minor isotope relative to the major, and (ii) kinetic fractionation, which is the result of the relatively faster rate of reaction of the lighter isotope.

Equilibrium fractionation provides the basis of isotope geothermometry. Experimental and theoretical studies (e.g. Sakai, 1968) of the equilibrium distribution of the isotopes of sulphur between galena, sphalerite and pyrite have established that the  $^{34}\text{S}$  content of these sulphides increases in that order, and that isotopic differences between the sulphides decrease with increasing temperature (Rye and Ohmoto, 1974; Smith et al., 1977). Sulphur isotope fractionations amongst sulphur-bearing phases, plotted with respect to pyrite in fig. 9.2, are largest with sulphate-sulphide pairs ( $\Delta^{34}\text{S}$  generally >10‰) and smallest between pyrite and sphalerite (e.g. 1‰ at 275°C). Consequently, an analytical uncertainty of  $\pm 0.1\%$  for the  $\Delta^{34}\text{S}$  value relating to mineral pairs (see Appendix H) causes an uncertainty in calculated sulphur isotopic temperatures of about  $\pm 10^\circ\text{C}$  for barite-pyrite,  $\pm 20^\circ\text{C}$  for sphalerite-galena, and  $\pm 50^\circ\text{C}$  for pyrite-sphalerite.

Kinetic fractionation effects accompany the reduction of sulphate, which may be achieved by sulphur-reducing bacteria, or by inorganic reactions with ferrous minerals or organic carbon compounds at elevated temperatures (Ohmoto and Rye, 1979). In a system open to sulphate supply, sulphide produced by purely chemical reduction is depleted in the heavier isotope by 22‰ relative to the  $\delta^{34}\text{S}_{\text{sulphate}}$  value (Harrison and Thode, 1957). A similar fractionation has been observed in  $\text{H}_2\text{S}$  generated from sulphate by laboratory cultures of sulphur-reducing bacteria (Kemp and Thode, 1968; McCready, 1975). However, bacterial reduction of seawater sulphate in present day, anaerobic sedimentary environments is observed to produce depletions in  $\delta^{34}\text{S}$  of up to 50‰ (Kaplan et al., 1963), which may be accounted for by a double kinetic isotopic effect involving an intermediate sulphite ion (Kemp and Thode, 1968). An antipathetic relationship between the rate of reduction

and the extent of kinetic fractionation has been demonstrated by Goldhaber and Kaplan (1974). These authors also show that rapid sedimentation rates, which favour the preservation of organic matter required for bacterial metabolism, increase the rate of sulphate reduction and therefore decrease the fractionation effect.

#### 9.2.3 Open and closed systems.

The distribution pattern of sulphur isotope ratios generated by bacterial reduction of sulphate is dependent upon whether the system is open or closed to the supply of sulphate and to the removal of sulphide (Schwarcz and Burnie, 1973). In an open system with an unlimited reservoir of sulphate, the isotopic composition of the sulphide is dependent only on the fractionation factor, and sulphate phases display  $\delta^{34}\text{S}$  values close to that of contemporaneous seawater sulphate. In a closed system with a limited supply of sulphate,  $\delta^{34}\text{S}$  values of the residual sulphate increase as reduction proceeds, and therefore each successive batch of reduced sulphur will be heavier than the previous (assuming that the fractionation factor,  $F$ , remains constant). Precipitated sulphides may show a range of  $\delta^{34}\text{S}$  values from that of  $\delta^{34}\text{S}(\text{seawater sulphate} - F)$  to that of  $\delta^{34}\text{S}(\text{residual sulphate} - F)$ , and precipitated sulphates will show a range of values which are heavier than that of the original seawater sulphate. If sulphide precipitation is not immediate, the  $\text{H}_2\text{S}$  generated by bacterial reduction may homogenise, so that sulphides precipitated subsequently may be of a uniform isotopic composition. Progressive increases in  $\delta^{34}\text{S}$  values of sedimentary sulphides (and of sulphate) with stratigraphic height within mineralized beds have generally been attributed to the closed system fractionation effect (e.g. Sangster, 1968; Smith and Croxford, 1975).

#### 9.2.4 Isotopic equilibration during metamorphism.

Several detailed studies of metamorphosed (to upper amphibolite grade) stratiform sulphide deposits have established that while large-scale primary  $\delta^{34}\text{S}$  variations are preserved, small-scale redistribution of sulphur isotopes and an approach to equilibrium fractionation has occurred during metamorphism (e.g. Rye and Ohmoto, 1974; Nielsen, 1978). The degree of attainment of isotopic equilibrium appears to be extremely variable in deposits of similar



mineralogy which have been metamorphosed to the greenschist facies (cf. Lusk and Crocket, 1969, and Bachinski, 1977). Equilibrium between coexisting sphalerite and galena seems to be more readily attained than between these phases and pyrite. This is borne out by experimental attempts to achieve isotopic equilibrium between metal sulphides and sulphur (Smith et al., 1977) which suggest that pyrite is the most sluggish sulphide to equilibrate.

Recently, Whelan et al. (1984) have reported a detailed isotopic study of the upper amphibolite grade ( $\sim 625^{\circ}\text{C}$ ,  $\sim 6.5$  kbar), Balmat-Edwards Zn-Pb deposits in NW New York, which are hosted by Grenville series marbles and evaporites. Equilibrium temperatures calculated from  $\Delta^{34}\text{S}$  values for the mineral pairs pyrite-galena, sphalerite-galena, pyrite-sphalerite and anhydrite-pyrite, average  $330^{\circ}$ ,  $340^{\circ}$ ,  $390^{\circ}$  and  $600^{\circ}\text{C}$  respectively. The authors consider that sulphate-pyrite  $\Delta^{34}\text{S}$  differences probably reflect equilibration at near-peak P-T conditions, whereas the sulphide-sulphide  $\delta^{34}\text{S}$  differences record retrograde re-equilibration which may have been accomplished during recrystallization of the sulphides. However, a positive correlation between sulphide grain size ( $<1$  to  $>5\text{mm}$ ) and  $\delta^{34}\text{S}$  values indicates that some retrograde isotope exchange occurred by solid state diffusion.

### 9.3 Previous sulphur isotope investigations of the Aberfeldy deposits.

In the first sulphur isotope study of barite and sulphide mineralization occurring in the Dalradian Supergroup of Scotland, Willan and Coleman (1981, 1983) analysed seventy six separates from a total of fifty nine samples from both the Foss and Ben Eagach deposits. The authors also analysed twenty six sulphides from twelve other localities of massive and disseminated base metal mineralization at a similar stratigraphic level to the SE.

In their initial report, Willan and Coleman (1981) concluded that the sulphate and the reduced sulphur in the Aberfeldy mineralization were both derived from late Precambrian-Lower Cambrian seawater sulphate, respectively by direct precipitation, and following bacterial reduction within warm brine layers. The range in  $\delta^{34}\text{S}_{\text{sulphide}}$  values ( $\sim 10\%$ ) found in both mineralized and host

rocks was attributed to varying physicochemical conditions and rates of nutrient supply and sediment deposition. Differences in the mean values of  $\delta^{34}\text{S}_{\text{barite}}$  in the Foss and Ben Eagach deposits, together with opposing trends in  $\delta^{34}\text{S}_{\text{sulphide}}$  variation with stratigraphic height (decreasing in BH3, cf. fig. 9.11b; increasing in BH4), are taken to indicate that the "Western Sector [Foss deposit] brine was more reducing and therefore in a more restricted environment with respect to mixing with seawater sulphate".

A different interpretation was subsequently presented by Willan (1982) and Willan and Coleman (1983), after the completion of fifteen further analyses. To account for the bimodal  $\delta^{34}\text{S}$  distribution (~32‰ and ~35‰) observed in the Aberfeldy barite, and the differences in isotopic composition between sulphides in the mineralization and in the enclosing metasediments, they invoke a dual source of sulphur and suggest that the bulk of the barite precipitated during rapid mixing of hydrothermal, metalliferous fluids with basinal seawater sulphate ( $\delta^{34}\text{S} = 35\%$ ), whereas during periods of waning exhalative activity and slower mixing, a greater proportion of isotopically light sulphate was derived from the oxidation of hydrothermal reduced sulphur ( $\delta^{34}\text{S} = 28\%$ ). The upward increase in  $\delta^{34}\text{S}$  of sulphides within mineralized beds (from 20‰ to ~28‰ in BH4) is attributed to the progressive reduction of circulating seawater sulphate at high temperatures (200–300°C) in the underlying sedimentary pile.

Willan and Coleman (1983) also found isotopically heavy, disseminated sulphide in metasediments along strike from, and at the same stratigraphic level as, the stratiform mineralization in the Creag an Fhithich area (BH8). Isotopically lighter sulphide ( $\delta^{34}\text{S} = 12\text{--}15\%$ ) occurring in metasediments stratigraphically higher and lower than the stratiform mineralization, and in the uppermost chert bed in the BH3 profile, is regarded as bacteriogenic in origin. Much lighter sulphide-sulphur ( $\delta^{34}\text{S} = -4$  to 0‰) occurring in minor, Cu- and Ni-enriched stratabound iron sulphide mineralization in the SW Highlands, may have been derived from leaching of intrusive basic rocks which are much more abundant in the sedimentary pile in that area than in the central Highlands.

Willan and Coleman (1983) used the experimentally determined fractionation factors given by Ohmoto and Rye (1979) (see fig. 9.4)

to calculate temperatures of 460-590°C from the  $\Delta^{34}\text{S}$  data for seven barite-pyrite pairs. Fractionation temperatures within this range, which brackets independent estimates for metamorphic conditions at Aberfeldy (fig. 9.6), were derived from only three of the eleven sulphide-sulphide pairs examined. In one sample of sulphide rock (481), non-equilibrium is indicated by a  $\Delta^{34}\text{S}_{\text{py-sph}}$  of -5.0‰, but the pyrite-galena fractionation in this sample (+1.5‰) suggests an equilibrium temperature of 550°C. Willan and Coleman conclude that on the scale sampled, no detectable equilibration took place during metamorphism because most of the sulphide pairs either have negative  $\Delta^{34}\text{S}$  values or yield isotopic temperatures which are unreasonably low or high for regional metamorphism. Furthermore, the isotopic composition of barite and sulphides are not related to their relative modal proportions, and independent variations of  $\delta^{34}\text{S}_{\text{barite}}$  and  $\delta^{34}\text{S}_{\text{pyrite}}$  were found in a stratigraphic profile (BH4).

#### 9.4 Objectives and methods of the present study.

The original objectives of the present, more detailed study of sulphur isotopes in the Foss deposit (outlined in part 1.4.4) were; (a) to critically test the hypothesis that equilibrium fractionation between coexisting sulphur-bearing phases during metamorphism has not influenced the sulphur isotope ratios, and (b) to see through the metamorphic imprint (if any) to obtain information on the temporal and spatial variations in  $\delta^{34}\text{S}$  ratios and their relationship to mineralizing processes and the source(s) of sulphur.

Knowledge of the scales of both primary isotopic variation and of metamorphic equilibration (if any) is an essential prerequisite to the interpretation of macroscopic variation in isotopic ratios. A detailed evaluation of the evidence for redistribution of sulphur isotopes during metamorphism is therefore a major aspect of this study. This was achieved by separately analysing coexisting sulphur-bearing minerals in many of the samples examined, and particularly in those which have petrographical and chemical evidence of heterogeneous sulphide compositions (i.e. variable iron content of sphalerites), or of diagenetic/metamorphic reactions involving sulphur-bearing minerals.

Detailed vertical  $\delta^{34}\text{S}$  profiles of several mineralized intersections were constructed to discern isotopic trends which may provide further information on the source of sulphur and the environment of ore deposition. The Creagan Loch area at the eastern end of the Foss deposit, which is characterised by rapid lateral facies and thickness changes related to both syn-depositional and late metamorphic fault movements (part 2.4.4), was selected for detailed examination because: (a) material was available from several closely spaced drillholes with good geological control on structural and stratigraphic location and way-up; (b) isotopic studies could be integrated with mineralogical and other geochemical studies using the same sample material; (c) sulphur isotope data obtained by Willan and Coleman from the BH3 intersection in this area can be incorporated for comparative purposes.

Lateral variations in the isotopic composition of barite in Foss East and West were evaluated using drillcore material from precisely correlated horizons, combined with a detailed vertical profile through several units of the composite barite bed in the Frenich Burn area (fig. 9.1). By examining the isotopic variation through one horizon using several profiles in a comparatively small area (<200m across), it should be possible to assess the significance of isotopic variation throughout the deposit as a whole and to distinguish such large-scale variations from local compositional irregularities. For example, considerable variation in the isotopic composition of samples from a time-equivalent horizon would indicate that  $\delta^{34}\text{S}$  values were dominantly influenced by the local depositional environment, whereas temporal changes in brine composition or the source of sulphur may be manifested by laterally correlatable isotopic trends. Two possibilities which were investigated are that  $\delta^{34}\text{S}$  values may be correlated with barite bed thickness, or that barite in the five distinct barite-bearing horizons (M3-M7) may be characterized by differing isotopic compositions.

This study further investigated the isotopic composition of sulphides in mineralized strata relatively distal from the exhalative centres, and in metasedimentary lithologies containing sulphides regarded as non-exhalative in origin or at least distal from the exhalative centres. The isotopic composition of iron sulphides occurring in two metabasic layers at Foss was also

examined, one closely associated with the mineralization and the other from the overlying Ben Lawers Schist.

#### Sampling method and presentation of results.

Most mineral separates analysed in this study were obtained from samples of 2-4cm<sup>3</sup> using conventional separating methods and hand-picking (see Appendix H). Massive monomineralic sulphide and barite were sampled by breaking off a small fragment, and a small (2cm diameter) diamond-impregnated saw attached to a dentists drill was used to cut material from a polished block of one sample (705-30B). The majority of the sixty-one samples used for isotopic determinations are from Dresser Minerals drillcores; two are from IGS boreholes and the remaining five are outcrop samples from Foss West. Sample locations, brief descriptions and the  $\delta^{34}\text{S}$  values obtained are given in table 9.1, and sample or drillhole locations are shown in fig. 9.2 (reference should also be made to figures in chapter 2). The results obtained from DHs 104 (Frenich Burn), 705 and 708 (Creagan Loch) are plotted against stratigraphic profiles of these mineralized intersections in figs 9.11 and 9.12, together with the BH3 data of Willan and Coleman (1983).

The  $\delta^{34}\text{S}$  values for both sulphides and barite from the Foss deposit obtained in this study differ in distribution from those obtained by Willan and Coleman (1981, 1983) (fig. 9.4). The differences may be due to sampling restrictions imposed by the limited amount of outcrop and borehole material available to these authors: in particular, the lower barite horizon in the Ben Eagach deposit was not exposed and most of the samples analysed by Willan and Coleman (op. cit.) are from the sulphide-rich BH4 intersection. Furthermore, a large proportion of the isotopically light sulphides analysed in this study are from one profile (DH 708, fig. 9.11d). It should also be noted that a greater proportion of sphalerite separates were analysed than in the previous investigation. If isotopic equilibration had occurred during metamorphism, sphalerite should have lower  $\delta^{34}\text{S}$  ratios (by 1-2‰) than coexisting pyrite (see fig. 9.2). Many samples used in this study contain both barite and sulphides, and the pre-metamorphic distribution of isotopic ratios in these rocks could have been modified by metamorphic equilibration. This possibility is examined in detail in the following section.

## 9.5 Isotopic equilibration and sulphur mobility during metamorphism.

### 9.5.1 Evidence for and against small-scale isotopic equilibration.

#### 9.5.1.1 Recognition of metamorphic equilibration.

Willan and Coleman (1983) found significant differences (>0.3% and up to 5%.) in the isotopic ratios of sulphides from samples taken 10cm apart in stratigraphical sequences from BHs 3 and 4 and the Foss adit. A difference in  $\delta^{34}\text{S}$  of 1% was discovered in barite chips taken 7cm apart across the banding in a sample of barite rock (203-18B) examined in this study. These results suggest either that primary isotopic variation on a centimetre scale has survived through metamorphism, or that metamorphic processes (such as laminar fluid flow) have generated isotopic heterogeneity. However, further evidence is required to establish whether equilibration of sulphur isotope ratios occurred on a millimetre or grain-to-grain scale, which would allow the use of isotopic data from coexisting barite and disseminated sulphides to estimate metamorphic equilibration temperatures (provided that sampling was on a scale less than or equal to the equilibrium domains). As such equilibration would tend to blur pre-metamorphic isotopic variation on scales greater than that of the equilibrium domains, the small-scale metamorphic equilibration of sulphur isotope compositions has significant implications for the interpretation of large-scale variations which may be related to mineralizing processes and to varying sources of sulphur.

The principal criteria for recognising isotopic equilibration are: (i) The  $\delta^{34}\text{S}$  values of coexisting sulphur-bearing minerals should increase in the sequence established for equilibrium distribution, i.e. galena<sphalerite=pyrrhotite<pyrite<barite, and (ii) the fractionation between phases should yield reasonable metamorphic temperatures (in the present case,  $530 \pm 30^\circ\text{C}$ ). A wide scatter in the fractionation temperatures, or a temperature range consistent with that of the hydrothermal fluids (i.e.  $200\text{--}300^\circ\text{C}$ : see part 10.4.3), would suggest that isotopic equilibration had not occurred during metamorphism. However, this interpretation requires caution, since extensive re-setting of sulphide-sulphide isotopic equilibria to comparatively low temperatures ( $300\text{--}400^\circ\text{C}$ ) has been recorded in some metamorphosed deposits (part 9.2.4).

#### 9.5.1.2 Isotopic temperatures and relationship with grain size.

Fractionation temperatures calculated from the data for seven barite-sulphide pairs and sixteen sulphide pairs analysed in this study are presented in table 9.2 and, together with previous results, in fig. 9.6. Assuming that equilibration occurred during metamorphism, a range of temperatures (410 - 580°C) approximating to that of peak metamorphism (part 8.3.5) are calculated from the data for barite-sulphide pairs (discussed further in part 9.5.1.6). However, a broader range of temperatures are indicated by sulphide-sulphide pairs, and negative  $\Delta^{34}\text{S}$  values indicating isotopic disequilibrium were found in three pairs examined by Willan and Coleman (1983) and in two analysed in this study (samples 705-30 and 708-7). A notable feature of the new data is that most pyrite-sphalerite pairs yield fractionation temperatures of around 300°C (range, 240-400°C, but note  $\pm 50^\circ$  uncertainty due to the small fractionation). In view of the greater tendency of sphalerite-galena pairs to equilibrate (or retrogressively re-equilibrate) during metamorphism (part 9.2.4), the wide range in temperatures derived from three sphalerite-galena pairs (390-590°C) suggests that metamorphic equilibration on a grain-to-grain scale was incomplete and the derived temperatures may be meaningless.

Clearly, the degree of attainment of isotopic equilibrium during metamorphism (if at all) was not solely determined by the specific mineral pairs involved, but varied from rock to rock. One significant difference between samples which could be related to the extent of prograde and/or retrograde isotopic equilibration, is the grain size of the sulphides (cf. Whelan et al., 1984) and perhaps also their textural association, if metamorphic fluid interactions influenced isotopic exchange. Although grain sizes are generally quite variable within the samples examined (fig. 9.7), those with significantly coarser sulphides, 708-7 and 705-30 (plate 25), are also characterised by isotopic disequilibrium (table 9.2). An interesting feature of sample 708-7 is that the galena is much finer grained than the coexisting sphalerite and pyrite (fig. 9.7), and isotopic fractionation values suggesting an approach to metamorphic equilibrium are yielded only by the sulphide-galena pairs (table 9.2). Very similar features are shown by sample 494 from BH3 (data of Willan and Coleman, 1981) (fig. 9.2b, 9.11b), in which the galena

is also fine grained (R.C.R. Willan, pers. comm.).

To summarise, the relationship between fractionation temperatures from different mineral pairs in samples in which all three sulphides were analysed, suggests that partial equilibration of isotopic ratios between fine-grained sulphides probably took place during metamorphism. However, the clustering of pyrite-sphalerite temperatures close to 300°C could represent equilibration in the hot hydrothermal fluids prior to exhalation, or during burial metamorphism and diagenesis prior to amphibolite-facies metamorphism.

#### 9.5.1.3 Within-crystal and within-sample isotopic variations in sulphide rocks.

Repeat analyses of coarsely crystalline (~1cm grain size) pyrite and galena from sample 705-30, using different fragments from the same small specimen (~2cm<sup>3</sup>), gave significantly different values (table 9.1). These results indicate not only isotopic disequilibrium (table 9.2), but also heterogeneity on a crystal scale. Within-crystal isotopic zonation was confirmed by analysing carefully separated areas of pyrite and galena crystals cut from a polished block of the same rock unit (705-30B: fig. 9.8). A much larger difference was found between core and rim parts of a 1cm galena crystal ( $\Delta^{34}\text{S} = 1.7\%$ ) than between corresponding locations in the adjacent pyrite ( $\Delta^{34}\text{S} = 0.3\%$ ). Apparent temperatures derived from this data, assuming that isotopic equilibrium existed between (1) mutually adjacent rims of pyrite and galena crystals, and (2) nearby core areas of these crystals, are 260°C and 540°C respectively, which suggests that partial retrograde isotopic re-equilibration could have taken place following recrystallization during metamorphism. A sphalerite crystal in the same rock shows zoning in iron content and exsolution features also indicative of retrograde re-equilibration (part 8.3.3 and Moles, 1983), but insufficient material was available for isotopic analysis. Further evidence for retrograde or post-metamorphic fluid interactions with this rock is provided by thin orthoclase rims to celsian crystals (part 6.2.2) and argillic alteration of the celsian.

Pyrite and sphalerite have a patchy distribution in sample 708-6 (table 9.1 and fig. 9.9), which is regarded as an annealed breccia (of metamorphic origin; part 3.2.2) incorporating disrupted fragments of quartz hyalophane chert (plate 29). An isotopic



fractionation temperature of 340°C derived from analyses of coexisting pyrite (modal proportion: 29%) and sphalerite (23%) separated from the area marked 'D' in fig. 9.9, suggested that the isotopic compositions of the sulphides may have partially equilibrated during prograde metamorphism. However, pyrite from an adjacent patch of granular, monomineralic pyrite (labelled 'M' in fig. 9.9) is comparatively enriched in the heavier isotope with a  $\delta^{34}\text{S}$  ratio 2.2‰ higher than pyrite in area 'D'. Monomineralic areas of sphalerite do not occur in this rock, but if the assumption is made that the pyrite in area 'D' was originally similar in isotopic composition to that in area 'M', then it may be speculated that the sphalerite in area 'D' was relatively depleted in the heavy isotope before metamorphic equilibration with the coexisting pyrite. Mass balance calculations (table 9.3) suggest that the pre-metamorphic isotopic composition of this sphalerite could lie within the range observed from other samples in this stratigraphic profile ( $\delta^{34}\text{S}$  = 15–20‰: fig. 9.11d). The possible implications of this are discussed further in part 9.5.2.

The data obtained from samples 705-30, 705-308 and 708-6 indicate that millimetre- or centimetre-scale heterogeneity in isotopic composition may result in averaged  $\delta^{34}\text{S}$  values for mineral separates obtained from samples of several  $\text{cm}^3$  in size, which might obscure the small-scale attainment of equilibrium. This is more likely to have occurred in samples with a banded or patchy distribution of sulphur-bearing minerals. Either the lack of attainment of isotopic equilibrium during prograde and peak metamorphism, or continued, partial re-equilibration during retrograde metamorphism, may account for the scatter in fractionation temperatures derived by Willan and Coleman (1983) and in this study (fig. 9.6).

Incomplete prograde equilibration could have resulted from the growth of coarse, zoned crystals before metamorphic recrystallization, e.g. from precipitation in hydrothermal mounds (such as the bed represented by 705-30: part 10.4.3) or during diagenesis. The early growth of some coarse pyrite in the Foss deposit, such as commonly observed in Cyprus and Kuroko-type deposits, is suggested by the presence within pyrite crystals of barite inclusions with heterogeneous compositions (section 7.4) and encapsulated barium

carbonates which have been destroyed by metamorphic reactions in the matrix (part 3.3.2).

However, the detailed study of sample 705-30B suggests that isotopic equilibrium was achieved during peak metamorphism and preserved in grain cores in this very coarse massive sulphide rock. Isotopic zonation within 1cm-sized crystals in 705-30B is attributed to progressively retarded rates of diffusion during cooling, with a lower blocking temperature for galena ( $\sim 260^\circ\text{C}$ ?) than for pyrite. Similarly, the low temperature derived from  $\Delta^{34}\text{S}$  values for seven pyrite-sphalerite pairs ( $310^\circ \pm 70^\circ\text{C}$ ; table 9.2) could reflect a blocking temperature, although this does not appear to decrease with decreasing grain size (fig. 9.7) (cf. Whelan et al., 1984). However, this hypothesis is incompatible with the higher temperatures obtained from three sphalerite-galena pairs ( $390^\circ$ ,  $488^\circ$  and  $585^\circ\text{C}$ ), which from comparison with other studies (see section 9.2.4) should yield the lowest temperatures if retrograde isotopic exchange had occurred.

#### 9.5.1.4 Relationship between chemical and isotopic composition of sphalerite.

A model of ore deposition which attempts to account for the coexistence of primary Fe-rich and Fe-poor sphalerites, presented in part 7.3.2 and by Moles (1983), advocates changing physicochemical conditions (including sulphur concentrations) during the precipitation of the zinc sulphides. These changes, and possibly variations at the sulphur source, might be expected to generate differing isotope ratios in the earlier- and later-formed sphalerite. Evidence of variation in  $\delta^{34}\text{S}$  source composition with time is seen in other hydrothermal systems, for example from the recent discoveries of unusually light  $\delta^{34}\text{S}_{\text{pyrite}}$  associated with hydrothermal chimneys from Silvermines, Ireland (Boyce et al., 1983), and of pronounced isotopic zonation ( $\sim 20\%$ ) corresponding to a zonation in Fe-content of colloform sphalerites in the unmetamorphosed, carbonate-hosted stratabound deposits at Bleiberg, Austria (Schroll et al., 1983).

Disseminated primary, iron-rich and iron-poor sphalerites were carefully separated by magnetic and hand-picking techniques from a small sample of fine-grained sulphidic barite rock (705-20: plate 47). These sphalerite fractions were found to have identical isotope ratios (table 9.1). This could indicate either that primary

variations in iron content were not related to differences in isotopic composition (contrary to the model described above), or that isotopic homogenization occurred during metamorphism. Two lamellae of sphalerite with contrasting iron-contents, which are located 1mm apart in a banded quartz dolomite hyalophane metachert (429-8: plate 106 and table 9.1) were also analysed separately and yielded indistinguishable  $\delta^{34}\text{S}$  ratios. In this case, the difference in iron content is attributed to localized enrichment due to buffering in the presence of pyrrhotite (see Moles, 1983 and part 7.3.2), and the absence of a corresponding isotopic difference suggests that if isotopic equilibration took place, this was not associated with changes in chemical composition during metamorphism. These results therefore permit, but do not prove, the hypothesis that millimetre-scale isotopic exchange between disseminated or banded sulphides occurred during metamorphism.

#### 9.5.1.5 Isotopic ratios of coexisting barite and sulphides.

No systematic relationship between the isotopic ratios and modal proportions of barite and sulphide was found by Willan and Coleman (1983). They noted that pyrite in several barite rocks was isotopically lighter than in most barite-poor samples, contrary to the relationship expected if equilibration had occurred during metamorphism. However, further data obtained in this study from six samples in which coexisting barite and sulphide were analysed (table 9.2), appear to support the contention that isotopic equilibration took place, since the  $\delta^{34}\text{S}$  ratios of barite and sulphide are positively correlated (fig. 9.10) and yield 'reasonable' metamorphic temperatures (410-580°C: fig. 9.6) over a wide range of whole rock  $\delta^{34}\text{S}$  compositions (25-36‰: table 9.3). The problem with this argument is that the 'primary' isotopic compositions of both barite and sulphides (determined in sulphide-free barite rocks and in barite-free sulphide rocks respectively) show the same range, and an average  $\Delta^{34}\text{S}_{\text{barite-sulphide}}$  value using non-coexisting phases is similar to that for coexisting phases. Therefore, the reasonable metamorphic temperatures and positive correlation referred to above, may merely reflect a primary, non-equilibrium relationship between the isotopic compositions of barite and sulphides controlled by depositional processes (section 9.7). Under such circumstances, even if equilibration had taken place during metamorphism, it would have

had a minimal effect on the primary isotopic distribution.

Two samples provide additional evidence that primary  $\delta^{34}\text{S}$  ratios in coexisting barite and sulphides are preserved. The unusually large  $\Delta^{34}\text{S}_{\text{barite-sphalerite}}$  of +16.4‰ in 104-25, due to the comparatively low  $\delta^{34}\text{S}$  ratio (17.4‰) in the disseminated sphalerite but 'normal' isotopic composition for barite in this profile (fig. 9.12), places this sample apart from others on fig. 9.10. Conversely, sulphides in the thin barite bed represented by sample 708-9B (table 9.1) are isotopically similar to sulphides in the underlying and overlying sulphidic cherts which do not contain barite (fig. 9.11d). These features are difficult to explain in terms of metamorphic equilibration, whereas stratigraphical variations in isotope ratios in both barite and sulphides are readily explained in terms of primary depositional processes, in particular an interplay between two sources of sulphur (section 9.7).

#### 9.5.1.6 The influence of metamorphism on isotopic ratios: a conclusion.

There is ample evidence that original spatial variations in bulk  $\delta^{34}\text{S}$  ratios have survived metamorphism (figs. 9.11, 9.12), although fine details such as primary zoning and possible isotopic variations associated with compositional variations in sphalerite have probably been modified by equilibration on a millimetre scale. Also, original contrasts in the stratigraphic profiles of pyrite-sulphur and base metal sulphide-sulphur, such as are observed in the Rammelsberg and McArthur deposits (fig. 9.15: see part 9.7.2.3) may have been destroyed during metamorphism of the Foss deposit. Since the pyrite content commonly equals or exceeds the base metal sulphide content of sulphidic rocks at Foss, the marked variations in  $\delta^{34}\text{S}_{\text{sulphide}}$  through stratigraphic profiles can largely be attributed to variations in pyrite composition. Possible evidence for a greater pre-metamorphic variation in the isotopic composition of pyrite than in the base metal sulphides may be seen in samples 490 and 491 in the BH3 profile (data of Willan and Coleman: fig. 9.11b) and in sample 708-6 (fig. 9.11d), which record wider stratigraphic fluctuations in the  $\delta^{34}\text{S}$  values of pyrite than of sphalerite.

It is concluded that the similarity between the apparent temperatures derived from  $\Delta^{34}\text{S}$  values for many coexisting sulphur-

bearing phases, and the temperature range of amphibolite-facies metamorphism (fig. 9.6), does not necessarily indicate that isotopic equilibration occurred during metamorphism. The apparent temperatures may not be meaningful due to sampling on a scale larger than the equilibrium domains, or may record isotopic fractionation in the hydrothermal fluids from which the sulphides precipitated.

#### 9.5.2 Sulphur mobility during diagenetic and metamorphic reactions.

Direct textural evidence for two diagenetic and/or metamorphic reactions involving sulphur-bearing phases were described in section 3.3: (1) the reaction of barite with silicates under reducing conditions to form hyalophane; and (2) the breakdown of barium carbonates to form calcite, dolomite and barite. Other reactions involving sulphur which may have occurred, although direct textural evidence is absent, include the formation of phlogopite + pyrite from biotite +  $H_2S$  (cf. Iso et al., 1979, and section 7.7) and the replacement of iron monosulphides by pyrite, which commonly occurs during diagenesis on combination of biogenic sulphur and as a retrograde reaction. Isotopic results from several rocks which show textural or mineralogical evidence of post-depositional sulphur mobility are now examined.

##### 9.5.2.1 Formation of barium feldspars from barite.

Textural evidence which suggests the diagenetic and/or metamorphic decomposition of barite to form barium feldspars has been described in a few metachert rocks (part 3.3.1 and plates 61-64), and three samples were selected for isotopic study (N81-80, 09-06 and G114; table 9.1). Insufficient barite was separated from N81-80 to obtain a reliable isotopic measurement (a microprobe analysis is given in table 7.6), but disseminated pyrite in this sample was found to be relatively enriched in  $^{34}S$  ( $\delta^{34}S = 27.1\%$ ). This could be explained by the incorporation of sulphur released from barite concomitant with reactions (1) and (2) suggested in part 3.3.1. However, a graphitic chert which is rich in hyalophane pseudomorphs similar in appearance to those in N81-80, (sample 09-06, plates 62, 63) contains sphalerite which is not significantly enriched in the heavy isotope ( $\delta^{34}S = 17.7\%$ ) relative to other sulphidic rocks from Foss (fig. 9.4). Note that this sample also contains minor pyrrhotite which was not analysed. If this pyrrhotite was found to be

enriched in  $^{34}\text{S}$ , then both the incorporation of barite-derived sulphur and the lack of subsequent inter-phase equilibration could be demonstrated.

In the third sample, G114 (table 9.1, plates 35, 66), celsian forms lensoid and wispy structures which locally replace the finely laminated quartz-pyrite matrix, and have a morphological resemblance to diagenetic gypsum (part 3.3.1). Recrystallized pyrite from this rock is also exceptionally enriched in  $^{34}\text{S}$  (28.9%), again possibly due to the incorporation of isotopically heavy sulphur released during sulphate decomposition. For comparison, the isotopic composition of pyrite was determined in another sample (G100E) which lacks textural evidence of sulphate replacement, but is from the same stratigraphic horizon as G114 (figs. 2.4 and 9.1). Pyrite in G100E was also found to be enriched in the heavy isotope ( $\delta^{34}\text{S} = 28.1\%$ ). Therefore, isotopically heavy sulphide-sulphur may be a characteristic feature of this distal facies equivalent to the M3 horizon on the northern limb of the Creag na h-Iolaire Anticline (part 9.7.2).

These results highlight the difficulty in interpreting isotopic data from rocks which have had a complex history of diagenetic and metamorphic reactions involving isotopic fractionation superimposed on the originally variable isotopic compositions. Nevertheless, the scarcity of  $\delta^{34}\text{S}_{\text{py}}$  values in excess of +27%, and of textural evidence for sulphate-silicate reactions in rocks containing barium feldspars, gives further support to the view held by Coats et al. (1981) and Fortey and Beddoe-Stephens (1982), that the barium feldspars in the Aberfeldy deposits were largely derived from silicate precursors and were seldom formed by subsequent reactions involving the breakdown of barite. (Note that isotopically heavy pyrite (>27%) found by Willan and Coleman, 1983, in the BH4 profile occurs in celsian-poor carbonate rocks.)

#### 9.5.2.2 Carbonate-sulphate reactions.

Inclusions of barium carbonates found encapsulated within pyrite crystals in several calcareous barite rocks (part 7.5.3) appear to have been shielded from reactions which generated barite, calcite and dolomite in the matrix by the incorporation of sulphite. If the sulphite in the permeating diagenetic/metamorphic fluid phase was derived by oxidation of a reduced sulphur species such as  $\text{H}_2\text{S}$ ,

the isotopic composition of the barite generated in these reactions may have been strongly enriched in  $^{32}\text{S}$  relative to primary barite precipitated from seawater sulphate. This hypothesis could perhaps account for the unusually low  $\delta^{34}\text{S}_{\text{barite}}$  values of 26-29‰ found by Willan and Coleman (1983) in calcareous barite near the stratigraphic top of the BH3 barite intersection (fig. 9.11b), where the presence of witherite has been verified (IGS 3965: see Appendix B part III and table 7.8).

Two calcareous barite samples, in which norsethite and baryto-calcite inclusions have been identified, were examined in the present study (203-18B and 408-10: table 9.1). The  $\delta^{34}\text{S}$  values of 32-33‰ determined for barite in these samples are not unusually low (fig. 9.2) but are significantly lower than barite from the same stratigraphical level in DH 104 (located between DHs 408 and 203: figs. 9.1 and 9.12). As lateral and stratigraphic variation can also be attributed to depositional processes (parts 9.6.2 and 9.7.1), isotopically lighter barite-sulphur in these samples and in the upper part of BH3 cannot be unequivocally related to carbonate-sulphate reactions. Further work is required to resolve this problem.

## 9.6 Stratigraphical and lateral variations in $\delta^{34}\text{S}$ ratios.

### 9.6.1 The Creagan Loch area.

#### 9.6.1.1 BH3 profile.

A stratigraphical sequence of seven barite and eleven sulphide separates from the BH3 intersection were analysed by Willan and Coleman (1981, 1983). One additional sample was analysed in this study (03-MB) from near the base of the horizon (table 9.1, fig. 9.11b). The  $\delta^{34}\text{S}$  ratio of pyrrhotite in this mineralized metabasite (22.1‰) is similar to that of sulphides in the overlying sulphidic dolomite-celsian rock (range, 20-25‰), and suggests that sulphur in the altered basaltic material derives from the same source. Sulphides in the 4m thick, basal dolomitic unit appear to show a general increase in  $\delta^{34}\text{S}$  with stratigraphic height, interrupted by an occurrence of isotopically heavy pyrite (sample 491) which coincides with a sudden increase in sulphide content and the local development of breccia textures (possibly synsedimentary in origin).

In the overlying massive barite bed (thickness, 6.4m), barite is basally enriched in the heavy isotope ( $\delta^{34}\text{S} = 35.6\%$ ) but becomes isotopically lighter with stratigraphic height. Exceptionally light  $\delta^{34}\text{S}_{\text{barite}}$  ratios of 26.7% were found in two samples above and below the boundary with the overlying cherts, where another sample of barite is isotopically heavy. Sulphides in these cherts are unusually depleted in  $^{34}\text{S}$  (<15%) compared with the bulk of the sulphide in mineralized rocks examined by Willan and Coleman. However, pyrite in a quartz celsian rock representing an upper mineralized horizon (probably M5) sampled by Willan and Coleman (1983) from 150m SE of BH3 (fig. 2.4), is again isotopically heavy ( $\delta^{34}\text{S} = 26.3\%$ ).

#### 9.6.1.2 DH 705 profile.

Twenty analyses of sulphides in eleven samples from the M3 horizon intersected in DH 705, show a range in  $\delta^{34}\text{S}$  ratios similar to that of the BH3 intersection about 110m to the east (figs. 9.11a,c). The heaviest value (24.9%) occurs in a thin (10cm), massive granular pyrite layer which directly overlies the footwall metabasite marker bed, and the lowest value ( $\delta^{34}\text{S}_{\text{pyrite}} = 18.3\%$ ) is found in the uppermost chert bed. Pyrite and galena in samples 705-30 and 308, from the coarsely crystalline massive sulphide rock, interpreted as a possible vent deposit (part 3.5.2), are isotopically similar to bedded sulphides in the same intersection. Five barite separates ( $\delta^{34}\text{S}$  range, 32.9-36.5%) from barite rock above and below the massive sulphide rock, show no clear systematic relationships between isotopic composition and either the presence of disseminated sulphides or stratigraphic height.

The isotopic ratios of sulphides in four metasedimentary rocks from the DH 705 drillcore were also determined. Pyrite in siliceous graphitic schists sampled at 0.2m and 1.6m stratigraphically below the base of the M3 horizon, has  $\delta^{34}\text{S}$  ratios (21.3 and 20.2% respectively) which are similar to sulphides within the stratiform mineralization. The same was found for minor disseminated sphalerite in an otherwise unmineralized graphitic dolostone near the top of the Ben Eagach Schist (sample 705-14; plate 39, table 9.1). However, sphalerite in lamellae within a coarse gritstone resembling those of the Carn Mairg Quartzite (sample 705-31; cf. plate 37) about 12m stratigraphically above the M3 bed, is isotopically light



at 15.0‰. This value is identical to that determined by Willan and Coleman (1983) for sphalerite in a graphitic schist sample from the Ben Eagach Schist exposed in the Middleton Burn, east of Ben Eagach.

9.6.1.3 DH 708 profile.

Isotopically light sulphur ( $\delta^{34}\text{S}$  range, 14.6–18.0‰) also occurs in sulphides from the lower part of the M3 horizon intersected in DH 708, and again at the top of this 7.5m thick mineralized bed, ~85m to the east of BH3 (figs. 9.11a,d). Of the ten samples examined, only one (708-6) has isotopic ratios comparable to those found in most BH3 and DH 705 sulphides (i.e.  $\delta^{34}\text{S} > 20\text{‰}$ ). This difference in isotopic composition between M3 sulphides in DH 708 and in intersections further west at Creagan Loch, is additional evidence that these parts of the deposit were not originally contiguous (part 2.4.6). The significance of the lower  $\delta^{34}\text{S}$  ratios, particularly in the mineralized metasediments which form the basal part of the M3 horizon in this area, is discussed in part 9.7.3.

The 2.2‰ difference between pyrite subsamples from sample 708-6, described previously (part 9.5.1), may indicate separate sulphur sources for the iron and zinc sulphides which partially equilibrated during metamorphism. Conversely, sphalerite and pyrite in the thin (6cm) bed of massive barite rock in the upper part of this chert-dominated profile, are very similar in isotopic composition to sulphides occurring in the sulphate-free rocks above and below (samples 708-9B, 708-8 and 10: fig. 9.11d). This contrasts with the wide range in sphalerite iron-contents observed in the same samples (fig. 7.4i).

## 9.6.2 Frenich Burn area and central Foss East.

### 9.6.2.1 DH 601.

Distal equivalents of the M3 horizon have been recognised at depth in Foss East by correlating the metabasite marker bed (part 2.4.5). In the Frenich Burn area, M3 is intersected at about 300m beneath the surface by DH 601 (fig. 2.25). Here the horizon is 0.5m thick and consists of banded quartz-dolomite-pyrrhotite rock with minor celsian rock; barite is absent. A  $\delta^{34}\text{S}$  ratio of 16.4‰ obtained from a pyrrhotite separate (sample 601-6B), is similar to that of sulphides in the lower part of the DH 708 intersection.

#### 9.6.2.2 DH 104 profile.

The thick barite bed near the surface in the Frenich Burn East area was formed by the stacking of four or five separate mineralized horizons (part 2.4.1). Drillhole 104 (fig. 2.22) was selected for a detailed isotopic profile because four barite units can be clearly distinguished, which total over 20m in stratigraphic thickness, and the intersection is structurally simple (except near the stratigraphic top) and largely free of faulting. A total of sixteen  $\delta^{34}\text{S}$  measurements of barite plus three of coexisting disseminated sphalerite were completed, the majority from the lowermost (M3) unit (fig. 9.12). Due to limited time, only one sample from the M7 unit was analysed.

$\delta^{34}\text{S}_{\text{barite}}$  ratios in DH 104 samples range from 32.8–41.8‰ (table 9.1), but within M3 and M5 most results group close to a mean value of 36.4‰. The heaviest barite-sulphur was found in a sample near the base of M7, but no systematic relationships are seen between isotopic composition and either stratigraphic height or the presence of coexisting sulphides. In two of the samples containing disseminated sphalerite (104-38 and 44) both the barite and sphalerite are comparatively enriched in  $\delta^{34}\text{S}$ , and the isotopic fractionation values (13.9–14.4‰) suggest that partial equilibration could have occurred during metamorphism (table 9.2). However, in a third sample (104-25) the disseminated sphalerite is isotopically light and the unusually large  $\Delta^{34}\text{S}_{\text{barite-sulphide}}$  (16.4‰) may be evidence against metamorphic equilibration (part 9.5.1.5).

#### 9.6.2.3 Other barite samples from Foss East.

Samples from seven other Foss East drillholes (table 9.1) were analysed to check for major differences in  $\delta^{34}\text{S}_{\text{barite}}$  ratios which might reflect changes in the depositional environment corresponding to lateral facies and thickness variations, or alternatively might allow the individual barite horizons to be characterised isotopically. Apart from 702-16C, from the base of M3 ( $\delta^{34}\text{S}_{\text{barite}} = 36.5\%$ ), the values obtained from these samples (203-18B and 408-10 from M5, and 410-8 from M7: 32–33‰) are significantly lower than the majority of DH 104 barite samples (fig. 9.12). Barite samples representing the top and bottom of the 3m thick M3 barite bed intersected in DH 703 (figs. 2.28, 2.29) have intermediate  $\delta^{34}\text{S}$  values (34.1 and 35.1‰ respectively), and a similar result was

obtained for a sample from the base of the M3 barite intersection in DH 505 at Creagan Loch (table 9.1 and fig. 9.11a). These results, together with those from DH 705 (fig. 9.11c), suggest that the trend of upward-decreasing  $\delta^{34}\text{S}_{\text{barite}}$  found by Willan and Coleman in the BH3 (and BH4) profiles may not be typical of the barite lenses in the Foss East area.

### 9.6.3 Foss West.

#### 9.6.3.1 Barite in the upper and lower horizons.

On the southern limb of the Creagan na h-Iolaire Anticline in Foss West, barite occurs predominantly in the upper horizon or in a composite unit, but in an area of limited lateral and down-dip extent N of Meall Tairneachan, a lens of barite rock also occurs in the lower (M3) horizon (part 2.3.2). Fisher and Coleman (1980) analysed a sequence of six pyrite samples ( $\delta^{34}\text{S}$  range, 22.3–26.0‰) together with one barite (36.0‰) from the base of the upper horizon exposed in the Foss adit. A similar  $\delta^{34}\text{S}_{\text{barite}}$  value (35.4‰) was measured by Willan and Coleman (1983) from a sample of the same barite bed outcropping near BH9. To supplement this data, and to test the possibility that barite occurring in the upper and lower horizons could be isotopically distinct, samples were analysed from the thin (~60cm), lower barite bed cropping out on Creagan Chanaich (N81–83; figs. 2.2, 2.4), from the stratigraphic base and top of the upper barite bed intersected in DH 404 and from the composite barite unit in DH 429 (both about 0.5km west of the adit: figs. 2.10 and 2.12).

$\delta^{34}\text{S}_{\text{barite}}$  ratios of 33.4‰ and 32.6‰ were obtained from the base and top of the ~4m thick barite bed intersected in DH 404, and a value of 35.1‰ was determined for barite in a stratigraphically equivalent position at the top of the thicker intersection in DH 429. Sphalerite separates from the thin overlying chert bed in DH 429 (sample 429–8) average 20.7‰, possibly indicating a return to isotopically lighter sulphide-sulphur such as observed at the top of the M3 bed at Creagan Loch. Barite in a thin (17cm) unit within basal cherts in the same bed, regarded as a composite M3–M5 unit (fig. 2.15), was found to be relatively depleted in  $^{34}\text{S}$  (31.6‰), and the lightest value obtained in this study was recorded from the

equivalent horizon at outcrop (sample N81-83: 29.6‰, table 9.1). Although these results appear to support the interpretation that the single mineralized horizon in sector I of Foss West is a composite M3-M5 unit (part 2.3.4), further data is required to establish the presence of an 'isotopic stratigraphy' in the Foss barite beds.

Clearly, barite in each horizon shows considerable lateral variation in isotopic composition which is not related to stratigraphic height. However, a loose positive correlation may be seen between barite bed thicknesses and  $\delta^{34}\text{S}_{\text{barite}}$  values, particularly if the unusually light values from BH3 are excluded (fig. 9.13). This may be explained by postulating that a greater proportion of isotopically light sulphate, derived from the oxidation of aqueous reduced sulphur species, was incorporated into barite precipitated as thin beds some distance from the exhalative centres or during relatively weak exhalative activity. This is discussed further in part 9.7.1.

#### 9.6.3.2 Distal mineralization and cherts with sulphate pseudomorphs.

Outcropping mineralization on the northern limb of the Creag na h-Iolaire Anticline north of Creag an Chanaich (fig. 9.1), which appears to represent a distal facies equivalent to M3 (part 2.2.1), includes hyalophane and celsian bearing schists and a finely laminated, pyrite-quartz metachert containing barian fuchsite. Pyrite separates from two samples of this lithology, collected from outcrops 150m apart (G100E and G114: fig. 2.1 and table 9.1), were analysed and found to be unusually rich in  $^{34}\text{S}$ . Although possibly due to incorporation of heavy sulphur released by the breakdown of sulphates during diagenesis or metamorphism (part 9.5.3), these high  $\delta^{34}\text{S}$  values (28-29‰) are considered more likely to be a primary characteristic inherited from depositional processes (section 9.7.2).

On Creag an Chanaich, BH9 intersected a mineralized meta-sediment consisting of graphitic hyalophane chert with abundant sulphate pseudomorphs (sample 09-06), forming part of the lower chert unit in the M5 horizon. As noted above (part 9.5.2.1), sphalerite in this sample is relatively  $^{34}\text{S}$ -depleted, which contrasts with the isotopically heavy sulphide-sulphur (27.1‰) found in pyrite separated from another chert containing similar

pseudomorphs (N81-80), which directly overlies the thin M3 barite bed exposed at the surface nearby (table 9.1; see fig. 2.8).

#### 9.6.3.3 Pyrite in a Ben Lawers Schist metabasite.

Pyrite is an uncommon constituent of metasediments in units C and D, but occurs in minor amounts (<1%) as disseminated 1mm cubes in an amphibolite sheet in the Ben Lawers Schist, about 8m above the boundary with the Ben Eagach Schist to the west of the Foss deposit (sample N80-13: table 9.1). Duplicate analyses of this pyrite yielded  $\delta^{34}\text{S}$  ratios of -4.3 and -4.7‰, which are considerably lower than 12.7‰ obtained for pyrite in a Ben Lawers Schist quartzite from BH6, east of Ben Eagach, by Willan and Coleman (1983). The trace of sulphur in the amphibolite is probably of magmatic origin.

#### 9.6.4 Summary of new results from the Foss deposit.

Features of the data obtained in this study which are significantly different to the results of Willan and Coleman (1981, 1983: summarised in section 9.3), are reviewed below.

Barite. Profiles through barite beds at Foss do not show consistent stratigraphical variations in  $\delta^{34}\text{S}_{\text{barite}}$ . However, isotopically light sulphur (29-33‰) is characteristic of relatively thin (<2m) barite beds whereas values of 34-36.5‰ are typical of barite from thicker beds (fig. 9.13). In the composite barite bed at Frenich Burn,  $\delta^{34}\text{S}_{\text{barite}}$  ratios exceed 36.5‰ (up to 42‰) in five of the sixteen samples examined, although these show no systematic relationship with stratigraphic height or horizon number. Such isotopically heavy barite has not been found elsewhere in the Aberfeldy deposits, and is rare in stratiform deposits worldwide (comparable values are recorded in the Proterozoic, Lady Loretta deposit, Australia; table 9.4).

Sulphides. The additional data obtained in this study does not support the dichotomy between  $\delta^{34}\text{S}_{\text{sulphide}}$  ratios in the stratiform mineralization and in the host metasediments at Foss, suggested by Willan and Coleman (1983). Although sulphides in the uppermost chert unit intersected in BH3 are unusually light (<15‰), the reversion to relatively  $^{34}\text{S}$ -depleted sulphides at the stratigraphic top to mineralized horizons appears to be a feature in common with all profiles examined. In these profiles, local abrupt increases in  $\delta^{34}\text{S}_{\text{pyrite}}$  generally coincide with increases in the modal sulphide

concentration, but the available evidence does not support a gradual increase in  $\delta^{34}\text{S}$  ratios with height as postulated by Willan and Coleman (op. cit.). The dominance of lateral over temporal variations in isotopic composition is also illustrated by the significantly lighter  $\delta^{34}\text{S}_{\text{sulphide}}$  values (15-20‰) in most samples from DH 708 compared with those from BH3 and DH 705 (20-25‰). Relatively light sulphide (16-18‰) also occurs in a barite rock from the Frenich Burn composite bed, in a distal facies equivalent to M3 at depth in this area, and in a mineralized sediment beneath the M5 barite bed at Creag an Chanaich.

A sample of quartzite-hosted stratabound sphalerite is isotopically similar to sulphides of presumed bacteriogenic origin ( $\delta^{34}\text{S} < 16\%$ ) in metasediments examined by Willan and Coleman. However, pyrite in sulphide-rich graphitic schists beneath M3 at Creagan Loch has  $\delta^{34}\text{S}$  ratios similar to those in the overlying mineralized horizon (20-23‰). Similar results were obtained by Willan and Coleman from graphitic schists lateral to the stratiform mineralization on Creag an Fhithich (BH8), which also contain isotopically heavy sulphides. Sulphidic cherts overlying the M3 horizon on Creag an Chanaich, and forming a distal equivalent to this mineralized horizon on the N limb of the Creag na h-Iolaire Anticline, contain pyrite which is unusually enriched in the heavy isotope ( $\delta^{34}\text{S} = 28-29\%$ ), possibly due to incorporation of sulphur derived from the direct reduction of evaporite minerals (observed as pseudomorphs). Very minor amounts of isotopically light sulphur of probable magmatic origin are present in metabasites in the area.

## 9.7 Sources of sulphur and the depositional environment.

### 9.7.1 Barite.

Three sources for the barite-sulphur in stratiform deposits have been suggested in other studies: (1) contemporaneous open ocean seawater sulphate; (2) seawater sulphate enriched in  $^{34}\text{S}$  as a result of bacterial sulphate reduction and precipitation of  $^{34}\text{S}$ -depleted sulphide in a restricted basin; and (3) the oxidation of reduced sulphur carried in the hydrothermal solutions. Unfortunately the isotopic composition of late Precambrian oceanic sulphate is poorly constrained. Although Claypool et al. (1980) suggest an average

composition of 30‰ at ~620My, values of >33‰ may well have been attained during the excursion to isotopically heavy sulphate at this time (Viezer et al., 1980) (fig. 9.1).

#### $\delta^{34}\text{S}$ lighter than seawater.

Following Holser (1977), Willan and Coleman (1983) suggest that seawater in the restricted, partly evaporitic Dalradian basin was enriched in isotopically heavy sulphate, and barite with  $\delta^{34}\text{S} \approx 35\%$  precipitated as a result of the vigorous mixing of hydrothermal fluids with oxygenated seawater. To account for an apparent bimodal distribution of  $\delta^{34}\text{S}_{\text{barite}}$  ratios, Willan and Coleman suggest that barite also precipitated during periods of slower mixing of a static brine layer with the overlying seawater, deriving a greater proportion of isotopically light sulphur (<33‰) from the oxidation of sulphide species in the hydrothermal solutions.

Clearly, this model does not necessarily predict a bimodal distribution of barite compositions, but rather a continuum between two end-members of which the isotopically heavier value is likely to be volumetrically dominant in thicker barite beds. Construed in this manner, the model accounts for both the skewed (or polymodal?) distribution of  $\delta^{34}\text{S}_{\text{barite}}$  values (fig. 9.4) and the positive relationship between isotopic composition and barite bed thickness (fig. 9.13) shown by the new data from Foss. However, a hydrothermal source need not be required for the isotopically light sulphur, since this could also be derived from the oxidation of bacteriogenic reduced sulphur within the entrained basinal seawater (fig. 9.16). Willan and Coleman (1983, p. 1644) acknowledge the possibility of this contribution of isotopically light aqueous sulphide species in accounting for the relatively  $^{34}\text{S}$ -poor pyrite associated with massive barite rock in BH 4 and elsewhere.

#### $\delta^{34}\text{S}$ heavier than seawater.

The unusually high  $\delta^{34}\text{S}_{\text{barite}}$  ratios (>36.5‰ and up to ~42‰) found in several DH 104 samples in the Frenich Burn stacked barite bed (fig. 9.12), may have resulted from the episodic depletion of the lighter isotope in the basinal seawater sulphate source due to bacterial reduction under closed system conditions (see part 9.2.3). A lagoonal seawater source has also been suggested for unusually heavy barite-sulphur (37-40‰) in the Lady Loretta deposit in northern Australia (Carr and Smith, 1977) (table 9.4). In the

Frenich Burn area, such conditions may have prevailed in a relatively shallow-water environment which is suggested by evidence of sedimentary reworking (part 2.4.1) and by increasingly oxidizing conditions inferred from sphalerite compositions (part 7.3.2). Sulphide coexisting with barite in two of these samples is also enriched in  $^{34}\text{S}$ , although as noted above (part 9.5.1.5 and fig. 9.10), this could be due to metamorphic equilibration.

Another possible explanation for the isotopically heavy barite and sulphide is in situ bacterial sulphate reduction and precipitation under closed system conditions during early diagenesis, such as postulated by Rye et al. (1978) to account for extremely high  $\delta^{34}\text{S}$  values (up to 56‰) in concretionary barite at Northumberland Canyon, Nevada. Conversely, Cecile et al. (1983) found that thick, Palaeozoic barite beds in Western Canada have  $\delta^{34}\text{S}$  values equivalent to that of contemporaneous marine sulphate, whereas barite in thin beds or nodules within carbonaceous sediments is isotopically heavy. They attribute this to precipitation-dissolution processes operating in redox-stratified wet sediments or seawater.

#### Along-strike differences.

In a recent isotopic study of the Precambrian stratiform orebodies at Aggeneys and Gamsberg, South Africa, Gehlen et al. (1983) found pronounced lateral differences in  $\delta^{34}\text{S}$  values of both sulphide and barite between the deposits. This is interpreted in terms of an increase in the proportion of sulphur derived from lagoonal seawater or evaporite solutions ( $\delta^{34}\text{S} > 30\text{‰}$ ), relative to that derived from magmatic-exhalative sulphur ( $\sim 0\text{‰}$ ). A similar explanation was offered by Solomon et al. (1969) for isotopic differences between the Cambrian, volcanic-hosted sulphide and barite deposits of Rosebery and Mt. Lyell in Tasmania. Further isotopic data from the Ben Eagach deposit is necessary to ascertain whether there are major, along-strike differences in barite composition (fig. 9.2), between the Foss and Ben Eagach deposits, suggested by significant differences in  $\delta^{34}\text{S}$  distribution (fig. 9.4) (cf. Willan and Coleman, 1981). However, considering the presence of thick sulphidic chert beds at the locations where barite was sampled in the Ben Eagach deposit, and the large amount of unexposed barite rock since discovered at a stratigraphically lower horizon (part



1.3.2), sampling bias based on available exposure could be responsible for these apparent along-strike differences at Aberfeldy.

#### 9.7.2 Sulphides.

##### Hydrothermal sulphur.

Reduced sulphur, precipitated as sulphides in sedimentary ore deposits, may be derived from (i) the bacterial reduction of seawater sulphate, or (ii) sulphur species transported with the metals in the hydrothermal solutions. The brines in present-day hydrothermal systems such as in the Red Sea, contain varying amounts of  $H_2S$  and soluble sulphate species such as  $NaSO_4^-$  and  $MgSO_4^-$  (e.g. Shanks and Bischoff, 1977). However, the abundance of barium aluminosilicates in the Aberfeldy deposits and the problem of transporting barium together with aqueous sulphates in the hydrothermal fluids, indicate that if sulphur was present in these fluids, it was largely in the reduced state. This reduced sulphur may have been derived from the dissolution of sulphide within buried sediments, or from the inorganic reduction of sulphate held in earlier evaporite deposits (e.g. the Ballachulish Slate; Hall, 1982), in connate waters, or in convecting seawater within the sedimentary pile.

The reduction of aqueous sulphate by reaction with ferrous minerals or organic material at temperatures of  $>200^\circ C$ , results in  $\delta^{34}S_{H_2S}$  ratios which are  $<22\%$  lighter than the sulphate source (e.g. Ohmoto and Rye, 1979; Styrt et al., 1981; Shanks et al., 1981). This reduced sulphur is therefore generally enriched in  $^{34}S$  compared with reduced sulphur of bacterial origin (part 9.2.2). As Willan and Coleman (1983) concluded, the smaller values of  $\Delta^{34}S_{SO_4-sulphide}$  in the Aberfeldy mineralization ( $\sim 10-15\%$ ) compared to that of sulphides of presumed bacterial origin in the host metasediments at Aberfeldy and elsewhere in the Dalradian ( $\Delta^{34}S = 15-35\%$ ), indicates that much of the mineralization incorporates reduced sulphur of hydrothermal rather than bacterial origin. Isotopically heavy sulphide ( $\delta^{34}S = 20-27\%$ ) also occurs in graphitic schists along strike from the stratiform mineralization in the Ben Eagach deposit (BH8), and in pyritic graphitic schists below the M3 horizon intersected in DH 705 (determined in this study). This suggests that the sulphides in these sediments incorporated reduced sulphur predominantly of hydrothermal origin.

The contention that most of the sulphide-sulphur in the stratiform mineralization is hydrothermal is consistent with the isotopic data from sulphides in an unusual, localized occurrence of massive pyrite rock sandwiched by barite in DH 705. Pyrite in this lens, which is regarded as a mound or possibly an exhalative 'chimney' (part 2.4.4.2), is isotopically similar to 'normal' bedded sulphides in the same mineralized horizon ( $\delta^{34}\text{S} = 20\text{--}23\%$ ). This result contrasts with the extremely light sulphur reported in hydrothermal sulphide chimneys from Silvermines, Ireland (Boyce et al., 1983), interpreted as due to vigorous bacterial activity at the chemocline above a basal brine pool.

#### Sulphur of mixed hydrothermal-bacterial origin.

Marked increases in the  $\delta^{34}\text{S}$  of sulphides were found to coincide with increases in the sulphide content of the mineralized rocks in the profiles examined by Willan and Coleman and in DH 705 (figs. 9.11b,c). A possible explanation for this is that rapidly deposited, thin massive sulphide beds incorporated relatively undiluted hydrothermal sulphur, whereas disseminated sulphides were precipitated from a mixture of hydrothermal and (volumetrically subordinate) bacterial reduced sulphur, entrained during discharge into the basinal seawater.

Conversely, the significantly lighter  $\delta^{34}\text{S}_{\text{sulphide}}$  ratios (15–20%) in the chert-dominated mineralization intersected in DH 708 at Creagan Loch (together with an absence of bimodal sphalerite compositions in this profile, part 7.3.2), are regarded as strong evidence for the incorporation of reduced sulphur of predominantly bacterial origin in this part of the deposit. The upward increase in  $\delta^{34}\text{S}_{\text{sulphide}}$  in the DH 708 profile corresponds to an increase in base metal content above the basal (~2m thick) mineralized sediment layer, but only one sample (708-6) has isotopic compositions comparable to those in the BH3 and DH 705 profiles. The unusually constant  $\delta^{34}\text{S}$  values in the upper part of the DH 708 profile, supports the hypothesis that the sulphides precipitated in a brine pool containing a large, homogeneous reservoir of reduced sulphur of mixed hydrothermal and bacteriogenic origin ( $\delta^{34}\text{S} \approx 20\%$ ). Note that whereas Willan and Coleman (1983) consider that sufficient  $\text{H}_2\text{S}$  was unlikely to be suddenly generated by bacterial action to precipitate the massive sulphide layers, a large reservoir of

aqueous sulphide species would be available beneath the oxic-anoxic chemocline in a stratified euxinic basin.

A purely bacteriogenic origin is also proposed for isotopically light sulphide-sulphur ( $\delta^{34}\text{S} = 13\text{--}15\text{‰}$ ) occurring in the uppermost chert bed in the BH3 profile, and a similar reversion to light sulphide is apparent at the stratigraphic top to the DH 705 and DH 708 profiles (figs. 9.11b-d). This abrupt decline in the input of hydrothermal sulphur, which marks the temporary end of exhalative activity, could be due to volumetric collapse of the feeder system perhaps accompanied by a 'thermal overturn' of the basinal brine layer. A similar pattern is observed in the hanging wall sequence of the McArthur River deposit, Australia (fig. 9.15). Smith and Croxford (1975) attributed this feature to an abrupt return to normal, deep water conditions with reduced bacterial activity at the cessation of hydrothermal brine input.

#### Stratigraphic trends in $\delta^{34}\text{S}$ .

A general trend of increasing  $\delta^{34}\text{S}_{\text{sulphide}}$  with increasing stratigraphic height has been described in several sedimentary ore deposits, such as McArthur River, Lady Loretta (Carr and Smith, 1979) and Rammelsberg (Anger et al., 1966) (figs. 9.14, 9.15). This trend has been variously attributed to the closed-system fractionation effect (part 9.2.3) operating in a ponded brine layer or restricted marine depression, or to changing  $\delta^{34}\text{S}$  ratios in the hydrothermal fluid due to kinetic fractionation effects in the source region.

However, there is little evidence at Foss for a general systematic increase in  $\delta^{34}\text{S}_{\text{sulphide}}$  ratios with stratigraphic height, such as observed by Willan and Coleman in a 10m thick profile through the basal part of the very thick (>20m?) mineralized bed at BH4 on Ben Eagach. These authors attribute this feature to a progressive increase in the completeness of sulphate reduction at depth in the sedimentary pile. However, such a slow mechanism for evolution in isotopic composition is incompatible with the scale of variation observed during the presumably rapid formation of each mineralized horizon (as indicated by the scarcity of incorporated clastic material despite rapid sedimentation rates). Kinetic isotope effects related to the increasing temperature of the convecting seawater with time, should be expressed as isotopic

differences between mineralized horizons rather than within horizons, but no evidence for this has been observed at Foss.

A possible explanation for isotopically heavy pyrite in some BH4 cherts is suggested by the presence of abundant probable evaporite pseudomorphs in the cherts cropping out nearby. High  $\delta^{34}\text{S}$  sulphide ratios (28-29‰) were found in this study in two (of three) samples containing sulphate pseudomorphs, and reactions involving the reduction of sulphate during diagenesis and/or metamorphism could account for these results. It is speculated that contemporaneous evaporites may have been a significant source of sulphur incorporated into the host rocks to the stratiform mineralization, since penetrative deformation has probably erased much of the evidence for sulphate pseudomorphs (part 3.3.1). The contribution of isotopically light sulphur of magmatic origin to the mineralization, suggested by an analysis of pyrite in an amphibolite sheet, is likely to have been volumetrically insignificant.

#### 9.8 Summary and conclusions.

##### The effects of metamorphic equilibration and reactions.

The results obtained in both this and the previous study of sulphur isotope variations in the Aberfeldy deposits, indicate that small-scale isotopic equilibration may have occurred during metamorphism, since fractionation temperatures of 450-580°C were obtained from the data for many coexisting barite-sulphide and some sulphide-sulphide pairs. However, non-equilibrium is displayed by a significant proportion of the samples, and it is suggested that isotopic exchange on a millimetre-scale may have had little effect on primary isotopic distributions, particularly in coexisting sulphides and barite. Therefore, large-scale variations in the  $\delta^{34}\text{S}$  ratios of barite and sulphides in stratigraphical and along-strike transects may be interpreted in terms of variations at source and/or fractionation processes operating in the feeder system or on the sea floor.

In a small proportion of rocks, the initial isotopic composition of sulphides and barite are likely to have been changed during diagenetic and/or metamorphic reactions involving sulphur. The reduction of barite to form barium feldspars plus sulphide, which is suggested by textural evidence in two samples examined, is supported

by the presence of  $^{34}\text{S}$ -rich pyrite, and a similar process may explain unusually heavy sulphide-sulphur ( $\delta^{34}\text{S} = 27\text{--}29\%$ ) occurring in some other beds. The sulphidation of barium carbonates may account for isotopically light barite ( $26\text{--}29\%$ ) in the BH3 profile, but other calcareous barite rocks appear to have 'normal'  $\delta^{34}\text{S}_{\text{barite}}$  values.

#### Source of the sulphur in barite.

Barite analysed in this study shows neither a clear-cut bimodal distribution of  $\delta^{34}\text{S}$  ratios nor a systematic relationship between  $^{34}\text{S}$ -content and stratigraphic height, but a positive correlation is observed between isotopic ratios and barite bed thickness. This can be explained by a mixed sulphur source model similar to that proposed by Willan and Coleman (1983). The bulk of the sulphate in thicker ( $>2\text{m}$ ) barite beds is derived directly from contemporaneous, Dalradian basin seawater ( $\delta^{34}\text{S} = 35\text{--}36\%$ ), but with less vigorous mixing distal from the vent area and in relatively deeper water environments, a greater proportion of isotopically light sulphate was incorporated from the oxidation of either bacterial or hydrothermal reduced sulphur species (fig. 9.16). Isotopically heavy barite-sulphur ( $36.5\text{--}42\%$ ) which occurs in the thick, composite barite bed in the Frenich Burn area (DH 104), may have resulted from episodic depletion of  $^{32}\text{S}$  in the local sulphate source due to sulphide formation in a shallow-water, possibly lagoonal environment. Alternatively, the  $^{34}\text{S}$ -enriched barite could be of diagenetic origin. Apparent differences in  $\delta^{34}\text{S}_{\text{barite}}$  distribution between the Foss and Ben Eagach deposits are probably due to unintentional sampling bias.

#### Source of the sulphur in sulphides.

$\delta^{34}\text{S}_{\text{sulphide}}$  ratios of  $20\text{--}28\%$  were found in the majority of mineralized rocks from the Aberfeldy deposits examined by Willan and Coleman (1983), and they regarded this sulphur as derived from the hydrothermal fluids. Sulphide-sulphur of presumed bacteriogenic origin in metasediments hosting the mineralization at Aberfeldy, and elsewhere in the Dalradian, is isotopically lighter ( $<16\%$ ). However, in this study, ratios of  $15\text{--}20\%$  were found in samples from several parts of the stratiform mineralization at Foss, notably in the M3 horizon intersected by DH 708, 85m to the east of BH3 at Creagan Loch. These intermediate  $\delta^{34}\text{S}$  values, together with other

geochemical and stratigraphical evidence, suggest that the mineralization in this fault-bounded block was formed in a brine pool and incorporated reduced sulphur of mixed hydrothermal and bacteriogenic origin (fig. 9.16). The reversion to lower  $\delta^{34}\text{S}_{\text{sulphide}}$  values near the stratigraphic top to the BH3 profile, which is also observed in the two new profiles in this area, is attributed to a sudden cessation of hydrothermal input probably accompanied by destabilization of the brine layer.

Pyrite forming a massive sulphide lens, which possibly represents an exhalative 'chimney', intersected in DH 705 has an isotopic composition which is similar to bedded sulphides in the same profile ( $\delta^{34}\text{S} = 20\text{--}23\%$ ). Local marked increases in  $\delta^{34}\text{S}_{\text{sulphide}}$ , which are seen in all profiles and generally coincide with increases in the modal proportions of sulphides, may record the pulsatory influx of metalliferous fluids from which rapidly precipitated sulphides incorporated 'undiluted' hydrothermal sulphur. This sulphur probably originated from the near-complete inorganic reduction of aqueous sulphate, in connate waters or slowly convecting seawater, at high temperatures ( $>200^\circ\text{C}$ ) in the sedimentary pile beneath. However, there is little evidence at Foss for a general stratigraphic increase in  $\delta^{34}\text{S}_{\text{sulphide}}$ , such as recorded in some other sedimentary exhalative sulphide deposits. Sulphides in altered metabasite and in 'cherty' graphitic schists underlying the M3 horizon at Creagan Loch, and in a graphitic dolostone sampled from this area, are similar in isotopic composition to the stratiform mineralization and are also considered to have incorporated hydrothermal sulphur. Conversely, stratabound sphalerite in a quartzite bed incorporates lighter, bacteriogenic sulphur ( $\delta^{34}\text{S} = 15\%$ ) which was probably derived from the surrounding sediments.

TABLE 9.1: Sample location, description and sulphur isotope data.

## CREAGAN LOCH AREA

Sample	Down-hole depth	Stratigraphic height(a)	Lithology	Phase, <sup>(b)</sup> $\delta^{34}\text{S}_{\text{‰}}$ (c)	Notes
705-14	45.00		Graphitic (qtz. musc.) dolomite rock with minor dissem. sulphides.	S 20.2	
705-31	82.8		Coarse, graded quartzite with bands of sphalerite and minor pyrrhotite.	S 15.0	
705-17A	98.05	5.0	Quartz hyalophane muscovite schist with dissem. sulphides.	P 18.3	
705-32	98.50	4.7	Banded quartz barite rock with minor calcite and pyrite.	B 34.3	
705-30	101.00	3.6	Massive coarse pyrite with galena, quartz and celsian.	P 21.9,22.0 G 23.3,22.7	} Repeat analyses
705-30B	101.50	3.3	As above (see fig. 9.8).	P 23.2,23.5 G 21.7,20.0	} Core & rim xtal.
705-19	102.35	2.8	Sulphidic carbonate rock adjacent to massive barite.	P 23.1 S 22.1 G 21.1 B 33.0	
705-19A	102.65	2.7	Massive barite rock.	B 34.8	
705-20	103.80	2.4	Banded massive barite with dissem. sulphides.	B 32.9 S 19.3,19.1	Coexisting red & yel.
705-28	106.15	1.6	Calcareous barite rock with dissem. pyrite, minor sphalerite.	B 36.5 P 23.9	
705-21	106.85	1.35	Coarse dolomite rock with recrystallized sphalerite and pyrite.	P 22.4	
705-21A	107.80	0.75	Quartz celsian chert banded with pyrite and sphalerite.	P 21.0	
705-22	108.70	0.05	Massive granular pyrite adjacent to metabasite rock.	P 24.9	
705-23	109.10	-0.2	Graphitic, laminated quartz, muscovite, pyrite chert.	P 21.3	
705-24B	112.00	-1.6	Banded quartzose graphitic schist with pyrrhotite and pyrite.	P 20.2	
03-MB	BH 3, 20.0	-	Metabasite marker: pyrrhotite quartz hyalophane dolomite rock.	Po 22.1	
505-17	140.80	1.5	Barite with sulphide and carbonate bands (basal M3).	B 34.2	
708-10B	34.0	7.3	Sulphide band in quartz hyalophane muscovite schist.	S 14.6 P 15.7	
708-10	33.2	6.6	Massive sulphide and quartz metachert with hyalophane.	S 19.3 P 20.0	
708-9B	32.2	5.7	Thin bed (<10cm) of massive barite rock with dissem. pyrite & sphalerite.	B 30.5 S 18.8 P 19.7	
708-8	31.0	4.9	Quartz celsian chert with minor dolomite & sulphides	S 19.3 P 20.2	
708-7	30.0	4.0	Massive sulphide and sulphide-veined quartz metachert with minor barite.	S 18.5 P 18.1 G 16.9	(Corrected for 10% sphalerite contamination.)
708-6	28.5	3.0	Massive sulphide with dolomite and quartz celsian chert.	S 22.5 P 23.3 P 25.5	} Coexisting in subsample. (Monomineralic)

Sample	Down-hole depth	Stratigraphic height	Lithology	Phase, $\delta^{34}\text{S}_{\text{‰}}$
708-6B	27.8	2.5	Banded massive sulphide and laminated quartz-hyalophane chert.	S 17.1
708-5B	27.1	2.0	Laminated sulphidic quartz-hyalophane and dolomite chert.	S 15.9
708-5A	26.1	1.3	Laminated sulphidic quartz-hyalophane chert.	S 17.0 P 18.0
708-4A	24.8	0.6	Quartz celsian muscovite schist with dissem. sulphides.	S 17.0 G 15.8

FRENICH BURN AREA and CENTRAL FOSS EAST

104-17	24.15	16.2	Barite, 9cm from base M7.	B 41.8
104-18	28.50	14.1	Barite adjacent to chert, top M6.	B 40.7
104-20	29.33	13.4	Barite immediately above 1cm metasediment band.	B 35.7
104-23	31.25	11.7	Barite rock.	B 32.8
104-25	32.65	10.3	Barite with pyrite aggregate and dissem. sphalerite, 15cm above M6.	B 33.8 S 17.4
104-27	33.60	9.4	Coarse barite rock.	B 34.5
104-29A	35.00	8.2	Barite immediately above meta-sediment band, at base M5.	B 34.6
104-30	35.31	7.8	Barite at top M3, below meta-sediment band.	B 34.7
104-32	36.66	6.6	Barite with disseminated pyrite.	B 36.4
104-34	38.00	5.4	Barite with disseminated pyrite.	B 36.4
104-36	39.24	4.2	Barite with minor magnetite.	B 35.7
104-37	39.75	3.7	Barite rock	B 40.9
104-38	40.16	3.4	Barite with disseminated pyrite and sphalerite	B 40.0 S 25.7
104-40	41.58	2.1	Coarse barite rock.	B 36.5
104-43	42.92	0.8	Barite above quartz celsian rock.	B 36.2
104-44	43.67	0.1	Near base M3: calcareous barite with bands of pyrite and sphalerite.	B 38.4 S 24.6

Sample	Location (D.H. depth)	Lithology	Phase, $\delta^{34}\text{S}_{\text{‰}}$	
601-6B	460.80 distal M3, Frenich Burn area	Quartz dolomite pyrrhotite rock.	Po 16.4	
203-18B	164.80 base M3 barite	Calcareous barite with quartz and sulphide bands.	B 32.9 B 31.9	} Sub-samples 7cm apart.
408-10	167.20 central M5, Foss East	Barite rock with disseminated pyrite, sphalerite and carbonates.	B 32.0	
410-8	95.55 top M7, Foss East	Barite rock with disseminated magnetite.	B 32.8	
702-16C	87.75 base M3 barite	Calcareous barite rock inter-banded with sulphidic carbonate rock.	B 36.5	
703-6	50.85 top M3 barite	Barite rock	B 34.1	
703-8	54.00 base M3 barite	Barite rock with bands of quartz and sulphides.	B 35.1	



## FOSS WEST

Sample	Location (D.H. depth)	Lithology	Phase, $\delta^{34}\text{S}\%$	
09-06	BH9, 28.7 base M5 Creag an Chanaich	Graphitic quartz muscovite hyalophane chert with tabular pseudomorphs and disseminated sulphides.	S 17.7	
N81-80	M3 outcrop on Creag an Chanaich: hangingwall	Quartz hyalophane schist with dissem. pyrite, sphalerite, and tabular/wispy barite- hyalophane complexes.	P 27.1	
N81-83	Same outcrop: central in 60cm barite interval	Coarse barite with minor disseminated pyrite	B 29.6	
404-B	129.20 base M3 barite Western Foss West	Massive barite with minor disseminated pyrite.	B 33.4	
404-A	124.20 top M3 barite	Massive barite.	B 32.6	
429-18	317.2 base M5 barite Western Foss West	Massive barite with dissemi- nated celsian and sulphides.	B 31.6	
429-8C	290.04 top M5 barite	Massive barite adjacent to chert.	B 35.1	
429-8	288.66 top M5 hanging wall cherts	Banded quartz muscovite dolomite hyalophane chert with bands and disseminated pyrite and sphalerite.	S 20.6 S 20.8	Red & yellow laminae, 1mm apart.
G114	Outcrop of ? M3 on N limb of Creag na h-Iolaire Anticline, Foss Estate	Massive quartz-pyrite rock grading into laminated quartz metachert with pyrite and ?sulphate pseudomorphs.	P 28.9	
G100E	As for G114, 150m further west	Laminated quartz-pyrite rock with minor sphalerite, calcite, hyalophane.	P 28.1	
N80-13	In Ben Lawers Schist near boundary with BES, by track in extreme W of Foss West	Calcareous amphibolite containing 1% pyrite as disseminated 1-2mm cubes.	P -4.3 P -4.7	Duplicate analyses.

no. rocks = 61; no. analyses = 88.

- (a) Distance (in metres) vertically above top of metabasite marker bed. Within each profile, the stratigraphically highest (youngest) samples are at the top.  
 (b) B, barite; P, pyrite; S, sphalerite; G, galena; Po, pyrrhotite.  
 (c) Expressed relative to CDI standard.

TABLE 9.2: Sulphur isotope fractionations and derived temperatures (in °C).

$\Delta^{34}\text{S}$ Calibration*	Pyrite- sphalerite (b)	Pyrite- galena (c)	Sphalerite -galena (b)+(c)	Barite- pyrite (a)	Barite- sphalerite (a)
Uncertainty in temperature†	$\pm 50$	$\pm 15$	$\pm 20$	$\pm 10$	$\pm 10$
708-10B	+1.15 240				
708-10	+0.69 385				
708-9B	+0.92 300			+10.8 540	+11.7 535
708-8	+0.85 320				
708-7	-0.35 ***	+1.2 640	+1.6 390		
708-6 'D'	+0.79 345				
708-5A	+1.00 275				
708-4A			+1.21 490		
705-30		-1.37, -0.62 ***			
705-30B	{ Rims Cores	+3.50 260			
		+1.51 540			
705-19	+0.97 285	+1.92 450	+0.95 585		
705-20					+13.7 485
705-28				+12.6 495	
104-25					+16.4 410
104-38					+14.4 450
104-44					+13.9 460

\*(a) Sakai, 1968.

(b) Kajiware and Krouse, 1971.

(c) Czamanske and Rye, 1974.

\*\*\* Disequilibrium.

† Calculated for  $T = 400^\circ\text{C}$  assuming analytical precision =  $\pm 0.1\%$ .

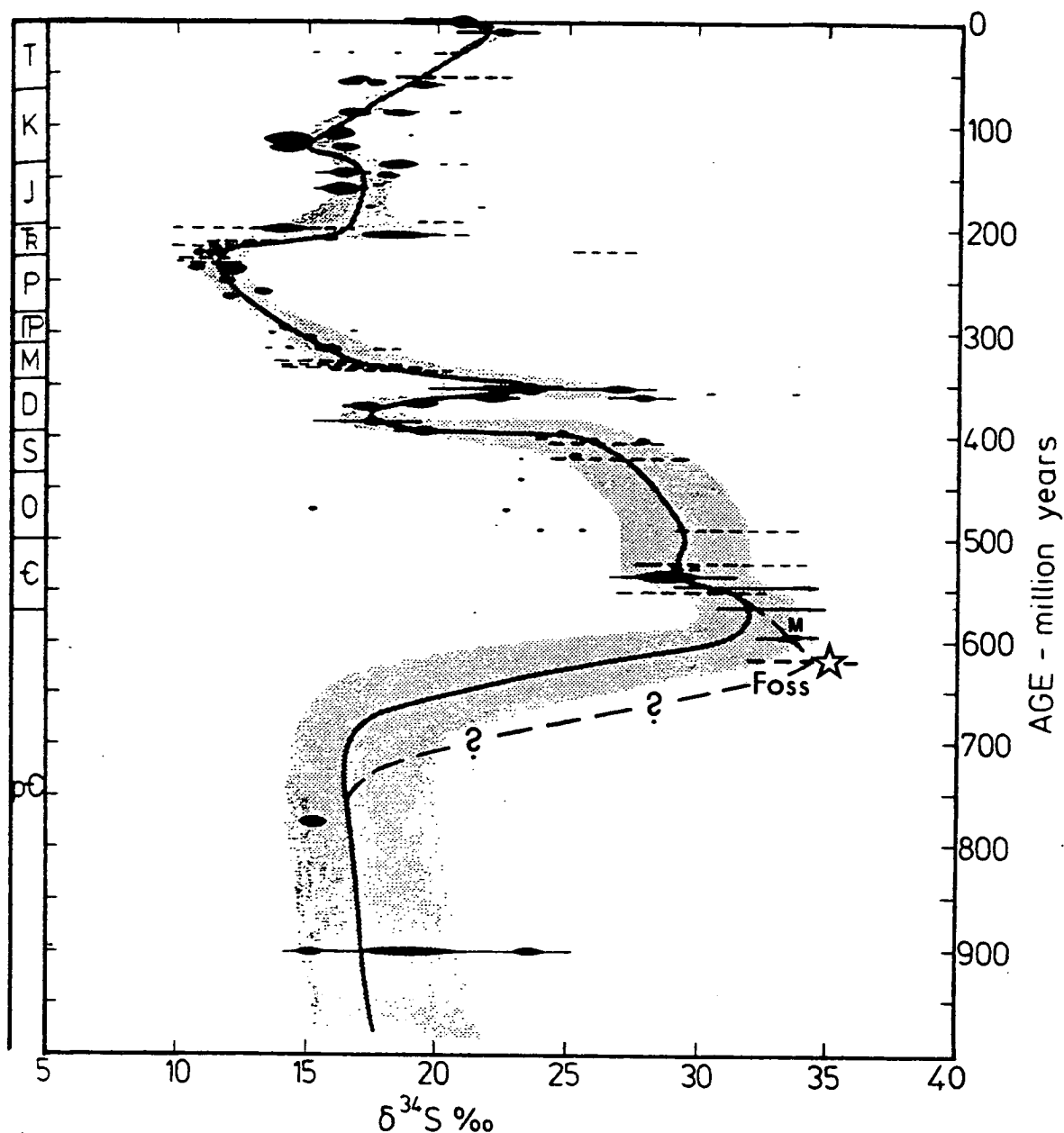
TABLE 9.3: Sulphur isotope mass balance calculations.

Sample	(1) Phase	(2) Mode Vol%	(3) Wt%	(4) Prop. of $\Sigma$ wt S	(5) Present $\delta^{34}\text{S}_{\text{‰}}$	(6) Mean Rock $\delta^{34}\text{S}_{\text{‰}}$	(7) Mean Sulphide $\delta^{34}\text{S}_{\text{‰}}$	(8) $\delta^{34}\text{S}$ Model A	(9) $\delta^{34}\text{S}$ Model B
708-6	P	29	60	.71	23.3	23.1	23.1	<u>25.5</u>	
	S	23	40	.29	22.5				
708-9B	P	16	17.5	.43	19.7	24.9	19.6	16.2	<u>22.0</u>
	S	6	5.5	.08	18.8				
	B	78	77	.49	30.5			<u>34.0</u>	28.0
705-20	P	8	9	.26	20.1 <sup>c</sup>	27.9	19.8	17.9	<u>22.0</u>
	S	7	7	.12	19.2				
	B	82	84	.62	32.9			<u>34.0</u>	31.5
705-28	P	13	21	.49	23.9	29.9	23.8	26.1	<u>22.0</u>
	S	2	2	.03	23.0 <sup>c</sup>				
	B	52	77	.48	36.5			<u>34.0</u>	38.5
104-38	P	3	4	.11	26.6 <sup>c</sup>	35.8	26.0	34.2	<u>22.0</u>
	S	10	10	.19	25.7				
	B	86	86	.70	40.1			<u>36.5</u>	41.7
104-44	P	6	11	.31	25.5 <sup>c</sup>	33.4	25.3	28.3	<u>22.0</u>
	S	3	4	.07	24.6				
	B	52	85	.62	38.4			<u>36.5</u>	40.4
104-25	P	1	1	.04	18.3 <sup>c</sup>	31.9	17.7	9.2	<u>22.0</u>
	S	4	4	.08	17.4				
	B	95	95	.88	33.8			<u>35.0</u>	33.3

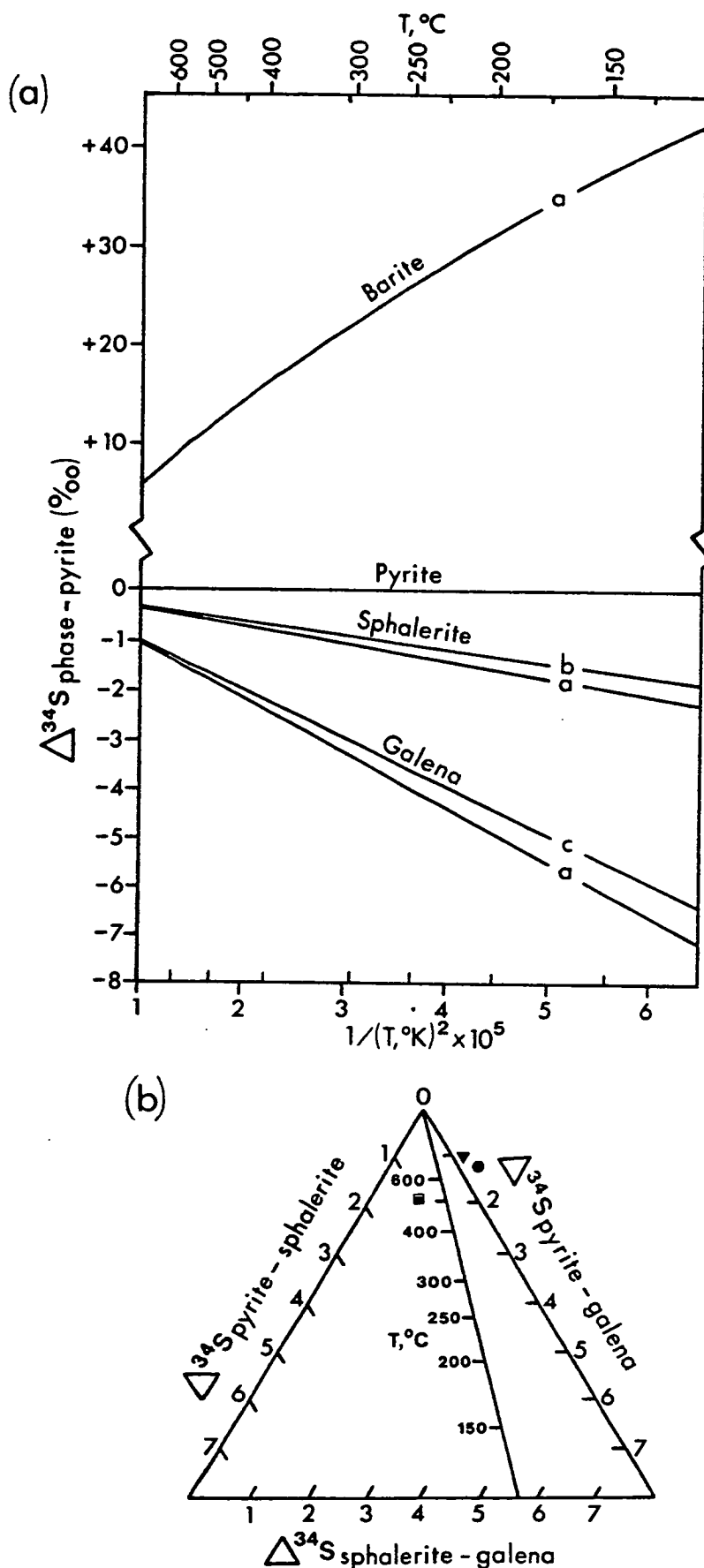
- Notes: 1. P = pyrite, S = sphalerite, B = barite. As the modal proportions of galena are small (<1%) in these samples, galena has been omitted from the calculations.
2. Estimated to nearest % by grain counting (at least 1000 points).
3. Proportional weight expressed as % of total weight of sulphur-bearing phases.
4. Proportion of total weight of S in each phase.
5. Measured  $\delta^{34}\text{S}$  except where marked (c): calculated assuming equilibrium fractionation between pyrite and sphalerite at  $T = 300^\circ\text{C}$  (see table 2).
6. Product of values in 4 and 5: whole-rock weighted mean.
7. Total sulphide weighted mean.
- 8, 9. Calculated  $\delta^{34}\text{S}$  values assuming one fixed value (underlined) and constant whole-rock  $\delta^{34}\text{S}$  (see text).

TABLE 9.4: Summary of  $\delta^{34}\text{S}$  features in Foss and in some other sediment-hosted exhalative sulphide/barite deposits.

Deposit (reference)	Age, metamorphic facies	Range [average] for sulphides,‰	Stratigraphic variation in $\delta^{34}\text{S}_{\text{sulphide}}$	Isotopic Equilibration	Range [ave.] for barite,‰	Sulphur sources
FOSS (this study)	L. Cambrian, amphibolite	+13 to +29 [+22], similar for each phase	Locally increases upwards, decrease at hangingwall	Metamorphic: variable, related to grain size	+26 to +42 [+35]	Restricted basin and hydrothermal
GAMSBERG (Gehlen et al., 1983)	Proterozoic, amphibolite	+26 to +32 [+29]	None reported (lateral variation between deposits)	Probably complete metamorphic	+35 (2 samples)	Lagoonal seawater, some hydrothermal
LADY LORETTA (Carr and Smith, 1977)	Proterozoic, greenschist	Py, +4 to +18 (late py, +22) Sph & gal, +10 to +19	Systematic increase upwards in py but not in sph & gal	Primary $\Delta^{34}\text{S}_{\text{sph-gal}} = 2.3$ to $4.7$ , ave. $3.5$ ( $170^\circ\text{C}$ )	+37 to +40 (3 samples)	Dual: Hydrothermal (for sph, gal) lagoonal seawater (for py, bar)
MOUNT ISA (Smith et al., 1978)	Proterozoic, L. greenschist	+5 to +22	Highly variable	Py>sph>po>gal suggests metamorphic	None reported	Seawater, possibly dual
McARTHUR (Smith and Croxford, 1973, 1975)	Proterozoic, not metamorphosed	Py, -4 to +16 Sph & gal, -1 to +9 [+2] and [+6] respectively	Systematic increase upwards in py but not in sph & gal. Markedly lighter py in hanging wall	Primary $\Delta^{34}\text{S}_{\text{sph-gal}} = 3.0$ to $5.7$ ( $100 - 260^\circ\text{C}$ )	None reported	Dual (as for Lady Loretta) - or diagenetic (Williams and Rye, 1974)
RAMMELSBURG (Anger et al., 1966)	Devonian, greenschist	Py, -15 to +25 Sph & gal, +7 to +20	Systematic increase upwards in sph & gal; py lighter in overlying barite rock	None?	+19 to +37; less variable associated with sulphides [+23]	Dual (as for Lady Loretta); 50% pyrite-S also hydrothermal
TOM (Large, 1981)	Devonian, L. greenschist	+9 to +30 [+13]	Heavier in upper third of ore horizon and near vent	None	+18.5 to +32 [+26]	Dual: sulphides hydrothermal, barite from seawater
SILVERMINES (Coomer and Robinson, 1976)	L. Carboniferous, not metamorphosed	-13 to -36 (-8 to +4 in vein sulphides)	Sulphide values increase upwards and outwards from vent	$\Delta^{34}\text{S}$ highly variable; $40-430^\circ\text{C}$ ; but sph>gal>py	+17 to +21	Dual: barite and stratabound sulphide from seawater, vein sulph. hydrothermal



**Fig. 9.1:** Summary sulphur isotope-age curve for marine sulphate (adapted from Claypool et al., 1980). Shaded area represents estimate of uncertainty on world ocean surface sulphate composition (heavy curved line) derived from marine evaporites of various ages (lenses). Query marks on possible alternative curve for late Precambrian (Willan and Coleman, 1983). Star indicates probable surface seawater sulphate composition during deposition of the Foss deposit. M indicates lower L. Cambrian evaporites of Motskaya, U.S.S.R. (Claypool et al., 1980).



**Fig. 9.2:** (a) Sulphur isotope fractionations between pyrite and barite, sphalerite and galena, plotted against  $1/T^2$ . Fractionation factors: a Sakai, 1968; b Kajiwara and Krouse, 1971; c Czamanske and Rye, 1974. (Modified from Ohmoto and Rye, 1974).

(b) The sulphur isotope geothermometer for coexisting pyrite, sphalerite and galena (from Smith et al., 1977). Trisulphide data from Foss: ▼ sample 494, BH3 (Willan and Coleman, 1983). ● 708-7. ■ 705-19.

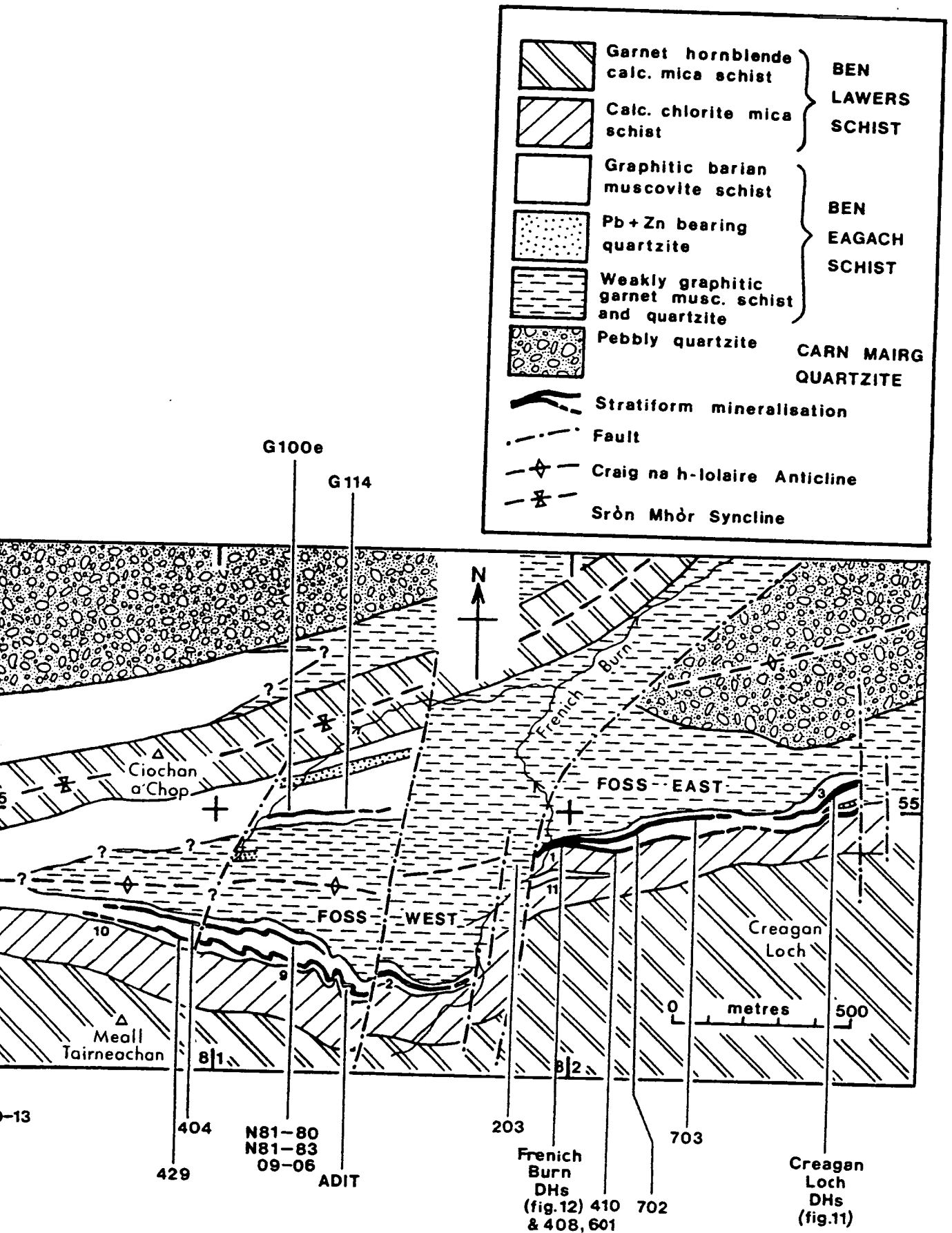


Fig. 9.3: Geological map of the Foss deposit (from Moles, 1983) with locations of drillhole intersections and outcrop samples from which sulphur isotope data was obtained. IGS borehole sites located by small numbers on map. Grid numbers refer to OS sheet 52.

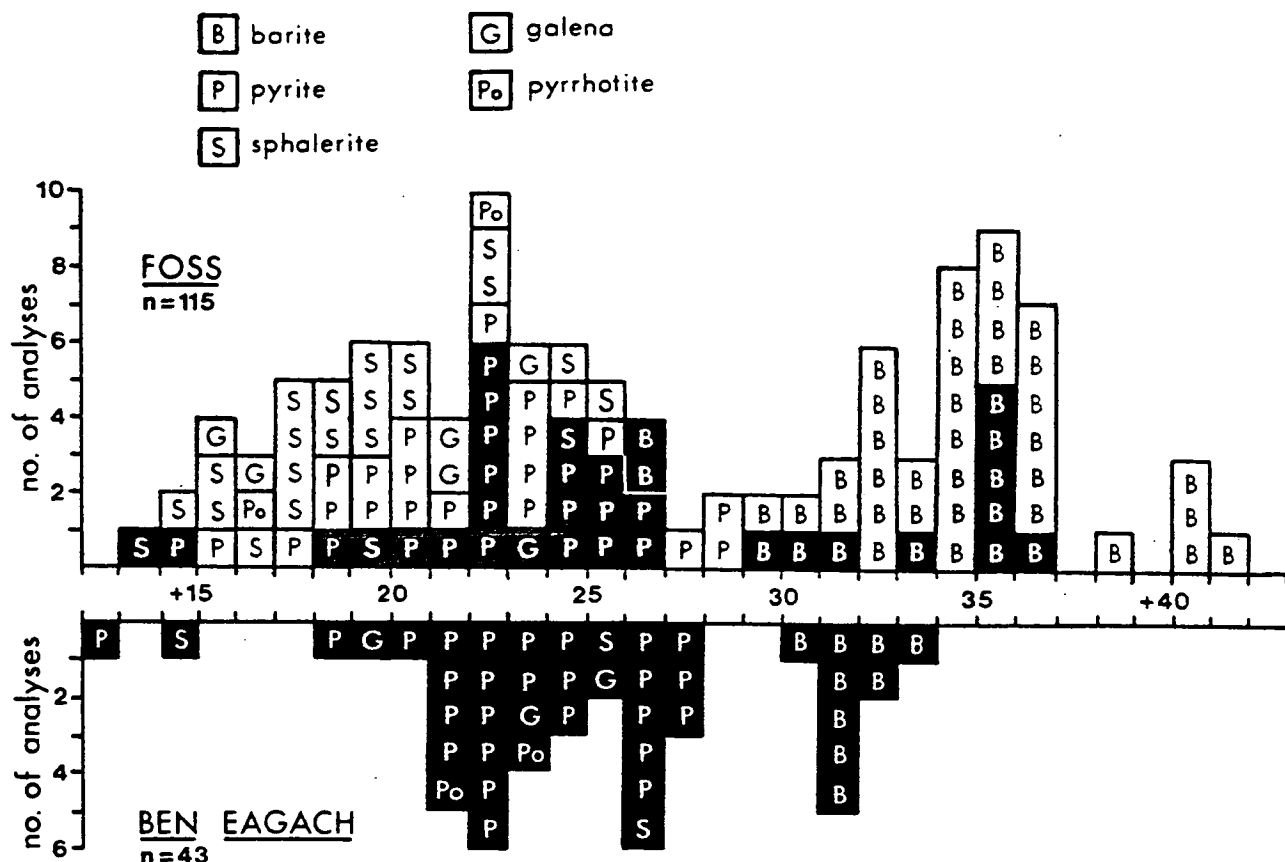


Fig. 9.4: Frequency distribution of sulphur isotope ratios from the Foss deposit (above baseline) and Ben Eagach deposit (below baseline). In black: data obtained by Willan and Coleman (1983); in white: this study. Averaged values of duplicate analyses plotted. A value of -4.5‰ for pyrite in amphibolite sample N80-13 is not shown.

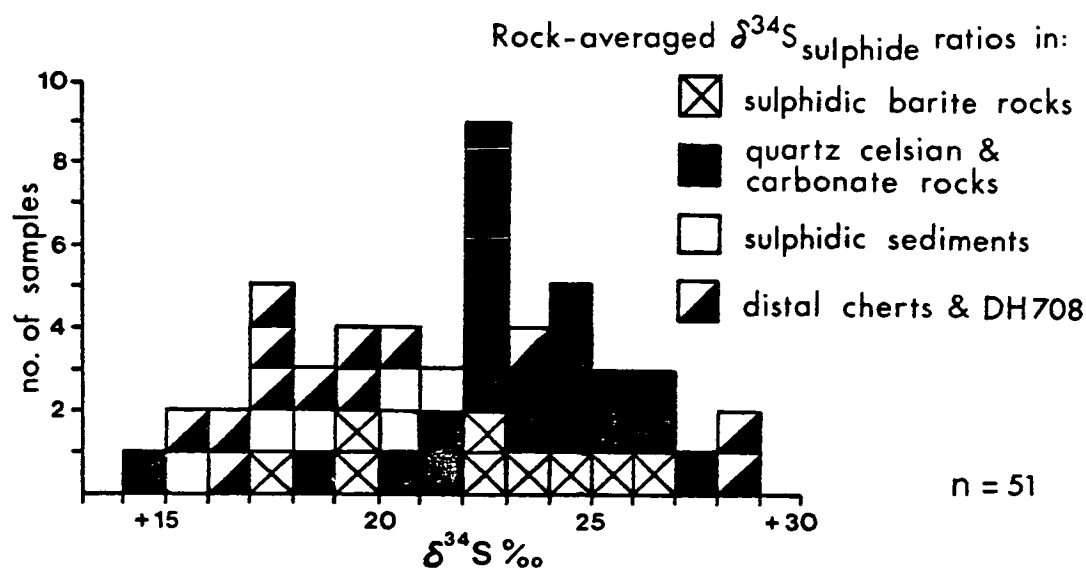
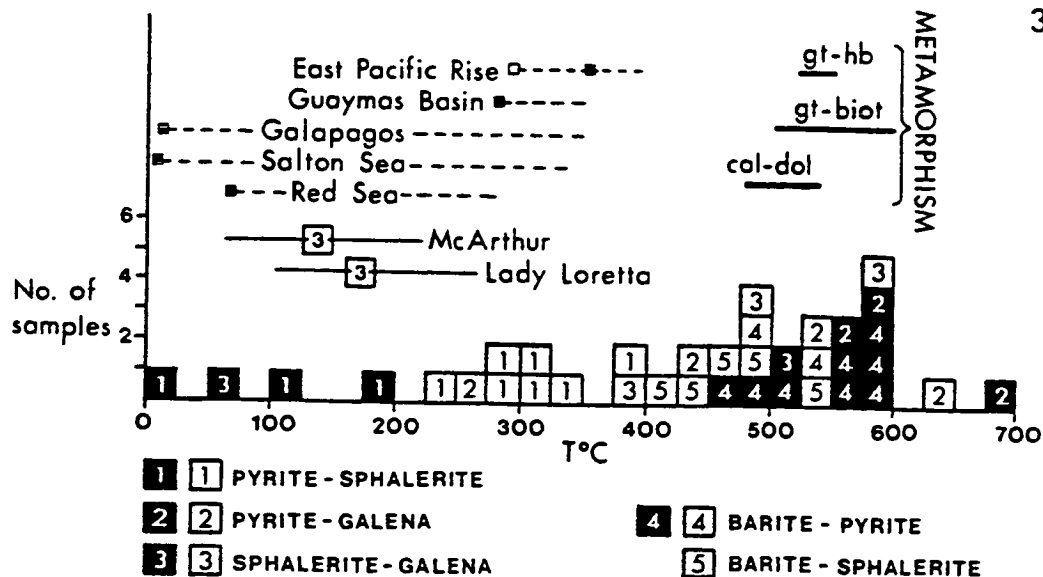
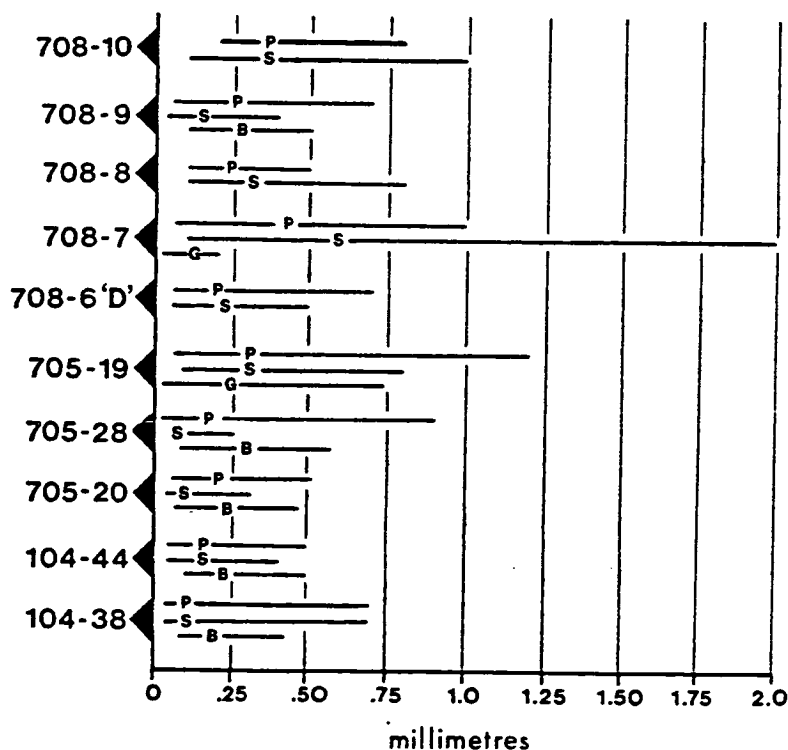


Fig. 9.5: Frequency of  $\delta^{34}\text{S}$  ratios in sulphides from different lithologies at Foss. Values plotted are mean total sulphur composition for each sample. Data from this study and Willan and Coleman (1983).





**Fig. 9.6:** Frequency distribution of temperatures indicated by sulphur isotope fractionation in samples from Foss and Ben Eagach. Black boxes: data of Willan and Coleman, 1983; white boxes: data of this study. For comparison, the temperatures found in modern hydrothermal systems, temperatures indicated by sphalerite-galena fractionation in two ancient deposits, and estimated metamorphic temperatures at Foss (from Moles, 1985) are shown. Modern hydrothermal fluids: East Pacific Rise (MacDonald et al., 1980), Guaymas (Lonsdale et al., 1980), Galapagos (Corliss et al., 1979), Salton Sea (White, 1981), and Red Sea (Shanks and Bischoff, 1980); squares indicate vented temperature (black square = sulphide-depositing system, white square = barite + silica-depositing system), dashed lines indicate temperature ranges at depth. Ancient deposits: McArthur (Smith and Croxford, 1973) and Lady Loretta (Carr and Smith, 1977); box indicates mean value, bar indicates range reported.



**Fig. 9.7:** Grain size data for selected samples (descriptions in table 9.1, fractionation temperatures in table 9.2). Bar shows range of diameters in each phase, mean value indicated by position of symbol: P = pyrite, S = sphalerite, G = galena, B = barite.

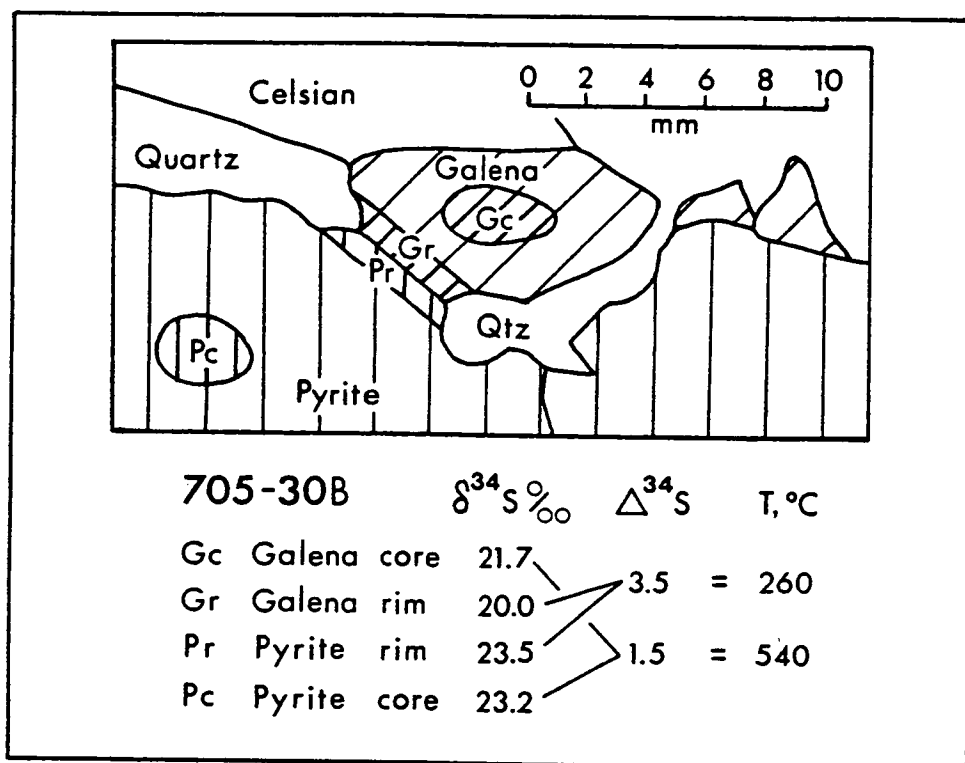


Fig. 9.8: Sketch of polished block of sample 705-308 showing the location of material removed for isotopic analysis and the results.

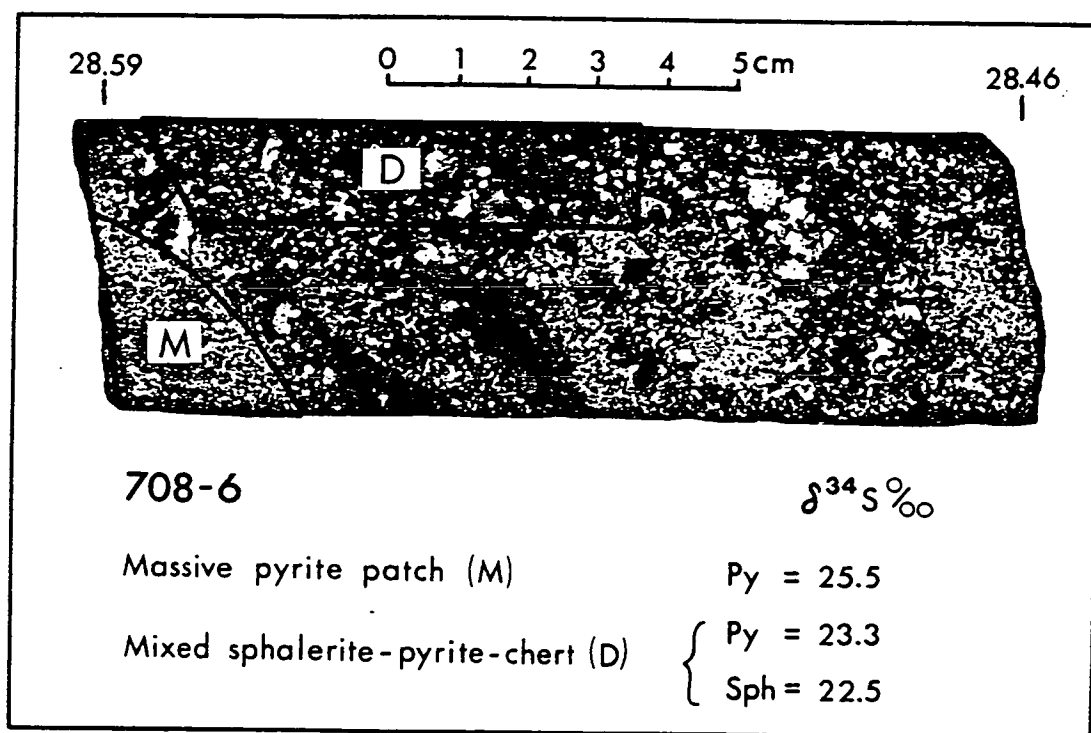
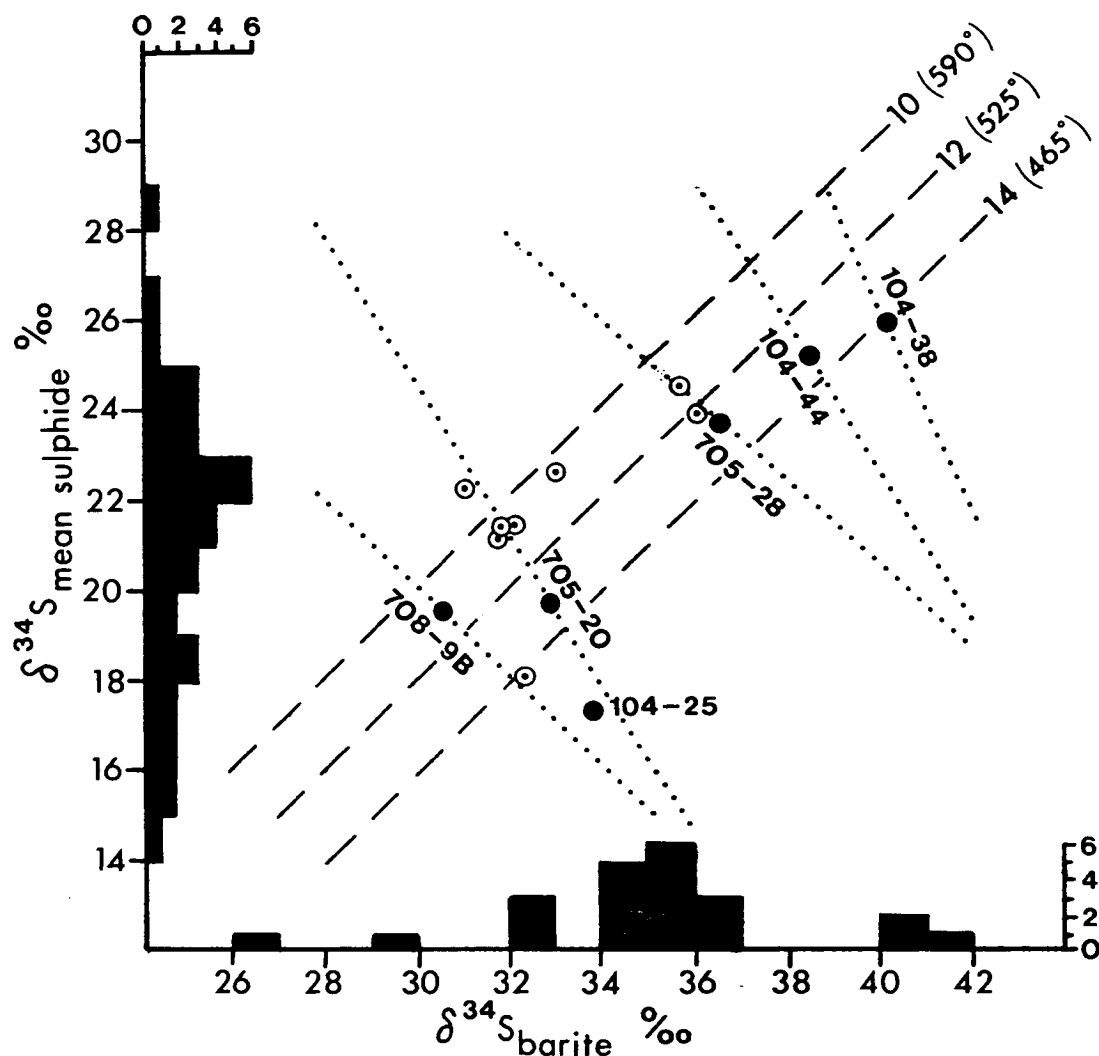


Fig. 9.9: Photograph of core slice 708-6 showing areas 'D' and 'M' from which sulphides were separated for analysis. Pyrite is light coloured and granular, sphalerite is dark, matrix chert is medium grey with white quartz and dolomite crystals.



**Fig. 9.10:** Histograms of  $\delta^{34}\text{S}$  values observed in sulphides in rocks not containing barite (ordinate) and in barite in rocks not containing sulphides (abscissa), combined with a bivariate plot of  $\delta^{34}\text{S}_{\text{sulphide}}$  vs.  $\delta^{34}\text{S}_{\text{barite}}$  values in sulphidic barite rocks (points). Black circles: data this from study; white circles: data of Willan and Coleman (1983). Dotted lines indicate calculated range of possible pre-metamorphic compositions of coexisting barite and sulphide for five samples (see Table 9.3). Dashed lines indicate constant  $\Delta^{34}\text{S}_{\text{barite-sulphide}}$  values of 10, 12 and 14‰.

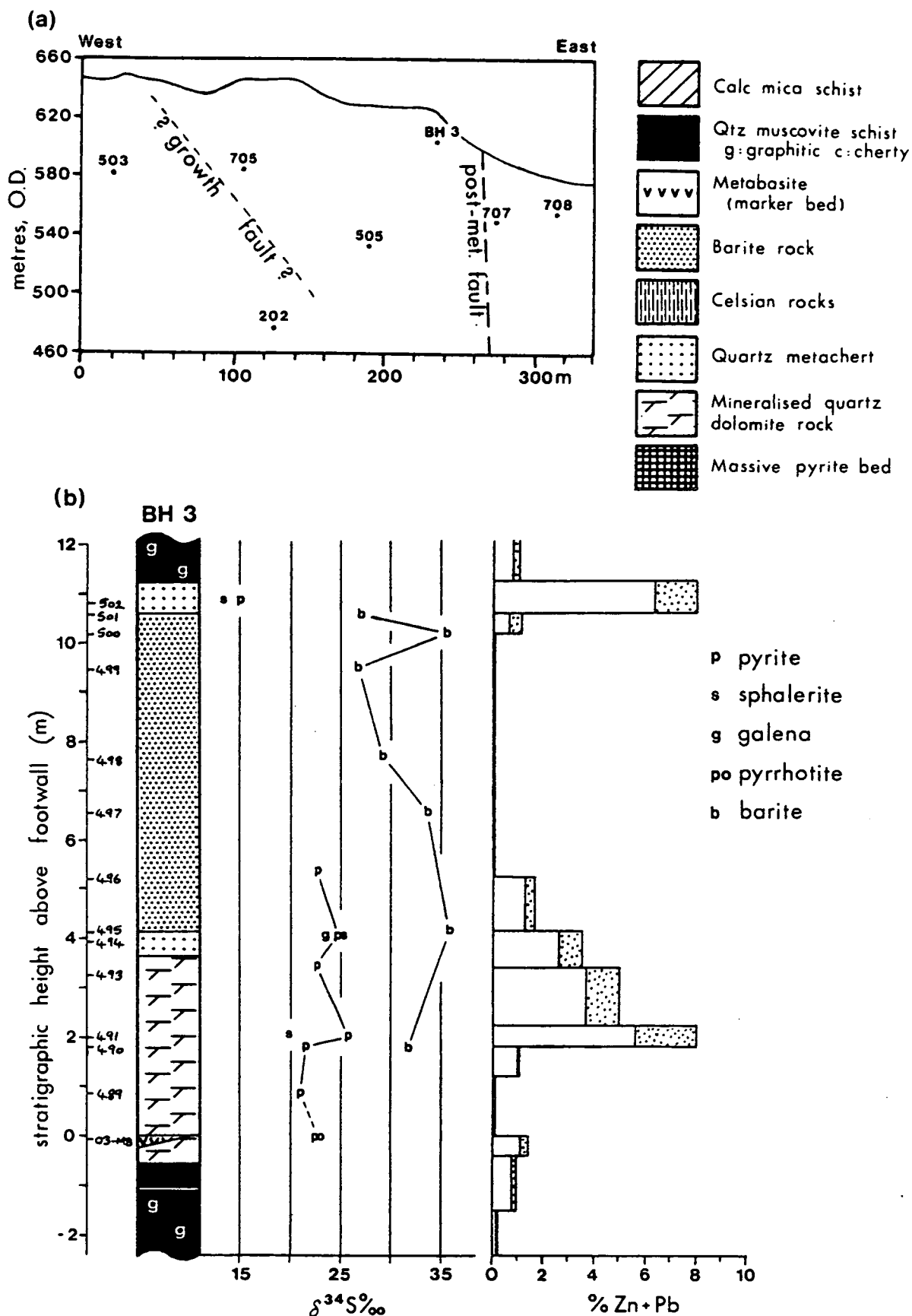


Fig. 9.11: Stratigraphic sections with  $\delta^{34}\text{S}$  and assay data, from drillhole intersections of the M3 horizon in the Creagan Loch area.

(a) Locations of drillhole intersections projected onto a vertical plane of orientation 070°. Line of postulated growth fault indicated.

(b) BH3 profile: isotopic results (except for 03-MB) from Willan and Coleman, 1983; assay data from Coats et al., 1981.

(c) DH 705 profile (including metasediments below the M3 horizon). } next page

(d) DH 708 profile.

Assay data in (c) and (d) provided by Dresser Minerals.

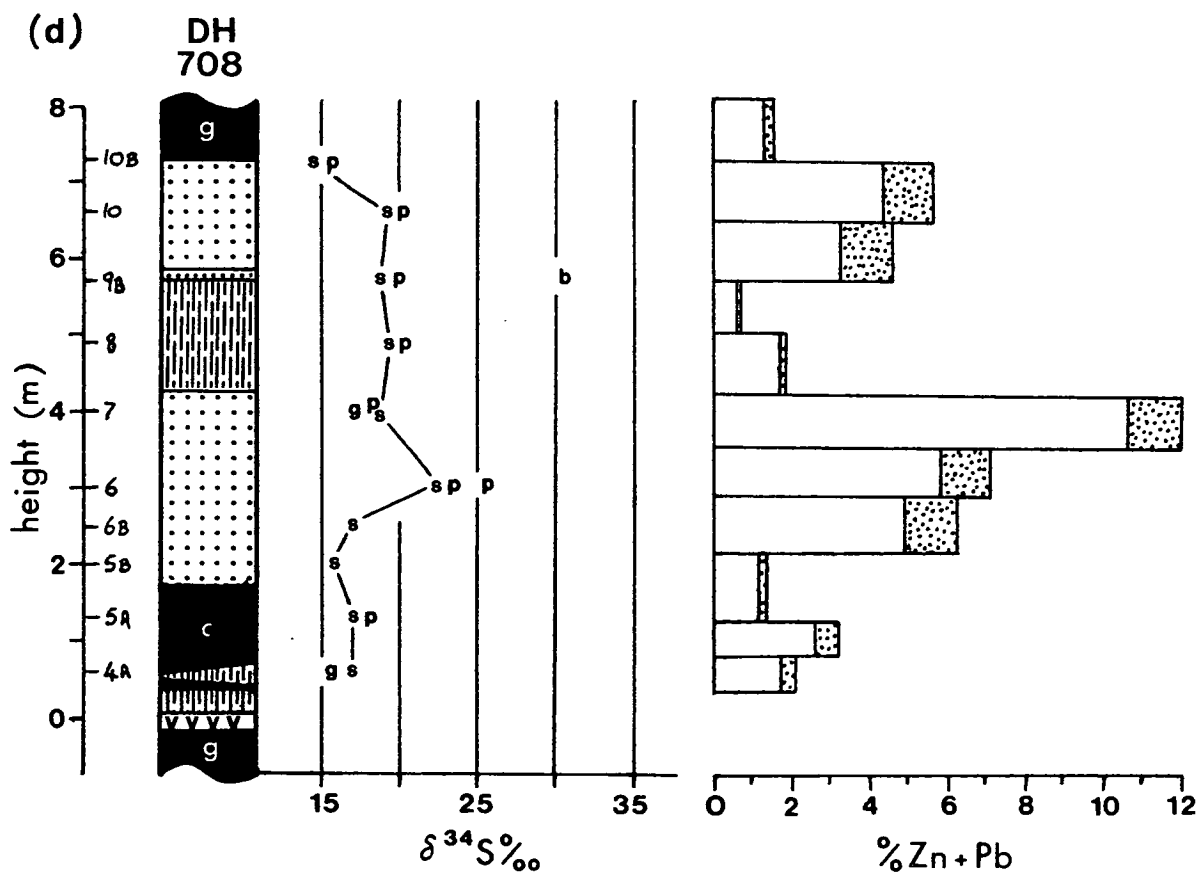
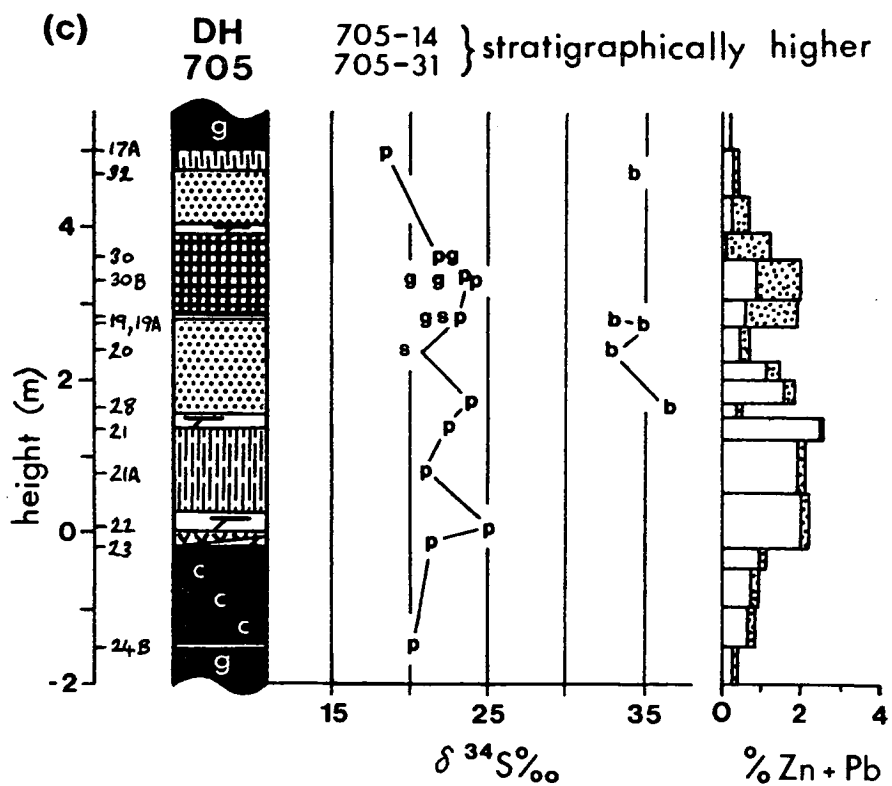
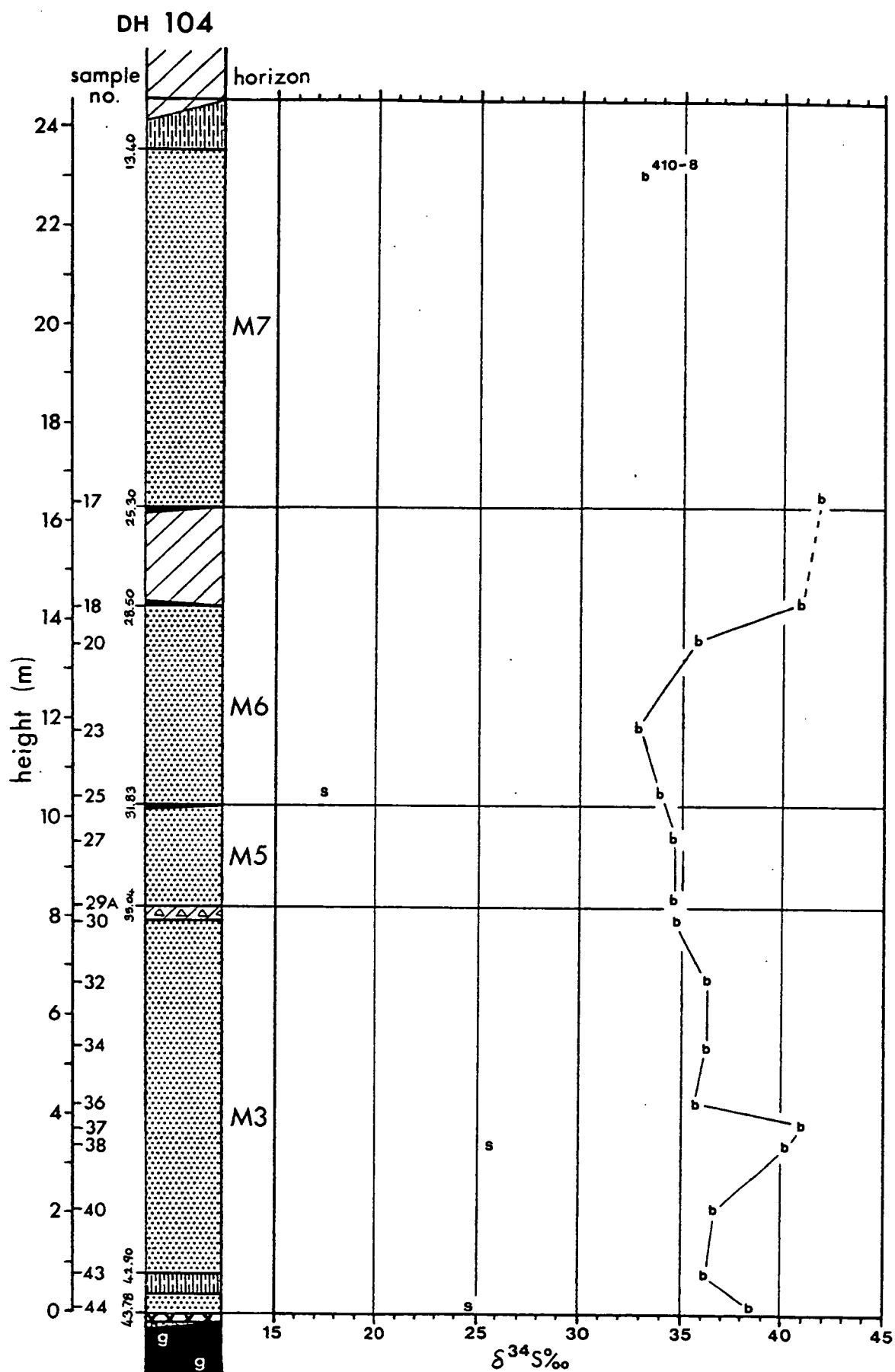


Fig. 9.11 continued



**Fig. 9.12:** Stratigraphical section and  $\delta^{34}\text{S}$  data for DH 104, Frenich Burn area. Lithological symbols as in fig. 9.11. Also shown, sample 410-8 from 130m E of DH 104.

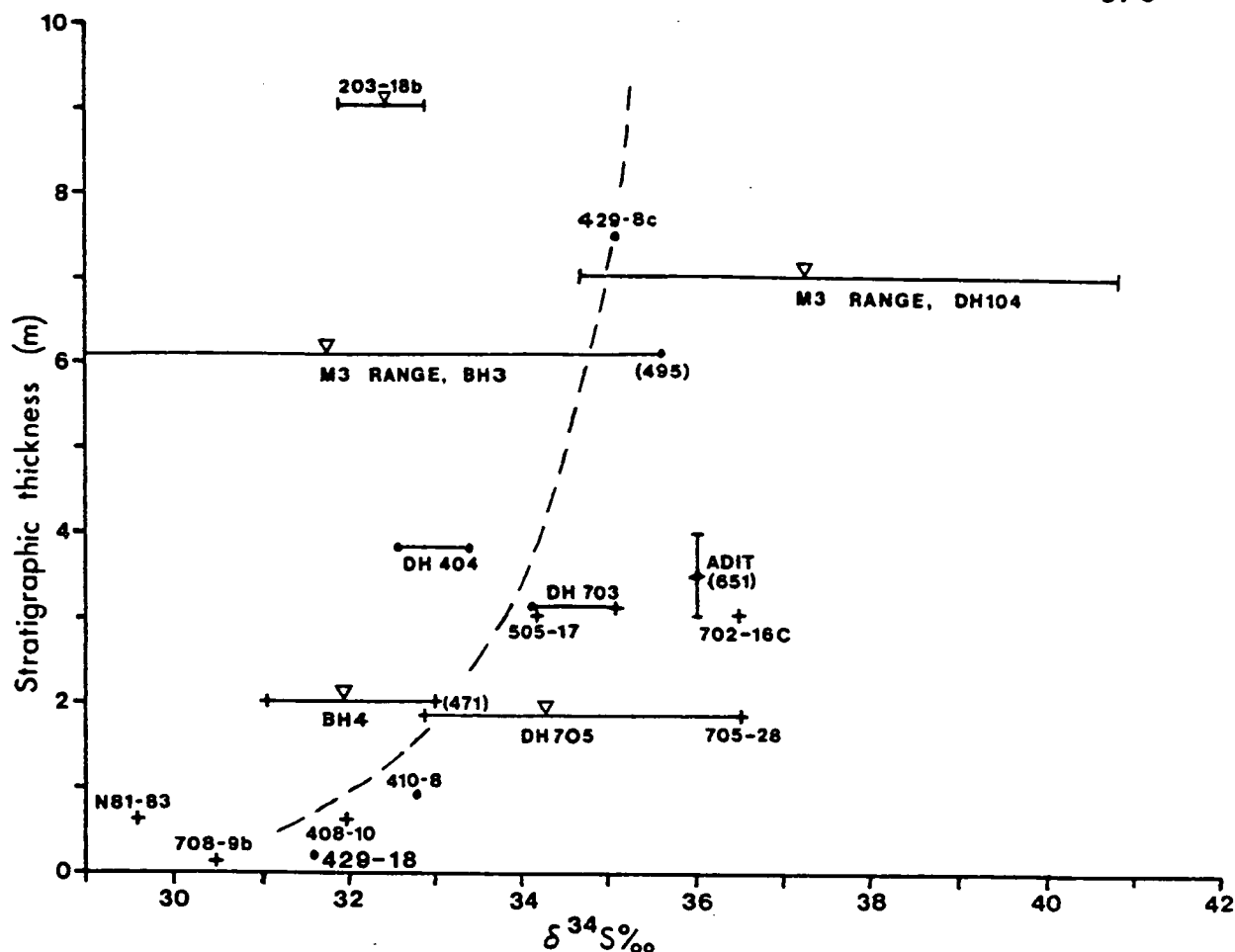


Fig. 9.13: Relationship between barite unit thickness and  $\delta^{34}\text{S}_{\text{barite}}$  in samples from the Foss deposit and BH4, Ben Eagach deposit. Barite rocks with modal sulphide content  $>5\%$  are plotted as crosses. Bars indicate range of several analyses from same intersection, inverted triangle shows arithmetic mean. Isotopic data from BHs 3 and 4 and the Foss adit from Willan and Coleman, 1983.

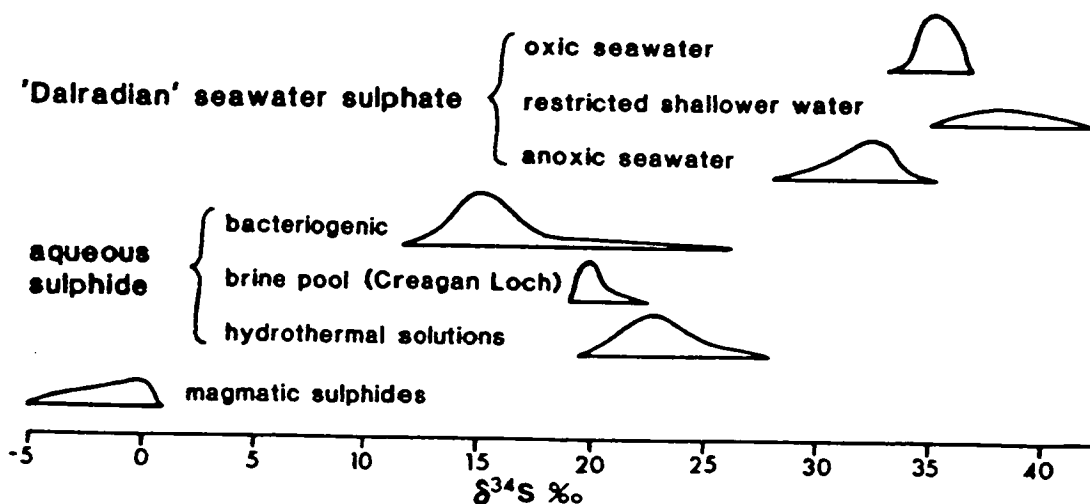
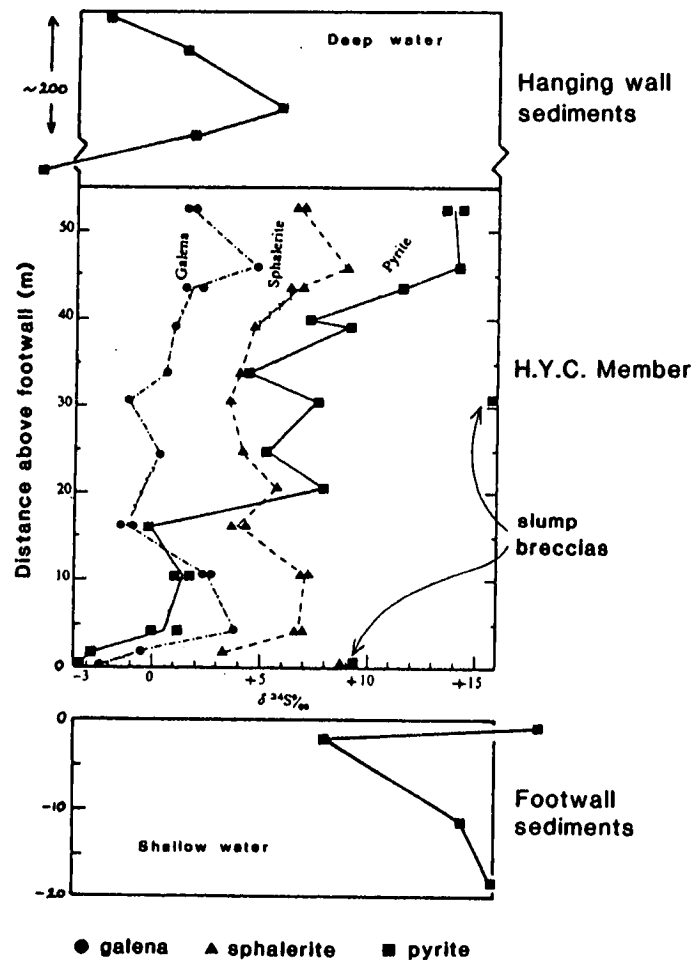
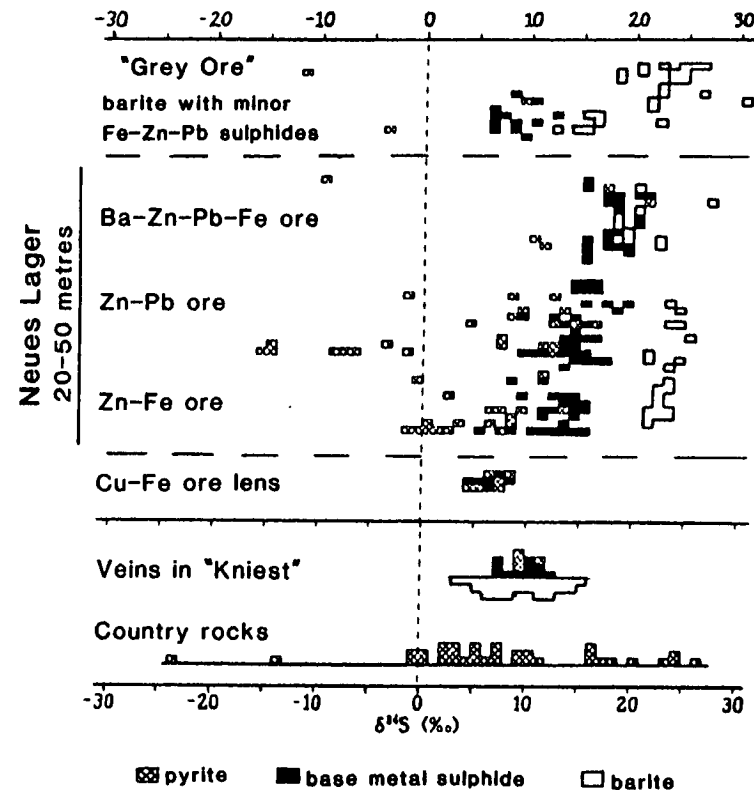


Fig. 9.14: Postulated  $\delta^{34}\text{S}$  distributions of aqueous sulphate and sulphide reservoirs from which sulphur-bearing minerals were precipitated during formation of the Foss deposit.

(a) McArthur Pb-Zn-Ag deposit, Australia



(b) Rammelsberg deposit, West Germany



**Fig. 9.15:** (a) Stratigraphic variation in  $\delta^{34}\text{S}$  ratios of sulphides in the McArthur deposit. Data of Smith and Croxford, 1973 and 1975. (b) Stratigraphic variation in  $\delta^{34}\text{S}$  ratios of pyrite, base metal sulphides and barite in the Rammelsberg deposit. The 'Kniest' is strongly silicified rock underlying the ore lenses. Data of Anger et al., 1966 (diagram adapted from Nielsen, 1978).



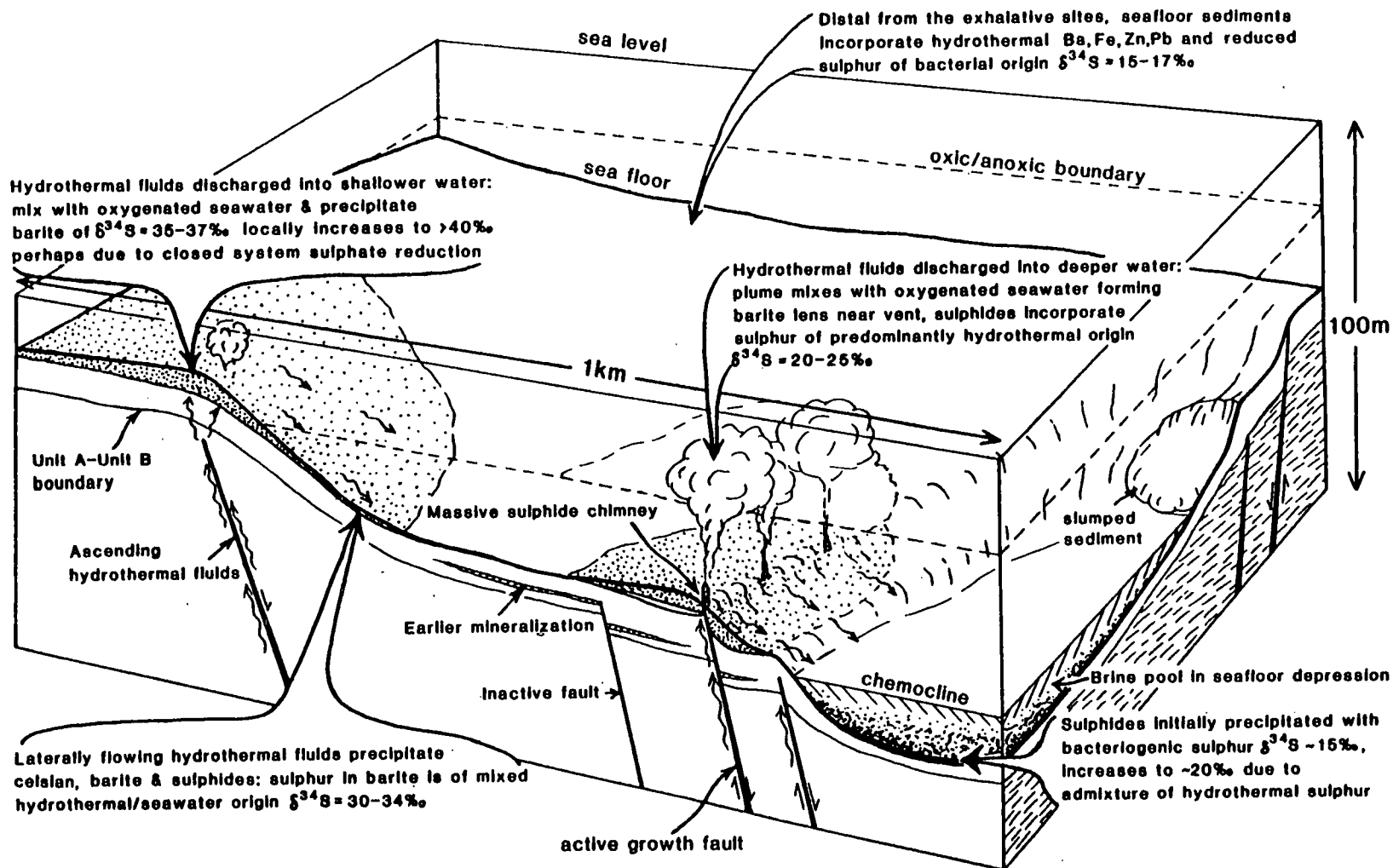


**Fig. 9.16:** Schematic block diagram based on proposed palaeotopography of the Foss East area during deposition of M3 (see fig. 2.35), to illustrate the influence of depositional environments and proximity to exhalative centres on the sulphur isotope compositions of barite and sulphides. The model invokes a dual source of sulphur, a stratified sea with anoxic bottom waters except in shallower water areas, and brine pools in seafloor depressions (see text). Seawater depth is conjectural: note vertical scale exaggeration.

## **CHAPTER 10: Petrogenesis of the Foss deposit and its host rocks.**

### **10.1 Introduction.**

In considering the genesis of the Aberfeldy deposits, Coats et al. (1980, 1981) recognized the importance of distinguishing between primary features related to deposition and diagenesis, and the superimposed effects of tectonism and metamorphism. The problem of discriminating between these processes has been a recurring theme in all aspects of this study, and the effects of metamorphism must be considered before primary features of the deposit can be properly evaluated and genetic models for the mineralization are derived.

Therefore, the first section (10.2) of this chapter reviews the deformational and metamorphic history of the study area and evaluates the evidence for (and implications of) mineralogical, chemical and isotopic changes which accompanied metamorphism. The tectonic and palaeogeographical setting of the mineralized zone, and the nature of the depositional and diagenetic environment are discussed in section 10.3, together with evidence for the sources of chemical components forming the mineralization. In section 10.4, the primary features of the Foss deposit are compared and contrasted with those of other sedimentary exhalative deposits, and genetic models for their formation are discussed. The potential for further exploration of the Aberfeldy deposits and elsewhere in the Dalradian is briefly addressed in section 10.5. Finally, section 10.6 summarizes the most significant results of this study and suggests some appropriate directions for further research.

### **10.2 The conditions and effects of metamorphism.**

#### **10.2.1 Deformational and metamorphic history.**

Polyphase deformation which accompanied amphibolite facies metamorphism during the Grampian Orogeny (part 1.2.2), resulted in fold structures ranging in amplitude from kilometric (e.g. the Creag na h-Iolaire Anticline) to millimetric (crenulated foliation in all pelitic rocks). The early, major fold structures ( $D_1$ - $D_2$ ) are associated with the development of a foliation parallel to bedding in micaceous lithologies, whereas later ( $D_3$ ) fold structures and

crenulation cleavages are oblique to the earlier fabric with westward-plunging fold axes and lineations. Box-shaped corrugations of the mineralized strata, due to superimposed folding of 10-30m amplitude, are defined by underground exploration in the Creag an Chanaich area. In Foss East, asymmetric isoclinal folds of similar amplitude are sporadically developed but fold structures are generally smaller in scale.

The contrasting structural competency of the heterogeneous components of the mineralized zone is reflected in a variety of responses to deformation, ranging from axial planar crenulation cleavage in pelitic lithologies to ductile structures such as attenuation, boudinage, and locally fold-thickening, in barite and carbonate rocks. Quartz celsian rocks which contained cymrite as a major constituent (>10-15%) during fabric development, behaved in a ductile manner in response to deformation and exhibit a relic schistose texture. Sedimentary structures other than compositional layering (bedding) have been largely erased from pelitic rocks, whereas microlamination and diagenetic structures are preserved in cherty rocks. Several rocks examined have breccia textures which are probably synsedimentary in origin, but in other cases the brecciation is likely to have been metamorphic, particularly in talc-bearing carbonate rocks and in some cherty quartz rocks where carbonates and sulphides have been remobilized. Quartz and dolomite segregations are fairly common in pelitic and dolomitic rocks respectively, and retrograde metamorphic and post-metamorphic veinlets are widespread but usually inconspicuous features of the mineralized strata.

On the microscopic scale, inclusion trails in porphyroblast minerals such as garnet and feldspars, provide evidence for relatively rapid mineral growth preceding and during D<sub>3</sub>. This episode was followed by a static phase during which the peak metamorphic temperatures were attained (530-550°C at pressures of 8-10 kbar), resulting in grain coarsening, annealing of deformed grains, and the growth of hornblende 'garbenschiefer' in unit D pelites. During the subsequent decline in pressure at near-constant temperatures, coexisting mineral compositions partially re-equilibrated and celsian replaced much of the cymrite formerly present in the mineralized lithologies. As uplift and erosion proceeded, the rock

mass cooled along a P-T path approximately parallel to the cymrite-celsian reaction line, possibly re-entering the stability field of cymrite before late metamorphic fault movements.

At least two major phases of brittle deformation are recognised, the first comprising E- to ENE-trending vertical displacements which duplicate the mineralized zone succession in the Frenich Burn area. The second phase consisted of N-S to NE-SW trending faults with both sinistral and vertical displacements generally downthrowing to the E (most notably, the Frenich Burn Fault and the Creagan Loch Faults), which divide the deposit into discrete ~~of~~ structural/lithostratigraphical blocks.

#### 10.2.2 Primary and metamorphic mineralogy.

Mineral species and compositionally distinct subspecies found in the vicinity of the Foss deposit may be categorized according to their inferred time(s) of formation, i.e. pre-, syn-, or post-metamorphic (table 7.10). Clearly, some minerals such as pyrite formed during more than one stage, and the pre-metamorphic existence of several phases (such as cymrite and talc) cannot be confirmed. Other species which were likely to have been present before metamorphism have been completely recrystallized and changed in composition, for instance the plagioclase in metabasites now exhibits a schistose fabric and is anorthite-poor. In general, the mineralogy of hydrothermal-exhalative lithologies is regarded as largely unaltered by metamorphism, whereas most of the abundant silicate minerals in the host rocks were neoformed during metamorphism from detrital and authigenic minerals.

Porphyroblastic minerals such as garnet and pyrite often retain inclusions of minerals no longer present in the matrix. These record previous primary or metamorphic assemblages and, in the case of garnet, elucidate the reactions by which the porphyroblasts grew (part 6.5.1). Several of the phases found in trace amounts, such as the barium carbonates, and kaolinite inclusions within hyalophane pseudomorphs after diagenetic sulphate crystals (part 10.3.4), have survived metamorphism because they were encapsulated in non-reactive minerals at an early stage. Other minerals described in this study are of retrograde metamorphic or supergene origin, due to exsolution (pentlandite in pyrrhotite, pyrrhotite in some sphalerite, bornite-

chalcocite intergrowths), structural changes on cooling (monoclinic pyrrhotite) or replacement (celsian replacing cymrite, chlorite replacing various ferromagnesian silicates, pyrite and marcasite replacing pyrrhotite).

Several mineral species listed in table 7.10 are restricted to particular lithologies or are mutually exclusive. Examples of these include the occurrence of magnetite only in barite rock; the absence of muscovite from barite rock (except for Cr- and V-rich varieties); the mutual exclusion of celsian and graphitic material (although graphite is commonly associated with hyalophane); the restriction of hornblende to amphibolites and non-carbonaceous calc mica schists of unit D (Ben Lawers Schist); and the scarcity of garnet in rocks containing pyrite (except where pyrite has retrogressively replaced pyrrhotite) so that garnet is absent from the sulphidic, Ba-enriched pelites of unit B. These features relate partly to the wide range in original bulk compositions, but principally to limiting stability conditions and intergranular fluid compositions (in terms of  $fO_2$ ,  $fCO_2$ ,  $fS_2$  etc.; cf. figs. 3.2 and 5.1). Iron is partitioned into sulphides rather than silicates with increasing  $fS_2$ , accounting for the low  $Fe/(Fe+Mg)$  of micas in most mineralized lithologies. Chapter 8 described the application of data on Mg-Fe partitioning within garnet-biotite and garnet-hornblende pairs, and on a variety of other mineral equilibria, to derive estimates of the peak P-T conditions during metamorphism.

### 10.2.3 The effects of metamorphism on isotopic ratios.

A preliminary study of carbon and oxygen isotopic ratios in carbonate-bearing samples from the Aberfeldy deposits (Appendix F), demonstrated that isotopic homogenization on at least a decimetric scale took place during metamorphism. Carbonates of sedimentary and hydrothermal origin, and of probable metamorphic origin in a metabasite and calcareous pelites, have similar  $\delta^{18}O$  and  $\delta^{13}C$  values indicating that carbonate compositions were buffered by infiltrating metamorphic fluids (see below).

Conversely, a more extensive sulphur isotope study (Chapter 9) confirms that isotopic equilibration between coexisting sulphur-bearing phases probably did not occur during metamorphism, despite the 'reasonable' metamorphic temperatures (450–550°C) suggested by

apparent fractionations between barite and sulphides. Isotopic disequilibrium characterises some coarse-grained sulphide rocks, but in another massive sulphide rock, within-crystal isotopic zonation in galena could be interpreted as partial retrograde re-equilibration to low temperatures after complete equilibration at the metamorphic climax. It is concluded that metamorphism has not greatly affected sulphur isotope ratios which can therefore be related to the primary controls on ore deposition and sources of sulphur (part 10.3.2).

#### 10.2.4 Changes in bulk composition.

Bulk compositional changes during diagenesis and metamorphism are illustrated by metabasites within the mineralized zone. Although they have uniform concentrations of the relatively immobile elements indicating a homogeneous original composition, the metabasites are extensively hydrated and carbonated and are variably enriched in K, Ba, Rb and S, and depleted in Na (sections 5.2, 5.3). Ratios of Rb:K in the metabasites are similar to those in the metasediments, and K and Ba contents are loosely correlated with metabasite bed thickness and the barium levels in adjoining lithologies. Alkaline metasomatism of the basic igneous rocks is related to chemical potential gradients and pervasive fluid infiltration during metamorphism. Isotopic studies (Appendix F) suggest that carbon incorporated as  $\text{CO}_2$  in the metabasites during metamorphism was derived from the oxidation of carbonaceous matter in the enclosing metasediments. A similar conclusion was reached in more detailed studies by Graham et al. (1983) of carbonated metabasites in the Knapdale area of the SW Highlands.

The extensive development, in both pelitic and metabasic lithologies, of assemblages containing both products and reactants of the reaction: biotite + chlorite + 8 calcite + 8  $\text{CO}_2$  = muscovite + 8 dolomite + 3 quartz + 4  $\text{H}_2\text{O}$  (section 5.2), testifies to the buffering action of prograde mineral reactions on the  $X_{\text{CO}_2}$  of the metamorphic fluid (cf. Graham et al., op. cit.). At the estimated peak P-T conditions and using analysed compositions, the above reaction buffers the fluid at water-rich compositions ( $X_{\text{CO}_2} < 0.1$ : fig. 5.1). Higher  $X_{\text{CO}_2}$  values in the fluid phase or greater fluid:rock ratios are indicated by the unbuffered muscovite-

dolomite-quartz assemblage (type B4) commonly found in a thin (<0.5m) altered metabasite bed adjoining mineralized lithologies. Therefore, petrographical, geochemical and isotopic evidence indicates that extensive infiltration of hydrous fluid and metasomatism accompanied late diagenetic and/or metamorphic alteration of the metabasites.

From evidence of sodium depletion accompanying the loss of plagioclase and presence of significant quantities of muscovite (~30%) and pyrrhotite (5-10%) in the thin beds of altered metabasite mentioned above, it is speculated that the comparatively low sodium content of sulphidic, graphitic schists in the mineralized zone (compared with sulphide-poor, garnet- and plagioclase-bearing graphitic schists in unit A) may also be due to the extensive removal of sodium in the infiltrating metamorphic fluids. A similar conclusion was reached by Ferry (1981, 1982), who demonstrated that progressive metamorphism of pyritic black shales in south-central Maine was at least broadly isochemical with respect to all major non-volatile elements except sodium, but that Na, C and S contents were depleted during metamorphism to sillimanite grade. Ferry (1982 and 1983a,b) also showed that large volumes of hot, acid, CO<sub>2</sub>-poor fluid infiltrated the metasediments (with volumetric fluid/rock ratios >3) to drive the mineral reactions responsible for changing the whole-rock chemistry.

Desulphidation reactions documented by Ferry (1981) can account for the presence of varying amounts of pyrrhotite (considered to be entirely metamorphic in origin) and pyrite in black shales and their metamorphic equivalents at all grades. Disseminated pyrrhotite in the Ben Eagach Schist at Foss also probably formed by the desulphidation of diagenetic pyrite concomitant with oxidation of reduced carbon, but much of the disseminated pyrrhotite and possibly all massive pyrrhotite bands occurring in the mineralized strata are regarded as primary in origin. Sulphur mobility during diagenetic/metamorphic reactions is also indicated by textural and isotopic evidence for the reduction of barite to form pyrite and hyalophane in some cherty lithologies, and by textural evidence for the sulphidation of barium carbonates to form barite plus calcite or dolomite in several mineralized rocks (part 10.3.3).

### 10.3 Tectonic setting and depositional environment of the Foss deposit.

#### 10.3.1 Sedimentation and magmatic activity.

##### 10.3.1.1 Lithostratigraphy and synsedimentary faulting.

The explored extent of the Foss deposit (2.2km strike-length and to ~300m depth) exhibits a remarkable diversity of lithostratigraphical successions, in which a variable number of mineralized beds are interlayered with pelitic, psammitic and calcareous metasediments and metabasites within a chronostratigraphical zone varying in combined thickness from ~10m to >100m (fig. 10.5). Although this diversity may have been increased by vertical displacements following metamorphism (section 2.5), there is clear evidence for primary, rapid lateral facies and thickness changes in both the mineralized beds and in the enclosing metasediments.

Variations in the rates of sediment input and in the proportions of quartzite and graphitic schist are attributed to localized basinal down-warpage related to synsedimentary faulting. This is particularly evident in Foss West and the Frenich Burn area, where decreases in the thickness of graphitic schist are accompanied by the convergence and coalescence of the lower and upper mineralized horizons to form a single, composite bed. A direct spatial association between rapid changes in metasediment thickness and the probable location of a hydrothermal exhalative vent (section 3.5), is observed in the Creagan Loch area. Here, unit B metasediments both below and above the lower (M3) horizon increase greatly in thickness (to total >100m) in relation to the thickness of unit B metasediments in central Foss East (30-50m) (fig. 10.5). In a separate structural block further east, the incorporation of sedimentary material into the lower part of the M3 mineralized bed is attributed to slumping associated with the onset of hydrothermal activity. The relationship between the depositional environment and mineralization facies is discussed further in part 10.3.2.1.

Lithostratigraphical variations within blocks of the deposit which are unaffected by major post-metamorphic faults, are generally more rapid in a down-dip direction than along strike. Both isopachs of metasediment thicknesses and boundaries between parts of the mineralized zone with differing lithostratigraphical character-



istics, generally plunge westwards with the regional structure (figs. 2.16, 2.18). This suggests that these boundaries marked hinge zones or growth faults which were approximately parallel to the NE-SW 'Caledonoid' trend, reflecting continental distention in a NW-SE direction (cf. Phillips et al., 1976; Anderton, 1982). However in the Creagan Loch area, rapid along-strike changes suggest that synsedimentary faulting also occurred in a transverse direction, and the poorly mineralized (?downfaulted) section of the Ben Eagach Schist on Farragon Hill may represent a 'palaeohigh' between third-order depositional basins (cf. fig. 10.2). Sedimentological evidence for faulting of both Caledonoid and trans-Caledonoid trends, has been described from the Argyll Group of the SW Highlands by Anderton (1979) and Borradaile (1979) (fig. 10.1).

#### 10.3.1.2 Magmatic activity.

Increasing crustal instability and stretching during Argyll Group times is reflected in the voluminous metabasaltic sills, lavas and tuffs of tholeiitic affinity in the SW Highlands (Graham, 1976a), and in the occurrence of less abundant metabasites of similar petrochemistry in the central Highlands (Graham and Bradbury, 1981). The metabasites of both eruptive and intrusive origin which constitute about 5% of the mineralized zone at Foss, have retained a uniform immobile element distribution which clearly indicates a 'within-plate' basalt affinity. This contrasts with the 'ocean floor' basalt type represented by the majority of metabasites occurring in the younger Farragon Beds formation and the comagmatic Ben Vrackie intrusive complex which is located at the top of the Ben Eagach Schist 15km NE of the Foss area.

The stratigraphical and geochemical evidence indicates that (i) a transition from continental to oceanic magma types occurred in Ben Lawers Schist times during the early stages of a major phase of igneous activity and after the inception of extensional tectonics, and (ii) sill intrusions occurred during, or shortly after, the deposition of the mineralized zone at Foss (fig. 10.5); although their relatively small volume and limited occurrence precludes a significant contribution of heat for driving hydrothermal convection systems. However, a temporal association between tectono-magmatic activity and the discharge of hydrothermal brines is indicated by

the presence of a thin but laterally extensive metabasite marker bed of probable pyroclastic origin, immediately beneath the lower (M3) mineralized horizon.

#### 10.3.1.3 Sedimentation.

Ben Eagach Schist pelites lack the geochemical characteristics of sapropelic black shales (e.g. high P, Ti, V and organic carbon contents), and apart from the low Na content (attributed to metasomatic alteration: part 10.2.4) and enrichment in barium and base metals of probable hydrothermal origin in unit B (section 4.5), the formation is similar in bulk composition to other Dalradian pelites and 'world average' pelites and shales. The relatively high K and Al content of Ben Eagach Schist pelites suggests that the precursor sediment consisted predominantly of illite. This may have been detrital and/or diagenetic in origin and is considered to have formed in a reduced, alkaline and possibly hypo-saline marine basin supplied with aluminous run-off and feldspathic detritus from the adjoining arid landmasses (cf. Russell et al., 1984) (fig. 10.3). Other indications of highly saline and alkaline pore-waters are provided by evidence for the diagenetic growth of sulphate (?gypsum) and barium carbonates associated with the mineralization (part 10.3.3). The presence of aqueous alumina species in the basinal seawater is consistent with the abundance of barium aluminosilicate (now celsian) in the deposit, the formation of which is discussed in part 10.3.2.2.

Metasediments in the mineralized zone include some coarse-grained quartzite beds which petrographically resemble the Carn Mairg Quartzite and locally exhibit graded bedding (Coats et al., 1981), suggesting their rapid deposition perhaps from turbidity currents. Decimetre-thick, graphitic dolostone bands within unit B may represent dolomitized carbonate turbidites derived from a carbonate shelf area (cf. Anderton, 1979). Non-carbonaceous, dolomitic quartz mica (+ chlorite) schists of the Ben Lawers Schist, and similar lithologies within the mineralized zone (unit C), were probably deposited in an oxidizing environment because of the abundance of carbonate and paucity of sulphides (reflected in the low Zn and Pb contents). The precursor sediment is likely to have been a calcareous siltstone or marl, which incorporated magnesium during dolomitization.

### 10.3.2 Interaction of the hydrothermal fluids with the marine environment.

#### 10.3.2.1 Facies variations in the mineralized horizons.

The interdigitation of discrete lenses of barite rock, quartz celtsian rocks, and carbonate- and sulphide-rich rocks within individual mineralized horizons at Foss (fig. 10.5), suggests that variable physicochemical conditions in the depositional environment, and variations in the rate of brine input and its density, controlled the composition of the mineralization to a greater extent than temporal variations in the chemistry of the hydrothermal fluids (discussed in the following section). In the M3 horizon east of Creagan Loch (DHs 707, 708) (part 2.4.4), the dominance of sulphide over barite, the absence of primary bimodal sphalerite compositions (part 7.3.2), and the relatively high proportion of incorporated bacteriogenic sulphur (part 9.7.2), support the interpretation of this area as a relatively deep-water, euxinic basin in which the metalliferous brines pooled downslope and perhaps some distance from the exhalative site (fig. 9.16).

A contrasting sedimentary environment is represented in the Frenich Burn area: here the barite which was precipitated from successive hydrothermal emanations formed a single, composite bed up to 22m thick, with little or no incorporation of detrital sediment. Wedges of metasediment, varying in thickness from a few centimetres to tens of metres, separate this barite bed into the four or five component horizons to the east and down-dip (figs. 2.7, 2.24). Sedimentary reworking, suggested by intraformational breccias in both barite rock and in the intervening (unit C) metasediment bands, and by possible unconformities in the sequence, also indicate an intermittently high-energy and relatively shallow-water environment. An increasingly oxygenated environment depleted in aqueous reduced sulphur species but with high sulphate concentrations, is supported by the iron content of disseminated sphalerite increasing with stratigraphic height (part 7.3.2), the presence of magnetite in sulphide-poor barite rocks, and by  $\delta^{34}\text{S}$  ratios of 35-36.5‰ which are compatible with the incorporation of contemporaneous, open seawater sulphate (although ratios up to 42‰ are also found in this profile; see part 10.3.2.3). Thick barite beds may indicate the passive exhalation of hydrothermal fluids into oxygenated seawater,

or the vigorous expulsion of buoyant brines (type IIA of Sato, 1972 & 1977) which rose above the anoxic bottom waters of the stratified, euxinic marine basin. In either situation, much of the base metal content of the hydrothermal solutions may have been oxidised and dispersed over large distances.

#### 10.3.2.2 The formation of barium aluminosilicate rocks.

The greater quantity of barium aluminosilicates (now celsian) than of barite in the Aberfeldy deposits, which suggests that the outflowing hydrothermal solutions did not mix with sulphate-bearing seawater, has been accounted for by Russell et al. (1984). They postulate that the celsian precursor (discussed below) precipitated when barium chloride and silicic acid introduced in the acidic hydrothermal solutions reacted with highly alkaline, aluminous and hypersaline, basinal seawater. These alkaline brines containing soluble aluminium hydrates are considered to have been derived by gravity flow from evaporitic shelf seas marginal to the Dalradian basin, which received intermittent runoff from adjoining, deeply weathered landmasses (such as the Lewisian of NW Scotland) (fig. 10.3).

Earlier, Russell, Willan et al. (1981) had considered that heated, convecting seawater "had the power to attack and leach not merely the trace metals and sulphides, but also a significant fraction of the aluminosilicates in the source rocks". However, experimental investigations of oceanic hydrothermal systems (e.g. Hajash, 1975) have shown that acid, saline brines are incapable of carrying significant amounts of Al. The precipitation of Ba-aluminosilicates rather than barite may be explained by the slow discharge of cooler, dense brines (type I of Sato, op. cit.) into a stable, anoxic brine layer isolated by a chemocline from the overlying oxygenated seawater. Coats et al. (1981) suggested that the barium aluminosilicate precursor could have been cymrite (which is found in unmetamorphosed black shales and stratiform deposits: part 10.4.2), or a mixture of quartz and a barium zeolite such as harmotome (which occurs in modern deep-sea sediments; e.g. Boles, 1977), or possibly an amorphous gel.

Coats et al. (op. cit.) also suggested that quartz celsian rock may have formed by the complete diagenetic alteration of sedimentary material. However, the composition of most quartz celsian rocks

(viz. low contents of Ti, K, Rb, Zr) suggests that they are unlikely to have formed by the incorporation of barium (supplied by hydrothermal fluids) into aluminosilicate-bearing sediments. Geochemical analyses, discussed in part 3.4.2, indicate the presence of major sedimentary component in a volumetrically small proportion of schistose celsian-bearing rocks which occur marginal to the mineralized horizons or in their distal portions. The formation of celsian in these mineralized sediments, and locally in basaltic (tuffaceous) material, appears to have been limited by the supply of  $\text{Al}_2\text{O}_3$  (or rather a soluble species such as  $\text{Al}(\text{OH})_4^-$ ) to the site of deposition. Barium and silica were available in excess as indicated by the formation of barite and siliceous cherts.

#### 10.3.2.3 Source of barium, metals and sulphur.

The source for most of the non-volatile components of the stratiform mineralization (namely, Ba, Si, Fe, Zn, Pb, Cu, Mn, Ca, probably Mg, and minor elements) is considered to have been the underlying, Lower Dalradian and Moinian sediments (fig. 10.3). Russell et al. (1984) have pointed out the relatively high barium contents of psammitic rocks in the Appin Group (up to 1000ppm recorded by Lambert et al., 1981, and Hickman & Wright, 1983) and in the Moines (as indicated by IGS stream geochemical results: Plant & Moore, 1979). These components were transported, principally as chloride complexes, in heated convecting seawater and/or deep formation waters (see part 10.4.3). This is supported by lead isotope studies (Swainbank et al., 1981), which indicate the derivation of base metals from craton-derived Dalradian sediments mixed with lead from a basic igneous (ultimately mantle) source. However, the low Cu, Co and Ni content of the mineralization is evidence against a major contribution of leachates from basic igneous rocks to the hydrothermal solutions, unlike minor massive sulphide deposits at similar stratigraphic levels in the SW Highlands (e.g. McPhun's Cairn, fig. 1.1: Willan, 1980, 1983; Willan and Hall, 1980).

Much of the sulphide-sulphur in the mineralized strata ( $\delta^{34}\text{S} = 20-28\%$ ) is regarded as hydrothermal in origin (part 9.7.2) and was probably generated by the inorganic reduction of sulphate in connate or convecting seawater at depth in the sedimentary pile. Small-scale fluctuations in isotopic composition are attributed to

variations in the proportion of reduced sulphur incorporated from the basinal seawater reservoir, which may have become increasingly enriched in  $^{34}\text{S}$  during each exhalative event. Isotopically lighter sulphide-sulphur (15-20‰) occurring close to the top of the lower mineralized bed in the Creagan Loch area, and in sulphides throughout the DH 708 profile, was derived from this basinal reservoir of reduced aqueous sulphur of mixed hydrothermal and bacteriogenic ( $\delta^{34}\text{S} \approx 15\%$ ) origin (fig. 9.16). A dual sulphur source is also suggested by the large isotopic range (15-28‰) in disseminated sulphide in the metasedimentary host rocks and in 'distal' mineralized strata.

As noted above, the  $\delta^{34}\text{S}$  values of  $\sim 35 \pm 1\%$  found for much of the barite in thicker beds at Foss, probably represents the isotopic composition of contemporaneous 'Dalradian basin' seawater. Isotopically lighter barite ( $\delta^{34}\text{S} = 28-33\%$ ) probably precipitated from a mixture of seawater sulphate and oxidized hydrothermal or bacterial aqueous sulphides, whereas exceptionally heavy sulphur (37-42‰) in the composite barite bed at Frenich Burn may be attributed to closed system fractionation in a shallower water setting or in trapped pore waters during diagenesis.

#### 10.3.3. Diagenetic changes in the mineralized strata.

Quartz-carbonate-pyrrhotite pseudomorphs after gypsum have been described from the less intensively metamorphosed stratigraphical equivalent to the Ben Eagach Schist, and also in carbonaceous shales of the Ballachulish Subgroup in the West Highlands (Anderson, 1975; Hall, 1982). Morphologically similar pseudomorphs, consisting of tabular hyalophane complexes up to 5mm in length and with internal quartz, kaolinite and barite inclusions, occur infrequently in metasedimentary cherts at Foss (part 3.5.1). These structures have survived metamorphism because the host sediments were enriched in silica of organic or hydrothermal origin, and evidence for more extensive diagenetic sulphate formation in shaly sediments may have been destroyed by penetrative metamorphism.

Unusually heavy sulphur isotope ratios in sulphides separated from two of the three pseudomorph-bearing rocks examined (part 9.4.1) support the interpretation that the reduction of sulphate (coupled with oxidation of carbonaceous material) occurred during

late diagenesis or metamorphism. The textural and isotopic evidence suggests that hyalophane and pyrite formed by reactions between barite and kaolinite (both preserved as relict inclusions) under reducing conditions, as described by Bjorlykke and Griffin (1973), and suggested by Fortey and Beddoe-Stephens (1982). This reaction may also have generated the hyalophane which forms up to 70% (modal) of other graphitic hyalophane schists and cherts locally adjoining or comprising the stratiform mineralized horizons. Hyalophane and potassic celsian also forms irregularly zoned, equant crystals in some massive sulphide rocks, and these could have originated as crystals of K-feldspar (adularia?) precipitated during boiling of the hydrothermal fluids (part 10.4.3.1).

The barium carbonates, witherite, norsethite, barytocalcite and possibly benstonite, occur in trace amounts as small inclusions in sulphide and barite crystals in a significant number (>10%) of massive sulphide, barite and carbonate rocks examined (parts 3.5.2 and 7.5.3). Textural evidence suggests that these carbonates were a more abundant (although still minor) component of the mineralization before metamorphism. By analogy with occurrences in stratiform barite-sulphide deposits in the Yukon (cf. Large, 1981b and Lydon et al., 1979: part 10.4.2), it seems likely that the barium carbonates were precipitated during an early diagenetic stage from alkaline, reducing and sulphate-depleted pore waters within the mineralized beds.

Replacement of detrital potassic feldspar by sodic feldspar in quartzites interbedded with the pelites is attributed to reactions with saline pore waters during diagenesis. Pore waters expelled from the base-metal enriched shales and channelled through interbedded permeable sandstones, redeposited stratabound Fe-Zn-Pb sulphides in some quartzites and dolostones within unit B of the Ben Eagach Schist.

#### 10.4 Comparisons with other sedimentary-exhalative deposits and models of ore genesis.

##### 10.4.1 Classification and characteristics.

The Foss and Ben Eagach deposits are members of the sediment-hosted, submarine-exhalative ('sedimentary-exhalative') class of

stratiform, base metal, barium and/or precious metal deposits, the characteristic features of which have been described by Finlow-Bates (1980), Large (1980, 1981a), Morganti (1981) and Russell, Solomon & Walshe (1981). An increasing number of metamorphosed deposits have been recognized as belonging to the sedimentary-exhalative class. The strictly stratiform character of these deposits (although many also have cross-cutting feeder zones) and the clastic sedimentary rock association, distinguishes this class from carbonate-hosted, strata-bound Mississippi Valley type deposits and from distal volcanogenic stratiform deposits (e.g. Large, 1977; Plimer, 1978). The class includes several of the world's largest ore deposits, the most prominent of which are of mid-Proterozoic age, e.g. the McArthur River and Mt Isa deposits in Australia, and Sullivan in Canada (table 10.1) which, prior to mining, had total stratiform sulphide tonnages of 190Mt, 89Mt and 155Mt respectively (Large, 1981a). Although these deposits and their lesser kin have received much attention in the literature (reviewed in references given above), several aspects of their genesis remain controversial. These include the fine and often rhythmic laminations of the sulphides, the occurrence of several discrete ore lenses (fig. 10.6), and the limited distribution of the deposits in time and space (cf. Sawkins, 1984).

Characteristic tectono-sedimentary, lithological, geochemical and isotopic features of the sedimentary-exhalative deposits have been reviewed by Large (1980, 1981a, 1981b), and these are listed in table 10.2 alongside evidence for comparable features in the Foss deposit. Notable characteristics which Foss has in common with the class are (a) a regional tectono-sedimentary regime characterized by continental distension, with local evidence of growth faulting and basin development during mineralization; (b) contemporaneous minor igneous activity, including thin pyroclastic deposits which are diagenetically enriched in potassium (tuffites), which suggests that a high geothermal gradient may have prevailed; (c) the spatial and temporal segregation of barite from sulphides (except close to exhalative vents) reflecting locally oxidizing and reducing environments, and varying extents of hydrothermal fluid-seawater mixing (also indicated by the dual source of sulphur); and (d) the dispersed halo of metal (and barium) enrichment in the host



sediments and evidence for 'footwall' silicification.

However, three characteristics of the class (according to Large, *op. cit.*) are not apparent in the Foss and Ben Eagach deposits: (1) A major structural lineament associated with the second-order (10-100km size) basin (the 'Aberfeldy basin' of Coats et al., 1984: see fig. 10.2). (2) Stockwork mineralization underlying the mineralized horizons and representing the feeder zone(s). (3) A homogeneous lead isotope signature (*cf.* Swainbank et al., 1981). Note that the first characteristic may have been obscured by large-scale, E-W isoclinal folding which formed the Creag na h-Iolaire Anticline (possibly related to a former lineament?), and evidence of the second may have been removed by post-tectonic re-activation of growth faults or by erosion (e.g. in the Creagan Loch area?). Further work on lead isotope compositions is in progress (C.H. Mills, University of Strathclyde; *pers. comm.* 1985).

The Foss and Ben Eagach deposits are similar to the Devonian barite-sphalerite-galena deposits of Meggen and Rammelsberg in Germany (Krebs, 1981; Hannak, 1981), and Tom in the Yukon area of Canada (Carne, 1979; Large, 1980, 1981b). These formed in epicratonic basins (the Variscan Trough and Macmillan Pass Basin, respectively) accumulating carbonaceous, pyritic shales, siltstone, sandstone and locally limestone turbidites (also a chert-pebble conglomerate at Tom; fig. 10.7). The mineralization consists of massive and laminated sulphides and bedded barite rock. The barite overlies the sulphides at Rammelsberg (fig. 9.14b), is peripheral to the stratiform sulphides at Meggen and is interbanded with sulphides at Tom. Mineralized, cross-cutting feeder pipes underlie the stratiform facies at Rammelsberg (the siliceous 'Kniest') and at Tom. However, although two stratigraphical zones containing mineralization are present at Tom and possibly also at Rammelsberg (the Altes Lager and the Neues Lager), these deposits also do not exhibit the multiple, laterally extensive mineralized horizons seen in the McArthur River Group deposits and at Foss.

#### 10.4.2 Comparative mineralogy.

Reactions between aluminous and alkaline basinal seawater and Ba-rich hydrothermal fluids are invoked to account for the great abundance of barium feldspar which is an outstanding feature of the

Aberfeldy deposits (celsian content estimated at  $\sim 10^8$  tonnes: Russell et al., 1984). However, the paragenesis is not unique since relatively minor amounts of celsian are associated with metamorphosed (to upper amphibolite facies), base metal exhalative mineralization at Rosh Pinah in Namibia (Page and Watson, 1976), and with the unmetamorphosed barite, Pb-Zn sulphide deposit of Tom in Yukon Territory, Canada (Large, 1981b). Fortey and Beddoe-Stephens (1982) speculated that barium aluminosilicates in deposits of this type may be more common than presently realised. Cymrite has also been identified in inter-ore sediments at Tom (Large, op. cit.), and hyalophane occurs in the mineralized footwall metasediments at Rosh Pinah. Further similarities in paragenesis between the Aberfeldy, Rosh Pinah and Tom deposits are the occurrences of barium carbonates associated with barite-sulphide mineralization, although Page and Watson (op. cit.) questioned the syngenetic origin for these carbonates at Rosh Pinah.

A simple sulphide mineralogy is characteristic of the sedimentary exhalative deposits (Large, 1981a), with variations chiefly in the relative proportions of pyrite, pyrrhotite, sphalerite, galena and (usually minor) chalcopyrite. Fine rhythmic banding is commonly observed in the stratiform deposits, and at Mt Isa, individual metre-thick and laterally extensive ( $\sim 1$ km) ore horizons contain monomineralic bands of galena, sphalerite and pyrite. Bubela and McDonald (1969) compared this banding with experimentally produced metal ion segregations in gels, while Finlow-Bates (1979b) appealed to rapid deposition from repeated flows of dense, laterally-flowing brines (cf. Turner and Gustafson, 1978). Large (1981b) has suggested a geyser-like submarine discharge of hydrothermal fluids to account for finely laminated (mm scale) sulphides and barite in the Tom deposit, and a similar process may explain sulphide laminations in barite and cherty rocks at Foss.

Wide variations in the pyrite:pyrrhotite ratio are observed between deposits, notably in the McArthur River-Broken Hill group. These appear to relate to variations in metamorphic grade due to the progressive desulphidation of pyrite, but several authors argue for primary differences in the relative proportions of iron sulphides (e.g. Finlow-Bates and Croxford, 1977; Plimer and Finlow-Bates, 1978). Arsenopyrite, minerals of the tennantite-tetrahedrite series,

and other sulphides and sulphosalts are generally found in minor or trace amounts in many deposits, including Rammelsberg (Large, 1981a); McArthur River, Mt Isa and Broken Hill (Hutchison, 1983); Rosh Pinah (Page and Watson, 1976); and also Foss (part 7.3.3).

The Sullivan deposit in SE British Columbia is unusual amongst sedimentary-exhalative deposits in that it contains an abundance of cassiterite (the ore locally contains several percent  $\text{SnO}_2$ ), tourmaline (dravite, largely in the brecciated feeder pipe), and fluoride minerals (Plimer, 1984). This suggests the involvement of magmatic fluids derived from late granitic differentiates (Campbell and Ethier, 1983). However, Slack (1982) notes that tourmaline is associated with several stratabound base metal (and precious metal) deposits in the Appalachian-Caledonian orogen, and suggests that the boron was leached from the underlying, thick sediment piles. Fluorine-bearing micas and apatite, and trace cassiterite, have been observed in the mineralization at Foss, but tourmaline is absent from the mineralized assemblage. However, tourmaline is fairly common in trace amounts in the host metasediments (part 6.4.6), and Plant et al. (1984) have noted that boron levels are relatively high ( $>30\text{ppm}$ ) in stream sediments derived from the Easdale Subgroup outcrop in northern Scotland, which they relate to sedimentation associated with an extensional, marginal basin.

#### 10.4.3 Composition, temperature and origin of the hydrothermal fluids.

##### 10.4.3.1 Physicochemistry of the hydrothermal solution.

Many authors have sought to define the nature of the hydrothermal fluids which formed submarine-exhalative base metal deposits (e.g. Finlow-Bates, 1980; Large, 1981a; Russell, Solomon & Walshe, 1981). The current consensus is that the chloride-complex models of Sato (1972, 1973) and R. Large (1977) for ore solutions forming massive sulphide deposits in volcanic terrains, are broadly applicable to sedimentary-exhalative deposits. To be capable of leaching and transporting significant amounts ( $>1\text{ppm}$ ) of base metals as chloride complexes, the fluids must be hot ( $>200^\circ\text{C}$ ), saline, weakly acid and reduced (cf. Sato, op. cit.; Anderson, 1973 and 1975). These conditions have been substantiated by direct observations of modern hydrothermal systems including those at ocean-floor spreading

centres, in which temperatures of 200–300°C have been measured (e.g. Lonsdale et al., 1980; MacDonald et al., 1980: see fig. 9.6).

Crerar et al. (1978) suggest that at temperatures of 250°C, a total reduced sulphur concentration of  $10^{-3}$ – $10^{-4}$  molal is sufficient to precipitate all the metals in solution as sulphides. Higher activities of reduced sulphur in the solution would decrease its capacity to carry metals as chloride complexes (Anderson, 1973, 1975). Metallic chloride complexes destabilize with decreasing temperature, so that the precipitation of sulphides will occur primarily because of cooling of the ascending or exhaled solutions. It should be noted that the large amounts of barium presumably carried by the hydrothermal fluids which formed the Aberfeldy deposits, precludes the presence of significant amounts of soluble sulphate species such as  $\text{NaSO}_4^-$  and  $\text{MgSO}_4^-$ , which were demonstrated by Shanks and Bischoff (1977) to be a major component of fluids in the Red Sea hydrothermal system.

Adiabatic boiling of metalliferous hydrothermal solutions is considered to be a major factor in determining the style of mineralization in submarine exhalative deposits (Finlow-Bates and Large, 1978; Finlow-Bates, 1980), and another related factor is the buoyancy of the exhaled brine with respect to seawater. Rising hydrothermal brines may reach the seafloor without boiling if the water depth is greater than 500 – 600m, but at shallower water depths (thought to be typical of sedimentary exhalative Ba-Zn-Pb deposits), hot brines will inevitably boil before they reach the seafloor. The sudden loss of a vapour phase (principally steam, but carrying  $\text{CO}_2$ ,  $\text{H}_2\text{S}$ , etc.) results in a rapid cooling and increase in salinity of the solution. Consequently, the least soluble sulphide phases such as chalcopyrite precipitate together with some sphalerite and galena as a cross-cutting stockwork, or as disseminated mineralization in the feeder zone (e.g. Russell, Solomon & Walshe, 1981).

Unfortunately, there is no direct evidence for the nature of the feeder system at Foss, although the several features of the M3 bed in the vicinity of BH3 at Creagan Loch suggest that this area was proximal to an exhalative vent (part 3.5.2). The thick lens of mineralized dolomite rock underlying the barite intersected in BH3, may indicate the rapid quenching of hot, weakly acid exhalative

fluid by cool, alkaline seawater (part 10.3.2.2) resulting in the precipitation of carbonates and sulphides incorporating hydrothermal  $\text{CO}_2$  and  $\text{S}^-$  respectively.

#### 10.4.3.2 Fluid inclusion evidence.

Fluid inclusion data for the mineralizing fluids which formed sediment-hosted lead-zinc deposits is presently limited, although mineral assemblages and isotopic evidence suggest that temperatures generally exceeded  $200^\circ\text{C}$ . Amphibolite facies metamorphism precludes the use of fluid inclusions to obtain direct evidence for the composition of the hydrothermal fluids which formed the Aberfeldy deposits. From fluid inclusion studies of the Silvermines Pb-Zn-sulphide and barite deposit, Ireland, Samson and Russell (1983) concluded that mineral precipitation occurred when a fluid with a temperature of  $250^\circ\text{C}$  and a salinity of 10 wt% NaCl, rising up the fault system, encountered a warm, highly saline solution ( $<80^\circ\text{C}$ , ~25 wt% NaCl), possibly related to a brine pool. Mako and Shanks (1984) reported fluid inclusion salinities of >26 wt% NaCl from the Vulcan shale-hosted stratiform barite deposit in the Selwyn Basin. In the same area, Gardner (quoted in Sawkins, 1984) measured fluid inclusion temperatures of  $180\text{--}280^\circ\text{C}$  and salinities of 9.4 wt% NaCl from the feeder zones below the Jason deposit (similar to Tom and situated 7km to the west).

It is noteworthy that the Vulcan deposit contains fluorite, which is more commonly found in Mississippi Valley-type deposits, and Morrow et al. (1978) have suggested that both shale- and carbonate-hosted stratiform barite deposits in the Selwyn Basin are genetically related and were formed from the same "oil-field brine" source fluids. This relationship is supported by lead isotope studies of these deposits (Godwin et al., 1982). Both shale-hosted and Mississippi Valley-type deposits also occur in close association in the McArthur River area, where they have also been attributed to the same mineralizing fluids (Williams, 1978; Rye and Williams, 1981).

The fluid inclusion results from the Silvermines, Vulcan and Jason deposits suggest that the mineralizing fluids which formed sedimentary exhalative deposits may have been as variable in composition as those in modern hydrothermal systems. Brine pools in the Red Sea deep are thought to have acquired their salt content

from hydrothermal circulation through underlying evaporite beds, and evaporites in the vicinity of carbonate-hosted deposits such as Pine Point, Canada (Hutchison, 1983) have been cited as the source for chloride-rich brines which transported the metals. A coastal sabkha environment was invoked by Renfro (1974) to explain the origin of the Zambian Copper Belt deposits, and the recognition of abundant evaporite pseudomorphs in the formations containing the McArthur River and Mt Isa deposits (Walker et al., 1977; McClay and Carlile, 1978) have led to interpretations involving sabkha processes for the fixation of metals by bacterial reduction of sulphate. However, the carbonaceous and sulphidic nature of the silica-enriched meta-sediments containing possible pseudomorphs of calcium sulphate crystals at Foss (part 10.3.3) suggests that they were unlikely to have formed in a tidal flat environment (cf. Anderton, 1975), and they are considered to have formed from pore waters derived from the overlying, hypersaline basinal seawater (cf. fig. 10.3).

#### 10.4.3.3 Temperature and origin of the hydrothermal fluids.

Fluid inclusion thermometric data from the carbonate-hosted, stratiform Mississippi Valley-type deposits suggests that they formed from substantially cooler hydrothermal fluids (typically 100-150°C: Cathles and Smith, 1983) than those which formed the clastic sediment-hosted deposits. The higher temperatures of these fluids could be attributed to several features: (a) a deeper plumbing system, discharging connate waters trapped at greater depths (5-12km) than those which formed Mississippi Valley-type deposits; (b) a higher heat flow due to distension of the underlying continental crust (note, however, that Andrews-Speed et al., 1984, have found extremely variable heat flows in the North Sea basin); (c) associated igneous activity including the intrusion of sills and extrusion of tuffs.

The comparison between the tectono-sedimentary setting and magmatic activity of the Gulf of California, and that of the Easdale Subgroup (section 5.5, and Graham and Borradaile, 1984), is noteworthy because Einsele et al. (1980) described evidence for the large-scale expulsion of heated pore waters associated with (and creating space for) shallow-level sill intrusion in the Guaymas Basin. These authors found that 20-45m thick sills had dewatered a similar thickness of surrounding sediment, and had heated the

expelled pore waters up to 400°C. The <10m thick metabasite sills constituting <5% of the mineralized zone at Foss are clearly not sufficiently voluminous to have directly generated the observed mineralization, and furthermore, metabasites are almost completely absent from the mineralized zone in the nearby, similarly-sized Ben Eagach deposit (see section 1.3). Magmatic activity accompanying the mineralization at Foss is therefore regarded as indicative of the prevailing high geothermal gradient and extensional tectonics, which are also manifested by the episodic expulsion of deep formation waters possibly further heated by sill or dyke intrusion at deeper levels in the sediment pile (fig. 10.4). A similar, indirect relationship between magmatic activity and the expulsion of metalliferous solutions was suggested by Lambert (1976) for the genesis of the McArthur River deposit.

Russell (1978 and 1983) and coauthors (Russell, Willan et al., 1981; Russell, Solomon & Walshe, 1981) have invoked a genetic model for sedimentary exhalative deposits which involves 'downward excavating' convection cells (fig. 10.3) driven by the elevated heat flow characteristic of thick sedimentary prisms infilling rifted continental crust. Pre-ore metal enrichments are attributed to the early, low temperature (<200°C) stage of shallow convection, but during the middle to late stages convection cells are considered to penetrate to depths of 10-15km and the circulating fluids (derived from the overlying seawater) become sufficiently hot (>250°C) to transport significant amounts (>1ppm) of copper. This may explain the concentration of Cu high in the stratigraphic sequence in the McArthur River group of deposits (Russell, Solomon & Walshe, 1981), although the reverse pattern is seen at Broken Hill, Australia (Plimer, 1979) and at Rammelsberg (Large, 1981a), and other deposits (including Foss) do not show a systematic distribution of copper content. According to this hypothesis, the hydrothermal system decays when the convection cells cannot penetrate deeper due to ductile deformation in the crystalline basement (Russell, 1978; Russell, Solomon & Walshe, 1981).

Extensive deep fluid penetration and hydrothermal transport systems have been recognised in the oceanic crust (e.g. Hajash, 1975; Hutchinson et al., 1980), and the convective circulation of

seawater above local 'hot spots' or intrusions can account for the formation of many volcanogenic massive sulphide deposits. However, the absence of such local heat sources, and the presence of discrete stacked lenses of mineralization suggesting the intermittent operation of major fluid-flow systems which formed many of the sedimentary-exhalative deposits, have recently led several authors to suggest an alternative genetic model involving the episodic expulsion of connate and deep formation waters (e.g. Badham, 1981; Carne and Cathro, 1982; Lydon, 1983; Sawkins, 1984; Whelan et al., 1984). This model has been widely suggested for the formation of Mississippi Valley-type lead-zinc deposits (e.g. Dunham, 1970; Dozy, 1970; Anderson and Macqueen, 1982; Cathles and Smith, 1983).

Shales and turbiditic lithologies, which are particularly common in epicratonic settings, can provide large amounts of connate fluids during compaction. As the weight of the overlying, rapidly deposited sediments increases, buried formations become over-pressured and therefore under-compacted. Fluids, including oil and gas, may also move into structural traps beneath impermeable strata. Intermittent movements of extensional faults cause the breaching of these traps and the sudden release of pressure, and the fluids may escape up the fault planes. The collapse of previously over-pressured sediments would also create local seafloor depressions favourable to sulphide accumulation adjacent to the surface traces of fault planes. This hypothesis seems more plausible than the large-scale convection theory, particularly to explain the generation of seven mineralized horizons at Foss which do not show a systematic trend of increasing size or metal content with stratigraphic height (fig. 10.5). The heterogeneity in lead isotope ratios within the Aberfeldy deposits (widely variable even in one short borehole intersection), also favours a dewatering model since large-scale seawater convection would be expected to generate hydrothermal fluids of relatively homogeneous isotopic composition. However, it is debatable whether sufficient connate water remains in buried formations at depths sufficiently great to have reached temperatures of  $>200^{\circ}\text{C}$ , even in a high heat-flow regime.



## 10.5 Other deposits in the Easdale Subgroup and potential for further exploration.

### 10.5.1 Historical review.

Prior to the discovery of the Aberfeldy deposits (Coats et al., 1978, 1980) investigations by the British Geological Survey under the Mineral Reconnaissance Programme identified a zone of disseminated, weakly cupriferous, pyritic mineralization which extends across the entire width of the Scottish Dalradian consistently at the base of the Farragon Beds volcanic sequence (Smith, Pitfield et al., 1977). This pyritic zone, which has been compared to the fahlbands of Scandinavia (Smith, 1981) and to Cyprus-type deposits (Graham and Bradbury, 1981), may be the product of upwelling metalliferous solutions generated by deep hydrothermal circulation associated with rifting and basic magmatism, as suggested by regional geochemical data (Plant et al., 1984).

More recent investigations by the B.G.S. have established the presence of a barium enriched horizon at the stratigraphic top of the Ben Eagach Schist near Loch Lyon, about 40km WSW of the Foss deposit (figs. 1.1 and 10.2), together with a zone of sphalerite-enriched quartzite lower in the same formation in Glen Lyon, and two stratigraphically higher sphaleritic quartzite horizons overlying the Ben Lawers Schist, further SW near Tyndrum (Smith et al., 1984; Coats et al., 1984b). Unfortunately these occurrences do not appear to be of economic significance, although the genesis of the sphaleritic horizons (exhalative or diagenetic-epigenetic) is presently unclear and their lateral extension is not fully explored.

These discoveries have highlighted the areal concentration of previously known mineral showings and worked deposits, some of vein type and others evidently stratiform (e.g. McPhun's Cairn and Meall Mor: fig. 10.8), within the outcrop of the Middle Dalradian Easdale Subgroup between Islay and the Aberfeldy district. Since much of this area is poorly exposed, and a few mineral showings and vein deposits (such as the Lecht Fe-Mn deposit south of Tomintoul) also occur in the Middle Dalradian of NW Scotland, the 500km strike-length of the Easdale Subgroup from Shetland to W Ireland is considered to have potential for further exploration (Willan, 1983; Smith et al., 1984; Coats et al., 1984b).

### 10.5.2 Exploration methods and targets.

A primary exploration method in Scotland has been the regional drainage geochemistry survey (cf. Plant and Moore, 1979; Coats et al., 1982), the results of which are available through the National Geochemical Data Bank. In addition to locating most previously known mineralization and several new occurrences (such as the Aberfeldy and Glen Lyon horizons), analysis of the regional geochemical data in relation to geological and geophysical information provides a foundation for models of Dalradian metallogenesis, and secondary exploration criteria for locating concealed mineralization (Plant et al., 1984). Geological reconnaissance and detailed follow-up drainage surveys at anomalous sites, have been followed by lithogeochemical and overburden sampling and geophysical surveys (particularly using Induced Polarization and VLF-EM techniques) to define drilling targets (Smith et al., 1984). An alternative approach to exploration within the favourable Middle Dalradian succession, based on long across-strike geophysical-geochemical traverses (Coats et al., 1984a), has proved valuable in identifying a "palaeohigh" in the vicinity of Loch Lyon which separates two second-order basins in the Ben Eagach Schist (fig. 10.2).

Considering the extensive 'halo' of Ba, Zn and Pb enrichment in graphitic schists surrounding the Aberfeldy deposits (figs. 2.2, 2.4; also Willan, 1981a), the recognition of similar lithogeochemical features elsewhere in Dalradian graphitic and calcareous schists would provide promising targets for further exploration (Willan, 1983). However, preliminary lithogeochemical analyses of the Ben Eagach Schist in the Glenshee, Glen Lyon and Loch Lyon areas have not located similar levels of barium or metal enrichment (Coats et al., 1984a, Table 3), despite the occurrence of a thin (1-2m) horizon of barium silicate mineralization (with minor matrix barite) at the top of the formation at Beinn Heasgarnich (fig. 10.2) (Coats et al., 1984b). The isotopically heavy sulphur of mixed hydrothermal-bacteriogenic origin, present in the stratiform mineralization and in disseminated sulphides in the host rocks at Foss and Ben Eagach, may also be a pathfinder for concealed, possibly large hydrothermal-exhalative deposits (cf. Willan, 1983). Further research into both lithogeochemical and isotopic variations in the along-strike extension of the Ben Eagach Schist is needed.

### 10.5.3 Suggested further sub-surface exploration at Foss.

From a detailed analysis of the distribution of mineralization in outcrop and drillcore (Chapter 2), it is suggested that further sub-surface exploration of the Foss deposit is warranted in three areas:

(1) The northern limb of the Creag na h-Iolaire Anticline in Foss West, where low-grade stratiform mineralization, at a stratigraphical level probably corresponding to the lower (M3) horizon, extends for some 350m along-strike in two fault-bounded blocks (fig. 2.4 and part 2.2.1). This may merely represent a distal part of the same, lenticular bed on the southern limb, which has been largely removed by erosion, but higher grade mineralization (probably sulphide-dominated) could be developed again at depth. This could be tested by two mid-depth (~100m) drillholes collared about 50m to the south of the outcrops at grid refs. 81220W 54950N (sample G100) and 81440W 55010N (G119) (cf. Coats et al., 1981, Table 8).

(2) The eastern block at Creagan Loch, in which high-grade base metal mineralization was intersected 20-50m below the surface in two drillholes (707 and 708), but appears to be absent at ~200m depth (DH 204) (fig. 2.32). Another mid-depth drillhole collared at 82800W 54990N and inclined at 50°N may establish the down-dip continuity of the M3 horizon, although potentially economic base metal reserves are unlikely to be developed in this narrow (110m strike-length) block (part 2.4.4).

(3) Deep intersections in Foss East indicate that potentially economic mineralization is absent at depth, but further reserves at depth are likely to be present in the western part of Foss West. This should be explored with two deep drillholes collared south of BHs 9 and 10 to intersect the mineralized zone (containing one, relatively thick barite bed) at depths of >300m below the surface (elevation <350m O.D.; figs. 2.12, 2.13).

### 10.6 Summary and suggestions for further research.

The following results from this investigation are considered to be of primary significance to the petrogenesis of the Foss deposit and its host rocks:

(1) The identification of petrographical, mineralogical and geochemical features which relate to sedimentary, diagenetic and metamorphic processes, and which elucidate the effects and conditions of metamorphism. Deformation, fluid infiltration and mineral reactions accompanying metamorphism resulted in widespread mass transfer of volatiles and alkaline elements, particularly sodium, whereas compositional and isotopic equilibrium domains in sulphides remained minute in some rocks. A variety of geobarometers and geothermometers utilising mineral equilibria in both mineralized and host rocks indicate peak P-T conditions of  $9 \pm 1$  kbar and  $530 \pm 30^\circ\text{C}$ . In conjunction with experimental studies, textural interpretations of cymrite-celsian equilibria enable the P-T path following peak metamorphism to be constrained.

(2) Despite the disruptive effects of several deformation episodes and post-metamorphic faulting, laterally continuous mineralized horizons or their distal equivalents can be correlated and primary variations in lithostratigraphy may be discerned. Rapid lateral thickness and facies changes in both mineralized strata and the host metasediments can be related to syndepositional tectonism and basinal development reflecting continental distension. The intermittent discharge of hot ( $>200^\circ\text{C}$ ), metalliferous formation waters from the underlying sediment pile is suggested to explain the generation of seven mineralized beds of unequal size and lateral extent. Volumetrically minor metabasite layers of eruptive (pyroclastic) and intrusive origin within the mineralized zone have an immobile-element petrochemistry indicative of a subcontinental source region, but subsequent more voluminous basaltic magmatism with ocean-floor affinities suggests incipient continental rifting.

(3) The integration of stratigraphical, geochemical and mineralogical studies to elucidate the mode of formation of the mineralization, and the recognition of features associated with proximity to hydrothermal vents. The chemical and isotopic composition of both the stratiform mineralization and the metasedimentary host rocks support the contention that the local marine basin was stratified with a basal, anoxic and alkaline brine layer beneath an upper layer of oxygenated seawater. The single, thick (up to 22m) barite bed in the Frenich Burn area is shown to represent an accumulation of precipitates from successive hydrothermal emanations separated by

periods of sedimentary reworking in a relatively shallow water, oxidized environment. In the Creagan Loch area, the mineralized horizons are separated by up to 100m of metasediments and the lenticular development of mineralized carbonate rocks and barite in the lower horizon, which pass laterally into sulphidic quartz celtsian cherts, is consistent with formation in a deeper water environment. Proximity to an exhalative centre is suggested by enrichment of the underlying sediments in silica, barium and sulphur, and by a restricted zone with unusually high Pb/Pb+Zn ratios which is associated with a coarse pyrite lens interpreted as a probable sulphide mound. Further east across a late metamorphic fault, sulphide-dominated mineralization incorporating a relatively high proportion of bacteriogenic sulphur and sedimentary material, and lacking bimodal sphalerite compositions, is considered to have formed in a relatively deep-water, euxinic basin which was possibly some distance from the exhalative site.

#### Suggestions for further research.

Further investigations could take two forms, namely (1) the application of different analytical techniques to the sampled material, and (2) application of the techniques used or developed in this study to other areas.

Full characterization of the several mineral species newly described from the Foss deposit, notably the barium carbonates (including possibly benstonite: part 7.5.3), barite (part 6.4.7) and ?crichtonite-group oxides (part 7.2.3), requires detailed XRD studies. The discovery of monazite in rocks of hydrothermal origin (section 7.6) raises the possibility that the mineralization could be more precisely dated by U/Pb geochronology, since this isotopic ratio is unlikely to have been reset during metamorphism. Considering the remarkable range of lead isotope ratios in galena from the Aberfeldy deposits, even within a single borehole intersection (Swainbank et al., 1981), considerable scope exists for further radiogenic isotope studies which may provide supporting evidence for the basinal dewatering model of ore genesis (part 10.4.3). There is also scope for further sulphur isotope studies, particularly to ascertain large-scale lateral variations using bulk samples of barite from correlated mineralized beds in different parts of the deposit.

The application of techniques used in this study to the nearby Ben Eagach deposit (part 1.3.4) would be of considerable interest. Previously published data on this deposit may give a biased representation, particularly with regard to the distribution of sulphur isotope values (part 9.6.4). A detailed comparison of lithostratigraphical successions is required to correlate exhalative events between the two deposits, since a much greater thickness (>200m) of metasediment is present between the lower and upper horizons at Ben Eagach and a metabasite marker bed is not found beneath the lower horizon. Such a study would clarify the spatial relationships between the distribution and composition of the stratiform mineralization and the locus of synsedimentary faults (S.J. Laux, pers. comm.), which are partially obscured in the Foss deposit by more extensive tectonic disruption.

--°o0o°--

Table 10.1: Stratigraphical features and metal contents of selected sedimentary exhalative deposits†.

Deposit, location	Sedimentary host rocks (mineralized zone)		Stratiform mineralization no. of horizons	lithologies	Contained metal*, barite			
	thick- ness (m)	lithologies			Mt Zn Pb		Kt Ag	Mt ore barite
Gamsberg, South Africa	60 (<150)	diverse qtz feldspar gt pyroxene rocks with overlying barite & magnetite rocks	1	graphitic qtz sillimanite musc schist & qtz gt amphibole rock, both with up to 50% sulphides	10.6	0.8	?	not given; 1.5-2.5m thick
Mount Isa, Australia	650	dolomitic shales and siltstones, minor evaporites, thin tuffs	28	finely laminated sulphides in Pb Zn stratiform facies	5.6	6.1	13	-
McArthur, Australia	130	carbonaceous silty dolomite rock; minor sandstone, shale; abundant evaporitic units; thin tuffs	8	finely laminated and bedded sulphides	18.0	7.6	7.6	-
Sullivan <sup>a</sup> , B.C., Canada	80	shale with pyrrhotite laminae, fine-grained quartz wackes	8	finely laminated and massive Fe Pb Zn sulphides	8.8	10.2	10.5	-
Rammelsberg, W. Germany	25	pyritic black shales, minor silt- stone and sandstone	3	Cu Zn Pb Fe sulphides and barite as laminated and massive ore	4.2	2.0	2.6	0.2
Meggen, W. Germany	6-7	grey & black shales, bituminous and fossiliferous limestones	1	laminated, lenticular and nodular sulphides and barite in shale	5.0	0.7	0.15	10
Tom, Yukon, Canada	50-150	grey siltstone and pyritic carbon- aceous shales; basal conglomerate	2	finely laminated barite and Pb Zn sulphides, minor pyrite	0.8	0.8	0.75	several?
Silvermines, Ireland	90-300	dolomitic shales, biomicrite, "reef" limestone breccias and chert	2	laminated sulphides and laterally equivalent barite rock (Macgobar)	1.2	0.4	0.4	2.5

† Information mainly from Large (1981a) and Sawkins (1984); Gamsberg data from Rozendaal & Stumpfl (1985).

\* Prior to mining. Mt = millions of tonnes; Kt = thousands of tonnes.

<sup>a</sup> Stratigraphical information refers to east part of the orebody.

**TABLE 10.2: Characteristic features associated with sedimentary exhalative, stratiform Pb-Zn-Ba deposits (from Large, 1980), and recognised in the Foss deposit.**

Characteristic feature	Foss deposit
(1) First order basin (several 100km in size) interpreted as epicratonic or intra-cratonic in type.	Dalradian basin containing Appin and lower Argyll Group clastic sediments, carbonates and minor tholeiitic volcanics (Harris et al., 1978; Graham and Bradbury, 1981; Russell et al., 1981).
(2) Second order basin (several 10km in size) formed by synsedimentary vertical tectonism and bounded by lineaments and hinge zones.	Fault controlled basin subsidence leading to deep-water sedimentation in mid-Argyll times (Anderton, 1979). Decreasing psammitic content of Ben Eagach Schist west from Ben Vrackie (Coats et al., 1980). No obvious lineament in the vicinity of Foss, unless represented by major fold closure (the Creag na h-Iolaire Anticline ?).
(3) Local development of third order basins (100m to several km in size) with euxinic environments, bounded by growth faults.	Rapid lateral thickening of metasediments (including turbiditic quartzites and dolostones) within the mineralized zone at Creagan Loch, coinciding with increase in coarse sediments and in base metal sulphide mineralization in M3. Growth fault in the vicinity becomes inactive by time M5 deposited?
(4) Minor igneous activity contemporaneous with mineralization: usually forms thin tuffite horizons and minor intrusives.	Thin (2cm-1m), extensive metabasic horizon of probable tuffaceous origin, used as marker bed at base of M3. Less widespread, thicker (<10m) metabasites were probably intrusive sills emplaced in semi-lithified sediment.
(5) Contemporaneous stratiform sulphide, barite and hydrothermal chert deposition.	Illustrated by distribution and facies variations in seven correlated mineralized horizons, with distal chert beds and barium-enriched metasediments. Contemporaneous barite & sulphidic chert deposition clearly demonstrated by lateral variations in M3 at Creagan Loch.
(6) Distinctive vertical and/or lateral element zonation in the ore beds and anomalous halo in the host sediments.	Little evidence for element zonation except for increase in Pb/Zn associated with locus of growth fault at Creagan Loch. Mineralization facies related to basin depth and proximity to vents. Extensive dispersion of K, Ba, Zn, Pb, Mn & S in unit B of the Ben Eagach Schist (cf. Willan, 1981).
(7) Characteristic alteration, normally silicification, of footwall sediments. Underlying or subjacent stockwork mineralization (feeder zone).	Pyritic, graphitic quartz-hyalophane cherts locally developed beneath some mineralized horizons, or as lateral equivalents to others. Associated barian muscovite schists indicate diagenetic enrichment in barium. No evidence for a feeder zone, but sulphide lens intersected in DH 705 is probably a hydrothermal mound.
(8) Homogeneous lead isotope signature that is nearly conformable with the lead growth-curve.	Pb isotope data (Swainbank and Fortey, 1981) suggests two major components, i.e. magmatic and old 'Lewisian' lead with a significant spread of model ages (600-450ma). Lead is less radiogenic than in other sedimentary exhalative deposits (work in progress).
(9) Sulphur isotope values indicative of a dual source of sulphur; a deep-seated source for galena- and sphalerite-S, and contemporaneous seawater sulphate for barite and most pyrite-S (derived from seawater sulphate by bacteriogenic reduction).	Barite-S ranges from +27 to +42‰, mode = 34-35‰ (data of Willan and Coleman, 1983, and this study) indicating deviation from late Precambrian seawater. Ratios of <33‰ attributed to oxidation of bacterial and/or hydrothermal reduced sulphur; ratios of >37‰ due to closed system, diagenetic fractionation. Sulphides range from +13 to +29‰ but ratios of 20-25‰ are typical of the mineralization; the low $\Delta^{34}\text{S}$ sulphate-sulphide (~12‰) and other features suggest that a hydrothermal source for much of the sulphide-S is likely, although evidence for a dual source may have been obscured by millimetre-scale equilibration during metamorphism. Brine pool sulphide mineralization and disseminated sulphides in metasediments adjacent to the mineralized beds probably incorporate a mixture of hydrothermal and bacteriogenic reduced sulphur ( $\delta^{34}\text{S} = 13-20\text{‰}$ ).



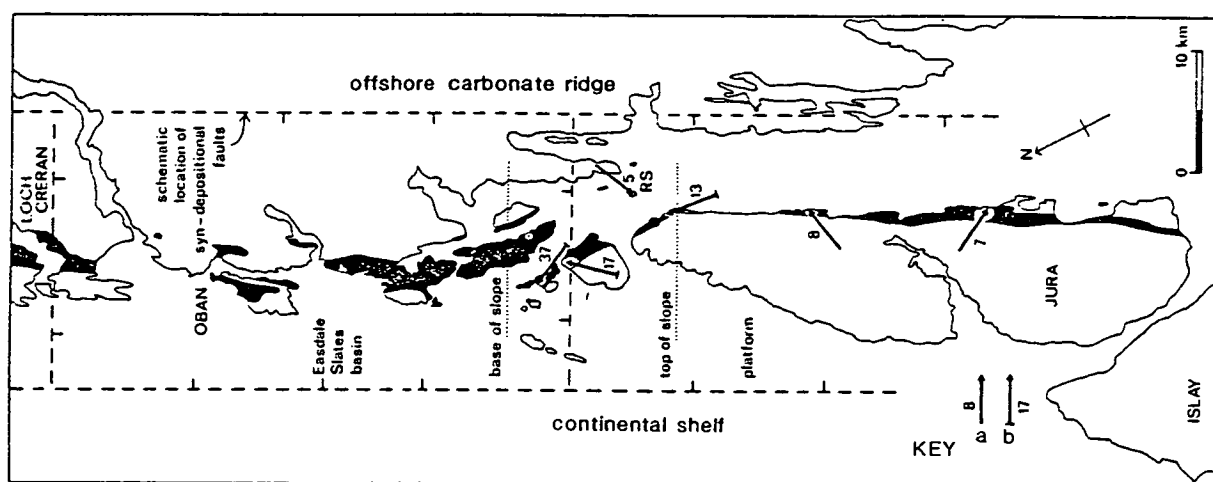
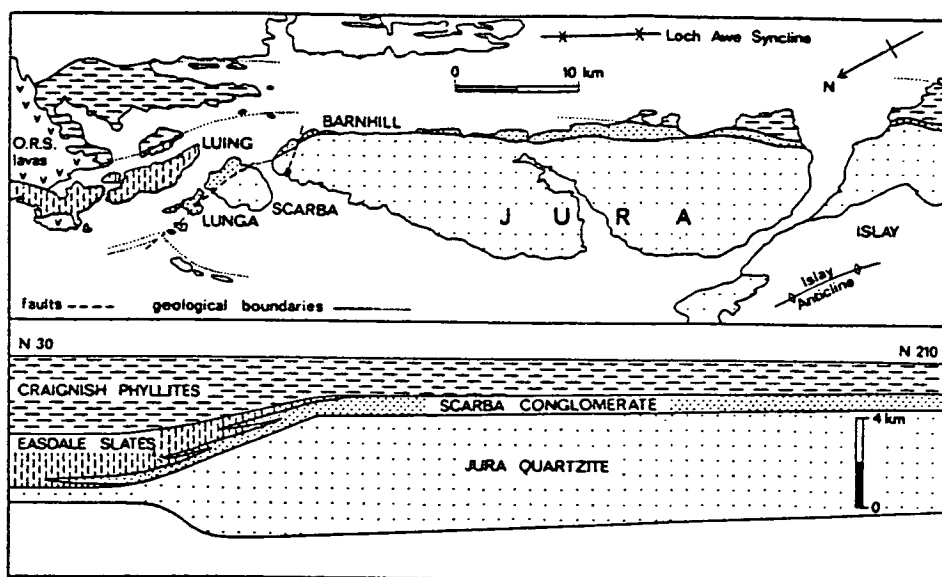


**Fig. 10.1:** Geological map and stratigraphical section of the Middle Dalradian succession in western Argyll (top), and palaeogeographical interpretation with location of syndepositional faults during Scarba Conglomerate/Easdale Slates times (bottom), from Anderton (1979). KEY: vectors show a, palaeocurrent and b, palaeoslope measurements, with number of measurements per locality in each case.

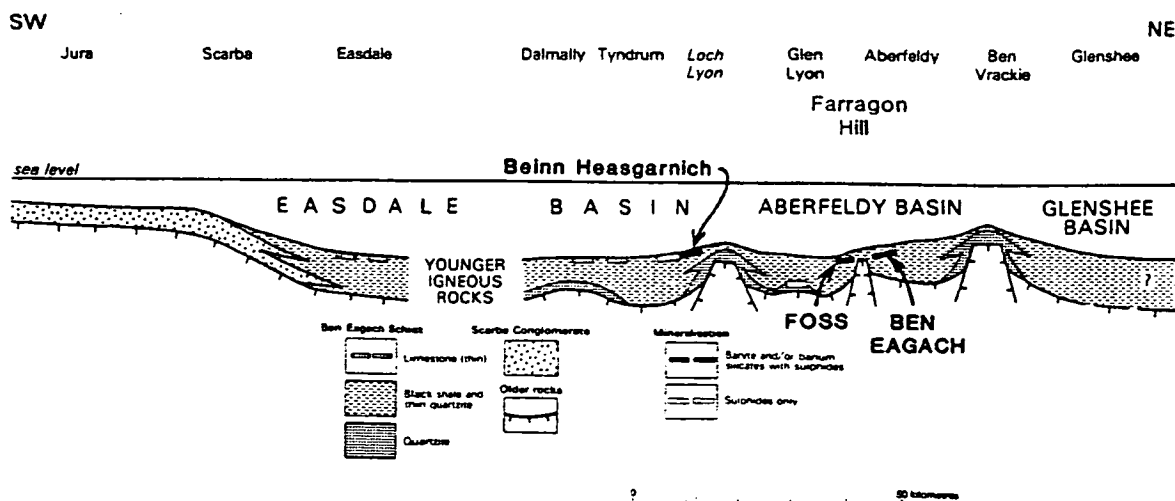


**Fig. 10.2:** Schematic longitudinal section of the Middle Dalradian between Jura and Glenshee during Ben Eagach Schist times, showing positions of inferred second-order basins, from Coats et al. (1984b).

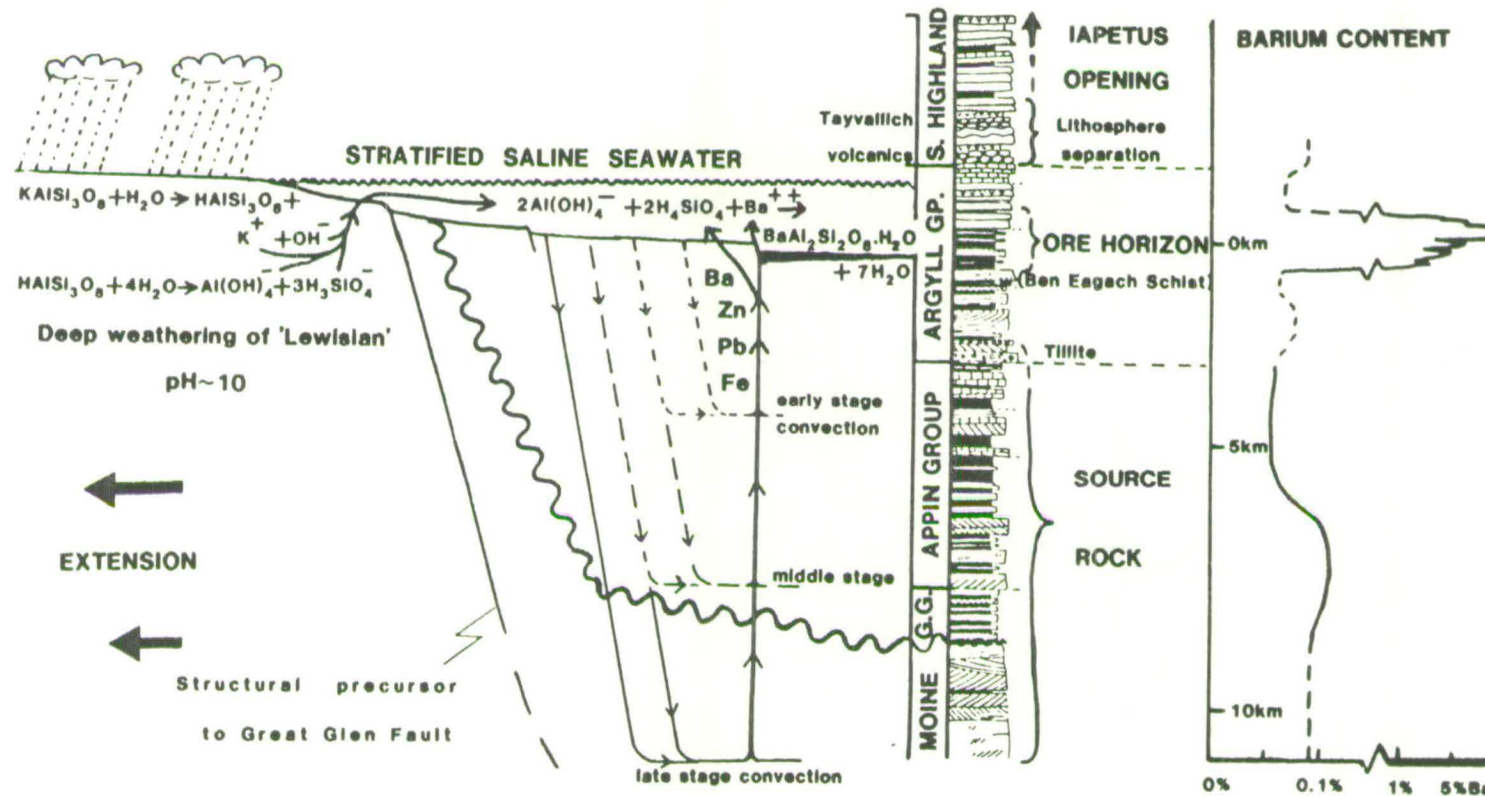
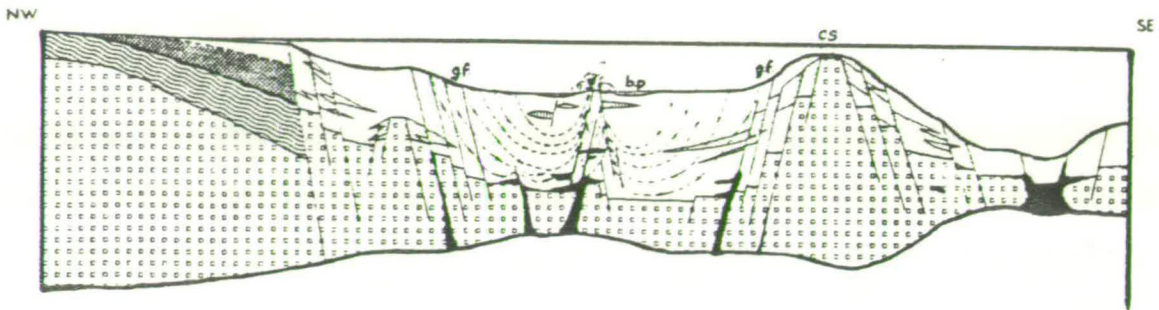
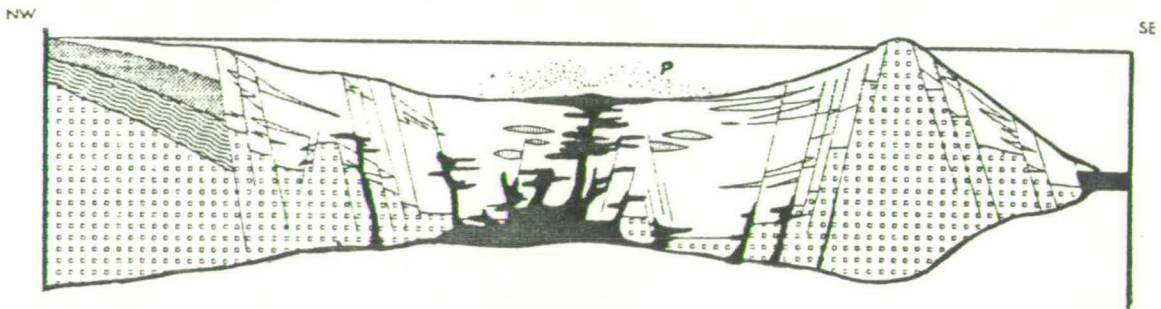


Fig. 10.3: Seawater convection model for the genesis of the Aberfeldy deposits with particular reference to the formation of cymrite or its precursor, from Russell et al. (1984). Note extreme vertical exaggeration. GG = Grampian Group (see fig. 1.4).

## a. Argyll Group ( Easdale Subgroup )



## b. Southern Highland Group



"Young Moines"  
 "Old Moines"  
 Lewisian basement

Dairadian {  
 Basic igneous rocks and ocean-floor basalts  
 Stratobound mineral deposits  
 Coarse clastic sediments (beach submarine fan and turbidite)  
 Dairadian sediments (undifferentiated)  
 Connecting fluid paths

**Fig. 10.4:** NW-SE sections (with vertical exaggeration) showing inferred structural settings of the Dalradian during Easdale Subgroup and Southern Highland Group times, from Plant et al. (1984). Dilational tectonism is envisaged as accompanying convective circulation of seawater (a), before shallow-level intrusion and extrusion of basaltic magmas (b) coincident with opening of the Iapetus Ocean to the SE. [Abbreviations: bp, brine pools; cs, carbonate shelf; gf, growth faults; p, pyroclastics].

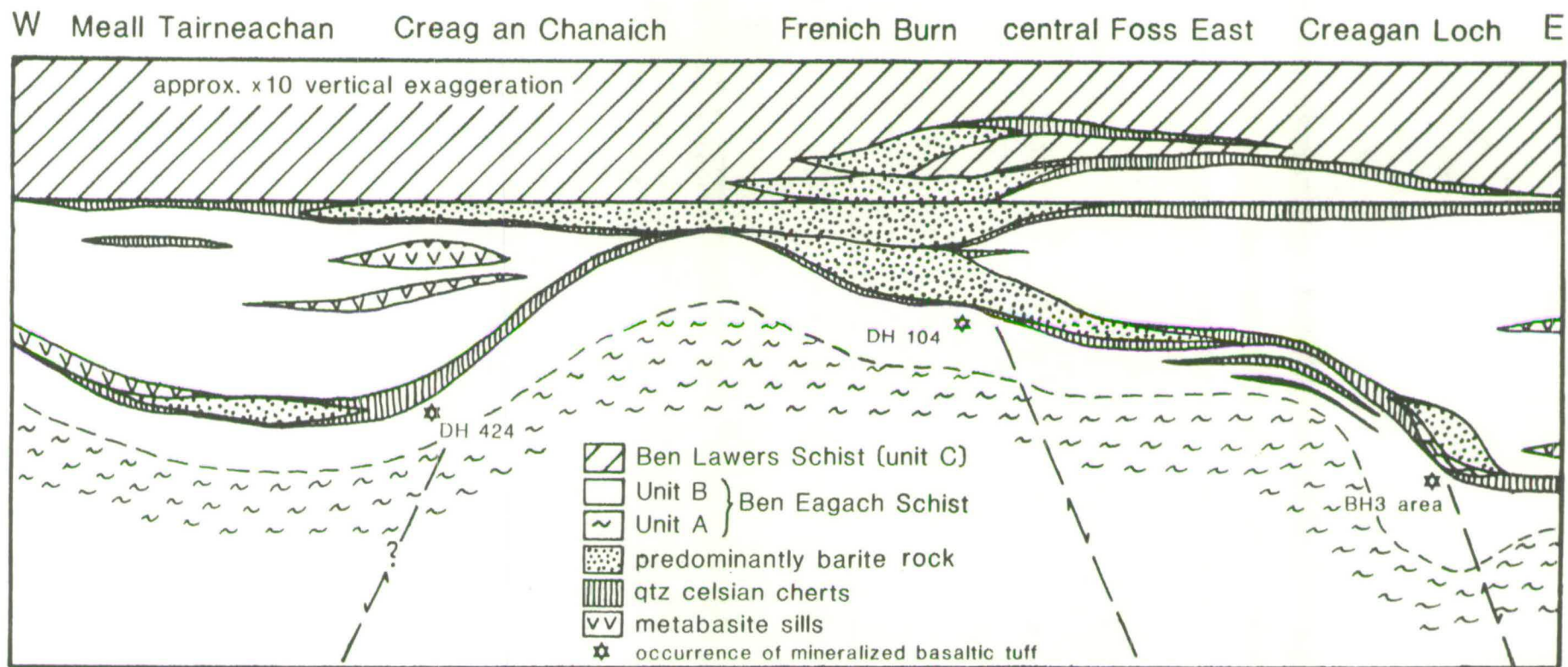


**Fig. 10.5:** Simplified, schematic cross-section of the Foss deposit showing distribution of stratiform mineralization and postulated growth faults active during late Ben Eagach Schist times.



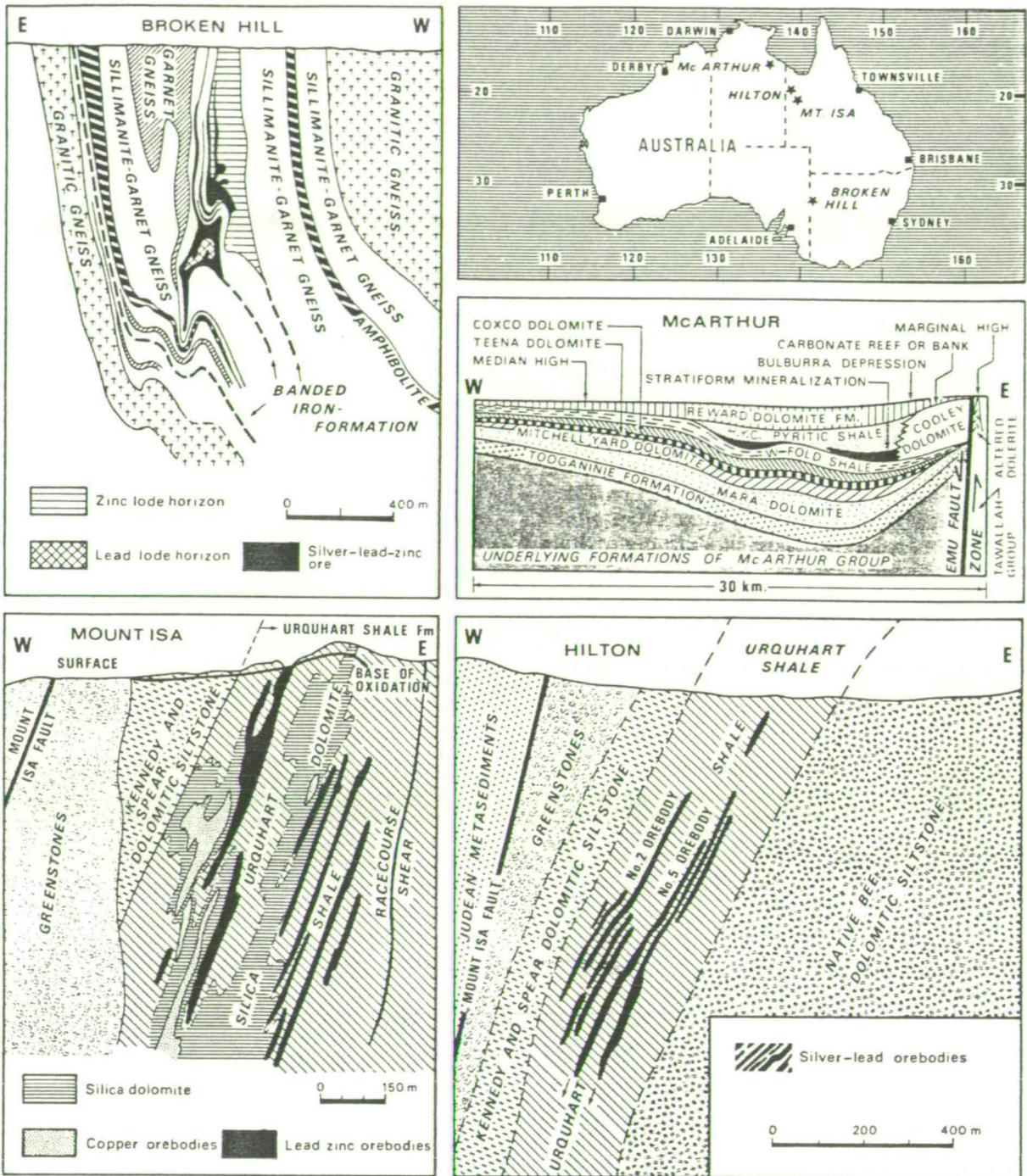


Figure 10.6. The great Australian Proterozoic stratiform ore bodies. Schematic cross-section through the McArthur area of the Northern Territory (after Lambert, 1976). Cross-section of the Hilton deposit of Queensland (after Mathias and Clark, 1975). Cross-section of the Mount Isa mine (after Bennett, 1965). Cross-section of the Broken Hill mine (after Both and Rutland, 1976) from Hutchison, 1983.



Fig. 10.7: Schematic cross-section of the Tom stratiform Pb-Zn-barite deposit, Yukon (modified from Carne, 1979)

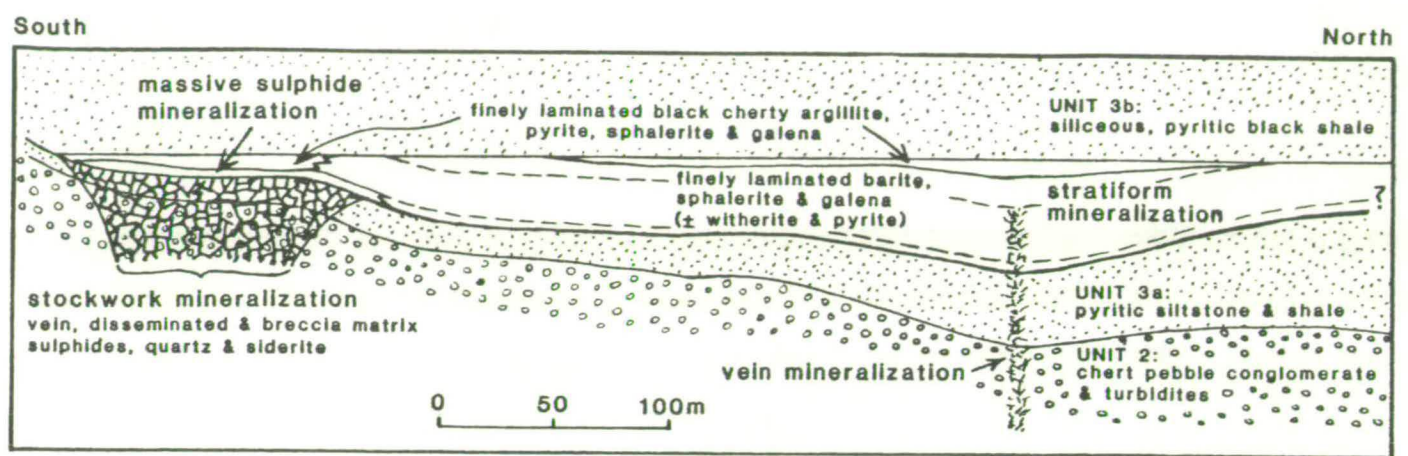


Fig. 10.8: Distribution of stratabound and vein-type mineralization in the Dalradian of the Grampian Highlands and Shetland (inset), from Smith et al. (1984).

# REFERENCES.

- Abbey, S. (1983) Studies in "standard samples" of silicate rocks and minerals. Geol. Surv. Canada, Paper 83-15.
- Addy, S.K. and Ypma, P.J.K. (1977) Origin of the massive sulfide deposits at Ducktown, Tennessee: an oxygen, carbon and hydrogen isotope study. Econ. Geol. 72, 1245-1268.
- Altaner, S.P., Hower, J., Whitney, G. and Aronson, J.L. (1984) Model for K-bentonite formation: Evidence from zoned K-bentonites in the disturbed belt, Montana. Geology 12, 412-415.
- Anderson, A.T. (1967) The dimensions of oxygen isotope equilibrium attainment during prograde metamorphism. J. Geol. 75, 323-332.
- Anderson, G.M. (1973) The hydrothermal transport and deposition of galena and sphalerite near 100°C. Econ. Geol. 68, 480-492.
- Anderson, G.M. (1975) Precipitation of Mississippi Valley-type ores. Econ. Geol. 70, 937-942.
- Anderson, G.M. and MacQueen, R.W. (1982) Ore deposits models - 6. Mississippi Valley type lead-zinc deposits. Geoscience Canada 9, 108-117.
- Anderton, R. (1975) Tidal flat and shallow marine sediments from the Craigish phyllites, Middle Dalradian, Argyll, Scotland. Geol. Mag. 112, 337-348.
- Anderton, R. (1979) Slopes, submarine fans, and syn-depositional faults: sedimentology of parts of the Middle and Upper Dalradian in the SW Highlands of Scotland. In Harris, A.L., Holland, C.H. and Leake, B.H. (eds.) 'The Caledonides of the British Isles - reviewed'. Geol. Soc. London 483-488.
- Anderton, R. (1982) Dalradian deposition and the late Precambrian-Cambrian history of the N Atlantic region: a review of the early evolution of the Iapetus Ocean. J. geol. Soc. London 139, 421-431.
- Andreae, M.O. (1974) Chemical and stable isotope composition of the high-grade metamorphic rocks from the Arendal area, southern Norway. Contrib. Mineral. Petrol. 47, 299-316.
- Andrews-Speed, C.P., Oxburgh, E.R. and Cooper, B.A. (1984) Temperatures and depth-dependant heat flow in the western North Sea. Amer. Assoc. Petrol. Geol. 68, 1764-1781.
- Anger, G., Nielsen, H., Puchelt, H. and Rieke, W. (1966) Sulphur isotopes in the Rammelsberg ore deposit (Germany). Econ. Geol. 61, 511-536.
- Arima, M. and Edgar, A.D. (1981) Substitution mechanisms and solubility of titanium in phlogopites from rocks of probable mantle origin. Contrib. Mineral. Petrol. 77, 288-295.
- Atherton, M.P. (1977) The metamorphism of the Dalradian rocks of Scotland. Scott. J. Geol. 13, 331-370.
- Atherton, M.P. and Brotherton, M.S. (1972) The composition of some kyanite-bearing regionally metamorphosed rocks from the Dalradian. Scott. J. Geol. 8, 203-213.
- Atherton, M.P. and Brotherton, M.S. (1982) Major element composition of the pelites of the Scottish Dalradian. Geol. Journal 17, 185-221.
- Atherton, M.P. and Smith, R.A. (1979) Chloritoid-staurolite assemblages from Barrow's Zones in Central Perthshire, Scotland. Geol. Mag. 116, 469-476.
- Black, P.M. (1974) Oxygen isotope study of metamorphic rocks from the Ouegoa District, New Caledonia. Contrib. Mineral. Petrol. 47, 197-206.

- Backinski, D.J. (1969) Bond strength and sulfur isotope fractionation in coexisting sulfides. *Econ. Geol.* 64, 56-65.
- Backinski, D.J. (1977) Sulfur isotopes in ophiolitic cupriferous iron sulfide deposits, Notre Dame Bay, Newfoundland. *Econ. Geol.* 72, 243-257.
- Badham, J.P.N. (1981) Shale-hosted Pb-Zn deposits: products of exhalation of formation waters? *Trans. Inst. Mining Metall.* 90, B70-B76.
- Bailey, E.B. (1910) Recumbent folds in the schists of the Scottish Highlands. *Q. Jl. geol. Soc. London* 66, 586-608.
- Bailey, E.B. (1925) Perthshire Tectonics: Loch Tummel, Blair Atholl and Glen Shee. *Trans. R. Soc. Edinb.* 53, 671-698.
- Baker, A.J. (1985) Pressures and temperatures of metamorphism in the easter Dalradian. *J. geol. Soc. London* 142, 137-148.
- Barton, P.B.Jr. (1970) Sulphide Petrology. *Mineral. Soc. Amer. Spec. Pap.* 3, 187-198.
- Berry, W.J.N. and Wilde, P. (1978) Progressive ventilation of the oceans - an explanation for the distribution of the lower Palaeozoic black shales. *Am. J. Sci.* 278, 257-275.
- Bethune, P.de, Laduron, D. and Bocquet, J. (1975) Diffusion processes in resorbed garnets. *Contrib. Mineral. Petrol.* 50, 197-204.
- Bickle, M.J. and Powell, R. (1977) Calcite-dolomite geothermometry for iron-bearing carbonates: the Glockner area of the Tavern Window, Austria. *Contrib. Mineral. Petrol.* 59, 281-292.
- Bjorlykke, K.O. and Griffin, W.L. (1973) Barium feldspars in Ordovician sediments, Oslo region, Norway. *J. Sed. Petrol.* 43, 461-465.
- Bjorlykke, K.O. and Englund, J.O. (1979) Geochemical response to Upper Pre-Cambrian rift basin sedimentation and Lower Palaeozoic epicontinental sedimentation in South Norway. *Chem. Geol.* 27, 271-295.
- Black, Philippa M. (1974) Oxygen isotope study of metamorphic rocks from the Ouega District, New Caledonia. *Contrib. Mineral. Petrol.* 47, 197-206.
- Boast, A.M. (1978) A textural and isotopic study of Irish base metal mineralization of lower Carboniferous age, with specific reference to the Tynagh deposit. Unpubl. Ph.D. thesis, London Univ.
- Boast, A.M., Coleman, M.L. and Halls, C. (1981) Textural and stable isotopic evidence for the genesis of the Tynagh Base Metal deposit, Ireland. *Econ. Geol.* 76, 27-55.
- Boctor, N.Z. (1980) Sphalerite geobarometry in Bodenmais ore, Bavaria. *Amer. Mineral.* 65, 1031-1037.
- Boles, J.R. (1977) Zeolites in deep-sea sediments. In Mumpton, F.A. (ed.) 'Mineralogy and geology of natural zeolites.' *Mineral. Soc. Am. short course notes*, 4, 137-163.
- Borradaile, G.J. (1979) Strain studies of the Caledonides in the Islay region, S.W. Scotland: implications for strain histories and deformation mechanisms in greenschists. *J. geol. Soc. London* 136, 77-89.
- Bottinga, Y. (1969) Calculated fractionation factors for carbon and hydrogen isotope exchange in the system calcite-carbon dioxide-graphite-methane-hydrogen-water vapour. *Geochim. Cosmochim. Acta* 33, 49-64.
- Bowie, S.H.U., Dawson, J., Gallagher, M.J., Ostle, D., Lambert, R.St.J. and Lawson, R.I. (1966) Potassium rich sediments in the Cambrian of NW Scotland. *Trans. Inst. Mining Metall.* 75, B125-B145.
- Boyce, A.J., Coleman, M.L. and Russell, M.J. (1983) Formation of fossil hydrothermal chimneys from Silvermines, Ireland, by reaction of hydrothermal iron with bacteriogenic brine-pool sulphide. *Inst. Geol. Sci. Stable Isotope Report no.* 93.



- Boyce, A.J., Anderton, R. and Russell, M.J. (1983) Rapid subsidence and early Carboniferous base-metal mineralization in Ireland. *Trans. Instn. Mining Metall.* 92, 855-866.
- Bradbury, H.J. (1979) Stratigraphic, structural, igneous and metamorphic history of the Dalradian rocks of the Ben Vrackie - Ben Vuirich district, Tayside. Ph.D. thesis, University of Liverpool.
- Bradbury, H.J., Smith, R.A. and Harris, A.L. (1976) 'Older' granites as time markers in Dalradian evolution. *J. geol. Soc. Lond.* 132, 677-684.
- Bradbury, H.J., Harris, A.L. and Smith, R.A. (1979) Geometry and emplacement of nappes in the Central Scottish Highlands. In Harris, A.L., Holland, C.H. and Leake, B.H. (eds) 'The Caledonides of the British Isles - reviewed' *Geol. Soc. London*, 8, 213-220.
- Brown, E.H. (1969) Some zoned garnets from the greenschist facies. *Am. Mineral.* 54, 1662-1677.
- Bubela, B. and McDonald, J.A. (1969) Formation of banded sulphides: metal iron separation and precipitation by inorganic and microbial sources. *Nature* 221, 465-466.
- Butler, B.C.M. (1967) Chemical study of minerals from the Moine Schists of the Ardnamurchan area, Argyllshire, Scotland. *J. Petrol.* 8, 233-267.
- Buyce, M.R. and Friedman, G.M. (1975) Significance of authigenic K-feldspar in Cambrian-Ordovician carbonate rocks of the proto-Atlantic shelf in North America. *J. Sed. Petrol.* 45, 808-821.
- Campbell, F.A. and Ethier, V.G. (1983) Environment of deposition of the Sullivan orebody. *Mineralia Deposita* 18, 39-55.
- Carne, R.C. (1976) The Tea barite deposit. Dept. Indian and Northern Affairs, EGS 1976-16, 20-31.
- Carne, R.C. (1979) Geological setting and stratiform mineralisation: Tom Claims, Yukon Territory. Dept. Indian and Northern Affairs, EGS 1979-4, 30pp: Whitehorse.
- Carne, R.C. and Cathro, R.J. (1982) Sedimentary exhalative (sedex) zinc-lead-silver deposits, northern Canadian Cordillera. *Can. Mining Metall. Bull.* 75, 66-75.
- Carr, G.R. and Smith, J.W. (1977) A comparative isotopic study of the Lady Loretta Zn-Pb-Ag deposit. *Mineralia. Deposita.* 12, 105-110.
- Carron, M.K., Mrose, M.E. and Reiser, A.N. (1964) New data on cymrite, a hydrated silicate of barium and aluminium (abstract). *Geol. Soc. Am. Spec. Pap.* 82, p. 26.
- Cathles, L.M. and Smith, A.T. (1983) Thermal constraints on the formation of Mississippi Valley-type lead-zinc deposits and their implications for episodic basin dewatering and deposit genesis. *Econ. Geol.* 78, 983-1002.
- Cecile, M.P., Shakur, M.A. and Krouse, H.R. (1983) The isotopic composition of western Canadian barites and the possible derivation of oceanic sulphate  $\delta^{34}\text{S}$  and  $\delta^{18}\text{O}$  age curves. *Can. J. Earth Sci.* 20, 1528-1535.
- Chang, L.L.Y. (1964) Syntheses of  $\text{MBa}(\text{CO}_3)_2$  compounds. *Am. Mineral.* 49, 1142-1143.
- Chatterjee, N.D. and Froese, E. (1975) A thermodynamic study of the pseudo-binary join margarite-paragonite in the system  $\text{KAlSi}_3\text{O}_8\text{-Al}_2\text{O}_3\text{-SiO}_2\text{-H}_2\text{O}$ . *Am. Mineral.* 60, 985-993.
- Chinner, G.A. (1966) The distribution of pressure and temperature during Dalradian metamorphism. *Q.J. geol. Soc. Lond.* 122, 159-186.
- Chinner, G.A. (1973) Metamorphic index minerals in the eastern Dalradian (discussion). *Scott. J. Geol.* 9, 248-249.

- Chopin, C. and Maluski, H. (1980)  $^{40}\text{Ar}$ - $^{39}\text{Ar}$  dating of high pressure metamorphic micas from the Paradisco Area (Western Alps): evidence against the blocking temperature concept. *Contrib. Mineral. Petrol.* 74, 109-122.
- Claypool, G.E., Holser, W.T., Kaplan, I.R., Sakai, H. and Zak, I. (1980) The age curves of sulphur and oxygen isotopes in marine sulphate and their mutual interpretation. *Chem. Geol.* 28, 199-260.
- Coats, J.S., Smith, C.G., Fortey, N.J., Gallagher, M.J., May, F. and McCourt, W.J. (1978) Stratabound barium-zinc mineralisation in Dalradian schist near Aberfeldy, Scotland: Preliminary report. *Inst. Geol. Sci. Mineral Recon. Prog. Report No. 26*.
- Coats, J.S., Smith, C.G., Fortey, N.J., Gallagher, M.J., May, F. and McCourt, W.J. (1980) Strata-bound barium-zinc mineralization in Dalradian schist near Aberfeldy, Scotland. *Trans. Inst. Mining Metall.* 89, B110-B122.
- Coats, J.S., Smith, C.G., Gallagher, M.J., May, F., McCourt, W.J., Parker, M.E. and Fortey, N.J., (1981) Stratabound barium-zinc mineralization in Dalradian schist near Aberfeldy, Scotland: Final report. *Inst. Geol. Sci. Mineral. Recon. Prog. Report No. 40*.
- Coats, J.S. and others (1982) Geochemical drainage survey of central Argyll, Scotland. *Inst. Geol. Sci. Mineral Recon. Prog. Report No. 50*.
- Coats, J.S., Pease, S.F. and Gallacher, M.J. (1984a) Exploration of the Scottish Dalradian. In 'Prospecting in areas of glaciated terrain', London, *Inst. Mining Metall.*, 21-34.
- Coats, J.S., Fortey, N.J., Gallacher, M.J. and Grout, A. (1984b) Stratiform barium enrichment in the Dalradian of Scotland. *Econ. Geol.* 79, 1585-1595.
- Coleman, M.L. (1980) Corrections for mass spectrometer analysis of  $\text{SO}_2$ . *Inst. Geol. Sci. Stable Isotope Report No. 65*.
- Coleman, M.L. and Moore, M.P. (1978) Direct reduction of sulphates to sulphur dioxide for isotopic analysis. *Anal. Chem.* 50, 1594-1595.
- Conway, E.J. (1945) Mean losses of Na, Ca, etc. in one weathering cycle and potassium removal from the ocean. *Am. J. Sci.* 243, 583-598.
- Corliss, J.B., Dymond, J., Gordon, L.I., van Herjen, R.P., Ballard, R.D., Green, K., Williams, D., Bainbridge, A., Crane, K. and van Andel, T. (1979) Submarine thermal springs on the Galapagos rift. *Science* 203, 2073-2083.
- Costa, U.R., Barnett, R.L. and Kerrich, R. (1983) The Mattagami Lake Mine Archean Zn-Cu sulphide deposit, Quebec: Hydrothermal coprecipitation of talc and sulphides in a sea-floor brine pool - evidence from geochemistry,  $^{18}\text{O}/^{16}\text{O}$ , and mineral chemistry. *Econ. Geol.* 78, 1144-1203.
- Costa, U.R., Fyfe, W.S., Kerrich, R. and Nesbitt, H.W. (1980) Archaean hydrothermal talc evidence for high ocean temperatures. *Chem. Geol.* 30, 341-349.
- Craig, J.R. and Scott, S.D. (1974) Sulfide phase equilibria. In Ribbe, P.H. (ed.) *Short Course Notes 1: Sulfide Mineralogy*. Mineral. Soc. Am.
- Craig, J.R. and Vaughan, D.J. (1981) 'Ore microscopy and ore petrography.' Wiley, New York, 406pp.
- Crawford, M.L. (1974) Calcium zoning in almandine: a model based on plagioclase equilibria. In Mackenzie and Zussman (eds.) 'The feldspars'. Manchester Univ. Press, 629-644.

- Crawford, M.L. (1966) Composition of plagioclase and associated minerals in some schists from Vermont, U.S.A. and South Westland, New Zealand, with inferences about the peristerite solvus. *Contrib. Mineral. Petrol.* 13, 269-294.
- Crerar, D.A., Susak, H.J., Borcsik, M. and Schwartz, S. (1978) Solubility of the buffer assemblage pyrite + pyrrhotite + magnetite in NaCl solutions from 200 to 350°C. *Geochim. Cosmochim. Acta* 42, 1427-1439.
- Croxford, N.J.W. (1964) Origin and significance of volcanic potash rich rocks from Mount Isa. *Trans. Inst. Mining Metall.* 74, B133-B143.
- Czamanske, G.K. and Rye, R.O. (1974) Experimental determinations of the sphalerite-galena sulfur isotope fractionations. *Econ. Geol.* 69, 17-25.
- Davis, J.C. (1973) 'Statistics and Data Analysis in Geology'. Wiley, New York, 560pp.
- Deer, W.A., Howie, R.A. and Zussman, J. (1962a) Rock-forming minerals: Vol. 3 Sheet silicates. Longmans, London.
- Deer, W.A., Howie, R.A. and Zussman, J. (1962b) Rock-forming minerals: Vol. 5, Non-silicates. Longmans, London.
- Deer, W.A., Howie, R.A. and Zussman, J. (1962c) Rock-forming minerals: Vol. 1, Ortho- and ring-silicates. Longmans, London.
- Deer, W.A., Howie, R.A. and Zussman, J. (1963) Rock-forming minerals: Vol. 4, Framework silicates. Longmans, London.
- Deer, W.A., Howie, R.A. and Zussman, J. (1966) Rock-forming minerals: Vol. 2, Chain Silicates. Longmans, London.
- Deines, P. (1970) Mass spectrometer correction factors for determination of small isotopic variations of carbon and oxygen. *Inst. J. Mass Spectrom. Ion. Phys.* 4, 283-295.
- Dempster, I.J. (1983) Studies of orogenic evolution in the Scottish Dalradian. Ph.D. thesis, University of Edinburgh.
- Dempster, I.J. (1985) Uplift patterns and orogenic evolution in the Scottish Dalradian. *J. geol. Soc. London* 142, 111-128.
- Dewey, J.F. (1982) Plate tectonics and the evolution of the British Isles. *J. geol. Soc. London* 139, 371-412.
- Donnay, G. and Kullerud, G. (1958) High-temperature chalcopyrite. *Carnegie Inst. Washington, Ann. Rep. Dir. Geophys. Lab. 1957-1958*, vol. 57, 246.
- Dozy, J.J. (1970) A geologic model for the genesis of the lead-zinc ores of the Mississippi Valley, U.S.A. *Trans. Inst. Mining Metall.* 79, B163-B170.
- Drits, V.A., Kashaev, A.A. and Sikolova, G.V. (1975) Crystal structure of cymrite. *Kristallografiya* 20, 280-286. (Transl. *Sov. Phy. Cryst.* 20, 171-175).
- Dunham, K.C. (1970) Mineralization by deep formation waters: a review. *Trans. Inst. Mining Metall.* 79, B127-B136.
- Dymer, R.F., Boak, J.L. and Kerr, M.T. (1983) Green micas in the Archean Isua and Malene supracrustal rocks, Southern West Greenland, and the occurrence of a barian-chromian muscovite. *Rapp. Grønlands geol. Unders.* 112, 71-82.
- Einsele, G., Gieskes, J.M., Curray, J. et al. (1980) Intrusions of basaltic sills into highly porous sediments, and resulting hydrothermal activity. *Nature* 283, 441-445.
- Ellis, D.J. and Green, D.H. (1979) An experimental study of the effect of Ca upon garnet-clinopyroxene Fe-Mg exchange equilibria. *Contrib. Mineral. Petrol.* 71, 13-22.

- Epstein, S., Graf, D.L. and Degens, E.T. (1964) Oxygen isotope studies on the origin of dolomites. Craig, H., Miller, S.L. and Wasserburg, G.R. (eds). 'Isotopic and Cosmic Chemistry', 169-180, Amsterdam.
- Essene, E.J. (1967) An occurrence of cymrite in the Franciscan formation, California. *Am. Mineral.* 52, 1885-1890.
- Fettes, D.J. (1979) A metamorphic map of the British Isles. In Harris, A.L., Holland, C.H. and Leake, B.E. (eds.) 'The Caledonides of the British Isles - Reviewed'. *Spec. Publ. geol. Soc. London*, 8, 307-322.
- Ferry, J.M. (1981) Petrology of graphitic sulphide-rich schists from south-central Maine: an example of desulphidation during regional metamorphism. *Am. Mineral.* 66, 908-930.
- Ferry, J.M. (1982) A comparative geochemical study of pelitic schists and metamorphosed carbonate rocks from south-central Maine, U.S.A. *Contrib. Mineral. Petrol.* 80, 59-71.
- Ferry, J.M. (1983a) Mineral reactions and element migration during metamorphism of calcareous sediments from the Vasselboro Formation, south-central Maine. *Am. Mineral.* 68, 334-354.
- Ferry, J.M. (1983b) Regional metamorphism of the Vasselboro Formation, south-central Maine, U.S.A.: a case study of the role of fluid in metamorphic petrogenesis. *J. geol. Soc. London* 140, 551-576.
- Ferry, J.M. and Spear, F.S. (1978) Experimental calibration of the partitioning of Fe and Mg between biotite and garnet. *Contrib. Mineral. Petrol.* 66, 113-117.
- Fettes, D.J. (1979) A metamorphic map of the British Isles. In Harris, A.L., Holland, C.H. & Leake, B.E. (eds.) 'The Caledonides of the British Isles - reviewed'. *Spec. Publ. geol. Soc. London* 8, 307-322.
- Fettes, D.J., Graham, C.M., Sassi, F.P. and Scolari, A. (1976) The basal spacing of potassic white micas and facies series variation across the Caledonides. *Scott. J. Geol.* 12, 227-236.
- Finlow-Bates, T. (1979a) Chemical mobilities in a submarine exhalative hydrothermal system. *Chem. Geol.* 27, 65-83.
- Finlow-Bates, T. (1979b) Cyclicity in the lead-zinc-silver-bearing sediments at Mount Isa mine, Queensland, Australia, and rates of sulfide accumulation. *Econ. Geol.* 74, 1408-1419.
- Finlow-Bates, T. (1980) The chemical and physical controls on the genesis of submarine exhalative orebodies and their implications for formulating exploration concepts. A review. *Geol. Jb.* D40, 131-168.
- Finlow-Bates, T. and Croxford, N.J.W. (1977) Evidence for, and implications of, a primary FeS phase in the lead-zinc bearing sediments at Mount Isa. *Mineralia Deposita* 12, 143-149.
- Finlow-Bates, T. and Stumpfl, E.F. (1979) The copper and lead-zinc orebodies at Mount Isa mine, Queensland: Products of one hydrothermal system. *Soc. Geol. Belgique Annales* 102, 497-517.
- Fisher, I.St.J. and Coleman, M.L. (1980) Sulphur isotope analysis of pyrite and barite from Frenich Burn near Aberfeldy. *Inst. Geol. Sci. Stable Isotope Report* no. 47.
- Fisk, S. (1984) Oxygen isotope geochemistry of possible hydrothermal cherts associated with base metal sulfide mineralization in Perthshire, Scotland (Abstract). In 'Stratabound Sulphides of the Appalachian-Caledonian Orogen, Ottawa'. Program and Abstracts, p. 14.
- Fitton, J.G., James, D.E. and Thirlwall, M.F. (1984) A users' guide to the X-ray fluorescence analysis of rock samples. (Second Ed.). Internal publ., Grant Inst. Geology, University of Edinburgh.

- Fleischer, M. (1961) New mineral names: Baoite (= Pao-t'ou-Kuang). [V.I. Simonov. Baoite, a mineral with a metasilicate ring ( $\text{Si}_4\text{O}_{12}$ ). *Kristallografiya* 5, 544-546 (1960) (in Russian).] *Am. Mineral.* 46, 466.
- Fleischer, M. and Chao, E.C.T. (1960) New mineral names: Pao-t'ou-k'uang, Bafertisite. [Peng Ch'I-Jui. The discovery of several new minerals of rare elements. *Ti-chih K'o-hseuh*, 10, 289 (1959) (in Chinese).] *Am. Mineral.* 45, 754.
- Floyd, P.A. and Winchester, J.A. (1975) Magma type and tectonic setting discrimination using immobile elements. *Earth Planet. Sci. Lett.* 27, 211-218.
- Floyd, P.A. and Winchester, J.A. (1978) Identification and discrimination of altered and metamorphosed volcanic rocks using immobile elements. *Chem. Geol.* 21, 291-306.
- Floyd, P.A. and Winchester, J.A. (1983) Element mobility associated with meta-shear zones within the Ben Hope amphibolite suite, Scotland. *Chem. Geol.* 39, 1-15.
- Forbes, W.C. and Flower, M.F.J. (1974) Phase relations of titano-phlogopite,  $\text{K}_2\text{Mg}_4\text{TiAl}_2\text{Si}_6\text{O}_{20}(\text{OH})_4$ : a refractory phase in the upper mantle? *Earth Planet. Sci. Lett.* 22, 60-66.
- Ford, C.E. (1972) Furnace design, temperature distribution, calibration and seal design in internally heated pressure vessels. In 'Progress in Experimental Petrology.' London: Natural Environment Research Council Publications, Series D, No. 2, 89-96.
- Fortey, N.J. and Beddoe-Stephens, B. (1982) Barium silicates in stratabound Ba-Zn mineralization in the Scottish Dalradian. *Mineral. Mag.* 46, 63-72.
- Froehlich, F. and Sandrea, A. (1973) Presence de cymrite dans les mineralisations devoniennes stratiformes a blende-galene-baratine d'Arrens (Haute-Pyrenees). *C.R. Acad. Sci. Paris* 277, Serie D, 2445-2448.
- Gallagher, M.J. (1983) Barite deposits and potential of Scotland. *Bull. Inst. Min. Metall.* 923, 4.
- Gaspar, J.C. and Wyllie, P.J. (1982) Barium phlogopite from the Jacupiranga carbonatite, Brazil. *Am. Mineral.* 67, 997-1000.
- Gatehouse, B.M., Grey, I.E. and Kelly, P.R. (1979) The crystal structure of Davidite. *Am. Mineral.* 64, 1010-1017.
- Gay, P. and Roy, N.N. (1968) The mineralogy of the potassium-barium feldspar series. III. Subsolidus Relationships. *Mineral. Mag.* 36, 914-932.
- Ghent, E.D. and Stout, M.Z. (1981) Geobarometry and geothermometry of plagioclase-biotite-garnet-muscovite assemblages. *Contrib. Mineral. Petrol.* 76, 92-97.
- Ghent, E.D., Robbins, D.B. and Stout, M.Z. (1979) Geothermometry, geobarometry, and fluid compositions of metamorphosed calc-silicates and pelites, Mica Creek, British Columbia. *Am. Mineral.* 64, 874-885.
- Gehlen, K.V., Neilsen, H., Chunnett, I. and Rozendaal, A. (1983) Sulphur isotopes in metamorphosed Precambrian Fe-Pb-Zn-Cu sulphides and baryte at Agenneys and Gamsberg, South Africa. *Mineral. Mag.* 47, 481-486.
- Giovani, W.F.De, Salati, E., Marini, O.J. and Friedman, I. (1974) Unusual isotopic composition of carbonates from the Irati Formation, Brazil. *Geol. Soc. Am. Bull.* 85, 41-44.
- Goble, R.J., Scott, S.D. and Hancock, R.G.V. (1979) Diffusion rates of Zn and Fe in sphalerite (abstr.) *Geol. Soc. Canada - Mineral. Soc. Canada, Abstr. with Programs* 4, 53.

- Godwin, C.I., Sinclair, A.J. and Ryan, B.D. (1982) Lead isotope models for the genesis of carbonate-hosted Zn-Pb, shale-hosted Ba-Zn-Pb, and silver-rich deposits in the northern Canadian Cordillera. *Econ. Geol.* 77, 82-94.
- Goldhaber, M.B. and Kaplan, I.R. (1974) Controls and consequences of sulfate reduction in recent marine sediments. *Soil Sci.* 119, 42-55.
- Goldsmith, J.R. (1959) Some aspects of the geochemistry of carbonates. In Abelson, P.H. (ed.) 'Researches in geochemistry.' New York, Wiley, 336-358.
- Goldsmith, J.R. and Newton, R.C. (1969) P-T-X relations in the system  $\text{CaCO}_3$ - $\text{MgCO}_3$  at high temperatures and pressures. *Amer. J. Sci.* 267-A, 160-190.
- Goldsmith, J.R. (1982) Review of the behaviour of plagioclase under metamorphic conditions. *Am. Mineral.* 67, 643-652.
- Goldsmith, J.R. (1982) Plagioclase stability at elevated temperatures and water pressures. *Am. Mineral.* 67, 653-675.
- Goni, J. and Remond, G. (1969) Localization and distribution of impurities in blende by cathodoluminescence. *Mineral. Mag.* 37, 153-155.
- Goodfellow, W.D. and Jonasson, I.R. (1984) Ocean stagnation and ventilation defined by  $^{34}\text{S}$  secular trends in pyrite and barite, Selwyn Basin, Yukon. *Geology* 12, 583-586.
- Graham, C.M. (1973) Chemical petrology of metamorphosed basic rocks of the Dalradian series, with particular reference to the Knapdale area of Argyll. Ph.D. thesis, University of Edinburgh.
- Graham, C.M. (1974) Metabasite amphiboles of the Scottish Dalradian. *Contrib. Mineral. Petrol.* 47, 165-185.
- Graham, C.M. (1976a) Petrochemistry and tectonic significance of Dalradian metabasaltic rocks of the S.W. Scottish Highlands. *Jl. Geol. Soc. Lond.* 132, 61-84.
- Graham, C.M. (1976b) Petrochemical affinities of Dalradian metabasaltic rocks: Discussion of paper by J.A. Winchester and P.A. Floyd. *Earth Planet. Sci. Lett.* 32, 210-212.
- Graham, C.M. and Borradaile, G.J. (1984) The petrology and structure of Dalradian metabasaltic dykes of Jura: implications for early Dalradian evolution. *Scott. J. Geol.* 20, 257-270.
- Graham, C.M. and Bradbury, H.J. (1981) Cambrian and late Precambrian basaltic igneous activity in the Scottish Dalradian: a review. *Geol. Mag.* 118, 27-37.
- Graham, C.M., Greig, K.M., Sheppard, S.M.F. and Turi, B. (1983) Genesis and mobility of the  $\text{H}_2\text{O}$ - $\text{CO}_2$  fluid phase during regional greenschist and epidote amphibolite facies metamorphism: a petrological and stable isotope study in the Scottish Dalradian. *J. geol. Soc. London* 140, 577-599.
- Graham, C.M. and Harte, B. (1985) Conditions of Dalradian metamorphism - Introduction. *J. geol. Soc. London* 142, 1-5.
- Graham, C.M. and Powell, R. (1984) A garnet-hornblende geothermometer: calibration, testing, and application to the Pelona Schist, Southern California. *J. metamorphic Geol.* 2, 13-31.
- Grant, J.A. and Weiblen, P.W. (1971) Retrograde zoning in garnet near the second sillimanite isograd. *Am. J. Sci.* 270, 281-296.
- Grapes, R. and Masayuki, O. (1983) Peristerite compositions in quartzofeldspathic schists, Franz-Josef-Fox Glacier Area, New Zealand. *J. metamorphic Geol.* 1, 47-61.

- Gray, J.R. and Yardley, B.W.D. (1979) A Caledonian blueschist from the Irish Dalradian. *Nature*, London, 278, 736-737.
- Grey, I.E., Lloyd, D.J. and White, J.S. (1976) The structure of crichtonite and its relationship to Davidite. *Am. Mineral.* 61, 1203-1212.
- Grout, A. and Gallagher, M.J. (1980) Barium determination in rock and overburden by portable XRF spectrometer. *Trans. Inst. Mining Metall.* 97, B130-B133.
- Groves, D.I., Binns, R.A., Bassett, F.M. and McQueen, K.G. (1975) Sphalerite compositions from Western Australian nickel deposits, a guide to equilibria below 300°C. *Econ. Geol.* 70, 391-396.
- Guidotti, C.V. (1969) A comment on 'Chemical study of minerals from the Moine Schists of the Ardnamurchan area, Argyllshire, Scotland', by B.C.M. Butler, and its implications for the phengite problem. *J. Petrol.* 10, 164-170.
- Guidotti, C.V., Cheney, J.T. and Guggenheim, S. (1977) Distribution of titanium between coexisting muscovite and biotite in pelitic schists from northwestern Maine. *Am. Mineral.* 62, 438-448.
- Gundlach, H. (1959) Untersuchungen zur Geochemie des Strontiums auf hydrothermalen Lagerstätten. *Geol. Jb.* 76, 637-712.
- Hajash, A. (1975) Hydrothermal processes along mid-ocean ridges: an experimental investigation. *Contrib. Mineral. Petrol.* 53, 205-226.
- Hall, A.J. (1982) Gypsum as a precursor to pyrrhotite in metamorphic rocks: Evidence from the Ballachulish Slate, Scotland. *Mineralia Deposita* 17, 401-409.
- Hannak, W. (1981) The geology of the Rammelsberg deposit. *In* Wolf, K.H. (ed.) 'Handbook of Stratabound and Stratiform ore deposits'. Elsevier, Amsterdam. Ch.9, 551-642.
- Harris, A.L. (1963) Structural investigations in the Dalradian rocks between Pitlochry and Blair Atholl. *Trans. Edinb. geol. Soc.* 19, 256-278.
- Harris, A.L., Bradbury, H.J. and McGonical, M.H. (1976) The evolution and transport of the Tay Nappe. *Scott. J. Geol.* 12, 103-113.
- Harris, A.L. and Pitcher, W. (1975) the Dalradian Supergroup. *In* Harris, A.L. et al. (eds.) 'Correlation of the Precambrian rocks of Great Britain'. Spec. Report, Geol. Soc. London no. 6.
- Harris, A.L., Baldwin, C.T., Bradbury, H.J., Johnson, H.D. and Smith, R.A. (1978) Ensialic basin sedimentation: the Dalradian Supergroup. *In* Bowes, D.R. and Leake, B.E. (eds.) 'Crustal evolution in northwestern Britain and adjacent regions'. Liverpool: Seal House Press, 115-138.
- Harrison, A.G. and Thode, H.G. (1957) Kinetic isotope effect in chemical reduction of sulphate. *Trans. Far. Soc.* 53, 1648-1651.
- Harrover, R.D., Norman, D.I., Savin, S.M. and Sawkins, F.J. (1982) Stable oxygen isotope and crystallite size analysis of De Long Mountain, Alaska, cherts: an exploration tool for submarine exhalative deposits. *Econ. Geol.* 77, 1761-1766.
- Harte, B. and Hudson, N.F.C. (1979) Pelite facies series and the temperatures and pressures of Dalradian metamorphism. *In* Harris, A.L., Holland, C.H. and Leake, B.E. (eds.) 'The Caledonides of the British Isles - Reviewed'. Spec. Publ. geol. Soc. London 8, 323-337.
- Harte, B., Dempster, T.J. and Booth, J.E. (1983) P-T estimates and mineral facies variation in space and time in the central and SE Scottish Highlands (abstr). *Geol. soc. Newsl. London* 12/4, 21.

- Haymon, R.M. and Kastner, M. (1981) Hot spring deposits on the East Pacific Rise at 21°N: preliminary description of mineralogy and genesis. *Earth Planet. Sci. Lett.* 53, 363-381.
- Hayton, J.D. (1960) The constitution of Davidite. *Econ. Geol.* 55, 1030-1038.
- Heinrich, E.W. (1965) Further information on the geology of chromian muscovites. *Am. Mineral.* 50, 758-762.
- Heinrich, E.W., Boyer, W.H. and Crowley, F.A. (1962) Baoite (Pao-T'ou-K'uang) from Ravalli County, Montana. *Am. Mineral.* 47, 987-993.
- Heinrich, E.W. and Levinson, A.A. (1955) Studies in the mica group; X-ray data on roscoelite and barium-muscovite. *Amer. J. Sci.* 253, 39-43.
- Heinrich, K.F.J. (1966) X-ray absorption uncertainty. *In* McKinley, T.D., Heinrich, K.F.J. and Wittey, D.B. (eds.) 'The electron microprobe'. London: Wiley, 296-377.
- Heinrichs, T.K. and Riemer, T.O. (1977) A sedimentary barite deposit from the Archean Fig Tree Group of the Barberton Mountain Land (South Africa). *Econ. Geol.* 72, 1426-1441.
- Hekinian, R., Fevrier, M., Bischoff, J.L., Picot, C. and Shanks, W.C. (1980) Sulfide deposits from the East Pacific Rise near 21°N. *Science* 207, 1433-1444.
- Henderson, P. (1982) *Inorganic Geochemistry*. Pergamon Press, Oxford, 353pp.
- Hey, M.H. (1954) A new review of the chlorites. *Min. Mag.* 30, 277-292.
- Hickman, A.H. and Wright, A.E. (1983) Geochemistry and chemostratigraphic correlation of slates, marbles and quartzites of the Appin Group, Argyll, Scotland. *Trans. Roy. Soc. Edinb.: Earth Sci.* 73, 251-278.
- Higgins, A.K. and Phillips, W.E.A. (1979) East Greenland Caledonides - an extension of the British Caledonides. *In* Harris, A.L., Holland, C.H. and Leake, B.E. (eds.) 'Caledonides of the British Isles - Reviewed'. *Spec. Publ. geol. Soc. London* 8, 19-32.
- Hodges, K.V. and Spear, F.S. (1982) Geothermometry, geobarometry and the  $\text{Al}_2\text{SiO}_5$  triple point at Mt. Moosilauke, New Hampshire. *Am. Mineral.* 67, 118-134.
- Hoefs, J. (1980) Stable Isotope Geochemistry. *In* 'Minerals and Rocks' 9 (2nd edition). Springer-Verlag, Berlin.
- Hoefs, J. and Frey, M. (1976) The isotopic composition of carbonaceous matter in a metamorphic profile from the Swiss Alps. *Geochim. Cosmochim. Acta* 40, 945-951.
- Hoering, T.C. (1967) The inorganic geochemistry of Precambrian rocks. Abelson (ed.). 'Researches in Geochemistry', 87 pp., New York.
- Hollister, L.S. (1966) Garnet zoning: an interpretation based on the Rayleigh fractionation model. *Science* 154, 1647-1651.
- Holser, W.T. (1977) Catastrophic chemical events in the history of the ocean. *Nature*, London 267, 403-408.
- Holser, W.T. and Kaplan, J.R. (1966) Isotope geochemistry of sedimentary sulfates. *Chem. Geology* 1, 93-135.
- Hood, C.W., Steidl, P.F. and Tschopp, D.G. (1974) Precipitation of norsethite at room temperature. *Am. Mineral.* 59, 471-474.
- Hower, J., Eslinger, E.V., Hower, M.E. and Perry, E.A. (1976) Mechanism of burial metamorphism of argillaceous sediment: 1. Mineralogical and chemical evidence. *Bull. Geol. Soc. Amer.* 87, 725-737.
- Hsu, L.C. (1968) Selected phase relationships in the system Al-Mn-Fe-Si-O-H: a model for garnet equilibria. *J. Petrol.* 9, 40-83.



- Hudson, J.D. (1977) Stable isotopes and limestone lithification. *Jl. geol. Soc. London* 133, 637-660.
- Hughes, C.J. (1972) Spilites, keratophyres, and the igneous spectrum. *Geol. Mag.* 109, 513-527.
- Hutcheon, I. and Scott, S.D. (1978) Effect of copper on the sphalerite geobarometer (abstract). *Geol. Soc. Am., Abstr. with prog.* 10, 426.
- Hutchinson, R.W., Fyfe, W.S. and Kerrich, R. (1980) Deep fluid penetration and ore deposition. *Minerals Sci. & Eng.* 12, 107-120.
- Hutchison, C.S. (1983) 'Economic deposits and their tectonic setting'. Macmillan, London, 356 pp.
- Hutchison, M.N. and Scott, S.D. (1981) Sphalerite geobarometry in the Cu-Fe-Zn-S system. *Econ. Geol.* 76, 143-153.
- Iijima, A. (1974) Clay and zeolite alteration zones surrounding Kuroko deposits in the Hakuroko district, northern Akita. *Mining Geology Spec. Issue* 6, 267-289.
- Iijima, A. and Hay, R.L. (1968) The analcime composition in tuffs of the Green River Formation of Wyoming. *Am. Mineral.* 53, 184-200.
- Jeffrey, P.G. (1970) 'Chemical methods of rock analysis'. International Series of Monographs in Analytical Chemistry, 36, Pergamon Press Ltd.
- Jensen, M.L. (1967) Sulfur isotopes and mineral genesis. In Barnes, H.L. (ed.) 'Geochemistry of hydrothermal ore deposits', New York, Holt, Rinehart and Winston, Inc., 143-165.
- Johnson, M.R.W., Sanderson, D.J. and Soper, N.J. (1979) Deformation in the Caledonides of England, Ireland and Scotland. In Harris, A.L., Holland, C.H. and Leake, B.H. (eds.) 'The Caledonides of the British Isles - Reviewed', *Spec. Publ. geol. Soc. London*, 8, 165-186.
- Kajiwara, Y. and Krouse, H.R. (1971) Sulfur isotope partitioning in metallic sulfide systems. *Canadian Jour. Earth Sci.* 8, 1397-1408.
- Kager, P.C.A. (1980) Mineralogical investigations on sulfides, Fe-Mn-Zn-Mg-Ca-carbonates, greenalite and associated minerals in the Pb-Zn deposits in the Sierra de Cartagena, Province of Murcia, S.E. Spain. *GUA Papers of Geology, Series 1*, 12-1980, Amsterdam.
- Kaplan, I.R., Emery, K.O. and Rittenberg, S.C. (1963) The distribution and isotopic abundance of sulfur in recent marine sediments off southern California. *Geochim. Cosmochim. Acta* 27, 297-331.
- Keith, M.L. and Weber, J.W. (1964) Carbon and oxygen isotopic composition of selected limestones and fossils. *Geochim. Cosmochim. Acta* 28, 1787-1816.
- Keith, M.L. (1982) Violent volcanism, stagnant oceans and some inferences regarding petroleum, stratabound ores and mass extinctions. *Geochim. Cosmochim. Acta* 46, 2621-2637.
- Kelly, D.P. and Vaughan, D.J. (1983) Pyrrhotite-pentlandite ore textures: a mechanistic approach. *Mineral. Mag.* 47, 453-463.
- Kemp, A.L.W. and Thode, H.G. (1968) The mechanism of the bacterial reduction of sulfate and of sulfite from isotopic fractionation studies. *Geochim. Cosmochim. Acta* 32, 71-91.
- Kennedy, M.J. (1979) The continuation of the Canadian Appalachians into the Caledonides of Britain and Ireland. In Harris, A.L., Holland, C.H. and Leake, B.E. (eds.) 'Caledonides of the British Isles - Reviewed'. *Spec. Publ. geol. Soc. London* 8, 33-64.
- Krebs, W. (1981) The geology of the Meggen ore deposit. In Wolf, K.H. (ed.) 'Handbook of stratabound and stratiform ore deposits'. Amsterdam, Elsevier. Ch. 9, 509-550.

- Kultiassou, S.V. and Dubinkina, R.P. (1946) A new vanadium-bearing variety of oellacherite. *Soc. russe mineralogie Mem.* 75, 187-192.
- Lambert, I.B. (1973) Post-depositional availability of sulphur and metals and the formation of secondary textures and structures in stratiform sedimentary sulphide deposits. *J. geol. Soc. Aust.* 20, 205-215.
- Lambert, I.B., Donnelly, T.H., Dunlop, J.S.R and Groves, D.I. (1978) Stable isotope compositions of early Archaean sulphate deposits of probable evaporitic and volcanogenic origins. *Nature* 276, 808-811.
- Lambert, R.St.J., Winchester, J.A. and Holland, J.G. (1981) Comparative geochemistry of pelites from the Moinian and Appin Group (Dalradian) of Scotland. *Geol. Mag.* 118, 477-490.
- Lambert, R. and McKerrow, W. (1976) The Grampian Orogeny. *Scott. J. Geol.* 12, 271-292.
- Large, D.E. (1980) Geological parameters associated with sediment-hosted, submarine exhalative Pb-Zn deposits: an empirical model for mineral exploration. *Geol. Jb.* D40, 59-129.
- Large, D.E. (1981a) Sediment-hosted submarine exhalative lead-zinc deposits: a review of their geological characteristics and genesis. *In: Wolf, K.H. (ed.), 'Handbook of stratabound and stratiform ore deposits'*. Elsevier, Amsterdam. Ch. 8, 469-508.
- Large, D.E. (1981b) On the geology, geochemistry and genesis of the Tom Pb-Zn-Barite deposit, Yukon Territory, Canada. Ph.D. dissertation, Braunschweig, 153pp.
- Large, D.E. (1981c) The geochemistry of the sedimentary rocks in the vicinity of the Tom Pb-Zn-Ba deposit, Yukon Territory, Canada. *J. Geochem. Explor.* 15, 203-217.
- Large, R.R. (1977) Chemical evolution and zonation of massive sulfide deposits in volcanic terrains. *Econ. Geol.* 72, 549-572.
- Lawley, D.N. and Maxwell, A.E. (1963) Factor analysis as a statistical method. Butterworths, London.
- Leake, B.E. (1972) The mineralogical modification of the chemistry of metamorphic rocks. *Geol. Mag.* 109, 331-337.
- Litherland, M. (1980) The stratigraphy of the Dalradian rocks around Loch Creran, Argyll. *Scott. J. Geol.* 16, 105-123.
- Lippman, F. (1962) Benstonite,  $\text{Ca}_7\text{Ba}_6(\text{CO}_3)_{13}$ . A new mineral from the barite deposit in Hot Spring County, Arkansas. *Am. Mineral.* 47, 585-598.
- Lonsdale, P.F., Bischoff, J.L., Burns, V.M., Kastner, M. and Sweeney, R.E. (1980) A high temperature hydrothermal deposit on the seabed at a Gulf of California spreading center. *Earth Planet. Sci. Lett.* 49, 8-20.
- Lusk, J. and Crocket, J.H. (1969) Sulfur isotope fractionation in coexisting sulfides from the Heath Steele Bl orebody, New Brunswick, Canada. *Econ. Geol.* 64, 147-155.
- Lusk, J. and Ford, C.E. (1978) Experimental extension of the sphalerite geobarometer to 10 kbar. *Am. Mineral.* 63, 516-519.
- Lydon, J.W. (1983) Chemical parameters controlling the origin and deposition of sediment-hosted lead-zinc deposits. *Mineral. Assoc. Canada Short Course Handbook*, 8, 175-250.
- Lydon, J.W., Lancaster, R.D. and Karkkainen, P. (1979) Genetic controls of Selwyn Basin stratiform barite/sphalerite/galena deposits: An investigation of the dominant barium mineralogy of the Tea deposit, Yukon. *In Current Research, Part B, Geol. Surv. Canada, Paper 79-1B*, 223-229.

- McClay, K.R. (1982) Tectonic and sedimentary structures in sulphide orebodies of Mount Isa, Australia, and Sullivan, Canada. *Trans. Inst. Mining Metall.* 91, B146-B151.
- McClay, K.R. and Carlile, D.G. (1978) Mid-proterozoic sulphate evaporites at Mount Isa mine, Queensland, Australia. *Nature, London* 274, 240-241.
- McCrea, J.M. (1950) On the isotopic chemistry of carbonates and paleo-temperature scale. *J. Chem. Phys.* 18, 849-857.
- McCready, R.G.L. (1975) Sulfur isotope fractionation of *Desulfovibrio* and *Desulfotomaculum* species. *Geochim. Cosmochim. Acta* 39, 1395-1401.
- MacDonald, K.C., Becker, K., Speiss, F.N. and Ballard, R.D. (1980) Hydrothermal heat flux of the "black smoker" vents on the East Pacific Rise. *Earth Planet. Sci. Letters* 48, 1-7.
- MacDonald, R., Gottfried, D., Farrington, M.J., Brown, F.W. and Skinner, N.G. (1981) Geochemistry of a continental tholeiite suite: late Palaeozoic quartz dolerite dykes of Scotland. *Trans. R. Soc. Edinb.: Earth Sci.* 72, 57-74.
- McKirdy, D.M. and Powell, T.G. (1974) Metamorphic alteration of carbon isotopic composition in ancient sedimentary organic matter: new evidence from Australia and South Africa. *Geology* 2, 591-595.
- McLeod, R.L. and Stanton, R.L. (1984) Phyllosilicates and associated minerals in some Palaeozoic stratiform sulphide deposits of southeastern Australia. *Econ. Geol.* 79, 1-22.
- McLimans, R.K., Barnes, H.L. and Ohmoto, H. (1980) Sphalerite stratigraphy of the Upper Mississippi Valley zinc-lead district, Southwest Wisconsin. *Econ. Geol.* 75, 351-361.
- Mako, D.A. and Shanks, W.C. (1984) Stratiform sulfide and barite-fluorite mineralization of the Vulcan prospect, Northwest Territories: Exhalation of basinal brines along a faulted continental margin. *Canadian J. Earth Sci.* 21, 78-91.
- Mansker, W.L., Ewing, R.C. and Keil, K. (1979) Barian-titanian biotites in nephelinites from Oahu, Hawaii. *Am. Mineral.* 64, 156-159.
- Maruyama, S., Liou, J.G. and Suzuki, K. (1982) The peristerite gap in low grade metamorphic rocks. *Contrib. Mineral. Petrol.* 81, 268-276.
- Matthews, A. and Katz, A. (1977) Oxygen isotope fractionation during the dolomitisation of calcium carbonate. *Geochim. Cosmochim. Acta* 41, 1431-1438.
- Matthews, D.W. (1967) Zoned ultrabasic bodies in the Lewisian of the Moine nappe in Skye. *Scott. J. Geol.* 3, 17-33.
- Mevel, C. and Kienast, J.R. (1980) Chromian jadeite, phengite, pumpellyite, and lawsonite in a high-pressure metamorphosed gabbro. *Mineral. Mag.* 43, 979-984.
- Milton, C. and Eugster, H.P. (1959) Mineral assemblages of the Green River Formation. In Abelson, P.H. (ed.) 'Researches in Geochemistry'. Wiley. 118-150.
- Miyashiro, A. (1961) Evolution of metamorphic belts. *J. Petrol.* 2, 277-311.
- Mohamid, H.B. (1980) Geochemistry and petrology of the Southern Highland (Upper Dalradian) pelitic-psammitic schists of Glen Esk, Angus, Scotland. Unpubl. Ph.D. thesis, Univ. of Strathclyde.
- Mohr, D.W. and Newton, R.C. (1983) Kyanite-staurolite metamorphism in sulfidic schists of the Anokeesta Formation, Great Smoky Mountains, North Carolina. *Am. J. Sci.* 283, 97-134.

- Moles, N.R. (1983) Sphalerite composition in relation to deposition and metamorphism of the Foss straiform Ba-Zn-Pb deposit, Aberfeldy, Scotland. *Mineral. Mag.* 47, 487-500.
- Moles, N.R. (1985) Metamorphic conditions and uplift history in central Perthshire: evidence from mineral equilibria in the Foss celsian-barite-sulphide deposit, Aberfeldy. *J. geol. Soc. Lond.* 142, 39-52.
- Morganti, J.M. (1981) Sedimentary-type stratiform ore deposits: some models and a new classification. *Geoscience Canada* 8, 67-75.
- Morrow, D.W., Krouse, H.R., Ghent, E.D., Taylor, G.C. and Dawson, K.R. (1978) A hypothesis concerning the origin of barite in Devonian carbonate rocks of northeastern British Columbia. *Can. J. Earth Sci.* 15, 1391-1406.
- Mrose, M.E., Chao, E.C.T., Fahey, J.J. and Milton, C. (1961) Norsethite  $\text{BaMg}(\text{CO}_3)_2$ , a new mineral from the Green River Formation, Wyoming. *Am. Mineral.* 46, 420-429.
- Munoz, J.L. (1984) F-OH and Cl-OH exchange in micas with applications to hydrothermal ore deposits. In Bailey, S.W. (ed.) *Mineral. Soc. Amer., Reviews in Mineralogy* 13, 'Micas', 469-493.
- Neiva, A.M.R. (1978) Barian chromium-bearing hydromuscovite from Mozambique. *Mineral. Mag.* 42, 292-293.
- Nesbitt, B.E. (1982) Metamorphic sulfide-silicate equilibria in the massive sulfide deposits at Ducktown, Tennessee. *Econ. Geol.* 77, 364-378.
- Newton, R.C. and Haselton, H.T. (1981) Thermodynamics of the garnet-plagioclase- $\text{Al}_2\text{SiO}_5$ -quartz geobarometer. In Newton, R.C., Navrotsky, A. and Wood, B.J. (eds.) 'Thermodynamics of Minerals and Melts' (Advances in Physical Geochemistry, 1). Springer-Verlag. 131-147.
- Nicholson, R. (1979) Caledonian correlations: Britain and Scandinavia. In Harris, A.L., Holland, C.H. and Leake, B.E. (eds.) 'The Caledonides of the British Isles - reviewed'. *Geol. Soc. London Spec. Publ.* 8, 3-18.
- Nielsen, H. (1978) Sulphur isotopes in nature. In: Wederpohl, K.H. (ed.) *Handbook of Geochemistry*, 11-2, 16-B-1 to 40. Springer-Verlag.
- Nitsch, K.-H. (1980) Reaktion von bariumfeldspat (celsian) mit  $\text{H}_2\text{O}$  zu cymrit unter metamorphen bedingungen. *Fortschr Mineral* 58, Bh 1, 98-100.
- Norrish, K. and Hutton, J.T. (1969) An accurate X-ray spectrographic method for the analysis of a wide range of geological samples. *Geochim. Cosmochim. Acta* 33, 431-453.
- Norry, M.J. and Fitton, J.G. (1983) Compositional differences between oceanic and continental basic lavas and their significance. In Hawkesworth, C.J. and Norry, M.J. (eds.) 'Continental basalts and mantle xenoliths'. Shiva Publishing Ltd.
- Northrop, D.A. and Clayton, R.N. (1966) Oxygen isotope fractionations in systems containing dolomite. *J. Geol.* 74, 174-196.
- Oehler, J.H. and Logan, R.G. (1977) Microfossils, cherts and associated mineralization in the Proterozoic McArthur (H.Y.C.) lead-zinc-silver deposit. *Econ. Geol.* 72, 1393-1409.
- Ohmoto, H. (1972) Systematics of sulphur and carbon isotopes in hydrothermal ore deposits. *Econ. Geol.* 67, 551-578.
- Ohmoto, H. and Rye, R.O. (1979) Isotopes of sulfur and carbon. In Barnes, H.L. (ed.) 'Chemistry of hydrothermal ore deposits'. New York, Wiley Interscience. 509-563.
- O'Neil, J.R. (1979) Stable isotope geochemistry of rocks and minerals. In Jaeger, E. et al. (eds.) 'Lectures in isotope geology'. Springer-Verlag, Berlin. 235-263.

- O'Neil, J.R. and Ghent, E.D. (1975) Stable isotope study of coexisting metamorphic minerals from the Esplanade Range, British Columbia. *Geol. Soc. Am. Bull.* 86, 1708-1712.
- Page, D.C. and Watson, M.D. (1976) The Pb-Zn deposit of Rosh Pinah Mine, South-West Africa. *Econ. Geol.* 71, 306-327.
- Pankhurst, R.J. and Pidgeon, R.T. (1976) Inherited isotope systems and the source region prehistory of the early Caledonian granites in the Dalradian series of Scotland. *Earth Planet. Sci. Lett.* 31, 55-68.
- Pantin, H.M. (1956) The petrology of the Ben Vrackie epidiorites and their contact rocks. *Trans. geol. Soc. Glasg.* 22, 48-79.
- Parker, M.E. (1980) VLF-electromagnetic mapping of strata-bound mineralization near Aberfeldy, Perthshire, Scotland. *Trans. Inst. Mining Metall.* 89, B123-B129.
- Pearce, J.A. and Cann, J.R. (1973) Tectonic setting of basic volcanic rocks determined using trace element analyses. *Earth Planet. Sci. Lett.* 19, 290-300.
- Pearce, J.A. and Norry, M.J. (1979) Petrogenetic implications of Ti, Zr, Y and Nb variations in volcanic rocks. *Contrib. Mineral. Petrol.* 69, 33-47.
- Perry, E.A. and Hower, J. (1972) Late-stage dehydration in deeply buried pelitic sediments. *Bull. Am. Assoc. Petroleum Geol.* 56, 2013-2021.
- Phillips, W.E.A., Stillman, C.J. and Murphy, T.A. (1976) A Caledonian plate tectonic model. *J. geol. Soc. London* 132, 579-609.
- Pigage, L.C. and Greenwood, H.J. (1982) Internally consistent estimates of pressure and temperature: the staurolite problem. *Am. J. Sci.* 282, 943-969.
- Plant, J. and Moore, P.J. (1979) Regional geochemical mapping and interpretation in Britain. *Phil. Trans. Roy. Soc. Lond.* 288B, 95-112.
- Plant, J.A., Smith, R.T., Stevenson, A.G., Forrest, M.D. and Hodgson, J.F. (1984) Regional geochemical mapping for mineral exploration in northern Scotland. In 'Prospecting in areas of glaciated terrain 1984'. *Inst. Mining Metall., London*.
- Plimer, I.R. (1978) Proximal and distal stratabound ore deposits. *Min. Dep.* 13, 345-353.
- Plimer, I.R. (1979) Sulphide rock zonation and hydrothermal alteration at Broken Hill, Australia. *Trans. Inst Mining Metall.* 88, B161-B176.
- Plimer, I.R. (1984) The role of fluorine in submarine exhalative systems with special reference to Broken Hill, Australia. *Mineralia Deposita* 19, 19-25.
- Plimer, I.R. and Finlow-Bates, I. (1978) Relationship between Fe sulphide species, sulphur source, depth of formation and age of submarine exhalative sulphide deposits. *Mineralia Deposita* 13, 399-410.
- Powell, R., Condcliffe, D.M. and Condcliffe, E. (1984) Calcite-dolomite geothermometry in the system  $\text{CaCO}_3\text{-MgCO}_3\text{-FeCO}_3$ : an experimental study. *J. metamorphic Geol.* 2, 33-41.
- Powell, R. and Evans, J.A. (1983) A new geobarometer for the assemblage biotite-muscovite-chlorite-quartz. *J. metamorphic Geol.* 1, 331-336.
- Pringle, I.R. (1972) Rb/Sr determinations on shales associated with the Varanger Ice Age. *Geol. Mag.* 109, 465-472.
- Ramdohr, P. (1980) 'The ore minerals and their intergrowths'. 2nd Edition, Pergamon, Oxford.
- Rees, C.E., Jenkins, W.J. and Monster, J. (1978) The sulfur isotope composition of ocean water sulfate. *Geochim. Cosmochim. Acta* 42, 377-381.

- Reinecke, T. (1982) Cymrite and celsian in manganese-rich metamorphic rocks from Andros Island, Greece. *Contrib. Mineral. Petrol.* 79, 333-336.
- Renfro, A.R. (1974) Genesis of evaporite-associated stratiform metalliferous deposits - a sabkha process. *Econ. Geol.* 69, 33-45.
- Reynolds, R.C. (1965) Geochemical behaviour of boron during the metamorphism of carbonate rocks. *Geochim. Cosmochim. Acta* 29, 1101-1114.
- Richardson, S.W., Gilbert, M.C. and Bell, P.M. (1969) Experimental determination of kyanite-andalusite and andalusite-sillimanite equilibria; the aluminium silicate triple point. *Am. J. Sci.* 267, 259-272.
- Richardson, S. and Powell, S. (1976) Thermal causes of the Dalradian metamorphism in the Central Highlands of Scotland. *Scott. J. Geol.* 12, 237-268.
- Robert, J.L. (1976a) Phlogopite solid solutions in the system  $K_2O$ - $MgO$ - $Al_2O_3$ - $SiO_2$ - $H_2O$ . *Chem. Geol.* 17, 195-212.
- Robert, J.L. (1976b) Titanium solubility in synthetic phlogopite solid solutions. *Chem. Geol.* 17, 213-227.
- Roberts, J.L. (1974) The structure of the Dalradian rocks in the SW Highlands of Scotland. *J. geol. Soc. Lond.* 130, 93-124.
- Roberts, J.L. and Treagus, J.E. (1979) Stratigraphical and structural correlation between the Dalradian rocks of the SW and Central Highlands of Scotland. In Harris, A.L., Holland, C.H. and Leake, B.E. (eds.) 'The Caledonides of the British Isles - reviewed'. *Spec. Publ. Geol. Soc. London* 8, 199-204.
- Robinson, B.W. and Kusakabe, M. (1975) Quantitative preparation of  $SO_2$  for  $^{34}S/^{32}S$  analyses from sulphides by combustion with cuprous oxide. *Anal. Chem.* 47, 1179-1181.
- Roulston, J.S. (1981) Petrochemistry of the metabasites of the Ben Vrockie area. M.Sc. thesis, University of Edinburgh.
- Roy, N.N. (1967) The mineralogy of the potassium-barium feldspar series. II: Studies on hydrothermally synthesized members. *Mineral. Mag.* 43-49.
- Rozendaal, A. (1980) The Gamsberg zinc deposit, South Africa: a banded stratiform base-metal sulphide ore deposit. In Ridge, J.D. (ed.) *Proc. 5th IAGOD Symp.* 1, 619-633.
- Rozendaal, A. and Stumpfl, E.F. (1985) Mineral chemistry and genesis of Gamsberg zinc deposit, South Africa. *Trans. Inst. Mining Metall.* 93, B161-B175.
- Rumble, D. III (1978) Mineralogy, petrology and oxygen isotope geochemistry of the Clough Formation, Black Mountain, western New Hampshire, U.S.A. *J. Petrol.* 19, 317-340.
- Rumble, D. III (1982) Stable isotope fractionation during metamorphic devolatilization reactions. In Ferry, J.M. (ed.) *Reviews in Mineralogy* 10, Min. Soc. Amer., 327-353.
- Rumble, D. III and Spear, F.S. (1983) Oxygen-isotope equilibration and permeability enhancement during regional metamorphism. *J. geol. Soc. London* 140, 619-628.
- Runnells, D.D. (1964) Cymrite in a copper deposit, Brooks Range, Alaska. *Am. Mineral.* 49, 158-165.
- Russell, M.J. (1978) Downward-excavating hydrothermal cells and Irish-type ore deposits: importance of an underlying thick Caledonian prism. *Trans. Inst. Mining Metall.* 87, B168-B171.
- Russell, M.J. (1983) Major sediment-hosted exhalative zinc + lead deposits: Formation from hydrothermal convection cells that deepen during crustal extension. In Sangster, D.F. (ed.) 'Short course in sediment-hosted

- stratiform lead-zinc deposits'. Mineral. Assoc. Canada Short Course Handbook 9, 251-282.
- Russell, M.J., Solomon, M. and Walshe, J.L. (1981) The genesis of sediment-hosted, exhalative zinc + lead deposits. *Mineralia Deposita* 16, 113-127.
- Russell, M.J., Willan, R.C.R., Anderton, R., Hall, A.J., Nicholson, K. and Smyth, D.K. (1981) Genetic model and tectonic setting for the Dalradian stratiform mineral deposits, Grampian Highlands. In Symposium Volume, CCSS 6th Meeting, Strathclyde 1-2 May, 1981, 24-29.
- Russell, M.J., Hall, A.J., Willan, R.C.R., Allison, I., Anderton, R. and Bowes, G.E. (1984) On the origin of the Aberfeldy celsian + baryte + base metal deposits, Scotland. Vol. of papers presented at the 6th Intern. Symp. 'Prospecting in Areas of Glaciated Terrain 1984'. Inst. Mining Metall. London.
- Rye, D.M. and Williams, N. (1981) Studies of base metal sulfide deposits at McArthur River, Northern Territory, Australia: III. The stable isotope geochemistry of the H.Y.C., Ridge and Cooley deposits. *Econ. Geol.* 76, 1-26.
- Rye, R.O. and Ohmoto, H. (1974) Sulfur and carbon isotopes and ore genesis: a review. *Econ. Geol.* 69, 826-842.
- Rye, R.O., Schuiling, R.D., Rye, D.M. and Jansen, J.B.B. (1976) Carbon, hydrogen and oxygen studies of the regional metamorphic complex at Naxos, Greece. *Geochim. Cosmochim. Acta* 40, 1031-1049.
- Rye, R.O., Shawe, D.R. and Poole, F.G. (1978) Stable isotope studies of bedded barite at East Northumberland Canyon in Toiyabe Range, Central Nevada. *J. Research U.S. Geol. Survey* 6, No. 2, 221-229.
- Saha, D. (1985) Clast composition and provenance of psammites in the Colonsay Group and Bowmore Sandstone, SW Argyllshire. *Scott. J. Geol.* 21, 1-8.
- Sakai, H. (1968) Isotopic properties of sulphur compounds in hydrothermal processes. *Geochem. J.* 2, 29-49.
- Samson, I.M. and Russell, M.J. (1983) Fluid inclusion data from Silvermines base-metal-baryte deposits, Ireland. *Trans. Inst. Mining Metall.* 92, B67-B71.
- Sangster, D.F. (1968) Relative sulphur isotope abundances of ancient seas and strata-bound sulphide deposits. *Geol. Assoc. Can. Proc.* 19, 79-91.
- Sanz, J. (1979) NMR study of micas, II. Distribution of  $\text{Fe}^{2+}$ ,  $\text{F}^-$ , and  $\text{OH}^-$  in the octahedral sheet of phlogopites. *Am. Mineral.* 64, 119-126.
- Sato, T. (1972) Behaviours of ore forming solutions in seawater. *Mining Geology, Tokyo* 22, 31-42.
- Sato, T. (1977) Kuroko deposits: their geology, geochemistry and origin. In 'Volcanic processes in ore genesis'. *Geol. Soc. Lond. Spec. Publ.* 7, 153-161.
- Sawkins, F.J. (1984) Ore genesis by episodic dewatering of sedimentary basins: application to giant Proterozoic lead-zinc deposits. *Geology* 12, 451-454.
- Schroll, E., Schulz, O. and Pak, E. (1983) Sulphur isotope distribution in the Pb-Zn deposit, Bleiberg (Carinthia, Austria). *Mineralia Deposita* 18, 17-25.
- Schlager, W. and Bolz, H. (1977) Clastic accumulation of sulphate evaporites in deep water. *J. Sed. Petrol.* 47, 600-609.
- Schwarcz, H.P. (1966) Oxygen and carbon isotopic fractionation between coexisting metamorphic calcite and dolomite. *J. Geol.* 74, 38-48.

- Schwarcz, H.P. and Burnie, S.W. (1973) Influence of sedimentary environments on sulfur isotope ratios in clastic rocks - a review. *Mineralia Deposita* 8, 264-277.
- Scott, S.D. (1973) Experimental calibration of the sphalerite geobarometer. *Econ. Geol.* 68, 466-474.
- Scott, S.D. (1983) Chemical behaviour of sphalerite and arsenopyrite in hydrothermal and metamorphic environments. *Mineral. Mag.* 47, 427-435.
- Scott, S.D. and Barnes, H.L. (1971) Sphalerite geothermometry and geobarometry. *Econ. Geol.* 66, 653-669.
- Segnit, E.R. and Gelb, I. (1970) Reaction of kaolinite with barium carbonate and barium sulphate. *J. Australian Ceramic Soc.* 6, 12-18.
- Seki, Y. and Kennedy, G.C. (1964a) Phase relations between cymrite,  $\text{BaAlSi}_3\text{O}_8(\text{OH})$ , and celsian,  $\text{BaAl}_2\text{Si}_2\text{O}_8$ . *Am. Mineral.* 48, 1407-1426.
- Seki, Y. and Kennedy, G.C. (1964b) The breakdown of potassium feldspar,  $\text{KAlSi}_3\text{O}_8$ , at high temperatures and high pressures. *Am. Mineral.* 49, 1688-1706.
- Senior, A. and Leake, B.E. (1978) Regional metasomatism and the geochemistry of the Dalradian metasediments of connemara, Western Ireland. *J. Petrol.* 19, 585-625.
- Shanks, W.C. and Bischoff, J.L. (1977) Ore transport and deposition in the Red Sea geothermal system: a geochemical model. *Geochim. Cosmochim. Acta* 41, 1507-1519.
- Shanks, W.C., Bischoff, J.L. and Rosenbauer, R.J. (1981) Seawater sulphate reduction and sulphur isotope fractionation in basaltic systems: Interaction of seawater with fayalite and magnetite at 200 to 350°C. *Geochim. Cosmochim. Acta* 45, 1977-1995.
- Sharma, T. and Clayton, R.N. (1965). Measurement of  $^{18}\text{O}/^{16}\text{O}$  ratios of total oxygen of carbonates. *Geochim. Cosmochim. Acta* 29, 1347-1353.
- Shaw, D.M. (1954) Trace elements in pelitic rocks. *Bull. geol. Soc. Am.* 65, 1151-1182.
- Shaw, D.M. (1956) Geochemistry of pelitic rocks. Part III: major elements and general geochemistry. *Bull. geol. Soc. Am.* 67, 919-934.
- Sheppard, S.M.F. and Schwarcz, H.P. (1970) Fractionation of carbon and oxygen isotopes and magnesium between coexisting metamorphic calcite and dolomite. *Contrib. Mineral. Petrol.* 26, 161-198.
- Shervas, J.W. (1982) Ti-V plots and the petrogenesis of modern and ophiolitic lavas. *Earth Planet. Sci. Lett.* 59, 101-118.
- Shikazono, N. (1977) Composition of siderite and the environment of formation of vein-type deposits in Japan. *Econ. Geol.* 72, 632-641.
- Sibson, R.H., Moore, J.M. and Rankin, A.H. (1975) Seismic pumping - a hydrothermal fluid transport mechanism. *J. geol. Soc. Lond.* 131, 653-659.
- Sivaprakash, C. (1981a) Chemographic analysis of metabasite assemblages from central Scottish Highlands. *Lithos* 14, 29-33.
- Sivaprakash, C. (1981b) Zoned garnets in some Scottish Dalradian pelites. *Mineral. Mag.* 44, 301-307.
- Sivaprakash, C. (1982) Geothermometry and geobarometry of Dalradian metapelites and metabasites from the Central Scottish Highlands. *Scott. J. Geol.* 18, 109-124.
- Slack, J.F. (1982) Tourmaline in Appalachian-Caldonian massive sulphide deposits and its exploration significance. *Trans. Inst. Mining Metall.* 91, B81-B89.



- Smith, C.G. (1981) Excursion Guide: Dalradian of the Scottish Highlands - Stratabound mineralization and Geology. (Prepared for the) 6th meeting of CCSS IGCP Project 60, Strathclyde, May 1981.
- Smith, C.G., Gallagher, M.J., Coats, J.S. and Parker, M.E. (1984) Detection and general characteristics of strata-bound mineralization in the Dalradian of Scotland. *Trans. Inst. Mining Metall.* 93, B125-B133.
- Smith, C.G., Pitfield, P.E.J., Burley, A.J., Howard, S.H.D., Parker, M.E., Michie, U.M. and Fortey, N.J. (1977) Investigation of stratiform sulphide mineralization in parts of central Perthshire. *Inst. Geol. Sci. Mineral Recon. Prog. rep. no. 8*.
- Smith, C.W., Bannister, F.A. and Hey, M.H. (1949) Cymrite, a new barium mineral from the Benallt manganese mine, Rhiw, Carmarvonshire. *Mineral. Mag.* 28, 676-681.
- Smith, J.W., Burns, M.S. and Croxford, N.J.W. (1978). Stable isotope studies of the origins of mineralization at Mount Isa. I. *Mineralia Deposita* 13, 369-381.
- Smith, J.W. and Croxford, N.J.W. (1973) Sulphur isotope ratios in the McArthur lead-zinc-silver deposit. *Nature* 245 (Phys. Sci.) 10-12.
- Smith, J.W. and Croxford, N.J.W. (1975) An isotopic investigation of the environment of deposition of the McArthur mineralization. *Mineralia Deposita* 10, 269-276.
- Smith, J.W., Doolan, S. and McFarlane, E.F. (1977) A sulfur isotope geothermometer for the trisulfide system galena-sphalerite-pyrite. *Chem. Geol.* 19, 83-90.
- Smith, J.W. and Stenstrom, R.C. (1965) Electron-excited luminescence as a petrologic tool. *J. Geol.* 73, 627-635.
- Smith, R.E. (1968) Redistribution of major elements in the alteration of some basic lavas during burial metamorphism. *J. Petrol.* 9, 191-219.
- Smith, W.D. (1968) Penecontemporaneous faulting and its likely significance in relation to Mount Isa ore deposition. *Geol. Soc. Australia Spec. Publ.* 2, 225-235.
- Snetsinger, K.G. (1966) Barium-vanadium muscovite and vanadium tourmaline from Manipoza County, California. *Am. Mineral.* 51, 1623-1639.
- Solomon, M., Rafter, T.A. and Jensen, M.L. (1969) Isotope studies on the Rozebery, Mt. Farrel and Mt. Lyell ores, Tasmania. *Mineralia Deposita* 4, 172-199.
- Sommer, S.E. (1972) Cathodoluminescence of carbonates, 1. Characterization of cathodoluminescence from carbonate solid solutions. 2. Geological applications. *Chem. Geol.* 9, 257-273, 275-284.
- Soong, R. and Olivecrona, J.A. (1975) An occurrence of cymrite in black shale, N.W. Nelson, South Island, New Zealand. *Mineral. Mag.* 40, 311-312.
- Soper, N.J. and Anderton, N. (1984) Did the Dalradian slides originate as extensional faults? *Nature, London* 307, 357-360.
- Stanton, R.L. (1976) Petrochemical studies of the ore environment at Broken Hill, N.S.W. *Trans. Inst Mining Metall.* 85, B33-46, B118-131, B132-141, B221-233.
- Stanton, R.L. (1982) Metamorphism of a stratiform sulphide orebody at Mount Misery, Einasleigh, Queensland, Australia: 1 Observations. 2 Implications. *Trans. Inst. Mining Metall.* 91, B47-80.
- Steyn, J.G.D. and Watson, M.D. (1967) A new occurrence of norsethite, BaMg(CO<sub>3</sub>)<sub>2</sub>. *Am. Mineral.* 52, 1770-1775.

- Sturt, B.A. (1961) The geological structure of the area south of Loch Tummel. *Q. Jl. geol. Soc. Lond.* 117, 131-156.
- Sturt, B.A. and Harris, A.L. (1961) The metamorphic history of the Loch Tummel area. *Liverpool and Manchester geol. J.* 2, 689-711.
- Styrt, M.M., Brackmann, A.J., Holland, H.D., Clark, B.C., Pisutha-Arnold, V., Eldridge, C.S. and Ohmoto, H. (1981) The mineralogy and the isotopic composition of sulphur in hydrothermal sulphide/sulphate deposits on the East Pacific Rise at 21°N latitude. *Earth Planet. Sci. Lett.* 53, 382-390.
- Sun, S.S., Nesbitt, R.W. and Sharaskin, A.Y. (1979) Geochemical characteristics of Mid-ocean Ridge Basalts. *Earth Planet. Sci. Lett.* 44, 119-138.
- Swainbank, I.G., Fortey, N.J. and Boast, A.M. (1981) Lead isotope ratios of galena from stratabound mineralization in the Scottish Dalradian (abstract). *Trans. Inst. Mining Metall.* 90, B57.
- Sweatman, T.R. and Long, J.V.P. (1969) Quantitative electron-probe microanalysis of rock-forming minerals. *J. Petrol.* 10, 332-379.
- Swenson, D.H., Laux, S.J., Burns, A.R., Perley, P.C. and Boast, A.M. (1981) The Foss barite deposit, Aberfeldy, Scotland: depositional and structural history of a Dalradian strata-bound orebody (abstract) *Trans. Inst. Mining Metall.* 90, B57.
- Swett, K. (1968) Authigenic feldspars and cherts resulting from dolomitization of illitic limestones: a hypothesis. *J. Sedim. Petrol.* 38, 128-135.
- Tanner, P.W.G. and Miller, R.G. (1980) Geochemical evidence for loss of Na and K from Moinian calc-silicate pods during prograde metamorphism. *Geol. Mag.* 117, 267-275.
- Taylor, S. (1984) Structural and paleotopographic controls of lead-zinc mineralization in the Silvermines orebodies, Republic of Ireland. *Econ. Geol.* 79, 529-548.
- Taylor, S. and Andrew, C.J. (1978) Silvermines orebodies, Co. Tipperary, Ireland. *Trans. Inst. Mining Metall.* 87, B111-B124.
- Taylor, H.P. and Coleman, R.G. (1968).  $^{18}\text{O}/^{16}\text{O}$  ratios of coexisting minerals in glaucophane-bearing metamorphic rocks. *Bull. Geol. Soc. Am.* 79, 1727-1756.
- Theisen, R. and Vollath, D. (1967) 'Tables of X-ray Mass Absorption Coefficients'. Verlag Stahleisen M.B.H., Dusseldorf.
- Thirlwall, M.F. (1979) 'The petrochemistry of the British Old Red Sandstone volcanic province'. Ph.D. thesis, University of Edinburgh.
- Thomas, P.R. (1979) New evidence for a Central Highland root zone. In Harris, A.L., Holland, C.H. and Leake, B.E. (eds.) 'The Caledonides of the British Isles - reviewed'. *Spec. Publ. geol. Soc. Lond.* 8, 205-212.
- Thompson, A.B. (1976) Mineral reactions in pelitic rocks. II: Calculation of some P-T-X (Fe-Mg) phase relations. *Am. J. Sci.* 276, 401-454.
- Thompson, A.M. (1975) Talc paragenesis in some siliceous dolomitic rocks, and its sedimentologic significance. *Contrib. Mineral. Petrol.* 52, 133-142.
- Thompson, G. (1973) Trace element distributions in fractionated oceanic rocks, 2. Gabbros and related rocks. *Chem. Geol.* 12, 99-111.
- Thompson, R.N., Morrison, M.A., Dickin, A.P. and Hendry, G.L. (1983) Continental flood basalts... arachnids rule OK? In Hawkesworth, C.J. and Norry, M.J. (eds.) 'Continental basalts and mantle xenoliths'. Shiva geology series.
- Toulmin, P. and Barton, P.B.Jr. (1964) A thermodynamic study of pyrite and pyrrhotite. *Geochim. Cosmochim. Acta* 28, 641-671.

- Tracy, R.J. (1982) Compositional zoning and inclusions in metamorphic minerals. In J.M. Ferry (ed.) *Reviews in Mineralogy* 10, Min. Soc. Am., 355-397.
- Tracy, R.J., Robinson, P. and Thompson, A.B. (1976) Garnet composition and zoning in the determination of temperature and pressure of metamorphism, central Massachusetts. *Am. Mineral.* 61, 762-775.
- Tso, J.L., Gilbert, M.C. and Craig, J.R. (1979) Sulfidation of synthetic biotites. *Am. Mineral.* 64, 304-316.
- Turekian, K.K. and Wedepohl, K.H. (1961) Distribution of the elements in some major units of the earth's crust. *Bull. geol. Soc. Am.* 72, 175-192.
- Turi, B., Graham, C.M. and Sheppard, S.M.F. (1973) Carbon and oxygen isotope studies of the Dalradian metabasic rocks, and the role of the pore fluid during regional metamorphism (abstract). 3rd European Colloquium of Geochronology and Isotope Geology, Oxford.
- Turner, F.J. (1968) 'Metamorphic petrology - Mineralogical and field aspects'. McGraw Hill, New York.
- Turner, J.S. and Gustafson, L.B. (1978) The flow of hot saline solutions from vents in the seafloor - some implications for exhalative massive sulphide and other ore deposits. *Econ. Geol.* 73, 1082-1100.
- Urabe, T. (1974a) Iron content of sphalerite coexisting with pyrite from some Kuroko deposits. In Ishihara, S. et al. (eds.) 'Geology of Kuroko deposits'. *Mining Geol. Tokyo, Spec. Issue* 6, 377-384.
- Urabe, T. (1974b) Mineralogical aspects of the Kuroko deposits in Japan and their implications. *Mineralia Deposita* 9, 309-324.
- Urabe, T. and Sato, T. (1978) Kuroko deposits of the Kosaka Mine, Northeast Honshu, Japan - products of submarine hot springs on Miocene sea floor. *Econ. Geol.* 73, 161-179.
- Valley, J.W. and O'Neil, J.R. (1981)  $^{13}\text{C}/^{12}\text{C}$  exchange between calcite and graphite: a possible thermometer in Grenville marbles. *Geochim. Cosmochim. Acta* 45, 411-419.
- Van de Kamp, P.C. (1970) The Green Beds of the Scottish Dalradian Series: geochemistry, origin and metamorphism of mafic sediments. *J. Geol.* 78, 281-303.
- Vaughan, D.J. and Craig, J.R. (1978) 'Mineral chemistry of metal sulphides'. Cambridge University Press.
- Velde, D. (1979) Trioctahedral micas in melilite-bearing eruptive rocks. *Geophys. Lab. Yearbook* 78, 468-475.
- Vermaas, F.H.S. (1953) A new occurrence of barium-feldspar at Otjosundu, S.W. Africa, and an X-ray method for determining the composition of hyalophane. *Am. Mineral.* 38, 845.
- Viezer, J. and Hoefs, J. (1976) The nature of  $^{18}\text{O}/^{16}\text{O}$  and  $^{13}\text{C}/^{12}\text{C}$  secular trends in sedimentary carbonate rocks. *Geochim. Cosmochim. Acta* 40, 1387-1395.
- Viezer, J., Hosler, W.T. and Wilgus, C.K. (1980) Correlation of  $^{13}\text{C}/^{12}\text{C}$  and  $^{34}\text{S}/^{32}\text{S}$  secular variations. *Geochim. Cosmochim. Acta* 44, 579-587.
- Vine, J.D. and Tourtelot, E.B. (1970) Geochemistry of black shale deposits - a summary report. *Econ. Geol.* 65, 253-272.
- Viswanathan, K. and Kielhorn, H.-M. (1983) Variations in the chemical compositions and lattice dimensions of (Ba, K, Na)-feldspars from Otjosundu, Namibia and their significance. *Am. Mineral.* 68, 112-121.
- Vokes, F.M. (1969) A review of the metamorphism of sulphide deposits. *Earth Sci. Rev.* 5, 99-143.

- Vokes, F.M. (1983) In discussions and contributions: Genetic problems related to base-metal deposits in sediments. *Trans. Inst. Mining Metall.* 92, B108-109.
- Wada, H. and Suzuki, K. (1983) Carbon isotope thermometry calibrated by dolomite-calcite solvus temperatures. *Geochim. Cosmochim. Acta* 47, 697-706.
- Walker, R.N., Muir, M.D., Diver, W.L., Williams, N. and Wilkins, N. (1977) Evidence of major sulphate evaporite deposits in the Proterozoic MacArthur Group, Northern Territory, Australia. *Nature* 265, 526-529.
- Walters, L.J., Clayford, G.E. and Choquette, P.W. (1972) Reaction rates and  $\delta^{18}\text{O}$  variation for the carbonate-phosphoric acid preparation method. *Geochim. Cosmochim. Acta* 36, 129-140.
- Watkins, K.P. (1983) Petrogenesis of Dalradian albite porphyroblast schists. *J. geol. Soc. London* 140, 601-618.
- Watkins, K.P. (1985) Geothermometry and geobarometry of inverted metamorphic zones in the W central Scottish Dalradian. *J. geol. Soc. London* 142, 157-165.
- Wells, P.R.A. (1979) P-T conditions in the Moines of the Central Highlands, Scotland. *J. geol. Soc. London* 136, 663-671.
- Wells, P.R.A. and Richardson, S.W. (1979) Thermal evolution of metamorphic rocks in the Central Highlands of Scotland. In Harris, A.L., Holland, C.H. and Leake, B.E. (eds.) 'The Caledonides of the British Isles - reviewed'. *Geol. Soc. Lond. Spec. Publ.* 8, 339-344.
- Wendlandt, R.F. (1977) Barium-phlogopite from Haystack Butte, Highwood Mountains, Montana. *Carnegie Inst. Geophys. Lab. Yearbook* 76, 534-539.
- Wenke, E. (1970) Distribution of Al between coexisting micas in metamorphic rocks from the central Alps. *Contrib. Mineral. Petrol.* 26, 50-61.
- Whelan, J.F., Rye, R.O. and deLorraine, W. (1984) The Balmat-Edwards zinc-lead deposits - synsedimentary ore from Mississippi Valley-type fluids. *Econ. Geol.* 79, 239-265.
- White, D.E. (1981) Active geothermal systems and hydrothermal ore deposits. *Econ. Geol.* 75, 392-423.
- Whitmore, D.R.E., Berry, L.G. and Hawley, J.E. (1946) Chrome micas. *Am. Mineral.* 31, 1-21.
- Wiggins, L.B. and Craig, J.R. (1980) Reconnaissance of the Cu-Fe-Zn-S system: sphalerite phase relationships. *Econ. Geol.* 75, 742-751.
- Willan, R.C.R. (1980) Stratabound sulphide mineralisation in the Dalradian Supergroup of the Grampian Highlands, Scotland. *Norges geol. Unders.* 300, 241-258.
- Willan, R.C.R. (1981a) The lithogeochemistry of the host rocks to the Aberfeldy baryte + base metal deposit, Scotland. In Hall, A.J. and Gallagher, M.J. (eds.) *Correlation Caledonian Stratabound Sulphides Symposium volume*, Strathclyde, May 1981, 46-53.
- Willan, R.C.R. (1981b) Discussion of trace element results. In Smith, C.G. (ed.) *Dalradian of the Scottish Highlands - stratabound mineralization and geology, excursion guide: Correlation Caledonian Stratabound Sulphides symposium*, May 1981, 25-32.
- Willan, R.C.R. (1982) Isotopic evidence for the source of sulphur in the Aberfeldy baryte and sulphide deposits, and the evolution of the hydrothermal system. (Abstract) Mineral Deposits Studies Group meeting, Univ. of Glasgow, 24 September 1982.

- Willan, R.C.R. (1983) Stratiform baryte and sulphide in Dalradian metasediments of the Grampian Highlands, Scotland: Geological setting, mineralogy, sulphur isotopes and geochemistry. Ph.D. thesis, University of Strathclyde.
- Willan, R.C.R. and Coleman, M.L. (1981) Sulphur isotope study on stratabound baryte and sulphide from the Dalradian metamorphic terrain, Scotland. Inst. Geol. Sci. Stable Isotope Report no. 60.
- Willan, R.C.R. and Coleman, M.L. (1983) Sulfur isotope study of the Aberfeldy barite, zinc, lead deposit and minor sulfide mineralization in the Dalradian metamorphic terrain, Scotland. Econ. Geol. 78, 1619-1656.
- Willan, R.C.R. and Hall, A.J. (1980) Sphalerite goebarometry and trace-element studies on stratiform sulphide from McPhun's Cairn, Loch Fyne, Argyll, Scotland. Trans. Inst. Mining Metall. 89, B31-B40.
- Williams, N. (1978) Studies of the base metal sulfide deposits at McArthur River, Northern Territory, Australia: 1. The Cooley and Ridge deposits. Econ. Geol. 73, 1005-1035.
- Williams, N. and Rye, D.M. (1974) Alternative interpretation of the sulphur isotope ratios in the McArthur lead-zinc-silver deposit. Nature 247 (Phys. Sci.), 535-537.
- Wilson, J.R. and Leake, B.E. (1972) The petrochemistry of the epidiorites of the Tayvallich peninsula, North Knapdale, Argyllshire. Scott. J. Geol. 8, 215-252.
- Yardley, B.W.D. (1977) An empirical study of diffusion in garnet. Am. Mineral. 62, 793-800.
- Yardley, B.W.D. and Senior, A. (1982) Basic magmatism in Connemara, Ireland: evidence for a volcanic arc? J. geol. Soc. London 139, 67-70.
- Yardley, B.W.D., Vine, F.J. and Baldwin, C.T. (1982) The plate tectonic setting of NW Britain and Ireland in late Cambrian and early Ordovician times. J. geol. Soc. London 139, 455-473.
- Zimmermann, R.A. (1970) Sedimentary features in the Meggen barite-pyrite-sphalerite deposit and a comparison with the Arkansas barite deposits. Neues Jb. Mineral. Abh. 113, 179-214.

# Sphalerite composition in relation to deposition and metamorphism of the Foss stratiform Ba-Zn-Pb deposit, Aberfeldy, Scotland

NORMAN R. MOLES

Grant Institute of Geology, University of Edinburgh, West Mains Road, Edinburgh EH9 3JW

**ABSTRACT.** Sphalerite is a common constituent of the mineralized rocks and host metasediments of the Foss baryte-base metal deposit, located near Aberfeldy in the central Scottish Highlands. Microprobe analyses of sphalerite show a wide range in minor element content (0–17 mol. % FeS, 0–3 mol. % MnS), and sphalerites of contrasting composition are often found in the same rock. This suggests that equilibrium domains in some rocks were minute (< 1 mm), during regional metamorphism. Pressures derived from the selective application of the sphalerite geobarometer are consistent with other mineralogical evidence of peak metamorphic pressures in the range 7–10 kbar, at 540–580 °C. However, there is considerable evidence of partial retrograde re-equilibration of sphalerite, by continued buffering with pyrite + pyrrhotine and by outward diffusion of iron. Marginal depletion of Fe and Mn in sphalerite within coarse carbonate rocks is attributed to partitioning reactions following recrystallization. Sphalerite which has retained its pre-metamorphic composition shows systematic variations in composition through profiles of mineralized beds, which may be related to depositional environments. Bimodal primary compositions can be explained by precipitation of zinc sulphides under the contrasting chemical environments of hydrothermal vents and cooler, exhaled brine layers on the sea floor.

THE Aberfeldy stratiform baryte-base metal deposits, which have been described by Coats *et al.* (1980, 1981), are situated in the central Scottish Highlands (fig. 1). They are contained within steeply inclined metasedimentary rocks of the Middle Dalradian (c. 600 Ma) which were subjected to polyphase deformation and garnet-grade metamorphism during the Grampian Orogeny (Bradbury *et al.*, 1979; Sirapakash, 1982). The deposits have many of the characteristics of the shale-hosted, sedimentary exhalative class of stratiform ore deposits (Large, 1981). They are considered to have formed from metalliferous brines which were expelled into actively developing sedimentary basins during a period of increasing crustal instability (Russell *et al.*, 1981a; Laux *et al.*, in prep.). This paper concerns the sulphide mineralogy of the Foss

deposit, which is the western of the two major deposits at Aberfeldy, in both of which sphalerite is widespread and locally abundant.

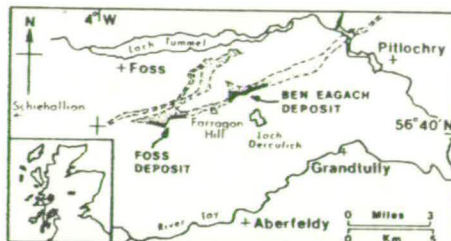


FIG. 1. Map of the central Scottish Highlands showing location of the Aberfeldy deposits. Outcrop of the Ben Eagach Schist is shown by the stippled ornament.

The importance of sphalerite in geological studies derives from its refractory nature, and its capacity to record physical and chemical characteristics of the environment of deposition or metamorphism by changes in minor element composition (Barton, 1970; Scott, 1983). The changing temperature and chemistry of mineralizing solutions has left a delicate record in the growth-banded sphalerite of some vein and Mississippi Valley type deposits (e.g. McLimans *et al.*, 1980). Sequential trends of sphalerite composition have been described from the Kuroko deposits (Urabe, 1974), and from some sedimentary exhalative deposits such as Sullivan (Campbell and Ethier, 1983). The Fe content of sphalerite in equilibrium with pyrite and pyrrhotine has been calibrated as a geobarometer (Scott, 1973; Lusk and Ford, 1981), which has been applied to many metamorphosed sulphide deposits with variable success (Scott, 1976; Plimer, 1980; Hutchison and Scott, 1981).

In this paper, the compositions and textural

© Copyright the Mineralogical Society

500

N. R. MOLES

- Nitsch, K.-H. (1980) *Fortschr. Mineral.* **58**, 98–100.  
 Oehler, J. H., and Logan, R. G. (1977) *Econ. Geol.* **72**, 1393–1409.  
 Page, D. C., and Watson, M. D. (1976) *Ibid.* **71**, 306–27.  
 Plimer, I. R. (1979) *Mineral. Deposita*, **14**, 207–18.  
 — (1980) *Ibid.* **15**, 237–41.  
 Reinecke, T. (1982) *Contrib. Mineral. Petrol.* **79**, 333–6.  
 Rozendaal, A. (1978) In *Mineralisation in metamorphic terranes* (W. J. Verwoerd, ed.), Geol. Soc. S. Afr. Spec. Publ. No. 4, 235–65.  
 Russell, M. J., Willan, R. C. R., Anderton, R., Hall, A. J., Nicholson, K., and Smythe, D. K. (1981a) In *Correlation of Caledonian stratabound sulphides, symposium volume* (A. J. Hall and M. J. Gallagher, eds.), Glasgow 1–2 May 1981, 24–9.  
 —, Solomon, M., and Walshe, J. L. (1981b) *Mineral. Dep.* **16**, 113–27.  
 Sato, T. (1972) *Min. Geol. Tokyo*, **22**, 31–42.  
 — (1973) *Geochem. J., Tokyo*, **7**, 245–70.  
 — (1977) In *Volcanic processes in ore genesis*, Geol. Soc. Lond., Special Pub. 7, 153–61.  
 Schroll, E., Schulz, O., and Pak, E. (1983) *Mineral. Deposita*, **18**, 17–25.  
 Scott, S. D. (1973) *Econ. Geol.* **68**, 466–74.  
 — (1976) *Am. Mineral.* **61**, 661–70.  
 — (1983) *Mineral. Mag.* **47**, 427–35.  
 — and Barnes, H. L. (1971) *Econ. Geol.* **66**, 653–69.  
 — and Kissin, S. A. (1973) *Ibid.* **68**, 475–79.  
 Sibson, R. H., Moore, J. M., and Rankin, A. H. (1975) *J. geol. Soc. Lond.* **131**, 653–9.  
 Sivapakash, C. (1982) *Scott. J. Geol.* **18**, 109–24.  
 Solomon, M., and Walshe, J. L. (1979) *Econ. Geol.* **74**, 797–813.  
 Stumpff, E. F. (1979) *Mineral. Deposita*, **14**, 207–17.  
 Sturt, B. A. (1961) *J. geol. Soc. Lond.* **117**, 131–56.  
 Styr, M. M., Brackmann, A. J., Holland, H. D., Clark, B. C., Pisutha-Arnond, V., Eldridge, C. S., and Ohmoto, H. (1981) *Earth Planet. Sci. Lett.* **53**, 382–90.  
 Sweatman, T. R., and Long, J. V. P. (1969) *J. Petrol.* **10**, 332–79.  
 Swenson, D. H., Laux, S. J., Burns, A. R., Perley, P. C., and Boast, A. M. (1981) *Trans. Inst. Minn. Metall. B.* **90**, 57.  
 Turner, J. S., and Gustafson, L. B. (1978) *Econ. Geol.* **73**, 1082–100.  
 Urabe, T. (1974) In *Geology of Kuroko Deposits* (S. Ishihara *et al.*, eds.), *Min. Geol., Tokyo*, Spec. Issue no. 6, 377–84.  
 Wells, P. R. A. (1979) *J. geol. Soc. Lond.* **136**, 663–71.  
 — and Richardson, S. W. (1979) In *The Caledonides of the British Isles: reviewed* (A. L. Harris *et al.*, eds.), Geol. Soc. Lond., 339–44.  
 Wiggins, L. B., and Craig, J. R. (1980) *Econ. Geol.* **75**, 742–51.  
 Willan, R. C. R. (1980) *Nor. geol. Unders.* **300**, 241–58.  
 — (1981) In *Correlation of Caledonian stratabound sulphides, excursion guide* (A. J. Hall and M. J. Gallagher, eds.), Glasgow 1–2 May 1981.  
 — and Coleman, M. C. (1981) *Inst. Geol. Sci. Stable Isotope Rep.* No. 60.

[Revised manuscript received 12 July 1983]



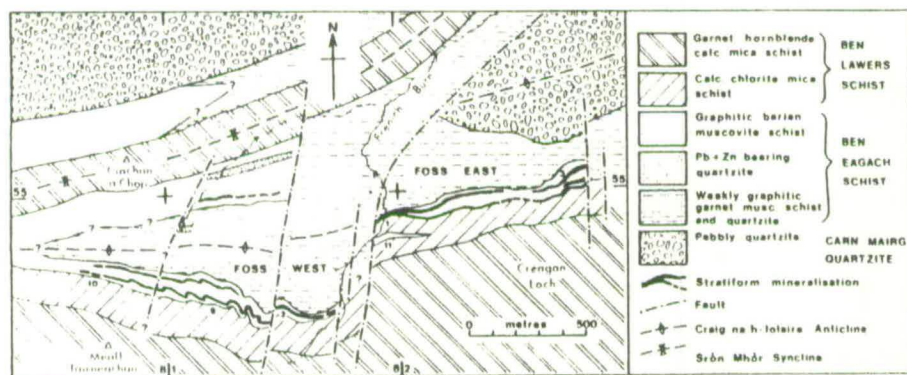


FIG. 2. Geological map of Foss deposit, Aberfeldy, based on maps by Sturt (1961) and Coats *et al.* (1981) and unpublished field maps. IGS borehole sites located by numbers. Grid numbers refer to OS sheet 52.

relationships of sphalerite in the Foss deposit are described, and an attempt is made to distinguish sphalerite compositions of primary origin from those modified by metamorphic processes. Consideration is given to the size of equilibrium domains and the significance of diffusion processes affecting sphalerite during metamorphism. The application of the sphalerite geobarometer is evaluated and results are compared with geothermometric and geobarometric data derived from calcite, dolomite, garnet hornblende, and cymrite celsian phase equilibria. The range and spatial distribution of pre-metamorphic sphalerite compositions are discussed and are tentatively related to depositional processes in the mineralizing system.

### Geology

The Foss deposit, which has a strike-length of about 2 km and an explored depth of 300 m, extends between the northern slopes of Meall Tairneachan and Creagan Loch (fig. 2). The mineralization occurs as multiple sheets or lenses within graphitic and calcareous mica schists of the Ben Eagach Schist formation, and the mineralized zone ranges from about 30 m to over 200 m in true thickness. It is terminated to the east by a N. S. fault zone, and plunges to the west in the core of the Craig na h-Iolair Anticline (Sturt, 1961).

Although potentially a source of industrial baryte, much of the mineralization consists of carbonate, quartz, and barium-silicate lithologies which are variably enriched in base-metal sulphides. Rapid lateral facies variations within both mineralized horizons and metasediments, and localized structural attenuation associated with folding, are features of the deposit (Swenson *et al.*, 1981).

However, closely spaced drillholes have allowed the correlation of individual horizons (Laux *et al.*, in prep. and unpublished work). Stratigraphic correlation has been assisted by the recognition of thin (2 cm–2 m) metabasic layers of probable tuffaceous origin, which are closely associated with several of the mineralized horizons.

Thickness and facies variations and the local occurrence of synsedimentary breccias suggest a genetic relationship between the distribution of mineralization and penecontemporaneous faulting. Growth faults were active elsewhere in the Dalradian basin in the late Proterozoic–early Cambrian (Anderton, 1979) and are a characteristic feature associated with sedimentary exhalative deposits (Large, 1981). These faults may have acted as conduits for mineralizing brines which were expelled into the marine basin, possibly by means of seismic pumping (Sibson *et al.*, 1975). It is envisaged that baryte was deposited in relatively shallow, oxygenated parts of the basin, while sulphides accumulated on the downthrown sides of postulated growth faults where pooling of the brines inhibited mixing with sea-water sulphate (Moles, 1982, and Laux *et al.*, in prep.). As cross-cutting mineralization (of pre-metamorphic origin) and alteration pipes are absent from below the stratiform horizons at the present level of exposure, the deposits may be classified as distal (Large, 1981; Plimer, 1979).

### Sulphide mineralogy

In the Aberfeldy deposits, sphalerite is the second most abundant sulphide mineral after pyrite; galena and pyrrhotine are less abundant, and chalcocite occurs in trace amounts. Although widespread in both the mineralized rocks and host metasediments,

sphalerite is seldom a major constituent. In sulphidic bands, the sphalerite content occasionally increases to > 50 % over intervals of 1–20 cm. Sphalerite more frequently occurs as disseminated grains, or as tenuous laminae which are parallel to the lithological layering. Fine sedimentary layering has generally been preserved in lithologies which are rich in quartz, barium feldspars, baryte, and carbonates, whereas micaceous rocks are usually highly schistose. Remobilization of sulphides, along high-angle cleavage planes or into veinlets and segregations, is generally minor and localized in extent, except in some mineralized carbonate rocks where breccia textures have developed.

Sphalerite grains range in shape from equant and subhedral to highly irregular and embayed. Grain size ranges from 0.03 to 3 mm corresponding to a similar range in the host rocks. Individual crystals may reach 2 cm in veins and segregations. Small sphalerite grains are often encapsulated by pyrite, which often forms discrete rounded to euhedral cubic porphyroblasts. Sphalerite grains of differing colour often occur in the same rock, and visible zoning of sphalerite is sometimes observed in transmitted light. Microprobe analyses have confirmed that these variations in colour correspond to variations in the minor element contents of sphalerite. This allows a visual estimate to be made of the abundance of particular compositions (Fe-rich or Fe-poor) in polished thin sections. A variety of textural and compositional relationships in sphalerite-bearing assemblages are illustrated in figs. 3, 8, and are described in detail below.

Irregular or rectangular-shaped grains of pyrrhotine are common in graphitic schist and dolomitic celsian rocks, but pyrrhotine is rare in baryte rock. Pyrrhotine commonly coexists with sphalerite and galena, and is often associated with minor chalcocite. The occurrence of pyrrhotine in certain metabasic lithologies suggests that reactions involving Fe–Mg silicates may have generated some pyrrhotine during metamorphism, but massive bands formed of pyrrhotine are undoubtedly primary in origin. No evidence of pyrrhotine replacing pyrite has been observed, but in many rocks some or all of the pyrrhotine has been pseudomorphed by pyrite and marcasite. The porous structure or 'bird's-eye' texture of secondary pyrite distinguishes it from the pre-existing, well-crystallized pyrite. This replacement of pyrrhotine is clearly post-tectonic and some has resulted from supergene alteration. From the drillcore samples examined, it is estimated that pyrite has replaced roughly 20 % of the pyrrhotine originally present.

Pyrrhotine occasionally occurs as small inclusions in ferroan sphalerite, which may be crystallographically orientated (fig. 7a). Depletion in the

Fe content of the host sphalerite around these orientated inclusions suggests that this pyrrhotine formed by exsolution from the sphalerite. Chalcocite is more common as inclusions in sphalerite, and has been observed in sphalerites of a wide range of compositions. Chalcocite inclusions, which are usually equant and can reach 30 µm in diameter, may be randomly dispersed, orientated along crystallographic planes, or concentrated towards the centres of host sphalerite grains. Although some chalcocite may have been exsolved from sphalerite (Wiggins and Craig, 1980), the abundance of inclusions (often about 5 % by volume) suggests that the chalcocite originated as a primary two-phase intergrowth which was recrystallized during metamorphism (Hutchison and Scott, 1981).

**Sphalerite analyses.** Analyses were performed on a Cambridge Instruments Microscan Mk 5 electron microprobe at Edinburgh University. The wavelength dispersive technique was employed, with an accelerating voltage of 20 KeV, a probe current (measured at the Faraday Cage) of 30 nA, and an electron beam diameter of 1 µm. Metal standards were used for Zn, Fe, Mn, Cu, and Cd, and a pyrite standard was used for sulphur. Data reduction was performed by an on-line computer using the ZAF correction procedures of Sweatman and Long (1969). Under the analytical conditions employed, detection limits were 0.03 wt. % for iron and 0.02 wt. % for manganese, and precision for iron was usually better than ±1 % of the wt. % Fe present for sphalerites with > 6 wt. % Fe (= 10 mol. % FeS).

Microprobe analyses were obtained from the polished thin (c. 30 µm) sections used for transmitted and reflected light observations. The iron content of Foss sphalerite varies from 0.0 to 17.0 mol. % FeS, which corresponds to a range in appearance from colourless, through yellow and orange, to dark red in transmitted light. The Mn content is low in most Fe-rich sphalerite (> 10 mol. % FeS) but ranges up to 2.7 mol. % MnS in Fe-poor sphalerite (see Coats *et al.*, 1980). Fe-poor, Mn-rich sphalerite is grey in transmitted light. These relationships between sphalerite composition and colour are similar to those noted by Page and Watson (1976).

A small amount (0.1–0.3 wt. %) of Cd was detected in many sphalerites, but Sb was below detection limits (c. 0.05 wt. %) in most analyses. Cu was detected in trace amounts (up to 0.14 wt. %) in some sphalerites, but microscopic chalcocite inclusions account for the higher apparent Cu contents in some analyses of inclusion-rich sphalerite. The metal: sulphur ratio of sphalerite confirms that it is stoichiometric (Zn,Fe,Mn)S, within the limits of analytical precision (±0.3 % of the amount present for sulphur).

**Textural and compositional relationships.** Six samples which illustrate a range in textural and compositional relationships between sphalerite and associated phases, and which contain features crucial to their interpretation, are now described in some detail. Information on these samples is summarized in Table 1 and in figs. 3–8.

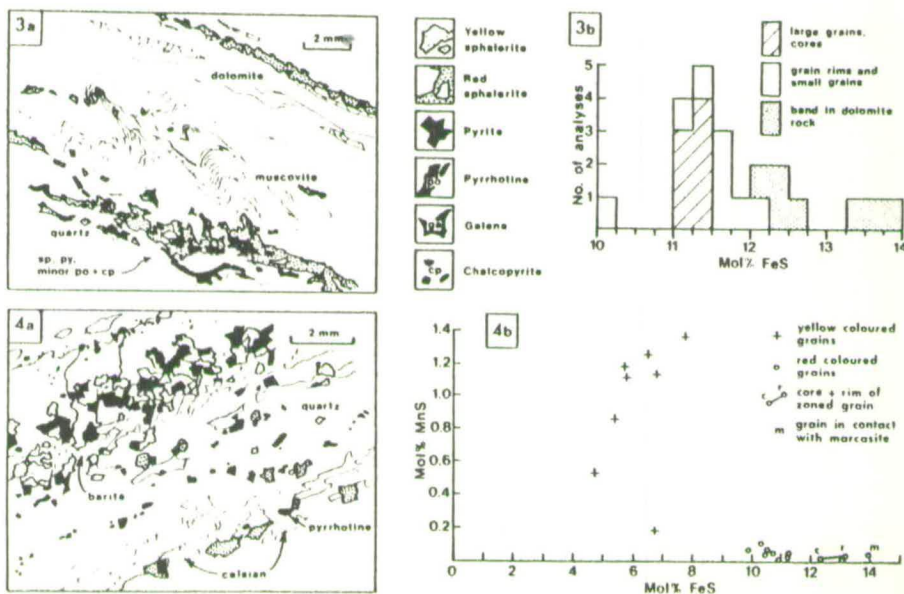


TABLE 1. Summary of textural and chemical features of sphalerite-bearing rock samples described in the text

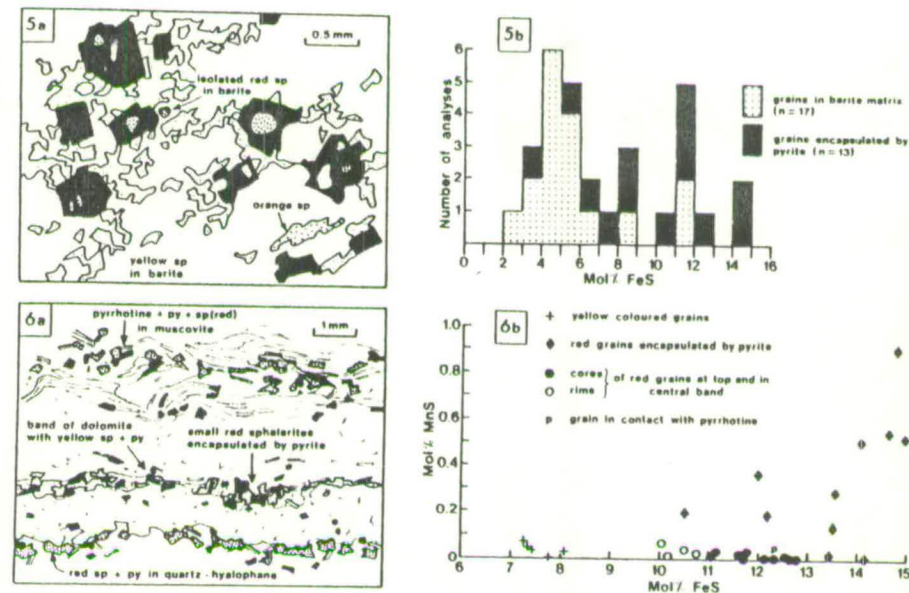
Fig.	Sample*	Lithology	Sulphide assemblage	No. of analyses	Range in mol. % FeS	Range in mol. % MnS	Interpretation
3	705-9	Graphitic musc. qtz. dol. schist	py + po + sp, minor ga, cp	22	10-14	0-0.1	Buffered, in part retrogressive
4	80-30A	Pyritic qtz. celsian rock	py + sp, py + po + sp, retro. mar	20	5-14	0-1.3	Primary (Fe-poor) + buffered (Fe-rich)
5	705-20	Sulphidic baryte rock	py + sp, minor ga	30	3-15	0-0.2	Primary, bimodal
6	429-8	Qtz. musc. dol. hyalophane metachert	py + sp, py + po + sp, minor ga, cp	30	7-15	0-0.9	Primary, bimodal + locally buffered
7	202-3	Muscovitic quartzite with sulphide lenses	py + po + sp + ga + cp, retrograde po, py + mar	38	11-17	0-0.1	Retrogressively buffered with annealed cp intergrowth
8	705-21	Coarse sp. celsian dolomite rock	sp; sp + py, minor ga	20	2-14	0-0.3	Diffusion zoned: loss of Fe + Mn to carbonate

\* Samples from Creagan Loch (Foss East) except 429-8, from Meall Tairneachan (Foss West) (see fig. 2). All samples except for 80-30A are from drillcore.

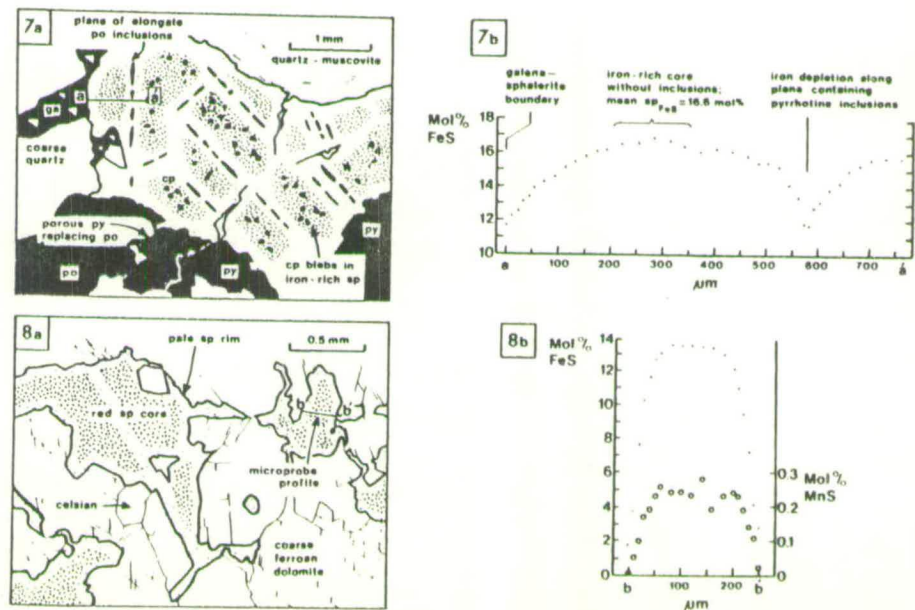
Abbreviations: py, pyrite; po, pyrrhotine; sp, sphalerite; ga, galena; cp, chalcopyrite; mar, marcasite.



FIGS. 3 and 4. (a) line drawings from polished thin sections (PTS). FIG. 3. Sample 705-9; (b) histogram of mol. % FeS for twenty-two sphalerite analyses. FIG. 4. Sample 80-30A; (b) plot of mol. % MnS vs. mol. % FeS for twenty sphalerite grains.



FIGS. 5 and 6. (a) line drawings from PTS. FIG. 5. Sample 705-20; (b) histogram of mol. % FeS for 30 sphalerite grains. FIG. 6. Sample 429-8; (b) plot of mol. % MnS vs. mol. % FeS for thirty sphalerite grains.



FIGS. 7 and 8. (a) line drawings from PTS. FIG. 7. Sample 202-3; (b) microprobe profile of FeS-content of sphalerite along line a'. FIG. 8. Sample 705-21; (b) microprobe profile of Fe (●) and manganese (○) contents of sphalerite along line b'.



Fig. 3a illustrates a sample of graphitic, calcareous metasediment in which sedimentary layering is expressed by variations in the proportions of muscovite to dolomite and quartz. Laminae of sphalerite + pyrite, with minor associated pyrrhotite and galena, parallel this layering, but are partly disrupted by small-scale folding and strain-slip cleavage oblique to the layering. The porous texture of some of the pyrite indicates that much of the pyrrhotite coexisting with the sphalerite during metamorphism has been replaced by secondary pyrite. All of the sphalerite is red in transmitted light, and microprobe analyses (fig. 3b) show a range in iron content from 10–14 mol. % with a modal composition of 11.4 mol. % FeS. The central parts of coarser crystals of sphalerite contain less Fe than both the rims of these crystals and small grains, and sphalerite contained in a dolomitic band is relatively Fe-rich.

The quartz felsic rock illustrated in fig. 4a contains trace (< 1%) pyrrhotite in addition to disseminated pyrite and sphalerite. All three sulphides are occasionally in mutual contact, but most of the sphalerite occurs as isolated grains and aggregates with pyrite. Much of this sphalerite is yellow-orange in colour, but grains which are in mutual contact with pyrrhotite (+ pyrite) are red. Isolated grains of sphalerite (or of sphalerite + pyrite) within a few millimetres of pyrrhotite are also red in colour. Two analysed grains of sphalerite in mutual contact with pyrrhotite + pyrite contain 11.2 and 10.8 mol. % FeS, and other red-coloured grains in the vicinity of pyrrhotite range from 9.9 to 13.0 mol. % FeS (fig. 4b). One grain containing 14 mol. % FeS adjoins marcasite of supergene origin. Yellow-coloured sphalerites contain 5.7 mol. % FeS, and in contrast to the red sphalerites, are variably enriched in manganese up to 1.3 mol. % MnS.

The textures portrayed in fig. 5a are typical of sulphide-rich baryte layers which commonly occur near to the stratigraphic base of the lower baryte horizon in Foss East. Pyrrhotite is absent from these rocks. Pyrite forms subhedral crystals up to 2 mm in diameter, which often enclose one or several grains of sphalerite. Encapsulated sphalerites may exceptionally attain > 200  $\mu$ m in diameter but are usually much smaller. Sphalerite surrounding the pyrites may be highly irregular in shape and intergrown with baryte, or (in other rocks) the sphalerite forms a continuous matrix enclosing crystals of pyrite. A large proportion of the sphalerite (typically > 90%) is yellow in colour corresponding to a relatively low Fe content, but many of the encapsulated grains are red and Fe-rich (fig. 5b). A few isolated orange and red coloured grains also occur in the baryte matrix. In

a similar rock to the one illustrated, discrete sphalerite grains of contrasting colour and composition are in mutual grain contact, but this occurrence is exceptional. However, pyrite crystals often enclose several sphalerite grains of contrasting composition.

A sample of laminated quartz muscovite-hyalophane metachert, which forms the hanging wall to the upper baryte horizon in Foss West, is illustrated in fig. 6a. Red-coloured sphalerite, containing 10.0–12.7 mol. % FeS, occurs as disseminated grains, some of which are in contact with pyrrhotite + pyrite, in crenulated muscovite-rich rock at the top of the field of view. Sphalerite of similar composition, associated with pyrite and muscovite (but not with pyrrhotite), also forms a thin band in hyalophane rock near the bottom of the illustration. In the centre is another thin band of sphalerite which is orange-yellow in colour and contains 7–8 mol. % FeS. Disseminated yellow sphalerite of this composition occurs together with pyrite elsewhere in the sample where pyrrhotite is absent. Small, red-coloured sphalerite grains are encapsulated in pyrite crystals associated with both red and yellow bands of sphalerite and elsewhere in the sample. These sphalerites are distinctive in that they contain appreciable manganese (up to 0.9 mol. % MnS), and up to 15 mol. % FeS (fig. 6b).

Strongly zoned sphalerite crystals are illustrated in figs. 7 and 8, but on detailed examination these are seen to have major differences. The large sphalerite crystal of fig. 7a is associated with coarse pyrite, pyrrhotite (partly replaced by porous pyrite) and galena. Equant chalcopyrite blebs populate dark red cores of the sphalerite crystal in which the Fe content is 15.5–17.0 mol. % FeS. More transparent sphalerite containing 11.5–12.2 mol. % FeS occurs at the margins of the crystal, and also along intersecting crystallographic planes containing planar inclusions of pyrrhotite and chalcopyrite. Usually pyrrhotite and chalcopyrite form separate, parallel grains (typically 5  $\times$  50  $\mu$ m in size) in these Fe-depleted zones, but occasionally chalcopyrite mantles pyrrhotite inclusions.

The highly irregular and embayed form of sphalerite shown in fig. 8a is typical of carbonate mineralization in which sedimentary layering has been obliterated by recrystallization during metamorphism. The sphalerite shows pronounced depletion in both Fe and Mn towards grain rims and along internal cracks and cleavage planes. Small grains (< 100  $\mu$ m) are pale-coloured, whereas the central areas of larger grains or aggregates are orange-red and differ in Fe content by up to 12 mol. % FeS from the rims (fig. 8b). In other examples to the one illustrated, each sphalerite grain or aggregate is homogeneous in colour and

composition, but the Fe content appears to increase in direct proportion to grain size.

**Interpretation.** Several general observations which emerge from the foregoing detailed descriptions are critical to the interpretation of textural and compositional relationships of sphalerite in the Foss deposit.

(1) Sphalerite which is in grain contact or in close association with pyrrhotite (or pyrite pseudomorphs of pyrrhotite) is invariably red-coloured and ferroan (> 10 mol. % FeS). Such sphalerite is also usually Mn-poor.

(2) Sphalerite occurring as isolated grains or coexisting with pyrite, but not in the immediate vicinity of pyrrhotite, has a wide range in compositions from Fe-poor to Fe-rich. Overall, Mn and Fe contents are not systematically related, but in individual samples compositional grouping of sphalerite may be based on variations in both Fe and Mn (e.g. figs. 4b and 6b).

(3) Bands of massive sphalerite and individual disseminated grains are usually homogeneous, but adjacent grains or bands may differ in composition. Sphalerite hosted by recrystallized carbonate rock is often strongly zoned, and zoned sphalerite also occurs in coarse sulphide rocks bearing evidence of retrograde alteration. The zonation is diffuse rather than abrupt or oscillatory, and is usually an outward decrease in Fe (and Mn) content.

It is apparent from these observations that equilibrium domains have been minute in some rocks despite the effects of regional metamorphism. At least some of the observed variation in sphalerite composition within and between samples appears to have been inherited from the time of deposition. Several processes can be distinguished which have erased or modified original sphalerite compositions during metamorphism. These are: (a) buffering of the Fe content of sphalerite coexisting with pyrrhotite + pyrite; (b) homogenization of individual grains or of massive bands of sphalerite by intracrystalline diffusion; (c) partitioning of Fe and Mn between sphalerite and carbonate or other sulphide phases; and (d) exsolution and retrograde alteration of sphalerite assemblages.

The background to the use of the sphalerite geobarometer and its application to the Foss deposit are considered first. After other processes which have modified original sphalerite compositions are considered, it is then possible to discuss the significance of primary sphalerite compositions and their stratigraphic variation.

#### Sphalerite geobarometry

The amount of FeS in solid solution in sphalerite ( $sp_{FeS}$ ) is a function of temperature, pressure, and

FeS activity ( $a_{FeS}$ ). Barton and Toulmin (1966) and Scott and Barnes (1971) have shown that  $sp_{FeS}$  is a function only of pressure in the range 254–550 °C, provided that the  $a_{FeS}$  is buffered by coexisting pyrite + hexagonal 1C' pyrrhotite. Under these conditions, sphalerite has a fixed FeS content of 20.8 mol. % at 1 bar, but with increasing pressure  $sp_{FeS}$  decreases progressively. This compositional change has been calibrated as a geobarometer to 10 kbar by Scott (1973), Lusk and Ford (1978), and Hutchison and Scott (1981) (fig. 9). Above 550 °C,  $sp_{FeS}$  varies with both temperature and pressure, but at high pressures the temperature-independent field extends above 600 °C.

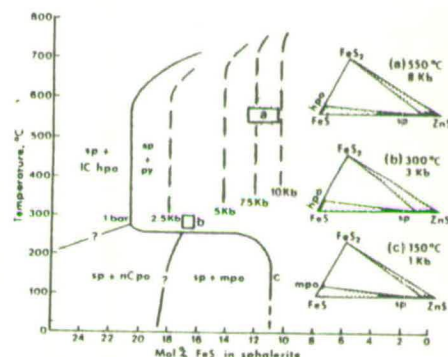


FIG. 9.  $T-X$  projection of the FeS-ZnS-S system showing the sphalerite + pyrrhotite + pyrite solvus at 1 bar (heavy line), and at higher pressures (broken lines). Stippled area is the temperature-independent field in which the sphalerite pyrite hexagonal-pyrrhotite barometer can be applied. Modified from Scott and Barnes (1971), Scott (1973), Scott and Kissin (1973), and Lusk and Ford (1978). Box labelled a indicates estimated peak  $P$ ,  $T$  conditions at Aberfeldy, box labelled b indicates retrograde conditions deduced from sample 202-3 (see text). Inset: isothermal sections of the condensed system FeS-FeS<sub>2</sub>-ZnS at points a, b, and c.

Below 254 °C (at 1 bar), 1C' pyrrhotite undergoes structural and compositional changes, and monoclinic 4C' pyrrhotite becomes stable in the assemblage pyrrhotite pyrite sphalerite. Low-temperature re-equilibration of sphalerite in this assemblage results in a marked decrease in  $sp_{FeS}$ . Scott and Kissin (1973) and Groves *et al.* (1975) have found convincing evidence of a largely temperature-independent monoclinic pyrrhotite pyrite-sphalerite solvus corresponding to between about 10.5 and 12.0 mol. % FeS in sphalerite (fig. 9, point c).

Tests with magnetic colloid and XRD tracings have shown that in all samples from Foss that were



examined, the pyrrhotine is monoclinic. However, estimates of peak metamorphic conditions in the Aberfeldy area are well in excess of 300 °C (Table II) and therefore hexagonal 1C pyrrhotine would have been stable during metamorphism. Before applying the sphalerite geobarometer, textural and geochemical evidence of retrograde alteration of sphalerite compositions must be thoroughly examined.

**Retrograde re-equilibration.** Evidence for low-temperature (< 250 °C) reactions involving sphalerite and monoclinic pyrrhotine include the exsolution of pyrrhotine from ferroan sphalerite and the depletion in  $sp_{FeS}$  adjacent to pyrite and pyrrhotine. Both features are illustrated by the sphalerite in fig. 7a. Re-equilibration of this sphalerite crystal with monoclinic pyrrhotine + pyrite, achieved in part by the exsolution of pyrrhotine, has clearly not gone to completion and the Fe-rich cores are relicts from buffering reactions with coexisting hexagonal pyrrhotine + pyrite.

The Fe content of these relict cores allows an estimation to be made of the confining pressure at the point in the cooling history below which hexagonal pyrrhotine was no longer stable. Inserting the mean of five analyses (16.6 mol. % FeS; fig. 7b) into the equation of Hutchison and Scott (1981) gives a pressure of 3.1 ± 0.3 kbar. The hexagonal pyrrhotine monoclinic pyrrhotine transition, and therefore the horizontal limb of the solvus in the Zn-Fe-S system (fig. 9), may be displaced to higher temperatures due to the effect of confining pressure. This has not been determined, but an upper limit of 300 °C at 3.4 kbar can be interpolated from the experimental data of Scott (1973). Therefore it may be postulated that, at some time during uplift, the rock mass enclosing the Foss deposit passed through the  $P-T$  area of 3.1 ± 0.3 kbar and 260–300 °C (fig. 10).

A record of metamorphic conditions during uplift has been preserved in this sphalerite crystal (fig. 7a) because of its large size and incomplete re-equilibration at low temperatures. Of critical importance is the ability to distinguish between small, unzoned sphalerites which have been buffered by monoclinic pyrrhotine + pyrite at low temperatures (< 250 °C), and sphalerite which (although currently in the same assemblage), has retained the equilibrium composition generated by buffering with hexagonal pyrrhotine + pyrite at about 9 kbar, since in both cases the sphalerite will contain about 11 mol. % FeS (fig. 9). Features which allow the recognition of sphalerites of this composition which have been involved in low-temperature reactions, are:

(a) Zoning or heterogeneity, and the presence of exsolved pyrrhotine.

(b) The presence of chalcopyrite inclusions, which appear to promote retrograde reactions (see Boctor, 1980; Hutchison and Scott, 1981).

(c) The association with retrograde metamorphic or supergene phases particularly marcasite and pyrite pseudomorphs of pyrrhotine, and retrograde chlorite and siderite, which indicate the passage of late metamorphic or meteoric fluids.

**Equilibrium domains and retrograde diffusion.** Sulphide-rich rocks from the Foss deposit which contain major amounts of pyrrhotine (frequently associated with minor chalcopyrite) are seldom suitable for deriving peak pressure estimates because of the high incidence of retrograde re-equilibration of sulphides in such rocks. Disseminated sphalerite in competent lithologies such as baryte rock and quartz metachert, in which pyrite is common but pyrrhotine is comparatively rare, has a greater tendency to retain compositions generated by prograde buffering reactions. In such cases, sphalerites in grain contact with pyrrhotine + pyrite are similar in colour and composition to nearby isolated sphalerite (± pyrite) grains, but at a greater distance from the pyrrhotine, sphalerite grains differ in composition and have apparently remained unaffected by buffering reactions during metamorphism (e.g. figs. 4 and 6). These observations suggest that an interstitial fluid phase in the immediate vicinity of pyrrhotine + pyrite was buffered with respect to  $a_{FeS}$ , and that this fluid provided the transport medium for enrichment in  $sp_{FeS}$ .

The rock volume, or equilibrium domain, within which disseminated sphalerite has been buffered by interstitial fluid in equilibrium with one or more grains of pyrrhotine (± pyrite) ranges from less than 1 mm<sup>3</sup> (e.g. sample 80-30A) to at least the size of a hand specimen, and is possibly on the scale of metres in schistose lithologies. In well-banded rocks, buffered equilibrium domains may be planar in shape, particularly where banding is defined by variations in mica content (e.g. sample 429-8). In other rocks, the shape of buffered equilibrium domains relate to cross-cutting veinlets. Characteristically, equilibrium volumes are sharply defined and grains as little as 30 µm apart, at the boundary of a fluid-buffered domain, may differ greatly in colour and composition.

Two independent processes appear to have affected sphalerite compositions subsequent to equilibration during climactic metamorphism. These are: (1) Partial down-pressure re-equilibration of sphalerite (particularly if in grain contact with pyrrhotine), resulting in an increase in  $sp_{FeS}$  (e.g. sample 705-9). (2) Outward diffusion and depletion in  $sp_{FeS}$  in small (< 100 µm diameter) grains and in the rims of larger grains. This depletion is typically

in the order of 0.5–2.0 mol. % FeS, but may exceed 10 mol. % FeS in carbonate-hosted sphalerite (e.g. sample 705-21). Outward diffusion of FeS in sphalerite has previously been invoked by Barton and Skinner (1979) to explain anomalous high-pressure estimates from sphalerite immediately adjacent to pyrrhotine. In the Foss deposit, outward diffusion of FeS in sphalerite (to varying extents) seems to be widespread, and is not restricted to mutual grain boundaries with pyrrhotine.

As these processes have opposing effects on sphalerite composition, the application of the sphalerite geobarometer using the mean of a number of analyses of sphalerites which show evidence of having been buffered by pyrite + hexagonal pyrrhotine, need not necessarily yield peak metamorphic pressures. The centres of relatively large (> 100 µm) sphalerite grains within fluid-buffered equilibrium domains (but not always in contact with pyrrhotine) are taken as the most suitable compositions for geobarometry. These compositions (taken from 705-9, 80-30A, 429-8, and other samples) range from 10.4 to 12.7 mol. % FeS, from which pressures of 9.7–6.9 kbar are calculated using the equation of Hutchison and Scott (1981) (fig. 10).

**Comparison of silicate and sphalerite geobarometers.** Estimates of peak metamorphic pressures in the Aberfeldy area from several silicate geobarometers (Table II), compare favourably with pressures in excess of 7 kbar suggested by the selective application of the sphalerite geobarometer.

Aluminosilicate-bearing rocks have not been found in the vicinity of the deposit, but kyanite is recorded by Sivaprakash (1982) from Grandtully (about 6 km to the SE), and by Wells and Richardson (1979) from Schiehallion (about 10 km to the W; see fig. 1). Recent recalculations of the plagioclase-garnet-kyanite-quartz equilibrium (Newton and Haselton, 1981) suggest that the pressures derived by these authors may be several (1–3) kilobars too high.

Metamorphic temperatures derived from calcite-dolomite geothermometry by Sivaprakash (1982) and from unpublished data, range from 550 to 420 °C, which suggests that retrograde re-equilibration of carbonates is common. The temperature range 540–580 °C derived from garnet-biotite and garnet-hornblende geothermometry, is regarded as representative of peak metamorphic temperatures. Temperatures in this range are also indicated by  $\delta^{34}S$  fractionations between some coexisting sulphide and sulphide baryte pairs (Willan and Coleman, 1981, and unpublished work).

Further petrological work has supported the suggestion by Fortey and Beddoe-Stephens (1982) that much of the celsian occurring at Aberfeldy was formed by the post-deformational replacement of the platy mineral, cymrite, by the reaction:



TABLE II. Estimates of metamorphic temperatures and pressures in the Aberfeldy area

Author	Area	Mineral equilibria	T °C	P kbar
Wells and Richardson (1979)	Schiehallion (Dalradian)	Plag-gt-ky-qtz Garnet-biotite <sup>a</sup>	560 ± 50	12 ± 1.5
Wells (1979)	Schiehallion (Moine)	Hb-plag-qtz-gt-ep Garnet-biotite <sup>a</sup> Gt-hornblende	550 ± 50	11.3 ± 2.0
Sivaprakash (1982)	Aberfeldy-Grandtully	Plag-gt-ky-qtz Ep-gt-plag-qtz Garnet-biotite <sup>a</sup>	500–580 420–550	10 ± 1 8–10
Moles (1983) and unpublished data	Foss deposit, Aberfeldy	Calcite-dolomite <sup>b</sup> Gt-hornblende <sup>c</sup> Calcite-dolomite <sup>b</sup> Cymrite-celsian <sup>d</sup> Sph-py-po	480–530	> 7.0* 8.5 ± 1.5 6.8 ± 0.3 6.1 ± 0.1
Willan (1980, 1981)	Aberfeldy deposits	Sph-py-po		6.1 ± 0.1
Willan and Coleman (1981)	Aberfeldy deposits	$\delta^{34}S$ of sulphide and baryte pairs	550 ± 50	

\* at T = 540 °C (see text).

Calibrations used: <sup>a</sup> Ferry and Spear (1978); <sup>b</sup> Bickle and Powell (1977); <sup>c</sup> Graham and Powell (in prep.); <sup>d</sup> Nitsch (1980).



Cymrite relics have been found in many celsian-bearing rocks, and the presence of aligned inclusions of quartz, rutile, and sulphides in coarse celsian rock suggests the replacement of a folded cymrite fabric. The reaction has been calibrated experimentally by Nitsch (1980) and further experimental work is in progress (Moles, 1983) to ascertain the displacement of the reaction curve by substitution of (K + Si) for (Ba + Al) in both cymrite and celsian (cf. Reinecke, 1982). Using the pure end-member calibration of Nitsch (fig. 10), a minimum pressure of 7 kbar at  $T = 540^\circ\text{C}$  is indicated by the reaction.

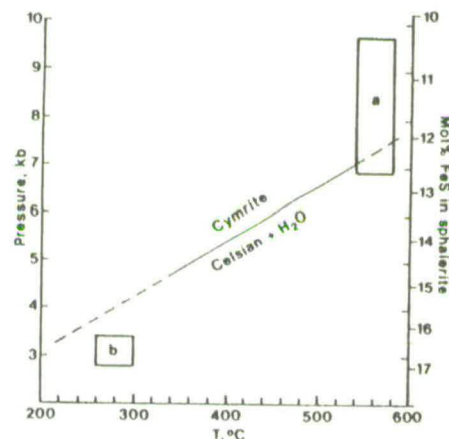


FIG. 10. The equilibrium curve for the reaction, cymrite = celsian +  $\text{H}_2\text{O}$ , from Nitsch (1980). Mol. % FeS scale refers to sphalerite buffered by pyrite + hexagonal pyrrhotine (fig. 9). Boxes labelled a and b correspond to those in fig. 9 and represent estimates of peak and retrograde  $P$ ,  $T$  conditions in the Foss deposit.

The widespread replacement of cymrite in the Aberfeldy deposits suggests that lithostatic pressures were decreasing and/or temperatures were increasing in the area after the development of tectonic fabrics (Moles, 1983). Annealing and continued re-equilibration of sphalerites buffered by pyrrhotine + pyrite during this period may account for some of the spread in pressures derived by sphalerite geobarometry. Previously published results from the application of the sphalerite geobarometer at Aberfeldy (Willan, 1980, 1981; Table II) appear to be underestimates. Willan used a small number of sphalerite grains stated to be in mutual contact with pyrite + pyrrhotine and lacking evidence of retrograde alteration. Unfortunately, the

detailed textural relationships of these sphalerites are not described.

#### Primary sphalerite compositions

Depositional growth zoning in sphalerite, characterized by abrupt and often oscillatory variations in minor element content, has been observed in several non-metamorphosed stratabound base-metal deposits, such as McArthur River (Croxford and Jephcott, 1972) and Bleiberg, Austria (Schroll *et al.*, 1983), and in Mississippi Valley type deposits (McLimans *et al.*, 1980). However, sphalerite zonation of this type is absent at Aberfeldy, and it is inferred that depositional growth zoning, if originally present in the sphalerite, has been erased by recrystallization and intracrystalline diffusion during prograde metamorphism (Barton, 1970).

The presence of encapsulated sphalerites of contrasting composition may provide evidence for the homogenization of the matrix sphalerite in massive sulphide rocks. In rocks containing disseminated sphalerite with a bimodal distribution of compositions, some sphalerite grains of intermediate composition (fig. 5b) may have formed by the coalescence of several grains of end-member composition. Coalescence during grain coarsening may account for the scarcity of mutual grain contacts between sphalerites of contrasting composition.

Partitioning of minor elements between sphalerite and coexisting phases during metamorphism must also be considered as a mechanism by which primary sphalerite compositions may have been modified. Marginal depletion in the Fe and Mn contents of sphalerite in a matrix of recrystallized carbonate, has been described above (fig. 8). Cathodoluminescence studies have revealed striking oscillatory zonation patterns, which correspond to variations in Fe and Mn concentrations determined on the microprobe, in coarsely recrystallized dolomite and calcite. The association of zoned sphalerite with recrystallized carbonate suggests that Fe and Mn have diffused out of the sphalerite and entered the carbonate matrix during metamorphism. Preferential partitioning of zinc from the matrix into the sphalerite may also have occurred, but the zinc content of carbonates is below detection limit on the microprobe. Diffusion profiles in sphalerite have often been frozen in (fig. 8b), but in some carbonate rocks individual sphalerite grains appear to have homogenized after marginal depletion in Fe and Mn, resulting in a positive correlation between grain size and minor element content.

Encapsulated sphalerites are often enriched in Mn in comparison with sphalerites of similar Fe

content in the matrix. This may be of primary origin, or could be due to a preferential partitioning of manganese into sphalerite from the surrounding pyrite during metamorphism. Campbell and Ethier (1983) have demonstrated a positive correlation between the manganese contents of coexisting sphalerite, pyrite and pyrrhotine in a laminated sulphide rock from the Sullivan deposit. In the Foss deposit, the manganese contents of iron sulphides are very low (Willan, 1980), and the grain size of encapsulated sphalerites does not appear to correlate with the degree of manganese enrichment. Therefore, pyrite-sphalerite partitioning of Mn (and Fe) has probably not affected primary sphalerite compositions. Buffering of  $sp_{\text{FeS}}$  by fluids in equilibrium with pyrite + pyrrhotine appears to result in the depletion of  $sp_{\text{MnS}}$  (e.g. sample 80-30A, fig. 4), but the reason for this is not clear.

In summary, the following criteria allow the selection of primary sphalerite compositions which are least likely to have been modified during metamorphism:

- (1) The absence of adjoining or nearby pyrrhotine (or retrograde marcasite and pyrite pseudomorphs of pyrrhotine).
- (2) The occurrence of sphalerite as small disseminated grains rather than as a continuous matrix.
- (3) The absence of zoning, or of a strong positive correlation between grain size and minor element content (particularly if the matrix is recrystallized carbonate rock).
- (4) The occurrence of matrix sphalerite of similar composition to sphalerite grains encapsulated in pyrite.

These criteria are most frequently satisfied in baryte rocks containing disseminated sulphides. However, primary sphalerites have been recognized in other mineralized lithologies such as quartz celsian cherts (e.g. samples 80-30A and 429-8) and also in some metasediments, notably thick (> 1 m) beds of graphitic dolomite rock containing sphalerite laminae.

**Primary sphalerites and ore formation.** Within many samples, a bimodal distribution of sphalerite compositions is observed, the Fe-poor fraction usually predominating (fig. 5). Primary Fe-rich sphalerites are commonly finer-grained, more equant in shape and more often encapsulated in pyrite than the Fe-poor sphalerite in the same rock. The sum of these textural features suggest that the Fe-rich sphalerite may have been precipitated earlier than both the Fe-poor sphalerite and much of the pyrite.

To account for the origin of a range of primary sphalerite compositions within the same rock, it is necessary to speculate on the mechanisms of ore

formation. Many authors have sought to define the nature of ore-forming fluids and the physico-chemical environment of deposition of submarine exhalative deposits (e.g. Finlow-Bates, 1980; Large, 1981; Russell *et al.*, 1981b). The chloride-complex models of Sato (1972, 1973) and Large (1977) for ore solutions forming massive sulphide deposits in volcanic terrains, are generally accepted as broadly applicable to sedimentary-exhalative deposits.

The progressive change in temperature, total sulphur concentration, and oxygen fugacity in the brines which formed the Kuroko deposits has been described by Sato (1977). Decrease in the Fe content of sphalerite with stratigraphic height in the Kuroko deposits (Urabe, 1974) is ascribed largely to a decline in temperature (typically by  $50^\circ\text{C}$  from the stockwork to the top of the stratiform ore). However, this trend may also be related to an increase in total sulphur concentration and oxygen fugacity in the brines (Finlow-Bates, 1980), which also favours the formation of baryte.

The following scenario is envisaged during formation of the ore-bearing stratiform lenses of the Foss deposit. During the expulsion of relatively hot (>  $200^\circ\text{C}$ ), saline, weakly acidic, and sulphur-poor metalliferous brines at exhalative vents, fine-grained and Fe-rich sphalerite (or wurtzite; cf. Styrst *et al.*, 1981; Scott, 1983) was precipitated and carried upwards in the buoyant brine plume together with sulphides of iron and lead (Solomon and Walshe, 1979). The brine then spread laterally as it entrained sea-water (Turner and Gustafson, 1978) and became cooler, less saline, more oxidized and enriched in sulphur (derived by bacteriogenic reduction from sea-water sulphate; Willan and Coleman, 1981). Sphalerite with a lower Fe content precipitated from the bottom-hugging or buoyant brine layer, together with baryte, pyrite, and (with increasing  $f_{\text{O}_2}$ ) magnetite. Alternatively, Fe-poor sphalerite may have crystallized within the unconsolidated ore as reduced sulphur became available (cf. McArthur River ore; Croxford, 1968).

In this model, the Fe-rich sphalerite fraction is regarded as allochthonous whereas the Fe-poor sphalerite crystallized *in situ*. If this is the case, one might expect to find a lateral variation in the Fe content of the Fe-poor sphalerite fraction with increasing distance from the exhalative centre, but less variation in the Fe-rich fraction. However, a simple pattern in the distribution of primary sphalerite compositions has not emerged from a study of the lower mineralized horizon in Foss East (fig. 2) using over 50 samples. Variation in primary sphalerite compositions is greater between samples taken through drill hole intersections of this horizon, than from east to west in the area.

Stratigraphic variation in sphalerite compositions



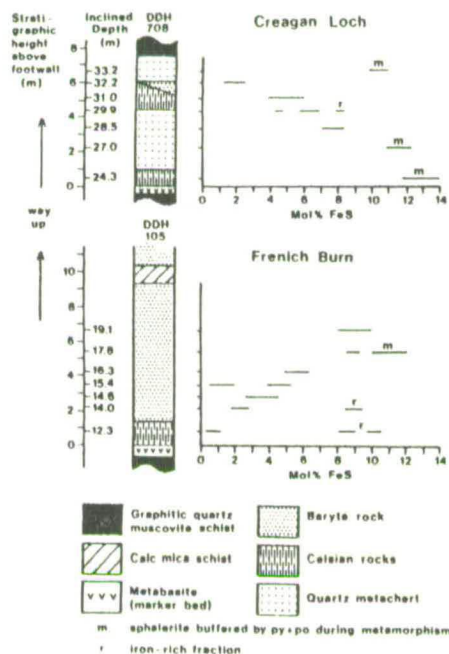


FIG. 11. Primary sphalerite compositions in samples from two drillhole intersections of the lower mineralized horizon (M3) in Foss East, located near IGS boreholes 1 and 3 (see fig. 2).

can be discerned locally (fig. 11). Sphalerite becomes progressively Fe-poor towards the hanging wall near the eastern limit of the deposit in Foss East (near IGS borehole 3), where a lense of baryte overlies thick sulphidic cherts deposited on the downthrown side of a probable syndimentary fault (Laux *et al.*, in prep.). This stratigraphic trend, which is similar to that observed in the Kuroko deposits, may be due to an increase in  $f_{O_2}$  and decrease in temperature and salinity as the ponded brine mixed with the overlying sea-water. This hypothesis is supported by sulphur isotope studies which show a marked decrease in  $\delta^{34}S$  of baryte and pyrite near the stratigraphic hanging wall (Willan and Coleman, 1981; Moles, in prep.).

In contrast to the trend described above, the Fe content of primary sphalerite increases stratigraphically upwards through the footwall chert and the overlying baryte in the vicinity of the French Burn headwater (figs. 2 and 11). Sphalerite is absent from the upper part of the relatively thick baryte unit in this area (Coats *et al.*, 1981; IGS borehole 1), which formed by the stacking of five

mineralized horizons and wedging out of the intervening metasediments (Laux *et al.*, in prep.). This trend in sphalerite compositions may reflect a decrease in sulphur concentration due to the restriction of bacterial activity in a relatively shallow, oxidizing environment during deposition of the baryte. Oxidizing conditions are also suggested by the absence of carbonaceous matter in the intervening and overlying metasediments in this area.

Primary sphalerites have been described from several other stratabound base-metal deposits, but analytical data from unmetamorphosed deposits is scarce. Croxford (1968), Croxford and Jephcott (1972), and Oehler and Logan (1977) describe bedded, disseminated and colloform sphalerites in black shales from the McArthur River deposit, Northern Territory, Australia. The sphalerite varies from colourless to red-brown in appearance, corresponding to a range in iron content from 1.4 to 11.2 mol. % FeS. Fe-rich compositions occur late in the paragenesis in concentrically zoned colloform and vein sphalerite. A similar increase in  $sp_{FeS}$  with paragenetic sequence has been observed by Schroll *et al.* (1983) in zoned colloform sphalerite at Bleiberg, Austria.

Pyrrhotine is absent from the McArthur River deposit, but is a major constituent of the low-grade metamorphosed deposit of Hilton, Queensland. At Hilton, pyrrhotine and chalcopyrite are associated with Fe-rich sphalerite in the upper part of the ore horizon (Mathias *et al.*, 1973). Elsewhere in the deposit, sphalerite ranging in colour from pale yellow to dark brown occurs as disseminations and late-stage veinlets. The association of Fe-rich sphalerite with pyrrhotine in metamorphosed sulphide deposits containing a wide range of sphalerite compositions, has also been observed at Gamsberg, South West Africa (Rozendaal, 1978, and Stumpff, 1979) and at Balmat, New York (Doe, 1962, and Scott, 1976). The preservation of primary sphalerite compositions in some rocks, while in others sphalerite has been buffered by coexisting pyrite + pyrrhotine, is one feature which these deposits have in common with Foss.

### Conclusions

Disillusionment with the sphalerite-pyrite-pyrrhotine barometer has been expressed by several authors in recent years (e.g. Stumpff, 1979; Plimer, 1980) and, indeed, 'sphalerite geobarometry does not appear to provide a panacea for estimating pressures in metamorphic rocks' (Brown *et al.*, 1978). This is due to the extensive resetting of sulphide compositions at lower pressures in many metamorphosed orebodies. The present study

amplifies the need for detailed textural studies before applying the geobarometer, but also illustrates the variety of other geological information, pertaining to metamorphism and to the environment of deposition, which can be derived from sphalerite studies.

In many granoblastic baryte, quartz and feldspar rocks in the Foss deposit, the variable FeS and MnS contents of disseminated sphalerite grains appear to have remained essentially unaltered through metamorphism to garnet-grade conditions. Very localized buffering of sphalerite adjoining pyrrhotine grains is evidence of small (1 cm–1 mm) equilibrium domains in these lithologies. In contrast, sphalerite in the enclosing mica schists has undergone widespread buffering by fluids in equilibrium with pyrite + pyrrhotine, which suggests that large equilibrium domains are associated with penetrative deformation. In rocks which lack evidence of retrograde alteration, the occurrence of buffered sphalerites containing 10.4–12.7 mol. % FeS indicates that peak metamorphic pressures of 7–10 kbar were attained in the Aberfeldy area. Similar pressures are also indicated by silicate geobarometers including the cymrite-celsian reaction (Moles, 1983). Continued buffering of sphalerite coexisting with pyrrhotine (+pyrite) to low pressures may be used in charting the  $P$ - $T$  path in the Aberfeldy area during cooling and uplift.

Depositional growth zoning, if originally present in sphalerite of the Foss deposit, has been erased by intracrystalline diffusion during metamorphism. Partitioning of Fe and Mn between sphalerite and enclosing phases has produced diffuse zonation in sphalerite in recrystallized carbonate rocks.

Primary sphalerite compositions vary in vertical transects through mineralized horizons, which suggests that mineral chemistry relates to depositional processes. Bimodal sphalerite compositions occur in many mineralized rocks: the Fe-rich sphalerites are usually subordinate in quantity and grain size to the Fe-poor sphalerite, and are often encapsulated by pyrite. The Fe-rich fraction is thought to have precipitated from the metalliferous brines during their expulsion from hydrothermal vents, and to have been carried in suspension in the laterally spreading brines. The Fe-poor sphalerite subsequently precipitated from cooler, bottom-hugging brine layers, or within the ore sediment as reduced sulphur became available.

**Acknowledgements.** A research studentship from the Department of Education, Northern Ireland, is gratefully acknowledged. Dresser Minerals are thanked for financial support during fieldwork, and for permission to sample drillcore obtained by the company. The project has benefitted from the guidance and co-operation of company staff.

Thanks are expressed to C. M. Graham, K. R. Gill, S. J. Laux, A. J. Hall, and R. C. R. Willan for critically reviewing the manuscript, and to the secretarial staff of the Grant Institute of Geology, Edinburgh University, for assistance with typing. N. J. Fortey (IGS, London) kindly loaned a number of polished thin sections. Analytical work at the Edinburgh Microprobe Unit was made possible by support from the Natural Environment Research Council, and P. Hill is thanked for his assistance.

### REFERENCES

- Anderton, R. (1979) In *The Caledonides of the British Isles—reviewed* (A. L. Harris *et al.*, eds.), Geol. Soc. Lond. 483 8.
- Barton, P. B., Jr. (1970) *Mineral. Soc. Am. Spec. Pap.* 3, 187 98.
- and Skinner, B. J. (1979) In *Geochemistry of Hydrothermal Ore Deposits*, 2nd edn (H. L. Barnes, ed.), Wiley, New York. 278 403.
- and Toulmin, P. (1966) *Econ. Geol.* 61, 815 49.
- Bickle, M. J., and Powell, R. (1977) *Contrib. Mineral. Petrol.* 59, 281 92.
- Boctor, N. Z. (1980) *Am. Mineral.* 65, 1031 7.
- Bradbury, H. J., Harris, A. L., and Smith, R. A. (1979) In *The Caledonides of the British Isles—reviewed* (A. L. Harris *et al.*, eds.), Geol. Soc. Lond. 213 20.
- Brown, P. E., Essene, E. J., and Kelly, W. C. (1978) *Am. Mineral.* 63, 250 7.
- Campbell, F. A., and Ethier, V. G. (1983) *Mineral. Deposita*, 18, 39 55.
- Coats, J. S., Smith, C. G., Fortey, N. J., Gallagher, M. J., May, F., and McCourt, W. J. (1980) *Trans. Inst. Mining Metall. B*, 89, 110 22.
- *et al.* (1981) *Inst. Geol. Sci. Miner. Recon. Rep.* No. 40, 116 pp.
- Croxford, N. J. W. (1968) *Proc. Aust. Inst. Mining Metall.* 226, 97 108.
- and Jephcott, S. (1972) *Ibid.* 243, 1 26.
- Doe, B. R. (1962) *Geol. Soc. Am. Bull.* 73, 833 54.
- Ferry, J. M., and Spear, F. S. (1978) *Contrib. Mineral. Petrol.* 66, 113 17.
- Finlow-Bates, T. (1980) *Geol. Jahrb.* 1040, 131 68.
- Fortey, N. J., and Beddoe-Stephens, B. (1982) *Mineral. Mag.* 46, 63 72.
- Groves, D. I., Binns, R. A., Bassett, F. M., and McQueen, K. G. (1975) *Econ. Geol.* 70, 391 6.
- Hutchison, M. N., and Scott, S. D. (1981) *Ibid.* 76, 143 53.
- Large, D. E. (1981) In *Handbook of stratabound and stratiform ore deposits* 9 (K. H. Wolf, ed.), 469 508. Elsevier, Amsterdam.
- Large, R. R. (1977) *Econ. Geol.* 72, 549 72.
- Lusk, J., and Ford, C. E. (1978) *Am. Mineral.* 63, 516 19.
- McLimans, R. K., Barnes, H. L., and Ohmoto, H. (1980) *Econ. Geol.* 75, 351 61.
- Mathias, B. U., Morris, D., and Russell, R. E. (1973) *Bull. Bur. Mineral. Resour. Australas.* 141, 33 58.
- Moles, N. R. (1982) *Mineral. Soc. Bull.* 57, December 1982.
- (1983) *Geol. Soc. Lond., Newsletter*, September 1983.
- Newton, R. C., and Haselton, H. T. (1981) In *Thermodynamics of Minerals and Melts* (R. C. Newton, A. Navrotsky, and B. J. Wood, eds.), Springer-Verlag.



# Metamorphic conditions and uplift history in central Perthshire: evidence from mineral equilibria in the Foss celsian–barite–sulphide deposit, Aberfeldy

Norman R. Moles

Grant Institute of Geology, University of Edinburgh, West Mains Road, Edinburgh EH9 3JW, Scotland

**SUMMARY:** Interlayered lithologies of diverse mineralogy enclosing the Middle Dalradian syngenetic Ba–Zn–Pb deposit at Foss, S of Loch Tummel in Perthshire, allow estimates of the P–T conditions of metamorphism using several new geothermometers and geobarometers. Temperatures of 500–560°C are derived from calcite–dolomite geothermometry and from data on Mg–Fe partitioning within garnet–hornblende and garnet–biotite pairs. Plagioclase–biotite–garnet–muscovite and biotite–muscovite–chlorite equilibria indicate peak metamorphic pressures of 8–10 kbar which are in agreement with the results of sphalerite geobarometry.

Textural evidence indicates that the rare platy mineral cymrite ( $\text{BaAl}_2\text{Si}_2\text{O}_8 \cdot \text{H}_2\text{O}$ ) was widespread in mineralized lithologies during penetrative deformation, and has since largely been replaced by celsian. The P–T location of the experimentally determined reaction line,  $\text{cymrite}_{\text{ss}} = \text{celsian}_{\text{ss}} + \text{H}_2\text{O}$ , places further constraints on the peak metamorphic conditions and suggests that the final episode of penetrative deformation ( $D_3$ ) was followed by a period of near-isothermal uplift during which celsian became stable. The cymrite field appears to have been re-entered during late brittle deformation. Peak metamorphic conditions recorded by mineral equilibria at Foss differ from those of areas 10 km to the N and S.

The syngenetic, barite–base metal deposits at Foss and Ben Eagach, situated to the N of Aberfeldy in the central Scottish Highlands (Fig. 1), are contained within steeply inclined, amphibolite facies metasediments of the Argyll Group of the Dalradian Supergroup. Lithologies of diverse composition are interlayered in the vicinity of the deposits. These include metamorphosed pelitic, psammitic and calcareous sediments, basaltic rocks and hydrothermal precipitates enriched in barium and sulphides. Granoblastic barite rock, forming beds often several metres in thickness, is of commercial interest and Zn–Pb sulphides locally reach sub-economic concentrations (Coates *et al.* 1980). An unusual feature of the deposits is the large proportion of barium contained in silicates, particularly celsian and barian muscovite, which although recrystallized are considered to have been authigenic in origin (Fortey & Beddoe-Stephens 1982). The dual influence of depositional and metamorphic processes on the mineralogy and geochemistry of the deposits has been illustrated by studies of sphalerite composition (Moles 1983) and the distribution of sulphur isotopes (Willan & Coleman 1983; Moles 1984).

In this paper, estimates of the intensive parameters of metamorphism are derived from the unmineralized host rocks to the Foss deposit using published calibrations for garnet–hornblende, garnet–biotite and calcite–dolomite geothermometers, and plagioclase–biotite–garnet–muscovite, and biotite–muscovite–chlorite–quartz geobarometers. These are compared with

previous results from sphalerite geobarometry applied to mineralized rocks in the deposit (Moles 1983). Textural evidence for the widespread replacement by celsian of the hydrous barium silicate, cymrite, is then shown to place constraints on the peak conditions of metamorphism and on the uplift and cooling history.

## Geological setting

The stratiform mineralization occurs in the upper part of the Ben Eagach Schist formation and locally extends into the overlying Ben Lawers Schist; both formations belong to the Easdale Subgroup (Harris & Pitcher 1975) which was deposited during a period of increasing crustal instability in the late Precambrian–early Cambrian (Anderton 1979; Graham & Bradbury 1981). The Ben Eagach Schist (BES) is comprised of graphitic quartz–muscovite–schists with subordinate quartzite, graphitic dolostone and metabasaltic lithologies in addition to the barian and sulphidic rocks (Table 1). The upper unit containing the mineralization ranges in stratigraphic thickness from about 20 m to over 100 m and is anomalously enriched in barium in the vicinity of the deposits (Willan 1981). Non-graphitic, calcareous two-mica schists in the lower unit of the Ben Lawers Schist (BLS), are succeeded by porphyroblastic garnet and hornblende schists (Table 1) which are characteristic of this formation along much of its outcrop in central Perthshire.

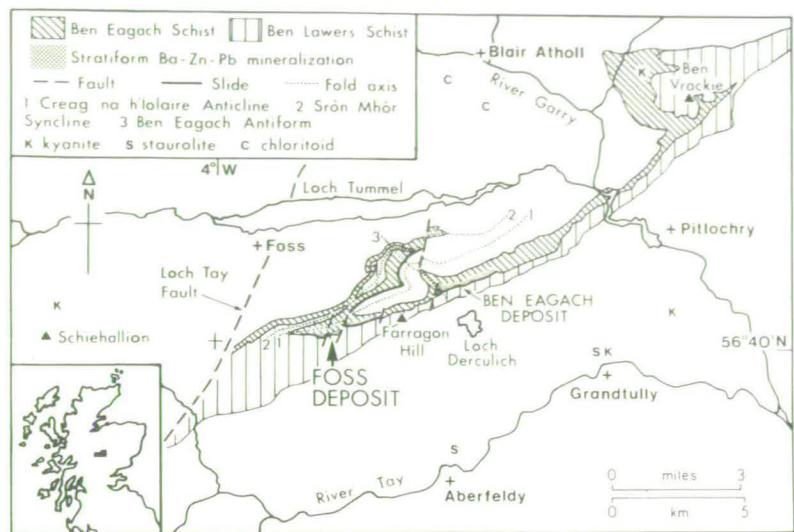


FIG. 1. Map of the central Scottish Highlands showing location of the Foss deposit and of other places and features mentioned in the text. Ornamented areas indicate outcrops of the Ben Eagach and Ben Lawers Schists. Adapted from Sturt (1961), Bradbury *et al.* (1979), and Coats *et al.* (1980).

The rocks enclosing the Foss deposit are situated near to the southern hinge zone of the Tummel Steep Belt (Bradbury *et al.* 1979), and most of the mineralization is located on the southern limb of a major early fold, the Creag na h'Iolaire Anticline (Sturt 1961) (Fig. 1). This is a tight, overturned antiform which plunges towards the W and has an axial planar dip of 50–60° to S. This structure may be equated chronologically with a composite D<sub>1</sub>–D<sub>2</sub> foliation which can be discerned in most lithologies and generally lies parallel to bedding.

A structure with an axial trace sub-parallel to the

Creag na h'Iolaire Anticline and situated on its northern limb is the Sròn Mhòr Syncline (Fig. 1). This was also regarded by Sturt as a primary fold but has since been interpreted as a D<sub>3</sub> isoclinal synform with a near-vertical axial plane (Roberts & Treagus 1979). This synform refolds the Creag na h'Iolaire Anticline and is associated with westward-plunging, ENE-trending asymmetric folds with limbs 20–40 m in length, which are a prominent feature affecting the disposition of the barite beds at Foss (see Willan & Coleman 1983, fig. 6). On a smaller scale, D<sub>3</sub> deformation is manifested in schistose rocks by a

TABLE 1: Common mineral assemblages in the Ben Eagach and Ben Lawers Schists at Foss

Formation	Unit	Lithology*	Assemblage†
Ben Lawers Schist	D	Amphibolite	hb chl pl qz bi cz cal ilm rut ap (se ss)
		<sup>1</sup> Hornblende garnet mica schist	qz pl mu hb dol gt chl bi cal ilm rut ap (cz)
	C	<sup>2</sup> Calc mica schist	qz dol mu bi pl (chl cal rut ilm se)
Ben Eagach Schist	B	Mineralization	{barite qz (dol mag ss celsian mu bi)
		<sup>3</sup> Chloritic metabasite	{celsian qz ss rut (dol cal mu cymrite)
		Graphitic schist	pl chl qz dol bi mu cal ilm rut ap (cz ss gt se)
	A	Graphitic schist	qz mu ss rut ap (dol pl bi chl)
		<sup>4</sup> Garnet quartzitic graphitic schist	qz pl mu chl bi gt dol rut ap (ss ilm cal)

\* Not listed in stratigraphic sequence; interbanded within each formation. 1–4 identify rock types in Tables 3 and 4.

† Mineral constituents listed in order of decreasing modal abundance; brackets indicate minerals only present in some samples. qz, quartz; pl, plagioclase; mu, muscovite; hb, hornblende; dol, dolomite; cal, calcite; cz, clinozoisite; ilm, ilmenite; rut, rutile; mag, magnetite; ss, sulphides (principally pyrite, pyrrhotite); ap, apatite; se, sphene.



ong crenulation cleavage which is usually oblique to folding, and in granoblastic rocks by a rodding parallel to the plunge of  $D_3$  folds.

Post- $D_3$  folding has merely produced open flexures previous fold axes and cleavage orientation in the vicinity of the Foss deposit, but further E is responsible for the prominent NW-trending Ben Eagach antiform and complimentary synform (Fig. 1). Subsequent deformation was non-penetrative, with major faults to NE-trending sinistral faults and shear zones which are probably coeval with the Loch Tay Fault system.

### Mineralogy and fabric development in relation to structure

Textural features relating mineral growth to the deformational history must be examined before estimates of metamorphic temperatures and pressures derived using mineral equilibria can be properly interpreted. Inclusion trails and cross-cutting relationships in porphyroblasts provide useful indications of the relative timing of mineral growth. Composition-zoning is found in many porphyroblast minerals (e.g. Sivaprakash 1982) and, together with compositional changes in mineral inclusions, has been used in elucidating the prograde and retrograde reactions involving the porphyroblasts (e.g. Sivaprakash 1981). However, the pronounced zonation which is characteristic of many medium-grade metamorphic garnets necessitates the careful selection of compositions likely to have been in equilibrium with matrix phases.

#### Garnet

Garnet is seldom found in the barium enriched rocks at Foss, but commonly occurs as small, rounded skeletal crystals in the footwall graphitic schists and orthoquartzites (BES, unit A), and as generally larger (7 mm diameter), euhedral porphyroblasts in the upper BLS calcareous mica schists (Table 1). These garnets often have open, S-shaped inclusion trails of quartz, rutile and ilmenite, which at the garnet rims may be continuous with the matrix fabric. In some samples, these syntectonic garnets have overgrowths which are free of quartz impurities but contain oxide inclusions aligned with the external fabric. Garnet growth is therefore regarded as largely syn- $D_3$  with some post- $D_3$  static overgrowth. This conclusion contrasts with that of Sturt & Harris (1961) who place the southern limit of syntectonic garnets (syn- $S_2$  in their terminology) to the N of the area covered in the present study.

Microprobe profiles of garnets from Foss usually show pronounced concentric zonation similar to that observed by Sivaprakash (1981) in the Aberfeldy–Lochry area. The garnets have a 'normal' zonation

with relatively Ca + Mn rich cores and Fe + Mg rich rims (Table 2, analyses 3–5), but often have thin (<50  $\mu\text{m}$ ) continuous or incomplete rims in which the zonation is reversed. In previous studies of metamorphic garnets (e.g. Grant & Weiblen 1971; de Bethune *et al.* 1975), peripheral Mn enrichment has been ascribed to retrograde resorption. At Foss, euhedral garnets showing no sign of resorption have developed reverse zonation where the garnet is in direct contact with primary biotite and chlorite, and a retrograde cation exchange mechanism is favoured (cf. Yardley 1977). Peak metamorphic equilibrium compositions are taken to be the non-retrograde rim composition or the minimum-Mn garnet composition within 100  $\mu\text{m}$  of the garnet rim. Except in samples with obvious compositional banding or heterogeneity, non-retrogressive garnet rim compositions were found to show little variation within thin sections.

#### Hornblende

Hornblende is absent from BES lithologies at Foss, but is common in the calcareous metasediments and metabasites of the BLS formation. The calc-micaschists are characterized by elongate sprays of dark-coloured hornblende ('garbenschiefer'), which are weakly zoned with relatively ferroan and aluminous cores (Table 2, analyses 1–2). The hornblende porphyroblasts have grown across the crenulated micaceous fabric during post- $D_3$  static metamorphism and contain oxide inclusion trails which are continuous with the matrix. They are often pseudomorphed by chlorite, biotite and carbonates to a greater extent than coexisting garnets.

#### Sheet silicates

Biotite and chlorite are common in units A, C and D (Table 1) and are major constituents of metabasite sheets in the upper BES. Chlorite occurs both as a component of the foliated fabric (composite  $D_1$ – $D_3$ ) of muscovite, biotite, plagioclase and quartz, and as cross-cutting flakes and sprays which appear to have replaced this fabric. Although the fabric is strongly crenulated, the absence of deformed sheet silicate grains and of undulose extinction in quartz indicates that a period of annealing followed penetrative deformation. Primary and porphyroblastic chlorite are generally indistinguishable in composition and vary little within thin sections, but biotite and muscovite show more variation on this scale (Table 4), which may be due to localized retrogressive equilibration. Evidence for this will be discussed later.

#### Aluminosilicates

Aluminosilicate-bearing rocks have not been found in the vicinity of the deposits, but kyanite and

TABLE 2: Representative microprobe analyses of minerals in sample 429-5\*

	1 <i>Hb</i> Core	2 <i>Hb</i> Rim	3 <i>Gt</i> Rim	4 <i>Gt</i> Core	5 <i>Gt</i> Rim	6 <i>Bi</i>	7 <i>Mu</i>	8 <i>Chl</i>	9 <i>Dol</i>	10 <i>Cal</i>
SiO <sub>2</sub>	42.36	42.60	37.51	38.25	37.78	37.29	46.86	25.14	nd	nd
TiO <sub>2</sub>	0.36	0.43	0.10	0.13	0.08	1.76	0.39	0.09	nd	nd
Al <sub>2</sub> O <sub>3</sub>	16.83	15.54	21.30	21.03	21.24	17.57	32.23	21.87	nd	nd
FeO <sup>T</sup>	17.11	16.36	29.05	26.44	29.55	17.71	1.68	22.48	10.23	3.09
MnO	0.21	0.13	2.56	5.18	2.28	0.05	0.02	0.10	0.53	0.61
MgO	7.76	8.78	2.01	1.47	2.26	11.51	1.78	16.75	13.37	1.72
CaO	9.98	9.93	7.35	8.27	7.36	0.00	nd	nd	28.61	52.13
K <sub>2</sub> O	0.40	0.34	nd	nd	nd	8.33	9.54	0.01	nd	nd
Na <sub>2</sub> O	2.18	2.11	nd	nd	nd	0.20	0.77	0.01	nd	nd
Total	97.19	96.22	99.88	100.77	100.55	94.43	93.27	86.45	52.74	57.55
(0=)	(23)	(23)	(24)	(24)	(24)	(23)	(22)	(28)	(3)	(3)
Si	6.321	6.400	5.999	6.070	6.004	5.882	6.356	5.295	—	—
Ti	0.041	0.049	0.012	0.016	0.010	0.210	0.041	0.014	—	—
Al	2.960	2.752	4.018	3.935	3.980	3.267	5.154	5.430	—	—
Fe <sup>2+</sup>	2.136	2.056	3.889	3.509	3.928	2.336	0.191	3.960	0.431	0.126
Mn	0.027	0.017	0.348	0.697	0.308	0.007	0.003	0.019	0.023	0.026
Mg	1.727	1.966	0.479	0.348	0.535	2.709	0.360	5.259	1.003	0.126
Ca	1.596	1.599	1.261	1.406	1.254	0.000	—	—	1.544	2.722
K	0.076	0.066	—	—	—	1.676	1.651	0.003	—	—
Na	0.630	0.616	—	—	—	0.061	0.202	0.005	—	—
Total	15.514	15.521	16.006	15.981	16.019	16.148	13.958	19.985	3.001	3.000

Mineral analyses by Cambridge Instruments Microscan 5 electron microprobe (at Edinburgh University) using wavelength dispersive spectrometry.

\* Sample of garnet-hornblende-mica-schist (BLS): see Tables 1 and 3.

Mineral abbreviations as in Table 1; analyses 1 and 2, and 3, 4 and 5 are core and rim compositions within single crystals. Gt (5) and Bi (6) in mutual contact; other analyses from same thin section.

FeO<sup>T</sup>; total iron expressed as FeO.

nd; Not determined.

staurolite are recorded by Chinner (1974) and Sivaprakash (1981, 1982) from Grandtully, which is about 10 km to the E (Fig. 1). Kyanite was also found by Wells & Richardson (1979) at Schiehallion, which is about 10 km to the W of Foss across the Loch Tay Fault. Chloritoid appears at Grandtully, but it occurs as inclusions in garnet and is only present as a retrograde phase in the matrix. The chloritoid occurrence is restricted to highly aluminous rocks with low bulk Mg/(Mg + Fe) (Atherton & Smith 1979; Sivaprakash 1981). The limited development of kyanite and staurolite in the Aberfeldy area has been attributed to the paucity of favourable bulk compositions, in particular the lack of suitably high Mg/(Mg + Fe) ratios (Atherton & Brotherton 1972; Atherton 1977), and to the stabilizing effect of high pressure on garnet-biotite-chlorite assemblages (Dempster 1983a).

#### *Cymrite and celsian*

The platy mineral cymrite, BaAl<sub>2</sub>Si<sub>2</sub>O<sub>8</sub>·H<sub>2</sub>O

(Essene 1967; Drits *et al.* 1975), was initially reported from the Aberfeldy barite deposits by Coats *et al.* (1980). Further petrological work has supported the suggestion made by Fortey & Beddoe-Stephens (1983) that cymrite was a precursor to much of the celsian (BaAl<sub>2</sub>Si<sub>2</sub>O<sub>8</sub>) seen at Foss, and isolated or encapsulated cymrite relicts have been found in many celsian-bearing rocks. The platy habit of celsian occurring in quartz, dolomite and mica matrices, and the presence of aligned quartz, mica, rutile and sulphide inclusions in a coarse celsian mosaic (Fig. 2a,b), suggests the replacement by celsian of a folded (D<sub>3</sub>) cymrite fabric. Celsian pseudomorphs appear not to have suffered penetrative deformation except in brittle shear zones, which indicates that celsian growth was post-D<sub>3</sub> and probably post-dated the Ben Eaga Antiform fold episode. Euhedral crystals of celsian up to 2 cm across, occurring in remobilized carbonate and sulphide rocks, crystallized subsequent to the deformation without inheriting the fabric of a cymrite precursor.



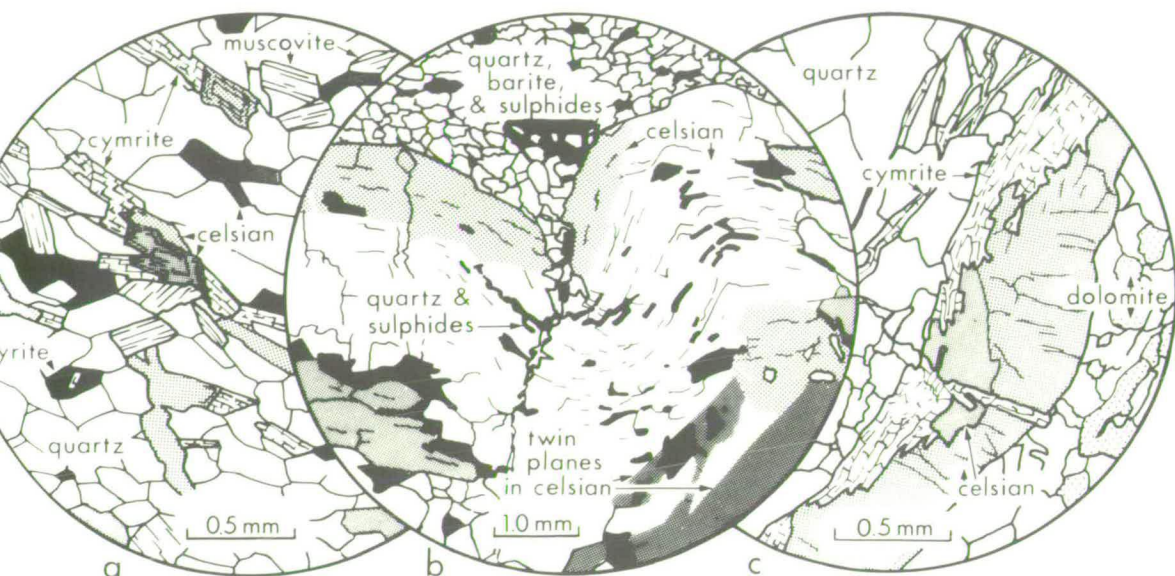


FIG. 2. Sketches from thin sections illustrating cymrite-celsian replacement textures. Areas of optical continuity in celsian (observed in crossed polars) are shown by grey shadings. (a). Partial replacement of platy cymrite by celsian crystals, some of which show faint oscillatory growth zoning. Both cymrite and celsian coexist with barian muscovite, quartz and pyrite, forming an annealed, foliated fabric. (b). Coarse, twinned celsian mosaic with relict folded fabric defined by rutile and sulphide inclusion trails. Sulphides and quartz also fill shrinkage fissures in the celsian, which has probably replaced cymrite. (c). Fractured quartz celsian dolomite rock containing cymrite which appears to have replaced celsian along cracks and at grain edges. The celsian has a platy form similar to other samples in which celsian has pseudomorphed cymrite.

## Geothermometry

### Garnet-hornblende

The geothermometer of Graham & Powell (1984) is based on the partitioning of Fe and Mg between garnet and hornblende, calibrated using the garnet-clinopyroxene thermometer of Ellis & Green (1979) applied to garnet-clinopyroxene-hornblende rocks. The distribution coefficient is approximately independent of pressure, but requires a correction for the grossular component in garnet. Microprobe analyses of non-retrogressive rim compositions of garnet and hornblende porphyroblasts in three calc-mica-schist samples from the vicinity of the Foss deposit were used to derive temperature estimates (Table 3), which are in the range 520–550°C.

As mutual contacts between garnet and hornblende crystals are rare in this lithology, analyses were obtained from unaltered porphyroblast rims separated from only a few millimetres of matrix. Anomalous temperature estimates might arise if closely associated porphyroblast rims had failed to equilibrate during the  $t$ - $D_3$  thermal climax, or had subsequently re-equilibrated with ferromagnesian silicates in the

matrix within domains smaller than the distance between porphyroblasts. The preservation of peak metamorphic equilibrium compositions is supported by observations of within-sample homogeneity in hornblende rim compositions, but some dispersion in calculated temperatures is caused by variation in garnet rim compositions (Tables 2 and 3). This dispersion is nevertheless no greater than the uncertainty of  $\pm 30^\circ\text{C}$  inherent in the calibration of the geothermometer as estimated by Graham & Powell (1984).

### Garnet-biotite

The variation with temperature of Fe and Mg partitioning between garnet and biotite has been calibrated empirically by Thompson (1976) and other workers, and experimentally by Ferry & Spear (1978). The latter calibration is applicable to garnets of restricted composition ( $\geq 80$  mol% almandine + pyrope components), and it has generally been found that garnets with a large grossular component, such as are typical of the Scottish Dalradian (e.g. Table 2), yield anomalously low temperatures. Of the samples from Foss examined (Table 3), only those with  $X_{Ca}$

TABLE 3: Garnet, hornblende, biotite, plagioclase and muscovite compositions and derived temperature and pressure estimates

Sample	(1) Rock type	(2) $X_{Ca}^{Gt}$	(3) $X_{Mn}^{Gt}$	Mg/Fe			(4) $X_{(Al^{vi}+Ti)}^{Bt}$	(5) $X_{Ca}^{Pl}$	(6) $X_K^{Mu}$	(7) $X_{Al^{vi}}^{Mu}$	Gt-Hb T°C G&P	Gt-Bi T°C (assuming P = 8 kbar)			Pl-Bi-Gt-Mu P kbar (G&S using T from	
				Gt	Hb	Bi						F&S	H&S	P&G	F&S	H&S
429-5	1*	0.208	0.051	0.1362	0.956	1.160	0.212	0.190	0.891	0.855	541	468	542	603	8.0	8.3-9.0
429-5	†	0.211	0.058	0.1232	0.956	1.160	0.212	0.190	0.891	0.855	525	443	517	579	7.6	7.9-8.3
N80-36	1	0.253	0.046	0.1349	1.209	1.372	0.155	albite			530	425	512	574	na	na
4685	1	0.218	0.077	0.1411	1.000	1.349	0.152	0.179	0.851	0.848	547	440	516	586	7.8	8.1-8.5
706-4B	3	0.225	0.100	0.1376	—	1.137	0.166	0.156	0.834	0.864	—	475	556	644	8.5	8.9-9.3
503-10	3	0.158	0.103	0.1496	—	1.016	0.156	0.089	0.844	0.873	—	530	592	672	9.9	10.3-11.0
503-10		0.158	0.103	0.1496	—	1.098	0.158	0.089	0.844	0.873	—	507	568	646	9.3	9.6-10.0
708-15	3	0.166	0.074	0.1660	—	1.047	0.224	0.157	0.873	0.888	—	552	618	693	9.1	9.4-10.0
G16	4	0.260	0.064	0.1337	—	1.146	0.199	albite			—	466	564	635	na	na
G16		0.208	0.039	0.1523	—	1.146	0.199	albite			—	501	581	637	na	na
G48	4	0.186	0.056	0.1325	—	1.056	0.254	0.107	0.885	0.885	—	485	556	614	9.6	10.1-10.5
503-27	4	0.173	0.060	0.1486	—	0.9314	0.161	albite			—	554	623	689	na	na

(1), Identified in Table 1; (2), Ca/(Ca + Fe + Mg + Mn) in garnet rim; (3), Mn/(Ca + Fe + Mg + Mn) in garnet rim; (4), (Al<sup>vi</sup> + Ti)/(Al<sup>vi</sup> + Ti + Fe + Mg + Mn) in biotite; (5), Ca/(Ca + K + Na) in plagioclase; 'albite' indicates <0.03; (6), K/(K + Na + Ca + Ba) in muscovite; Al<sup>vi</sup>/(Al<sup>vi</sup> + Ti + Fe + Mg + Mn) in muscovite.

Calibrations of: G&P, Graham & Powell (1984); F&S, Ferry & Spear (1978); H&S, Hodges & Spear (1982); P&G, Pigage & Greenwood (1982); G&S, Ghent & Stout (1981).

\* Using analyses 2, 5, 6, 7 and 8, Table 2.

† As above except analysis 3 instead of 5.

na, not applicable.

<0.18 give temperature estimates using the Ferry & Spear calibration which are in the range indicated by garnet-hornblende thermometry; the remaining Ca-rich garnet-bearing samples appear to indicate much lower temperatures (420–500°C). The correction factor for the grossular component in garnet used by Hodges & Spear (1982) yields garnet-biotite temperatures which are 60–100°C higher and, with the exception of samples 503–27 and 708–15, range from 510° to 590°C. The correction factors for both Ca and Mn substitution in garnet used by Pigage & Greenwood (1982) appear to give excessively high temperatures (Table 3) relative to other methods and to petrological prejudices.

Ferry & Spear (1978) suggested a limit to the Al<sup>vi</sup> + Ti content of biotite for successful application of their geothermometer, which is exceeded in most samples from Foss (Table 3). However, any effects due to this appear to be negligible compared with the variations in temperature estimates caused by high Ca levels in garnet, and by within-sample variation in garnet rim and biotite compositions. This compositional heterogeneity results in a range of calculated temperatures (typically of 25–50°C) for each sample, which may be attributed to partial retrograde re-equilibration among the ferromagnesian silicates, since biotites which are isolated from garnet and chlorite often have relatively lower Mg/Fe ratios (e.g. sample 503–27, Table 3). Similar variation in biotite compositions has been ascribed to retrogression or disequilibrium in other studies of garnet-biotite thermometry,

e.g. Tracy *et al.* (1976), Ghent *et al.* (1979), and Dempster (1983a, 1983b).

### Calcite-dolomite

Calcite is seldom a major component of the lithologies in the area studied, but occurs in minor amounts coexisting with ferroan dolomite in most BES metasediments and in BES chloritic metabasites (Table 1). The MgCO<sub>3</sub> content of calcite coexisting with dolomite was experimentally calibrated as a geothermometer by Goldsmith & Newton (1969). Bickle & Powell (1977) incorporated adjustments for iron-bearing carbonates, and their calibration was adopted here since Foss carbonates are iron-rich (Table 2, analyses 9–10) and contain <1.5 mol% MnCO<sub>3</sub>. Compositions of 40 calcite grains in 10 samples from Foss, plotted in Fig. 3, suggest that equilibration occurred at temperatures ranging from 470° to 540°C, assuming pressures of 7–9 kbar (justified below). However, an experimental calibration of the iron correction to the calcite-dolomite geothermometer (Powell *et al.* 1984) indicates that the temperatures may be about ~30°C too high (Powell, pers. comm.).

Several anomalously high values for the MgCO<sub>3</sub> content of calcite (>4.6 mol%; Fig. 3) are probably due to overlap of the defocused microprobe beam (diameter, 10–15 µm) with adjacent dolomite grains and low values (<2.5 mol%, not plotted) may



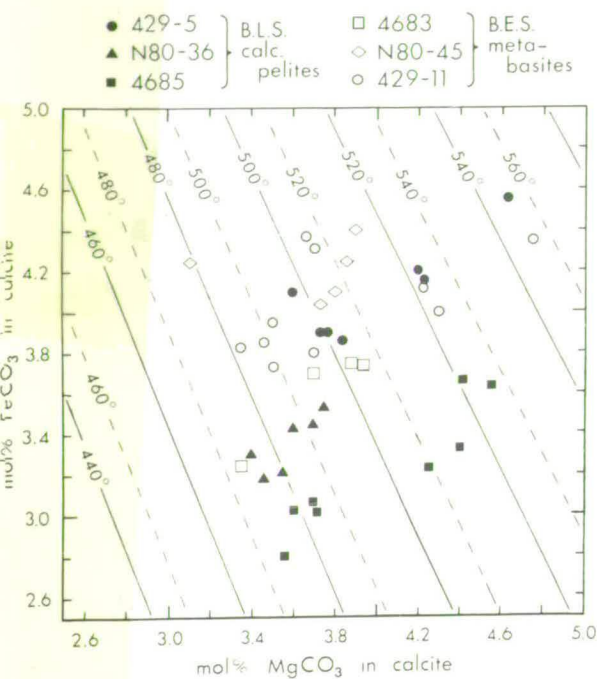


FIG. 3.  $\text{FeCO}_3$  content plotted against  $\text{MgCO}_3$  content in calcite coexisting with dolomite in six samples from Foss, contoured for temperature in  $^{\circ}\text{C}$  at  $P=9$  kbar (solid lines) and  $P=7$  kbar (dashed lines) (after Bickle & Powell 1977).

attributed to retrogressive alteration or to late-metamorphic carbonate growth. The central areas of coarser ( $>0.5$  mm) grains of calcite are enriched in Mg and Fe compared with the rims of these crystals and the whole of smaller grains, both of which yield lower temperature estimates. This dispersion in compositions suggests that partial retrograde equilibration occurred while temperatures were sufficiently high to allow Mg-Fe exchange between calcite and matrix phases on a  $\sim 0.1$  mm scale. Temperatures derived using the Bickle & Powell (1977) calibration and the maximum Mg and Fe contents of reliable calcite analyses ( $520$ – $540^{\circ}\text{C}$  at pressures of  $7$ – $9$  kbar), are chosen as representative of peak metamorphic conditions. Reasonable agreement is therefore shown by the results of garnet-hornblende, garnet-biotite and calcite-dolomite geothermometry (Fig. 4), which indicate the attainment of peak metamorphic temperatures of  $530 \pm 30^{\circ}\text{C}$  during and shortly after the  $D_3$  deformation episode in this area.

### Geobarometry

Two recently calibrated silicate barometers utilize the assemblages plagioclase-biotite-garnet-muscovite

(Ghent & Stout 1981) and biotite-muscovite-chlorite-quartz (Powell & Evans 1983), which occur in a wide range of rock compositions. Both geobarometers are tested using samples from the vicinity of the Foss deposit, and pressure estimates are compared with information derived from sulphide and barium silicate equilibria in the stratiform mineralized lithologies.

#### Plagioclase-biotite-garnet-muscovite

Ghent & Stout (1981) used the garnet-plagioclase- $\text{Al}_2\text{SiO}_5$ -quartz geobarometer (Ghent *et al.* 1979) in conjunction with garnet-biotite thermometry (Ferry & Spear 1978) to derive an empirical geobarometer for the assemblage plagioclase-biotite-garnet-muscovite. The resolution of this geobarometer depends on the uncertainty attached to activity-composition relationships and to the garnet-biotite temperature estimate, and on analytical uncertainty in determining garnet, biotite, muscovite and plagioclase compositions. In addition, Ghent & Stout (1981) found that samples containing albitic plagioclase yielded higher pressure estimates than nearby samples containing more calcic plagioclase, which they attributed to incomplete correction of strong positive deviations from the ideal molecular mixing model for compositions of  $\text{An}_{<8}$ .

Application of the plagioclase-biotite-garnet-muscovite barometer at Foss is restricted by the low and variable anorthite content of plagioclase (often  $<\text{An}_{10}$ ). Pressure estimates of between  $7.7$  kbar and  $8.5$  kbar (with a probable uncertainty of  $\pm 0.8$  kbar, Ghent & Stout 1981) have been obtained from three samples containing oligoclase in the compositional range  $\text{An}_{15-20}$  (Table 3). Coexisting albite ( $\text{An}_{<3}$ ) and oligoclase ( $\text{An}_{18-23}$ ), defining the peristerite gap (Grapes & Masayuki 1983) was observed in quartzofeldspathic domains in sample 429-5. Significantly higher pressure estimates of  $9.6 \pm 0.8$  kbar, obtained from 503-10 and G48 (Table 3), could be due to less calcic plagioclase compositions or to the higher temperatures obtained by garnet-biotite thermometry, or to a combination of these factors. Widely variable Ca contents of both plagioclase and coexisting garnet in Dalradian pelites near Spean Bridge, Inverness-shire (Richardson & Powell 1976), were considered by Ghent & Stout (1981) to be partly responsible for the comparatively lower temperatures and higher pressures for the Spean Bridge area estimated by them using plagioclase-biotite-garnet-muscovite thermobarometry.

Since Ghent & Stout (1981) constructed their geobarometer using temperature estimates from Ferry & Spear's (1978) calibration of Fe-Mg exchange between garnet and biotite, the use of 'corrected' garnet-biotite calibrations such as those of Hodges & Spear (1982), leads to inconsistent pressure estimates from the Fe and Mg end-member equations for the

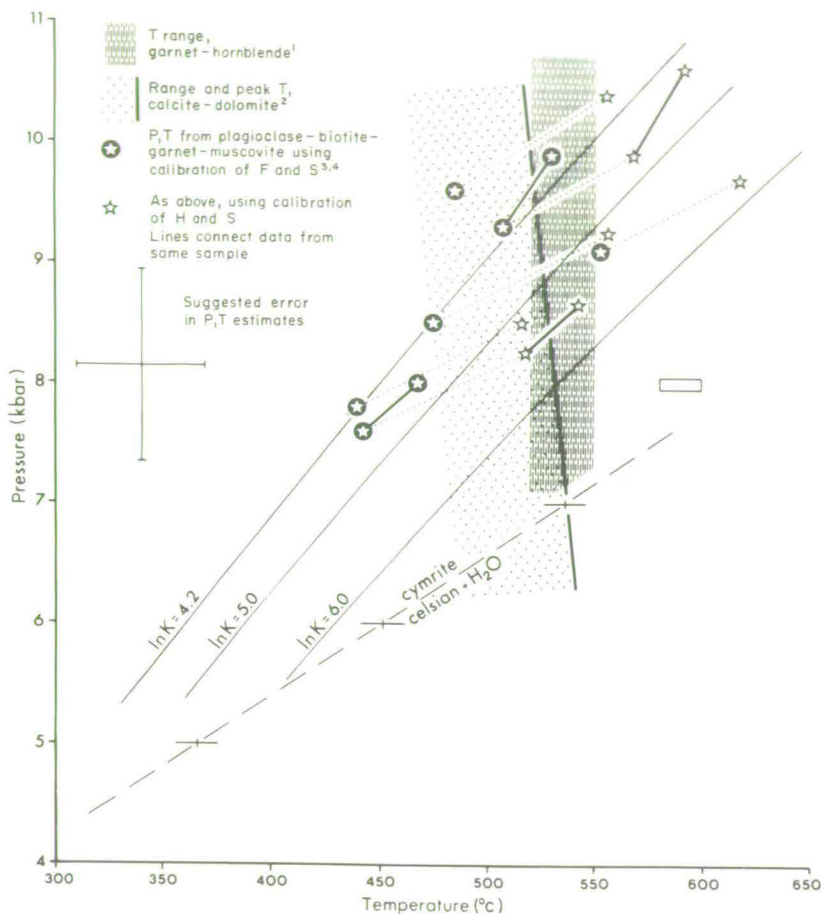


FIG. 4. P-T diagram showing results from several geothermometers and geobarometers applied at Foss. Calibrations of: 1, Graham & Powell (1984); 2, Bickle & Powell (1977); 3, Ghent & Stout (1981); 4, Ferry & Spear (1978); (star in circle) 5, Hodges & Spear (1982) (star) (see Table 3 for details). Curved lines are  $\ln K$  contours from biotite-muscovite-chlorite-quartz geobarometry (Powell & Evans 1983) and represent minimum, mean and maximum values obtained (see Table 4). Dashed line with error bars for the pure cymrite-celsian reaction from Nitsch (1980); rectangular box locates 8 kbar reversal obtained in this study.

plagioclase-biotite-garnet-muscovite geobarometer. Average pressure estimates given by this barometer using temperatures obtained from the Hodges & Spear equation (assuming  $W_{\text{MgMn}} = 0$ ) are about 0.8 kbar higher than pressure estimates based on the uncorrected garnet-biotite geothermometer (Table 3 and Fig. 4).

#### Biotite-muscovite-chlorite-quartz

This geobarometer, recently formulated by Powell & Evans (1983), is based on the extent of Mg-Al celadonite substitution in white mica in equilibrium with biotite and chlorite. Activity data for muscovite, celadonite, phlogopite and clinocllore end-members,

calculated from representative microprobe analyses of seven samples using the activity formulations of Powell & Evans, are presented in Table 4. The range in derived equilibrium constants for the reaction, celadonite + clinocllore = muscovite + phlogopite + quartz + H<sub>2</sub>O ( $\ln K_D = 4.2-6.0$ ), defines a band of positive slope in P-T space (Fig. 4) which intersects with the temperature range of 520-580°C at pressures of between 7.8 kbar and 10.7 kbar. Presently unclear is the extent to which the isopleths are displaced to lower temperatures and to higher pressures by the presence of other components in the fluid phase, particularly CO<sub>2</sub> as carbonates are present in all samples (although none contain graphite). Fe<sub>2</sub>O<sub>3</sub> contents of minerals in the samples have not been determined, but Powell &



TABLE 4: Activity data\* and pressure estimates from biotite-muscovite-chlorite-quartz geobarometry

Sample	Rock type†	$X_{\text{chlorite clinoch.}}$	$X_{\text{biotite phlog.}}$	$X_{\text{white mica celadonite}}$	$X_{\text{white mica muscovite}}$	$\ln K_D$	$P \text{ kbar at } T =$	
							500°C	550°C
429-5‡	1	0.050	0.063	0.081	0.588	4.22	9.1	10.2
429-5		0.050	0.075	0.079	0.542	4.77	8.5	9.5
N80-36	1	0.061	0.084	0.080	0.607	4.97	8.3	9.3
C79-31	2	0.091	0.104	0.074	0.528	5.38	8.0	9.0
706-4B	3	0.045	0.060	0.076	0.553	4.38	9.0	10.1
503-10	3	0.044	0.053	0.060	0.589	5.04	8.3	9.3
N80-45	3	0.040	0.055	0.063	0.619	5.10	8.2	9.2
N80-45		0.041	0.054	0.049	0.603	6.00	7.3	8.3
429-11	3	0.042	0.062	0.063	0.582	5.35	8.0	9.0
429-11		0.042	0.059	0.055	0.609	5.79	7.7	8.7

\* Activity formulations and equilibrium constant for the expression:

$$K_D = [(X_{\text{white mica muscovite}}) \cdot (X_{\text{biotite phlogopite}})^3] / [(X_{\text{white mica celadonite}})^4 \cdot (X_{\text{chlorite clinoclinochlore}})] \text{ from Powell \& Evans (1983).}$$

† Identified in Table 1.

‡ Mineral compositions given in Table 2.

Evans found their barometer to be insensitive to  $\text{Fe}^{2+}/\text{Fe}^{3+}$  ratios.

The barometer is sensitive, however, to within-sample variation in muscovite compositions. Pressure estimates which differ by up to 1 kbar may be obtained by using activity data derived from several muscovite analyses within individual thin sections (e.g. N80-45, Table 4). This variation is presumably due to localized retrogressive equilibration of peak metamorphic equilibrium compositions. Dempster (1983a) has shown that in central Perthshire, retrograde alteration of muscovite results in a decrease in the celadonite content, coupled with an increase in the paragonite content of affected grains.

#### Sphalerite-pyrite-pyrrhotite

Scott & Barnes (1971) have demonstrated that the amount of FeS in solid solution in sphalerite is essentially a function of pressure in the temperature range 254–550°C (at 1 kbar pressure; 300–>600°C at higher pressures), provided that the sphalerite is buffered by coexisting pyrite + hexagonal pyrrhotite. Under these conditions the FeS content of sphalerite decreases progressively with increasing pressure, and this has been calibrated experimentally as a geobarometer to 10 kbar by Scott (1973) and Lusk & Ford (1978). Although it is one of the more refractory sulphides, sphalerite is nevertheless susceptible to retrograde metamorphic and supergene compositional alteration, particularly if it contains chalcopryrite inclusions (e.g. Boctor 1980; Craig & Vaughan 1981). A major pitfall with application of this geobarometer is that the FeS contents of sphalerite generated by equilibration with monoclinic pyrrhotite + pyrite at low temperatures (<254°C), are similar to equilibrium

compositions retained from buffering with hexagonal pyrrhotite at about 9 kbar (cf. Groves *et al.* 1975). Therefore evidence of low temperature alteration in metamorphosed sulphide assemblages must be critically examined before application of the geobarometer.

The textural and compositional relationships of sphalerite occurring in the Foss deposit have been discussed in detail by Moles (1983), and the analytical results presented here (Fig. 5) are restricted to sphalerites which satisfy established criteria for retention of peak metamorphic equilibrium compositions. These range in FeS content from 10 mol% to 13 mol% with a distinct concentration between 11.0 mol% and

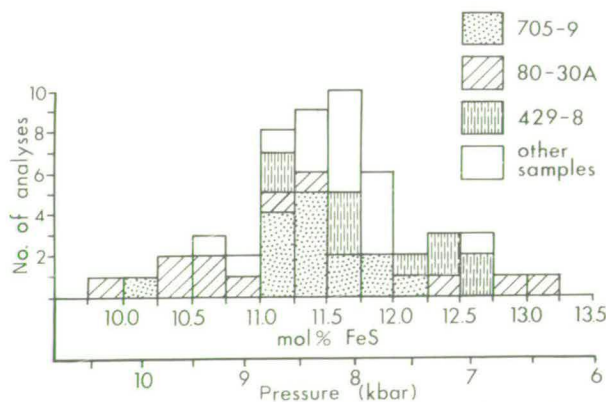


FIG. 5. Histogram of mol% FeS in 52 analyses of sphalerite from Foss. Sphalerites satisfy textural criteria for retention of peak metamorphic compositions buffered in the assemblage pyrrhotite-pyrite-sphalerite. Textural and compositional data for samples 705-9, 80-30A and 429-8 published in Moles (1983). Pressure calibration of Hutchison & Scott (1981).

11.7 mol% FeS, from which pressures of 8–9 kbar ( $\pm 0.5$  kbar analytical and calibration uncertainty) are calculated using the equation of Hutchison & Scott (1981). These estimates, which are significantly higher than earlier results from sphalerite geobarometry at Ben Eagach (Willan 1980), are in good agreement with pressures derived from the silicate barometers discussed above.

### Cymrite–celsian

Microprobe analyses of cymrite and celsian from the Foss deposits, published by Fortey & Beddoe-Stephens (1982) and plotted with additional new data in Fig. 6, show that K and Na are minor but essential components of both phases. The K/Na atomic ratio varies from 2 to 9 and the majority of analysed cymrites contain 3–7 mol% of combined sanidine + albite hydrate in solid solution. Celsian pseudomorphs of cymrite contain similar or slightly greater K + Na contents. Hyalophane with up to 73 mol% orthoclase + albite (i.e.  $Cn = 27\%$ ) occurs in some mineralized rocks and strongly zoned crystals with compositions intermediate between hyalophane ( $Cn < 50\%$ ) and celsian ( $Cn > 90\%$ ) have also been observed, but feldspars of these compositions do not show textural evidence of having replaced a cymrite precursor.

The location in P–T space of the reaction, cymrite = celsian +  $H_2O$  (Essene 1967), has been determined in reversed hydrothermal experiments by Nitsch

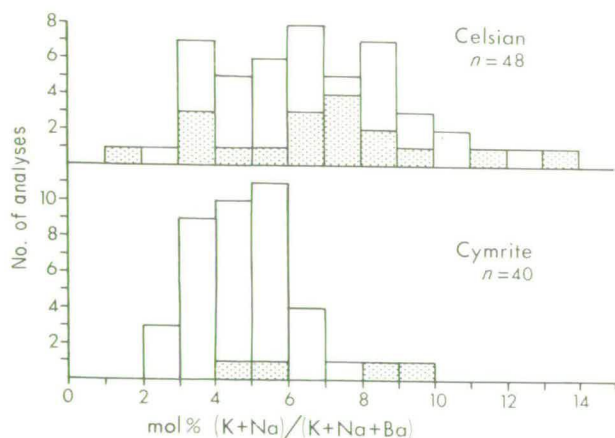


FIG. 6. Histograms of mol% orthoclase + albite component in celsian, and mol% (sanidine + albite) hydrate component in cymrite in analysed samples from the Aberfeldy deposits. Stippled: data published by Fortey & Beddoe-Stephens (1982).

(1980) who confirmed that cymrite is the stable phase under higher pressure/lower temperature conditions (Fig. 4). In earlier experiments, Seki & Kennedy (1964a, 1964b) used the wrong formula  $BaAlSi_3O_8(OH)$  for cymrite, but surmised that cymrite and sanidine hydrate,  $KAlSi_3O_8 \cdot H_2O$ , form a complete or partial solid solution series. They demonstrated that the formation of sanidine hydrate from sanidine +  $H_2O$  requires very high water pressures (c. 18 kbar at  $400^\circ C$ ). Therefore, as suggested by Reinecke (1982), the minimum water pressures for the stability of potassic cymrite should be higher than for pure cymrite.

Further hydrothermal experiments (currently in progress) with synthetic cymrite<sub>ss</sub> and celsian<sub>ss</sub> have bracketed the pure cymrite–celsian equilibrium at 8.0 kbar,  $590 \pm 10^\circ C$ , which is near to the extrapolated position of the reaction line determined by Nitsch (1980) at 5.5–7.0 kbar (Fig. 4). Rapid attainment of equilibrium in this system was found by Nitsch and confirmed in the present study, with complete reaction in runs lasting 8–12 h. However, attempts to evaluate the displacement of the reaction line by substitution of (K + Si) for (Ba + Al) in both cymrite and celsian, have been hindered by a marked reduction in reaction rate and the metastable growth and persistence of K-bearing cymrite in the celsian field. These effects are pronounced even with a 5 mol% substitution of the potassic end-members, and may account for the metastable persistence of some cymrite<sub>ss</sub> in the Foss deposits, which had previously seemed difficult to reconcile with observations of rapid reaction in the pure system under experimental conditions.

From the textural features of celsian that has replaced cymrite (Fig. 2b), it is inferred that cymrite was stable throughout the development of tectonic fabrics ( $D_1$ – $D_3$ ) at Foss. The experimentally determined reaction line therefore constrains the minimum P, maximum T of metamorphism and indicates that hydrostatic pressures exceeded 7.0 kbar during peak metamorphism at  $530^\circ C$ , which is in satisfactory agreement with the results of other geobarometers applied in this area. The post- $D_3$  replacement of cymrite by celsian indicates that the stability field of celsian was entered by decreasing pressure and/or increasing temperature. However, evidence from other geobarometers of higher peak pressures, and the preservation of some cymrite at Foss, suggests that temperatures were constant or probably decreasing by this time (Fig. 7). Rare examples have been found of cymrite occurring in late-stage veinlets, and of cymrite replacing celsian (itself retaining the morphology of a cymrite precursor, Fig. 2c) in a rock affected by late (?Loch Tay Fault age) shearing. These suggest that the cymrite stability field was re-entered and that the downgrade P–T evolution probably did not depart substantially from the cymrite–celsian reaction line.



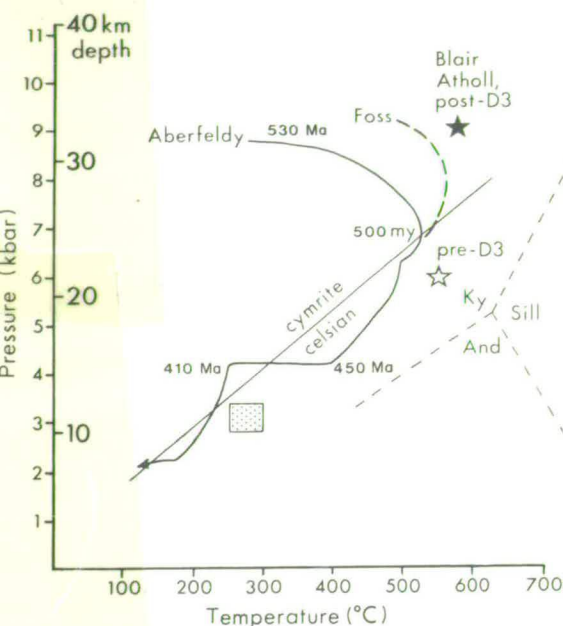


FIG. 7. Possible P-T conditions during and subsequent to metamorphism in central Perthshire. Heavy curved line: uplift path modelled by Dempster (1985), Aberfeldy area. Heavy dashed line: suggested alternative path for the Foss area (see text). Equilibrium line for the reaction, cymrite = celsian +  $H_2O$ , from Nitsch (1980) and work in progress. Aluminosilicate triple point (light dashed lines) from Richardson *et al.* (1969). Shaded box represents conditions at Foss deduced from the composition of retrogressively zoned sphalerite (Moles 1983). Stars represent probable pre-D<sub>3</sub> conditions indicated by chloritoid-biotite assemblages, and subsequent peak P-T conditions at Blair Atholl, 10 km N of Foss (Dempster 1983a).

## Discussion

### Comparison of methods for estimating peak P-T conditions

One aim of this paper has been to compare peak metamorphic P-T estimates using a variety of methods, several of which are comparatively new or are specific to the unusual mineralized rocks of the Aberfeldy deposits. Satisfactory agreement is shown between the results of the three geothermometers examined, provided that care is taken in selecting peak metamorphic equilibrium compositions in zoned minerals and in calcite, and that a correction is incorporated for the high grossular content of garnet in garnet-biotite thermometry. Comparable metamorphic temperatures are indicated by sulphur isotope

fractionation between coexisting barite and sulphides in samples from the Foss deposit (Moles 1984), although Willan & Coleman (1983) argue that isotopic equilibration did not occur during metamorphism.

Pressures calculated using the plagioclase-biotite-garnet-muscovite geobarometer of Ghent & Stout (1981) are probably imprecise due to calibration uncertainties and between-sample variation in the calcium contents of garnet and plagioclase. Despite these reservations, peak metamorphic pressures indicated by this barometer (7.5–10 kbar; Table 3) are in good agreement with results from sphalerite geobarometry applied to sphalerites which satisfy textural criteria for the retention of peak metamorphic buffered compositions (Fig. 5). Similar or slightly higher pressures are also derived from the temperature-sensitive celadonite geobarometer of Powell & Evans (1983), assuming that the sheet silicates preserve compositions equilibrated close to the peak metamorphic temperatures  $\sim 530^\circ\text{C}$  and that  $P_{H_2O} = P_{\text{Total}}$ . These assumptions may not be justified because of the presence of carbonates and evidence for retrogressive changes in mica compositions, manifested by a spread in the celadonite content of white micas within thin sections. However, pressures estimated from the celadonite geobarometer assuming equilibration to lower than peak temperatures (e.g. 8–9 kbar at  $500^\circ\text{C}$ ; Table 4) are incompatible with evidence from the cymrite-celsian 'barometer' which requires that the stability field of celsian was entered by a relatively greater decrease in pressure than in temperature (see above and Fig. 7). Therefore the celadonite geobarometer is suspected of yielding pressure estimates which are perhaps 1–2 kbar too high at Foss. Similar conclusions have been reached by other users (C. M. Graham pers. comm.).

Metamorphic temperatures of  $480\text{--}580^\circ\text{C}$  for the Aberfeldy-Grandtully-Pitlochry area (Fig. 1) have previously been estimated by Sivaprakash (1982), who used garnet-biotite and calcite-dolomite geothermometry. Slightly higher temperatures (up to  $620^\circ\text{C}$ ) were estimated for the Schiehallion area by Wells (1979) and Wells & Richardson (1979), who also calculated pressures of  $12 \pm 1.5$  kbar for this area using plagioclase-garnet-kyanite-quartz geobarometry. Using the same barometer, Sivaprakash derived pressures of 10–11 kbar for the Grandtully area. However, a more recent calibration of the plagioclase-garnet-kyanite-quartz equilibrium by Newton & Haselton (1981) indicates that these pressure estimates may be several ( $\sim 3\text{--}4$ ) kilobars too high (Dempster 1983a). Using the plagioclase-biotite-garnet-muscovite barometer of Ghent & Stout (1981), Dempster (1983a) has derived pressures of 7 kbar and 9–10 kbar for the Aberfeldy and Loch Tummel areas, respectively. These agree with revised pressure estimations from the data of Sivaprakash (1982) and of Wells &



Richardson (1979), and with the results of the present work.

### Metamorphic evolution in central Perthshire

Dempster (1983a) and Harte *et al.* (1983) have discussed evidence for overprinting of pre-D<sub>3</sub>, lower pressure (5–6 kbar) chloritoid–biotite assemblages by higher pressure (9–10 kbar) assemblages at around the time of D<sub>3</sub> deformation, in the northern part of the Tummel Steep Belt near Blair Atholl (Fig. 1). They suggest that this syn-D<sub>3</sub> pressure increase could relate to the formation of the Steep Belt, which Bradbury *et al.* (1979) consider to be a 'deep-seated rotation zone' where movements 'spanned the time of Barrovian metamorphism'.

Although significantly higher peak metamorphic pressures are indicated by mineral barometry for the vicinity of the Foss deposit than for the Aberfeldy–Grandtully area, there is no mineralogical evidence for a syn-D<sub>3</sub> increase of pressure at Foss, which lies to the southern margin of the Steep Belt about 10 km SSW of Blair Atholl. If the pre-D<sub>3</sub> conditions postulated by Dempster (1983a) and Harte *et al.* (1983) for the Blair Atholl area ( $\leq 6$  kbar at 550°C) had prevailed at Foss, celsian rather than cymrite would have been the stable barium silicate (Fig. 4) and textural evidence might be expected for syn-D<sub>3</sub> replacement of celsian by cymrite (perhaps similar to that described from the island of Andros, Greece, by Reinecke 1982). No evidence of prograde replacement of celsian by cymrite has been observed at Foss. However, a more limited increase in pressure (*within* the stability field of cymrite) during D<sub>3</sub> movements (Fig. 7), cannot be precluded on the basis of the textural and thermobarometric data available.

The relations of cymrite and celsian in the Foss deposit were mentioned above as evidence for an uplift and cooling path lying close to the cymrite–celsian equilibrium line. The P–T history, so constrained, is very similar to that modelled by Dempster for the area near the River Tay at Aberfeldy (Fig. 1) using isotopic mineral age data. An interesting feature of Dempster's model P–T path (Fig. 7) is the period commencing at about 450 Ma ago, during which cooling proceeded without significant uplift, until regional uplift resumed with a major faulting episode between 410 and 390 Ma. During this period of tectonic inactivity the P–T path (Fig. 7) re-entered the stability field of cymrite. Late-stage growth of cymrite is only observed at Foss in some cross-cutting veinlets and in a shear zone where the passage of fluids allowed partial retrogressive hydration of celsian (Fig. 2c). Incomplete reaction may be explained by the low temperatures ( $\sim 250^\circ\text{C}$ ) prevailing at the time, which with the resumption of uplift allowed the metastable persistence of this second-generation cym-

rite. These textural relationships therefore support the episodic nature of post-orogenic uplift advocated by Dempster (1983a, 1985) on the basis of isotopic dating.

The composition of relict Fe-rich areas in coarsely crystalline, retrogressively-zoned sphalerite coexisting with pyrrhotite, pyrite and chalcopryite in a sample from the Foss deposit, was used by Moles (1983) to define a P–T area through which the rock passed at some time during uplift. This area is constrained by pressures of  $3.1 \pm 0.3$  kbar estimated by extrapolation of the sphalerite geobarometer (calibration of Hutchison & Scott 1981) and by the temperature of the hexagonal–monoclinic transition in pyrrhotite, estimated to be 260–300°C at this pressure. This P–T area lies close to the uplift and cooling path modelled for Aberfeldy by Dempster (1985) and is also close to the cymrite–celsian reaction line (extrapolated from Nitsch 1980) (Fig. 7). However, its location within the celsian field conflicts with the suggestion that cymrite was stable at this point in the uplift and cooling history. Possible explanations for this relatively small discrepancy include continued equilibration of the sphalerite with hexagonal pyrrhotite persisting metastably to lower temperatures (e.g. 200–250°C), or the metastable growth of cymrite associated with the late metamorphic brittle deformation and fluid infiltration.

### Conclusions

Temperature and pressure ranges derived from a variety of mineral equilibria in metasedimentary metabasaltic and mineralized lithologies associated with the Foss barite deposit, are in reasonable agreement and indicate peak metamorphic conditions of  $530 \pm 30^\circ\text{C}$  and  $9 \pm 1$  kbar. Lower temperatures given by garnet–biotite thermometry using the calibration of Ferry & Spear (1978) are attributed to the high grossular component of garnets in the pelites.

The post-D<sub>3</sub> replacement of cymrite by celsian in stratiform mineralized rocks is considered to post-date the attainment of peak metamorphic temperatures during a period of decreasing lithostatic pressure. The subsequent P–T evolution probably followed a path close to the cymrite–celsian equilibrium until the cymrite stability field was re-entered before late metamorphic fault movements. The post-tectonic evolution recorded by mineral equilibria at Foss fits well with that modelled in a study of isotopic mineral ages in central Perthshire (Dempster 1983a, 1985) even though there appear to be significant differences both in prograde history and in peak metamorphic conditions attained in areas 10 km to the N and S of Foss.

ACKNOWLEDGEMENTS. I thank Gordon Biggar and Colin Graham for assistance with the cymrite–celsian experiments.



and Colin Graham and Ben Harte for discussions on thermobarometry and structural relationships. Giles Droop, Roger Powell, David Pattison and Timothy Dempster are thanked for their useful comments on the manuscript. Neil Forthey (B.G.S., London) kindly loaned a number of polished thin sections (samples 4683 and 4685). Analytical work at the

Edinburgh Microprobe Unit was made possible by support from the Natural Environment Research Council. A research studentship from the Department of Education, Northern Ireland is gratefully acknowledged and Dresser Minerals are thanked for their financial and logistic support during fieldwork.

## References

- ANDERTON, R. 1979. Slopes, submarine fans and syn-depositional faults: sedimentology of parts of the Middle and Upper Dalradian of the SW Highlands of Scotland. In: HARRIS, A. L., HOLLAND C. H. & LEAKE, B. E. (eds) *The Caledonides of the British Isles—Reviewed*. Spec. Publ. geol. Soc. London, **8**, 483–8.
- ATHERTON, M. P. 1977. The metamorphism of the Dalradian rocks of Scotland. *Scott. J. Geol.* **13**, 331–70.
- & BROTHERTON, M. S. 1972. The composition of some kyanite-bearing regionally metamorphosed rocks from the Dalradian. *Scott. J. Geol.* **8**, 203–13.
- & SMITH, R. A. 1979. Chloritoid–staurolite assemblages from Barrow's Zones in Central Perthshire, Scotland. *Geol. Mag.* **116**, 469–76.
- BETHUNE, P., LADURON, D. & BOCQUET, J. 1975. Diffusion processes in resorbed garnets. *Contrib. Mineral. Petrol.* **50**, 197–204.
- BICKLE, M. J. & POWELL, R. 1977. Calcite–dolomite geothermometry for iron-bearing carbonates. *Contrib. Mineral. Petrol.* **59**, 281–92.
- BOCTOR, N. Z. 1980. Sphalerite geobarometry in Bodenmais ore, Bavaria. *Am. Mineral.* **65**, 1031–7.
- BRADBURY, H. J., HARRIS, A. L. & SMITH, R. A. 1979. Geometry and emplacement of nappes in the Central Scottish Highlands. In: HARRIS, A. L., HOLLAND, C. H. & LEAKE, B. E. (eds). *The Caledonides of the British Isles—reviewed*. Spec. Publ. geol. Soc. London, **8**, 213–20.
- CHINNER, G. A. 1974. Metamorphic index minerals in the eastern Dalradian. *Scott. J. Geol.* **9**, 248–9.
- COATS, J. S., SMITH, C. G., FORTEY, N. J., GALLAGHER, M. J., MAY, F. & MCCOURT, W. J. 1980. Strata-bound barium-zinc mineralization in Dalradian schist near Aberfeldy, Scotland. *Trans. Instn Minn Metall. B*, **89**, 110–22.
- CRAIG, J. R. & VAUGHAN, D. J. 1981. *Ore Microscopy and Ore Petrography*. Wiley, New York.
- DEMPSTER, T. J. 1983a. *Studies of orogenic evolution in the Scottish Dalradian*. Unpubl. PhD thesis, Edinburgh Univ.
- 1983b. Low temperature re-equilibration in the kyanite and sillimanite zone pelites of Glen Esk, Angus (abstr.). *Newsl. geol. Soc. London*, **2/4**, 22.
- 1985. Uplift patterns and orogenic evolution in the Scottish Dalradian. *J. geol. Soc. London*, **142**, 111–128.
- DRITS, V. A., KASHAEV, A. A. & SOKOLOVA, G. A. 1975. Crystal structure of cymrite. *Kristallografiya*, **20**, 280–6 (transl. *Sov. Phy. Cryst.* **20**, 171–5).
- ELLIS, D. J. & GREEN, D. H. 1979. An experimental study of the effect of Ca upon garnet–clinopyroxene Fe–Mg exchange equilibria. *Contrib. Mineral. Petrol.* **71**, 13–22.
- ESSENE, E. J. 1967. An occurrence of cymrite in the Franciscan formation, California. *Am. Mineral.* **52**, 1885–90.
- FERRY, J. M. & SPEAR, F. S. 1978. Experimental calibration of the partitioning of Fe and Mg between biotite and garnet. *Contrib. Mineral. Petrol.* **66**, 113–7.
- FORTEY, N. J. & BEDDOE-STEPHENS, B. 1982. Barium silicates in stratabound Ba–Zn mineralization in the Scottish Dalradian. *Mineralog. Mag. London*, **46**, 63–72.
- GHEENT, E. D. & STOUT, M. Z. 1981. Geobarometry and geothermometry of plagioclase–biotite–garnet–muscovite assemblages. *Contrib. Mineral. Petrol.* **76**, 92–7.
- , ROBBINS, D. B. & STOUT, M. Z. 1979. Geothermometry, geobarometry, and fluid compositions of metamorphosed calc-silicates and pelites, Mica Creek, British Columbia. *Am. Mineral.* **64**, 874–85.
- GOLDSMITH, J. R. & NEWTON, R. C. 1969. P–T–X relations in the system  $\text{CaCO}_3$ – $\text{MgCO}_3$  at high temperatures and pressures. *Am. J. Sci.* **267-A**, 160–90.
- GRAHAM, C. M. & BRADBURY, H. J. 1981. Cambrian and late Precambrian basaltic igneous activity in the Scottish Dalradian: a review. *Geol. Mag.* **118**, 27–37.
- & POWELL, R. 1984. A garnet–hornblende geothermometer: calibration, testing, and application to the Pelona Schist, Southern California. *J. metamorphic Geol.* **2**, 13–31.
- GRANT, J. A. & WEIBLEN, P. W. 1971. Retrograde zoning in garnet near the second sillimanite isograd. *Am. J. Sci.* **270**, 281–96.
- GRAPES, R. & MASAYUKI, O. 1983. Peristerite compositions in quartzofeldspathic schists, Franz Josef–Fox Glacier area, New Zealand. *J. metamorphic Geol.* **1**, 47–61.
- GROVES, D. I., BINNS, R. A., BASSETT, F. M. & MCQUEEN, K. G. 1975. Sphalerite compositions from Western Australian nickel deposits, a guide to equilibria below 300°C. *Econ. Geol.* **70**, 391–6.
- HARRIS, A. L. & PITCHER, W. 1975. The Dalradian Supergroup. In: HARRIS, A. L., SHACKLETON, R. M., WATSON, J., DOWNIE, C., HARLAND, W. B. & MOORBATH, S. (eds) *Correlation of the Precambrian Rocks of Great Britain*. Spec. Rep. geol. Soc. London, **6**, 52–128.
- HARTE, B., DEMPSTER, T. J. & BOOTH, J. E. 1983. P–T estimates and mineral facies variation in space and time in the Central and SE Scottish Highlands (abstr.). *Geol. Soc. Newsl. London*, **12/4**, 21.
- HODGES, K. V. & SPEAR, F. S. 1982. Geothermometry, geobarometry and the  $\text{Al}_2\text{SiO}_5$  triple point at Mt. Moosilauke, New Hampshire. *Am. Mineral.* **67**, 1118–34.
- HUTCHISON, M. N. & SCOTT, S. D. 1981. Sphalerite geobarometry in the Cu–Fe–Zn–S system. *Econ. Geol.* **76**, 143–53.
- LUSK, J. & FORD, C. E. 1978. Experimental extension of the sphalerite geobarometer to 10 kbar. *Am. Mineral.* **63**, 516–9.
- MOLES, N. R. 1983. Sphalerite composition in relation to deposition and metamorphism of the Foss stratiform

- Ba-Zn-Pb deposit, Aberfeldy, Scotland. *Mineralog. Mag. London*, **47**, 487-500.
- 1984. Sulphur isotopes in the metamorphosed, stratiform barite-sulphide deposit at Foss in Perthshire, Scotland. Rep. Br. geol. Surv. Stable Isotope Unit.
- NEWTON, R. C. & HASELTON, H. T. 1981. Thermodynamics of the garnet-plagioclase-Al<sub>2</sub>SiO<sub>5</sub>-quartz geobarometer. In: NEWTON, R. C., NAVROTSKY, A. & WOOD, B. J. (eds). *Thermodynamics of Minerals and Melts*. (Advances in Physical Geochemistry, 1.) Springer-Verlag, New York.
- NITSCH, K.-H. 1980. Reaktion von Bariumfeldspat (Celsian) mit H<sub>2</sub>O zu Cymrit unter metamorphen Bedingungen. *Fortschr. Mineral.* **58**, 98-100.
- PIGAGE, L. C. & GREENWOOD, H. J. 1982. Internally consistent estimates of pressure and temperature: the staurolite problem. *Am. J. Sci.* **282**, 943-69.
- POWELL, R. & EVANS, J. 1983. A new geobarometer for the assemblage biotite-muscovite-chlorite-quartz. *J. metamorphic Geol.* **1**, 331-6.
- , CONDLIFFE, D. M. & CONDLIFFE, E. 1984. Calcite-dolomite geothermometry in the system CaCO<sub>3</sub>-MgCO<sub>3</sub>-FeCO<sub>3</sub>; an experimental study. *J. metamorphic Geol.*, **2**, 33-41.
- REINECKE, T. 1982. Cymrite and celsian in manganese-rich metamorphic rocks from Andros Island, Greece. *Contrib. Mineral. Petrol.* **79**, 333-6.
- RICHARDSON, S. W., GILBERT, M. C. & BELL, P. M. 1969. Experimental determination of kyanite-andalusite and andalusite-sillimanite equilibria; the aluminium silicate triple point. *Am. J. Sci.* **267**, 259-72.
- & POWELL, R. 1976. Thermal causes of the Dalradian metamorphism in the Central Highlands of Scotland. *Scott. J. Geol.* **12**, 237-68.
- ROBERTS, J. L. & TREAGUS, J. E. 1979. Stratigraphic and structural correlation between the Dalradian rocks of the SW and Central Highlands of Scotland. In: HARRIS, A. L., SHACKLETON, R. M., WATSON, J., DOWNIE, C., HARLAND, W. B. & MOORBATH, S. (eds) *The Caledonides of the British Isles—Reviewed*. Spec. Publ. geol. Soc. London, **8**, 199-204.
- SCOTT, S. D. 1973. Experimental calibration of the sphalerite geobarometer. *Econ. Geol.* **68**, 466-74.
- & BARNES, H. L. 1971. Sphalerite geothermometry and geobarometry. *Econ. Geol.* **66**, 653-69.
- SEKI, Y. & KENNEDY, G. C. 1964a. Phase relations between cymrite, BaAlSi<sub>3</sub>O<sub>8</sub>(OH), and celsian, BaAl<sub>2</sub>Si<sub>2</sub>O<sub>8</sub>. *Am. Mineral.* **49**, 1407-26.
- & — 1964b. The breakdown of potassium feldspar, KAlSi<sub>3</sub>O<sub>8</sub>, at high temperatures and pressures. *Am. Mineral.* **49**, 1688-1706.
- SIVAPRAKASH, C. 1981. Zoned garnets in some Scottish Dalradian pelites. *Mineralog. Mag. London*, **44**, 301-7.
- 1982. Geothermometry and geobarometry of Dalradian metapelites and metabasites from the Central Scottish Highlands. *Scott. J. Geol.* **18**, 109-24.
- STURT, B. A. 1961. The geological structure of the area south of Loch Tummel. *Q. J. geol. Soc. London*, **117**, 131-56.
- & HARRIS, A. L. 1961. The metamorphic history of the Loch Tummel area. *Liverpool Manchester geol. J.* **2**, 689-711.
- THOMPSON, A. B. 1976. Mineral reactions in pelitic rocks. II. Calculation of some P-T-X (Fe-Mg) phase relations. *Am. J. Sci.* **276**, 401-54.
- TRACY, R. J. 1982. Compositional zoning and inclusions in metamorphic minerals. In: FERRY, J. M. (ed). *Reviews in Mineralogy*, **10**. Miner. Soc. Am., 355-97.
- , ROBINSON, P. & THOMPSON, A. B. 1976. Garnet composition and zoning in the determination of temperature and pressure of metamorphism, central Massachusetts. *Am. Mineral.* **61**, 762-75.
- WELLS, P. R. A. 1979. P-T conditions in the Moines of the Central Highlands, Scotland. *J. geol. Soc. London*, **136**, 663-71.
- & RICHARDSON, S.W. 1979. Thermal evolution of metamorphic rocks in the Central Highlands of Scotland. In: Harris, A. L., Shackleton, R. M., Watson, J., Downie, C., Harland, W. B. & Moorbath, S. (eds) *The Caledonides of the British Isles—Reviewed*. Spec. Publ. geol. Soc. London, **8**, 339-44.
- WILLAN, R. C. R. 1980. Stratabound sulphide mineralisation in the Dalradian Supergroup of the Grampian Highlands, Scotland. *Nor. geol. Unders.* **300**, 241-58.
- 1981. Geochemistry of host rocks to the Aberfeldy barite deposit, Scotland (abstr.). *Trans. Instn Mining Metall. B.* **90**, 57.
- & COLEMAN, M. L. 1983. Sulphur isotope study of the Aberfeldy baryte, zinc, lead deposit and minor sulphide mineralization in the Dalradian metamorphic terrain, Scotland. *Econ. Geol.* **78**, 1619-56.
- YARDLEY, B. W. D. 1977. An empirical study of diffusion in garnet. *Am. Mineral.* **62**, 793-800.

Received 22 January 1984; revised typescript accepted 25 May 1984.